ADVANCES IN SUPERCONDUCTING INFINITE-LAYER AND RELATED NICKELATES

EDITED BY: Matthias Hepting, Danfeng Li, Antia Botana, George Sawatzky and Junjie Zhang

PUBLISHED IN: Frontiers in Physics

frontiers Research Topics

frontiers

ISSN 1664-8714
ISBN 978-2-88976-818-9
DOI 10.3389/978-2-88976-818-9

About Frontiers

Frontiers is more than just an open-access publisher of scholarly articles: it is a pioneering approach to the world of academia, radically improving the way scholarly research is managed. The grand vision of Frontiers is a world where all people have an equal opportunity to seek, share and generate knowledge. Frontiers provides immediate and permanent online open access to all its publications, but this alone is not enough to realize our grand goals.

Frontiers Journal Series

The Frontiers Journal Series is a multi-tier and interdisciplinary set of open-access, online journals, promising a paradigm shift from the current review, selection and dissemination processes in academic publishing. All Frontiers journals are driven by researchers for researchers; therefore, they constitute a service to the scholarly community. At the same time, the Frontiers Journal Series operates on a revolutionary invention, the tiered publishing system, initially addressing specific communities of scholars, and gradually climbing up to broader public understanding, thus serving the interests of the lay society, too.

Dedication to Quality

Each Frontiers article is a landmark of the highest quality, thanks to genuinely collaborative interactions between authors and review editors, who include some of the world's best academicians. Research must be certified by peers before entering a stream of knowledge that may eventually reach the public - and shape society; therefore, Frontiers only applies the most rigorous and unbiased reviews.
Frontiers revolutionizes research publishing by freely delivering the most outstanding research, evaluated with no bias from both the academic and social point of view. By applying the most advanced information technologies, Frontiers is catapulting scholarly publishing into a new generation.

What are Frontiers Research Topics?

Frontiers Research Topics are very popular trademarks of the Frontiers Journals Series: they are collections of at least ten articles, all centered on a particular subject. With their unique mix of varied contributions from Original Research to Review Articles, Frontiers Research Topics unify the most influential researchers, the latest key findings and historical advances in a hot research area! Find out more on how to host your own Frontiers Research Topic or contribute to one as an author by contacting the Frontiers Editorial Office: frontiersin.org/about/contact

ADVANCES IN SUPERCONDUCTING INFINITE-LAYER AND RELATED NICKELATES

Topic Editors:
Matthias Hepting, Max Planck Institute for Solid State Research, Germany
Danfeng Li, City University of Hong Kong, Hong Kong, SAR China
Antia Botana, Arizona State University, United States
George Sawatzky, University of British Columbia, Canada
Junjie Zhang, Shandong University, China

Citation: Hepting, M., Li, D., Botana, A., Sawatzky, G., Zhang, J., eds. (2022). Advances in Superconducting Infinite-Layer and Related Nickelates. Lausanne: Frontiers Media SA. doi: 10.3389/978-2-88976-818-9

Table of Contents

frontiers in Physics

MINI REVIEW
published: 22 December 2021
doi: 10.3389/fphy.2021.808683

Soft X-Ray Spectroscopy of Low-Valence Nickelates

Matthias Hepting[1]*, *Mark P. M. Dean*[2] *and Wei-Sheng Lee*[3]

[1]Max-Planck-Institute for Solid State Research, Stuttgart, Germany, [2]Condensed Matter Physics and Materials Science Department, Brookhaven National Laboratory, Ridge, NY, United States, [3]Stanford Institute for Materials and Energy Sciences, SLAC National Accelerator Laboratory and Stanford University, Menlo Park, CA, United States

Low-valence nickelates—including infinite-layer (IL) and trilayer (TL) compounds—are longstanding candidates for mimicking the high-temperature superconductivity of cuprates. A recent breakthrough in the field came with the discovery of superconductivity in hole-doped IL nickelates. Yet, the degree of similarity between low-valence nickelates and cuprates is the subject of a profound debate for which soft x-ray spectroscopy experiments at the Ni *L*- and O *K*-edge provided critical input. In this review, we will discuss the essential elements of the electronic structure of low-valance nickelates revealed by x-ray absorption spectroscopy (XAS) and resonant inelastic x-ray scattering (RIXS). Furthermore, we will review magnetic excitations observed in the RIXS spectra of IL and TL nickelates, which exhibit characteristics that are partly reminiscent of those of cuprates.

Keywords: infinite-layer nickelates, trilayer nickelates, low-valence nickelates, spectroscopy, RIXS, XAS, electronic structure, magnetic correlations

OPEN ACCESS

Edited by:
Veerpal Singh Awana, National Physical Laboratory (CSIR), India

Reviewed by:
Atsushi Fujimori, The University of Tokyo, Japan
Kenji Ishii, National Institutes for Quantum Science and Technology, Japan

***Correspondence:**
Matthias Hepting
hepting@fkf.mpg.de

Specialty section:
This article was submitted to Condensed Matter Physics, a section of the journal Frontiers in Physics

Received: *03 November 2021*
Accepted: *30 November 2021*
Published: *22 December 2021*

Citation:
Hepting M, Dean MPM and Lee W-S (2021) Soft X-Ray Spectroscopy of Low-Valence Nickelates. Front. Phys. 9:808683. doi: 10.3389/fphy.2021.808683

1 INTRODUCTION

Spectroscopy has proven to be a versatile tool for studying the charge, spin, lattice, and orbital degrees of freedom in quantum materials. Arguably, one of the most fascinating families of quantum materials are cuprate high-temperature superconductors [1–3]. Critical insights into cuprates have been provided by electron, neutron, and photon spectroscopy techniques—including photoemission and electron spectroscopy, scanning tunneling microscopy, optical and Raman spectroscopy, as well as inelastic x-ray and neutron scattering [4–10]. More recently, fresh perspectives on the enigmatic ground states of cuprates opened up especially due to resonant soft x-ray spectroscopy studies. For instance, resonant inelastic x-ray scattering (RIXS) [11] revealed that damped spin excitations persist even for high hole-doping levels far away from the parent antiferromagnetically (AFM) ordered phase [12, 13]. Furthermore, RIXS allowed to probe the three-dimensional (3D) dispersion of low-energy plasmons [14–16], which arise due to the characteristic quasi-2D layered crystal structure of cuprates. Moreover, resonant elastic x-ray scattering (REXS) and RIXS studies found that different types of static and dynamic charge orders emerge ubiquitously in cuprates [17–21]. Nevertheless, a comprehensive understanding of the most prominent phases in cuprates—including the pseudogap, strange metal phase, and superconductivity—remains elusive.

One approach to gain a deeper understanding of cuprates involves the targeted design of materials that mimic cuprate-typical properties, such as their layered quasi-2D crystal structure, $3d^9$ electronic configuration, spin $S = 1/2$ magnetic moments with antiferromagnetic (AFM) coupling, strong ligand-oxygen hybridization, and a lifted degeneracy of the active e_g orbitals [22]. In principle, the discovery of superconductivity in a material that emulates at least a subset of

these properties could allow to identify the hallmarks of cuprates that are crucial for invoking their exceptional high-temperature superconductivity.

In this context, long-standing candidates are Ni-based compounds, as Ni is a direct neighbor of Cu in the periodic table. In early works, it was speculated that doped RE_2NiO_4 (RE = rare-earth ion), which is the $n = 1$ member of the Ruddlesden-Popper (RP) homologous series $RE_{n+1}Ni_nO_{3n+1}$ [23], could become superconducting [24], as it is isostructural to the cuprate La_2CuO_4 and possesses similar charge and spin stripe ordered states [25]. The formal electronic configuration of La_2NiO_4, however, is $3d^8$ (Ni^{2+}) with $S = 1$ [26, 27], providing a possible rationalization for the observed absence of superconductivity. Perovskite nickelates $RENiO_3$ are the $n = \infty$ member of the RP series with a formal $3d^7$ (Ni^{3+}) configuration and $S = 1/2$, although x-ray spectroscopic experiments indicated a $3d^8\underline{L}$ configuration [28], with $\underline{L}$ denoting an O ligand hole. In their seminal work, Chaloupka and Khaliullin proposed a significant modification of the electronic structure of perovskite nickelates via tensile strain and incorporation into thin epitaxial heterostructures [29], breaking of the degeneracy of the e_g orbitals, which in the extreme case could yield a half filled $3d_{x^2-y^2}$ band and a single-sheet, cuprate-like Fermi surface [30]. In fact, spectroscopic studies detected new electronic and magnetic ground states in perovskite nickelate heterostructures, distinct from those of bulk nickelates [31–41]. Nevertheless, superconductivity has not been found to date [42–44], possibly due to the insufficient splitting of the orbital energy levels in the realized heterostructures [45, 46]. More recently, oxygen-reduced variants of the $n = 3$ members of the RP series have attracted intense attention. These $RE_4Ni_3O_8$ trilayer (TL) nickelates are composed of three closely stacked square-planar Ni-O layers with intervening RE ions, which are separated by rocksalt type RE-O blocking structures [47]. The electronic configuration of TL nickelates is $3d^{8.67}$ per Ni on average ($Ni^{1.33+}$). It was found by x-ray spectroscopy that metallic $Pr_4Ni_3O_8$ exhibits low-spin configuration and a significantly lifted orbital degeneracy, suggesting a close analogy to cuprates [48]. Notably, the close parallel between TL nickelates and cuprates was further corroborates by RIXS, revealing the presence of strong AFM exchange coupling J in $La_4Ni_3O_8$ and $Pr_4Ni_3O_8$ [49]. Nonetheless, superconductivity has not been detected in TL nickelates. This could be due to their electronic configuration, which corresponds to 1/3-hole-doping of a Ni^{1+} background and therewith falls into the overdoped regime of cuprates [48, 50, 51]. Experimental efforts to stabilize superconductivity via lowering the $Ni^{1.33+}$ valence by electron-doping are ongoing. Along these lines, also the $n = 5$ oxygen-reduced RP variants $RE_6Ni_5O_{12}$ are promising candidates for superconductivity, as these quintuple layer nickelates exhibit a $3d^{8.8}$ ($Ni^{1.2+}$) configuration—analogous to optimally doped cuprates—already without additional electron-doping.

A breakthrough in the field came with the discovery of superconductivity in hole-doped nickelates with the IL crystal structure [52]. In more detail, epitaxial thin films of Sr- or Ca-substituted $RENiO_2$ obtained via topotactic oxygen reduction of the perovskite phase show superconductivity below 9–15 K [52–58]. The parent compounds of these nickelates formally exhibit the $3d^9$ (Ni^{1+}) configuration with $S = 1/2$, which qualifies them as isostructural and isoelectronic to the parent cuprates. Early neutron powder diffraction studies of parent IL nickelates, however, indicated absence of long-range AFM order [59, 60] and electrical transport measurements of films show weakly metallic behavior [61]. This is in stark contrast to parent cuprates, which are AFM Mott (charge-transfer) insulators [1]. Moreover, whereas first theoretical studies proposed that the electronic and magnetic correlations of IL nickelates and cuprates share close similarities [62], other theoretical works suggested significant distinctions, including a multiband character of nickelates [63]. Along these lines, insights from experiments can help to resolve the controversy about similarities and differences between IL nickelates and cuprates. In particular, recent x-ray and electron energy-loss spectroscopic studies [64–66] unveiled a reduced Ni-O hybridization, presence of a weakly interacting RE $5d$ metallic band, and overdamped spin excitations with a bandwidth as large as 200 meV in IL nickelates.

In the following, we will review recent soft x-ray absorption spectroscopy (XAS) and RIXS studies at the O K-edge and Ni L-edge of IL and TL nickelates. We will discuss the essential elements of their distinct electronic structure. Furthermore, the spin excitation spectra of IL and TL nickelates observed with RIXS will be reviewed.

2 ELECTRONIC STRUCTURE

XAS at the O K-edge measures core-hole excitations from O $1s$ to unoccupied O $2p$ states and is also a sensitive probe of the covalent mixing between O $2p$ and transition-metal d states [67]. In particular the O-K pre-edge fine structure can provide valuable information about Ni-O hybridized states and the associated electronic structure, for instance in the cases of NiO and perovskite $RENiO_3$ [28, 67, 68]. In both materials, Ni $3d$-orbitals strongly hybridize with oxygen ligands, giving rise to a pre-peak in the absorption spectra near the O K-edge (**Figure 1A**). Due to different relative energy scales between the charge-transfer energy Δ and the Coulomb interaction U, according to the Zaanen–Sawatzky–Allen (ZSA) scheme [69], the former material falls into the regime of charge-transfer insulators, whereas the latter is a negative charge-transfer compound. In contrast, the O K-edge absorption spectra of the IL nickelates $LaNiO_2$ and $NdNiO_2$ lack a prominent pre-edge peak (**Figure 1A**), suggesting a substantially weaker effective mixing between oxygen and the unoccupied $3d$ states of the upper Hubbard band (UHB) of the Ni^{1+} cations [64]. In the case of cuprates, a prominent pre-peak feature is present in O K-edge absorption spectra [70]. This is known to originate from the charge-transfer nature of these materials, with Δ smaller than U, and O $2p$ states mixed with both the lower Hubbard band (LHB) and the UHB of the Cu $3d_{x^2-y^2}$ states. A sizable pre-peak has also been observed in TL nickelates (**Figure 1C**), indicating mixing between O $2p$ and the Ni UHB [48, 49]. Upon hole-doping of cuprates, spectral weight shifts from the UHB pre-peak to a

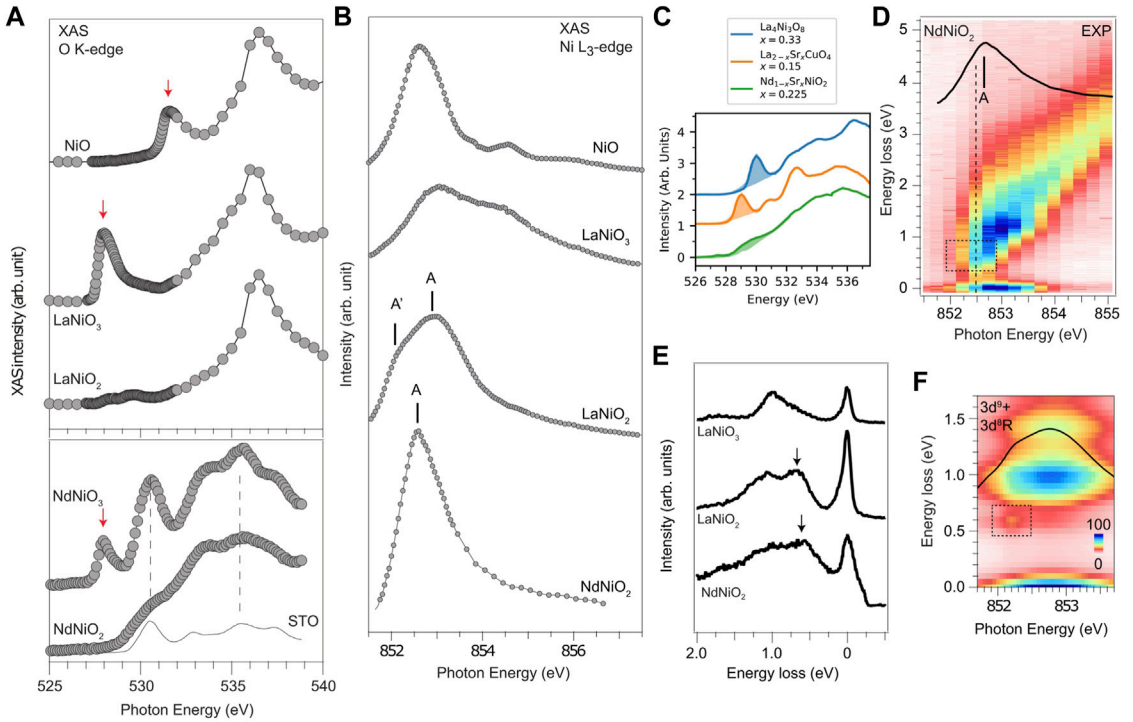

FIGURE 1 | Electronic structure of nickelates. **(A)** Upper panel: O *K*-edge XAS of NiO, $LaNiO_3$ and $LaNiO_2$. Red arrows mark the pre-edge peaks indicative of Ni–O hybridization. Lower panel: O *K*-edge XAS of $NdNiO_3$ and $NdNiO_2$. Dashed vertical lines indicate features of the $SrTiO_3$ (STO) substrate (solid grey line) in the XAS spectra of $NdNiO_3$ and $NdNiO_2$ due to the film thickness being thinner than that of the La-based films in the upper panel. Spectra are vertically offset for clarity. **(B)** Ni L_3-edge XAS of NiO, $LaNiO_3$, $LaNiO_2$, and $NdNiO_2$. The La M_4-line was subtracted from the $LaNiO_3$ and $LaNiO_2$ spectra. **(C)** Comparison of the O *K*-edge pre-peak intensities (shaded areas) of a TL nickelate ($La_4Ni_3O_8$), a hole-doped cuprate ($La_{1.85}Sr_{0.15}CuO_4$), and a hole-doped IL nickelate ($Nd_{0.775}Sr_{0.225}NiO_2$). **(D)** RIXS intensity map of $NdNiO_2$ measured as a function of incident photon energy across the Ni L_3-edge. **(E)** Representative RIXS spectra of $LaNiO_3$, $LaNiO_2$, and $NdNiO_2$. Black arrows highlight the 0.6 eV features of $LaNiO_2$ and $NdNiO_2$. **(F)** Calculated RIXS map and XAS (solid black line) of $LaNiO_2$ for a $3d^9 + 3d^8\underline{R}$ ground state, with $\underline{R}$ denoting a charge-transfer to the La cation. The dashed box highlights the same feature as the box in panel D. Panels adapted from Refs. [49, 64].

lower-energy peak (**Figure 1C**) that is associated with transitions into the doped hole levels [70, 71]. These hole-states constitute Zhang-Rice singlets (ZRS), which are plaquettes of two doped holes and four O atoms in square planar coordination around a Cu atom, playing the same role as a fully occupied or empty site in an effective single-band Hubbard model [72]. Notably, a recent scanning transmission electron microscopy electron-energy loss spectroscopy (STEM-EELS) study suggested that a similar ZRS peak emerges in IL nickelates upon hole-doping [65], although it carries significantly less spectral weight (**Figure 1C**). Overall, there is good evidence for reduced oxygen hybridization in nickelates compared to cuprates, which likely comes from an enhanced Δ value. Direct and quantivative determination of Δ and *U* represents an important issue for future soft x-ray studies.

Further insights into the electronic structure can be obtained from Ni *L*-edge XAS, corresponding to 2*p*-3*d* multiplet transitions, reflecting the valence configuration of the Ni ions. In the cases of NiO and perovskite $RENiO_3$ ($2p^63d^8$–$2p^53d^9$ and $2p^63d^8\underline{L}^n$–$2p^53d^9\underline{L}^n$ transitions, respectively) distinct multi-peak structures emerge across the L_3-edge (**Figure 1B**) [28, 64, 73]. Conversely, the line shapes of the IL nickelates $LaNiO_2$ and especially of $NdNiO_2$ (**Figure 1B**) resemble rather the single-peak XAS spectrum of IL cuprates with only one possible final XAS state ($2p^63d^9$-$2p^53d^{10}$ transition). In more detail, the L_3-edge XAS of $LaNiO_2$ and $NdNiO_2$ is dominated by a main peak A (**Figure 1B**), while $LaNiO_2$ shows an additional minor low energy shoulder A′ at slightly lower energies.[1] **Figure 1D** displays the RIXS intensity map of $NdNiO_2$ as a function of the incident photon energy and **Figure 1E** shows RIXS spectra for selected incident energies. Importantly, the RIXS spectra of $LaNiO_2$ and $NdNiO_2$ exhibit a distinct feature around 0.6 eV energy loss (**Figures 1D,E**), which is visible in the RIXS spectra with incident energies coinciding with the XAS peak A (A'). Furthermore, this feature emerges exclusively in the IL compounds and not the perovskite nickelate $LaNiO_3$ (**Figure 1E**). Using exact diagonalization, the general XAS and RIXS features can be reproduced (**Figure 1F**) and the 0.6 eV feature can be assigned to the hybridization between the Ni

[1]The A′ feature in XAS is only visible in $LaNiO_2$ films without a $SrTiO_3$ (STO) capping layer. Based on our recent measurements on $LaNiO_2$ films with a STO capping layer, the A′ feature, which arises from the resonance of the ~ 0.6 eV feature in the RIXS map, coincides with the main XAS peak and becomes invisible. In other words, the XAS of La- and Nd-based infinite layer nickelates (with a STO capping layer) are essentially the same

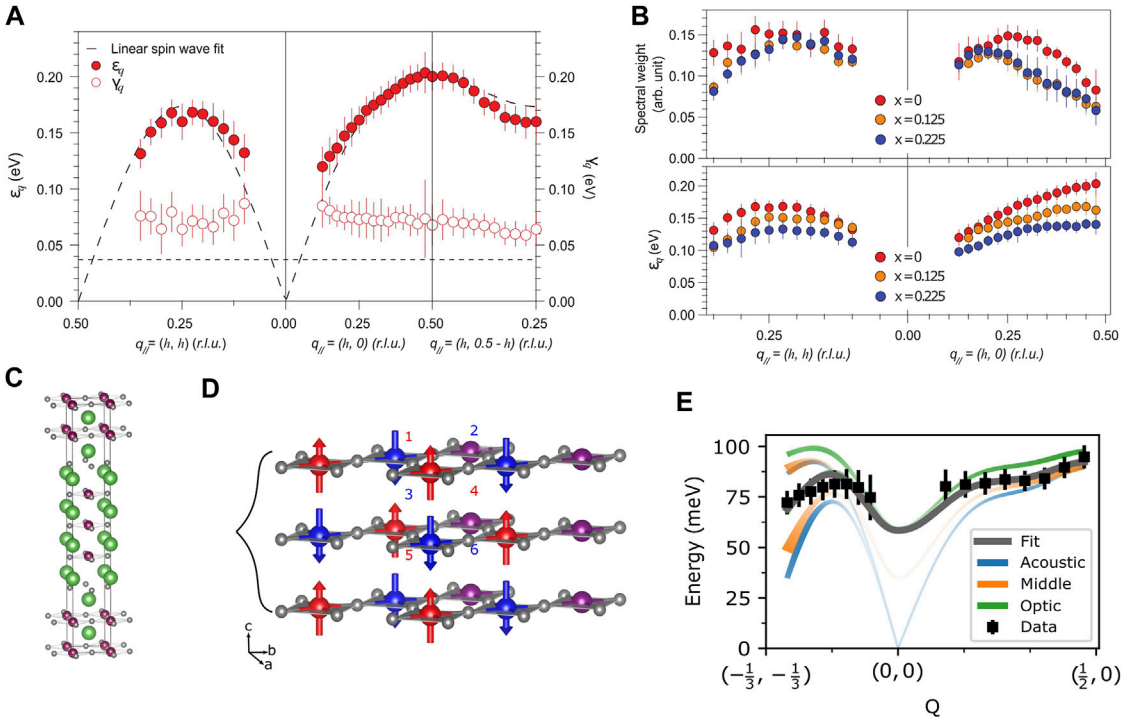

FIGURE 2 | Magnetic excitations in nickelates. **(A)** Magnetic excitations in $NdNiO_2$. Solid and open symbols are mode energy and the damping parameters, respectively, extracted from fitting RIXS spectra to a damped harmonic oscillators (DHO). The dashed curve is the linear spin wave fit to the extracted energy-momentum dispersion. The horizontal dashed line represents the energy resolution of the RIXS measurement. **(B)** Doping dependence of the spectral weight **(upper)** and mode energy **(lower)** deduced from the DHO fitting. **(C)** The structural unit cell of $La_4Ni_3O_8$ with Ni/O/La atoms shown as purple/gray/green spheres. **(D)** The electronically active TL nickel-oxide plane structures in $La_4Ni_3O_8$, showing the diagonal stripe-ordered state [47]. Ni sites with additional hole character are in purple, whereas spinful Ni up (down) sites are depicted in red (blue). **(E)** Measured magnetic excitations in $La_4Ni_3O_8$. Black squares are the extracted energies of the magnetic excitations. The dark gray line is the fit to the experimental dispersion, which is composed of three modes plotted in blue, orange, and green, respectively. The doubling of the modes from $(-\frac{1}{3}, -\frac{1}{3})$ to (0,0) arises from magnetic twinning and the line thickness reflects the predicted intensity of the modes. Panels adapted from Refs. [49, 66].

$3d_{x^2-y^2}$ and La 5*d* orbitals, involving a charge-transfer from Ni to the *RE* cation [64]. From LDA + *U* it is found that a Fermi pocket of mainly La 5*d* character forms near the Γ point, which is quite extended and three-dimensional. On the other hand, the Ni $3d_{x^2-y^2}$ states in the NiO_2 planes are quasi-2D and strongly correlated [64, 74]. Nevertheless, the relevance of the rare-earth 5*d* bands for the low-energy physics of IL nickelates is still under debate and proposals range from effective single-band to multi-orbital models, including various Ni 3*d* and rare-earth 5*d* as well as interstitial orbitals [62, 63, 75–89]. Hence, future experiments probing the Fermi surface topology, such as angle resolved photoemission (ARPES) and quantum oscillation measurements, are highly desirable.

3 MAGNETIC CORRELATIONS

3.1 Magnetic Excitations in Infinite-Layer Nickelates

Despite of the involvement of rare-earth 5*d* states, the fact that the electronic structures of the Ni 3*d* states resemble a cuprate-like $3d^9$ system raises a curious question: whether the Mott-physics, a key ingredient in the cuprate phenomenology [90], also play an important role in sculpting the electronic structures in IL nickelates. Since a strong AFM interaction is a consequence of Mott physics due to strong onsite Coulomb interaction, information about the magnetic structures in IL nickelate is imperative to gain further insight into this issue. Early investigations of bulk polycrystalline $LaNiO_2$ and $NdNiO_2$ found no evidence of AFM order [59, 60], which appeared to suggest a significantly weaker magnetic interaction than in cuprates. On a different ground, theories have been debating the energy scale of magnetic interactions in the IL nickelates. Some theories predict a small AFM interaction (~ an order of magnitude smaller than that of cuprates) because of the larger charge transfer energy Δ [91–94]. Conversely, other theories argue that the magnetic interactions are comparable to those in cuprates [74, 92, 95]. Experimental information about magnetic excitations is crucial to clarify this important issue.

Recently, magnetic excitations in $Nd_{1-x}Sr_xNiO_2$ have been revealed using RIXS at the Ni L_3-edge [66]. As shown in **Figure 2A**, a branch of dispersive magnetic excitations has been observed in $NdNiO_2$, whose energy-momentum dispersion resembles the spin wave excitations of AFM coupled spins in a square lattice. Importantly, the bandwidth of the magnetic excitations is approximately 200 meV,

corresponding to a nearest neighbor spin interaction $J_1 \sim 65$ meV. This is about half of the J_1 in cuprate superconductors and similar to that in the TL nickelates [49], but is notably higher than in the stripe-ordered single-layer ($n = 1$) nickelates [25–27], perovskite nickelates ($n = \infty$) [96], and cubic NiO [97, 98]. Therefore, the observation of the high energy scale of J_1 in IL nickelates confirms the presence of a strong onsite Coulomb interaction, indicating that the strong correlation effect associated with the Mott-physics is likely also at play in the nickelate superconductors. Notably, distinct from the sharp magnetic modes observed in undoped cuprates, the magnetic excitations in the undoped parent compound of IL nickelates are damped, which is likely due to the coupling to the metallic Nd 5*d* states.

Upon hole doping, the magnetic excitations become less dispersive as a function of momentum and significantly damped. By fitting the spectrum to a damped harmonic oscillator function, it is found that mode energies soften accompanied by slightly reduced spectral weight (**Figure 2B**). The observed doping dependence is consistent with spin dilution in a Mott insulator. This is in fact different from those observed in cuprates, in which the mode energy and spectral weight do not decrease with increasing doping [99]. The doping dependence of the magnetic excitations in cuprates has been attributed to the longer-range charge dynamics emergent with increasing hole doping, for example, the three site terms in a Hubbard model [100, 101]. Such dynamics appear to be less prominent in the doped IL nickelates, likely due to the larger charge transfer energy Δ and the presence of the rare-earth 5*d* metallic state, calling for further investigation.

We note the next nearest-neighbour exchange interaction J_2 extracted from the magnetic excitations dispersion possesses an opposite sign to the nearest neighbor J_1, which should favor the formation of AFM ordering at (0.5, 0.5). Unfortunately, RIXS at the Ni L_3-edge cannot reach (0.5, 0.5) due to insufficient momentum transfer of the photons, preventing a direct scrutinization on the putative AFM order. Notably, recent susceptibility measurement on bulk powder samples indicated spin glass behaviors, but signatures of an AFM phase transition were still not observed. Thus, it would be interesting to investigating why IL nickelates are a failed AFM. However, one should be cautious about the difference between bulk and thin film samples, as well as the disorders in both types of materials, which were significantly reduced over time along with the optimization of material synthesis protocols.

Interestingly, the IL nickelates add one more case in which the magnetic correlations are in proximity to superconductivity in the phase diagram, similarly to a number of unconventional superconductors, such as cuprates, iron-based superconductors, and heavy fermion superconductors [102]. It might be tempting to attribute magnetic fluctuations as a candidate mechanism of superconductivity. However, among these superconducting compounds, including the nickelate superconductors, there appears no clear correlation between the energy scale of the magnetic excitation and the superconducting transition temperature, casting doubt on this notion. In any case, the relationship between magnetic fluctuations and the superconductivity remains an important issue in nickelate superconductors.

3.2 Magnetic Excitations in Trilayer Nickelates

In parallel with the measurement of magnetic excitations in the IL material $Nd_{1-x}Sr_xNiO_2$, magnetic excitations were also measured in the TL materials $La_4Ni_3O_8$ and $Pr_4Ni_3O_8$ [49]. The crystal structure of $La_4Ni_3O_8$ is shown in **Figure 2C**. This material has some features that indicate that it might be especially promising as a cuprate analog. The rock salt *RE*-O layers present in its structure make it more two-dimensional than IL compounds and the rare-earth orbitals that are populated in IL are predicted to have a less significant role in TL systems [48, 103, 104]. As explained in the introduction, this compound is naturally self-doped and has a nominal hole concentration of 1/3. A disadvantage of the $La_4Ni_3O_8$ series is that they have, to date, proven difficult to chemically dope. Like cuprates, and some other complex oxides, $La_4Ni_3O_8$ has charge and spin order [47, 105]. This structure, illustrated in **Figure 2D**, features diagonal rows of Ni sites with enhanced hole character and neighboring diagonal stripes of up and down spin-ordered sites with reduced hole character. The overall magnetic dispersion, measured with Ni L_3 edge RIXS, is plotted in **Figure 2E** and features a bandwidth of ~ 80 meV with a downturn near $(-\frac{1}{3}, -\frac{1}{3})$, which is the charge and spin stripe-ordering wavevector. $La_4Ni_3O_8$ was modeled by solving a Heisenberg Hamiltonian which accounts for stripes, and assumes complete charge disproportionation into d^9 and d^8 sites, similar to prior studies of other stripe-ordered cuprates and nickelates [18, 106]. This includes J_1, which connects sites 1 and 2 in **Figure 2D**, J_3, which couples atom 2, through the purple doped site, to atom 1 in the next unit cell and J_z, which reflects interactions along the *c*-axis, for example, site 1 to site 3. The diagonal J_2 interaction that was included in the analysis of $NdNiO_2$ is not expected to be important here, as it couples to the sites with an enhanced hole character and which would be spinless when hosting an extra hole ($S = 0$) [48]. Solving this Hamiltonian in the spin-wave approximation yields three modes. Since these modes could not be resolved separately, the RIXS intensity of these modes was computed and summed to predict the intensity of the magnetic feature in RIXS. Values of $J_1 = 69(4)$ meV and $J_3 = 17(4)$ meV were obtained by fitting a Hamiltonian of this type.[2] Similar to the $Nd_{1-x}Sr_xNiO_2$ case, the effects of J_z were too small to be constrained by the experiment, so the theoretical value of $J_z = 13.6$ meV was used. Very similar dispersions were found in $Pr_4Ni_3O_8$, which may imply that dynamical stripes exist in this compound even though long range stripe order has not been detected, as has been suggested independently in muon spin rotation studies [107].

The leading value of $J_1 = 69(4)$ meV in $La_4Ni_3O_8$ is strikingly close the 65(1) meV value obtained for $NdNiO_2$. It should be noted that this similar value arises from a much smaller magnetic

[2]The notation used here was been modified from the original work of Ref. [49] to facilitate comparison with Ref. [66].

bandwidth, as within the stripe-ordered state, each Ni will have only two magnetic neighbors. An approximate extrapolation of the magnetic dispersion of $Nd_{1-x}Sr_xNiO_2$ to a doping of $x \sim 1/3$ implies that it would have a bandwidth comparable to $La_4Ni_3O_8$ at this doping; yet, whether stripe order or fluctuations exist in the IL nickelates, like those found in the TL nickelates, remains an important open question. Overall, this suggests that the local correlated physics in these reduced RP cousins is very similar provided they are compared at the same effective doping, although their precise low-energy ground states might be more different.

4 CONCLUSION

In summary, soft x-ray spectroscopic studies have provided valuable insights into the physics of RP-phase and RP-derived nickelates. Nevertheless, for low-valence nickelates there is still limited consensus on the essential ingredients of their electronic structure. Along these lines, we anticipate that advances in sample synthesis and the application of complementary experimental techniques, including ARPES and quantum oscillation measurements, will be helpful. Moreover, the role of disorder and capping layers, as well as the apparent differences between film and bulk samples need further clarification. These insights could point the way towards improved low-valance nickelate superconductors, including multilayer systems [108]. Finally, a pertinent question is whether suitable sample preparation allows to realize other cuprate-typical ground states in nickelates, such as antiferromagnetism, pseudogap, as well as nematic, charge, and spin orders.

AUTHOR CONTRIBUTIONS

The manuscript was written by MH, MD, and W-SL.

FUNDING

Work at SLAC National Lab was supported by United States Department of Energy, Office of Science, Office of Basic Energy Sciences under Contract No. DE-AC02-76SF00515. Work at Brookhaven National Laboratory was supported by the United States Department of Energy, Office of Science, Office of Basic Energy Sciences. The use of resources at the SIX beamline of the National Synchrotron Light Source II, a United States Department of Energy (DOE) Office of Science User Facility operated for the DOE Office of Science by Brookhaven National Laboratory under Contract No. DE-SC0012704, is acknowledged. The Max Planck Society is acknowledged for funding of the open access fee.

ACKNOWLEDGMENTS

The authors thank K. Fürsich for useful discussions and comments.

REFERENCES

1. Keimer B, Kivelson SA, Norman MR, Uchida S, Zaanen J. From Quantum Matter to High-Temperature Superconductivity in Copper Oxides. *Nature* (2015) 518:179–86. doi:10.1038/nature14165
2. Lee PA, Nagaosa N, Wen XG. Doping a Mott Insulator: Physics of High-Temperature Superconductivity. *Rev Mod Phys* (2006) 78:17–85. doi:10.1103/RevModPhys.78.17
3. Armitage NP, Fournier P, Greene RL. Progress and Perspectives on Electron-Doped Cuprates. *Rev Mod Phys* (2010) 82:2421–87. doi:10.1103/RevModPhys.82.2421
4. Damascelli A, Hussain Z, Shen ZX. Angle-resolved Photoemission Studies of the Cuprate Superconductors. *Rev Mod Phys* (2003) 75:473–541. doi:10.1103/RevModPhys.75.473
5. Fink J, Knupfer M, Atzkern S, Golden M. Electronic Correlations in Solids, Studied Using Electron Energy-Loss Spectroscopy. *J Electron Spectros Relat Phenomena* (2001) 117-118:287–309. doi:10.1016/S0368-2048(01)00254-7
6. Fischer O, Kugler M, Maggio-Aprile I, Berthod C, Renner C. Scanning Tunneling Spectroscopy of High-Temperature Superconductors. *Rev Mod Phys* (2007) 79:353–419. doi:10.1103/RevModPhys.79.353
7. Basov DN, Timusk T. Electrodynamics of High-T_c Superconductors. *Rev Mod Phys* (2005) 77:721–79. doi:10.1103/RevModPhys.77.721
8. Devereaux TP, Hackl R. Inelastic Light Scattering from Correlated Electrons. *Rev Mod Phys* (2007) 79:175–233. doi:10.1103/RevModPhys.79.175
9. Fujita M, Hiraka H, Matsuda M, Matsuura M, Tranquada MJ, Wakimoto S, et al. Progress in Neutron Scattering Studies of Spin Excitations in High-T_c Cuprates. *J Phys Soc Jpn* (2012) 81:011007. doi:10.1143/JPSJ.81.011007
10. Miao H, Ishikawa D, Heid R, Le Tacon M, Fabbris G, Meyers D, et al. Incommensurate Phonon Anomaly and the Nature of Charge Density Waves in Cuprates. *Phys Rev X* (2018) 8:011008. doi:10.1103/PhysRevX.8.011008
11. Ament LJP, van Veenendaal M, Devereaux TP, Hill JP, van den Brink J. Resonant Inelastic X-ray Scattering Studies of Elementary Excitations. *Rev Mod Phys* (2011) 83:705–67. doi:10.1103/RevModPhys.83.705
12. Le Tacon M, Ghiringhelli G, Chaloupka J, Sala MM, Hinkov V, Haverkort M, et al. Intense Paramagnon Excitations in a Large Family of High-Temperature Superconductors. *Nat Phys* (2011) 7:725–30. doi:10.1038/NPHYS2041
13. Dean M, Dellea G, Springell R, Yakhou-Harris F, Kummer K, Brookes N, et al. Persistence of Magnetic Excitations in $La_{2-x}Sr_xCuO_4$ from the Undoped Insulator to the Heavily Overdoped Non-superconducting Metal. *Nat Mater* (2013) 12:1019–23. doi:10.1038/NMAT3723
14. Hepting M, Chaix L, Huang E, Fumagalli R, Peng Y, Moritz B, et al. Three-dimensional Collective Charge Excitations in Electron-Doped Copper Oxide Superconductors. *Nature* (2018) 563:374–8. doi:10.1038/s41586-018-0648-3
15. Lin JQ, Yuan J, Jin K, Yin ZP, Li G, Zhou K-J, et al. Doping Evolution of the Charge Excitations and Electron Correlations in Electron-Doped Superconducting $La_{2-x}Ce_xCuO_4$. *Npj Quan Mater* (2020) 5:4. doi:10.1038/s41535-019-0205-9
16. Nag A, Zhu M, Bejas M, Li J, Robarts HC, Yamase H, et al. Detection of Acoustic Plasmons in Hole-Doped Lanthanum and Bismuth Cuprate Superconductors Using Resonant Inelastic X-ray Scattering. *Phys Rev Lett* (2020) 125:257002. doi:10.1103/PhysRevLett.125.257002
17. Ghiringhelli G, Le Tacon M, Minola M, Blanco-Canosa S, Mazzoli C, Brookes NB, et al. Long-Range Incommensurate Charge Fluctuations in (Y,Nd) $Ba_2Cu_3O_{6+x}$. *Science* (2012) 337:821–5. doi:10.1126/science.1223532
18. Miao H, Lorenzana J, Seibold G, Peng YY, Amorese A, Yakhou-Harris F, et al. High-temperature Charge Density Wave Correlations in $La_{1.875}Ba_{0.125}CuO_4$ without Spin–Charge Locking. *PNAS* (2017) 114:12430–5. doi:10.1073/pnas.1708549114
19. Chaix L, Ghiringhelli G, Peng Y, Hashimoto M, Moritz B, Kummer K, et al. Dispersive Charge Density Wave Excitations in $Bi_2Sr_2CaCu_2O_{8+\delta}$. *Nat Phys* (2017) 13:952–6. doi:10.1038/nphys4157

20. Miao H, Fumagalli R, Rossi M, Lorenzana J, Seibold G, Yakhou-Harris F, et al. Formation of Incommensurate Charge Density Waves in Cuprates. *Phys Rev X* (2019) 9:031042. doi:10.1103/PhysRevX.9.031042
21. Lee WS, Zhou KJ, Hepting M, Li J, Nag A, Walters AC, et al. Spectroscopic Fingerprint of Charge Order Melting Driven by Quantum Fluctuations in a Cuprate. *Nat Phys* (2021) 17:53–7. doi:10.1038/s41567-020-0993-7
22. Norman MR. Materials Design for New Superconductors. *Rep Prog Phys* (2016) 79:074502. doi:10.1088/0034-4885/79/7/074502
23. Greenblatt M. Ruddlesden-popper $Ln_{n+1}Ni_nO_{3n+1}$ Nickelates: Structure and Properties. *Curr Opin Solid State Mater Sci* (1997) 2:174–83. doi:10.1016/S1359-0286(97)80062-9
24. Acrivos J, Lei M, Jiang C, Nguyen H, Metcalf P, Honig J. Paramagnetism, Antiferromagnetism, and Superconductivity in La_2NiO_4. *J Solid State Chem* (1994) 111:343–8. doi:10.1006/jssc.1994.1237
25. Sachan V, Buttrey DJ, Tranquada JM, Lorenzo JE, Shirane G. Charge and Spin Ordering in $La_{2-x}Sr_xNiO_{4.00}$ with x=0.135 and 0.20. *Phys Rev B* (1995) 51:12742–6. doi:10.1103/PhysRevB.51.12742
26. Sugai S, Sato M, Kobayashi T, Akimitsu J, Ito T, Takagi H, et al. High-energy Spin Excitations in the Insulating Phases of High-T_c Superconducting Cuprates and La_2NiO_4. *Phys Rev B* (1990) 42:1045–7. doi:10.1103/PhysRevB.42.1045
27. Fabbris G, Meyers D, Xu L, Katukuri VM, Hozoi L, Liu X, et al. Doping Dependence of Collective Spin and Orbital Excitations in the Spin-1 Quantum Antiferromagnet $La_{2-x}Sr_xNiO_4$ Observed by X Rays. *Phys Rev Lett* (2017) 118:156402. doi:10.1103/PhysRevLett.118.156402
28. Bisogni V, Catalano S, Green RJ, Gibert M, Scherwitzl R, Huang Y, et al. Ground-state Oxygen Holes and the Metal–Insulator Transition in the Negative Charge-Transfer Rare-Earth Nickelates. *Nat Commun* (2016) 7: 13017. doi:10.1038/ncomms13017
29. Chaloupka J, Khaliullin G. Orbital Order and Possible Superconductivity in $LaNiO_3/LaMO_3$ Superlattices. *Phys Rev Lett* (2008) 100:016404. doi:10.1103/PhysRevLett.100.016404
30. Hansmann P, Yang X, Toschi A, Khaliullin G, Andersen OK, Held K. Turning a Nickelate Fermi Surface into a Cupratelike One through Heterostructuring. *Phys Rev Lett* (2009) 103:016401. doi:10.1103/PhysRevLett.103.016401
31. Middey S, Chakhalian J, Mahadevan P, Freeland J, Millis A, Sarma D. Physics of Ultrathin Films and Heterostructures of Rare-Earth Nickelates. *Annu Rev Mater Res* (2016) 46:305–34. doi:10.1146/annurev-matsci-070115-032057
32. Catalano S, Gibert M, Fowlie J, Íñiguez J, Triscone JM, Kreisel J. Rare-earth Nickelates $RNiO_3$: Thin Films and Heterostructures. *Rep Prog Phys* (2018) 81: 046501. doi:10.1088/1361-6633/aaa37a
33. Boris AV, Matiks Y, Benckiser E, Frano A, Popovich P, Hinkov V, et al. Dimensionality Control of Electronic Phase Transitions in Nickel-Oxide Superlattices. *Science* (2011) 332:937–40. doi:10.1126/science.1202647
34. Benckiser E, Haverkort MW, Brück S, Goering E, Macke S, Frañó A, et al. Orbital Reflectometry of Oxide Heterostructures. *Nat Mater* (2011) 10: 189–93. doi:10.1038/NMAT2958
35. Liu J, Okamoto S, van Veenendaal M, Kareev M, Gray B, Ryan P, et al. Quantum Confinement of mott Electrons in Ultrathin $LaNiO_3/LaAlO_3$ Superlattices. *Phys Rev B* (2011) 83:161102. doi:10.1103/PhysRevB.83.161102
36. Frano A, Schierle E, Haverkort MW, Lu Y, Wu M, Blanco-Canosa S, et al. Orbital Control of Noncollinear Magnetic Order in Nickel Oxide Heterostructures. *Phys Rev Lett* (2013) 111:106804. doi:10.1103/PhysRevLett.111.106804
37. Hepting M, Minola M, Frano A, Cristiani G, Logvenov G, Schierle E, et al. Tunable Charge and Spin Order in $PrNiO_3$ Thin Films and Superlattices. *Phys Rev Lett* (2014) 113:227206. doi:10.1103/PhysRevLett.113.227206
38. Gibert M, Viret M, Torres-Pardo A, Piamonteze C, Zubko P, Jaouen N, et al. Interfacial Control of Magnetic Properties at $LaMnO_3/LaNiO_3$ Interfaces. *Nano Lett* (2015) 15:7355–61. doi:10.1021/acs.nanolett.5b02720
39. Disa AS, Georgescu AB, Hart JL, Kumah DP, Shafer P, Arenholz E, et al. Control of Hidden Ground-State Order in $NdNiO_3$ Superlattices. *Phys Rev Mater* (2017) 1:024410. doi:10.1103/PhysRevMaterials.1.024410
40. Hepting M, Green RJ, Zhong Z, Bluschke M, Suyolcu YE, Macke S, et al. Complex Magnetic Order in Nickelate Slabs. *Nat Phys* (2018) 14:1097–102. doi:10.1038/s41567-018-0218-5
41. Fürsich K, Lu Y, Betto D, Bluschke M, Porras J, Schierle E, et al. Resonant Inelastic X-ray Scattering Study of Bond Order and Spin Excitations in Nickelate Thin-Film Structures. *Phys Rev B* (2019) 99:165124. doi:10.1103/PhysRevB.99.165124
42. Chakhalian J, Rondinelli JM, Liu J, Gray BA, Kareev M, Moon EJ, et al. Asymmetric Orbital-Lattice Interactions in Ultrathin Correlated Oxide Films. *Phys Rev Lett* (2011) 107:116805. doi:10.1103/PhysRevLett.107.116805
43. Wu M, Benckiser E, Haverkort MW, Frano A, Lu Y, Nwankwo U, et al. Strain and Composition Dependence of Orbital Polarization in Nickel Oxide Superlattices. *Phys Rev B* (2013) 88:125124. doi:10.1103/PhysRevB.88.125124
44. Disa AS, Kumah DP, Malashevich A, Chen H, Arena DA, Specht ED, et al. Orbital Engineering in Symmetry-Breaking Polar Heterostructures. *Phys Rev Lett* (2015) 114:026801. doi:10.1103/PhysRevLett.114.026801
45. Han MJ, Wang X, Marianetti CA, Millis AJ. Dynamical Mean-Field Theory of Nickelate Superlattices. *Phys Rev Lett* (2011) 107:206804. doi:10.1103/PhysRevLett.107.206804
46. Fabbris G, Meyers D, Okamoto J, Pelliciari J, Disa AS, Huang Y, et al. Orbital Engineering in Nickelate Heterostructures Driven by Anisotropic Oxygen Hybridization rather Than Orbital Energy Levels. *Phys Rev Lett* (2016) 117: 147401. doi:10.1103/PhysRevLett.117.147401
47. Zhang J, Chen YS, Phelan D, Zheng H, Norman MR, Mitchell JF. Stacked Charge Stripes in the quasi-2D Trilayer Nickelate $La_4Ni_3O_8$. *PNAS* (2016) 113:8945–50. doi:10.1073/pnas.1606637113
48. Zhang J, Botana AS, Freeland JW, Phelan D, Zheng H, Pardo V, et al. Large Orbital Polarization in a Metallic Square-Planar Nickelate. *Nat Phys* (2017) 13:864–9. doi:10.1038/nphys4149
49. Lin JQ, Villar Arribi P, Fabbris G, Botana AS, Meyers D, Miao H, et al. Strong Superexchange in a $d^{9-\delta}$ Nickelate Revealed by Resonant Inelastic X-ray Scattering. *Phys Rev Lett* (2021) 126:087001. doi:10.1103/PhysRevLett.126.087001
50. Botana AS, Pardo V, Norman MR. Electron Doped Layered Nickelates: Spanning the Phase Diagram of the Cuprates. *Phys Rev Mater* (2017) 1: 021801. doi:10.1103/PhysRevMaterials.1.021801
51. Nica EM, Krishna J, Yu R, Si Q, Botana AS, Erten O. Theoretical Investigation of Superconductivity in Trilayer Square-Planar Nickelates. *Phys Rev B* (2020) 102:020504. doi:10.1103/PhysRevB.102.020504
52. Li D, Lee K, Wang BY, Osada M, Crossley S, Lee HR, et al. Superconductivity in an Infinite-Layer Nickelate. *Nature* (2019) 572:624–7. doi:10.1038/s41586-019-1496-5
53. Zeng S, Tang CS, Yin X, Li C, Li M, Huang Z, et al. Phase Diagram and Superconducting Dome of Infinite-Layer $Nd_{1-x}Sr_xNiO_2$ Thin Films. *Phys Rev Lett* (2020) 125:147003. doi:10.1103/physrevlett.125.147003
54. Li D, Wang BY, Lee K, Harvey SP, Osada M, Goodge BH, et al. Superconducting Dome in $Nd_{1-x}Sr_xNiO_2$ Infinite Layer Films. *Phys Rev Lett* (2020) 125:027001. doi:10.1103/PhysRevLett.125.027001
55. Lee K, Goodge BH, Li D, Osada M, Wang BY, Cui Y, et al. Aspects of the Synthesis of Thin Film Superconducting Infinite-Layer Nickelates. *APL Mater* (2020) 8:041107. doi:10.1063/5.0005103
56. Osada M, Wang BY, Goodge BH, Lee K, Yoon H, Sakuma K, et al. A Superconducting Praseodymium Nickelate with Infinite Layer Structure. *Nano Lett* (2020) 20:5735–40. doi:10.1021/acs.nanolett.0c01392
57. Li Y, Sun W, Yang J, Cai X, Guo W, Gu Z, et al. Impact of Cation Stoichiometry on the Crystalline Structure and Superconductivity in Nickelates. *Front Phys* (2021) 9:443. doi:10.3389/fphy.2021.719534
58. Osada M, Wang BY, Goodge BH, Harvey SP, Lee K, Li D, et al. Nickelate Superconductivity without Rare-Earth Magnetism: $(La,Sr)NiO_2$. *Adv Mater* (2021) 33:2104083. doi:10.1002/adma.202104083
59. Hayward MA, Green MA, Rosseinsky MJ, Sloan J. Sodium Hydride as a Powerful Reducing Agent for Topotactic Oxide Deintercalation: Synthesis and Characterization of the Nickel(i) Oxide $LaNiO_2$. *J Am Chem Soc* (1999) 121:8843–54. doi:10.1021/ja991573i
60. Hayward M, Rosseinsky M. Synthesis of the Infinite Layer Ni(i) Phase $NdNiO_{2+x}$ by Low Temperature Reduction of $NdNiO_3$ with Sodium Hydride. *Solid State Sci* (2003) 5:839–50. doi:10.1016/S1293-2558(03)00111-0
61. Ikeda A, Krockenberger Y, Irie H, Naito M, Yamamoto H. Direct Observation of Infinite NiO_2 Planes in $LaNiO_2$ Films. *Appl Phys Express* (2016) 9:061101. doi:10.7567/apex.9.061101

62. Anisimov VI, Bukhvalov D, Rice TM. Electronic Structure of Possible Nickelate Analogs to the Cuprates. *Phys Rev B* (1999) 59:7901–6. doi:10.1103/physrevb.59.7901
63. Lee KW, Pickett WE. Infinite-layer $LaNiO_2$: Ni^{1+} Is Not Cu^{2+}. *Phys Rev B* (2004) 70:165109. doi:10.1103/physrevb.70.165109
64. Hepting M, Li D, Jia CJ, Lu H, Paris E, Tseng Y, et al. Electronic Structure of the Parent Compound of Superconducting Infinite-Layer Nickelates. *Nat Mater* (2020) 19:381–5. doi:10.1038/s41563-019-0585-z
65. Goodge BH, Li D, Lee K, Osada M, Wang BY, Sawatzky GA, et al. Doping Evolution of the Mott-Hubbard Landscape in Infinite-Layer Nickelates. *PNAS* (2021) 118:e2007683118. doi:10.1073/pnas.2007683118
66. Lu H, Rossi M, Nag A, Osada M, Li DF, Lee K, et al. Magnetic Excitations in Infinite-Layer Nickelates. *Science* (2021) 373:213–6. doi:10.1126/science.abd7726
67. Abbate M, Zampieri G, Prado F, Caneiro A, Gonzalez-Calbet JM, Vallet-Regi M. Electronic Structure and Metal-Insulator Transition in $LaNiO_{3-\delta}$. *Phys Rev B* (2002) 65:155101. doi:10.1103/physrevb.65.155101
68. Kuiper P, Kruizinga G, Ghijsen J, Sawatzky GA, Verweij H. Character of Holes in $Li_xNi_{1-x}O$ and Their Magnetic Behavior. *Phys Rev Lett* (1989) 62:221–4. doi:10.1103/PhysRevLett.62.221
69. Zaanen J, Sawatzky GA, Allen JW. Band Gaps and Electronic Structure of Transition-Metal Compounds. *Phys Rev Lett* (1985) 55:418–21. doi:10.1103/PhysRevLett.55.418
70. Chen CT, Sette F, Ma Y, Hybertsen MS, Stechel EB, Foulkes WMC, et al. Electronic States in $La_{2-x}Sr_xCuO_{4+\delta}$ Probed by Soft-X-ray Absorption. *Phys Rev Lett* (1991) 66:104–7. doi:10.1103/PhysRevLett.66.104
71. Abbamonte P, Rusydi A, Smadici S, Gu GD, Sawatzky GA, Feng DL. Spatially Modulated 'Mottness' in $La_{2-x}Ba_xCuO_4$. *Nat Phys* (2005) 1:155–8. doi:10.1038/nphys178
72. Zhang FC, Rice TM. Effective Hamiltonian for the Superconducting Cu Oxides. *Phys Rev B* (1988) 37:3759–61. doi:10.1103/PhysRevB.37.3759
73. Green RJ, Haverkort MW, Sawatzky GA. Bond Disproportionation and Dynamical Charge Fluctuations in the Perovskite Rare-Earth Nickelates. *Phys Rev B* (2016) 94:195127. doi:10.1103/PhysRevB.94.195127
74. Been E, Lee WS, Hwang HY, Cui Y, Zaanen J, Devereaux T, et al. Electronic Structure Trends across the Rare-Earth Series in Superconducting Infinite-Layer Nickelates. *Phys Rev X* (2021) 11:011050. doi:10.1103/physrevx.11.011050
75. Nomura Y, Hirayama M, Tadano T, Yoshimoto Y, Nakamura K, Arita R. Formation of a Two-Dimensional Single-Component Correlated Electron System and Band Engineering in the Nickelate Superconductor $NdNio_2$. *Phys Rev B* (2019) 100:205138. doi:10.1103/PhysRevB.100.205138
76. Botana A, Norman M. Similarities and Differences between $LaNiO_2$ and $CaCuO_2$ and Implications for Superconductivity. *Phys Rev X* (2020) 10:011024. doi:10.1103/physrevx.10.011024
77. Kitatani M, Si L, Janson O, Arita R, Zhong Z, Held K. Nickelate Superconductors—A Renaissance of the One-Band Hubbard Model. *Npj Quan Mater* (2020) 5:59. doi:10.1038/s41535-020-00260-y
78. Wu X, Di Sante D, Schwemmer T, Hanke W, Hwang HY, Raghu S, et al. Robust $d_{x^2-y^2}$-wave Superconductivity of Infinite-Layer Nickelates. *Phys Rev B* (2020) 101:060504. doi:10.1103/PhysRevB.101.060504
79. Zhang H, Jin L, Wang S, Xi B, Shi X, Ye F, et al. Effective Hamiltonian for Nickelate Oxides $Nd_{1-x}Sr_xNiO_2$. *Phys Rev Res* (2020) 2:013214. doi:10.1103/PhysRevResearch.2.013214
80. Sakakibara H, Usui H, Suzuki K, Kotani T, Aoki H, Kuroki K. Model Construction and a Possibility of Cupratelike Pairing in a New d^9 Nickelate Superconductor (Nd, Sr)NiO_2. *Phys Rev Lett* (2020) 125:077003. doi:10.1103/PhysRevLett.125.077003
81. Lechermann F Late Transition Metal Oxides with Infinite-Layer Structure: Nickelates versus Cuprates. *Phys Rev B* (2020) 101:081110. doi:10.1103/PhysRevB.101.081110
82. Wang Y, Kang CJ, Miao H, Kotliar G. Hund's Metal Physics: From $SrNiO_2$ to $LaNiO_2$. *Phys Rev B* (2020) 102:161118. doi:10.1103/PhysRevB.102.161118
83. Werner P, Hoshino S. Nickelate Superconductors: Multiorbital Nature and Spin Freezing. *Phys Rev B* (2020) 101:041104. doi:10.1103/PhysRevB.101.041104
84. Adhikary P, Bandyopadhyay S, Das T, Dasgupta I, Saha-Dasgupta T. Orbital-selective Superconductivity in a Two-Band Model of Infinite-Layer Nickelates. *Phys Rev B* (2020) 102:100501. doi:10.1103/PhysRevB.102.100501
85. Karp J, Botana AS, Norman MR, Park H, Zingl M, Millis A. Many-body Electronic Structure of $NdNiO_2$ and $CaCuO_2$. *Phys Rev X* (2020) 10:021061. doi:10.1103/PhysRevX.10.021061
86. Liu Z, Xu C, Cao C, Zhu W, Wang ZF, Yang J. Doping Dependence of Electronic Structure of Infinite-Layer $NdNiO_2$. *Phys Rev B* (2021) 103:045103. doi:10.1103/PhysRevB.103.045103
87. Wan X, Ivanov V, Resta G, Leonov I, Savrasov SY. Exchange Interactions and Sensitivity of the Ni Two-Hole Spin State to Hund's Coupling in Doped $NdNiO_2$. *Phys Rev B* (2021) 103:075123. doi:10.1103/PhysRevB.103.075123
88. Lang ZJ, Jiang R, Ku W. Strongly Correlated Doped Hole Carriers in the Superconducting Nickelates: Their Location, Local many-body State, and Low-Energy Effective Hamiltonian. *Phys Rev B* (2021) 103:L180502. doi:10.1103/PhysRevB.103.L180502
89. Higashi K, Winder M, Kuneš J, Hariki A. Core-level X-ray Spectroscopy of Infinite-Layer Nickelate: LDA + DMFT Study. *Phys Rev X* (2021) 11:041009. doi:10.1103/PhysRevX.11.041009
90. Phillips P. Mottness. *Ann Phys (N Y.)* (2006) 321:1634–50. doi:10.1016/j.aop.2006.04.003
91. Jiang M, Berciu M, Sawatzky GA. Critical Nature of the Ni Spin State in Doped $NdNiO_2$. *Phys Rev Lett* (2020) 124:207004. doi:10.1103/PhysRevLett.124.207004
92. Zhang GM, Yang Y, Zhang FC. Self-doped mott Insulator for Parent Compounds of Nickelate Superconductors. *Phys Rev B* (2020) 101:020501. doi:10.1103/PhysRevB.101.020501
93. Hu LH, Wu C. Two-band Model for Magnetism and Superconductivity in Nickelates. *Phys Rev Res* (2019) 1:032046. doi:10.1103/PhysRevResearch.1.032046
94. Liu Z, Ren Z, Zhu W, Wang Z, Yang J. Electronic and Magnetic Structure of Infinite-Layer $NdNiO_2$: Trace of Antiferromagnetic Metal. *Npj Quan Mater* (2020) 5:31. doi:10.1038/s41535-020-0229-1
95. Katukuri VM, Bogdanov NA, Weser O, van den Brink J, Alavi A. Electronic Correlations and Magnetic Interactions in Infinite-Layer $NdNiO_2$. *Phys Rev B* (2020) 102:241112. doi:10.1103/PhysRevB.102.241112
96. Lu Y, Betto D, Fürsich K, Suzuki H, Kim HH, Cristiani G, et al. Site-selective Probe of Magnetic Excitations in Rare-Earth Nickelates Using Resonant Inelastic X-ray Scattering. *Phys Rev X* (2018) 8:031014. doi:10.1103/PhysRevX.8.031014
97. Hutchings MT, Samuelsen EJ. Measurement of Spin-Wave Dispersion in NiO by Inelastic Neutron Scattering and its Relation to Magnetic Properties. *Phys Rev B* (1972) 6:3447–61. doi:10.1103/PhysRevB.6.3447
98. Ghiringhelli G, Piazzalunga A, Dallera C, Schmitt T, Strocov VN, Schlappa J, et al. Observation of Two Nondispersive Magnetic Excitations in NiO by Resonant Inelastic Soft-X-Ray Scattering. *Phys Rev Lett* (2009) 102:027401. doi:10.1103/PhysRevLett.102.027401
99. Peng YY, Huang EW, Fumagalli R, Minola M, Wang Y, Sun X, et al. Dispersion, Damping, and Intensity of Spin Excitations in the Monolayer $(Bi,Pb)_2(Sr,La)_2CuO_{6+\delta}$ Cuprate Superconductor Family. *Phys Rev B* (2018) 98:144507. doi:10.1103/PhysRevB.98.144507
100. Jia CJ, Nowadnick EA, Wohlfeld K, Kung YF, Chen CC, Johnston S, et al. Persistent Spin Excitations in Doped Antiferromagnets Revealed by Resonant Inelastic Light Scattering. *Nat Commun* (2014) 5:3314. doi:10.1038/ncomms4314
101. Bala J, Oleś AM, Zaanen J. Spin Polarons in the T-T′-J Model. *Phys Rev B* (1995) 52:4597–606. doi:10.1103/PhysRevB.52.4597
102. Scalapino DJ. A Common Thread: The Pairing Interaction for Unconventional Superconductors. *Rev Mod Phys* (2012) 84:1383–417. doi:10.1103/RevModPhys.84.1383
103. Poltavets VV, Lokshin KA, Nevidomskyy AH, Croft M, Tyson TA, Hadermann J, et al. Bulk Magnetic Order in a Two-Dimensional Ni^{1+}/Ni^{2+} (d^9/d^8) Nickelate, Isoelectronic with Superconducting Cuprates. *Phys Rev Lett* (2010) 104:206403. doi:10.1103/PhysRevLett.104.206403
104. Botana AS, Pardo V, Pickett WE, Norman MR. Charge Ordering in Ni^{1+}/Ni^{2+} Nickelates: $La_4Ni_3O_8$ and $La_3Ni_2O_6$. *Phys Rev B* (2016) 94:081105. doi:10.1103/PhysRevB.94.081105
105. Zhang J, Pajerowski DM, Botana AS, Zheng H, Harriger L, Rodriguez-Rivera J, et al. Spin Stripe Order in a Square Planar Trilayer Nickelate. *Phys Rev Lett* (2019) 122:247201. doi:10.1103/PhysRevLett.122.247201

106. Carlson EW, Yao DX, Campbell DK. Spin Waves in Striped Phases. *Phys Rev B* (2004) 70:064505. doi:10.1103/PhysRevB.70.064505
107. Huangfu S, Guguchia Z, Cheptiakov D, Zhang X, Luetkens H, Gawryluk DJ, et al. Short-range Magnetic Interactions and Spin-Glass Behavior in the Quasi-Two-Dimensional Nickelate $Pr_4Ni_3O_8$. *Phys Rev B* (2020) 102:054423. doi:10.1103/physrevb.102.054423
108. Ortiz RA, Menke H, Misják F, Mantadakis DT, Fürsich K, Schierle E, et al. Superlattice Approach to Doping Infinite-Layer Nickelates. *Phys Rev B* (2021) 104:165137. doi:10.1103/PhysRevB.104.165137

Conflict of Interest: The authors declare that the research was conducted in the absence of any commercial or financial relationships that could be construed as a potential conflict of interest.

Publisher's Note: All claims expressed in this article are solely those of the authors and do not necessarily represent those of their affiliated organizations, or those of the publisher, the editors and the reviewers. Any product that may be evaluated in this article, or claim that may be made by its manufacturer, is not guaranteed or endorsed by the publisher.

frontiers in Physics

PERSPECTIVE
published: 23 December 2021
doi: 10.3389/fphy.2021.813483

A Nickelate Renaissance

J. F. Mitchell *

Materials Science Division, Argonne National Laboratory, Lemont, IL, United States

The 2019 discovery of high temperature superconductivity in layered nickelate films, $Nd_{1-x}SrNiO_2$, has galvanized a community that has been studying nickelates for more than 30 years both as cuprate analogs and in their own right. On the surface, infinite layer nickelates, and their multilayer analogs, should be promising candidates based on our understanding of cuprates: square planar coordination and a parent d^9 configuration that places a single hole in a dx^2-y^2 planar orbital makes nickelates seem poised for superconductivity. But creating crystals and films of sufficient quality of this d^9 configuration in Ni^{1+} has proven to be a synthetic challenge, only recently overcome. These crystalline specimens are opening windows that shed new light on the cuprate-nickelate analogy and reveal nuances that leave the relationship between cuprates and nickelates very much an area open to debate. This Perspective gives a qualitative, phenomenological account of these newly discovered superconductors and multilayer members of the infinite layer nickelate family. The focus is on our current understanding of electronic and magnetic properties of these materials as well as some future opportunities, explored from the viewpoint of synthetic challenges and some suggested developments in materials discovery and growth to make further progress in this rejuvenated field.

Keywords: superconductivity, high-Tc superconductors, crystal growth, thin film, metal insulator transition, stripes

OPEN ACCESS

Edited by:
Matthias Hepting,
Max Planck Institute for Solid State Research, Germany

Reviewed by:
Massimiliano Polichetti,
University of Salerno, Italy

***Correspondence:**
J. F. Mitchell
mitchell@anl.gov

Specialty section:
This article was submitted to Condensed Matter Physics, a section of the journal Frontiers in Physics

Received: *11 November 2021*
Accepted: *24 November 2021*
Published: *23 December 2021*

Citation:
Mitchell J (2021) A Nickelate Renaissance. Front. Phys. 9:813483. doi: 10.3389/fphy.2021.813483

INTRODUCTION

Like the soil, mind is fertilized while it lies fallow, until a new burst of bloom ensues [1]. These words were penned by John Dewey in his 1934 work on the philosophy of art, but they express a universal experience that is common across most walks of life, especially the sciences. The materials that inspire the collection of articles in this issue, low-dimensional rare earth nickelates, are a case in point. With a story spanning more than three decades, these compelling materials have been fellow travelers with the more famous copper oxide superconductors, yet have always remained in their shadow, a "poor cousin." That is, until now.

With superconductivity discovered in epitaxial thin films of the "infinite-layer" d^9 nickelate $(Nd,Sr)NiO_2$ by Harold Hwang [2] and his Stanford collaborators in mid-2019 and more recently by Julia Mundy [3] of Harvard in the five-layer nickelate $Nd_6Ni_5O_{12}$, a decades-long dream has been realized. Their discoveries and other exciting new findings in d^9 layered nickelate materials rest on breakthroughs in thin film and single crystal growth that have allowed old ideas to take on a new life, and renewed enthusiasm to explore the nickelates as a platform to understand high-T_c superconductivity beyond cuprates, indeed a "new burst of bloom." The purpose of this Perspective is to provide a phenomenological account of how this nickelate renaissance has emerged as viewed through the lens of new and transformative materials developments in d^9 nickel oxides, the discoveries they have enabled, and some new directions toward which they may point.

Cuprates

To appreciate the long-lived fascination with nickelates and the importance of today's resurgence of interest, a bit of stage-setting about cuprate superconductors is essential. Understanding the physics behind the copper oxides has been a defining challenge of condensed matter physics for the 35 years since their discovery. The hundreds of thousands of papers written about cuprates underscore simultaneously their impact on the condensed matter community, and the daunting challenge to untangling both the phenomenology and mechanism behind these unconventional superconductors. Generating this challenge is an elaborate web of interactions that result in the complex phase behavior of cuprates, behavior that contains—in addition to superconductivity—magnetism, charge order, non-Fermi-liquid metals, real-space stripes (both static and dynamic) pair density waves, and perhaps other yet-to-be-discovered exotica [4]. Unraveling how these emergent phases compete or cooperate, both in the normal and superconducting state, has driven the field from its inception to today.

Superconducting cuprates emerge by doping a parent antiferromagnetic insulating parent oxide containing Cu^{2+}, exemplified by La_2CuO_4 (La-214). Doping introduces holes (i.e., $La_{2-x}Sr_2CuO_4$) or electrons (i.e., $Nd_{2-x}Ce_xCuO_4$) to produce first a metal, and then a superconductor. Along with sophisticated quantitative models and mechanisms constructed to explain this progression of phases, there have emerged a set of phenomenological descriptors that are considered important "ingredients" in the "recipe" for high-T_c copper oxide superconductivity. These include:

- A quasi-2D structure in which the copper ions are surrounded by a highly axially-elongated octahedral coordination polyhedron of oxygen anions.
- An orbital configuration around Cu in which the dx^2-y^2 orbital is highest lying. With a nominal oxidation state of Cu^{2+}, this d^9 filling promotes a Jahn-Teller distortion that generates a configuration with a single hole in this half-filled dx^2-y^2 orbital.
- Strong correlations that precipitate an instability in the notionally metallic half-filled dx^2-y^2 band of the parent, leading to an insulating, magnetic ground state (so-called "checkerboard" antiferromagnetic order)
- The relatively narrow separation between Cu 3*d* and O 2*p* states that lends a considerable hybridization between these orbitals and leads to a significant O component to the hole wave function, placing cuprates solidly in the charge transfer insulator rather than the Mott regime of the Zaanen-Sawatztky-Allen framework [5].

A Cuprate Analog

These ingredients have driven materials and chemistry design rules for high-T_c superconductors in the search both for other cuprate families and for non-copper based analogs. Soon after the discovery of cuprate superconductivity, attention turned to known nickelates isostructural with La-214, specifically $La_{2-x}Sr_xNiO_4$ (LSNO). Although Ni is immediately to the left of Cu on the Periodic Table, and a similar solid-state chemistry is found, the parent phase contains Ni^{2+}, d^8, rather than d^9. Such d^8 systems in octahedral coordination are typically high spin with holes in both the dx^2-y^2 and dz^2 orbitals. Additionally, the lower electronegativity of Ni vs Cu means that the separation between the O 2p states and the Ni *d* manifold is larger, reducing hybridization. With these cuprate ingredients missing, it is perhaps unsurprising that superconductivity has not been found in LSNO. Indeed, the system remains insulating unless doped heavily to $x \approx 0.9$ [6], where a metal emerges. Study of this system and analogs has revealed collective phenomena interesting on their own right, such as real-space charge and spin stripes [7–12], whose period is set by the charge concentration, e.g., $La_{5/3}Sr_{1/3}NiO_4$ with 1/3 hole added to Ni^{2+} has a three-fold superlattice oriented at 45° to the Ni-O bonds. Many of these phenomena turn out to be relevant to cuprates as well.

d^9 NICKELATES: MATERIALS AND CHEMISTRY

If Ni^{2+} isn't right, why not Ni^{1+}, which would share the d^9 configuration of Cu^{2+}? Indeed, Anisimov suggested that Ni^{1+} in the square planar configuration found in the infinite layer compound, if doped with low-spin Ni^{2+}, could be a superconductor [13]. In counterpoint, Pickett argued that reduced hybridization and concomitant weighting of the 3*d* band at E_F meant that despite the isoelectronic configuration, "Ni^{1+} is not Cu^{2+}." [14] From the perspective of solid-state inorganic chemistry, Ni prefers to be in the 2+ charge state, and oxides with Ni^{1+} are rare. In the present context, a family of layered d^9 compounds has taken center stage (**Figure 1A**). This homologous series, $R_{n+1}Ni_nO_{2n+2}$ (R = La,Pr,Nd), first described by Lacorre [15], is characterized by interleaving blocks of *n* NiO_2 layers separated by R_2O_2 fluorite blocks. It is noteworthy that the $n = 1$ member of the series is isostructural with the well-known T′ phase of the superconducting cuprates, $(Nd,Ce)_2CuO_4$. The remainder of this Perspective focuses on this class of d^9 nickelates in both bulk and thin-film forms, their growth, properties, and impact on high T_c superconductivity.

Bulk Materials

The "infinite layer" nickelate $LaNiO_2$ ($n = \infty$, LNO) possesses square planar NiO_2 layers, in which the crystal field would produce a hole in the dx^2-y^2 band, desirable for cuprate superconductors. Synthesis of LNO in bulk polycrystalline form was reported by Crespin in 1983 (followed up 22 years later) using a complex apparatus to titrate H_2 gas to the sample [16–18]. Study of the evolution of $LaNiO_3$ to reduced phases was reported by Moriga, et al. [19–21] who were unable to reach $LaNiO_2$. The synthesis window of temperature, sample size, etc. employed by Crespin was quite narrow, and to our knowledge, no other successful synthesis of LNO in H_2 gas has been reported.

Hayward reported bulk synthesis of LNO and $NdNiO_2$ (NNO) using NaH as a reducing agent [22, 23]. The synthesis led to mixed phases with excess O, stacking faults, etc. NNO synthesized in this way was insulating and paramagnetic, not the hoped-for antiferromagnetism found in cuprate parent phases. Hayward

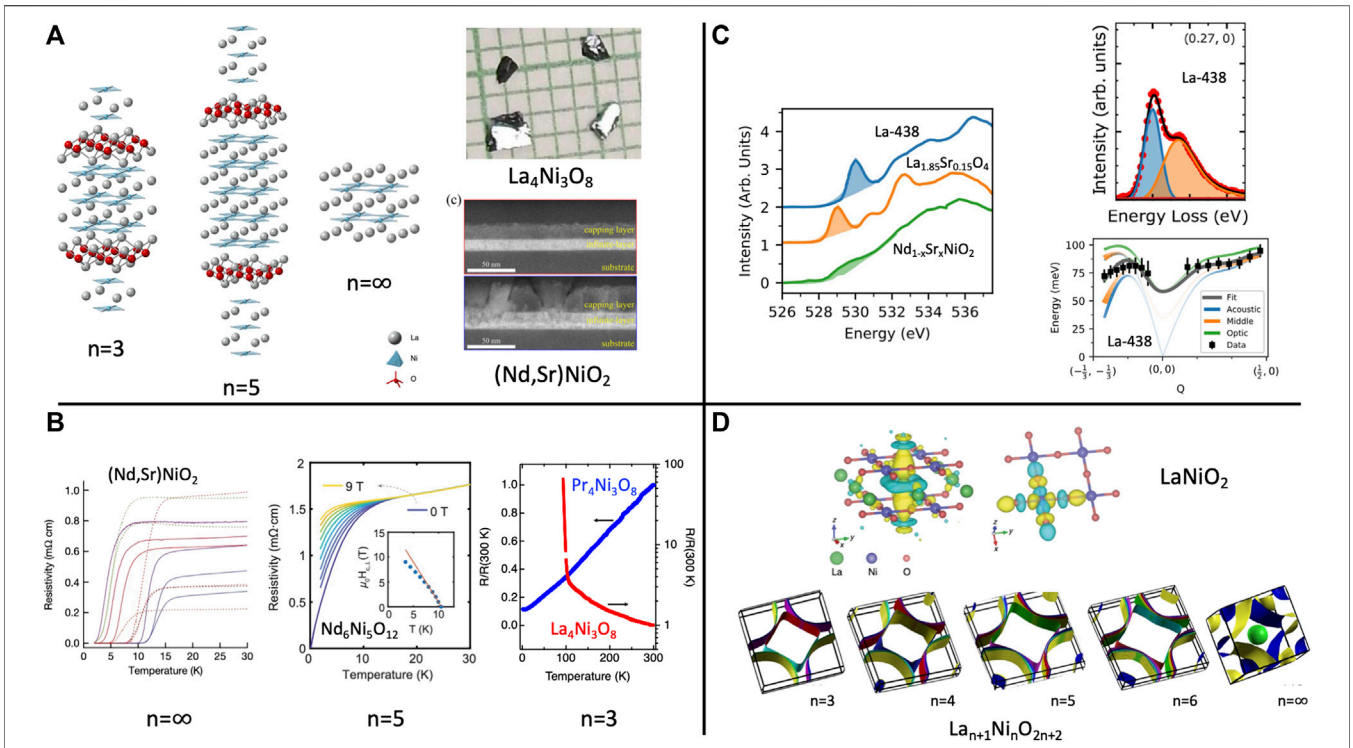

FIGURE 1 | Overview of d^9 nickelates structure and properties **(A)** left: members of the layered d^9 nickelate family showing square planar NiO_2 sheets separated by fluorite-like R_2O_2 layers; right top: single crystals of $La_4Ni_3O_8$; right bottom: cross-sectional images of PLD-grown (Nd,Sr)NiO_2 films [46]. **(B)** transport properties showing superconductivity in thin film infinite layer (Nd,Sr)NiO_2 [2] and five-layer $Nd_6Ni_5O_{12}$ [3] and competing ground states in single crystal bulk trilayer nickelates, metallic $Pr_4Ni_3O_8$ and charge-stripe insulating $La_4Ni_3O_8$. Note logarithmic scale for La-438. **(C)** Electronic structure of nickelates. left: prominent O *K*-edge prepeak in cuprates and trilayer $La_4Ni_3O_8$ appears suppressed in (Nd,Sr)NiO_2 films [49]. right: RIXS data reveal a magnon whose dispersion can be fit to yield the nearest-neighbor Ni-O superexchange constant [49]. **(D)** DFT calculations of electronic structure of d^9 layered nickelates. top: Wannier orbitals calculated for $LaNiO_2$ showing both dx^2-y^2 and dz^2 configurations [51]; bottom: calculated Fermi surface vs. layer number for the $La_{n+1}Ni_nO_{2n+2}$ series [52].

also successfully doped 10% Sr and Ca into LNO, but he reported no physical properties due to contamination by metallic Ni byproducts [24]. More recently, Li et al. [25] synthesized bulk $Nd_{1-x}Sr_xNiO_2$ (x = 0, 0.2, 0.4) using CaH_2 to reduce the perovskite parent. The samples were insulating and paramagnetic. Contemporaneously, Wang et al. [26] made the x = 0.0, 0.1, 0.2 compositions and found no evidence for the mixed phase behavior found by Hayward. Samples were insulating, and neutron diffraction revealed the absence of long-range magnetic order above 3 K in the parent phase. Some theoretical considerations implicate H^- insertion into the infinite layer nickelates during the reduction process [27, 28]. Such interstitial species could dramatically impact the electronic band structure; however, no direct experimental evidence for this interstitial has been reported in the superconducting films.

The multilayer analogs of "infinite layer" $R_{n+1}Ni_nO_{2n+2}$ (R = La,Pr,Nd) shown in **Figure 1A** are synthesized by reduction of the corresponding Ruddlesden-Popper phase, $R_{n+1}Ni_nO_{3n+1}$. In bulk materials, samples with La, Pr, and Nd have been synthesized with $n \leq 3$ [29–31]. Unlike the infinite layer materials, these compounds can be synthesized at 300°C using dilute mixtures of H_2 in inert gas, or using NaH in organic solvents at a more mild 150°C, as shown by Poltavets [30]. The ease of reduction can be traced to the mixed-valent nature of this family, which implies a fraction of Ni^{2+} for all *n*. Given the square planar coordination, it was conceivable that the divalent Ni could enter as low spin, satisfying the conditions placed by Anisimov for superconductivity [13].

Searching for cuprate analogs, particular attention was paid to the $n = 3$ material, $La_4Ni_3O_8$ (La-438), which formally contains Ni^{1+} and Ni^{2+} in a 2:1 ratio. Work by Poltavets and Greenblatt [29] revealed a semiconductor to metal transition at T = 105 K, which also had a magnetic component. Speculation at the time was that either a CDW or SDW was the cause of this transition, and band structure calculations corroborated this *q*-space mechanism by showing a nested Fermi surface [29]. Other suggestions included charge order among the planes [32]—outer planes Ni^{1+} and inner plane Ni^{2+}—or a spin-state transition mediated by inter-plane coupling through partially-occupied dz^2 orbitals [33]. It was the successful growth of single crystals at Argonne National Laboratory, using a high oxygen pressure floating zone furnace followed by H_2 reduction, that opened a new view on La-438: we showed unambiguously using x-ray and neutron diffraction that the transition results from real space charge- and spin-stripe formation, leading to an insulating ground state (**Figure 1B**, right), with a three-cell repeat set by the hole concentration: 1/3 hole doped into a Ni^{1+} background [34, 35]. The correspondence to the stripes found in hole-doped Ni^{2+}

LSNO (including the diagonal propagation vector) became obvious in hindsight. DFT calculations show that the stripe formation is accompanied by a buckling of the outer Ni-O layers, a prediction verified by high-resolution diffraction measurements [36]. μSR studies by Bernal were found to be consistent with this stripe model [37].

We were also able to grow the Pr analog, $Pr_4Ni_3O_8$ (Pr-438) [38]. As shown in **Figure 1B** (right), Pr-438 is metallic. Pr^{3+} is somewhat smaller than La^{3+}, and this conceivably leads to a wider bandwidth than that of La-438, favoring the metallic ground state rather than the charge- and spin-stripes found for La-438. Notably, however, RIXS measurements on Pr-438 show the same broadened magnon dispersion as found in La-438 (see below) despite no long-range magnetic order, implying that stripe correlations are present here as well. As discussed below, Pr-438 possesses many of the ingredients for cuprate superconductivity. However, its hole concentration is slightly beyond the cuprate superconducting dome, and it remains normal. DFT calculations [39] and ARPES measurements [40] substantiate this picture, revealing an electronic structure like that of overdoped cuprates. Unfortunately, attempts to dope electrons into Pr-438 and shift the hole concentration into the superconducting dome have thus far proven unsuccessful.

Thin Films

Thin film synthesis of LNO was achieved by Kawai et al. [41, 42] using CaH_2 reduction of a perovskite precursor film. It was found to be insulating. This result was subsequently confirmed by Kaneko et al. [43] and Ikeda et al. [44, 45] Regrettably, these groups do not seem to have pursued hole doping into the parent LNO or the effect of using other rare earths than La on the A site. It thus came as a remarkable surprise in August 2019, when the Stanford team led by Harold Hwang reported superconductivity at ≈ 15 K in PLD films of $Nd_{1-x}Sr_xNiO_2$ grown on STO substrates and capped by STO (**Figure 1B**, left) [2]. Synthesis of high quality, superconducting films is challenging, requiring optimization of multiple growth parameters to avoid competing phases of multilayer nickelates and other second phases (**Figure 1A**, right bottom) [46]. While the sample-to-sample variation of T_c shown in these early samples reflects subtle compositional or structural variables, subsequent work has refined the synthesis procedure and revealed a $T_c(x)$ that shows a superconducting dome reminiscent of, and at similar hole concentrations as, the cuprates. Subsequently, other groups have confirmed the Stanford result, and have extended it to show superconductivity in R = La, and Pr analogs [47]. With the Stanford group's announcement, the 30+ year pursuit of nickelate superconductivity had finally reached its hoped-for end, but a new quest for understanding this novel superconductor and its relationship to copper oxides had just begun.

Following on the direction suggested by the bulk trilayer nickelates, a strategy of growing multilayer thin-film nickelates has been pursued by Julia Mundy's group at Harvard through another tour de force in materials growth [3]. While in infinite layer (Nd,Sr)NiO_2 and the putative trilayer $(Pr,Ce)_4Ni_3O_8$ the doping is provided by aliovalent substitution on the A site, it is also possible to self-dope the higher order members of the $R_{n+1}Ni_nO_{2n+2}$ series, as the formal Ni oxidation state follows $(n+1)/n$. Thus, by stacking more layers, the average Ni oxidation state will progressively move into the superconducting dome of the cuprates and the infinite-layer nickelates, entering perhaps at $n = 4$ and certainly by $n = 5$ (See **Figure 2**). This hypothesis proved to be correct, as shown in **Figure 1B** (middle). Here the resistivity of the five-layer material, $Nd_6Ni_5O_{12}$ (nominal Ni oxidation state = 6/5), is shown as a function of temperature and field. A broad superconducting transition is found with T_c (H = 0) around 10 K, making this multilayer, self-doped material the second class of d^9-derived nickelate superconductors and validating a unified a picture of nickelate and cuprate superconducting phase diagrams controlled by *d* electron count.

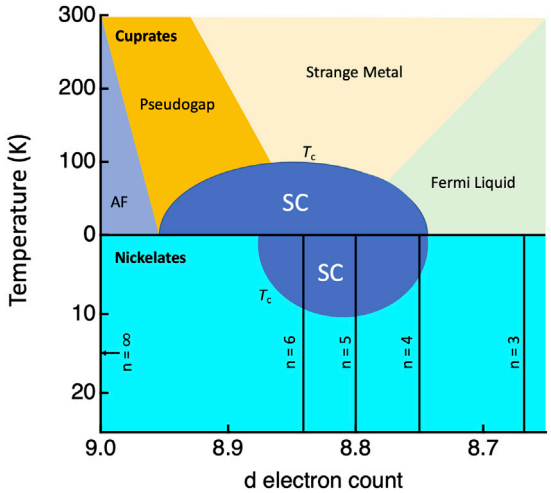

FIGURE 2 | Schematic unified electronic phase diagram of d^9 nickelates and cuprates as a function of *d* electron count. Inspired by Refs. [3, 4] and [38].

d^9 NICKELATES: PHYSICS

We now turn from materials and chemistry to physics to overview the current thinking about the question of how nickelates compare and contrast with the cuprates. Inspired by the cuprate ingredients discussed above, we touch on magnetism and electronic structure and the role of hybridization on the hole wavefunction.

Magnetism

The cuprate parent phase is an antiferromagnetic insulator. As mentioned above, this does not seem to be the case for the infinite layer nickelates, which in bulk are paramagnetic [23, 25, 26]. Nonetheless, Ni L_3-edge RIXS measurements on the superconducting films by Lu et al. [48] find a magnon spectrum consistent with the spin-1/2 antiferromagnetic square lattice found in cuprates. The nearest-neighbor exchange, J_1 = 63 meV, is roughly half that found in copper oxide materials. Mark Dean's group at Brookhaven National Lab has analyzed similar experiments on single crystals of trilayer La-

438 (**Figure 1C**, right), finding a comparable value of $J_1 = 69$ meV, although the nominal doping concentration is quite different [49]. A broadened magnon spectrum observed by this group is consistent with the spin stripes seen by neutrons. It is currently impossible to synthesize the equivalent hole concentration in the trilayer material in bulk or to reach the parent (e.g., $Pr_3CeNi_3O_8$), but DFT calculations indicate the antiferromagnetic square lattice as the ground state of this putative parent phase [39].

Electronic Structure

DFT calculations show that the broad features of the infinite layer nickelate Fermi surface to be much like that of the copper oxides, except for the rare earth *d*-band hole pocket that self-dopes the former [14, 50]. The size of this hole pocket decreases with doping into the superconducting dome. The Wannier orbitals shown in **Figure 1D** (top) bear strong resemblance to the one-electron dx^2-y^2 and dz^2 orbitals expected from simple crystal field considerations [51]. Looking at the multilayer systems [**Figure 1** (bottom)], the number of bands in the dx^2-y^2 manifold increases with *n,* as expected [52].

Whether the nickelates lie in the Mott-Hubbard or charge transfer regime remains a significant controversy in the field. Since before even the earliest mentions of superconductivity in infinite layer nickelates, a Mott picture has been favored due to the larger 3*d*- O 2*p* separation [14]. Modern DFT calculations on the d^9 nickelates support this view [53–56], which leads to less metal-ligand hybridization, and to the inference that Mott physics should be a better descriptor than a charge-transfer insulator model, distancing the d^9 nickelates from cuprates. Experimental support for this picture comes from STEM-EELS measurements that find $NdNiO_2$ lies in the Mott regime, and that with doping, holes appear on the Ni and Nd *d* bands as well as on O [53]. Many-body DMFT calculations have come down on both sides of this divide, but recent calculations seem to favor the Mott picture rather than charge-transfer, which is found for the isostructural cuprate analog $CaCuO_2$ [56]. Experimentally, the prominent O 2*p K*-edge prepeak found in cuprates that signifies strong 3*d*- O 2*p* hybridization is greatly suppressed in the infinite layer materials, although less so in the case of the trilayer material (**Figure 1C**, left). Adding to the uncertainty, the Brookhaven group argues from O *K*-edge RIXS and cluster calculations that neither limit is appropriate for the trilayer La-438; rather, this nickelate is better described as having a mixed Mott-Hubbard/charge-transfer character with significant hole character on O, explaining the large superexchange mentioned above in this material [57]. The jury is still out on hybridization in the d^9 nickelates, but it seems that oxygen states cannot be ignored in a proper description of these materials.

To date, the gold-standard for probing the low-energy physics of copper oxide superconductors, Angle-Resolved Photoemission Spectroscopy (ARPES), has not been applied to the thin film superconducting nickelates. It has, however, been measured on single crystals of the trilayer metal Pr-438 by the Dessau group. In unpublished data, they find a Fermi surface consistent with that of overdoped BSCCO and a large mass enhancement signaling strong correlations [40].

Finally, the crystal field is expected to strongly favor the low-spin configuration on Ni^{2+}. This configuration has indeed been confirmed in the trilayer materials by x-ray absorption spectroscopy, which also shows a strong in plane orbital polarization [38]. Both findings stand as analogous to the cuprate electronic state.

OUTLOOK

To conclude this Perspective, a discussion of open questions and potential directions to pursue is appropriate. Here are a few materials-inspired questions that could direct research in the near term.

Why aren't Bulk d^9 Nickelates Superconducting?

To date, no superconductivity has been found in bulk infinite layer phases at doping levels inside the superconducting dome of thin film specimens or in bulk multilayer systems ($n = 2,3$) that lie outside the dome. This does not mean it is impossible, so what might be the problem? It could be as simple as having the wrong lattice constant. The films are slightly compressively strained vs. freestanding bulk materials, and so perhaps pressure could tip the balance. Unfortunately, pressure studies on $Nd_{0.8}Sr_{0.2}NiO_2$ to 50 GPa show no sign of metallic, let alone superconducting, behavior [25]. Concerning is the structural perfection [2, 46, 53] found in the ultra-thin films that is probably unlikely to be found in bulk materials. Oxygen defects may become disordered or be insufficiently ordered during the low-T reduction. The complex process that takes $RNiO_3$ to $RNiO_2$ passes through multiple known (and perhaps unknown) ordered O vacancy structures [19, 21, 58]. And while single crystals have been made by CaH_2 reduction of $Nd_{0.8}Ca_{0.2}NiO_3$ grown at high P, and they are more metallic than powder samples, there is a low-temperature localization transition and no superconductivity [59]. This may reflect a true Ca content in the crystals that is insufficient to reach the superconducting dome. Further work here is called for.

The message is that we simply may not have optimized materials growth of bulk samples to the same level of perfection as the films. Desperately needed is a direct synthesis of the d^9 nickelate families that does not involve the perovskite reduction process. Such a method per force must be low temperature, as the infinite layer materials begin to disorder and to decompose at or below ~300°C, depending on the rare earth. Such a creative breakthrough in synthesis and growth could be game-changing.

Can Trilayer Materials Be Made SC?

Based on simple *d* count as the key parameter, the trilayer materials are overdoped by a bit (**Figure 2**). Substituting on the Pr site of Pr-438 with a tetravalent ion like Ce^{4+} could in principle adjust the hole count into the dome. Despite extensive efforts, we have failed in this endeavor (A small amount of Ce^{4+} could be substituted into La-438, causing the metal-insulator

transition to shift down from 105 K by 25 K). Other methods could include electric field gating or K-dosing (e.g., in an ARPES chamber) as done for cuprates and iridates [60, 61]. So far no one has succeeded at these strategies. A contrarian approach has been suggested by Dessau: while the focus has been on trying to increase the electron count to bring Pr-438 into the dome, another possibility is that the dz^2 band takes up some holes that need to be in the dx^2-y^2 band, and that hole doping is really needed to tune into superconductivity. However, the recent report of superconductivity in n = 5 $Nd_6Ni_5O_{12}$ films by Mundy et al. [3] (**Figures 1B**, **2**) argues that the electron doping argument is appropriate, although this does not rule out other approaches. Even in the absence of superconductivity, the trilayer materials may hold other interesting stories. For instance, how does the stripe phase of La-438 evolve into the correlated metal Pr-438 at T = 0 K?

What Other Prospects May Be out There?

We have argued in this Perspective that materials synthesis and crystal growth advances have led the way in the rebirth of nickelates. Largely this has emerged as we access and gain better control over materials with Ni in extreme oxidation states spanning from +1 to +4. These synthesis advances have largely been applied to known materials. We should also look to the possibility of other materials — either known or unknown — in the quest for a more complete picture of nickelate superconductivity and the more general understanding of the physics of these highly correlated materials. Hybrid materials such as layered oxide-chalcogenides stand out as an interesting direction to pursue.

As demonstrated by the intense study of LSNO and related Ni^{2+} materials and the long history of the $RNiO_3$ Ni^{3+} perovskites, the rare Earth nickelates as an extended family are more than just the d^9 Ni^{1+} materials, and many open questions remain. What is the magnetic ground state of the rare Earth perovskites? Do dynamic fluctuations exist in the metallic phase of $LaNiO_3$? How does dimensionality evolution from LSNO to $LaNiO_3$ influence the transition from a real space charge stripe insulator to a metal? Many if not all such questions stand at a better place to be answered than they did even a few years ago because of renewed interest and capability in growing crystals under high pressure either by zone techniques or high fugacity solution growth in anvil cells or optimizing thin film growth. We are already seeing new and yet unresolved physics in these crystals: a broad maximum in magnetic susceptibility unknown in powders is universally found in $LaNiO_3$ crystals grown independently by multiple groups around the world [62–64]. Evidence for a polar distortion in perovskite nickelates is growing [65]. A coupled CDW/SDW in the trilayer Ruddlesden-Popper phase $La_4Ni_3O_{10}$ replaces the charge stripes in single layer $La_{2-x}Sr_xNiO_4$, hinting at an evolution between q-space and real space driven instabilities tuned by dimensionality [66].

The nickelate field had already established its longevity and importance to condensed matter science well before superconductivity was discovered in 2019, and the next few years should prove exciting as we learn more about superconducting and non-superconducting systems alike. As we master the synthesis and growth of a wider range of nickel oxides in extreme oxidation states, it is certain that new answers to questions both old and new will be found and that unexpected surprises are virtually guaranteed to emerge.

There is much work to be done. So, let the fields lay fallow, but not for too long.

DATA AVAILABILITY STATEMENT

The original contributions presented in the study are included in the article/Supplementary Materials, further inquiries can be directed to the corresponding author.

AUTHOR CONTRIBUTIONS

This Perspective was conceived and written by JFM.

FUNDING

This work was sponsored by the U.S. Department of Energy, Office of Science, Basic Energy Sciences, Materials Science and Engineering Division.

ACKNOWLEDGMENTS

The author thanks Mike Norman and Daniel Phelan for helpful discussions in the preparation of this manuscript.

REFERENCE

1. Dewey J. *Art as Experience*. New York: Minton, Balch & Company (1934).
2. Li D, Lee K, Wang BY, Osada M, Crossley S, Lee HR, et al. Superconductivity in an Infinite-Layer Nickelate. *Nature* (2019) 572:624–7. doi:10.1038/s41586-019-1496-5
3. Pan GA, Segedin DF, LaBollita H, Song Q, Nica EM, Goodge BH, et al.Superconductivity in a Quintuple-Layer Square-Planar Nickelate. *Nat Mater* (2021). doi:10.1038/s41563-021-01142-9
4. Keimer B, Kivelson SA, Norman MR, Uchida S, Zaanen J, Uchida S, et al. From Quantum Matter to High-Temperature Superconductivity in Copper Oxides. *Nature* (2015) 518:179–86. doi:10.1038/nature14165
5. Zaanen J, Sawatzky GA, Allen JW. Band Gaps and Electronic Structure of Transition-Metal Compounds. *Phys Rev Lett* (1985) 55:418–21. doi:10.1103/physrevlett.55.418
6. Shinomori S, Okimoto Y, Kawasaki M, Tokura Y. Insulator-Metal Transition in La2-xSrxNiO4. *J Phys Soc Jpn* (2002) 71:705–8. doi:10.1143/jpsj.71.705
7. Cheong S-W, Hwang HY, Chen CH, Batlogg B, Rupp LW, Carter SA. Charge-Ordered States in (La,Sr)2NiO4for Hole Concentrationsnh=1/3 and 1/2. *Phys Rev B* (1994) 49:7088–91. doi:10.1103/physrevb.49.7088
8. Katsufuji T, Tanabe T, Ishikawa T, Yamanouchi S, Tokura Y, Kakeshita T, et al. Commensurability Effect on the Charge Ordering ofLa2−xSrxNiO4. *Phys Rev B* (1999) 60:R5097–R5100. doi:10.1103/physrevb.60.r5097

9. Tranquada JM, Buttrey DJ, Sachan V. Incommensurate Stripe Order inLa2−xSrxNiO4withx=0.225. *Phys Rev B* (1996) 54:12318–23. doi:10.1103/physrevb.54.12318
10. Wochner P, Tranquada JM, Buttrey DJ, Sachan V. Neutron-Diffraction Study of Stripe Order inLa2NiO4+δwithδ=215. *Phys Rev B* (1998) 57:1066–78. doi:10.1103/physrevb.57.1066
11. Boothroyd AT, Prabhakaran D, Freeman PG, Lister SJS, Enderle M, Hiess A, et al. Spin Dynamics in Stripe-orderedLa5/3Sr1/3NiO4. *Phys Rev B* (2003) 67: 100407. doi:10.1103/physrevb.67.100407
12. Yoshizawa H, Kakeshita T, Kajimoto R, Tanabe T, Katsufuji T, Tokura Y. Stripe Order at Low Temperatures inLa2−xSrxNiO4with0.289≤x≤0.5. *Phys Rev B* (2000) 61:R854–R857. doi:10.1103/physrevb.61.r854
13. Anisimov VI, Bukhvalov D, Rice TM. Electronic Structure of Possible Nickelate Analogs to the Cuprates. *Phys Rev B* (1999) 59:7901–6. doi:10.1103/physrevb.59.7901
14. Lee K-W, Pickett WE. Infinite-LayerLaNiO2: Ni1+is notCu2+. *Phys Rev B* (2004) 70:165109. doi:10.1103/physrevb.70.165109
15. Lacorre P. Passage from T-type to T′-type Arrangement by Reducing R4Ni3O10 to R4Ni3O8 (R = La, Pr, Nd). *J Solid State Chem* (1992) 97: 495–500. doi:10.1016/0022-4596(92)90061-y
16. Crespin M, Isnard O, Dubois F, Choisnet J, Odier P. LaNiO2: Synthesis and Structural Characterization. *J Solid State Chem* (2005) 178:1326–34. doi:10.1016/j.jssc.2005.01.023
17. Crespin M, Levitz P, Gatineau L. Reduced Forms of LaNiO3perovskite. Part 1.-Evidence for New Phases: La2Ni2O5and LaNiO2. *J Chem Soc Faraday Trans 2* (1983) 79:1181–94. doi:10.1039/f29837901181
18. Levitz P, Crespin M, Gatineau L. Reduced Forms of LaNiO3perovskite. Part 2.-X-ray Structure of LaNiO2and Extended X-ray Absorption fine Structure Study: Local Environment of Monovalent Nickel. *J Chem Soc Faraday Trans 2* (1983) 79:1195–203. doi:10.1039/f29837901195
19. Moriga T, Usaka O, Nakabayashi I, Kinouchi T, Kikkawa S, Kanamaru F. Characterization of Oxygen-Deficient Phases Appearing in Reduction of the Perovskite-type LaNiO3 to La2Ni2O5. *Solid State Ionics* (1995) 79:252–5. doi:10.1016/0167-2738(95)00070-m
20. Moriga T, Usaka O, Nakabayashi I, Hirashima Y, Kohno T, Kikkawa S, et al. Reduction of the Perovskite-type LnNiO3 (Ln=Pr, Nd) to Ln3Ni3O7 with Monovalent Nickel Ions. *Solid State Ionics* (1994) 74:211–7. doi:10.1016/0167-2738(94)90212-7
21. Moriga T, Usaka O, Imamura T, Nakabayashi I, Matsubara I, Kinouchi T, et al. Synthesis, Crystal Structure, and Properties of Oxygen-Deficient Lanthanum Nickelate LaNiO3−x(0 ≤x≤ 0.5). *Bcsj* (1994) 67:687–93. doi:10.1246/bcsj.67.687
22. Hayward MA, Green MA, Rosseinsky MJ, Sloan J. Sodium Hydride as a Powerful Reducing Agent for Topotactic Oxide Deintercalation: Synthesis and Characterization of the Nickel(I) Oxide LaNiO2. *J Am Chem Soc* (1999) 121: 8843–54. doi:10.1021/ja991573i
23. Hayward MA, Rosseinsky MJ. Synthesis of the Infinite Layer Ni(I) Phase NdNiO2+x by Low Temperature Reduction of NdNiO3 with Sodium Hydride. *Solid State Sci* (2003) 5:839–50. doi:10.1016/s1293-2558(03)00111-0
24. Hayward MAThe Synthesis and Characterisation of Some Novel Reduced Transition Metal Oxides. [PhD thesis]. Oxford, United Kingdom: University of Oxford (1999).
25. Li Q, He C, Si J, Zhu X, Zhang Y, Wen H-H. Absence of Superconductivity in Bulk Nd1−xSrxNiO2. *Commun Mater* (2020) 1:16. doi:10.1038/s43246-020-0018-1
26. Wang B-X, Zheng H, Krivyakina E, Chmaissem O, Lopes PP, Lynn JW, et al. Synthesis and Characterization of bulk Nd_{1-x} Sr_x NiO_2 and Nd_{1-x} Sr_x NiO_3. *Phys Rev Mat* (2020) 4:084409. doi:10.1103/physrevmaterials.4.084409
27. Si L, Xiao W, Kaufmann J, Tomczak JM, Lu Y, Zhong Z, et al. Topotactic Hydrogen in Nickelate Superconductors and Akin Infinite-Layer Oxides ABO2. *Phys Rev Lett* (2020) 124:166402. doi:10.1103/physrevlett.124.166402
28. Malyi OI, Varignon J, and Zunger A, arXiv:2107.01790 (2021).
29. Poltavets VV, Lokshin KA, Nevidomskyy AH, Croft M, Tyson TA, Hadermann J, et al. Bulk Magnetic Order in a Two-DimensionalNi1+/Ni2+(d9/d8) Nickelate, Isoelectronic with Superconducting Cuprates. *Phys Rev Lett* (2010) 104:206403. doi:10.1103/physrevlett.104.206403
30. Blakely CK, Bruno SR, Poltavets VV. Low-Temperature Solvothermal Approach to the Synthesis of La4Ni3O8 by Topotactic Oxygen Deintercalation. *Inorg Chem* (2011) 50:6696–6700. doi:10.1021/ic200677p
31. Sakurai Y, Chiba N, Kimishima Y, Uehara M. Electronic and Magnetic Properties of La4Ni3−xCuxO8 and Nd4−ySmyNi3O8. *Physica C: Supercond* (2013) 487:27–30. doi:10.1016/j.physc.2013.02.002
32. Wu H. Charge-spin-orbital States in the Tri-layered Nickelate La4Ni3O8: an Ab Initio Study. *New J Phys* (2013) 15:023038. doi:10.1088/1367-2630/15/2/023038
33. Pardo V, Pickett WE. Quantum Confinement Induced Molecular Correlated Insulating State inLa4Ni3O8. *Phys Rev Lett* (2010) 105:266402. doi:10.1103/physrevlett.105.266402
34. Zhang J, Chen Y-S, Phelan D, Zheng H, Norman MR, Mitchell JF. Stacked Charge Stripes in the quasi-2D Trilayer Nickelate $La_4Ni_3O_8$. *Proc Natl Acad Sci USA* (2016) 113:8945–50. doi:10.1073/pnas.1606637113
35. Zhang J, Pajerowski DM, Botana AS, Zheng H, Harriger L, Rodriguez-Rivera J, et al. Spin Stripe Order in a Square Planar Trilayer Nickelate. *Phys Rev Lett* (2019) 122:247201. doi:10.1103/physrevlett.122.247201
36. Botana AS, Pardo V, Pickett WE, Norman MR. Charge Ordering in Ni1+/Ni2+ Nickelates: La4Ni3 O8 and La3Ni2 O6. *Phys Rev B* (2016) 94:081105. doi:10.1103/physrevb.94.081105
37. Bernal OO, MacLaughlin DE, Morris GD, Ho P-C, Shu L, Tan C, et al. Charge-stripe Order, Antiferromagnetism, and Spin Dynamics in the Cuprate-Analog Nickelate La4Ni3O8. *Phys Rev B* (2019) 100:125142. doi:10.1103/physrevb.100.125142
38. Zhang J, Botana AS, Freeland JW, Phelan D, Zheng H, Pardo V, et al. Large Orbital Polarization in a Metallic Square-Planar Nickelate. *Nat Phys* (2017) 13: 864–9. doi:10.1038/nphys4149
39. Botana AS, Pardo V, Norman MR. Electron Doped Layered Nickelates: Spanning the Phase Diagram of the Cuprates. *Phys Rev Mater* (2017) 1: 021801. doi:10.1103/physrevmaterials.1.021801
40. Li H, Hao P, Zhang J, Gordon K, Linn AG, Zheng H, et al.,submitted.
41. Kawai M, Inoue S, Mizumaki M, Kawamura N, Ichikawa N, Shimakawa Y. Reversible Changes of Epitaxial Thin Films from Perovskite LaNiO3 to Infinite-Layer Structure LaNiO2. *Appl Phys Lett* (2009) 94:082102. doi:10.1063/1.3078276
42. Kawai M, Matsumoto K, Ichikawa N, Mizumaki M, Sakata O, Kawamura N, et al. Orientation Change of an Infinite-Layer Structure LaNiO2 Epitaxial Thin Film by Annealing with CaH2. *Cryst Growth Des* (2010) 10:2044–6. doi:10.1021/cg100178y
43. Kaneko D, Yamagishi K, Tsukada A, Manabe T, Naito M. Synthesis of Infinite-Layer LaNiO2 Films by Metal Organic Decomposition. *Physica C: Supercond* (2009) 469:936–9. doi:10.1016/j.physc.2009.05.104
44. Ikeda A, Krockenberger Y, Irie H, Naito M, Yamamoto H. Direct Observation of Infinite NiO2planes in LaNiO2films. *Appl Phys Express* (2016) 9:061101. doi:10.7567/apex.9.061101
45. Ikeda A, Manabe T, Naito M. Comparison of Reduction Agents in the Synthesis of Infinite-Layer LaNiO2 Films. *Physica C: Superconductivity its Appl* (2014) 506:83–6. doi:10.1016/j.physc.2014.09.002
46. Lee K, Goodge BH, Li D, Osada M, Wang BY, Cui Y, et al. Aspects of the Synthesis of Thin Film Superconducting Infinite-Layer Nickelates. *APL Mater* (2020) 8:041107. doi:10.1063/5.0005103
47. Lin H, Gawryluk DJ, Klein YM, Huangfu S, Pomjakushina E, Rohr FV, et al.,arXiv:2104.14324 (2021).
48. Lu H, Rossi M, Nag A, Osada M, Li DF, Lee K, et al. Magnetic Excitations in Infinite-Layer Nickelates. *Science* (2021) 373:213–6. doi:10.1126/science.abd7726
49. Lin JQ, Arribi PV, Fabbris G, Botana AS, Meyers D, Miao H, et al. Strong Superexchange in a d{9-δ} Nickelate Revealed by Resonant Inelastic X-Ray Scattering. *Phys Rev Lett* (2021) 126:087001. doi:10.1103/physrevlett.126.087001
50. Choi M-Y, Lee K-W, Pickett WE. Role of 4 F States in Infinite-Layer $NdNiO_2$. *Phys Rev B* (2020) 101:020503. doi:10.1103/physrevb.101.020503
51. Hepting M, Li D, Jia CJ, Lu H, Paris E, Tseng Y, et al. Electronic Structure of the Parent Compound of Superconducting Infinite-Layer Nickelates. *Nat Mater* (2020) 19:381–5. doi:10.1038/s41563-019-0585-z
52. LaBollita H, Botana AS. Tuning the Van Hove Singularities inAV3Sb5(A=K,Rb,Cs)via Pressure and Doping. *Phys Rev B* (2021) 104: 035148. doi:10.1103/physrevb.104.205129
53. Goodge BH, Li D, Lee K, Osada M, Wang BY, Sawatzky GA, et al. Doping Evolution of the Mott-Hubbard Landscape in Infinite-Layer Nickelates. *Proc Natl Acad Sci USA* (2021) 118:e2007683118. doi:10.1073/pnas.2007683118
54. Hepting M, Green RJ, Zhong Z, Bluschke M, Suyolcu YE, Macke S, et al.Complex Magnetic Order in Nickelate Slabs. *Nat Phys* (2019) 14 (11): 1097–1102. doi:10.1038/s41567-018-0218-5

55. Jiang M, Berciu M, Sawatzky GA. Critical Nature of the Ni Spin State in Doped NdNiO2. *Phys Rev Lett* (2020) 124:207004. doi:10.1103/physrevlett.124.207004
56. Karp J, Hampel A, Zingl M, Botana AS, Park H, Norman MR, et al. Comparative many-body Study of Pr4Ni3O8 and NdNiO2. *Phys Rev B* (2020) 102:245130. doi:10.1103/physrevb.102.245130
57. Shen Y, Sears J, Fabbris G, Li J, Pelliciari J, Jarrige I, et al.,arXiv:2110.08937 (2021)
58. Wang B-X, Rosenkranz S, Rui X, Zhang J, Ye F, Zheng H, et al. Antiferromagnetic Defect Structure in LaNi $O_{3-\delta}$ Single Crystals. *Phys Rev Mat* (2018) 2:064404. doi:10.1103/physrevmaterials.2.064404
59. Puphal P, Wu YM, Fürsich K, Lee H, Pakdaman M, Bruin J, et al.Topotactic Transformation of Single Crystals: From Perovskite to Infinite-Layer Nickelates. *Sci Adv* (2021). 7:eabl8091.
60. Hossain MA, Mottershead JDF, Fournier D, Bostwick A, McChesney JL, Rotenberg E, et al. *In Situ* doping Control of the Surface of High-Temperature Superconductors. *Nat Phys* (2008) 4:527–31. doi:10.1038/nphys998
61. Kim YK, Sung NH, Denlinger JD, Kim BJ. Observation of a D-Wave gap in Electron-Doped Sr2IrO4. *Nat Phys* (2016) 12:37–41. doi:10.1038/nphys3503
62. Dey K, Hergett W, Telang P, Abdel-Hafiez MM, Klingeler R. Magnetic Properties of High-Pressure Optical Floating-Zone Grown LaNiO3 Single Crystals. *J Cryst Growth* (2019) 524:125157. doi:10.1016/j.jcrysgro.2019.125157
63. Guo H, Li ZW, Zhao L, Hu Z, Chang CF, Kuo CY, et al.Antiferromagnetic Correlations in the Metallic Strongly Correlated Transition Metal Oxide $LaNiO_3$. *Nat Commun* (2017) 9:43. doi:10.1038/s41467-017-02524-x
64. Zhang J, Zheng H, Ren Y, Mitchell JF. High-Pressure Floating-Zone Growth of Perovskite Nickelate LaNiO3 Single Crystals. *Cryst Growth Des* (2017) 17:2730–5. doi:10.1021/acs.cgd.7b00205
65. Ardizzone I, Teyssier J, Crassee I, Kuzmenko AB, Mazzone DG, Gawryluk DJ, et al. Raman Spectroscopic Evidence for Multiferroicity in Rare Earth Nickelate Single Crystals. *Phys Rev Res* (2021) 3:033007. doi:10.1103/physrevresearch.3.033007
66. Zhang J, Phelan D, Botana AS, Chen Y-S, Zheng H, Krogstad M, et al. Intertwined Density Waves in a Metallic Nickelate. *Nat Commun* (2020) 11:6003. doi:10.1038/s41467-020-19836-0

Conflict of Interest: The author declares that the research was conducted in the absence of any commercial or financial relationships that could be construed as a potential conflict of interest.

frontiers in Physics

BRIEF RESEARCH REPORT
published: 10 January 2022
doi: 10.3389/fphy.2021.810220

Oxygen Hole Character and Lateral Homogeneity in $PrNiO_{2+\delta}$ Thin Films

*K. Fürsich[1], R. Pons[1], M. Bluschke[1], R. A. Ortiz[1], S. Wintz[2], E. Schierle[3], M. Weigand[3], G. Logvenov[1], G. Schütz[2], B. Keimer[1] and E. Benckiser[1]**

[1]Max Planck Institute for Solid State Research, Stuttgart, Germany, [2]Max Planck Institute for Intelligent Systems, Stuttgart, Germany, [3]Helmholtz-Zentrum Berlin für Materialien und Energie, Berlin, Germany

Using x-ray absorption spectroscopy with lateral resolution from the submillimeter to submicrometer range, we investigate the homogeneity, the chemical composition, and the nickel 3*d*- oxygen 2*p* charge transfer in topotactically reduced epitaxial $PrNiO_{2+\delta}$ thin films. To this end, we use x-ray absorption spectroscopy in a standard experimental setup and in a soft x-ray microscope to probe the element and spatially resolved electronic structure modifications through changes of the nickel-2*p* and oxygen-1*s* absorption spectrum upon soft-chemistry reduction. We find that the reduction process is laterally homogeneous across a partially reduced $PrNiO_{2+\delta}$ thin film sample for length scales down to 50 nm.

Keywords: infinite-layer nickelates, x-ray absorption spectroscopy, x-ray microscopy, topotactical soft chemistry reduction, rare-earth nickelates films

OPEN ACCESS

Edited by:
Danfeng Li,
City University of Hong Kong, Hong Kong SAR, China

Reviewed by:
Motoki Osada,
Stanford University, United States
Atsushi Fujimori,
The University of Tokyo, Japan
Zhihai Zhu,
Institute of Physics (CAS), China

****Correspondence:***
E. Benckiser
E.Benckiser@fkf.mpg.de

Specialty section:
This article was submitted to Condensed Matter Physics, a section of the journal Frontiers in Physics

Received: *06 November 2021*
Accepted: *08 December 2021*
Published: *10 January 2022*

Citation:
Fürsich K, Pons R, Bluschke M, Ortiz RA, Wintz S, Schierle E, Weigand M, Logvenov G, Schütz G, Keimer B and Benckiser E (2022) Oxygen Hole Character and Lateral Homogeneity in $PrNiO_{2+\delta}$ Thin Films. Front. Phys. 9:810220. doi: 10.3389/fphy.2021.810220

1 INTRODUCTION

Although theoretically considered already decades ago [1], superconductivity in nickelates with infinite-layer structure was only realized recently [2]. In particular, Sr and Ca-doped rare-earth nickelate thin films with composition $RNiO_2$ (R = La, Pr, Nd) show a superconducting transition below 9–15 K [3–6]. This discovery triggered a lot of research activity that uncovered similarities [1, 7], but also significant differences [8, 9] between nickelates and cuprates. It remains to be seen whether it is the similarity or the difference that will contribute to our understanding of unconventional superconductivity. Before that, however, many questions about these superconducting nickelates still have to be answered. These concern in particular the role of heteroepitaxy with the underlying substrate, the exact chemical composition and crystal structure as well as the homogeneity of the distribution of the dopant ions and the oxygen removal.

To date superconductivity in nickelates has only been realized in epitaxially stabilized thin films, including the related, topotactically-reduced Ruddlesden-Popper compounds [10]. Such heterostructures are a challenge for standard characterization tools such as neutron scattering due to their small sample mass. Hence, x-ray absorption (XAS) and resonant x-ray scattering studies provided significant insights into the ground state and electronic structure of infinite-layer nickelates, and therefore serve as important experimental probes to compare nickelates and cuprates.

XAS and resonant inelastic x-ray scattering (RIXS) at Ni-L edge energies revealed a doping dependent electronic structure of infinite-layer nickelates and indicate a d^8 spin-singlet ground state, where the doped holes occupy the $d_{x^2-y^2}$ orbitals in analogy to single-band Hubbard models [11]. A high-resolution RIXS study identified spin excitations in infinite-layer nickelates with a bandwidth of 200 meV [12], which can be explained in terms of dynamical correlations giving rise to large antiferromagnetic nearest-neighbor exchange interactions [13]. Along these lines, several studies point towards the importance of the itinerant electrons from the rare-earth ions, and their hybridization with the Ni d states, in particular for the exchange coupling, and for

superconductivity in general [14]. Further XAS studies at the Ni-*L* edge focused on the Ni-O hybridization and found that the hybridization can be modulated by the film thickness [6].

Due to the hybridization between Ni-3*d* and O-2*p* states, XAS at the O-*K* edge serves as another independent characterization tool in transition metal oxides. In particular, O-*K* edge XAS measurements revealed a prominent pre-peak, indicative of the strong $3d - 2p$ hybridization between nickel and oxygen, and the negative charge-transfer character of perovskite $R\mathrm{NiO_3}$. Since this feature is indiscernible in infinite-layer $R\mathrm{NiO_2}$ [14, 15, 11, 16], the well-isolated pre-peak (usually at around 528 eV) serves as a reliable characteristic to track the state of reduction of the sample under investigation. In addition, the absence of strong Ni-O hybridization in infinite-layer nickelates suggests a clear difference to superconducting cuprates with strong Cu-O hybridization [17]. A recent scanning-transmission electron microscopy (STEM) and electron energy loss spectroscopy (EELS) study on infinite-layer nickelate thin films reported that with increasing hole-doping an additional spectral weight emerges at around 529 eV, which is imposed on the rising edge of the O-*K* edge [15]. This feature is attributed to $d^9\,\underline{L}$ states, where $\underline{L}$ represents a hole residing on the oxygen ligands. This phenomenology is reminiscent of hole-doped cuprates, where the Zhang-Rice singlet arises when holes are doped into the CuO_2 planes.

The above studies have given important insights into the phase behavior in rare-earth nickelates and the topotactic stabilization of the infinite layer phase. While this soft-chemistry synthesis of the infinite-layer phase with different rare-earth elements and/or doping levels has already been extensively dealt with in several studies, information on the lateral, spatial distribution of oxygen content and Ni valence state has so far been little investigated. Since superconductivity was only observed in epitaxial thin layers, the question arises to what extent the reduction process is sample-specific here. In particular, lattice defects resulting from the lattice mismatch with the substrate, spatially varying cation stoichiometry as a result of the growth process, and islands resulting from mixed layer-by-layer and island growth typical of these nickelate layers, are areas where an inhomogeneous reduction can occur. Therefore, spatially resolved information about the oxidation state and the oxygen de-intercalation pathways in these compounds may reveal strategies for enhancing superconductivity in the nickelates.

Here we present results from XAS, measured in total-electron yield in a standard setup and in an x-ray microscope, to study spatial variations of the Ni valence state and oxygen stoichiometry in reduced nickelates over a large lateral scale. We observe high homogeneity down to a lateral length scale of ~ 50 nm.

2 METHODS

The investigated sample is a 15 nm-thick $PrNiO_3$ film on (110)-oriented $NdGaO_3$ that was grown by ozone-assisted atomic layer-by-layer molecular beam epitaxy (MBE). The growth was performed by sequentially opening the Pr and Ni effusion cells under an ozone atmosphere of 2.4×10^{-5} mbar, while the substrate was heated to about 600°C. Before growth, the effusion cell evaporation rates were determined in vacuum using a quartz crystal microbalance. The rates were then constantly adjusted during growth according to the reflection high-energy electron diffraction (RHEED) feedback. The as-grown sample was cut in several pieces, where one piece was kept pristine, while the others were topotactically reduced. We used CaH_2 as the reduction agent, which was physically separated from the sample in an evacuated quartz glass ampoule and heated at 250 °C for 12 h (not including the 30 min to ramp our oven up from room temperature), following previously established protocols [16, 18, 2].

All samples were characterized by in-house hard x-ray diffraction to track changes in the out-of-plane lattice constant *c* upon reduction (see **Figure 1**). For the pristine perovskite $PrNiO_3$ sample we find $c = 3.79\,\mathring{A}$, slightly smaller than the bulk value due to moderate tensile strain imposed by the $NdGaO_3$ substrate. Upon reduction, the out-of-plane lattice spacing is substantially reduced corresponding to a value of $c = 3.62\,\mathring{A}$, which is larger than $c = 3.31\,\mathring{A}$ reported for $PrNiO_2$ grown on $SrTiO_3$ in Ref. [5]. This deviation results from a combination of the different lattice mismatch with the substrates and an incomplete transition to the infinite-layer phase. Corroborated by our O-*K* edge XAS measurements and the comparison to literature we estimate the stoichiometry of our film to be close to $PrNiO_{2.3}$ [19–21]. We take advantage of this and use the partially reduced nickelate film to examine possible oxygen inhomogeneities and/or identify possibly non-reduced areas.

We used both endstations of the UE46 beamline of BESSY II at the Helmholtz-Zentrum Berlin. XAS measurements over a large sample area were carried out in the XUV diffractometer at UE46-PGM1, while we used the x-ray microscope (UE46-MAXYMUS endstation) [22] to map out the chemical composition and electronic structure with up to four orders of magnitude higher spatial resolution. For the standard XAS measurements the footprint of the beam on the sample was approximately 250 µm × 200 µm, while the energy-dependent XAS measurements at MAXYMUS were performed with a beam diameter of ≈ 5 µm ("defocused beam"). For the spatially resolved image maps at fixed energies, we further decreased the beam footprint to facilitate a spatial resolution of 50 nm. All XAS measurements were performed at room temperature with horizontally polarized light at normal incidence $\theta = 90°$ and in total-electron yield (TEY) mode. The probing depth in our measurements is limited by the electron escape depth, which is below 10 nm (approximately one third of our sample thickness) for energies of relevance here.

All spectra taken across the Ni-*L* edge are normalized to the post-edge region (around 876 eV), whereas the data measured across the O-*K* edge were normalized to the value at 536 eV. To facilitate a comparison between energy and image scans, we normalized the image scans to the exposure time and the number of photons (among others determined by the opening of the exit slits).

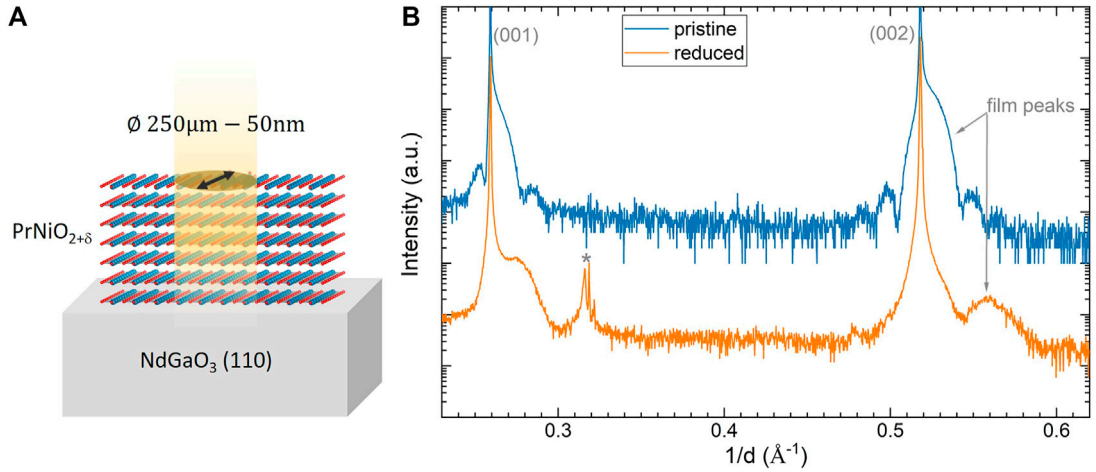

FIGURE 1 | (A) Sketch of the $PrNiO_{2+\delta}$ thin film on a $NdGaO_3$ substrate, indicating the large variation of the soft x-ray beam diameter used to investigate its lateral chemical homogeneity. **(B)** Hard x-ray diffraction around the (001) and (002) $NdGaO_3$ substrate reflection for the pristine (blue) and the 12 h at 250°C reduced (orange) sample. The film peaks close to the (002) substrate peak are indicated and the star marks a peak arising from the sample holder.

3 RESULTS

3.1 X-Ray Absorption Spectroscopy

Figure 2A shows the XAS measurements taken in the standard experimental setup at the Ni-*L* edge for both pristine and reduced pieces of the same sample. For the pristine piece, we observe the well-known double-peak structure at the Ni-L_3 edge, indicative of charge fluctuations in the metallic phase [23–25]. Upon topotactical reduction, both the Ni-L_2 and L_3 edges shift towards lower energies, suggesting the transition from a Ni^{3+} oxidation state towards Ni^{2+} and Ni^{1+} [11]. We note that these energy shifts imprint also changes of the crystal/ligand field, since the pristine sample has a perovskite structure, whereas the reduced sample adopts an infinite-layer phase, in which apical oxygen ions are successively removed [4, 16]. Without analyzing further details of the spectral features, we consider the difference spectrum, as it clearly reflects the essential changes upon reduction. We observe an increase in spectral weight at lower energies, which at the L_3 edge, is maximal at E_A and is associated with a loss of weight at higher energy, labeled E_B in **Figure 2**. A previous study on $SmNiO_x$ films showed that similar changes in the XAS were already observed between non-stoichiometric $SmNiO_{2.92}$ and $SmNiO_{2.63}$ [19]. From the comparison with this data, we estimate the oxygen stoichiometry of our film to be around 2.3, i.e. already relatively close to the desired stoichiometry, but with the option of testing the lateral homogeneity of the distribution of the remaining 0.3 oxygen ions per formula unit and thus evaluating the reduction process.

To get a first impression on the spatial homogeneity of the reduction process, we next investigate the very same samples by XAS measurements with a much smaller beam footprint [≈ 5µm available at the x-ray microscope, *i.e.* a factor of 50 smaller compared to data in **Figure 2A**. **Figure 2B** shows these XAS measurements at the Ni-*L* edge for both, pristine and reduced sample pieces. The data agrees well with the XAS measurements on the respective pieces with the much larger beam (≈ 250µm, see **Figure 2A**). This indicates already that the Ni oxidation state and consequently the oxygen stoichiometry of the reduced sample is spatially homogeneous at the µm length scale.

We repeat the same measurements for pristine and reduced samples with the small and large beam sizes at the O-*K* edge. **Figure 3** panels A and B show XAS measurements with a beamsize of ≈ 250µm and 5 µm, respectively. As was the case at the Ni-*L* edge, the two spectra taken with different beam sizes resemble each other closely. In particular, we identify the following features: A rather sharp prepeak with the spectral weight centered around 528 eV ("pre-peak") vanished upon reduction in agreement with previous studies [14, 15]. Additionally, we observe an increase in the spectral weight upon reduction in a broad range between 531 eV and 534 eV. Previous studies on Sr-doped $LaNiO_2$ [15] and self-doped $La_4Ni_3O_8$ [21] have associated emerging spectral weight below 531 eV as a contribution reminiscent of the Zhang-Rice singlet in hole-doped cuprates. The increase in the spectral weight we observe here is clearly higher in energy. In cuprates it is possible to adjust the doping required for superconductivity via the oxygen content. Similarly, one would also expect this to be possible for the nickelates. According to our estimation, we expect a doping level close to that of the $La_4Ni_3O_8$ samples from Ref. [21], where a clear pre-peak at 530 eV was observed. A very small spectral weight gain is also observed in our O-*K* data, however much smaller than the additional weight above 531 eV. Hence we conclude that a partial oxygen reduction of infinite-layer nickelate films causes a different modification of the electronic structure than the one realized in the $La_4Ni_3O_8$ single crystals. A possible explanation could be a Hund's

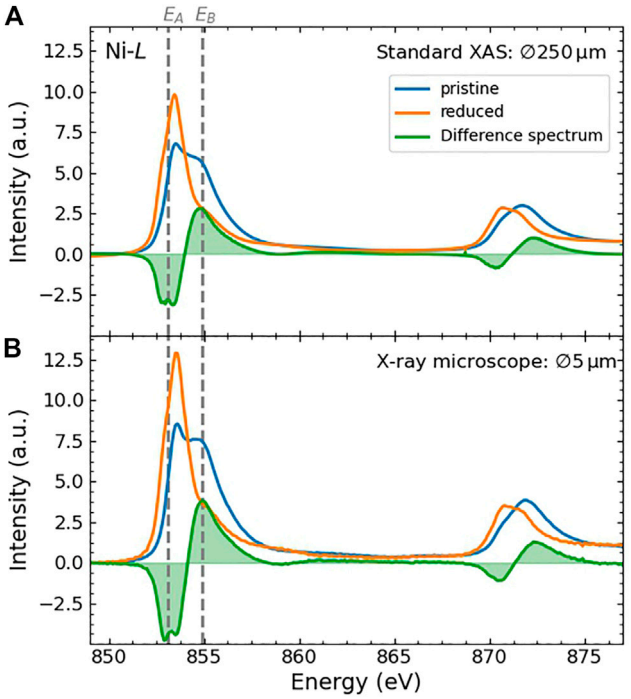

FIGURE 2 | XAS measurements across the Ni *L*-edge from a pristine and reduced $PrNiO_3$ thin film in a standard experimental setup **(A)** and with an x-ray microscope **(B)**. The latter measurement agrees well with XAS measured using a much larger beam, shown in panel **(A)**. From the difference spectrum (green curve), we extract two energies E_A = 853.1 eV and E_B = 854.9 eV, where the contrast between pristine and reduced is the largest. The two energies are indicated by gray dashed lines. Subsequently, we take image scans with varying size/resolution at peak A and B on the reduced sample to check for possible oxygen inhomogeneities (see **Figure 4**).

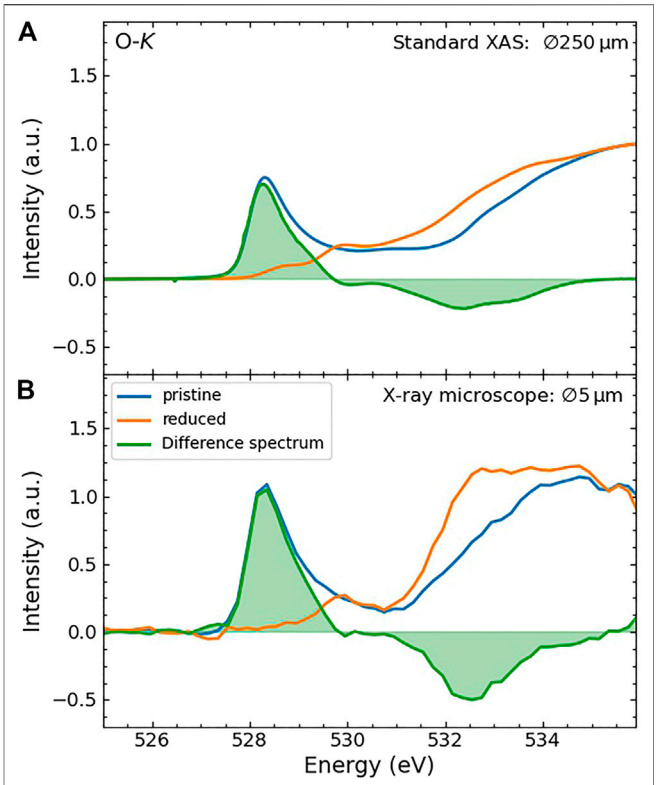

FIGURE 3 | Oxygen *K*-edge XAS measurements for both the pristine and reduced $PrNiO_3$ thin film in a standard experimental setup **(A)** and at the x-ray microscope **(B)**. The spectral weight around 528 eV ("pre-peak") vanishes upon reduction, in agreement with previous studies.

coupling stabilized trapping of holes at sites with a remaining apical oxygen, similar to what was inferred for layer-selective reduced $LaNiO_{2+\delta}$-$LaGaO_3$ superlattices [16].

3.2 X-Ray Microscopy

We now move to a detailed investigation of the lateral distribution of oxygen inhomogeneity in the reduced $PrNiO_{2+\delta}$ films and the associated Ni 3*d* state filling. To this end we exploit the unprecedented capabilities of an x-ray microscope such as MAXYMUS to spatially resolve features with a resolution down to 50 nm. We studied the spatial distribution of the oxygen content using image scans, *i.e.* the incident energy is fixed while we record the TEY signal at different locations across the sample. Since the absorption signal and consequently the corresponding (absolute) contrast, is much higher at the Ni-*L* edge, we use the Ni-L_3 edge for our spatially resolved study, instead of the O-*K* edge. To maximize sensitivity to potential inhomogenieties, we choose the energies for the subsequent mapping to be at the maximum difference between the reduced and pristine sample (see **Figure 2**, green line). Following this procedure, we identify two energies: peak *A* at E_A = 853.1 eV and peak *B* at E_B = 854.9 eV, which are indicated with dashed gray lines in **Figure 2**.

We performed several image scans with varying spatial resolution and incident energies E_A and E_B as shown in the upper row of **Figure 4**. In the image scans with different lateral resolution, we find similar intensities across the investigated sample region, which indicates a spatially homogeneous Ni valence and the associated homogeneity of the oxygen distribution. Additionally we show the difference image for the two images taken at peak *A* and *B*. We emphasize that for possibly unreduced sample areas, we would expect a negative contrast (dark red in the chosen colour scheme). As can be seen from the difference image, we do not identify such contrast regions and hence conclude at the length scale investigated here (> 50 nm) the oxygen stoichiometry is laterally constant. This observation is further supported by analysing the image scans using histrograms (lower row of the corresponding **Figure 4**). Here, we group the pixels according to their intensity and subsequently show the number of pixels versus the normalized intensity. This representation illustrates that the intensity is evenly distributed around the value expected for a fully and homogeneously reduced sample.

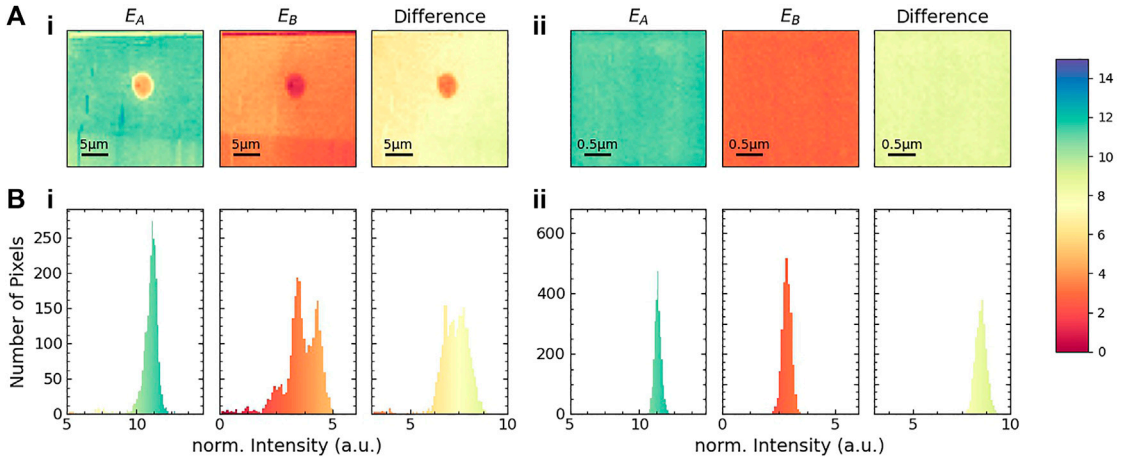

FIGURE 4 | Spatially resolved XAS measurements of the $PrNiO_{2+\delta}$ thin film. *upper row:* Image scans at peak A, peak B, and the difference image: A—B for two different image, and corresponding pixel sizes. The images on the left (right) have a lateral size of 25 µm × 25 µm (2.5 µm × 2.5 µm). This corresponds to a resolution, *i.e.*, pixel size, of 500 and 50 nm for left and right panels, respectively. The colorbar on the right side gives the normalized intensity for all image scans. **(Bi, Bii)***:* Histograms of the images shown in the **(Ai, Aii)**. For both image sizes, the intensity distribution is centered around the TEY value from the energy scan (**Figure 2**) of the reduced film. Note that all scans (image and energy scans) were taken in TEY mode at room temperature. The artifact (dot-like structure) in the larger images (upper left) probably results from surface contamination or surface defects, lowering the overall XAS intensity of the underlying sample. We emphasize that this is a region of reduced XAS signal, and can in particular not be identified as an unreduced patch, which would appear in dark red in the difference image and brighter than the background in the E_B image.

4 DISCUSSION

Due to a lack of studies on the lateral, spatially resolved properties of the infinite-layer nickelates[1], we compare and relate our x-ray microscopy study to similar experiments on other perovskite compounds, including the RNiO$_3$. In particular, we focus on photo-emission electron microscopy (PEEM) and magnetic resonant elastic x-ray scattering (REXS) to review the spatial distribution of different characteristics, such as the metal-to-insulator transition and magnetic domain structures.

In the following paragraphs, we illustrate that our study allows to rule out lateral inhomogeneities with length scales similar to those observed in other related oxide compounds. Several PEEM studies investigate the spatial variation of different characteristics in $SrTiO_3$, a prototypical and widely studied oxide material. Ferromagnetic domains, randomly distributed in $SrTiO_3$, have a typical size of approx. 40 nm at room temperature [27]. Further, domains in the $SrTiO_3$ surface polarization [28] originating from local defects, studied with PEEM using a 400 nm-sized beam revealed polarized regions with sizes of several µm. Consequently, we argue that possible spatial variations of our reduced samples within these typical length scales should have been visible in our study, and hence this points again towards a laterally homogeneous topotactical reduction.

A spatially resolved study of the metal-to-insulator transition (MIT) in $NdNiO_3$ epitaxial thin films was carried out by Mattoni *et al.* [29]. The authors use PEEM with a resolution of a few tens of nm, which is very comparable to our x-ray microscopy study. The PEEM contrast results from the difference of the XAS spectra for metallic and insulating regions and can be quantified as the ratio of the difference between metallic and insulating regions to the XAS intensity at a specific energy, resulting in a maximal PEEM contrast at the Ni-L_3 edge of approx. 1%. This contrast is enough to map the evolution and nucleation of metallic/insulating domains upon warming/cooling and to identify structures of approx. 250 nm (smaller length scale of the structure). Comparing the PEEM contrast of this study to our x-ray microscopy experiment [c.f. **Figure 2**, ratio of difference spectrum (green line) to XAS intensity (orange) at peak *A* of the reduced sample], we expect a contrast of approx. 50% , thereby more than one order of magnitude higher. We therefore conclude, that variations on similar length scales as those of locally distinct T_{MIT} would have been visible in our experiment, if present.

Comparing our results with the study of magnetic domains in $NdNiO_3$ using nanoprobe magnetic scattering of the characteristic antiferromagnetic (AFM) peak, which reveals magnetic textures with sizes of several hundred nm up to 250 µm [30]. The lateral resolution of this study is 100 nm and hence very comparable to our investigation. While the magnetic structure in the perovskite phase seems to be modulated within length scales of hundreds of nm, we do not find any indications of variation in the oxygen content at a similar length scale.

Finally, we compare our x-ray microscopy study to available scanning transmission electron microscopy measurements on nickelates. In particular, STEM-EELS constitutes a

[1]To the best of our knowledge, Ref. [26] is the only available spatially resolved study comparing layered and perovskite oxides. The authors use electrochemical strain microscopy to investigate surfaces of Co-based compounds with a resolution of 10 nm and reveal electrochemical activity on the length scales of approx. 50 to 100 nm.

complementary method to map out the chemical composition of oxide materials within atomic resolution. Superconducting Sr-doped $NdNiO_2$ thin films have been studied with STEM, indicating defects, primarily resulting from stacking faults of the Ruddlesden-Popper-type [3, 15]. However, a detailed investigation of the oxygen positions, including potential variations of the reduction state, is still lacking in thin film compounds. A comprehensive STEM-EELS characterization of infinite-layer $La_{1-x}Ca_xNiO_{2+\delta}$ single crystals indicates that some apical oxygen atoms remain after the topotactic reduction [31]. This suggests that the soft chemistry reduction process might be non-homogeneous on the length scale of single atoms, while still most parts of the sample transition to the infinite-layer phase. Atomic resolution is beyond the capabilities of our x-ray microscope. We emphasize that despite the somewhat better spatial resolution in STEM studies, x-ray microscopy has the advantage of being a destruction-free method. Additionally, the samples are easy to prepare (if we consider the TEY mode that is used in our study), and in particular several etching and milling processes, which are necessary for STEM specimen preparation, can be avoided, thereby maintaining the sensitive oxygen stoichiometry.

5 SUMMARY

In summary, we used total electron yield XAS both in a standard experimental configuration and in an x-ray microscope to probe topotactically reduced $PrNiO_{2+\delta}$. We confirm a spatially homogeneous oxidation state within the length scales probed in our experiment (resolution approx. 50 nm). Consequently, we conclude that the oxygen de-intercalation processes upon soft-chemistry reduction from the perovskite precursor to infinite-layer phase occurs homogeneously across the sample. Our study illustrates the power of non-destructive spatially-resolved XAS measured in an x-ray microscope to confirm lateral homogeneity in correlated oxide materials. In the future it would be interesting to study the depth-depended oxidation profiles to investigate possible differences in the reduction of layers next to the surface or interface and the inner layers in infinite layer nickelates.

DATA AVAILABILITY STATEMENT

The raw data supporting the conclusions of this article will be made available by the authors, without undue reservation.

AUTHOR CONTRIBUTIONS

EB, KF, and MB conceived the project. The samples were grown, reduced, and characterized by RP, where RO provided guidance on the reduction procedure. The spatially resolved data was taken by KF, SW, and MW with remote support from MB and RP. The standard XAS measurements were performed by KF, RP and ES. KF performed the data analysis. KF and EB wrote the manuscript with input from all co-authors. GS, BK, and EB coordinated the project.

FUNDING

We acknowledge financial support by the Center for Integrated Quantum Science and Technology (IQ^{ST}) and the Deutsche Forschungsgemeinschaft (DFG, German Research Foundation): Projektnummer 107745057—TRR 80.

ACKNOWLEDGMENTS

We thank HZB for the allocation of synchrotron radiation beamtime.

REFERENCES

1. Anisimov VI, Bukhvalov D, Rice TM. Electronic Structure of Possible Nickelate Analogs to the Cuprates. *Phys Rev B* (1999) 59:7901–6. doi:10.1103/PhysRevB.59.7901
2. Li D, Lee K, Wang BY, Osada M, Crossley S, Lee HR, et al. Superconductivity in an Infinite-Layer Nickelate. *Nature* (2019) 572:624–7. doi:10.1038/s41586-019-1496-5
3. Li D, Wang BY, Lee K, Harvey SP, Osada M, Goodge BH, et al. Superconducting Dome in $Nd_{1-x}Sr_xNiO_2$ Infinite Layer Films. *Phys Rev Lett* (2020) 125:027001. doi:10.1103/PhysRevLett.125.027001
4. Zeng S, Tang CS, Yin X, Li C, Li M, Huang Z, et al. Phase Diagram and Superconducting Dome of Infinite-Layer $Nd_{1-x}Sr_xNiO_2$ Thin Films. *Phys Rev Lett* (2020) 125:147003. doi:10.1103/PhysRevLett.125.147003
5. Osada M, Wang BY, Lee K, Li D, Hwang HY. Phase Diagram of Infinite Layer Praseodymium Nickelate Pr1−$_{x}$Sr$_{x}$N$_{i}$O2 $_{T}$hin Films. *Phys .Rev .Mater* (2020) 4: 121801. doi:10.1103/PhysRevMaterials.4.121801
6. Zeng SW, Yin XM, Li CJ, Tang CS, Han K, Huang Z, et al. *Observation of Perfect Diamagnetism and Interfacial Effect on the Electronic Structures in nd0.8sr0.2nio2 Superconducting Infinite Layers* (2021). arXiv:2104.14195.
7. Zhang Y, Lin LF, Hu W, Moreo A, Dong S, Dagotto E. Similarities and Differences between Nickelate and Cuprate Films Grown on a $Srtio_3$ Substrate. *Phys Rev B* (2020) 102:195117. doi:10.1103/PhysRevB.102.195117
8. Lee KW, Pickett WE. Infinite-layer $LaNio_2$: Ni^{1+} Is Not Cu^{2+}. *Phys Rev B* (2004) 70:165109. doi:10.1103/PhysRevB.70.165109
9. Botana AS, Norman MR. Similarities and Differences between $Lanio_2$ and $Cacuo_2$ and Implications for Superconductivity. *Phys Rev X* (2020) 10:011024. doi:10.1103/PhysRevX.10.011024
10. Pan GA, Segedin DF, LaBollita H, Song Q, Nica EM, Goodge BH, et al. Superconductivity in a Quintuple-Layer Square-Planar Nickelate. *Nat. Mater.* (2021). doi:10.1038/s41563-021-01142-9
11. Rossi M, Lu H, Nag A, Li D, Osada M, Lee K, et al. Orbital and Spin Character of Doped Carriers in Infinite-Layer Nickelates. *Phys. Rev. B* (2020) 104(22): L220505. doi:10.1103/PhysRevB.104.L220505
12. Lu H, Rossi M, Nag A, Osada M, Li DF, Lee K, et al. Magnetic Excitations in Infinite-Layer Nickelates. *Science* (2021) 373:213–6. doi:10.1126/science.abd7726
13. Katukuri VM, Bogdanov NA, Weser O, van den Brink J, Alavi A. Electronic Correlations and Magnetic Interactions in Infinite-Layer $NdNiO_2$. *Phys Rev B* (2020) 102:241112. doi:10.1103/PhysRevB.102.241112

14. Hepting M, Li D, Jia CJ, Lu H, Paris E, Tseng Y, et al. Electronic Structure of the Parent Compound of Superconducting Infinite-Layer Nickelates. *Nat Mater* (2020) 19:381–5. doi:10.1038/s41563-019-0585-z
15. Goodge BH, Li D, Lee K, Osada M, Wang BY, Sawatzky GA, et al. Doping Evolution of the mott–hubbard Landscape in Infinite-Layer Nickelates. *Proc Natl Acad Sci* (2021) 118.
16. Ortiz RA, Menke H, Misják F, Mantadakis DT, Fürsich K, Schierle E, et al. Superlattice Approach to Doping Infinite-Layer Nickelates. *Phys Rev B* (2021) 104:165137. doi:10.1103/PhysRevB.104.165137
17. Chen CT, Tjeng LH, Kwo J, Kao HL, Rudolf P, Sette F, et al. Out-of-plane orbital characters of intrinsic and doped holes in $la_{2-x}sr_xcuo_4$. *Phys Rev Lett* (1992) 68:2543–6. doi:10.1103/PhysRevLett.68.2543
18. Lee K, Goodge BH, Li D, Osada M, Wang BY, Cui Y, et al. Aspects of the Synthesis of Thin Film Superconducting Infinite-Layer Nickelates. *APL Mater* (2020) 8:041107. doi:10.1063/5.0005103
19. Li J, Green RJ, Zhang Z, Sutarto R, Sadowski JT, Zhu Z, et al. Sudden Collapse of Magnetic Order in Oxygen-Deficient Nickelate Films. *Phys Rev Lett* (2021) 126:187602. doi:10.1103/PhysRevLett.126.187602
20. Abbate M, Zampieri G, Prado F, Caneiro A, Gonzalez-Calbet JM, Vallet-Regi M. Electronic Structure and Metal-Insulator Transition in $Lanio_{3-\delta}$. *Phys Rev B* (2002) 65:155101. doi:10.1103/PhysRevB.65.155101
21. Lin JQ, Villar Arribi P, Fabbris G, Botana AS, Meyers D, Miao H, et al. Strong Superexchange in a $D^{9-\delta}$ Nickelate Revealed by Resonant Inelastic X-ray Scattering. *Phys Rev Lett* (2021) 126:087001. doi:10.1103/PhysRevLett.126.087001
22. Weigand M. *Realization of a New Magnetic Scanning X-ray Microscope and Investigation of Landau Structures under Pulsed Field Excitation*. Göttingen: Cuvillier Verlag (2015).
23. Green RJ, Haverkort MW, Sawatzky GA. Bond Disproportionation and Dynamical Charge Fluctuations in the Perovskite Rare-Earth Nickelates. *Phys Rev B* (2016) 94:195127. doi:10.1103/PhysRevB.94.195127
24. Medarde M, Dallera C, Grioni M, Delley B, Vernay F, Mesot J, et al. Charge Disproportionation in $Rnio_3$ Perovskites (*R*=rare Earth) from High-Resolution X-ray Absorption Spectroscopy. *Phys Rev B* (2009) 80:245105. doi:10.1103/PhysRevB.80.245105
25. Fürsich K, Lu Y, Betto D, Bluschke M, Porras J, Schierle E, et al. Resonant Inelastic X-ray Scattering Study of Bond Order and Spin Excitations in Nickelate Thin-Film Structures. *Phys Rev B* (2019) 99:165124. doi:10.1103/PhysRevB.99.165124
26. Kumar A, Leonard D, Jesse S, Ciucci F, Eliseev EA, Morozovska AN, et al. Spatially Resolved Mapping of Oxygen Reduction/evolution Reaction on Solid-Oxide Fuel Cell Cathodes with Sub-10 Nm Resolution. *ACS Nano* (2013) 7:3808–14. doi:10.1021/nn303239e
27. Taniuchi T, Motoyui Y, Morozumi K, Rödel TC, Fortuna F, Santander-Syro AF, et al. Imaging of Room-Temperature Ferromagnetic Nano-Domains at the Surface of a Non-magnetic Oxide. *Nat Commun* (2016) 7:11781. doi:10.1038/ncomms11781
28. Chen J, Liu W, Eul T, Chen M, Hu X, Wang S, et al. Engineering of Electron Confinement through Defect-Based Localized Polarization on Srtio3 Surface. *Adv Electron Mater* (2021) 7:2000968. doi:10.1002/aelm.202000968
29. Mattoni G, Zubko P, Maccherozzi F, van der Torren AJH, Boltje DB, Hadjimichael M, et al. Striped Nanoscale Phase Separation at the Metal–Insulator Transition of Heteroepitaxial Nickelates. *Nat Commun* (2016) 7:13141. doi:10.1038/ncomms13141
30. Li J, Pelliciari J, Mazzoli C, Catalano S, Simmons F, Sadowski JT, et al. Scale-invariant Magnetic Textures in the Strongly Correlated Oxide Ndnio3. *Nat Commun* (2019) 10:4568. doi:10.1038/s41467-019-12502-0
31. Puphal P, Wu YM, Fürsich K, Lee H, Pakdaman M, Bruin JAN, et al. *Synthesis and Characterization of Ca-Substituted Infinite-Layer Nickelate Crystals*. arXiv: 2106 (2021). p. 13171.

Conflict of Interest: The authors declare that the research was conducted in the absence of any commercial or financial relationships that could be construed as a potential conflict of interest.

Publisher's Note: All claims expressed in this article are solely those of the authors and do not necessarily represent those of their affiliated organizations, or those of the publisher, the editors, and the reviewers. Any product that may be evaluated in this article, or claim that may be made by its manufacturer, is not guaranteed or endorsed by the publisher.

frontiers in Physics

REVIEW
published: 10 January 2022
doi: 10.3389/fphy.2021.801236

Self-Doping and the Mott-Kondo Scenario for Infinite-Layer Nickelate Superconductors

Yi-feng Yang[1,2,3]* *and Guang-Ming Zhang*[4,5]*

[1]*Beijing National Laboratory for Condensed Matter Physics and Institute of Physics, Chinese Academy of Sciences, Beijing, China,* [2]*School of Physical Sciences, University of Chinese Academy of Sciences, Beijing, China,* [3]*Songshan Lake Materials Laboratory, Dongguan, China,* [4]*State Key Laboratory of Low-Dimensional Quantum Physics and Department of Physics, Tsinghua University, Beijing, China,* [5]*Frontier Science Center for Quantum Information, Beijing, China*

We give a brief review of the Mott-Kondo scenario and its consequence in the recently-discovered infinite-layer nickelate superconductors. We argue that the parent state is a self-doped Mott insulator and propose an effective *t- J-K* model to account for its low-energy properties. At small doping, the model describes a low carrier density Kondo system with incoherent Kondo scattering at finite temperatures, in good agreement with experimental observation of the logarithmic temperature dependence of electric resistivity. Upon increasing Sr doping, the model predicts a breakdown of the Kondo effect, which provides a potential explanation of the non-Fermi liquid behavior of the electric resistivity with a power law scaling over a wide range of the temperature. Unconventional superconductivity is shown to undergo a transition from nodeless (*d+is*)-wave to nodal *d*-wave near the critical doping due to competition of the Kondo and Heisenberg superexchange interactions. The presence of different pairing symmetry may be supported by recent tunneling measurements.

Keywords: nickelate superconductor, self-doping, Mott, Kondo, t-J-K model

OPEN ACCESS

Edited by:
Danfeng Li,
City University of Hong Kong, Hong Kong SAR, China

Reviewed by:
Yusuke Nomura,
RIKEN, Japan
Liang Si,
Vienna University of Technology, Austria

***Correspondence:**
Yi-feng Yang
yifeng@iphy.ac.cn
Guang-Ming Zhang
gmzhang@tsinghua.edu.cn

Specialty section:
This article was submitted to Condensed Matter Physics, a section of the journal Frontiers in Physics

Received: *25 October 2021*
Accepted: *02 December 2021*
Published: *10 January 2022*

Citation:
Yang Y-f and Zhang G-M (2022) Self-Doping and the Mott-Kondo Scenario for Infinite-Layer Nickelate Superconductors. Front. Phys. 9:801236. doi: 10.3389/fphy.2021.801236

1 INTRODUCTION

Recent discovery of superconductivity (SC) in infinite-layer Sr-doped $NdNiO_2$ films [1] and subsequently in hole doped $LaNiO_2$ and $PrNiO_2$ films [2–5] has stimulated intensive interest in condensed matter community. Despite of many theoretical and experimental efforts, there are still debates on its electronic structures and pairing mechanism [6–21]. The study of possible Ni-based superconductivity was initially stimulated by cuprates, whose high T_c mechanism remains one of the most challenging topics in past three decades [22–25]. Many attempts have been devoted to exploring new families of high T_c superconductors. Nickelate superconductors are but one latest example of these efforts.

In undoped cuprates, Cu^{2+} ions contain nine electrons with partially occupied $3d_{x^2-y^2}$ orbitals. The oxygen $2p$ orbitals are higher in energy than the Cu $3d_{x^2-y^2}$ lower Hubbard band. Thus, cuprates belong to the so-called charge-transfer insulator. A superexchange interaction between localized Cu $3d_{x^2-y^2}$ spins is mediated by oxygen ions and causes an antiferromagnetic (AF) ground state. Upon chemical doping, holes may be introduced on the oxygen sites in the CuO_2 planes [23–25] and combine with the $3d_{x^2-y^2}$ spins to form the Zhang-Rice singlets [26], destroying the long-range AF order rapidly. In theory, these led to an effective *t-J* model, describing the holes moving on the antiferromagnetic square lattice. High temperature SC with robust *d*-wave pairing has been predicted

and established over a wide doping range [27–29]. Extending such "cuprate-Mott" conditions in other oxides has led to extensive efforts on nickel oxides [30–40]. Nickelate superconductors have a similar layered crystal structure with Ni^{1+} possessing the same $3d^9$ configuration as Cu^{2+}. As a result, theories based on Mott scenario have naturally been developed to account for nicklate superconductors.

However, there are clear evidences since the beginning suggesting that these two systems are different. Instead of a Mott insulator with AF long-range order like in cuprates, $NdNiO_2$ displays metallic behavior at high temperatures with a resistivity upturn below about 70 K, showing no sign of any magnetic long-range order in the whole measured temperature range [41]. Similar results have previously been found in $LaNiO_2$ [42]. Possible signatures of (short-range) antiferromagnetic order were reported only very recently in $Nd_{0.8}Sr_{0.2}NiO_2$ thin films by X-ray magnetic linear dichroism measurements [43] and in bulk $Nd_{0.85}Sr_{0.15}NiO_2$ by nuclear magnetic resonance (NMR) [44]. First-principles calculations have also revealed some subtle differences in their band structures. The O-2*p* orbitals are located at a deeper energy compared to that of cuprates. Nd-5*d* bands are found to hybridize with Ni-3*d* bands and produce small electron pockets in the Brillouin zone. As a consequence, holes are doped directly into Ni-3*d* orbitals rather than O-2*p* orbitals. Nickelates should thus be modelled as a self-doped Mott insulator, which implies a multi-band system with two types of charge carriers, the itinerant Nd-5*d* conduction electrons and the Ni-$3d_{x^2-y^2}$ holes, on a background lattice of Ni-$3d_{x^2-y^2}$ magnetic moments [6]. Joint analysis of the resistivity upturn and Hall coefficient at low temperatures suggests possible presence of incoherent Kondo scattering between low-density conduction electrons and localized Ni spins. A physical picture is illustrated in **Figure 1** on the square lattice. Then the basis for the Mott-Kondo scenario of nickelate superconductors has been established, leading to the proposal of an extended *t-J-K* model for a microscopic description of their low-energy properties [6, 9].

Interestingly, the Kondo hybridization does not appear significant at first glance in band structure calculations [32]. It was later realized that nickelates may host a special interstitial-*s* orbital for conduction electrons that have substantially stronger hybridization than previously thought [17]. Resonant inelastic X-ray scattering (RIXS) measurements [13, 45] confirmed the presence of hybridization between Ni $3d_{x^2-y^2}$ and Nd 5*d* orbitals. At zero temperature, the self-doping effect and the Kondo coupling produce low-energy doublon (Kondo singlet) and holon excitations on the nickel spin-1/2 background. Because of the larger charge transfer energy, nickelates were considered to have a reduced superexchange interaction between Ni^{1+} spins by almost an order of magnitude than cuprates. Raman scattering measurements seemed to confirm this expectation and estimated $J \approx 25$ meV in bulk $NdNiO_2$ [46]. However, latest RIXS measurement of magnetic excitations found a larger nearest-neighbor coupling $J_1 \approx 63.6$ meV [47] in ~10-nm-thick films, as suggested also by some recent calculations [48]. In any case, the Kondo coupling may suppress the AF long-range order and cause a phase transition to a paramagnetic metal [6]. The parent or underdoped compounds may therefore be viewed as a Kondo semimetal (KS). For large hole doping, the Ni-3*d* electrons become more itinerant and the Kondo effect breaks down, followed by an abrupt change of the charge carriers. Indeed, a sign change of the Hall coefficient has been reported in experiment [49, 50].

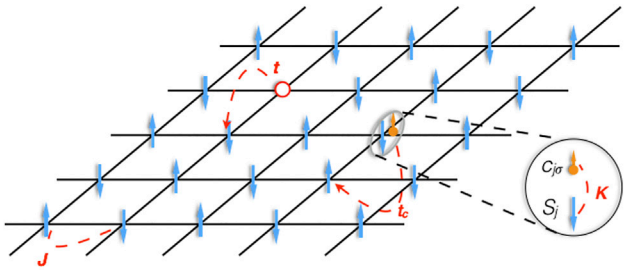

FIGURE 1 | Illustration of the self-doping and Mott-Kondo scenario for $NdNiO_2$ projected on a two-dimensional square lattice, showing one of the Ni $d_{x^2-y^2}$ electrons transferring to the Nd 5*d* orbitals. Blue arrows denote Ni-spins interacting through the Heisenberg superexchange coupling *J*. Orange arrow denotes Nd-5*d* electron, which couples to Ni-spin by the Kondo coupling *K* to form at low temperatures a Kondo singlet (doublon). Red circle represents Ni-$3d^8$ configuration, or a holon. t_c and *t* denote the hopping of doublon and holon, respectively. Figure adapted from Ref. [6]. Copyright 2020 by the American Physical Society.

The above differences have an immediate impact on candidate pairing mechanism of the superconductivity. At critical doping, the *t-J-K* model predicted possible SC transition from a gapped $(d + is)$-wave state to a gapless *d*-wave pairing state due to the competition of Kondo and superexchange interactions [9]. Latest scanning tunneling experiment (STM) also revealed two different gap structures of U and V-shapes [51], supporting the possibility of above scenario. Thus, nickelates may belong to a novel class of unconventional superconductors and one may anticipate potentially more interesting properties bridging the cuprates and heavy fermions.

In this paper, we briefly summarize the consequences of the Mott-Kondo scenario based on the extended *t-J-K* model for nickelate superconductors [6, 9]. We propose a global phase diagram upon electron and hole doping and derive a low-energy effective Hamiltonian with doublon and holon excitations in the low doping region. We then employ the renormalized mean-field theory (RMFT) to study the possibility of superconductivity and predict a phase transition of its pairing symmetry. The latter is shown to originate from the breakdown of Kondo hybridization, accompanied with non-Fermi liquid (NFL) behavior of the resistivity $\rho \sim T^{\alpha}$ near critical doping.

2 THEORY

2.1 Model Hamiltonian

To introduce the effective *t-J-K* model for describing the low-energy physics of nickelates, we start from a background lattice of Ni^{1+} $3d_{x^2-y^2}$ localized spins with a small number of self-doped holes and Nd-5 *d* conduction electrons [6]. Similar to cuprates, one expects an AF superexchange interaction between Ni^{1+} spins through the O-2*p* orbitals. This is different from heavy fermion systems, where the exchange interaction between localized spins

originates from the Ruderman-Kittel-Kasuya-Yosida (RKKY) interaction mediated by conduction electrons. It should be noted that latest RIXS measurements revealed a sizable next-nearest-neighbor coupling $J_2 \approx -10.3$ meV, implying a possible contribution from the RKKY mechanism [47]. The motion of holes on the spin lattice should be strongly renormalized as in the usual *t-J* model. There is an additional local Kondo interaction between local spins and conduction electrons. The total Hamiltonian therefore contains three terms:

$$H = H_t + H_J + H_K, \tag{1}$$

where the first term comes from the hopping of holes, the second term describes the spin lattice, and the third term gives the Kondo interaction.

For simplicity, we consider a minimal model with Ni-$3d^8$ and Nd-$5d^0$ as the vacuum. As in cuprates, the localized $3d_{x^2-y^2}$ spins on the NiO_2 plane can be described by a two-dimensional quantum Heisenberg model with nearest neighbour AF superexchange interactions,

$$H_J = J \sum_{\langle ij \rangle} S_i \cdot S_j, \tag{2}$$

whose ground state is a Mott insulator with AF long-range orders.

The self-doping effect is supported by first-principles band structure calculations [32], where the Nd 5*d* orbitals in $NdNiO_2$ are found to hybridize with the Ni 3*d* orbitals and give rise to small electron pockets in the Brillouin zone. Thus, we have a small number of Nd-5*d* conduction electrons. This is actually supported by experiment. At high temperatures, the Hall coefficient is dominated by conduction electrons giving $R_H \approx -4 \times 10^{-3}\,\mathrm{cm^3\,C^{-1}}$ for $NdNiO_2$ and $-3 \times 10^{-3}\,\mathrm{cm^3\,C^{-1}}$ for $LaNiO_2$. By contrast, in typical heavy fermion metals such as Ce*M*In_5 (*M* = Co., Rh, Ir), we have $R_H \approx -3.5 \times 10^{-4}\,\mathrm{cm^3\,C^{-1}}$ at high temperatures [52]. The larger and negative values of the Hall coefficient implies that there are only a few percent of electron-like carriers per unit cell in $NdNiO_2$ and $LaNiO_2$.

The hybridization between Ni $3d_{x^2-y^2}$ spins and conduction electrons gives the additional Kondo term:

$$H_K = -\sum_{ij\sigma}\left(t_c^{ij} c_{i\sigma}^{\dagger} c_{j\sigma} + h.c.\right) + \frac{K}{2} \sum_{j\alpha;\sigma\sigma'} S_j^{\alpha} c_{j\sigma}^{\dagger} \tau_{\sigma\sigma'}^{\alpha} c_{j\sigma'}, \tag{3}$$

where t_c^{ij} is the hopping of conduction electrons projected on the square lattice of the Ni^{1+} ions, *K* is the Kondo coupling, and τ^{α} ($\alpha = x, y, z$) are the spin-1/2 Pauli matrices. Only a single conduction band is considered for simplicity. For a low carrier density system, the average number of conduction electrons is small, i.e. $n_c = N_s^{-1} \sum_{j\sigma} \langle c_{j\sigma}^{\dagger} c_{j\sigma} \rangle \ll 1$. In reality, there may exist multiple conduction bands with three-dimensional Fermi pockets. Whether or not this can lead to other new physics requires more elaborate theoretical investigation.

The presence of magnetic impurities may be at first glance ascribed to the Nd 4*f* moments. However, the Nd^{3+} ion contains three *f* electrons forming a localized spin-3/2 moment, which acts more like a classical spin as in manganites and therefore disfavors spin-flip scattering as the quantum spin-1/2 moment. Their energy level is also far away from the Fermi energy, so it is reasonable to ignore the Nd 4*f* electrons. However, we should note that there exist different opinions on the importance of Nd-4*f* orbitals [53].

For parent compounds, self-doping also introduces an equal number of Ni $3d_{x^2-y^2}$ holes on the spin lattice. The hopping of holes on the lattice of Ni $3d_{x^2-y^2}$ spins can be described as interactions,

$$H_t = -\sum_{ij\sigma}\left(t_{ij} P_G d_{i\sigma}^{\dagger} d_{j\sigma} P_G + h.c.\right), \tag{4}$$

where $d_{i\sigma}$ and $d_{i\sigma}^{\dagger}$ are the annihilation and creation operators of the Ni $3d_{x^2-y^2}$ electrons, respectively, t_{ij} is the hopping integral between site *i* and *j*, and P_G is the Gutzwiller operator to project out doubly occupancy of local Ni $3d_{x^2-y^2}$ orbital. As in cuprates, the holes' motion is strongly renormalized due to the onsite Coulomb repulsion *U*.

Quite generally, the above effective *t-J-K* model can be replaced by the one-band Hubbard model plus a hybridization term with additional conduction electrons:

$$\begin{aligned} H = &\sum_{\mathbf{k}\sigma} E_{\mathbf{k}} d_{\mathbf{k}\sigma}^{\dagger} d_{\mathbf{k}\sigma} + U \sum_i n_{i\uparrow}^d n_{i\downarrow}^d \\ &+ \sum_{\mathbf{k}\sigma} \epsilon_{\mathbf{k}} c_{\mathbf{k}\sigma}^{\dagger} c_{\mathbf{k}\sigma} + \sum_{\mathbf{k}\sigma} V_{\mathbf{k}}\left(d_{\mathbf{k}\sigma}^{\dagger} c_{\mathbf{k}\sigma} + h.c.\right), \end{aligned} \tag{5}$$

where $E_{\mathbf{k}}$ and $\epsilon_{\mathbf{k}}$ are the dispersion of Ni $3d_{x^2-y^2}$ and conduction electrons, respectively, *U* is the onsite Coulomb interaction on Ni $3d_{x^2-y^2}$ orbital, and $V_{\mathbf{k}}$ is the hybridization. The model may also be viewed as a periodic Anderson model with dispersive *d* bands. It allows for a better treatment of charge fluctuations of the Ni $3d_{x^2-y^2}$ orbitals, in particular for large Sr doping or small Coulomb interaction. One-band model with additional electron reservoir has been studied in the literature [18–20]. More complicated models including multiple Ni-3*d* orbitals have also been proposed, focusing on different aspects of the nickelate physics such as hybridization, Hund coupling, superconductivity, and topological properties [7–17, 21]. In this work, we only consider the minimal *t-J-K* model and show that it can already capture some main features of the nickelates.

2.2 Global Phase Diagram

As is in heavy fermion systems, the *t-J-K* model contains two competing energy scales that support different ground states. The Heisenberg superexchange *J* favors an antiferromagnetic long-range order, while the Kondo coupling *K* tends to screen the local spins and form a nonmagnetic ground state. In nickelates, due to the large charge transfer energy between O-2*p* and Ni-$3d_{x^2-y^2}$ orbitals, *J* was expected to be smaller that (about 100 meV) in cuprates. First-principles calculations suggested *J* of the order of 10 meV [17], Raman scattering measurements estimated $J \approx 25$ meV in bulk $NdNiO_2$ [46], but latest RIXS experiment reported $J \approx 63.6$ meV [47]. There is at present no direct measurement of the Kondo interaction *K*. However, from the observed resistivity minimum at 70–100 K in $NdNiO_2$ and $LaNiO_2$ [1, 42], *K* may be roughly estimated to be of the order of a few hundred meV if we use the formula $T_K \approx \rho^{-1} e^{-1/K\rho}$, assume T_K to be a few Kelvin, and take a small density of states ρ of the order of 0.1 $\mathrm{eV^{-1}}$ for conduction electrons [6, 54]. This is

consistent with numerical calculations for the hybridization between Ni-3$d_{x^2-y^2}$ and interstitial *s* orbitals [17]. Thus for undoped nickelates, the Kondo coupling is a relatively large energy scale.

We may propose a global phase diagram starting from an antiferromagnetic ground state. The self-doping introduces equal numbers of conduction electrons and holes. The conduction electrons tend to form Kondo singlets with local spins due to the large *K*. Both tend to suppress the long-range AF order and causes a paramagnetic ground state. But because of the small number of conduction electrons, local spins cannot be fully Kondo screened to become delocalized. Thus, instead of a heavy fermion metal, we are actually dealing with a low carrier density Kondo system at low temperatures. Due to insufficient Kondo screening, the resistivity exhibits insulating-like behavior (upturn) because of incoherent Kondo scattering, which is typical for low carrier density Kondo systems and has been observed previously in $CeNi_{2-\delta}(As_{1-x}P_x)_2$ [55] and $NaYbSe_2$ [56].

Upon Sr (hole) doping, the number of conduction electrons may be reduced, while that of holes increases. The Kondo physics may be suppressed and replaced by the usual *t-J* model for large hole doping, resembling the physics of cuprates. On the other hand, for electron doping, we may expect to first recover the AF long-range order with reduced hole density, and then with increasing conduction electrons and Kondo screening, the AF order will be suppressed again and the system turns into a heavy fermion metal with sufficient electron doping. SC may emerge around the quantum critical point. Whether or not the AF phase may actually exist depends on how doping changes the fraction of electron and hole carriers. But in bulk $Nd_{1-x}Sr_xNiO_2$, NMR experiment has revealed short-range glassy AF ordering, supporting the possible existence of antiferromagnetism [44]. **Figure 2** summarizes possible ground states of the model on the temperature-doping plane, showing a connection between the heavy fermion and cuprate physics on two ends and the nickelates in between. However, it should be noted that current experiment on "overdoped" nickelate superconductors found a weak insulator rather than a Fermi liquid as in heavily hole-doped cuprates [50]. How exactly holes are doped in $Nd_{1-x}Sr_xNiO_2$ and whether or not multiple Ni-3*d* orbitals are needed remain an open question.

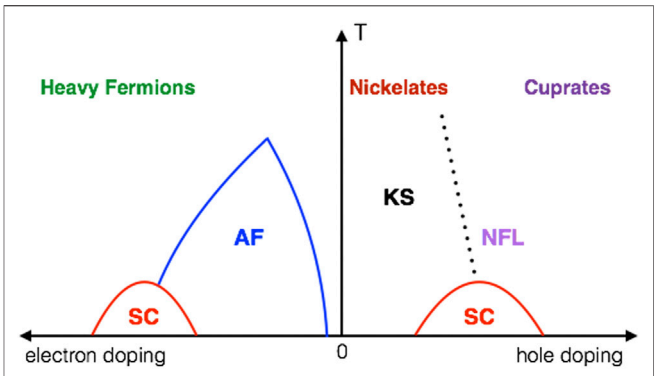

FIGURE 2 | A schematic phase diagram of the *t-J-K* model with electron and hole doping. KS stands for incoherent Kondo scattering or Kondo semimetal. Whether or not the AF phase may exist depends on details of electron and hole densities introduced by doping.

2.3 Low Energy Excitations

As shown in the phase diagram, the paramagnetic region (KS) is responsible for undoped or low doped nickelates. In this case, we have a small number (n_c) of conduction electrons per Ni-site and $n_c + p$ empty nickel sites (holons) on the NiO_2 plane, where p is the hole doping ratio. In the large *K* limit and at zero temperature, conduction electrons form Kondo singlets or doublons with local Ni spins. We may then derive an effective low-energy Hamiltonian in terms of doublons, holons, and localized spins, to describe a doped Mott metallic state with Kondo singlets [6]. A cartoon picture is given in **Figure 1**.

For this, we first introduce the pseudofermion representation for the spin-1/2 local moments:

$$S_j^+ = f_{j\uparrow}^\dagger f_{j\downarrow}, S_j^- = f_{j\downarrow}^\dagger f_{j\uparrow}, S_j^z = \frac{1}{2}\left(f_{j\uparrow}^\dagger f_{j\uparrow} - f_{j\downarrow}^\dagger f_{j\downarrow}\right),$$

where $f_{j\sigma}$ is a fermionic operator for the spinon on site *j*. The Ni $3d_{x^2-y^2}$ electron operator is given by $d_{j\sigma} = h_j^\dagger f_{j\sigma}$ with a local constraint, $h_j^\dagger h_j + \sum_\sigma f_{j\sigma}^\dagger f_{j\sigma} = 1$, if we ignore double occupancy. Here $h_j^\dagger$ is a bosonic operator creating a holon on site *j*.

The doublon operators for the on-site Kondo spin singlet and triplets may be defined as

$$b_{j0}^\dagger = \frac{1}{\sqrt{2}}\left(f_{j\uparrow}^\dagger c_{j\downarrow}^\dagger - f_{j\downarrow}^\dagger c_{j\uparrow}^\dagger\right);$$
$$b_{j1}^\dagger = f_{j\uparrow}^\dagger c_{j\uparrow}^\dagger,\ b_{j2}^\dagger = \frac{1}{\sqrt{2}}\left(f_{j\uparrow}^\dagger c_{j\downarrow}^\dagger + f_{j\downarrow}^\dagger c_{j\uparrow}^\dagger\right),\ b_{j3}^\dagger = f_{j\downarrow}^\dagger c_{j\downarrow}^\dagger.$$

The Kondo Term Then Becomes.

$$\frac{K}{2}\sum_{j\alpha;\sigma\sigma'} S_j^\alpha c_{j\sigma}^\dagger \tau_{\sigma\sigma'}^\alpha c_{j\sigma'} = \frac{K}{4}\sum_{\mu=1}^{3} b_{j\mu}^\dagger b_{j\mu} - \frac{3K}{4}\sum_j b_{j0}^\dagger b_{j0}, \quad (6)$$

which describes the doublon formation on each site, namely, the Kondo singlet or triplet pair formed by one conduction electron with a localized spinon. We see that the triplet pair costs a higher energy of *K*. Similarly, there may also exist three-particle states with one localized spinon and two conduction electrons on the same site, $e_{j\sigma}^\dagger = f_{j\sigma}^\dagger c_{j\uparrow}^\dagger c_{j\downarrow}^\dagger$, or one-particle states with one unpaired spinon only, $\tilde{f}_{j\sigma} = (1 - n_j^c) f_{j\sigma}$.

Following Refs. [57, 58], we first rewrite the Hamiltonian in terms of these new operators and then eliminate all high-energy terms containing $b_{j\mu}$ ($\mu = 1, 2, 3$) and $e_{j\sigma}$ using canonical transformation while keeping only the on-site doublon (b_{j0}) and unpaired spinons ($\tilde{f}_{j\sigma}$). This yields an effective low-energy model with a simple form

$$H_{\text{eff}} = -t\sum_{\langle ij\rangle,\sigma}\left(h_i \tilde{f}_{i\sigma}^\dagger \tilde{f}_{j\sigma} h_j^\dagger + h.c.\right) + J\sum_{\langle ij\rangle}\tilde{S}_i \cdot \tilde{S}_j$$
$$-\frac{t_c}{2}\sum_{\langle ij\rangle,\sigma}\left(b_{i0}^\dagger \tilde{f}_{i\sigma}\tilde{f}_{j\sigma}^\dagger b_{j0} + h.c.\right), \quad (7)$$

where the spin operators are $\tilde{S}_j^\alpha = \sum_{\sigma\sigma'}\tilde{f}_{j\sigma}^\dagger \frac{1}{2}\tau_{\sigma\sigma'}^\alpha \tilde{f}_{j\sigma'}$ with a local constraint $h_j^\dagger h_j + b_{j0}^\dagger b_{j0} + \sum_\sigma \tilde{f}_{j\sigma}^\dagger \tilde{f}_{j\sigma} = 1$. Here only the nearest-neighbor hopping parameters t and t_c are considered for

simplicity. For large but finite K, apart from some complicated interactions, an additional term should also be included

$$H_b = -\frac{3}{4}\left(K + \frac{t_c^2}{K}\right)\sum_j b_{j0}^\dagger b_{j0} + \frac{5t_c^2}{12K}\sum_{\langle ij\rangle} b_{i0}^\dagger b_{i0} b_{j0}^\dagger b_{j0}, \quad (8)$$

which describes the doublon condensation.

This effective Hamiltonian describes the ground state of nickelates at zero or low doping. It is similar to the usual *t-J* model for cuprates [26], but includes two types of mobile quasiparticles: doublons (Kondo singlets) and holons. It is now clear why the self-doping can efficiently suppress the AF long-range order to yield a paramagnetic ground state in nickelates. At high temperatures, doublons become deconfined, causing incoherent Kondo scattering in transport measurements. This is confirmed by the resistivity replotted in **Figure 3** as a function of temperature for both $NdNiO_2$ and $LaNiO_2$. Unlike cuprates, the resistivity exhibits metallic behavior at high temperature but shows an upturn below about 70 K. If we put the data on a linear-log scale, we find that the upturn follows exactly a logarithmic temperature ($\ln T$) dependence over a large temperature range for both compounds, which is a clear evidence for incoherent Kondo scattering typical for low carrier density Kondo systems [59]. The saturation at very low temperatures is an indication of Kondo screening. This Kondo scenario is also supported by the Hall measurement. In both compounds, the Hall coefficient R_H exhibits non-monotonic temperature dependence. It approaches a negative constant at high temperatures due to the contribution of conduction electrons, but exhibits the same $\ln T$ dependence at low temperatures. The linear relation $R_H \propto \rho$ is an indication of skew scattering by localized magnetic impurities in typical Kondo systems [60, 61].

An alternative explanation for the resistivity upturn is weak localization, where disordered holes in the NiO_2 plane may also give rise to a logarithmic correction. However, this explanation is not supported by the corresponding correction to the Hall coefficient and magnetoresistance.

2.4 Superconductivity

Experimentally, superconductivity was first observed to emerge and have an onset temperature of 14.9 K in 20% Sr doped $NdNiO_2$ thin films deposited on $SrTiO_3$ substrates [1]. From the *t-J-K* model, one may naively expect that sufficiently large doping may deplete conduction electrons and increase the number of holons, driving the system to an effective *t-J* model resembling that in cuprates. As a result, *d*-wave superconductivity may arise due to the superexchange interaction between Ni $3d_{x^2-y^2}$ electrons. However, this is not the whole truth. With increasing Sr doping, the ordinary Hall coefficient at high temperatures becomes smaller in magnitude but remains negative even in $Nd_{0.8}Sr_{0.2}NiO_2$ [1], which cannot be explained by a single carrier model but rather indicates a cancellation of electron and hole contributions. Thus, conduction electrons should still be present even at 20% Sr doping. It is thus anticipated that superconductivity in nickelates may be affected by the presence of conduction electrons and their Kondo hybridization with Ni $3d_{x^2-y^2}$ electrons.

The pairing symmetry can be studied by using the renormalized mean-field theory (RMFT) [62], which had successfully predicted the *d*-wave superconductivity in the *t-J* model for cuprates and can well describe the Fermi liquid similar to the slave-boson mean field theory. Our numerical calculations of superconductivity on the generalized *t-J-K* model have yielded a typical superconducting phase diagram in **Figure 4** [9]. The

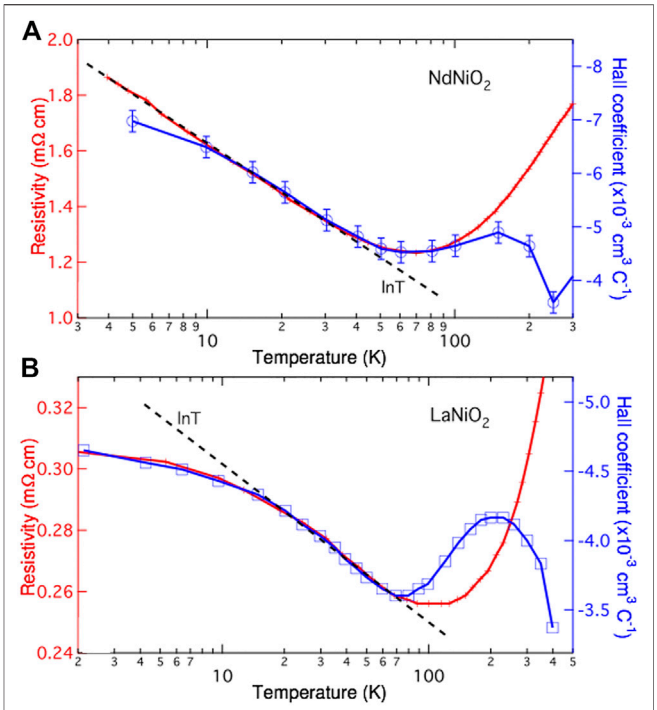

FIGURE 3 | Logarithmic scaling of the resistivity (red color) and Hall coefficient (blue color) below about 70 K for **(A)** $NdNiO_2$ with experimental data adopted from Ref. [1]; **(B)** $LaNiO_2$ reproduced from Ref. [42]. The dashed lines are the ln *T* fits. Figure adapted from Ref. [6]. Copyright 2020 by the American Physical Society.

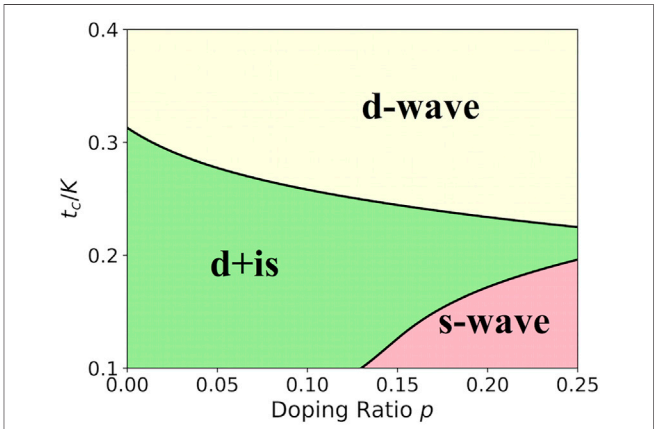

FIGURE 4 | Superconducting phase diagram of the *t-J-K* model. At small doping p and moderate t_c/K, the pairing symmetry is $(d + is)$-wave. At large t_c/K, the pairing is *d*-wave. For moderate t_c/K, the phase diagram predicts a superconducting transition from $(d + is)$ to *d* with increasing hole doping. Figure adapted from Ref. [9]. Copyright 2020 by the American Physical Society.

pairing symmetry is found to depend on the hole concentration p and the effective strength of the Kondo hybridization controlled by the conduction electron hopping (t_c/K). For simplicity, we have taken the Kondo coupling K as the energy unit ($K = 1$), and set the AF Heisenberg spin exchange $J = 0.1$. Both the nearest-neighbor hopping $t = 0.2$ and the next-nearest-neighbor hopping $t' = -0.05$ are taken into consideration for Ni $3d$ electrons. The density of conduction electrons is taken to be $n_c = 0.1$, while their nearest-neighbor hopping t_c is chosen as a tuning parameter. Note that these parameters may in principle vary with doping in real materials. Here we fix them for simplicity in our model study and focus on the qualitative picture.

For all doping, we find a dominant d-wave pairing symmetry for large t_c/K or small K. But for low doping and moderate t_c/K, we obtain a $(d + is)$-wave pairing state that breaks the time-reversal symmetry. This is different from the conventional picture based purely on the t-J model for cuprates, where the Heisenberg superexchange interaction favors d-wave pairing [63]. The s-wave pairing should be ascribed to the Kondo coupling, which is an on-site spin exchange between localized and conduction electrons [64]. This is supported by the extended s-wave solution at large doping for small t_c/K or strong Kondo coupling. It is the combination of both effects that gives rise to the special $(d + is)$-wave superconductivity and represents a genuine feature of the nickelate superconductivity differing from cuprates or heavy fermions.

Details of RMFT calculations are explained as follows [9]. We first introduce three Gutzwiller renormalization factor to approximate the operator that projects out the doubly occupied states: $g_t = n_h/(1 + n_h)$ for the hopping t and t', $g_J = 4/(1 + n_h)^2$ for the superexchange J, and $g_K = 2/(1 + n_h)$ for the Kondo coupling K. We then define four mean-field order parameters to decouple the Heisenberg superexchange and Kondo terms:

$$\chi_{ij} = \langle d^\dagger_{i\uparrow} d_{j\uparrow} + d^\dagger_{i\downarrow} d_{j\downarrow}\rangle, \quad B = \frac{1}{\sqrt{2}}\langle d^\dagger_{j\uparrow} c^\dagger_{j\downarrow} - d^\dagger_{j\downarrow} c^\dagger_{j\uparrow}\rangle,$$
$$\Delta_{ij} = \langle d^\dagger_{i\uparrow} d^\dagger_{j\downarrow} - d^\dagger_{i\downarrow} d^\dagger_{j\uparrow}\rangle, \quad D = \frac{1}{\sqrt{2}}\langle c^\dagger_{j\uparrow} d_{j\uparrow} + c^\dagger_{j\downarrow} d_{j\downarrow}\rangle.$$

The resulting mean-field Hamiltonian has a simple bilinear form in the momentum space,

$$\mathcal{H}_{\rm mf} = \sum_{\mathbf{k}} \Psi^\dagger_{\mathbf{k}} \begin{pmatrix} \chi(\mathbf{k}) & K_D & \Delta^*(\mathbf{k}) & K_B^* \\ K_D^* & \epsilon(\mathbf{k}) & K_B^* & 0 \\ \Delta(-\mathbf{k}) & K_B & -\chi(-\mathbf{k}) & -K_D^* \\ K_B & 0 & -K_D & -\epsilon(-\mathbf{k}) \end{pmatrix} \Psi_{\mathbf{k}}, \tag{9}$$

where we have introduced the Nambu spinors $\Psi^\dagger_{\mathbf{k}} = (d^\dagger_{\mathbf{k}\uparrow}, c^\dagger_{\mathbf{k}\uparrow}, d_{-\mathbf{k}\downarrow}, c_{-\mathbf{k}\downarrow})$ and defined the matrix elements

$$\begin{aligned} \chi(\mathbf{k}) &= -\sum_\alpha \left(t g_t + \frac{3}{8} J g_J \chi_\alpha\right)\cos(\mathbf{k}\cdot\alpha) \\ &\quad -t' g_t \sum_\delta \cos(\mathbf{k}\cdot\delta) + \mu_1, \\ \epsilon(\mathbf{k}) &= -t_c \sum_\alpha \cos(\mathbf{k}\cdot\alpha) + \mu_2, \\ \Delta(\mathbf{k}) &= -\frac{3}{8} J g_J \sum_\alpha \Delta_\alpha \cos(\mathbf{k}\cdot\alpha), \\ K_D &= -\frac{3}{4} g_K K \frac{D}{\sqrt{2}}, K_B = -\frac{3}{4} g_K K \frac{B}{\sqrt{2}}. \end{aligned} \tag{10}$$

Here α denotes the vectors of the nearest-neighbor lattice sites and δ stands for those of the next-nearest-neighbor sites. μ_1 and μ_2 are chemical potentials fixing the numbers of the constrained electrons $d_{i\sigma}$ and conduction electrons $c_{i\sigma}$, respectively.

The above mean-field Hamiltonian can be diagonalized using the Bogoliubov transformation, $(d_{\mathbf{k}\uparrow}, c_{\mathbf{k}\uparrow}, d^\dagger_{-\mathbf{k}\downarrow}, c^\dagger_{-\mathbf{k}\downarrow})^T = U_{\mathbf{k}}(\alpha_{\mathbf{k}\uparrow}, \beta_{\mathbf{k}\uparrow}, \alpha^\dagger_{-\mathbf{k}\downarrow}, \beta^\dagger_{-\mathbf{k}\downarrow})^T$. The ground state is given by the vacuum of the Bogoliubov quasiparticles $\{\alpha^\dagger_{\mathbf{k}\sigma}, \beta^\dagger_{\mathbf{k}\sigma}\}$, which in turn yields the self-consistent equations for the mean-field order parameters. We will not go into more details here, but only mention that the mean-field self-consistent equations can be solved numerically and yield two dominant pairing channels of s and d-waves as shown in the phase diagram **Figure 4**. Typical results for the mean-field parameters are plotted in **Figure 5A** as a function of the doping ratio p for $t_c/K = 0.25$. For clarity, we have defined $\Delta_s = |\Delta_x + \Delta_y|/2$ and $\Delta_d = |\Delta_x - \Delta_y|/2$ to represent the respective pairing amplitudes of s and d channels. We see a clear transition from the mixed $(d + is)$-wave SC to the pure d-wave SC.

Antiferromagnetic spin fluctuations have been observed in bulk $Nd_{1-x}Sr_xNiO_2$ by NMR [44] and may also exist and play the role of pairing glues in thin films. Hence the presence of a dominant d-wave pairing at large doping is expected from the experience in cuprates. However, our results also suggest several additional features of the nickelate superconductivity that are not present in cuprates and may be examined in experiment. First, for sufficiently large Kondo coupling K, the $(d + is)$-wave SC in the low doping region breaks the time reversal symmetry and as shown in **Figure 5C** (left panel), has a nodeless gap which is distinctly different from the usual d-wave pairing with nodes along the diagonal direction. Second, we predict a quantum phase transition between this gapped $(d + is)$-wave SC to the nodal d-wave superconductivity with increasing hole doping. These features can be detected by scanning tunneling, penetration depth, or μSR experiment and serve as a support for our theory. We remark that conduction electrons play an important role in our theory of nickelate superconductivity, which is not possible in the single-band Mott picture. The importance of electron pockets is in fact supported by experimental measurements of the upper critical field [65, 66].

Recent single particle tunneling experiment [51] on superconducting nickelate thin films have also observed two distinct types of spectra: a V-shape feature with a gap maximum of 3.9 meV, a U-shape feature with a gap of about 2.35 meV, and some spectra with mixed contributions of these two components. If we attribute their different observations to different hole concentrations due to possible surface effect, the two types of spectra may correspond exactly to the two pairing states in our theory. In this sense, the scanning tunneling spectra have provided a supportive evidence for our theoretical prediction of multiple superconducting phases. Of course, the $(d + is)$-wave pairing might not exist in real materials if the Kondo coupling K is too weak or t_c/K is too large. In that case, as is seen in **Figure 4**, d-wave pairing may become dominant on the hole Fermi surface, but electron pockets may still have nodeless gap depending on their position in the Brillouin zone.

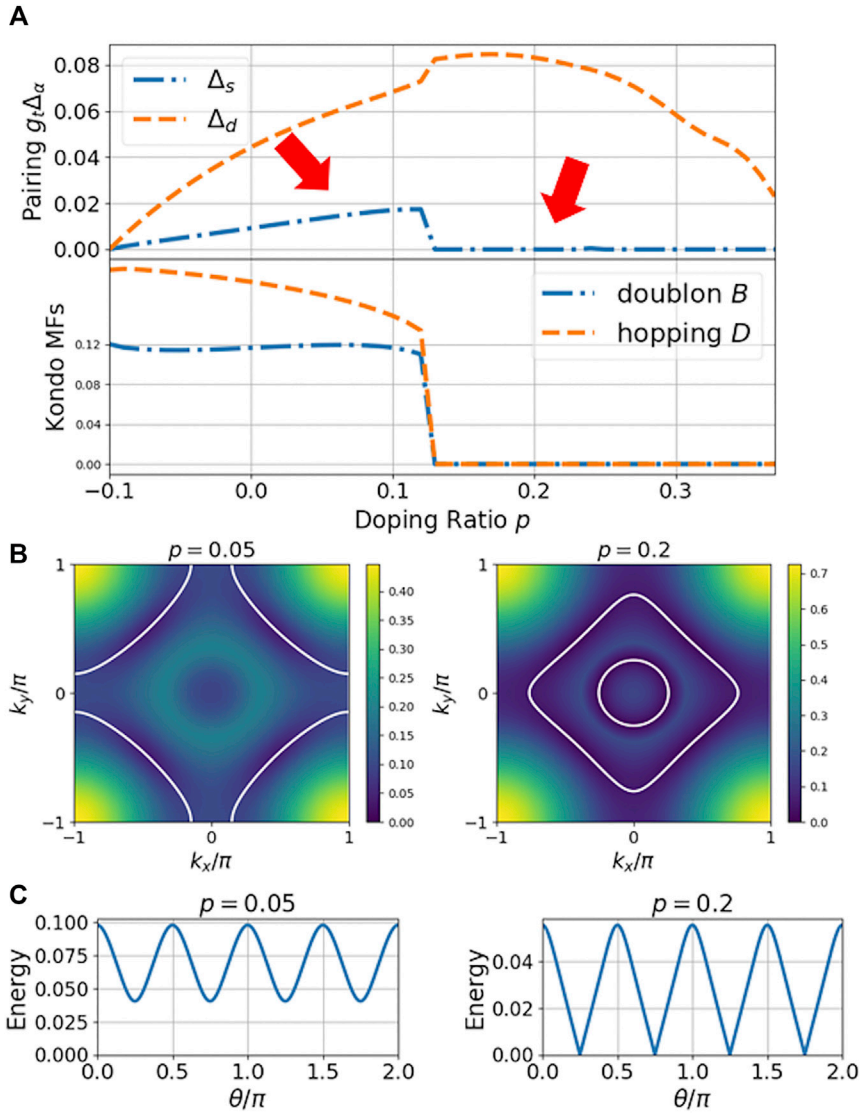

FIGURE 5 | RMFT results for $t_c/K = 0.25$. **(A)** Doping dependence of the mean-field parameters $g_t\Delta$ (upper panel) and B and D (lower panel). Comparison of **(B)** the quasiparticle excitation energy (background) and the Fermi surface (white solid line) defined as the minimal excitation energy and **(C)** superconducting gap along the Fermi surface at $p = 0.05$ ($d + is$)-wave and $p = 0.2$ (d-wave) as marked by the arrows in **(A)**. Figure adapted from Ref. [9]. Copyright 2020 by the American Physical Society.

2.5 Quantum Criticality

As shown in **Figure 5**, for moderate t_c/K, the SC transition from ($d + is$) to d-wave is accompanied with vanishing Kondo mean-field parameters B and D, which implies a breakdown of the Kondo hybridization in the large doping side. Correspondingly, the Fermi surface structures also change from a large hole-like Fermi surface around four Brillouin zone corners at low doping to two separate electron-like Fermi surfaces (from decoupled charge carriers) around the Brillouin zone center at large doping. These results may be compared with the Hall experiments in $Nd_{1-x}Sr_xNiO_2$ [49, 50], which revealed a crossover line of sign change in the temperature-doping phase diagram near the maximal T_c. The line marks a potential change in the Fermi surfaces and resembles that observed in some heavy fermion systems owing to the delocalization of localized moments [67]. It is thus attempted to link the experiment with our theoretical proposals and predict a zero-temperature quantum critical point with the SC transition and the Fermi surface change near the crossover line, although it should be cautious that they take place in different temperature region.

As a matter of fact, experiment has indeed observed quantum critical behavior in the normal state above T_c. A tentative fit of the resistivity in superconducting nickelate thin films has yielded power-law scaling with temperature, namely $\rho \sim T^\alpha$, with $\alpha = 1.1$–1.3 over a wide range [6]. **Figure 6** gives an example of the fit in $Nd_{0.8}Sr_{0.2}NiO_2$ and we obtain $\alpha \approx 1.13$ from slightly above T_c up to the room temperature. This reminds us the strange metal above T_c in optimal-doped cuprates and the non-Fermi liquid in

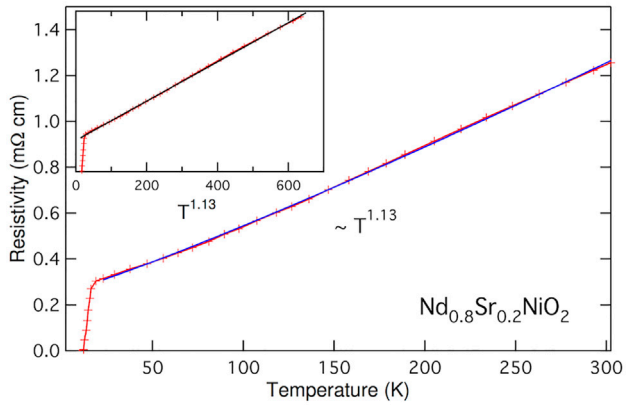

FIGURE 6 | Power-law temperature dependence of the electric resistivity above T_c = 14.9K up to the room temperature for $Nd_{0.8}Sr_{0.2}NiO_2$. The experimental data were reproduced from Ref. [1].

heavy fermion systems. Better numerical calculations are required in order to establish the exact mechanism of this scaling.

3 FUTURE PERSPECTIVE

We have introduced the picture of self-doped Mott insulator to describe the recently discovered nickelate superconductors. The self-doping effect has been generally accepted by the community and distinguishes nickelates from cuprates. We further propose a Mott-Kondo scenario and an extended *t-J-K* model based on transport measurements and electronic structure calculations. Our model bridges the usual Kondo lattice model for heavy fermions and the *t-J* model for cuprates, but shows unique features that can only be understood as an interplay of both physics. Our theory provides a natural explanation of the resistivity upturn in undoped nickelates at low temperatures, and our calculations based on the *t-J-K* model predict an exotic (d + is)-wave superconductivity that breaks the time reversal symmetry and a possible transition of the pairing symmetry at critical doping, around which the normal state exhibits non-Fermi liquid behavior above T_c. This implies that nickelate superconductors are a novel class of unconventional superconductors. Thus, exploration of new physics based on our theory will be an interesting direction for future investigations.

Currently there still exist different opinions on the effect of Sr doping. Some argued that holes may occupy other Ni 3*d* orbitals and the Hund coupling may favor a high spin state (S = 1) [8, 14, 16]. This scenario seems inconsistent with joint analyses of XAS and RIXS experiments [18] and a number of other calculations [11, 20]. Nevertheless, our model allows for a straightforward multi-orbital extension by considering a two-band Hubbard model of Ni 3*d* orbitals (or its projection at large U) plus hybridization with additional conduction bands. So far, bulk nickelates have not been found superconductive and many issues remain to be answered both in theory and in experiment [68]. Our proposal of the self-doping effect, the Mott-Kondo scenario, and the *t-J-K* model provides a promising starting basis for future investigations.

AUTHOR CONTRIBUTIONS

All authors listed have made a substantial, direct, and intellectual contribution to the work and approved it for publication.

FUNDING

This work was supported by the National Natural Science Foundation of China (Nos. 11774401, 11974397, and 12174429), the National Key Research and Development Program of MOST of China (Nos. 2017YFA0303103 and 2017YFA0302902), and the Strategic Priority Research Program of CAS (Grand No. XDB33010100).

REFERENCES

1. Li D, Lee K, Wang BY, Osada M, Crossley S, Lee HR, et al. Superconductivity in an Infinite-Layer Nickelate. *Nature* (2019) 572:624–7. doi:10.1038/s41586-019-1496-5
2. Osada M, Wang BY, Goodge BH, Lee K, Yoon H, Sakuma K, et al. A Superconducting Praseodymium Nickelate with Infinite Layer Structure. *Nano Lett* (2020) 20:5735–40. doi:10.1021/acs.nanolett.0c01392
3. Osada M, Wang BY, Lee K, Li D, Hwang HY. Phase Diagram of Infinite Layer Praseodymium Nickelate $Pr_{1-x}Sr_xNiO_2$ Thin Films. *Phys Rev Mater* (2020) 4: 121801. doi:10.1103/physrevmaterials.4.121801
4. Zeng S, Li C, Chow L, Cao Y, Zhang Z, Tang C, et al. Superconductivity in Infinite-Layer Lanthanide Nickelates. arXiv preprint arXiv:2105.13492 (2021).
5. Osada M, Wang BY, Goodge BH, Harvey SP, Lee K, Li D, et al. Nickelate Superconductivity without Rare-Earth Magnetism: (La, Sr)NiO_2. arXiv preprint arXiv:2105.13494 (2021).
6. Zhang G-M, Yang Y-f., Zhang F-C. Self-doped mott Insulator for Parent Compounds of Nickelate Superconductors. *Phys Rev B* (2020) 101(R):020501. doi:10.1103/PhysRevB.101.020501
7. Nomura Y, Hirayama M, Tadano T, Yoshimoto Y, Nakamura K, Arita R. Formation of a Two-Dimensional Single-Component Correlated Electron System and Band Engineering in the Nickelate Superconductor $NdNiO_2$. *Phys Rev B* (2019) 100:205138. doi:10.1103/PhysRevB.100.205138
8. Hu L-H, Wu C. Two-band Model for Magnetism and Superconductivity in Nickelates. *Phys Rev Res* (2019) 1:032046. doi:10.1103/PhysRevResearch.1.032046
9. Wang Z, Zhang G-M, Yang Y-f., Zhang F-C. Distinct Pairing Symmetries of Superconductivity in Infinite-Layer Nickelates. *Phys Rev B* (2020) 102(R): 220501. doi:10.1103/PhysRevB.102.220501
10. Botana AS, Norman MR. Similarities and Differences between $LaNiO_2$ and $CaCuO_2$ and Implications for Superconductivity. *Phys Rev X* (2020) 10:011024. doi:10.1103/PhysRevX.10.011024
11. Jiang M, Berciu M, Sawatzky GA. Critical Nature of the Ni Spin State in Doped $NdNiO_2$. *Phys Rev Lett* (2020) 124:207004. doi:10.1103/PhysRevLett.124.207004
12. Sakakibara H, Usui H, Suzuki K, Kotani T, Aoki H, Kuroki K. Model Construction and a Possibility of Cupratelike Pairing in a New d^9 Nickelate Superconductor (Nd,Sr)NiO_2. *Phys Rev Lett* (2020) 125:077003. doi:10.1103/PhysRevLett.125.077003

13. Hepting M, Li D, Jia CJ, Lu H, Paris E, Tseng Y, et al. Electronic Structure of the Parent Compound of Superconducting Infinite-Layer Nickelates. *Nat Mater* (2020) 19:381–5. doi:10.1038/s41563-020-0761-110.1038/s41563-019-0585-z
14. Zhang Y-H, Vishwanath A. Type-II t–J Model in Superconducting Nickelate $Nd_{1-x}Sr_xNiO_2$. *Phys Rev Res* (2020) 2:023112. doi:10.1103/PhysRevResearch.2.023112
15. Lechermann F. Multiorbital Processes Rule the $Nd_{1-x}Sr_xNiO_2$ Normal State. *Phys Rev X* (2020) 10:041002. doi:10.1103/PhysRevX.10.041002
16. Werner P, Hoshino S. Nickelate Superconductors: Multiorbital Nature and Spin Freezing. *Phys Rev B* (2019) 101:041104. doi:10.1103/PhysRevB.101.041104
17. Gu Y, Zhu S, Wang X, Hu J, Chen H. A Substantial Hybridization between Correlated Ni-D Orbital and Itinerant Electrons in Infinite-Layer Nickelates. *Commun Phys* (2020) 3:1–9. doi:10.1038/s42005-020-0347-x
18. Rossi M, Lu H, Nag A, Li D, Osada M, Lee K, et al. Orbital and Spin Character of Doped Carriers in Infinite-Layer Nickelates. arXiv preprint arXiv:2011.00595 (2020).
19. Kitatani M, Si L, Janson O, Arita R, Zhong Z, Held K. Nickelate Superconductors-A Renaissance of the One-Band Hubbard Model. *npj Quan Mater.* (2020) 5:59. doi:10.1038/s41535-020-00260-y
20. Higashi K, Winder M, Kuneš J, Hariki A. Core-Level X-Ray Spectroscopy of Infinite-Layer Nickelate: LDA+DMFT Study. *Phys Rev X* (2021) 11:041009. doi:10.1103/PhysRevX.11.041009
21. Gao J, Peng S, Wang Z, Fang C, Weng H. Electronic Structures and Topological Properties in Nickelates $Ln_{n+1}Ni_nO_{2n+2}$. *Natl Sci Rev* (2021) 8:nwaa218. doi:10.1093/nsr/nwaa218
22. Bednorz JG, Müller KA. Possible highT C Superconductivity in the Ba-La-Cu-O System. *Z Physik B - Condensed Matter* (1986) 64:189–93. doi:10.1007/BF01303701
23. Anderson PW. The Resonating Valence Bond State in La_2CuO_4 and Superconductivity. *Science* (1987) 235:1196–8. doi:10.1126/science.235.4793.1196
24. Anderson PW, Lee PA, Randeria M, Rice TM, Trivedi N, Zhang FC. The Physics behind High-Temperature Superconducting Cuprates: the plain Vanilla Version of RVB. *J Phys Condens Matter* (2004) 16:R755–R769. doi:10.1088/0953-8984/16/24/r02
25. Lee PA, Nagaosa N, Wen X-G. Doping a Mott Insulator: Physics of High-Temperature Superconductivity. *Rev Mod Phys* (2006) 78:17–85. doi:10.1103/RevModPhys.78.17
26. Zhang FC, Rice TM. Effective Hamiltonian for the Superconducting Cu Oxides. *Phys Rev B* (1988) 37:3759–61. doi:10.1103/PhysRevB.37.3759
27. Shen Z-X, Dessau DS, Wells BO, King DM, Spicer WE, Arko AJ, et al. Anomalously Large gap Anisotropy in the a-b Plane of $Bi_2Sr_2CaCu_2O_{8+\delta}$. *Phys Rev Lett* (1993) 70:1553–6. doi:10.1103/physrevlett.70.1553
28. Wollman DA, Van Harlingen DJ, Lee WC, Ginsberg DM, Leggett AJ. Experimental Determination of the Superconducting Pairing State in YBCO from the Phase Coherence of YBCO-Pb dc SQUIDs. *Phys Rev Lett* (1993) 71:2134–7. doi:10.1103/PhysRevLett.71.2134
29. Tsuei CC, Kirtley JR, Chi CC, Yu-Jahnes LS, Gupta A, Shaw T, et al. Pairing Symmetry and Flux Quantization in a Tricrystal Superconducting Ring of $YBa_2Cu_3O_{7-\delta}$. *Phys Rev Lett* (1994) 73:593–6. doi:10.1103/physrevlett.73.593
30. Anisimov VI, Bukhvalov D, Rice TM. Electronic Structure of Possible Nickelate Analogs to the Cuprates. *Phys Rev B* (1999) 59:7901–6. doi:10.1103/PhysRevB.59.7901
31. Hayward MA, Green MA, Rosseinsky MJ, Sloan J. Sodium Hydride as a Powerful Reducing Agent for Topotactic Oxide Deintercalation: Synthesis and Characterization of the Nickel(I) Oxide $LaNiO_2$. *J Am Chem Soc* (1999) 121:8843–54. doi:10.1021/ja991573i
32. Lee K-W, Pickett WE. Infinite-layer $LaNiO_2$: Ni^{1+} is not Cu^{2+}. *Phys Rev B* (2004) 70:165109. doi:10.1103/PhysRevB.70.165109
33. Botana AS, Pardo V, Norman MR. Electron Doped Layered Nickelates: Spanning the Phase Diagram of the Cuprates. *Phys Rev Mater* (2017) 1:021801. doi:10.1103/PhysRevMaterials.1.021801
34. Chaloupka J, Khaliullin G. Orbital Order and Possible Superconductivity in $LaNiO_3/LaMO_3$ Superlattices. *Phys Rev Lett* (2008) 100:016404. doi:10.1103/PhysRevLett.100.016404
35. Hansmann P, Yang X, Toschi A, Khaliullin G, Andersen OK, Held K. Turning a Nickelate Fermi Surface into a Cupratelike One through Heterostructuring. *Phys Rev Lett* (2009) 103:016401. doi:10.1103/PhysRevLett.103.016401
36. Middey S, Chakhalian J, Mahadevan P, Freeland JW, Millis AJ, Sarma DD. Physics of Ultrathin Films and Heterostructures of Rare-Earth Nickelates. *Annu Rev Mater Res* (2016) 46:305–34. doi:10.1146/annurev-matsci-070115-032057
37. Boris AV, Matiks Y, Benckiser E, Frano A, Popovich P, Hinkov V, et al. Dimensionality Control of Electronic Phase Transitions in Nickel-Oxide Superlattices. *Science* (2011) 332:937–40. doi:10.1126/science.1202647
38. Benckiser E, Haverkort MW, Brück S, Goering E, Macke S, Frañó A, et al. Orbital Reflectometry of Oxide Heterostructures. *Nat Mater* (2011) 10:189–93. doi:10.1038/nmat2958
39. Disa AS, Kumah DP, Malashevich A, Chen H, Arena DA, Specht ED, et al. Orbital Engineering in Symmetry-Breaking Polar Heterostructures. *Phys Rev Lett* (2015) 114:026801. doi:10.1103/PhysRevLett.114.026801
40. Zhang J, Botana AS, Freeland JW, Phelan D, Zheng H, Pardo V, et al. Large Orbital Polarization in a Metallic Square-Planar Nickelate. *Nat Phys* (2017) 13:864–9. doi:10.1038/nphys4149
41. Hayward MA, Rosseinsky MJ. Synthesis of the Infinite Layer Ni(I) Phase $NdNiO_{2+x}$ by Low Temperature Reduction of $NdNiO_3$ with Sodium Hydride. *Solid State Sci* (2003) 5:839–50. doi:10.1016/S1293-2558(03)00111-0
42. Ikeda A, Krockenberger Y, Irie H, Naito M, Yamamoto H. Direct Observation of Infinite NiO_2 Planes in $LaNiO_2$ Films. *Appl Phys Express* (2016) 9:061101. doi:10.7567/APEX.9.061101
43. Zhou X, Zhang X, Yi J, Qin P, Feng Z, Jiang P, et al. Antiferromagnetism in Ni-Based Superconductors. arXiv preprint arXiv:2110.14915 (2021).
44. Cui Y, Li C, Li Q, Zhu X, Hu Z, Yang Y-f., et al. NMR Evidence of Antiferromagnetic Spin Fluctuations in $Nd_{0.85}Sr_{0.15}NiO_2$. *Chin Phys. Lett.* (2021) 38:067401. doi:10.1088/0256-307X/38/6/067401
45. Goodge BH, Li D, Lee K, Osada M, Wang BY, Sawatzky GA, et al. Doping Evolution of the Mott-Hubbard Landscape in Infinite-Layer Nickelates. *Proc Natl Acad Sci USA* (2021) 118:e2007683118. doi:10.1073/pnas.2007683118
46. Fu Y, Wang L, Cheng H, Pei S, Zhou X, Chen J, et al. Core-level X-ray Photoemission and Raman Spectroscopy Studies on Electronic Structures in Mott-Hubbard Type Nickelate Oxide $NdNiO_2$. arXiv preprint arXiv:1911.03177 (2019).
47. Lu H, Rossi M, Nag A, Osada M, Li DF, Lee K, et al. Magnetic Excitations in Infinite-Layer Nickelates. *Science* (2021) 373:213–6. doi:10.1126/science.abd7726
48. Been E, Lee WS, Hwang HY, Cui Y, Zaanen J, Devereaux T, et al. Electronic Structure Trends across the Rare-Earth Series in Superconducting Infinite-Layer Nickelates. *Phys Rev X* (2021) 11:011050. doi:10.1103/physrevx.11.011050
49. Li D, Wang BY, Lee K, Harvey SP, Osada M, Goodge BH, et al. Superconducting Dome in $Nd_{1-x}Sr_xNiO_2$ Infinite Layer Films. *Phys Rev Lett* (2020) 125:027001. doi:10.1103/PhysRevLett.125.027001
50. Zeng S, Tang CS, Yin X, Li C, Li M, Huang Z, et al. Phase Diagram and Superconducting Dome of Infinite-Layer $Nd_{1-x}Sr_xNiO_2$ Thin Films. *Phys Rev Lett* (2020) 125:147003. doi:10.1103/PhysRevLett.125.147003
51. Gu Q, Li Y, Wan S, Li H, Guo W, Yang H, et al. Single Particle Tunneling Spectrum of Superconducting $Nd_{1-x}Sr_xNiO_2$ Thin Films. *Nat Commun* (2020) 11:1–7. doi:10.1038/s41467-020-19908-1
52. Hundley M, Malinowski A, Pagliuso P, Sarrao J, Thompson J. Anomalous F-Electron Hall Effect in the Heavy-Fermion System $CeTIn_5$ (T=Co, Ir, or Rh). *Phys Rev B* (2004) 70:035113. doi:10.1103/physrevb.70.035113
53. Jiang P, Si L, Liao Z, Zhong Z. Electronic Structure of Rare-Earth Infinite-Layer $RNiO_2$(R=La,Nd). *Phys Rev B* (2019) 100:201106. doi:10.1103/PhysRevB.100.201106
54. Yang Y-f., Fisk Z, Lee H-O, Thompson JD, Pines D. Scaling the Kondo Lattice. *Nature* (2008) 454:611–3. doi:10.1038/nature07157
55. Chen J, Wang Z, Li Y, Feng C, Dai J, Xu Za., et al. Heavy Fermion Quantum Criticality at Dilute Carrier Limit in $CeNi_{2-\delta}(As_{1-x}P_x)_2$. *Sci Rep* (2019) 9:1–10. doi:10.1038/s41598-019-48662-8
56. Xu Y, Sheng Y, Yang YF. Mechanism of the Insulator-To-Metal Transition and Superconductivity in the Spin Liquid Candidate $NaYbSe_2$ under Pressure. arXiv preprint arXiv:2108.03218 (2021).

57. Lacroix C. Some Exact Results for the Kondo Lattice with Infinite Exchange Interaction. *Solid State Commun* (1985) 54:991–4. doi:10.1016/0038-1098(85)90171-1
58. Sigrist M, Ueda K, Tsunetsugu H. Ferromagnetism of the Kondo Lattice in the Low-Carrier-Concentration Limit. *Phys Rev B* (1992) 46:175–83. doi:10.1103/PhysRevB.46.175
59. Hewson AC. *The Kondo Problem to Heavy Fermions*. Cambridge: Cambridge University Press (1993).
60. Fert A, Levy PM. Theory of the Hall Effect in Heavy-Fermion Compounds. *Phys Rev B* (1987) 36:1907–16. doi:10.1103/physrevb.36.1907
61. Nagaosa N, Sinova J, Onoda S, MacDonald AH, Ong NP. Anomalous Hall Effect. *Rev Mod Phys* (2010) 82:1539–92. doi:10.1103/RevModPhys.82.1539
62. Zhang FC, Gros C, Rice TM, Shiba H. A Renormalised Hamiltonian Approach to a Resonant Valence Bond Wavefunction. *Supercond Sci Technol* (1988) 1:36–46. doi:10.1088/0953-2048/1/1/009
63. Wu X, Di Sante D, Schwemmer T, Hanke W, Hwang HY, Raghu S, Thomale R. Robust $d_{x^2-y^2}$-wave Superconductivity of Infinite-Layer Nickelates-Wave Superconductivity of Infinite-Layer Nickelates. *Phys Rev B* (2020) 101:060504. doi:10.1103/PhysRevB.101.060504
64. Bodensiek O, Žitko R, Vojta M, Jarrell M, Pruschke T. Unconventional Superconductivity from Local Spin Fluctuations in the Kondo Lattice. *Phys Rev Lett* (2013) 110:146406. doi:10.1103/PhysRevLett.110.146406
65. Xiang Y, Li Q, Li Y, Yang H, Nie Y, Wen H-H. Physical Properties Revealed by Transport Measurements for Superconducting $Nd_{0.8}Sr_{0.2}NiO_2$ Thin Films. *Chin Phys. Lett.* (2021) 38:047401. doi:10.1088/0256-307X/38/4/047401
66. Wang BY, Li D, Goodge BH, Lee K, Osada M, Harvey SP, et al. Isotropic Pauli-Limited Superconductivity in the Infinite-Layer Nickelate $Nd_{0.775}Sr_{0.225}NiO_2$. *Nat Phys* (2021) 17:473–7. doi:10.1038/s41567-020-01128-5
67. Yang Y-f., Pines D, Lonzarich G. Quantum Critical Scaling and Fluctuations in Kondo Lattice Materials. *Proc Natl Acad Sci USA* (2017) 114:6250–5. doi:10.1073/pnas.1703172114
68. Gu Q, Wen HH. Superconductivity in Nickel Based 112 Systems. arXiv preprint arXiv:2109.07654 (2021).

Conflict of Interest: The authors declare that the research was conducted in the absence of any commercial or financial relationships that could be construed as a potential conflict of interest.

Publisher's Note: All claims expressed in this article are solely those of the authors and do not necessarily represent those of their affiliated organizations, or those of the publisher, the editors and the reviewers. Any product that may be evaluated in this article, or claim that may be made by its manufacturer, is not guaranteed or endorsed by the publisher.

frontiers in Physics

REVIEW
published: 21 January 2022
doi: 10.3389/fphy.2021.810394

Phase Diagram of Nickelate Superconductors Calculated by Dynamical Vertex Approximation

Karsten Held[1]*, *Liang Si*[1,2]*, *Paul Worm*[1], *Oleg Janson*[3], *Ryotaro Arita*[4,5], *Zhicheng Zhong*[6], *Jan M. Tomczak*[1] and *Motoharu Kitatani*[1,4]*

[1]Institute for Solid State Physics, Vienna University of Technology, Vienna, Austria, [2]School of Physics, Northwest University, Xi'an, China, [3]Institute for Theoretical Solid State Physics, Leibniz IFW Dresden, Dresden, Germany, [4]RIKEN Center for Emergent Matter Sciences (CEMS), Wako, Japan, [5]Department of Applied Physics, the University of Tokyo, Bunkyo, Japan, [6]Key Laboratory of Magnetic Materials and Devices and Zhejiang Province Key Laboratory of Magnetic Materials and Application Technology, Ningbo Institute of Materials Technology and Engineering (NIMTE), Chinese Academy of Sciences, Ningbo, China

We review the electronic structure of nickelate superconductors with and without effects of electronic correlations. As a minimal model, we identify the one-band Hubbard model for the Ni $3d_{x^2-y^2}$ orbital plus a pocket around the A-momentum. The latter, however, merely acts as a decoupled electron reservoir. This reservoir makes a careful translation from nominal Sr-doping to the doping of the one-band Hubbard model mandatory. Our dynamical mean-field theory calculations, in part already supported by the experiment, indicate that the Γ pocket, Nd 4f orbitals, oxygen 2p, and the other Ni 3d orbitals are not relevant in the superconducting doping regime. The physics is completely different if topotactic hydrogen is present or the oxygen reduction is incomplete. Then, a two-band physics hosted by the Ni $3d_{x^2-y^2}$ and $3d_{3z^2-r^2}$ orbitals emerges. Based on our minimal modeling, we calculated the superconducting T_c vs. Sr-doping x phase diagram prior to the experiment using the dynamical vertex approximation. For such a notoriously difficult to determine quantity as T_c, the agreement with the experiment is astonishingly good. The prediction that T_c is enhanced with pressure or compressive strain has been confirmed experimentally as well. This supports that the one-band Hubbard model plus an electron reservoir is the appropriate minimal model.

Keywords: electronic structure calculations, dynamical mean field theory, electronic correlation, high-temperature superconductivity, solid state theory

OPEN ACCESS

Edited by:
Matthias Hepting,
Max Planck Institute for Solid State Research, Germany

Reviewed by:
Fabio Bernardini,
University of Cagliari, Italy
Liviu Chioncel,
University of Augsburg, Germany

***Correspondence:**
Karsten Held
held@ifp.tuwien.ac.at
Liang Si
liang.si@ifp.tuwien.ac.at
Motoharu Kitatani
motoharu.kitatani@riken.jp

Specialty section:
This article was submitted to Condensed Matter Physics, a section of the journal Frontiers in Physics

Received: *06 November 2021*
Accepted: *10 December 2021*
Published: *21 January 2022*

Citation:
Held K, Si L, Worm P, Janson O, Arita R, Zhong Z, Tomczak JM and Kitatani M (2022) Phase Diagram of Nickelate Superconductors Calculated by Dynamical Vertex Approximation. Front. Phys. 9:810394. doi: 10.3389/fphy.2021.810394

1 INTRODUCTION

Twenty years ago, Anisimov, Bukhvalov, and Rice [1] suggested high-temperature (T_c) superconductivity in nickelates based on material calculations that showed apparent similarities to cuprates. Subsequent calculations [2–4] demonstrated the potential to further engineer the nickelate Fermi surface by heterostructuring. Two years ago, Li, Hwang et al. [5] discovered superconductivity in Sr-doped $NdNiO_2$ films grown on a $SrTiO_3$ substrate and protected by a $SrTiO_3$ capping layer. These novel $Sr_xNd_{1-x}NiO_2$ films are isostructural and formally isoelectric to the arguably simplest, but certainly not the best superconducting cuprate: infinite layer $CaCuO_2$ [6–9].

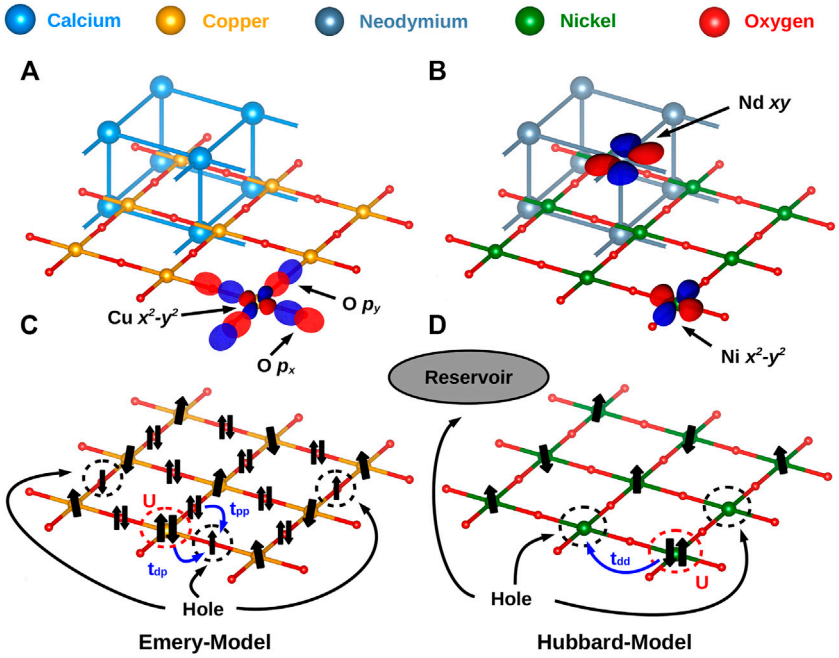

FIGURE 1 | Crystal lattice and most important orbitals for **(A)** cuprates and **(B)** nickelates. **(C)** For cuprates, the arguably simplest model is the Emery model with a half-filled copper $3d_{x^2-y^2}$ band and holes in the oxygen $2p$ orbitals that can hop to other oxygen (t_{pp}) and copper sites (t_{dp}) where double occupations are suppressed by the interaction U. **(D)** For nickelates, we have a Ni-$3d_{x^2-y^2}$-band Hubbard model which, however, only accommodates part of the holes induced by Sr-doping. The others go to the A pocket stemming from the Nd $5d_{xy}$ band and acting as a decoupled reservoir.

However, the devil is in the details, and here cuprates and nickelates differ. For revealing such material-specific differences, band-structure calculations based on density functional theory (DFT) are the method of choice. They serve as a starting point for understanding the electronic structure and, subsequently, the phase diagram of nickelate superconductors. Following the experimental discovery of nickelate superconductivity, and even before that, numerous DFT studies have been published [10–20]. Based on these DFT calculations, various models for the low-energy electronic structure for nickelates and the observed superconductivity have been proposed. Besides the cuprate-like Ni $3d_{x^2-y^2}$ band, DFT shows an A and a Γ pocket which originate from Nd $5d_{xy}$ and $5d_{3z^2-r^2}$ bands, but with major Ni $3d$ admixture in the region of the pocket. The importance of the Ni $3d_{3z^2-r^2}$ orbital has been suggested in some studies [21–24], and that of the Nd-$4f$ orbitals in others [20, 25]. Furthermore, there is the question regarding the relevance of the oxygen $2p$ orbitals. For cuprates, these are, besides the Cu $3d_{x^2-y^2}$ orbitals, the most relevant. Indeed, cuprates are generally believed to be charge-transfer insulators [26]. This leads to the three-orbital Emery model [27] visualized in **Figures 1A,C** as the minimal model for cuprates. The much more frequently investigated Hubbard model [28–30] may, in the case of cuprates, only be considered as an effective Hamiltonian mimicking the physics of the Zhang–Rice singlet [31].

At first glance, nickelates appear to be much more complicated with more relevant orbitals than in the case of the cuprates. In this article, we review the electronic structure of nickelates in comparison to that of cuprates and the arguments for a simpler description of nickelate superconductors, namely, a Hubbard model for the Ni $3d_{x^2-y^2}$ band plus a largely decoupled reservoir corresponding to the A pocket. This A pocket is part of the Nd $5d_{xy}$ band which has, however, a major admixture of Ni $3d_{xz/yz}$ and O $2p_z$ states around the momentum A. This leaves us with **Figures 1B,D** as the arguably simplest model for nickelates [32, 33]. This (our) perspective is still controversially discussed in the literature. However, as we will point out below, a number of experimental observations already support this perspective against some of the early suggestions that other orbitals are relevant. Certainly, other perspectives will be taken in other articles of this series on "Advances in Superconducting Infinite-Layer and Related Nickelates." The simple picture of a one-band Hubbard model, whose doping needs to be carefully calculated since part of the holes in Sr-doped $Sr_xNd_{1-x}NdO_2$ go to the A pocket, allowed us [33] to calculate T_c, see **Figure 5**, at a time when only the T_c for a single doping $x = 20\%$ was experimentally available. To this end, state-of-the-art dynamical vertex approximation (DΓA) [36–38], a Feynman diagrammatic extension of dynamical mean-field theory (DMFT) [39–42] has been used. For such a notoriously difficult to calculate physical quantity as T_c, the agreement of the single-orbital Hubbard model calculation with subsequent experiments [34, 35] is astonishingly good. This further supports the modeling by a single-orbital Hubbard model which, thus,

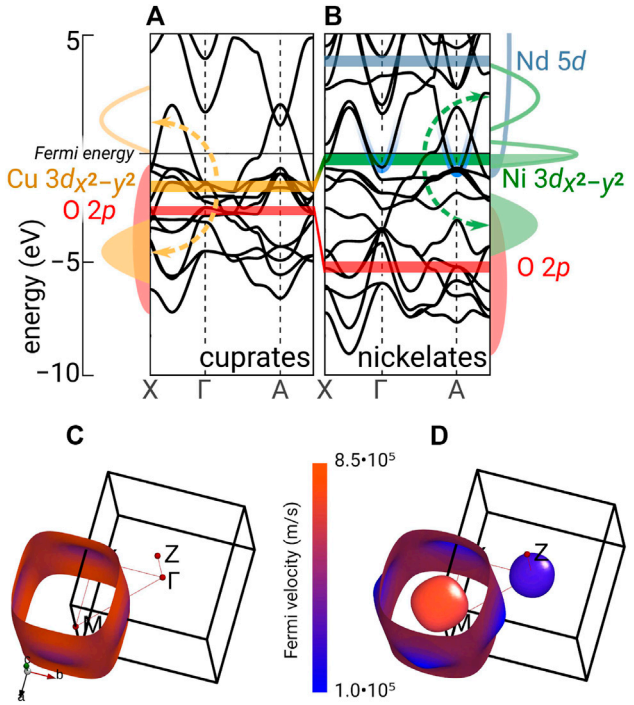

FIGURE 2 | Electronic structures of $CaCuO_2$ **(A)** and $NdNiO_2$ **(B)** exemplifying superconducting cuprates and nickelates. Top: The bars indicate the center of energy for the most important DFT bands. The dashed arrows indicate the correlation-induced splitting of the Cu or Ni $3d_{x^2-y^2}$ band into Hubbard bands, leading to the (schematic) spectral function at the side. Cuprates are charge-transfer insulators with a gap between the O $2p$ and the upper Cu $3d_{x^2-y^2}$ Hubbard band as the lower Cu $3d_{x^2-y^2}$ Hubbard band is below the O $2p$ band. For nickelates, bands with a large La (Nd) $5d$ contribution cross the Fermi energy at Γ and A, self-doping the Ni $3d_{x^2-y^2}$ band away from half-filling. **(C,D)**: Corresponding DFT Fermi surface. For cuprates, DFT shows a single Cu $3d_{x^2-y^2}$ hole–like Fermi surface; for nickelates, there is a similar, slightly more warped Ni $3d_{x^2-y^2}$ Fermi surface and additional small pockets around the Γ and A momentum.

should serve at the very least as a good approximation or a starting point.

The outline of this article is as follows: In **Section 2**,we first compare the electronic structure of nickelates to that of cuprates, starting from DFT but also discussing effects of electronic correlations as described, for example, by DMFT. Subsequently, we argue in **Section 3**, orbital-by-orbital, that the other orbitals besides the Ni $3d_{x^2-y^2}$ and the A pocket are, from our perspective, not relevant. This leaves us with the one-$3d_{x^2-y^2}$-band Hubbard model plus an electron reservoir representing the A pocket of **Figures 1B,D**, which is discussed in **Section 4**, including the translation of Sr-doping to the filling in the Hubbard model and the reservoir. In **Section 5**, we discuss the effect of non-local correlations as described in DΓA and the calculated superconducting phase diagram. **Section 6** shows that topotactic hydrogen, which is difficult to detect in the experiment, completely overhauls the electronic structure and the prevalence of superconductivity. Finally, **Section 7** summarizes the article.

2 ELECTRONIC STRUCTURE: NICKELATES VS. CUPRATES

Let us start by looking into the electronic structure in more detail and start with the DFT results. On a technical note, the calculations presented have been performed using the WIEN2K [43, 44], VASP [45], and FPLO [46] program packages, with the PBE [47] version of the generalized gradient approximation (GGA). For further details, see the original work [33]. **Figure 2** compares the bandstructure of the two simple materials: $CaCuO_2$ and $NdNiO_2$. Here, we restrict ourselves to only the Brillouin zone path along the most relevant momenta for these compounds: Γ (0, 0, 0), X (π, 0, 0), and A (π, π, π). In DFT, both the cuprate and nickelate parent compounds are metals with a prominent Cu or Ni $3d_{x^2-y^2}$ band crossing the Fermi energy. In other aspects, both materials differ (for a review cf [48]): In the case of cuprates, the oxygen bands are much closer to the Fermi energy. Hence, if electronic correlations split the DFT bands into two Hubbard bands as indicated in **Figure 2** by the arrows and the spectral function in the left side panel, we get a charge-transfer insulator [26]. For this charge-transfer insulator, the oxygen $2p$ orbitals are the first orbitals below the Fermi level (E_F) and receive the holes that are induced by doping. The Cu $3d_{x^2-y^2}$ lower Hubbard band is below these oxygen orbitals, and the Cu $3d_{x^2-y^2}$ upper Hubbard band is above the Fermi level. Let us note that we here refer to oxygen $2p$ orbitals and Cu $3d_{x^2-y^2}$ orbitals even though the hybridization between both is very strong. Indeed, the two sets of orbitals strongly mix in the resulting effective DFT bands of **Figure 2**.

Because cuprates are charge-transfer insulators, the one-band Hubbard model can only be considered an effective Hamiltonian mimicking the Zhang–Rice singlet [31]. As already pointed out in the *Introduction*, more appropriate is the Emery model of **Figure 1**. The correlation-induced splitting into the Hubbard bands [40], as well as the Zhang–Rice singlet [49], can be described already by DMFT [39, 40, 42]. Two-dimensional spin-fluctuations and superconductivity, however, cannot be described. For describing such physics, non-local correlations beyond DMFT are needed.

For the nickelates, the oxygen bands are at a much lower energy. Hence, as indicated in the right side panel of **Figure 2**, the lower Ni $3d_{x^2-y^2}$ Hubbard band can be expected to be closer to the Fermi energy than the oxygen p orbitals [32, 33]. Consequently, undoped nickelates would be Mott–Hubbard insulators if it was not for two additional bands that cross E_F around the Γ- and A-momentum. These form electron pockets, as visualized in **Figure 2** (bottom right), and self-dope the Ni $3d_{x^2-y^2}$ band away from half-filling. As the $3d_{x^2-y^2}$ is doped, it develops, even when the Coulomb interaction is large, a quasiparticle peak at the Fermi energy as displayed in the right side panel of **Figure 2**.

3 IRRELEVANCE OF VARIOUS ORBITALS

Next, we turn to various orbitals that may appear relevant at first glance but turn out to be irrelevant for the low-energy physics

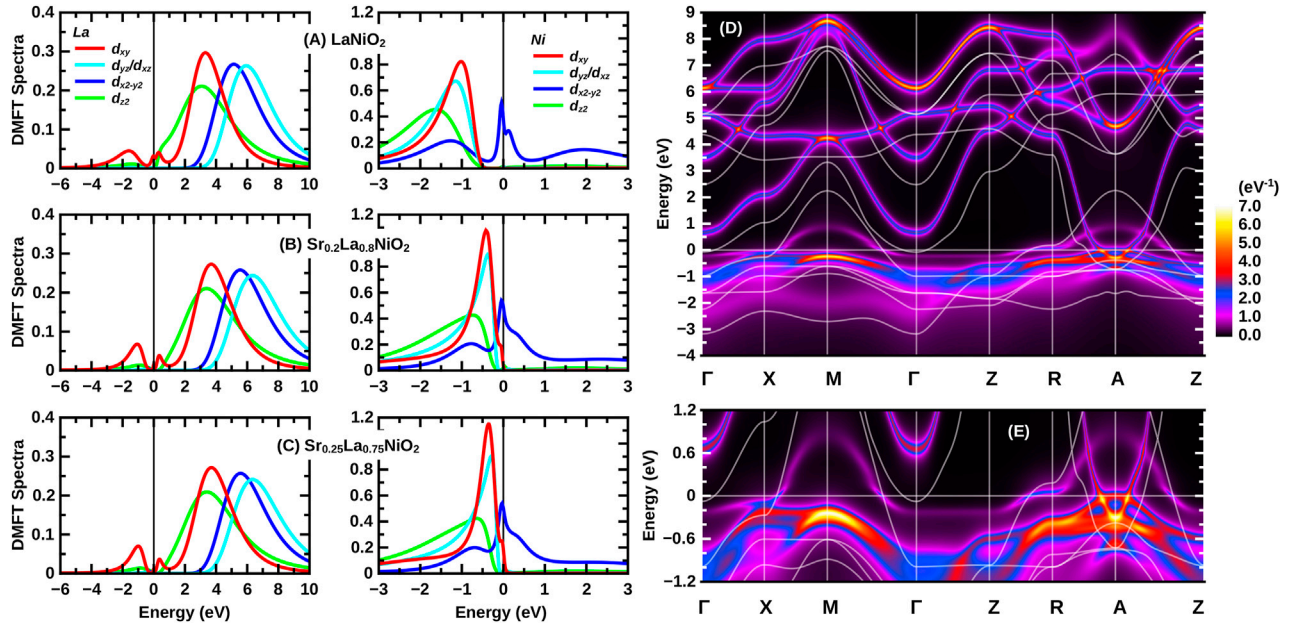

FIGURE 3 | DMFT *k*-integrated **(A–C)** and *k*-resolved **(D,E)** spectral functions $A(\omega)$ and $A(k, \omega)$ of undoped $LaNiO_2$ **(A)**, 20% Sr-doped $LaNiO_2$ ($Sr_{0.2}La_{0.8}NiO_2$) **(B)**, and 25% Sr-doped $LaNiO_2$ ($Sr_{0.25}La_{0.75}NiO_2$) **(C)**. The *k*-resolved spectral function $A(k, \omega)$ of $La_{0.8}Sr_{0.2}NiO_2$ is shown in **(D)**; **(E)** is a zoom-in of **(D)**. Data partially obtained from [33, 55].

when taking electronic correlations properly into account. To account for the latter, we use DFT + DMFT [50–54], which is the state of the art for calculating correlated materials.

Oxygen Orbitals

For nickelates, the oxygen 2*p* orbitals are approximately 3 eV lower in energy than in cuprates within DFT. Hence, some DFT + DMFT calculations did not include these from the beginning [32, 33], and those that did [22] also found the oxygen 2*p* orbitals at a lower energy than the lower Ni $3d_{x^2-y^2}$ Hubbard band. Hence, while there is still some hybridization and mixing between the O 2*p* states and the Ni $3d_{x^2-y^2}$ states, a projection onto a low-energy set of orbitals without oxygen appears possible.

Ni $3d_{3z^2-r^2}$ and t_{2g} Orbitals

Instead of the oxygen 2*p* orbitals, the DFT calculation in **Figure 2** and elsewhere [10, 11, 17, 48] show other Ni 3*d* orbitals closely below the Ni $3d_{x^2-y^2}$ band. In fact, these other 3*d* orbitals are somewhat closer to the Fermi level than in the case of cuprates. Electronic correlations can strongly modify the DFT band structure. In particular, the Hund's exchange J tends to drive the system toward a more equal occupation of different orbitals, especially if there is more than one hole (more than one unpaired electron) in the Ni 3*d* orbitals. This is not only because a larger local spin is made possible but also because the inter-orbital Coulomb interaction U' between two electrons in two different orbitals is smaller than the intra-orbital Coulomb interaction $U = U' + 2J$ for two electrons in the same orbital. This tendency is countered by the crystal field splitting (local DFT potentials) which puts the $3d_{x^2-y^2}$ orbital above the Ni $3d_{3z^2-r^2}$ orbital and the other (t_{2g}) Ni 3*d* orbitals because of the absence of apical O atoms in NiO_4 squares.

Figure 3 shows the DFT + DMFT spectral function for $Sr_xLa_{1-x}NiO_2$ from 0 to 25% Sr-doping. In these calculations [33], all Ni 3*d* and all La 5*d* orbitals have been taken into account in a WIEN2WANNIER [56] projection supplemented by interactions calculated within the constrained random phase approximation (cRPA) [55] to be $U' = 3.10$ eV (2.00 eV) and Hund's exchange $J = 0.65$ eV (0.25 eV) for Ni (La). On a technical note, the DMFT self-consistency equations [39] have been solved here at room temperature (300 K) by continuous-time quantum Monte Carlo simulations in the hybridization expansions [57] using the W2DYNAMICS implementation [58, 59] and the maximum entropy code of ANA_CONT [60] for analytic continuation.

Clearly, **Figure 3** indicates that for up to 20% Sr-doping, the other Ni 3*d* orbitals besides the $3d_{x^2-y^2}$ orbital are not relevant for the low-energy physics of $Sr_xLa_{1-x}NiO_2$; they are fully occupied below the Fermi energy. With doping, these other Ni 3*d* orbitals, however, shift more and more upward in energy. At around 25% Sr-doping, they touch the Fermi energy and hence a multi-orbital Ni description becomes necessary at larger dopings. That is, between 20 and 30% Sr-doping, the physics of $Sr_xLa_{1-x}NiO_2$ turns from single to multi-orbital. In the case of $Sr_xNd_{1-x}NiO_2$, this turning point is at slightly larger doping [33]. Later, in **Section 6**, we will see that for the Ni $3d^8$ configuration, which in **Section 6** is induced by topotactic hydrogen and here would be obtained for 100% Sr doping; the two holes in the Ni 3*d* orbitals form a spin-1 and occupy two orbitals: $3d_{x^2-y^2}$ and $3d_{3z^2-r^2}$. In **Figure 3**,we see at 30% doping, the first steps into this direction. Importantly, within the superconducting doping regime which,

noteworthy, is below 24% Sr-doping for $Sr_xNd_{1-x}NiO_2$ [34, 35] and 21% for $Sr_xLa_{1-x}NiO_2$ [61], a single $3d_{x^2-y^2}$ Ni-orbital is sufficient for the low-energy modeling. A one-band Hubbard model description based on DMFT calculations was also concluded in [32] for the undoped parent compound.

DFT + DMFT calculations by Lechermann [22, 23] stress, on the other hand, the relevance of the $3d_{3z^2-r^2}$ orbital. Let us note that also in [22] the number of holes in the $3d_{3z^2-r^2}$ orbital is considerably less than in that in the $3d_{x^2-y^2}$. However, for low Sr-doping, also a small quasiparticle peak develops for the $3d_{3z^2-r^2}$ band [22, 23]. An important difference to [33, 55] is that the $5d$ Coulomb interaction has been taken into account in [33, 55] and that the Coulomb interaction of [22] is substantially larger. The $5d$ Coulomb interaction pushes the Γ pocket above the Fermi energy (see next paragraph). As much of the holes in the $3d_{3z^2-r^2}$ orbital stem from the admixture of this orbital to the Γ pocket, this difference is very crucial for the occupation of the $3d_{3z^2-r^2}$ orbital in some calculations [21, 23]. On the other hand, in GW + extended DMFT calculations by Petocchi *et al.* [24], the $3d_{3z^2-r^2}$ orbital is pushed to the Fermi energy for large k_z instead, that is, around the R, Z, and A point. Except for this large k_z deviation, the Fermi surface, the effective mass of the Ni $3d_{x^2-y^2}$ orbital etc. of [24] are similar to our calculation [33, 62].

First experimental hints on the (ir) relevance of the $3d_{3z^2-r^2}$ can be obtained from resonant inelastic X-ray scattering (RIXS) experiments [63, 64]. Higashi et al. [65] analyzed these RIXS data by comparison with DFT + DMFT and obtained good agreement with the experiment. They conclude that $NdNiO_2$ is slightly doped away from $3d^9$ because of a small self-doping from the Nd $5d$ band and that only the $3d_{x^2-y^2}$ Ni orbital (not the $3d_{3z^2-r^2}$ orbital) is partially filled and that the Ni–O hybridization plays a less important role than for the cuprates.

Γ Pocket

A feature clearly present in DFT calculations for the nickelate parent compounds $LaNiO_2$ and $NdNiO_2$ is the Γ pocket, see **Figure 2D**. However, when the Coulomb interaction on the La or Nd sites is included, it is shifted upward in energy. Furthermore, Sr-doping depopulates the Ni $3d_{x^2-y^2}$ orbital and the A and Γ pocket, and, thus, also helps pushing the Γ pocket above the Fermi energy. Clearly in the DFT + DMFT k-resolved spectrum of **Figure 3**, the Γ pocket is above the Fermi energy. To some extent, the presence or absence of the Γ pocket also depends on the rare-earth cation. For $NdNiO_2$, we obtain a Γ pocket for the undoped compound [33], which only shifts above the Fermi energy with Sr-doping in the superconducting region, whereas for $LaNiO_2$, it is already above the Fermi level without Sr-doping. We can hence conclude that while there might be a Γ pocket without Sr-doping, DFT + DMFT results suggest that it is absent in the superconducting doping regime.

Briefly after the discovery of superconductivity in nickelates, it has also been suggested that the Nd $5d$ orbitals of the pockets couple to the Ni $3d_{x^2-y^2}$ spin giving rise to a Kondo effect [20, 66]. However, **Table 1** shows that the hybridization between the relevant Ni $3d_{x^2-y^2}$ and the most important La or Nd $5d_{xy}$ and $5d_{3z^2-r^2}$ vanishes by symmetry. Also, the full 5 Ni and 5 Nd band DMFT calculations in **Figure 3** do not show a hybridization (gap) between A pocket and Ni bands. This suggests that the Γ and A pocket are decoupled from the $3d_{x^2-y^2}$ orbitals. There is no hybridization and hence no Kondo effect.

Nd 4*f* Orbitals

Finally, the importance of the Nd $4f$ orbitals has been suggested in the literature. Treating these $4f$ orbitals in DFT is not trivial because DFT puts them in the vicinity of the Fermi level. This neglects that electronic correlations split the Nd $4f$ into upper and lower Hubbard bands as they form a local spin. This effect is beyond DFT. One way to circumvent this difficulty is to put the Nd $4f$ orbitals in the core instead of having them as valence states close to the Fermi energy. This is denoted as "GGA open core" instead of standard "GGA" in **Table 1**. The localized Nd $4f$ spins might, in principle, be screened through a Kondo effect. However, the hybridization of the Nd $4f$ with the Ni $3d_{x^2-y^2}$ orbital at the Fermi energy is extremely small, see **Table 2** and [67]. Hence, the Kondo temperature is zero for all practical purposes. In spin-polarized DFT + U, there is, instead, a local exchange interaction between the Nd $4f$ and the predominately Nd $5d$ Γ pocket [68]. However, as pointed out in the previous paragraph, the Γ pocket is shifted above the Fermi level in the superconducting Sr-doping regime. Hence in [33], we ruled out that the Nd $4f$ is relevant for superconductivity. This has been spectacularly confirmed experimentally by the discovery of superconductivity in nickelates without f electrons: $Ca_xLa_{1-x}NiO_2$ [69] and $Sr_xLa_{1-x}NiO_2$ [61] have a similar T_c.

4 ONE-BAND HUBBARD MODEL PLUS RESERVOIR

Altogether, this leaves us with **Figures 1B,D** as the arguably simplest model for nickelate superconductors, consisting of a strongly correlated Ni $3d_{x^2-y^2}$ band and an A pocket. This A pocket is derived from the Nd $5d_{xy}$ band which, however, crosses the Ni $3d$ orbitals and hybridizes strongly with the Ni t_{2g} orbitals so that at the bottom of the A pocket, that is, at the momentum A, it is made up primarily from Ni t_{2g}, whereas the Nd $5d_{xy}$ contribution is here at a lower energy. This makes the A pocket much more resistive to shifting up in energy than the Γ pocket.

On the other hand, the A pocket does not interact with the Ni $3d_{x^2-y^2}$ band; that is, does not hybridize in **Table 1**. Hence, we can consider the A pocket as a mere hole reservoir which accommodates part of the holes induced by Sr-doping, whereas the other part goes into the correlated Ni $3d_{x^2-y^2}$ band which is responsible for superconductivity. **Figure 4** shows the thus obtained Ni $3d_{x^2-y^2}$ occupation as a function of Sr-doping in the DFT + DMFT calculation with 5 Ni and 5 Nd(La) orbitals.

It is noted that $NdNiO_2$ shows for Sr-doping below about 10% more holes in the Ni $3d_{x^2-y^2}$ orbital and a weaker dependence on the Sr-doping since here the Γ pocket is still active, not only taking away electrons from Ni but also first absorbing some of the holes from the Sr-doping until it is completely depopulated (shifted above the Fermi energy) before superconductivity sets in.

TABLE 1 | Hybridization (hopping amplitude in eV) between the partially occupied Ni $3d_{x^2-y^2}$ and the La/Nd 5*d* orbitals [33]. Here, the results are obtained from Wannier projections onto 17-bands (La/Nd-4*f* + La/Nd-5*d* + Ni-3*d*) and 10-bands (La/Nd-5*d* + Ni-3*d*).

$LaNiO_2$	La $5d_{xy}$	La $5d_{yz}$	La $5d_{xz}$	La $5d_{x^2-y^2}$	La $5d_{z^2}$
Ni $3d_{x^2-y^2}$ (10-band model, GGA)	0.000	0.084	−0.084	−0.017	0.000
Ni $3d_{x^2-y^2}$ (17-band model, GGA)	0.000	0.085	−0.085	−0.037	0.000
$NdNiO_2$	**Nd $5d_{xy}$**	**Nd $5d_{yz}$**	**Nd $5d_{xz}$**	**Nd $5d_{x^2-y^2}$**	**Nd $5d_{z^2}$**
Ni $3d_{x^2-y^2}$ (10-band model, GGA open core)	0.000	0.070	−0.070	−0.038	0.000
Ni $3d_{x^2-y^2}$ (10-band model, GGA)	0.000	0.077	−0.077	−0.006	0.000
Ni $d_{x^2-y^2}$ (17-band model, GGA)	0.000	0.081	−0.081	−0.023	0.000

TABLE 2 | Hybridization (hopping amplitude in eV) between the Ni $3d_{x^2-y^2}$ and the Nd (La) 4*f* orbitals, as obtained from Wannier projections onto 17-bands (La/Nd-4*f* + La/Nd-5*d* + Ni-3*d*), including the 4*f* as valence states in DFT (GGA) [33].

$LaNiO_2$ (GGA)	f_{xz^2}	f_{yz^2}	f_{z^3}	$f_{x(x^2-3y^2)}$	$f_{y(3x^2-y^2)}$	$f_{z(x^2-y^2)}$	f_{xyz}
Ni-$d_{x^2-y^2}$	−0.030	0.030	0.000	−0.085	−0.085	−0.020	−0.000
$NdNiO_2$ (GGA)	**f_{xz^2}**	**f_{yz^2}**	**f_{z^3}**	**$f_{x(x^2-3y^2)}$**	**$f_{y(3x^2-y^2)}$**	**$f_{z(x^2-y^2)}$**	**f_{xyz}**
Ni-$d_{x^2-y^2}$	−0.021	0.021	0.000	−0.061	−0.061	0.016	−0.000

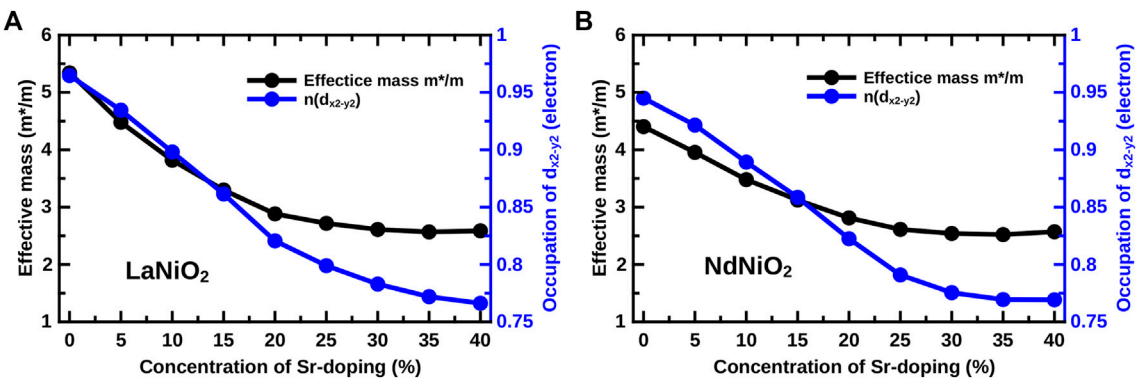

FIGURE 4 | Occupation of the Ni $3d_{x^2-y^2}$ orbital (blue; right *y*-axis) and its effective mass enhancement $m^*/m = 1/Z$ (black; left *y*-axis in panels) vs. Sr-doping for $LaNiO_2$ **(A)** and $NdNiO_2$ **(B)** as calculated in DFT + DMFT. From [33] (Supplemental material).

In the subsequent one-band calculation, presented in the next paragraph, we employ the occupation from the Ni $3d_{x^2-y^2}$ orbital as calculated in this full DMFT calculation with 5 Ni and 5 Nd orbitals. This accounts not only for the electron pocket in the DMFT calculation but also for minor hybridization effects between the Ni $3d_{x^2-y^2}$ and $3d_{3z^2-r^2}$ orbital, for example, along the Γ-*X* direction. In principle, this hybridization effect, which inter-mixes the orbital contribution to the bands, should not be taken into account in the one-band Hubbard model. This aims at modeling the effective $3d_{x^2-y^2}$ band which is crossing the Fermi level and which is predominantly Ni $3d_{x^2-y^2}$ (but also has admixtures from the other orbitals because of the hybridization). In the case of the Ni $3d_{x^2-y^2}$ orbital, this hybridization is very weak [33] (Supplemental Material) and can be neglected as a first approximation [62] (Supplemental Material). For other Ni 3*d* orbitals, this hybridization has a sizeable effect on their respective occupation. For example, the Ni $3d_{3z^2-r^2}$ orbital which is strongly hybridizing with the Nd $5d_{3z^2-r^2}$ orbital only has an occupation of 1.85 electrons per site in our multi-orbital calculation [62] (Supplemental material), whereas the effective Ni $3d_{3z^2-r^2}$ orbital, including contributions from the hybridization, is fully occupied with two electrons per site as it is completely below the Fermi level.

The hopping parameters for the Ni-$3d_{x^2-y^2}$ model from a one-band Wannier projection are shown in **Table 3** and compared to that of the same orbital in a 10-band and 17-band Wannier projection. Here, t_{R_x,R_y,R_z} denotes the hopping by R_i unit cells in the *i* direction. That is, t_{000} is the on-site potential, $t = -t_{100}$; $t' = -t_{110}$, and $t'' = -t_{200}$ are the nearest, next-nearest, and next-next-nearest neighbor hopping, respectively; and $t_z = -t_{001}$ is the hopping in the *z*-direction perpendicular to the NiO_2 planes. The hopping parameters are strikingly similar for $LaNiO_2$ and $NdNiO_2$ and the different Wannier projections.

Besides the doping from **Figure 4** and the hopping for the one-band Wannier projection from **Table 3**, we only need the interaction parameter for doing realistic one-band Hubbard

TABLE 3 | Major hopping elements (in units of eV) of the Ni-$3d_{x^2-y^2}$ orbital from 1-band (Ni-$3d_{x^2-y^2}$), 10-bands (La/Nd-*d* + Ni-*d*), and 17-bands (La/Nd-*f* + La/Nd-*d* + Ni-*d*) Wannier projections. The DFT-relaxed lattice parameters are as follows: $LaNiO_2$ ($a = b = 3.88$ Å, $c = 3.35$ Å), $NdNiO_2$ ($a = b = 3.86$ Å, $c = 3.24$ Å) [33].

$LaNiO_2$ (GGA)	t_{000}	t_{100}	t_{001}	t_{110}	t_{200}	t_{210}
1-band (Ni-$d_{x^2-y^2}$)	0.2689	−0.389	−0.036	0.097	−0.046	−0.003
10-bands (La-*d* + Ni-*d*)	0.295	−0.397	−0.045	0.098	−0.049	0.000
17-bands (La-*f* + La-*d* + Ni-*d*)	0.351	−0.394	−0.023	0.079	−0.042	−0.000
$NdNiO_2$ (GGA open core)	t_{000}	t_{100}	t_{001}	t_{110}	t_{200}	t_{210}
1-band (Ni-$d_{x^2-y^2}$)	0.305	−0.394	−0.033	0.095	−0.047	−0.003
10-bands (Nd-*d* + Ni-*d*)	0.316	−0.397	−0.038	0.094	−0.048	−0.000

model calculations for nickelates. In cRPA for a single $3d_{x^2-y^2}$ orbital, one obtains $U = 2.6$ eV [15, 17] at zero frequency. But, the cRPA interaction has strong frequency dependence because of the screening of all the other Ni and Nd (La) orbitals close by. To mimic this frequency dependence, the static U parameter needs to be slightly increased. Expertise from many DFT + DMFT calculations for transition metal oxides shows that it typically needs to be about 0.5 eV larger, so that $U = 3.2$ eV $= 8t$ is reasonable. Altogether, this defines a one-band Hubbard model for nickelates at various dopings. For the conductivity and other transport properties, the A pocket may be relevant as well, but superconductivity should arise from the correlated $3d_{x^2-y^2}$ band that is hardly coupled to the A pocket.

5 NON-LOCAL CORRELATIONS AND SUPERCONDUCTING PHASE DIAGRAM

DFT provides a first picture of the relevant orbitals, and DMFT adds to this effect of strong local correlations, such as the splitting into Hubbard bands, the formation of a quasiparticle peak, and correlation-induced orbital shifts, such as the upshift of the Γ pocket. However, at low temperatures, non-local correlations give rise to additional effects. Relevant factors are as follows: the emergence of strong spin fluctuations and their impact on the spectral function and superconductivity.

For including such non-local correlations, diagrammatic extensions of DMFT, such as the dynamical vertex approximation (DΓA) [36–38, 70], have been proven extremely powerful. Such calculations are possible down to the temperatures of the superconducting phase transition in the correlated regime and for very large lattices so that the long-range correlations close to a phase transition can be properly described. Even (quantum) critical exponents can be calculated [71–74]. DΓA has proven reliable compared with the numerically exact calculations where these are possible [75] and, in particular, provide for a more accurate determination of T_c [76] since the full local frequency dependence of the two-particle vertex is included. Such local frequency dependence can affect even the non-local pairing through spin fluctuations. In, for example, RPA, this frequency dependence and the suppression of the pairing vertex for small frequencies can only be improperly mimicked by (quite arbitrarily) adjusting the static U.

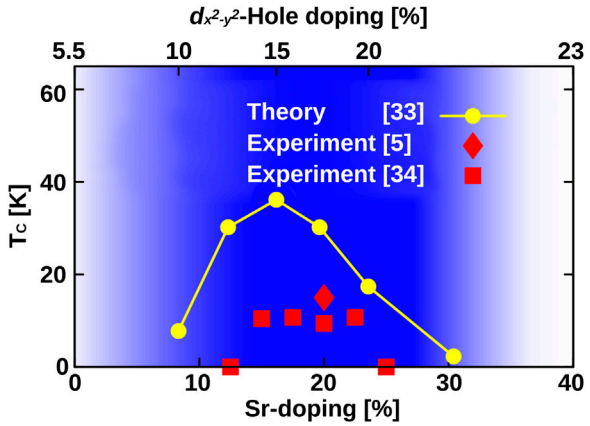

FIGURE 5 | Superconducting phase diagram T_c vs. x for $Sr_xNd_{1-x}NiO_2$ as predicted by DΓA [33] and experimentally confirmed a posteriori in [34, 35]. A priori, that is, at the time of the calculation, only one experimental data point [5] was available. For such a difficult to determine quantity as the superconducting T_c and without adjusting parameters, the accuracy is astonishing. The bottom x-axis shows the Sr-doping and the top x-axis the calculated hole doping of the $3d_{x^2-y^2}$ band according to **Figure 4**. Adjusted from [33].

This simple one-band Hubbard model in DΓA has been the basis for calculating the phase diagram T_c vs. Sr-doping in **Figure 5** [33]. At the time of the calculation, only a single experimental T_c at 20% Sr-doping was available [5]. The physical origin of the superconductivity in these calculations is strong spin fluctuations which form the pairing glue for high-temperature superconductivity. Charge fluctuations are much weaker; the electron–phonon coupling has not been considered and is also too weak for transition metal oxides to yield high-temperature superconductivity. The theoretical T_c in **Figure 5** at 20% doping was from the very beginning slightly larger than in the experiment. Most likely, this is because in the ladder DΓA [36, 37] calculation of T_c, the spin fluctuations are first calculated and then enter the superconducting particle–particle channel [76]. This neglects the feedback effect of these particle–particle fluctuations on the self-energy and the spin fluctuations, which may, in turn, suppress the tendency toward superconductivity somewhat. Such effects would be only included in a more complete parquet DΓA calculation [77–79]. Also, the ignored weak three-dimensional dispersion will

suppress Tc. Let us note that antiferromagnetic spin fluctuations have recently been observed experimentally [64, 80].

Given the slight overestimation of T_c from the very beginning, the agreement with the subsequently obtained experimental T_c vs. Sr-doping x phase diagram [34, 35] in **Figure 5** is astonishingly good. We further see that the superconducting doping regime also concurs with the doping regime where a one-band Hubbard model description is possible for $Sr_xNd_{1-x}NiO_2$, as concluded from a full DFT + DMFT calculation for 5 Ni plus 5 Nd bands. This regime is marked dark blue in **Figure 5** and, as already noted, extends to somewhat larger dopings [33] than for $Sr_xLa_{1-x}NiO_2$ shown in **Figure 3**. Concomitant with this is the fact that the experimental superconducting doping range for $Sr_xLa_{1-x}NiO_2$ extends to a larger x than for $Sr_xNd_{1-x}NiO_2$. For dopings larger than the dark blue regime in **Figure 5**, two Ni $3d$ bands need to be included. As we will show in the next section, this completely changes the physics and is not favorable for superconductivity. For dopings smaller than the dark blue regime in **Figure 5**, on the other hand, the Γ pocket may become relevant for $Sr_xNd_{1-x}NiO_2$, as well as its exchange coupling to the $4f$ moments.

Our theoretical calculations also reveal ways to enhance T_c. Particularly promising is to enhance the hopping parameter t. This enhances T_c because (i) t sets the energy scale of the problem, and a larger t means a larger T_c if U/t, t'/t, and t''/t and doping are kept fixed. Furthermore, the ratio $U/t = 8$ for nickelates is not yet optimal. Indeed, (ii) a somewhat smaller ratio U/t would imply a larger T_c at fixed t [33]. Since the interaction U is local, it typically varies much more slowly when, for example, applying compressive strain or pressure and can be assumed to be constant as a first approximation (for secondary effects, see [81, 82]). Thus, compressive strain or pressure enhance (i) t and reduce (ii) U/t. Both effects enhance T_c. This prediction made in [33] has been confirmed experimentally: applying a pressure of 12 GPa increases T_c from 18K to 31 K in $Sr_{0.18}Pr_{0.82}NiO_2$ [83]. This is so far the record T_c for nickelates, and there are yet no signs for saturation or maximum, indicating that even higher T_c's are possible at higher pressures.

Alternatives to enhance t are 1) to substitute the $SrTiO_3$ substrate by a substrate with smaller in-plane lattice constants since the nickelate film in-plane axis parameters will be locked to that of the substrate. Furthermore, one can 2) replace $3d$ Ni by $4d$ Pd, that is, try to synthesize Nd (La)PdO_2 [11]. Since the Pd $4d$ orbitals are more extended than the $3d$ Ni orbitals, this should enhance t as well.

Next, we turn to the DΓA spectra, more precisely Fermi surfaces, in **Figure 6**. Here, beyond quasiparticle renormalizations of DMFT, non-local spin fluctuations can further impact the spectrum. Only the spectral function of the Hubbard model is shown, describing the $3d_{x^2-y^2}$ band. Please keep in mind that on top of the Fermi surface in **Figure 6**, there is also a weakly correlated A pocket. As one can see in **Figure 6**, antiferromagnetic spin-fluctuations lead to a pseudogap at the antinodal momenta $(\pm\pi, 0)$ $(0, \pm\pi)$ if the filling of the $3d_{x^2-y^2}$ band is close to half-filling. Indeed $n_{3d_{x^2-y^2}} = 0.95$ is the filling for the undoped parent compound $NdNiO_2$ where the A- and Γ pocket have taken 5% of the electrons away from the Ni $3d_{x^2-y^2}$ band. An Sr-doping of 20% is in between $n_{3d_{x^2-y^2}} = 0.85$ and $n_{3d_{x^2-y^2}} = 0.8$, see **Figure 4**. Comparing these theoretical predictions with the experimental Fermi surface, even the **k**-integrated spectrum is very much sought after. However, here, we face the difficulty that the superconducting samples require a $SrTiO_3$ capping layer or otherwise may oxidize out of vacuum. This hinders photoemission spectroscopy (PES) experiments as these are extremely surface-sensitive. Hitherto, PES is only available without the capping layer for $Sr_xPr_{1-x}NiO_2$ [84]. These show a surprisingly low spectral density at the Fermi energy despite the metallic behavior of the doped system, raising the question of how similar these films are to the superconducting films.

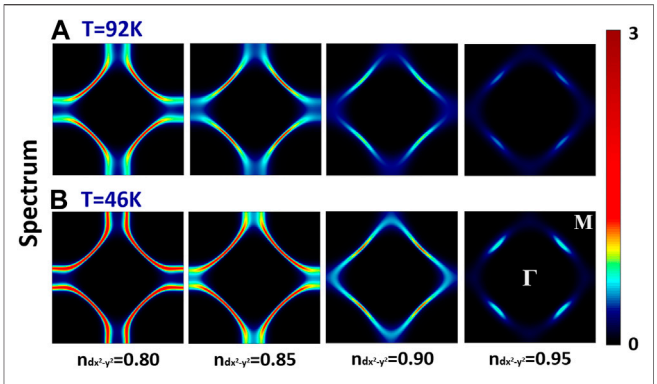

FIGURE 6 | DΓA k-resolved spectrum at the Fermi energy for $T = 0.02t$ = 92 K **(A)** and $T = 0.01t$ = 46 K **(B)** and four different dopings $n_{d_{x^2-y^2}}$ of the Ni-$3d_{x^2-y^2}$ band (left to right). From [33].

6 TOPOTACTIC HYDROGEN: TURNING THE ELECTRONIC STRUCTURE UPSIDE DOWN

The fact that it took 20 years from the theoretical prediction of superconductivity in rare-earth nickelates to the experimental realization already suggests that the synthesis is far from trivial. This is because nickel has to be in the unusually low oxidation state Ni^{+1}. The recipe of success for nickelate superconductors is a two-step process [85]: First, doped perovskite films Sr (Ca)$_x$Nd (La,Pr)$_{1-x}NiO_3$ films are deposited on a $SrTiO_3$ substrate by pulsed laser deposition. Already, this first step is far from trivial, not least because the doped material has to be deposited with homogenous Sr (Ca) concentration. Second, $Sr(Ca)_xNd(La,Pr)_{1-x}NiO_3$ needs to be reduced to $Sr(Ca)_xNd(La,Pr)_{1-x}NiO_2$. To this end, the reducing agent CaH_2 is used. Here, the problem is that this reduction might be incomplete with excess oxygen remaining or that hydrogen from CaH_2 is topotactically intercalated in the Sr (Ca)$_x$Nd (La,Pr)$_{1-x}NiO_2$ structure. A particular difficulty is that the light hydrogen is experimentally hard to detect, for example, it evades conventional X-ray structural detection.

In [55], we studied the possibility to intercalate hydrogen, that is, to synthesize unintendedly $Sr_xNd(La)_{1-x}NiO_2H$ instead of $Sr_xNd(La)_{1-x}NiO_2$. For the reduction of, for example, $SrVO_3$

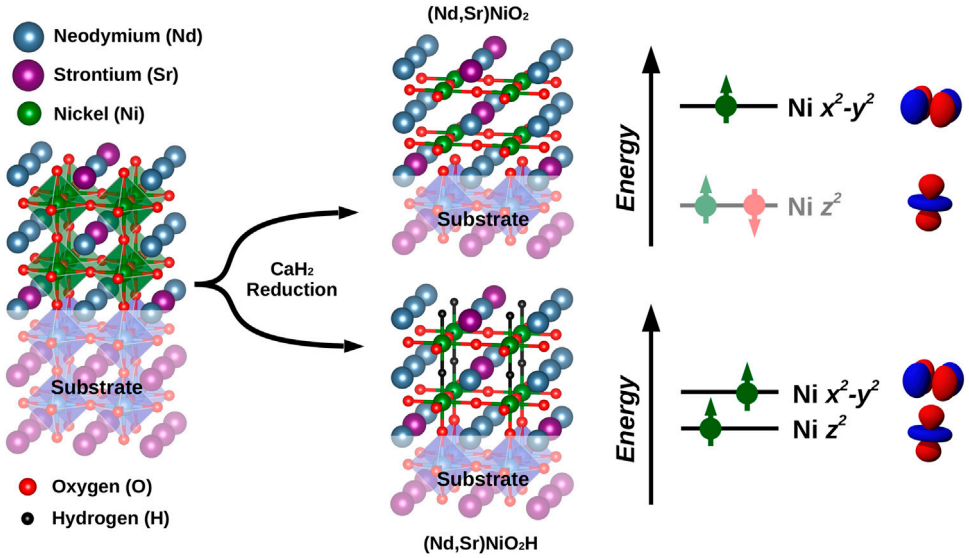

FIGURE 7 | Reduction of $Sr_xNd(La)_{1-x}NiO_3$ with CaH_2 may result not only in the pursued end product $Sr_xNd(La)_{1-x}NiO_2$ but also in $Sr_xNd(La)_{1-x}NiO_2H$, where H atoms occupy the vacant O sites between the layers. This has dramatic consequences for the electronic structure. In a first, purely local picture, visualized on the right side, there is instead of Ni $3d^9$ with one-hole in the $3d_{x^2-y^2}$ orbital, two holes in the $3d_{x^2-y^2}$ and $3d_{3z^2-r^2}$ orbital forming a local spin-1.

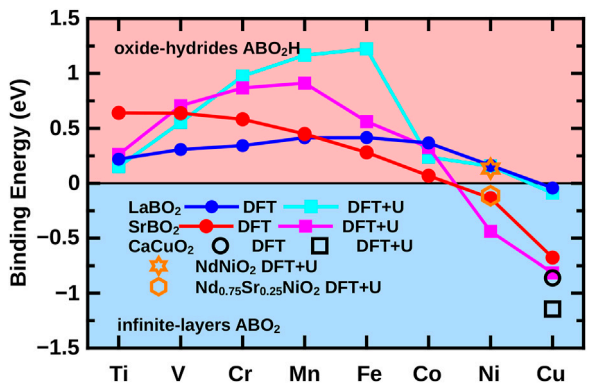

FIGURE 8 | Binding energy for topotactical H as calculated by non–spin-polarized DFT and spin-polarized DFT + U for various transition metals *B* (*x*-axis). Positive binding energies indicate that $ABNiO_2H$ is energetically favored; for negative binding energies, $ABNiO_2$ is more stable. The data for non–spin-polarized DFT calculations are from [55].

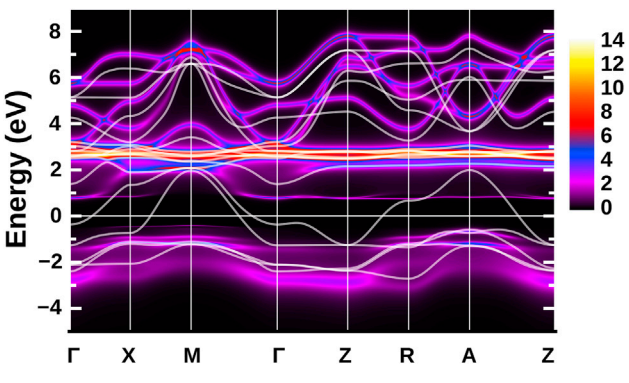

FIGURE 9 | DFT (white lines) and DMFT (color bar) *k*-resolved spectral function for $LaNiO_2H$. Here, a model with La-d + La-f + Ni-d was used, which is beyond the Ni-d only and La-d + Ni-d models shown in [55].

with CaH_2, it is well-established that $SrVO_2H$ may be obtained as the end product [86]. Both possible end products are visualized in **Figure 7**. The extra H takes away one more electron from the Ni sites. Hence, we have two holes on the Ni sites which in a local picture are distributed to two orbitals and form a spin-1, due to Hund's exchange.

The first question is how susceptible the material is to bind topotactic H. To answer this question, one can calculate the binding energy E ($ABNiO_2$) + 1/2 E (H_2)- E ($ABNiO_2H$) in DFT [55, 87]. The result is shown in **Figure 8**, which clearly shows that early transition metal oxides are prone to intercalate hydrogen, whereas for cuprates, the infinite layer compound without H is more stable. Nickelates are in-between. For the undoped compounds $NdNiO_2$, and even a bit more for $LaNiO_2$, it is favorable to intercalate H. However, for the Sr-doped nickelates, the energy balance is inverted. Here, it is unfavorable to bind hydrogen.

Let us emphasize that this is only the enthalpy balance. In the actual synthesis also the reaction kinetics matter, and the entropy which is large for the H_2 gas. Nonetheless, this shows that undoped nickelates are very susceptible to topotactic H. This possibly means that, experimentally, not a complete H-coverage as in $ABNiO_2H$ of **Figure 8** is realized, but some hydrogen may remain in the nickelates because of an incomplete reduction with CaH_2. Indeed, hydrogen remainders have later been detected experimentally by nuclear magnetic resonance (NMR) spectroscopy, and they have even been used to analyze the antiferromagnetic spin fluctuations [80].

Now that we have established that remainders of hydrogen can be expected for nickelates at low doping, the question is how this affects the electronic structure. The local picture of **Figure 7** already suggested a very different electronic configuration. This is further corroborated by DFT + DMFT calculations for $LaNiO_2H$ presented in **Figure 9**. Here, the DFT band structure shows a metallic behavior with two orbitals, Ni $3d_{x^2-y^2}$ and $3d_{3z^2-r^2}$, crossing the Fermi level. There are no rare-earth electron pockets any longer. Thus, we have an undoped Ni $3d^8$ configuration without Sr-doping. If electronic correlations are included in DMFT, the DFT bands split into two sets of Hubbard bands. Above the Fermi level, one can identify the upper $3d_{x^2-y^2}$ and $3d_{3z^2-r^2}$ Hubbard band below the flat *f* bands in **Figure 9**, with some broadening because of the electronic correlations. The lower Hubbard bands intertwine with the Ni t_{2g} orbitals below the Fermi energy.

Even if we dope $LaNiO_2H$, this electronic structure is not particularly promising for superconductivity. First, it is not two-dimensional because of the $3d_{3z^2-r^2}$ orbitals, which makes the system more three-dimensional. More specifically, there is a considerable hopping process from Ni $3d_{3z^2-r^2}$ *via* H to the Ni $3d_{3z^2-r^2}$ on the vertically adjacent layer, as evidenced in **Figure 9** by the DFT dispersion of this band in the Γ-Z direction; the other $3d_{x^2-y^2}$ band is (as expected) flat in this direction. Second, the tendency to form local magnetic moments of spin-1 counteracts the formation of Cooper pairs from two spin-1/2s. Hence, altogether, we expect topotactic H to prevent high-temperature superconductivity.

7 CONCLUSION

In this article, we have discussed the physics of nickelate superconductors from the perspective of a one-band Hubbard model for the Ni $3d_{x^2-y^2}$ band plus an *A* pocket. Because of symmetry, this *A* pocket does not hybridize with the $3d_{x^2-y^2}$ band and merely acts as a decoupled electron reservoir. Hence, once the filling of the $3d_{x^2-y^2}$ band is calculated as a function of Sr- or Ca-doping in $Sr(Ca)_xNd(La,Pr)_{1-x}NiO_2$, we can, for many aspects, concentrate on the physics of the thus doped Hubbard model. This includes antiferromagnetic spin fluctuations and the onset of superconductivity. Other physical properties, such as transport and the Hall conductivity, depend, as a matter of course, also on the *A* pocket. This is in stark contrast to the cuprates, where the oxygen *p* orbitals are much closer to the Fermi level so that we have a charge-transfer insulator that needs to be modeled by the more complex Emery model.

The one-band Hubbard model picture for nickelates was put forward early on for nickelates [11, 19, 32, 33], and its proper doping, including correlation effects, has been calculated in [33]. This picture has been confirmed by many experimental observations so far. The Nd 4*f* states are, from the theoretical perspective, irrelevant because they form a local spin and barely hybridize with the $3d_{x^2-y^2}$ band. This has been confirmed experimentally by the observation of superconductivity in $Sr(Ca)_xLa_{1-x}NiO_2$. The minor importance of the other Ni 3*d* orbitals, in particular the $3d_{3z^2-r^2}$ orbital, is indicated through the careful analysis [65] of RIXS data [63, 64]. Not confirmed experimentally is hitherto the prediction that the Γ pocket is shifted above the Fermi level in the superconducting doping regime.

Strong evidence for the one-band Hubbard model picture is the prediction of the superconducting phase diagram [33], confirmed experimentally in [34, 35]. A further prediction was the increase of T_c with pressure or compressive strain [33], which was subsequently found in the experiment with a record $T_c = 31$ K for nickelates under pressure [83]. The strength of antiferromagnetic spin-fluctuations as obtained in RIXS [64] also roughly agrees with that of the calculation [33]. Altogether, this gives us quite some confidence in the one-band Hubbard model scenario, which even allowed for a rough calculation of T_c. Notwithstanding, further theoretical calculations, in particular including non-local correlations also in a realistic multi-orbital setting [37, 70, 88], are eligible. On the experimental side more detailed, for example, **k**-resolved information is desirable as are further close comparisons between the experiment and theory.

A good analysis of the quality of the samples is also mandatory, especially against the background that superconducting nickelates have been extremely difficult to synthesize. Incomplete oxygen reduction and topotactic hydrogen [55, 87] are theoretically expected to be present because this is energetically favored, at least for low Sr-doping. This leads to two holes in two orbitals forming a high-spin state and a three-dimensional electronic structure, thus obstructing the intrinsic physics of superconducting nickelates.

AUTHOR CONTRIBUTIONS

All authors listed have made a substantial, direct, and intellectual contribution to the study and approved it for publication.

FUNDING

We acknowledge funding through the Austrian Science Funds (FWF), Project numbers P 32044 and P 30213, and Grant-in-Aids for Scientific Research (JSPS KAKENHI), Grant numbers 19H05825, JP20K22342, and JP21K13887. OJ was supported by the Leibniz Association through the Leibniz Competition. Calculations were partially performed on the Vienna Scientific Cluster (VSC).

ACKNOWLEDGMENTS

We thank Atsushi Hariki, Motoaki Hirayama, Josef Kaufmann, Yusuke Nomura, and Terumasa Tadano for valuable discussions.

REFERENCES

1. Anisimov VI, Bukhvalov D, Rice TM. Electronic Structure of Possible Nickelate Analogs to the Cuprates. *Phys Rev B* (1999) 59:7901–6. doi:10.1103/PhysRevB.59.7901
2. Chaloupka J, Khaliullin G. Orbital Order and Possible Superconductivity in $LaNiO_3/LaMO_3$ Superlattices. *Phys Rev Lett* (2008) 100:016404. doi:10.1103/PhysRevLett.100.016404
3. Hansmann P, Toschi A, Yang X, Andersen O, Held K. Electronic Structure of Nickelates: From Two-Dimensional Heterostructures to Three-Dimensional Bulk Materials. *Phys Rev B* (2010) 82:235123. doi:10.1103/PhysRevB.82.235123
4. Hansmann P, Yang X, Toschi A, Khaliullin G, Andersen OK, Held K. Turning a Nickelate Fermi Surface into a Cupratelike One through Heterostructuring. *Phys Rev Lett* (2009) 103:016401. doi:10.1103/PhysRevLett.103.016401
5. Li D, Lee K, Wang BY, Osada M, Crossley S, Lee HR, et al. Superconductivity in an Infinite-Layer Nickelate. *Nature* (2019) 572:624–7. doi:10.1038/s41586-019-1496-5
6. Balestrino G, Medaglia PG, Orgiani P, Tebano A, Aruta C, Lavanga S, et al. Very Large Purely Intralayer Critical Current Density in Ultrathin Cuprate Artificial Structures. *Phys Rev Lett* (2002) 89:156402. doi:10.1103/physrevlett.89.156402
7. Di Castro D, Cantoni C, Ridolfi F, Aruta C, Tebano A, Yang N, et al. High-T_c Superconductivity at the Interface between the $CaCuO_2$ and $SrTiO_3$ Insulating Oxides. *Phys Rev Lett* (2015) 115:147001. doi:10.1103/PhysRevLett.115.147001
8. Orgiani P, Aruta C, Balestrino G, Born D, Maritato L, Medaglia PG, et al. Direct Measurement of Sheet Resistance $R_\square$ in Cuprate Systems: Evidence of a Fermionic Scenario in a Metal-Insulator Transition. *Phys Rev Lett* (2007) 98: 036401. doi:10.1103/PhysRevLett.98.036401
9. Siegrist T, Zahurak S, Murphy D, Roth R. The Parent Structure of the Layered High-Temperature Superconductors. *Nature* (1988) 334:231–2. doi:10.1038/334231a0
10. Botana AS, Norman MR. Similarities and Differences between $LaNiO_2$ and $CaCuO_2$ and Implications for Superconductivity. *Phys Rev X* (2020) 10:011024. doi:10.1103/PhysRevX.10.011024
11. Hirayama M, Tadano T, Nomura Y, Arita R. Materials Design of Dynamically Stable D^9 Layered Nickelates. *Phys Rev B* (2020) 101:075107. doi:10.1103/PhysRevB.101.075107
12. Hu L-H, Wu C. Two-band Model for Magnetism and Superconductivity in Nickelates. *Phys Rev Res* (2019) 1:032046. doi:10.1103/PhysRevResearch.1.032046
13. Jiang M, Berciu M, Sawatzky GA. Critical Nature of the Ni Spin State in Doped $NdNiO_2$. *Phys Rev Lett* (2020) 124:207004. doi:10.1103/PhysRevLett.124.207004
14. Lee K-W, Pickett W. Infinite-layer $LaNiO_2$: Ni^{1+} Is Not Cu^{2+}. *Phys Rev B* (2004) 70:165109. doi:10.1103/PhysRevB.70.165109
15. Nomura Y, Hirayama M, Tadano T, Yoshimoto Y, Nakamura K, Arita R. Formation of a Two-Dimensional Single-Component Correlated Electron System and Band Engineering in the Nickelate Superconductor $NdNiO_2$. *Phys Rev B* (2019) 100:205138. doi:10.1103/PhysRevB.100.205138
16. Pavarini E, Dasgupta I, Saha-Dasgupta T, Jepsen O, Andersen OK. Band-structure Trend in Hole-Doped Cuprates and Correlation with T (C max). *Phys Rev Lett* (2001) 87:047003. doi:10.1103/PhysRevLett.87.047003
17. Sakakibara H, Usui H, Suzuki K, Kotani T, Aoki H, Kuroki K. Model Construction and a Possibility of Cupratelike Pairing in a New D^9 Nickelate Superconductor (Nd, Sr)NiO_2. *Phys Rev Lett* (2020) 125:077003. doi:10.1103/PhysRevLett.125.077003
18. Werner P, Hoshino S. Nickelate Superconductors: Multiorbital Nature and Spin Freezing. *Phys Rev B* (2020) 101:041104. doi:10.1103/PhysRevB.101.041104
19. Wu X, Di Sante D, Schwemmer T, Hanke W, Hwang HY, Raghu S, et al. Robust $D_{x^2-y^2}$ -wave Superconductivity of Infinite-Layer Nickelates. *Phys Rev B* (2020) 101:060504. doi:10.1103/PhysRevB.101.060504
20. Zhang G-M, Yang Y-F, Zhang F-C. Self-Doped Mott Insulator for Parent Compounds of Nickelate Superconductors. *Phys Rev B* (2020) 101:020501. doi:10.1103/PhysRevB.101.020501
21. Adhikary P, Bandyopadhyay S, Das T, Dasgupta I, Saha-Dasgupta T. Orbital-selective Superconductivity in a Two-Band Model of Infinite-Layer Nickelates. *Phys Rev B* (2020) 102:100501. doi:10.1103/PhysRevB.102.100501
22. Lechermann F. Late Transition Metal Oxides with Infinite-Layer Structure: Nickelates versus Cuprates. *Phys Rev B* (2020) 101:081110. doi:10.1103/PhysRevB.101.081110
23. Lechermann F. Multiorbital Processes Rule the $Nd_{1-x}Sr_xNiO_2$ normal State. *Phys Rev X* (2020) 10:041002. doi:10.1103/PhysRevX.10.041002
24. Petocchi F, Christiansson V, Nilsson F, Aryasetiawan F, Werner P. Normal State of $Nd_{1-x}Sr_xNiO_2$ from Self-Consistent *GW* + EDMFT. *Phys Rev X* (2020) 10:041047. doi:10.1103/PhysRevX.10.041047
25. Bandyopadhyay S, Adhikary P, Das T, Dasgupta I, Saha-Dasgupta T. Superconductivity in Infinite-Layer Nickelates: Role of *F* Orbitals. *Phys Rev B* (2020) 102:220502. doi:10.1103/PhysRevB.102.220502
26. Zaanen J, Sawatzky GA, Allen JW. Band Gaps and Electronic Structure of Transition-Metal Compounds. *Phys Rev Lett* (1985) 55:418–21. doi:10.1103/PhysRevLett.55.418
27. Emery VJ. Theory of High–T_c Superconductivity in Oxides. *Phys Rev Lett* (1987) 58:2794–7. doi:10.1103/PhysRevLett.58.2794
28. Gutzwiller MC. Effect of Correlation on the Ferromagnetism of Transition Metals. *Phys Rev Lett* (1963) 10:159–62. doi:10.1103/PhysRevLett.10.159
29. Hubbard J. Electron Correlations in Narrow Energy Bands. *Proc R Soc Lond Ser A, Math Phys Sci* (1963) 276:238–57. doi:10.1098/rspa.1963.0204
30. Kanamori J. Electron Correlation and Ferromagnetism of Transition Metals. *Prog Theor Phys* (1963) 30:275–89. doi:10.1143/ptp.30.275
31. Zhang FC, Rice TM. Effective Hamiltonian for the Superconducting Cu Oxides. *Phys Rev B* (1988) 37:3759–61. doi:10.1103/PhysRevB.37.3759
32. Karp J, Botana AS, Norman MR, Park H, Zingl M, Millis A. Many-Body Electronic Structure of $NdNiO_2$ and $CaCuO_2$. *Phys Rev X* (2020) 10:021061. doi:10.1103/PhysRevX.10.021061
33. Kitatani M, Si L, Janson O, Arita R, Zhong Z, Held K. Nickelate Superconductors – a Renaissance of the One-Band Hubbard Model. *npj Quan Mater* (2020) 5:59, 2020 . arXiv:2002.12230. doi:10.1038/s41535-020-00260-y
34. Li D, Wang BY, Lee K, Harvey SP, Osada M, Goodge BH, et al. Superconducting Dome in $Nd_{1-x}Sr_xNiO_2$ Infinite Layer Films. *Phys Rev Lett* (2020) 125:027001. arxiv:2003.08506. doi:10.1103/PhysRevLett.125.027001
35. Zeng S, Tang CS, Yin X, Li C, Li M, Huang Z, et al. Phase Diagram and Superconducting Dome of Infinite-Layer $Nd_{1-x}Sr_xNiO_2$ Thin Films, arxiv: 2004.11281. *Phys Rev Lett* (2020) 125:147003. doi:10.1103/physrevlett.125.147003
36. Katanin AA, Toschi A, Held K. Comparing Pertinent Effects of Antiferromagnetic Fluctuations in the Two- and Three-Dimensional Hubbard Model. *Phys Rev B* (2009) 80:075104. doi:10.1103/PhysRevB.80.075104
37. Rohringer G, Hafermann H, Toschi A, Katanin AA, Antipov AE, Katsnelson MI, et al. Diagrammatic Routes to Nonlocal Correlations beyond Dynamical Mean Field Theory. *Rev Mod Phys* (2018) 90:025003. doi:10.1103/revmodphys.90.025003
38. Toschi A, Katanin AA, Held K. Dynamical Vertex Approximation; a Step Beyond Dynamical Mean-Field Theory. *Phys Rev B* (2007) 75:045118. doi:10.1103/PhysRevB.75.045118
39. Georges A, Kotliar G, Krauth W, Rozenberg MJ. Dynamical Mean-Field Theory of Strongly Correlated Fermion Systems and the Limit of Infinite Dimensions. *Rev Mod Phys* (1996) 68:13. doi:10.1103/RevModPhys.68.13
40. Georges A, Krauth W. Numerical Solution of the $D = \infty$ Hubbard Model: Evidence for a Mott Transition. *Phys Rev Lett* (1992) 69:1240–3. doi:10.1103/PhysRevLett.69.1240
41. Jarrell M. Hubbard Model in Infinite Dimensions: A Quantum Monte Carlo Study. *Phys Rev Lett* (1992) 69:168–71. doi:10.1103/PhysRevLett.69.168
42. Metzner W, Vollhardt D. Correlated Lattice Fermions in $D = \infty$ Dimensions. *Phys Rev Lett* (1989) 62:324–7. doi:10.1103/PhysRevLett.62.324
43. Blaha P, Schwarz K, Madsen G, Kvasnicka D, Luitz J. *wien2k: An Augmented Plane Wave+ Local Orbitals Program for Calculating crystal Properties* (2001). Wien: TU Wien.
44. Schwarz K, Blaha P, Madsen GKH (2002). Electronic Structure Calculations of Solids Using the Wien2k Package for Material Sciences. *Comp Phys Comm* 147: 71–6. doi:10.1016/S0010-4655(02)00206-0
45. Kresse G, Hafner J. Ab Initio molecular Dynamics for Open-Shell Transition Metals. *Phys Rev B* (1993) 48:13115–8. doi:10.1103/PhysRevB.48.13115

46. Koepernik K, Eschrig H. Full-potential Nonorthogonal Local-Orbital Minimum-Basis Band-Structure Scheme. *Phys Rev B* (1999) 59:1743–57. doi:10.1103/PhysRevB.59.1743
47. Perdew JP, Burke K, Ernzerhof M. Generalized Gradient Approximation Made Simple. *Phys Rev Lett* (1996) 77:3865–8. doi:10.1103/PhysRevLett.77.3865
48. Nomura Y, Arita R. Superconductivity in Infinite-Layer Nickelates (2021). arXiv:2107.12923.
49. Hansmann P, Parragh N, Toschi A, Sangiovanni G, Held K. Importance of *D–P* Coulomb Interaction for High T_c Cuprates and Other Oxides. *New J Phys* (2014) 16:033009. doi:10.1088/1367-2630/16/3/033009
50. Anisimov VI, Poteryaev AI, Korotin MA, Anokhin AO, Kotliar G. First-principles Calculations of the Electronic Structure and Spectra of Strongly Correlated Systems: Dynamical Mean-Field Theory. *J Phys Condens Matter* (1997) 9:7359–67. doi:10.1088/0953-8984/9/35/010
51. Held K. Electronic Structure Calculations Using Dynamical Mean Field Theory. *Adv Phys* (2007) 56:829–926. doi:10.1080/00018730701619647
52. Held K, Nekrasov IA, Keller G, Eyert V, Blümer N, McMahan AK, et al. Realistic Investigations of Correlated Electron Systems with LDA+DMFT. *physica status solidi (b)* (2006) 243:2599–631. Previously appeared as Psi-k Newsletter No. 56 (April 2003). doi:10.1002/pssb.200642053
53. Kotliar G, Savrasov SY, Haule K, Oudovenko VS, Parcollet O, Marianetti CA. Electronic Structure Calculations with Dynamical Mean-Field Theory. *Rev Mod Phys* (2006) 78:865. doi:10.1103/RevModPhys.78.865
54. Lichtenstein AI, Katsnelson MI. Ab Initio calculations of Quasiparticle Band Structure in Correlated Systems: LDA++ Approach. *Phys Rev B* (1998) 57:6884–95. doi:10.1103/PhysRevB.57.6884
55. Si L, Xiao W, Kaufmann J, Tomczak JM, Lu Y, Zhong Z, et al. Topotactic Hydrogen in Nickelate Superconductors and Akin Infinite-Layer Oxides ABO_2. *Phys Rev Lett* (2020) 124:166402. doi:10.1103/PhysRevLett.124.166402
56. Kuneš J, Arita R, Wissgott P, Toschi A, Ikeda H, Held K. Wien2wannier: From Linearized Augmented Plane Waves to Maximally Localized Wannier Functions. *Comput Phys Commun* (2010) 181:1888–95. doi:10.1016/j.cpc.2010.08.005
57. Gull E, Millis AJ, Lichtenstein AI, Rubtsov AN, Troyer M, Werner P. Continuous-time Monte Carlo Methods for Quantum Impurity Models. *Rev Mod Phys* (2011) 83:349–404. doi:10.1103/RevModPhys.83.349
58. Parragh N, Toschi A, Held K, Sangiovanni G. Conserved Quantities of *SU*(2)-Invariant Interactions for Correlated Fermions and the Advantages for Quantum Monte Carlo Simulations. *Phys Rev B* (2012) 86:155158. doi:10.1103/PhysRevB.86.155158
59. Wallerberger M, Hausoel A, Gunacker P, Kowalski A, Parragh N, Goth F, et al. w2dynamics: Local One- and Two-Particle Quantities from Dynamical Mean Field Theory. *Comp Phys Comm* (2019) 235:388–99. doi:10.1016/j.cpc.2018.09.007
60. Kaufmann J, Held K. ana_cont: Python Package for Analytic Continuation (2021). arXiv:2105.11211.
61. Osada M, Wang BY, Goodge BH, Harvey SP, Lee K, Li D, et al. Nickelate Superconductivity without Rare-Earth Magnetism: $(La,Sr)NiO_2$. *Adv Mater* (2021) 33:2104083. doi:10.1002/adma.202104083
62. Worm P, Si L, Kitatani M, Arita R, Tomczak JM, Held K. Correlations Turn Electronic Structure of Finite-Layer Nickelates Upside Down (2021). arXiv:2111.12697.
63. Hepting M, Li D, Jia CJ, Lu H, Paris E, Tseng Y, et al. Electronic Structure of the Parent Compound of Superconducting Infinite-Layer Nickelates. *Nat Mater* (2020) 19:381. doi:10.1038/s41563-019-0585-z
64. Lu H, Rossi M, Nag A, Osada M, Li DF, Lee K, et al. Magnetic Excitations in Infinite-Layer Nickelates. *Science* (2021) 373:213–6. doi:10.1126/science.abd7726
65. Higashi K, Winder M, Kuneš J, Hariki A. Core-level X-ray Spectroscopy of Infinite-Layer Nickelate: LDA + DMFT Study. *Phys Rev X* (2021) 11:041009. doi:10.1103/PhysRevX.11.041009
66. Gu Y, Zhu S, Wang X, Hu J, Chen H. A Substantial Hybridization between Correlated Ni-*D* Orbital and Itinerant Electrons in Infinite-Layer Nickelates. *Commun Phy* (2020) 3:84. doi:10.1038/s42005-020-0347-x
67. Jiang P, Si L, Liao Z, Zhong Z. Electronic Structure of Rare-Earth Infinite-Layer $RNiO_2$ (R = La, Nd). *Phys Rev B* (2019) 100:201106. doi:10.1103/PhysRevB.100.201106
68. Choi M-Y, Lee K-W, Pickett WE. Role of 4*f* States in Infinite-Layer $NdNiO_2$. *Phys Rev B* (2020) 101:020503. doi:10.1103/PhysRevB.101.020503
69. Zeng SW, Li CJ, Chow LE, Cao Y, Zhang ZT, Tang CS, et al. Superconductivity in Infinite-Layer Lanthanide Nickelates (2021). arXiv:2105.13492.
70. Galler A, Thunström P, Gunacker P, Tomczak JM, Held K. Ab Initio dynamical Vertex Approximation. *Phys Rev B* (2017) 95:115107. doi:10.1103/PhysRevB.95.115107
71. Antipov AE, Gull E, Kirchner S. Critical Exponents of Strongly Correlated Fermion Systems from Diagrammatic Multiscale Methods. *Phys Rev Lett* (2014) 112:226401. doi:10.1103/PhysRevLett.112.226401
72. Rohringer G, Toschi A, Katanin A, Held K. Critical Properties of the Half-Filled Hubbard Model in Three Dimensions. *Phys Rev Lett* (2011) 107:256402. doi:10.1103/PhysRevLett.107.256402
73. Schäfer T, Katanin AA, Held K, Toschi A. Interplay of Correlations and Kohn Anomalies in Three Dimensions: Quantum Criticality with a Twist. *Phys Rev Lett* (2017) 119:046402. doi:10.1103/PhysRevLett.119.046402
74. Schäfer T, Katanin AA, Kitatani M, Toschi A, Held K. Quantum Criticality in the Two-Dimensional Periodic anderson Model. *Phys Rev Lett* (2019) 122:227201. doi:10.1103/PhysRevLett.122.227201
75. Schäfer T, Wentzell N, Šimkovic F, He Y-Y, Hille C, Klett M, et al. Tracking the Footprints of Spin Fluctuations: A Multimethod, Multimessenger Study of the Two-Dimensional Hubbard Model. *Phys Rev X* (2021) 11:011058. doi:10.1103/PhysRevX.11.011058
76. Kitatani M, Schäfer T, Aoki H, Held K. Why the Critical Temperature of High-T_c Cuprate Superconductors Is So Low: The Importance of the Dynamical Vertex Structure. *Phys Rev B* (2019) 99:041115. doi:10.1103/PhysRevB.99.041115
77. Li G, Kauch A, Pudleiner P, Held K. The Victory Project v1.0: An Efficient Parquet Equations Solver. *Comp Phys Comm* (2019) 241:146–54. doi:10.1016/j.cpc.2019.03.008
78. Li G, Wentzell N, Pudleiner P, Thunström P, Held K. Efficient Implementation of the Parquet Equations: Role of the Reducible Vertex Function and its Kernel Approximation. *Phys Rev B* (2016) 93:165103. doi:10.1103/physrevb.93.165103
79. Valli A, Schäfer T, Thunström P, Rohringer G, Andergassen S, Sangiovanni G, et al. Dynamical Vertex Approximation in its Parquet Implementation: Application to Hubbard Nanorings. *Phys Rev B* (2015) 91:115115. doi:10.1103/PhysRevB.91.115115
80. Cui Y, Li C, Li Q, Zhu X, Hu Z, feng Yang Y, et al. NMR Evidence of Antiferromagnetic Spin Fluctuations in $Nd_{0.85}Sr_{0.15}NiO_2$. *Chin Phys Lett* (2021) 38:067401. doi:10.1088/0256-307x/38/6/067401
81. Ivashko O, Horio W, Wan M, Christensen N, McNally D, Paris E, et al. Strain-engineering Mott-insulating La_2CuO_4. *Nat Comm* (2019) 10:786. doi:10.1038/s41467-019-08664-6
82. Tomczak JM, Miyake T, Sakuma R, Aryasetiawan F. Effective Coulomb Interactions in Solids under Pressure. *Phys Rev B* (2009) 79:235133. doi:10.1103/PhysRevB.79.235133
83. Wang NN, Yang MW, Chen KY, Yang Z, Zhang H, Zhu ZH, et al. Pressure-induced Monotonic Enhancement of T_c to over 30 K in the Superconducting $Pr_{0.82}Sr_{0.18}NiO_2$ Thin Films (2021). arXiv:2109.12811.
84. Chen Z, Osada M, Li D, Been EM, Chen S-D, Hashimoto M, et al. Electronic Structure of Superconducting Nickelates Probed by Resonant Photoemission Spectroscopy (2021). arXiv:2106.03963.
85. Lee K, Goodge BH, Li D, Osada M, Wang BY, Cui Y, et al. Aspects of the Synthesis of Thin Film Superconducting Infinite-Layer Nickelates. *APL Mater* (2020) 8:041107. doi:10.1063/5.0005103
86. Katayama T, Chikamatsu A, Yamada K, Shigematsu K, Onozuka T, Minohara M, et al. Epitaxial Growth and Electronic Structure of Oxyhydride $SrVO_2H$ Thin Films. *J Appl Phys* (2016) 120:085305. doi:10.1063/1.4961446
87. Malyi OI, Varignon J, Zunger A. Bulk $NdNiO_2$ Is Thermodynamically Unstable with Respect to Decomposition while Hydrogenation Reduces the Instability and Transforms it from Metal to Insulator (2021). arXiv:2107.01790.

88. Tomczak JM, Liu P, Toschi A, Kresse G, Held K. Merging *GW* with DMFT and Non-local Correlations beyond. *Eur Phys J Spec Top* (2017) 226:2565–90. doi:10.1140/epjst/e2017-70053-1

Conflict of Interest: The authors declare that the research was conducted in the absence of any commercial or financial relationships that could be construed as a potential conflict of interest.

Publisher's Note: All claims expressed in this article are solely those of the authors and do not necessarily represent those of their affiliated organizations, or those of the publisher, the editors, and the reviewers. Any product that may be evaluated in this article, or claim that may be made by its manufacturer, is not guaranteed or endorsed by the publisher.

frontiers in Physics

REVIEW
published: 02 February 2022
doi: 10.3389/fphy.2022.835942

Dynamical Mean Field Studies of Infinite Layer Nickelates: Physics Results and Methodological Implications

Hanghui Chen[1,2]*, *Alexander Hampel*[3], *Jonathan Karp*[4], *Frank Lechermann*[5] and *Andrew J. Millis*[3,6]

[1]NYU-ECNU Institute of Physics, NYU Shanghai, Shanghai, China, [2]Department of Physics, New York University, New York, NY, United States, [3]Center for Computational Quantum Physics, Flatiron Institute, New York, NY, United States, [4]Department of Applied Physics and Applied Mathematics, Columbia University, New York, NY, United States, [5]European XFEL, Schenefeld, Germany, [6]Department of Physics, Columbia University, New York, NY, United States

This article summarizes recent work on the many-body (beyond density functional theory) electronic structure of layered rare-earth nickelates, both in the context of the materials themselves and in comparison to the high-temperature superconducting (high-T_c) layered copper-oxide compounds. It aims to outline the current state of our understanding of layered nickelates and to show how the analysis of these fascinating materials can shed light on fundamental questions in modern electronic structure theory. A prime focus is determining how the interacting physics defined over a wide energy range can be estimated and "downfolded" into a low energy theory that would describe the relevant degrees of freedom on the ~0.5 eV scale and that could be solved to determine superconducting and spin and charge density wave phase boundaries, temperature dependent resistivities, and dynamical susceptibilities.

Keywords: nickelates, correlated electron physics, downfolding, dynamical mean field theory, density functional theory, quantum embedding

OPEN ACCESS

Edited by:
Antia Botana,
Arizona State University, United States

Reviewed by:
Liang Si,
Northwest University, China
Atsushi Fujimori,
The University of Tokyo, Japan

***Correspondence:**
Hanghui Chen
hanghui.chen@nyu.edu

Specialty section:
This article was submitted to Condensed Matter Physics, a section of the journal Frontiers in Physics

Received: *15 December 2021*
Accepted: *07 January 2022*
Published: *02 February 2022*

Citation:
Chen H, Hampel A, Karp J, Lechermann F and Millis AJ (2022) Dynamical Mean Field Studies of Infinite Layer Nickelates: Physics Results and Methodological Implications. Front. Phys. 10:835942. doi: 10.3389/fphy.2022.835942

1 INTRODUCTION

The identification of a new class of superconductors is a momentous event. Ways in which the new superconductors are similar to or different from previously known materials can drive new insights into the microscopic origin of this fundamentally mysterious quantum many-body phenomenon. The discovery [1, 2] of superconductivity in layered copper-oxide materials sparked a revolution in condensed matter physics and materials science, because the transition temperatures were very high relative to other materials known at the time. Additionally, many aspects both of the superconductivity and of the non-superconducting ("normal state") physics differed sharply from the predictions of conventional theory [3] in ways that made it obvious that interacting electron physics beyond mean field theory could have consequences of fundamental physics interest that approach (and in a few niche cases reach) commercial viability.

The very recent discovery [4] of superconductivity in the layered d^9 nickelates was also momentous because the superconductivity was theoretically anticipated [5] on the basis of a chemical and structural similarity to the cuprates. Understanding the properties of the superconducting nickelates provides an immense scientific opportunity to sharpen our understanding of the relation between crystal structure and local chemistry on the one hand and important phenomena such as superconductivity on the other.

The relationship between physical phenomena and crystal structure/local chemistry is the central question in the theory of quantum materials. The theory of quantum materials is one instance of the quantum many-body problem, one of the grand scientific challenges of our time. The quantum many-body problem is in essence a problem of data compression: as is well known, many-particle quantum mechanics is formulated in a Hilbert space of a size that grows exponentially with the number of degrees of freedom while quantum entanglement in general and Fermi statistics in particular implies that delicate phase relationships between different states are of crucial importance. Incorporating the chemical realism needed to understand and predict material properties requires acting on this Hilbert space with a Hamiltonian matrix that involves a number of parameters which grows as a very high power of the number of degrees of freedom. All solutions of the quantum many-body problem require both reducing the number of degrees of freedom and the number of interaction parameters to a manageable level ("downfolding" the physics to a simpler systems, typically a "low energy theory") and then handling the "model system" analysis of the still exponentially large and severely entangled Hilbert space of the downfolded theory.

Three decades of intense work have led to a rough consensus, generally although not universally accepted, that the low energy theory for the copper-oxide materials is some variant of the two dimensional one band Hubbard model. The relation of the model parameters to the precise chemistry and structure is reasonably well understood, and the properties of the simplest instantiations of this model are starting to come into focus [6–8]. The recent discovery of superconductivity in layered d^9 nickelates such as $NdNiO_2$ takes these questions to a new level. While many aspects of the crystal structure and chemistry are similar to those of the cuprates, in the nickelate family of materials multiple bands cross the Fermi surface and more interactions may be relevant. A crucial question is whether these effects are minor, so that the important physics of the nickelates is similar to that of the cuprates, or whether the low energy physics is richer and more complex in nickelates than in cuprates.

Various interacting models have been proposed for $NdNiO_2$. The simplest interacting lattice model is a single Ni $d_{x^2-y^2}$ orbital Hubbard model with an additional electron reservoir to mimic the self-doping effect from other bands that exist near the Fermi level. Kitatani *et al.* used this interacting model to directly estimate the superconducting transition temperatures [9]. Hepting *et al.* [10] and Been *et al.* [11] used a two-orbital model including Ni-$d_{x^2-y^2}$ orbital and a lanthanide element $d_{3z^2-r^2}$-like orbital with an interaction only on the Ni-$d_{x^2-y^2}$ orbital. A number of studies [12–17] focus on a different type of two-orbital models that consists of two Ni-d orbitals. Hu *et al.* [12] include Ni-$d_{x^2-y^2}$ and Ni-d_{xy} orbitals, while Zhang *et al.* [14], Werner *et al.* [13], and Kang *et al.* [15] and Wan *et al.* [17] include Ni-$d_{x^2-y^2}$ and Ni-$d_{3z^2-r^2}$ orbitals. These two-orbital models not only includes the local interaction on each Ni d orbital, but also takes into account the Hund's coupling between the two Ni d orbitals, relevant if the Ni high-spin $S = 1$ d^8 state is relevant. Wu *et al.* [18] include Ni-$d_{x^2-y^2}$ orbital, neodymium $d_{3z^2-r^2}$ orbital, and neodymium d_{xy} orbital. Local interactions are added on both Ni-$d_{x^2-y^2}$ orbital and neodymium d orbitals. This model is used to calculate the spin susceptibility and to estimate the superconducting transition temperature in the weak-coupling limit. Nomura *et al.* [19] compare two different three-orbital basis: one is identical to that of Ref. [18] and the other one is Ni $d_{x^2-y^2}$ orbital, lanthanide $d_{3z^2-r^2}$ orbital and interstitial s orbital. Strength of local interactions on all three orbitals is estimated. The model is used to study the screening effects on the Hubbard U of Ni-$d_{x^2-y^2}$ orbital. A different flavor of three-orbital model is employed by Lechermann [20], which consists of Ni $d_{x^2-y^2}$ and Ni $d_{3z^2-r^2}$ orbitals as well as a self-doping orbital. The model emphasizes the importance of multi-orbital processes in $RNiO_2$. Gu *et al.* [21] use a four-orbital model: Ni d_{xy} orbital, lanthanide $d_{3z^2-r^2}$ orbital, lanthanide d_{xy} orbital and interstitial s orbital. Local interaction is added on Ni-$d_{x^2-y^2}$. The model is used to study the interplay between hybridization and correlation effects and to calculate the phase diagram. Gao *et al.* [22] construct a general four-orbital model $B_{1g}@1a \oplus A_{1g}@1b$ which consists of two Ni-d orbitals and two lanthanide d orbitals. The model is used to study the topological property of the Fermi surface. All the above models focus on Ni-d and/or lanthanide d orbitals. A number of studies also explicitly take into account oxygen p states with local interactions added on Ni-d orbitals [20, 23–25]. Jiang *et al.* [23] study a hole doped system that consists of a Ni d^9 impurity properly embedded in an infinite square lattice of O p^6 ions. This impurity model is used to argue that in the NiO_2 layer, the strong pd hybridization may favor a $S = 0$ hole-doped state with $^1A1$ symmetry, similar to superconducting cuprates.

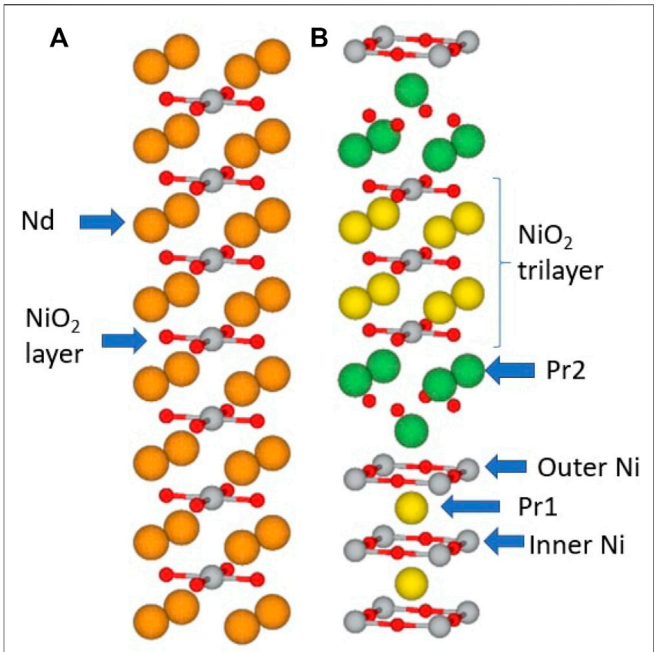

FIGURE 1 | (A): crystal structure of infinite layer $NdNiO_2$ in the P4/mmm structure. **(B)**: crystal structure of trilayer $Pr_4Ni_3O_8$ in the I4/mmm structure. Ni atoms are shown in silver, O in red, Nd in orange, Pr1 in yellow, and Pr2 in green. From Ref. [25] and the crystal structures are visualized using Vesta [115].

Which of the plethora of theoretical models is most relevant is an important question. This review will present a perspective on what has been learned from the density functional theory (DFT) plus dynamical mean field theory (DMFT) about the many body electronic structure and the relevant low energy model and also what has been learned about the methods in the context of applying them to the layered nickelates.

2 OVERVIEW

2.1 Crystal Structure and Basic Chemistry

The copper oxide and layered d^9 nickelate materials are transition metal oxide (TMO) compounds that share the common structural motif of the CuO_2/NiO_2 plane. We focus first on the conceptually simplest materials, "infinite layer" $CaCuO_2$ and $NdNiO_2$ [panel (A) of **Figure 1**] in which the transition metal ions occupy the vertices of a square planar array with the oxygen ions at the midpoints of the edges. In their bulk, three dimensional form these materials are stacks of transition metal/oxygen planes, with the Ca/Nd ions located half-way between planes, above the centers of the squares formed by four transition metal ions.

The CuO_2/NiO_2 plane motif may be combined in many ways, yielding a wide variety of compounds with somewhat similar properties but with many differences of detail. The very large number of cuprate materials will not be discussed here. In the nickelate materials, the infinite layer compounds can in principle be realized with all rare-earth elements R as A-site cation [26]. So far R = La, Pr, and Nd have been synthesized. In addition, multilayer variants $R_{1+m}Ni_mO_{2m+2}$ are known, consisting of groups of m $NdNiO_2$ planes separated by effectively insulating spacer layers of Nd and O. To date, m = 3, 4, 5 have been synthesized. The $m = 3$ material is shown in panel (B) of **Figure 1**; the plane labelled Pr2 is the spacer layer. Some charge transfer (CT) to the spacer layers occurs, leading to a doping of the NiO_2 planes that is different than that of the infinite layer compounds, but apart from this the basic electronic physics of the layered compounds is believed to be very similar to that of the infinite layer compounds [27]. In this article we consider the compounds as interchangeable.

Qualitative chemical ("formal valence") considerations suggest that the electronic configurations of the ions are $Ca^{2+}Cu^{2+}[O^{2-}]_2$ and $Nd^{3+}Ni^{1+}[O^{2-}]_2$ corresponding in both cases to a transition metal d^9 configuration (one hole in the d-shell), and standard considerations of ligand field theory indicate that the hole resides in the transition metal $d_{x^2-y^2}$ orbital. Varying the chemical formula (e.g., by replacing a fraction x of the Nd^{3+} with Sr^{2+} can lead to changes in the Cu/Ni formal valence to $d^{9\pm x}$ (electron or hole doping) and in both material families electron and hole doping leads to dramatic changes in physical properties; in particular, superconductivity occurs only in relatively narrow electron or hole doping ranges not including the nominal d^9 valence.

Formal valence considerations are only a rough approximation to the actual electronic states because in a solid the charge on an ion is not conserved. Quantitatively or qualitatively important roles may be played by charge transfer processes including fluctuations that move an electron from an O to a transition metal (producing a $d^{10}\underline{L}$ configuration, where $\underline{L}$ refers to a hole in the oxygen ligand) or from the transition metal to the rare earth/alkali producing e.g., an Ni d^8 Nd $^{2+}$ configuration or between two transition metal ions, producing a $d^8 - d^{10}$ pair. Especially for Ni based transition metal oxides (TMO) it is well known that Ni-O bonds are highly covalent and hybridization effects lead to drastic deviations from the formal atomic orbital occupation picture [28, 29]. The low energy theory of the copper-oxide materials is generally although not universally, accepted to involve one band, of mixed Cu-$d_{x^2-y^2}$ and O(2p) character and with an essentially two dimensional dispersion and with relatively strong, relatively local interactions derived from intra-d Coulomb matrix elements but substantially affected in magnitude by CT and screening processes involving the O ions (the rare earth/alkali ions such as the Ca in $CaCuO_2$ are believed to be electronically inert on these scales) [3]. Important to this finding is the observation that the relevant configurations of the Cu(3d) states are d^9 and d^{10}; this simple multiplet structure strongly constrains the possible interaction terms. The low energy theory is thus a variant of the two dimensional Hubbard model, possibly including longer ranged interactions.

In the layered d^9 nickelates such as $NdNiO_2$ the situation is richer. Multiple bands cross the Fermi surface, while the potential relevance of d^8 configurations raises the possibility that multiplet ("Hund's") interactions governing the relative energetics of different configurations of TMO d-electrons are relevant to the low energy physics. A fundamental question is whether this additional physics plays an important role in the low energy correlation physics such as superconductivity or whether the correlation physics of the nickelates is in essence similar to that of the cuprates.

2.2 Downfolding and the DFT + DMFT Methodology

In the context of quantum materials the process of defining an appropriately reduced model from a high energy, more chemically realistic, "all orbital" description is referred to as "downfolding". Downfolding starts from the use of a mean field like approximation such as density functional theory to define a single-particle basis (e.g., the Kohn-Sham eigenstates within a broad energy region) that is for all practical purposes complete. Then a subspace of this set of states is selected and the Hamiltonian is appropriately projected onto the subspace. The required projection is more sophisticated than simply taking the matrix elements of the Hamiltonian between states in the subspace: screening of the retained interactions by processes involving states that are not retained must be incorporated and correlation induced shifts in relative energy splittings of different states ("double counting corrections") must be managed correctly. Further, since the purpose is to obtain something that can be solved (perhaps approximately), the specifics of downfolding are intertwined with the method of solution of the resulting theory.

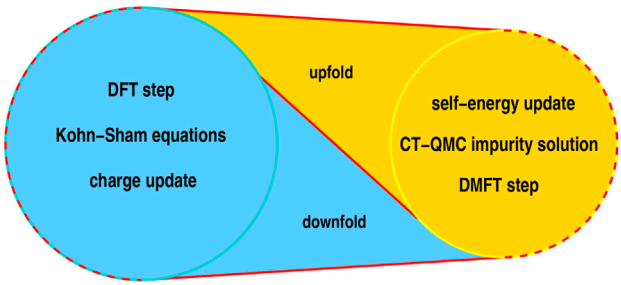

FIGURE 2 | Principle DFT + DMFT method as hybrid scheme, working as a ratchet with up- and downfolding links. One starts from a converged KS-DFT calculation and downfolds to the correlated subspace where a DMFT step is performed. This asks mainly for the solution of a quantum-impurity problem [here conducted *via* continuous-time quantum-Monte Carlo (CT-QMC)], yielding a local self-energy. That self-energy is upfolded to the Bloch space of the DFT problem and used to revise the electronic charge density. Using the latter, a new KS potential is generated and a novel DFT step performed, which is followed by the next downfolding, etc. This cycle is performed until self-consistency in the charge density and the self-energy is achieved. Adapted from Ref. [116].

While one important goal of a downfolding process is to obtain a truly low energy theory (defined, say on the ±0.5 eV interval around the chemical potential that is relevant for analysis of transport and of low energy instabilities such as superconductivity), in the case of transition metal oxides an intermediate step of downfolding to a reduced model defined in a wider energy range but with truncated interactions has been found to be very useful. This intermediate step is motivated by the physical/chemical intuition that in transition metal oxides the most relevant interactions are the site local charging ("U") and multiplet ("J") interactions that control the energy levels of a partly filled d shell on a transition metal ion and by the success of the DMFT approximation in treating the resulting physics.

The DFT + DMFT methodology is a specific downfolding method based on the idea that both the important interactions and the correlation physics they induce are spatially local in a sense defined more precisely below. It is closely related to the DFT + U method inmpmllemented in standard DFT codes; indeed the DFT + U method is in effect the hartreee approximation to the DFT + DMFT method. The locality of the interactions greatly reduces the number of relevant interaction parameters (i.e., the complexity of the interacting Hamiltonian that must be solved) while the locality of the correlation physics drastically reduces the severity of entanglement effects, enabling a tractable solution of the resulting correlation problem. The method is now a work-horse of correlated electron materials science and the nickelate materials provide an interesting test of both the assumptions that go into the methodology and the results it produces.

The DFT + DMFT methodology [30, 31] uses a DFT calculation to define a set of correlated orbitals (for example the Ni d-orbitals), the hybridization of these orbitals to each other and to other orbitals, presumed to be uncorrelated, and also involves a prescription for associating site local interactions to the correlated orbitals. The resulting downfolded system may be thought of a kind of generalized multi-orbital Hubbard model involving correlated sites coupled to uncorrelated ones and is solved in the DMFT (locality of correlation physics) approximation which reduces the problem to the solution of a quantum impurity model (set of local orbitals coupled to a non-interacting bath) plus a self-consistency condition. Finally, in a charge self-consistent (CSC) step which is sometimes omitted, the full charge density of the system is obtained and fed back in to the density functional theory; the correlated orbitals are redefined, and the process is repeated until complete self consistency is obtained. This process is visualized in **Figure 2**. Importantly, the CSC DFT + DMFT equations can be derived as the stationarity conditions of a general functional describing the electronic structure *ab-initio* [31] within the DMFT approximations.

In first instance, DMFT delivers results for the electron (one-particle) Green's function $\hat{G}$, which is directly connected to the physical spectral function:

$$\hat{A}(\omega) = i\left[\hat{G}(\omega) - \hat{G}(\omega)^{\dagger}\right] \Big/ 2\pi. \tag{1}$$

From solving the impurity problem within DMFT the atomic multiplet nature of the correlated manifold can also be analyzed from the many-body density matrix. The computed spectral functions can be compared directly to photoemission measurements [32, 33] and considerable intuition about the physics can be gained from the many body density matrices. Furthermore, symmetry broken phases such as superconductivity and magnetic phase can be addressed, and transport coefficients can be estimated. Momentum dependent susceptibilities and vertex functions can also be constructed, albeit with much more computational effort.

The important technical steps in implementing the dynamical mean field approximation are the construction of the correlated orbitals and their coupling to the uncorrelated orbitals and the computation of the interactions among electrons in these orbitals.

3 METHODS

The DFT + DMFT methodology is formulated in terms of the single particle Green function, defined on the Matsubara (imaginary frequency) axis for a periodic solid as

$$\hat{G}(\mathbf{k}, i\omega_n) = \left[i\omega_n + \mu - \hat{H}_{ref}(\mathbf{k}) - \hat{\Sigma}(\mathbf{k}, i\omega_n)\right]^{-1} \tag{2}$$

Here $\mathbf{k}$ is a wavevector in the first Brillouin zone of the solid, μ is the chemical potential, H_{ref} is a reference single-particle (non-interacting) Hamiltonian and the self energy operator $\hat{\Sigma}$ parametrizes the difference between physical electron propagation and the predictions of the reference single-particle Hamiltonian. If the theory is solved exactly, the choice of reference Hamiltonian is immaterial: it just provides a starting point for calculations. However, actual calculations involve approximations and require the use of a computational basis that is a subset of the full set of all single-particle eigenstates of H_{ref}; in this circumstance, the choice of H_{ref} and the choice of basis functions will influence the final result.

Here, we take H_{ref} to be the Kohn-Sham Hamiltonian produced by a specified density functional theory combined with a "double counting (DC) correction" and $\hat{\Sigma}^{\nu,\nu'}_{\mathbf{k}}$ is a matrix in the space spanned by the eigenstates $\psi_{\nu\mathbf{k}}(r)$ of H_{ref}, which is constructed using a locality ansatz described more explicitly below. The different "pure" DFT exchange-correlation functionals give very similar results and will not be discussed explicitly here. However, extensions of DFT such as self interaction correction (SIC) DFT [34] do lead to different results, as discussed below. For further reading we refer to review articles, i.e., Ref. [35].

In embedding theories such as DFT + DMFT one defines on physical grounds a subset of correlated orbitals (in the cuprate/nickelate context the transition metal d-orbitals) and retains only the site-local matrix elements of the self energy among these orbitals and the site-local interactions that contribute to these matrix elements. These site-local self energy matrix elements are then calculated via a mapping to a quantum impurity model with the local Hamiltonian (crystal field levels plus interactions) of the full model and a self-consistently determined coupling to a bath in the form of a so called "hybridization function"; the result is self-consistently embedded into the full electronic structure.

The key conceptual issues in the method are the construction of the local orbitals and the specification of the interactions between them. These issues are discussed in the next two subsections.

3.1 Quantum Embedding: Construction of the Localized Orbitals

The first step in this procedure is to precisely define a set of orbitals $\phi^{R_i}_m$ centered on sites R_i. These orbitals define a basis in which the self energy and local interactions are computed. Within the DFT + DMFT community many approaches to define these local orbitals have been introduced. All methods explicitly or implicitly use a set of so called "projector functions":

$$P^{R_i,m}_{\nu,\mathbf{k}} = \langle \phi^{R_i}_m | \psi_{\nu,\mathbf{k}} \rangle, \tag{3}$$

which specify the relation of the local orbitals $\phi^{R_i}_m$ to the Kohn-Sham (KS) eigenstates $\psi_{\nu,\mathbf{k}}$. The P operators are termed projectors because in the general case there are fewer localized orbitals m than there are Kohn-Sham eigenstates ν.

The projector functions allow one to "upfold" a self energy calculated in the orbital (R_i, m) basis to the Kohn-Sham basis as

$$\Sigma_{\nu\nu'}(\mathbf{k}, i\omega_n) = \sum_{R_i mm'} \left(P^{R_i\mathbf{k}}_{m\nu}\right)^{\dagger} \left[\Sigma^{R_i}_{\mathrm{QI}}(i\omega_n)\right]_{mm'} P^{R_i\mathbf{k}}_{\nu' m'}. \tag{4}$$

Here we have written Eq. 4 for the DMFT ansatz of a self energy that is site local in the orbital basis. In general the self-energy can also contain multiple sites embedded as a cluster impurity. However, in this case one has to carefully consider breaking of symmetries due to the geometry of the lattice.

The full Green function **Eq. 2**, a matrix in the set of Kohn-Sham bands, is then written as

$$\left[G^{latt}_{\nu\nu'}(\mathbf{k}, i\omega_n)\right] = \left[i\omega_n + \mu - \hat{H}_{ref}(\mathbf{k}) - \Sigma_{\nu\nu'}(\mathbf{k}, i\omega_n)\right]^{-1} \tag{5}$$

The 'downfolded' site-local lattice Green function $G^{mm'}_{\mathrm{QI};R_i}$ in the orbital basis is given as

$$G^{mm'}_{\mathrm{QI};R_i}(i\omega_n) = \frac{1}{N_k} \sum_{\nu,\nu',\mathbf{k}\in\mathcal{W}(k)} P^{R_i\mathbf{k}}_{\nu m} G^{latt}_{\nu,\nu'}(\mathbf{k}, i\omega_n) \left(P^{R_i\mathbf{k}}_{m'\nu'}\right)^{\dagger}, \tag{6}$$

which allows to construct the dynamic Weiss field of the quantum impurity problem in DMFT *via* a Dyson equation:

$$\mathcal{G}^0_{mm'}(i\omega_n)^{-1} = G^{mm'}_{\mathrm{QI};R_i}(i\omega_n)^{-1} + \Sigma^{R_i}_{\mathrm{QI}}(i\omega_n). \tag{7}$$

$\mathcal{G}^0_{mm'}$ connects the impurity and the bath, from which a hybridization function for the Anderson impurity model (AIM) can be constructed.

Solving the impurity problem gives a new self-energy (**Eq. 4**), defining a new lattice Green function, and hence a new local Green function. This procedure is performed until convergence is reached and $\mathcal{G}^0$ does not change further.

The DMFT converged lattice Green function **Eq. 5** can be used to construct a new charge density:

$$n(r) = \frac{1}{\beta}\frac{1}{N_k} \sum_{\nu,\mathbf{k}} \langle r|\Psi_{\nu,\mathbf{k}}\rangle \left[G^{latt}(\mathbf{k}, i\omega_n)\right]_{\nu\nu} \langle \Psi_{\nu,\mathbf{k}}|r\rangle, \tag{8}$$

which serves as input for DFT in a CSC DFT + DMFT calculation. From this a new charge density from DMFT a new set of Kohn-Sham (KS) orbitals, projectors and interactions are defined and the DMFT equations are solved again. This procedure is repeated until the charge density converges. The effect of this additional charge self consistency loop is sometimes small, but in many cases can have important quantitative influence in the results [36], and is technically needed to evaluate energies within the DFT + DMFT formalism [31].

3.1.1 Projected Atomic Orbitals

One choice for constructing the projector functions is the projected atomic orbitals (PLO) methodology [37–39], in which one introduces a set of atomic-like correlated orbitals $|\tilde{\phi}^R_m\rangle$, which are centered on the positions R of the ions of interest, have the symmetry appropriate to the correlated orbital of interest (e.g. transition metal d), and are set to zero for distances $|\vec{r} - \vec{R}|$ around R greater than some preset value. In this formalism a first set of projectors is then defined from **Eq. 3** as

$$\tilde{P}^{R_i,m}_{\nu,\mathbf{k}} = \langle \tilde{\phi}^{R_i}_m | \psi_{\nu,\mathbf{k}} \rangle. \tag{9}$$

The downfolded orbitals describing the correlated subspace are computed as

$$|\bar{\phi}^{R_i}_m\rangle = \sum_{\nu,\mathbf{k}\in\mathcal{W}(\mathbf{k})} \tilde{P}^{R_i,m}_{\nu,\mathbf{k}} |\psi_{\nu,\mathbf{k}}\rangle, \tag{10}$$

here, $\mathcal{W}(\mathbf{k})$ notates the fact that all practical calculations retain only a subset of KS states within a possibly $\mathbf{k}$-dependent window $\mathcal{W}(\mathbf{k})$. Since the sum over ν is not complete, as it runs only over $\mathcal{W}(\mathbf{k})$, the $|\bar{\phi}^{R_i}_m\rangle$ must be orthonormalized. The result after orthonormalization are functions $|\phi^{R_i}_m\rangle$ that deviate

to some degree from the originally defined atomic like states like states $|\tilde{\phi}_m^{R_i}\rangle$, and in particular have tails that extend outside the originally defined radius. These functions may be viewed as Wannier functions as defined as in **Eq. 11**, with the procedure described above corresponding to a prescription for constructing some elements of the U matrices. These new states are then used in **Eq. 3** to construct the projectors $P_{\nu,\mathbf{k}}^{R_i,m}$, which are actually used in the formalism.

The window $\mathcal{W}(\mathbf{k})$ effectively controls how localized the resulting states are, and one strategy is to formulate the problem in as wide a range as feasible, to make the $|\phi_m^{R_i}\rangle$ very localized. However, a narrower energy window has the advantages of focusing attention on states that are more directly related to the low energy physics of interest and of providing a theory with lower intrinsic energy scales.

3.1.2 Maximally Localized Wannier Functions for Downfolding

One may also obtain the projector functions via the Wannier construction introduced by Marzari and Vanderbilt [40], in which one defines N spatially localized Wannier functions (WFs) as Fourier transforms of linear combinations of N KS states *via*

$$|w_\alpha^{R_i}\rangle = \frac{V}{(2\pi)^3}\int_{\mathrm{BZ}} d\mathbf{k}\; e^{-i\mathbf{k}R_i}\sum_{\nu=1}^{N} U_{\nu\alpha}^{*(\mathbf{k})}|\Psi_{\nu,\mathbf{k}}\rangle, \tag{11}$$

Here the $U_{\nu\alpha}^{*(\mathbf{k})}$ are the components of a family of unitary transformations (one at each $\mathbf{k}$) and are chosen to optimize specific properties of the $|w_\alpha^{R_i}\rangle$. The most common choice, referred to as the maximally localized Wannier function (MLWF) method, is to choose the $U_{\nu\alpha}^{*(\mathbf{k})}$ to minimize the mean square spread of all WFs in the unit cell [40]. Alternatively, one can construct selectively localized Wannier functions (SLWFs) by performing the spread minimization only for certain WFs [41].

A subset of the Wannier functions, labelled by m, are identified with the correlated orbitals and the Wannier construction in **Eq. 11** implies that projectors can be identified as

$$P_{m\nu}^{\mathbf{k}} := U_{\mu\alpha=m}^{*(\mathbf{k})}. \tag{12}$$

This construction is implemented in the software package WANNIER90 (W90) [42].

The initial seed for $U_{\mu\alpha}^{(k)}$ are typically obtained by projections on atomic orbitals similar to the PLOs above. These are orthonormalized, and then the orthonormalized functions are used as a starting point for the spread minimization. The additional optimization process leads to differences between the MLWF and PLO procedures.

The number of Kohn-Sham bands N_B used in the Wannierization process can be chosen similar to the projector method above via a window $\mathcal{W}(\mathbf{k})$ which is ideally set to contain a group of bands separated by energy gaps from all other bands in the solid. If N_B is larger than the number of desired Wannier orbitals then a disentanglement procedure is performed, producing a set of N optimized Bloch states $|\Psi_{\mu,\mathbf{k}}^{(\mathrm{opt})}\rangle$ labelled by $\mu = 1 \ldots N$:

$$|\Psi_{\mu,\mathbf{k}}^{(\mathrm{opt})}\rangle = \sum_{\nu=1}^{N_B^{\mathbf{k}}} U_{\mu\nu}^{\mathrm{dis}(\mathbf{k})}|\Psi_{\nu,\mathbf{k}}\rangle. \tag{13}$$

This ensures "global smoothness of connection" and an optimal k-point connectivity by minimizing the gauge invariant term of the spread of the resulting WFs [43]. Afterwards, the spread-minimization is performed as usual using the $\Psi^{(\mathrm{opt})}$. This allows to define the projector functions as:

$$P_{\alpha\nu}^{\mathbf{k}} := U_{\mu\alpha}^{*(\mathbf{k})}U_{\mu\nu}^{\mathrm{dis}(\mathbf{k})}. \tag{14}$$

It is important to note that while the projection of the KS Hamiltonian onto a given set of Wannier functions may reproduce the Kohn-Sham bands perfectly, different Wannierization choices may lead to different constructions of the orbitals and to different tight binding parameters. This issue is discussed in more detail in Ref. [44].

3.1.3 Comparison

The projector and Wannier constructions of the localized orbitals are conceptually very similar, differing in the specifics of how the correlated orbitals are constructed. The projector method is connected in a intuitively appealing manner to the local orbitals of interest (especially if the projection window $\mathcal{W}$ is set to a wide value), and provides a more convenient construction of double counting correction formulas [45]. In most applications to date the projector method is used only to construct the correlated orbitals needed in the DMFT procedure. Part of the motivation for this choice is to focus the DMFT treatment on the strongly correlated orbitals not well treated by DFT. The method avoids the expensive and sometimes unstable spread minimization associated with the Wannier construction.

The MLWF method is less dependent on an a-priori choice of atomic orbitals, is based on minimization of a clear metric under which the orbitals are constructed, and also minimizes deviations from the KS dispersion. Because it constructs a basis set which is complete within some energy range, it provides at no additional complication a full tight-binding parametrization of the electronic band structure in a given energy range,

$$H_{\alpha\alpha'}^{\mathrm{TB}}(\mathbf{k}) = \sum_{\nu} P_{\nu'\alpha'}^{\mathbf{k}} H_{ref}^{\nu}(\mathbf{k})\; \left(P_{\alpha\nu}^{\mathbf{k}}\right)^{\dagger}, \tag{15}$$

providing physical intuition about the relevant orbitals. (With some effort, similar information can be obtained from the projector method, but this is not often done). **Figure 3** shows two examples of fitting the $NdNiO_2$ low-energy KS states using MLWF. The first [**Figure 3A**], constructs 17 Wannier orbitals for all 17 KS states that are present in a large energy window from -9 to 8 eV, whereas the second [**Figure 3B**] constructs a minimal model only for the three frontier orbitals (Ni-$d_{x^2-y^2}$, Nd-d_{z^2}, Nd-d_{xy}). As shown in Ref. [21] an improved description of the low energy dispersion is obtained by the inclusion of a non-Ni, non-Nd, band orbital near the Fermi level, apparently representing interstitial charge, which is further discussed in **Section 4.1**.

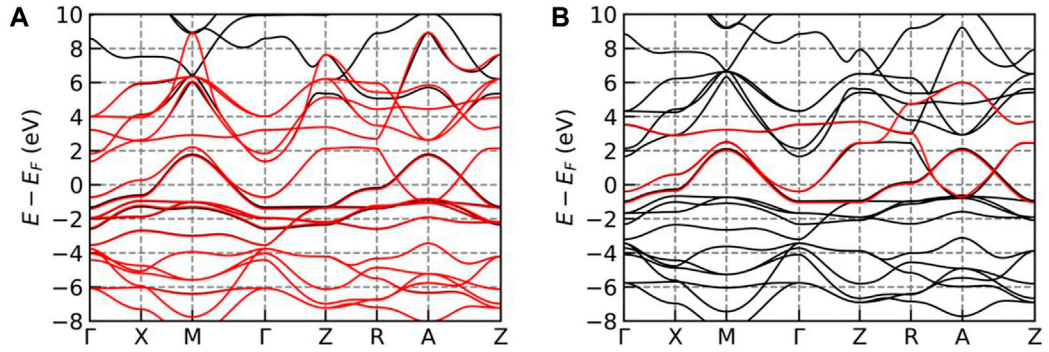

FIGURE 3 | DFT bands for $NdNiO_2$ (black lines) and Winner fits (red lines) for Wannierization using **(A)** 17 Wannier functions (5 Nd-*d* orbitals +5 Ni-*d* orbitals + 6 oxygen-*p* orbitals + interstitial-*s* orbital and **(B)** using 3 Wannier functions (Nd-$d_{3z^2-r^2}$, Nd-d_{xy} and Ni-$d_{x^2-y^2}$ orbital). Adapted from Ref. [21].

In the following we will call all calculations performed directly in the tight-binding (TB) basis Wannier-mode calculations, whereas calculations in which the DMFT equations are written in the Kohn-Sham basis will be referred to as Bloch-mode calculations. Note, that direct formulation of the DMFT equations as a solution of a Hamiltonian restricted to the space of the correlated orbitals is in general not possible, because the projectors are in general non-square matrices and hence do not serve as a unitary transformation [46].

While Wannier and projector methods had until recently been viewed as roughly equivalent methods of constructing the basis in which the dynamical mean field equations are formulated, and indeed in some cases the equivalence of projector and Wannier-based methods was demonstrated [47], Karp *et al.* [44] found that results of the DFT + DMFT methodology can be sensitive to the choice of method used to construct the local orbitals of the downfolded model. We will review and discuss these results in **Section 4.2**.

3.2 Interactions in the Correlated Subspace

3.2.1 Basic Definitions

Once an orbital downfolding has been defined one has to formulate an appropriate interaction among the downfolded correlated orbitals $|\phi_m^{R_i}\rangle$. Within the DMFT approximation the important interaction matrix elements are the on-site ones among the n correlated orbitals centered on the same site R_i. We begin by considering the matrix elements of the bare Coulomb interaction V among the correlated orbitals on a given site:

$$\hat{H}_V = \frac{1}{2}\sum_{\sigma\sigma'}\sum_{mm'm''m'''} V_{mm'm''m'''}\; c^\dagger_{m\sigma}c^\dagger_{m'\sigma'}c_{m'''\sigma'}c_{m''\sigma}. \tag{16}$$

Here, $c^\dagger_{m\sigma}$ and $c_{m\sigma}$ are creation and annihilation operators for the correlated orbitals $|w_\alpha\rangle = |w^{R_i}_{,m,\sigma}\rangle$ or $|\tilde{\phi}^{R_i}_m\rangle$, and $V_{mm'm''m'''}$ is the Coulomb interaction tensor:

$$\begin{aligned} V_{mm'm''m'''} &= \langle mm'|V|m''m'''\rangle \\ &= \int d\mathbf{r}_1 \int d\mathbf{r}_2\; w^*_{m\sigma}(\mathbf{r}_1)w^*_{m'\sigma'}(\mathbf{r}_2)\frac{1}{|\mathbf{r}_1-\mathbf{r}_2|}w_{m'''\sigma'}(\mathbf{r}_2)w_{m''\sigma}(\mathbf{r}_1). \end{aligned} \tag{17}$$

In the absence of symmetries there are $\mathcal{O}n^4$ matrix elements, but the main cases of physical interest involve a high degree of symmetry that enables one to reduce the complexity of the Coulomb tensor to just a few parameters. We will only describe the most important formulas here and refer the reader to Ref. [48] for an more detailed overview.

The most widely used form is the so called "Slater" parametrization [49], which makes use of the spherical symmetry of an isolated single atom. If the projectors in **Eq. 3** are chosen to produce sufficiently local WFs this is a good approximation, and is for example used in all DFT + U implementations.

The most important Coulomb integrals are elements of $V_{mm'm''m'''}$ that differ only in up to two different indices m. Using the symmetries this allows to define (in the absence of spin-orbit coupling):

$$U_{avg} = \frac{1}{(2l+1)^2}\sum_{mm'} V_{mm'mm'} = F^0 \tag{18}$$

$$U_{avg} - J_{avg} = \frac{1}{2l(2l+1)}\sum_{m\neq m'} V_{mm'm'm}. \tag{19}$$

Here, F^k, refers to the kth Slater integral, proportional in effect to the kth-pole of the electric charge distribution of the atomic configuration of the rotationally symmetric free-ion case. From the F^k the full Coulomb tensor can be constructed. For a d-shell of an isolated ion one can further show that

$$J_{avg} = \frac{F^2 + F^4}{14} \tag{20}$$

and that F^4/F^2 is fixed, so that the entire Coulomb interaction tensor is determined by only two parameters: $F^0 = U_{avg}$ and J_{avg}. The ratio F^4/F^2 is obtained empirically, varies only little for transition metals, and it is often fixed to $F^4/F^2 \approx 0.625$ [50].

Another often applied parametrization is the so called "Hubbard-Kanamori" form [51, 52], widely used in particular to describe the on-site interactions among electrons in the d-shell of a transition metal ion. This parametrization is formulated in terms of the averaged parameters:

$$\begin{aligned}\mathcal{U} &\equiv \frac{1}{n}\sum_{m} V_{mmmm}\\ \mathcal{U}' &\equiv \frac{1}{n(n-1)}\sum_{m\neq m'} V_{mm'mm'}\\ \mathcal{J} &\equiv \frac{1}{n(n-1)}\sum_{m\neq m'} V_{mm'm'm}\\ \mathcal{J}_C &\equiv \frac{1}{n(n-1)}\sum_{m\neq m'} V_{mmm'm'},\end{aligned} \tag{21}$$

which are the so-called Hubbard-Kanamori parameters for n orbitals. In the particular case of an octahedral crystal field, the d shell is split into a t_{2g} and e_g manifold. Within either the t_{2g} and e_g sub-manifold of the octahedral point group (but not for the whole d shell), one can verify that $\mathcal{U}' = \mathcal{U} - 2\mathcal{J}$ and $\mathcal{J} = \mathcal{J}_C$ so as in the free ion case the full interaction can be constructed from only two independent parameters $\mathcal{U}$, and $\mathcal{J}$. The resulting interaction operator has the following form:

$$\begin{aligned}\hat{H}_U^{\text{kan}} &= \frac{1}{2}\sum_{\sigma}\sum_{m}\mathcal{U}\ \hat{n}_{m\sigma}\hat{n}_{m\bar{\sigma}}\\ &+\frac{1}{2}\sum_{\sigma}\sum_{m\neq m'}\left[(\mathcal{U}-2\mathcal{J})\ \hat{n}_{m\sigma}\hat{n}_{m'\bar{\sigma}} + (\mathcal{U}-3\mathcal{J})\hat{n}_{m\sigma}\hat{n}_{m'\sigma}\right]\\ &+\frac{1}{2}\sum_{\sigma}\sum_{m\neq m'}\mathcal{J}\left(\underbrace{c^{\dagger}_{m\sigma}c^{\dagger}_{m'\bar{\sigma}}c_{m\bar{\sigma}}c_{m'\sigma}}_{spin-flip} + \underbrace{c^{\dagger}_{m\sigma}c^{\dagger}_{m\bar{\sigma}}c_{m'\bar{\sigma}}c_{m'\sigma}}_{pair-hopping}\right).\end{aligned} \tag{22}$$

Importantly, this form of the interaction is rotationally invariant, which means that within the subset of orbitals, arbitrary unitary transformations on the orbitals can be applied, without adapting the parameters.

Note, that in this form $\mathcal{U}$ represents directly the diagonal terms of the full Coulomb tensor in contrast to the Slater parameter F^0. In the case of spherical symmetry one can show that the two parametrizations are related by:

$$\begin{aligned}\mathcal{U} &= U_{avg} + \frac{8}{7}J_{avg}\\ \mathcal{J} &= \frac{5}{7}J_{avg}.\end{aligned} \tag{23}$$

3.2.2 Determining the Screened Interactions

In solids the interaction parameters are renormalized from their bare values by screening processes $V \rightarrow U$ involving the other electrons in the solid. The most important renormalization is of the monopole interaction $F_0 \equiv U_{avg}$ which gives the charging energy $E_C = \frac{1}{2}U_{avg}N_{tot}^2$ with $N_{tot} = \sum_m n_m$ the total charge in the correlated orbitals. The charging energy measures the change in energy when the local charge is changed, but changing the local charge implies changing the 'monopole' electric fields produced by these charges; these electric fields are screened by the dielectric constant ϵ so that in computing the energy one should replace e^2/r by $e^2/(\epsilon r)$ in **Eq. 16** where ϵ is the dielectric constant associated with charge fluctuations on orbitals not included in the low energy theory. Since typical values of ϵ are $\sim 5-10$ renormalizations of the charging energy from the free ion value ~20 eV to solid state values of the order of 5 eV are expected. The other "$\mathcal{J}$" terms represent energetics associated with electron rearrangement at fixed total charge, i.e., with changes in the quadrupole and octupole moments of the ion; these fields fall off much more rapidly and the J are as a result much more weakly screened, typically deviating by only 10–20% from the free-ion values. The important conclusion from this argument is that the basic interaction strength U or F^0 depends on how the screening is treated. In the next sections we discuss this issue in more detail.

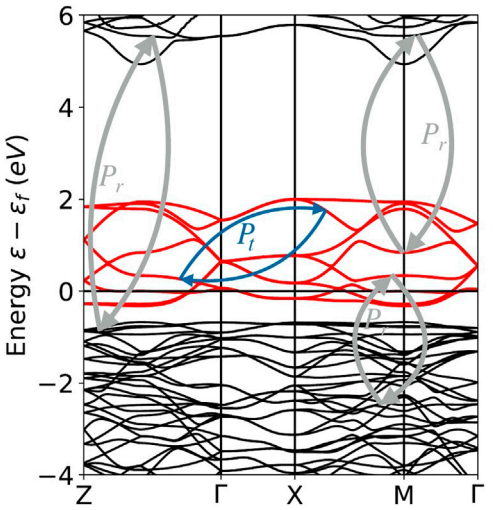

FIGURE 4 | Band structure of $LuNiO_3$, with constructed Wannier functions for the Ni e_g states as target states t. The decomposition in the polarization channels P_t within the correlated subspace, and the polarization channels P_r outside, from, and to the target subspace t are schematically depicted as blue and grey arrows.

Commonly used ab-initio methods for treating the strong renormalizations from solid state screening are the constrained LDA method [53] and the constrained random phase approximation (cRPA) method [54]. Here, we present the latter, for a review see e.g., Ref. [55].

cRPA is a linear response theory based on the polarization function P giving the response of electrons to a test charge in the system. Within the RPA approximation, which neglects all non-Hartree terms, the dielectric function is calculated from the full bare Coulomb interaction and the polarization function as:

$$\epsilon = 1 - VP\ . \tag{24}$$

The polarization function P in RPA is calculated from DFT as:

$$P(\mathbf{r},\mathbf{r}',\omega) = \sum_{\nu\mathbf{k}}^{\text{occ}}\sum_{\nu'\mathbf{k}'}^{\text{unocc}}\left[\frac{\Psi^{\dagger}_{\nu\mathbf{k}}(\mathbf{r})\Psi_{\nu'\mathbf{k}'}(\mathbf{r})\Psi^{\dagger}_{\nu'\mathbf{k}'}(\mathbf{r}')\Psi_{\nu\mathbf{k}}(\mathbf{r}')}{\omega - \epsilon_{\nu'\mathbf{k}'} + \epsilon_{\nu\mathbf{k}} + i\delta} - \frac{\Psi_{\nu\mathbf{k}}(\mathbf{r})\Psi^{\dagger}_{\nu'\mathbf{k}'}(\mathbf{r})\Psi_{\nu'\mathbf{k}'}(\mathbf{r}')\Psi^{\dagger}_{\nu\mathbf{k}}(\mathbf{r}')}{\omega + \epsilon_{\nu'\mathbf{k}'} - \epsilon_{\nu\mathbf{k}} - i\delta}\right], \tag{25}$$

where $\Psi_{\nu\mathbf{k}}$ and $\epsilon_{\nu\mathbf{k}}$ mark KS eigenstates and eigenvalues.

The effective screened Coulomb interaction U in a target "(t)" space (typically the manifold of correlated states)can now be calculated as follows. Consider the example depicted in **Figure 4**. The effective screened Coulomb interaction is calculated by first splitting the polarization of the system in two parts, P_t pertaining

only to transitions among the target orbitals and P_r containing all other transitions (including from target to non-target orbitals and the reverse):

$$P = P_t + P_r. \tag{26}$$

Now one can deduce the partially screened interaction W_r from P_r as:

$$W_r = \epsilon_r^{-1}V = [1 - V\ P_r]^{-1}V, \tag{27}$$

Here W_r, which is implicitly restricted to include only matrix elements among the target orbitals, is Coulomb interaction tensor $U_{mm'm''m'''}$ for the target orbitals, screened by transitions involving other orbitals. Because the screening involves only the non-target orbitals it is referred to as "constrained". Adding the polarization P_t to P_r would recover the fully screened interaction

$$U = [1 - V\ P_r]^{-1}V. \tag{28}$$

Note, that due to the energy dependency of the polarization, W_r is naturally frequency dependent. The frequency dependence is often neglected and U ($\omega = 0$) is used.

Now, one can analyze the symmetries of the calculated Coulomb tensor and fit to one of the two forms given above. Either by directly averaging the elements of the tensor, or using a minimization procedure to minimize differences between U^{cRPA} and a constructed U. Importantly, U should be evaluated in the same orbitals used for the embedding techniques. We advocate the use of a more advanced version of cRPA for disentangled bands implemented in VASP evaluating the polarization directly using the WFs [56].

It is evident that the screening depends crucially on the chosen subspace. For example, a larger energy window for the target space in the downfolding produces more atomic like orbitals but also has fewer screening channels, so leads to a larger interaction, whereas smaller energy windows give more extended orbitals with smaller, heavily screened, interactions. As we will show later in **Section 4.2** the screening in infinite layer nickelates is very sensitive as both, oxygen p states below, and Nd d states above, make large contributions to the screening. We discuss results from cRPA in **Section 4.3**.

3.3 Including Local Coulomb Interactions on Oxygen: DFT + sicDMFT Approach

In standard DFT + DMFT the many-body physics imposed by U on Ni is treated within the DMFT correlated subspace, however the description of the quantum processes on O remains on the Kohn-Sham DFT level. Note that correlations on the O ($2p$) orbitals are not necessarily weak because these orbitals, just as Ni($3d$) ones, carry the first new angular-momentum number with growing main quantum number (there is neither a $1p$ nor a $2d$ orbital), meaning the orbitals may sit close to the atomic nucleus and therefore are more compact and with a larger charging energy. This implies that also $2p$ frontier orbitals have a demanding pseudopotential that needs to moderate between localization and itinerancy (though not as severely as for $3d$ orbitals). And this nature becomes increasingly relevant when the connection to the environment via a Δ comparable to U is substantial, a feature taking place for later TMOs. This suggests that a DFT-level treatment may be insufficient to tackle the sophisticated Mott-Hubbard vs. charge-transfer balance. As a further aspect in infinite-layer nickelates, while Ni-$d_{x^2-y^2}$ is strongly hybridized with O($2p$), Ni-$d_{3z^2-r^2}$ is less so due to the missing apical oxygen. Hence the Ni-e_g $\{3z^2 - r^2, x^2 - y^2\}$ orbitals of the DMFT-active Ni($3d$) shell are quite differently affected by O($2p$). This may also call for an improved description of correlation effects originating from oxygen.

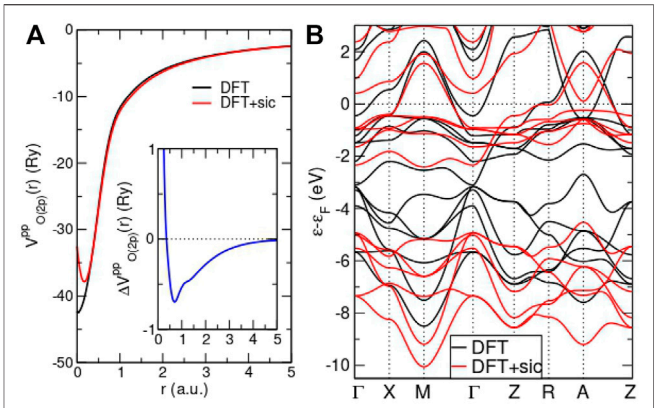

FIGURE 5 | Effects of SIC inclusion on the DFT level. **(A)** Radial part of oxygen $2p$ pseudopotential with (red) and without SIC (black). Inset: difference between DFT and DFT + sic pseudopotential. **(B)** Band structure for $NdNiO_2$ within DFT (black) and DFT + sic (red). Note that in the latter calculation, SIC was only applied to O and the Ni orbitals are treated on the DFT level. F.L. to be published.

However, treating explicit Coulomb interaction within DMFT also for O($2p$) raises several methodological and numerical challenges, and the explicit quantum-fluctuating aspect in these orbitals should be still generally weaker than in transition-metal $3d$ orbitals. In order to include localization tendencies on the oxygen sites beyond KS-DFT, one may therefore introduce the self-interaction correction (SIC) [34] as a simplified treatment compared to DMFT. The SIC scheme can efficiently be applied already on the pseudopotential level [57–59], leading to a refined O pseudopotential to be used in a standard CSC DFT + DMFT [60]. Use of this pseudopotential defines the DFT + sicDMFT method, which is thus capable of handling correlation physics on and between Ni and O closer to equal footing.

Figures 5A,B show the principal impact of the SIC inclusion on the DFT level. We see that the radial part of the O ($2p$) pseudopotential is somewhat reduced within the lower-limit of the bonding region (~ 0.5–2 a.u.), resulting in a stronger localization of charge near the O site. For the $NdNiO_2$ crystal calculation within DFT + sic, i.e., employing the revised oxygen pseudopotential in the conventional KS cycle, two key effects may be observed. First, the O($2p$) block of six bands (originally between Ħ [−3.5, −8] eV) get shifted to deeper energies, hence the $p - d$ splitting is increased. Second, especially around the Fermi level, some band-narrowing takes place due to the

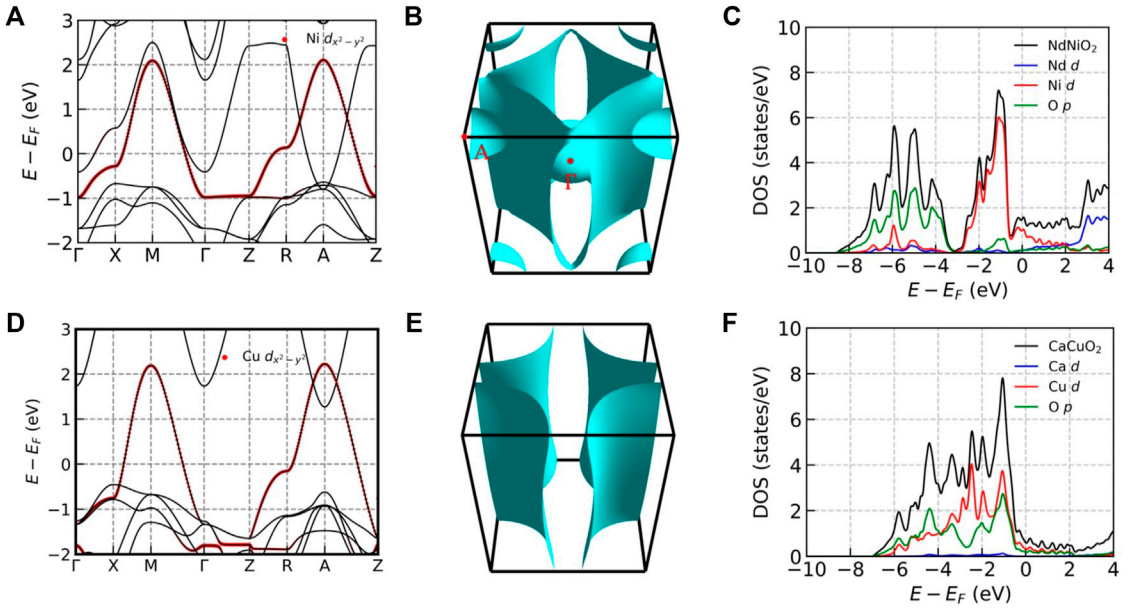

FIGURE 6 | (A–C): Electronic properties of $NdNiO_2$. **(A)**: Electronic band structure of $NdNiO_2$ close to the Fermi level. The red dots highlight the Ni $d_{x^2-y^2}$ band. A second band also crosses the Fermi level. **(B)**: Fermi surface of $NdNiO_2$. In addition to the cylindrical Fermi sheet that is derived from Ni $d_{x^2-y^2}$ band, there are two additional electron pockets: one is at $\Gamma = (0, 0, 0)$ and the other is at $A = (\pi, \pi, \pi)$. **(C)**: Densities of states of $NdNiO_2$. The black, blue, red and green curves correspond to total, Nd-*d* projected, Ni-*d* projected and O-*p* projected densities of states, respectively. The Fermi level is shifted to the zero point. **(D–F)**: Electronic properties of $CaCuO_2$. **(D)**: Electronic band structure of $CaCuO_2$ close to the Fermi level. The red dots highlight the Cu $d_{x^2-y^2}$ band. **(E)**: Fermi surface of $CaCuO_2$. **(F)**: Densities of states of $CaCuO_2$. The black, blue, red, and green curves correspond to total, Ca-*d* projected, Cu-*d* projected, and O-*p* projected densities of states, respectively. The Fermi level is shifted to the zero point. Adapted from Ref. [21].

renormalized hoppings resulting from the increased charge localization. It is important to note however that here these bands are an intermediate step in the full DFT + sicDMFT scheme, not a final physical result and are shown to provide insight into the physics underlying the method. In particular, the upward shift of the self-doping band away from the Fermi level is an artifact of the neglect of the local Coulomb interactions on Ni. The complete DFT + sicDMFT scheme yields the self-doping band again back at the Fermi level, which we will discuss in detail in **Section 4.3**.

4 RESULTS

In this section, we give an overview of results on infinite-layer nickelates in literature and a comparison to the better understood case of the layered copper oxides. We mainly focus on theoretical results [12, 13, 15–19, 21, 23, 27, 33, 44, 61–85] but present some comparison to experiments [4, 10, 86–98], when the relevant experimental results are available. We also mention that while we are aware of the important works on the study of interface effects [63, 65, 69], due to space limitation, we concentrate on the study of bulk nickelates here.

We present four levels of results: for orientation we show the DFT-level electronic structure; then we describe the basic many-body electronic structure following from the different DFT + DMFT calculations and the approximate physical picture that results. Next we consider the predictions of these calculations for the Fermiology–which bands are present at the Fermi surface and what are the mass enhancements. Finally, inspired by recent experimental results, we make some brief remarks about magnetism in **Section 4.4**.

4.1 DFT Results

Figure 6 compares basic aspects of the DFT-level electronic structure of the infinite layer nickelates $NdNiO_2$ and the analogous cuprate compound $CaCuO_2$. Panels a and d present the DFT bands of the two compounds. Panel d shows the familiar cuprate band structure, with one essentially two dimensional band of mixed Cu-$d_{x^2-y^2}$/O-$2p_\sigma$ character crossing the Fermi surface. Panel a shows that in $NdNiO_2$ the situation is richer, with other Fermi surface crossings in addition to the Ni-$d_{x^2-y^2}$-derived band (highlighted in red) [21, 24, 26, 83, 99, 100]. The Fermi surfaces shown in panels b and e reveal that in addition to the $d_{x^2-y^2}$ bands which disperse very weakly in the z direction and give rise to a cylindrical Fermi surface sheet, there are two additional closed (three dimensional) electron pockets centered at Γ and A. The three dimensional sheets arise from Nd-*d* orbitals, in particular $d_{3z^2-r^2}$ and d_{xy} orbitals, with an admixture of Ni-$d_{3z^2-r^2}$ and $d_{xz/yz}$ as well as interstitial states not directly attributed to any atomic orbital [21, 24, 25, 100, 101].

Charge transfer from the $d_{x^2-y^2}$-derived band to the Nd-derived band leads to a "self-doping" effect: in the stoichiometric infinite layer nickelate compound the $d_{x^2-y^2}$-derived band is not half-filled; rather its occupancy corresponds to about a 10–15% hole doping filling; thus

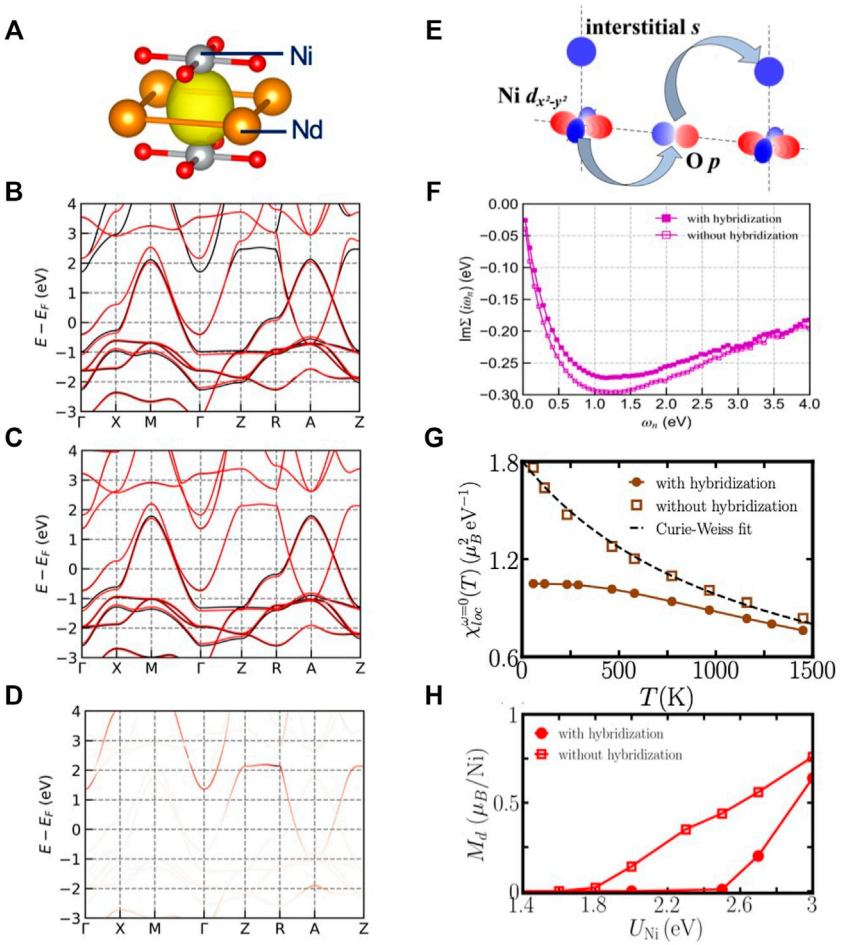

FIGURE 7 | (A): An iso-value surface of the interstitial *s* orbital in $NdNiO_2$. **(B)**: Fitting of DFT band structure of $NdNiO_2$, using 16 Wannier functions (Nd-*d*, Ni-*d*, and O-*p* orbitals). The black lines are DFT bands and the red lines are fitted bands from Wannier functions. **(C)**: Fitting of DFT band structure of $NdNiO_2$, using 17 Wannier functions (Nd-*d*, Ni-*d*, O-*p*, and the interstitial *s* orbitals). The black and red lines have the same meaning as in panel **(B)**. **(D)**: The fatband plot of the interstitial *s* orbital. **(E)**: An illustration of the hybridization between Ni $d_{x^2-y^2}$ orbital and the interstitital *s* orbital *via* a second-nearest-neighbor hopping. **(F)**: Imaginary part of the self-energy of Ni $d_{x^2-y^2}$ orbital calculated using DFT + DMFT method with hybridization (solid symbols) and without hybridization (open symbols). **(G)**: Local susceptibility $\chi^{\omega=0}_{\mathrm{loc}}(T)$ of $NdNiO_2$ as a function of temperature calculated with hybridization (solid symbols) and without hybridization (open symbols). The dashed line is a Curie-Weiss fitting. **(H)**: Magnetic moment on Ni *d* orbitals as a function of interaction strength $\mathcal{U}_{\mathrm{Ni}}$ calculated with hybridization (solid symbols) and without hybridization (open symbols). Adapted from Ref. [21].

stoichiometric nickelates should be compared to hole-doped cuprates.

It is important to note that the published DFT analyses of orbital admixture are obtained by projecting the states onto atomic orbitals as described in the projector section above. Gu *et al.* [21] find *via* a Wannier analysis that the additional band also has considerable contribution from charge density not centered on any atom. Because this component is not centered on an atom it is not easily revealed in the standard projector analysis. Panel a of **Figure 7** shows this component, known as an interstitial *s* orbital, which is located at the mid-point between two neighboring Ni atoms along the *z* axis. Panels b and c show the fitting of DFT band structure using maximally localized Wannier functions (MLWF) as explained in the previous Methods section. Panel b shows a band fit based on 16 MLWFs, of which 5 are initialized as being centered on Ni-*d* orbitals, five more centered on Nd-*d* orbitals and six O-*p* orbitals. The fitting is very good for the occupied bands but for one of the Nd-derived empty bands, the $Z \rightarrow R$ portion is not well reproduced. Panel c shows the result of adding one more MLWF that corresponds to the interstitial *s* orbital. The fitting is improved, in particular in that Nd-derived bands are now exactly reproduced throughout the first Brillouin zone. Panel d shows the weight of the interstitial *s* orbital on the different bands. We can see that the *s*-orbital has a high weight on the extra band on the $Z \rightarrow R$ portion at energy $E \approx 2$ eV above the Fermi level.

One of the key questions in the materials physics of the layered d^9 nickelates is whether the additional band is a "spectator", acting simply as a reservoir enabling charge transfer from the NiO_2 plane to the Nd spacer layer, or whether the additional band also plays an essential role in the physics, either because it is strongly hybridized with or strongly interacting with the Ni

degrees of freedom. The orbital composition of the additional band is relevant to this question: the "spectator band" contains Nd $d_{3z^2-r^2}$ and d_{xy} orbitals, as well as a small but non-zero admixture of Ni $d_{3z^2-r^2}$ and $d_{xz/yz}$ content; however the hybridization of these orbitals to the Ni $d_{x^2-y^2}$ band is very weak. However, in the Wannierization with the interstitial charge included, the hybridization between the interstitial *s* orbital and Ni $d_{x^2-y^2}$ is one order of magnitude stronger [21]. Panel e of **Figure 7** shows the hybridization between Ni $d_{x^2-y^2}$ and the interstitial *s* orbital *via* the second-nearest-neighbor hopping. Because of this hopping, the itinerant electrons in the Nd spacer layer can effectively interact with the electrons in Ni $d_{x^2-y^2}$ orbital and therefore it is suggested that this coupling may lead to Kondo-type physics [102, 103].

To complete the discussion of DFT-level theory we mention DFT + *U* calculations on infinite-layer nickelates. In these calculations all the atomic orbitals that are in the pseudopotentials are taken into account [11, 24, 26] and rotationally invariant Hubbard *U* interactions are added on all the five Ni *d* orbitals. Botana *et al.* [24] extracted various hopping matrices and energy splitting, which shows similarity between infinite-layer nickelates and cuprates. Kapeghian *et al.* [26], Been *et al.* [11] and Xia *et al.* [104] studied the electronic structure trends of the entire lanthanide series of infinite-layer nickelates.

4.2 DFT + DMFT: Local Electronic Structure

In transition metal oxides, it is believed that the interesting correlation physics arises from a competition between local interactions within the transition metal *d*-shell, which control the relative energetics of different *d*-multiplets, and the hybridization with other orbitals, which acts to mix the *d*-multiplets. In assessing the relevance of different interactions, an analysis of the ground state wave function is of interest. As noted previously, a formal valence analysis places either the Ni or the Cu in a d^9 state, thus with one hole in the *d*-shell and full oxygen-2*p* and empty Nd-5*d*/6*s* shells. Deviations from this simple picture provide insight into the relevant interaction processes. One question is the admixture of ligand (O-2*p* holes in the cuprate and nickelate cases and also Nd-5*d*/6*s* electrons in the nickelate case) states. One distinguishes [105] "charge transfer" materials where the energy difference between the ligand and transition metal *d* states controls the physics from Mott Hubbard materials where the charging energy of the transition metal *d*-shells controls the physics. A second issue is the relative weight of different transition metal multiplets. In "Hund's metals", multiplet configurations involving high spin (spin $S \geq 1$) *d*-states are relevant; in Mott Hubbard materials only the $S = 1/2$ and $S = 0$ states are relevant.

DFT + DMFT calculations provide theoretical estimates of orbital occupancies and of the local density matrices describing the multiplet probabilities of the correlated sites and the occupancies of the ligand sites. In the cuprate case there is general agreement both within DFT and in DFT + DMFT that the only relevant states are d^9 (with the hole in the Cu-$d_{x^2-y^2}$ orbital) and $d^{10}\underline{L}$. These two states appear with almost equal weight, while the Cu d^8 configuration plays a negligible role (for a recent calculation consistent with the substantial previous literature see [33]). This pattern of occupancies marks the cuprate material as a "charge transfer" compound [105] in which the major deviation from the atomic limit comes from moving the *d*-shell hole onto the oxygen network and back and the correlation physics should be thought of as arising from the oxygen-copper hybridization in the presence of strong local Cu correlations.

In the nickelate compounds the theoretical situation is less clear. There is a general consensus that the Ni-$d_{x^2-y^2}$ orbital is occupied by approximately one electron, and that the oxygen states are farther removed in energy from the $d_{x^2-y^2}$ orbital than in the cuprates and also more weakly hybridized, implying the admixture of the oxygen states into the near Fermi level bands is smaller than in cuprates [23, 24, 27, 75, 106]. There is also general consensus that charge transfer onto the Nd states occurs. However, whether $NdNiO_2$ is in the Mott-Hubbard region or in a critical region with mixed charge-transfer/Mott-Hubbard character is still under debate [23, 75, 107]. Another complication arises from the interstitial *s* orbital, which hybridizes with the Ni-$d_{x^2-y^2}$ orbital. Panels f, g and h of **Figure 7** compare the imaginary part of the self-energy of Ni-$d_{x^2-y^2}$ orbital, the local susceptibility and magnetic phase diagram of $NdNiO_2$ with the hybridization (solid symbols) and without the hybridization (open symbols) [21], calculated using DFT + DMFT method (U_{Ni} = 2 eV) that is explained in the Methods section. Panel f shows $\mathrm{Im}\Sigma(i\omega_n)$ of Ni-$d_{x^2-y^2}$ orbital. The effective mass $\frac{m^*}{m} \simeq 1 - \frac{d\mathrm{Im}(i\omega_n)}{d\omega_n}|_{\omega_n \to 0}$ is reduced from 2.0 without hybridization to 1.8 with hybridization. Panel g shows the local susceptibility $\chi_{\mathrm{loc}}^{\omega=0}(T) = \int_0^\beta \chi_{\mathrm{loc}}(\tau)d\tau = \int_0^\beta g^2\langle S_z(\tau)S_z(0)\rangle d\tau$. The hybridization reduces $\chi_{\mathrm{loc}}^{\omega=0}(T)$ at low temperatures, indicating the screening of the Ni spin in $d_{x^2-y^2}$ orbital. Panel h shows the magnetic moment on Ni atom as a function of interaction strength $\mathcal{U}$ on Ni-$d_{x^2-y^2}$ orbital. The hybridization increases the critical $\mathcal{U}$ that is needed to stabilize long-range antiferromagnetic ordering. Overall, the presence of the hybridization makes Ni-$d_{x^2-y^2}$ orbital less correlated and less magnetic, which is consistent with the Kondo screening picture.

Perhaps more importantly, unlike the cuprate case the transition metal Ni-$d_{3z^2-r^2}$ may also be relevant. The Ni-$d_{3z^2-r^2}$ has a non-negligible hybridization with the Nd-$d_{3z^2-r^2}$ band, so the three dimensional bands may be more than spectator bands, and instead participate to some degree in the correlation physics and Hund's physics may be relevant. Karp *et al.* [25, 27] find $\leq 15\%$ high spin d^8 and argue that only the Ni-$d_{x^2-y^2}$ orbital is important for the low-energy physics. Wang *et al.* [16] find 25.9% high spin d^8 (10.8% low spin d^8) in the ground state configuration of $LaNiO_2$ and argue based on this that the material should be classified as a Hund's metal. A difference between the calculations is the number of correlated d orbitals retained. The result of Wang *et al.* [16] is in partial agreement with the GW + EDMFT study of Petocchi et al. [79] which also finds ≱ 25% high spin d^8 character (≱ 25% low spin d^8) at optimal doping level. However, Petocchi et al. [79] report a nonmonotonic doping dependence of the high-spin d^8 weight, whereas Ref. [16] reports a monotonic doping dependence. Petocchi et al. [79] point out that the effect of this physics on the low energy properties is not clear.

TABLE 1 | Orbital occupancies of the most relevant Ni-*d* orbitals of $NdNiO_2$ from the Matsubara Green function (left) and occurrence probabilities of low spin (LS $S = 0$) and high spin (HS $S = 1$) multiplet configurations obtained from the impurity density matrix computed for stoichiometric $NdNiO_2$ using a Kanamori Hamiltonian with two correlated orbitals and $\mathcal{U} = 7$ eV and $\mathcal{J} = 0.7$ eV at $T =$ 290K. From Ref. [44].

	$d_{x^2-y^2}$	$d_{3z^2-r^2}$	LS $N = 2$	HS $N = 2$	$N = 3$	$N = 4$
MLWF	1.13	1.91	0.04	0.05	0.78	0.13
SLWF	1.27	1.93	0.03	0.02	0.69	0.26
Proj −10 to 10	1.14	1.65	0.11	0.15	0.64	0.09
Proj −10 to 3	1.15	1.81	0.07	0.08	0.72	0.12

These questions are not theoretically settled because, as shown by Karp *et al.* [44] the choice of method used to construct the local orbitals of the downfolded model affects the DMFT results for the nickelate. **Table 1** compares the orbital occupancies and multiplet occurence probabilities (defined as weight of the different configurations in the many-body density matrix projected onto the Ni states) obtained with different methodologies.

4.3 DMFT Theory of the Low Energy Physics

We next consider the consequences of the wide window electronic structure for the low energy physics. Panels (a) and (b) of **Figure 8** show the many body electronic structure (momentum and frequency dependent electron spectral function) computed for $NdNiO_2$ at two representative dopings using the basic DFT + DMFT and DFT + sicDMFT methods for a particular method and choice of parameters. From a comparison with other nickelates [60] and in view of experimental constraints (see discussion in [106]) a value $U_{avg} = 10$ eV and $J_{avg} = 1$ eV is here used to parametrize the local Coulomb interaction for the Ni(3*d*) orbitals in charge self-consistent DFT+(sic)DMFT calculations. The projector method for the five Ni(3*d*) orbitals, building on the 12 KS states above the O(2*s*) bands [i.e., an energy window (−10, 3) eV], is employed and a rotational-invariant Slater Hamiltonian is active in the resulting correlated subspace. The hole doping δ is achieved by the virtual-crystal approximation using an effective Nd atom [108], where the Nd (4*f*) states are frozen in the pseudopotential core. Note again that calculational settings resulting in the data shown in **Figure 8** differ only in using the LDA (SIC) oxygen pseudpotential in DFT+(sic)DMFT.

The upper panels of **Figures 8A,B** show the DFT + DMFT spectral function. In comparison to the DFT bands shown in Fig. 6, we see that the Ni-$d_{x^2-y^2}$-derived band is narrowed and broadened, and its separation in energy from the lower lying Ni-t_{2g} and O(2*p*) bands is increased. The lower panels show the DFT + sicDMFT results, which are markedly different. We see that in the stoichiometric compound the $d_{x^2-y^2}$ bands are completely absent: within this scheme these orbitals are completely localized and incoherent, hence not visible in the spectral function. The position of the "spectator" bands relative to the Fermi surface is also changed, with some electrons transferred to these orbitals [20]. This may calls for an alternative possible Kondo scenario at low *T*, including also a substantial role of the Ni-$d_{3z^2-r^2}$ orbital [20]. At doping $\delta = 0.15$ we see that in the DFT + sicDMFT calculation some aspects of the $d_{x^2-y^2}$ bands are restored, but again the relative positions of the spectator and $d_{x^2-y^2}$ bands are very different in the two methods. Panel (c) of **Figure 8** shows the momentum integrated total and Ni-projected spectral functions. Important differences between the results of the two methods include the $p - d$ splitting visible as the shift in higher binding energy peak from ~−4 eV to ~−6 eV (cf upper left panel) and the proximity of the $d_{3z^2-r^2}$ states to the Fermi surface. This characterizes the material as an effective orbital-selective Mott-insulator. In this theory, hole doping leaves the Ni-$d_{x^2-y^2}$

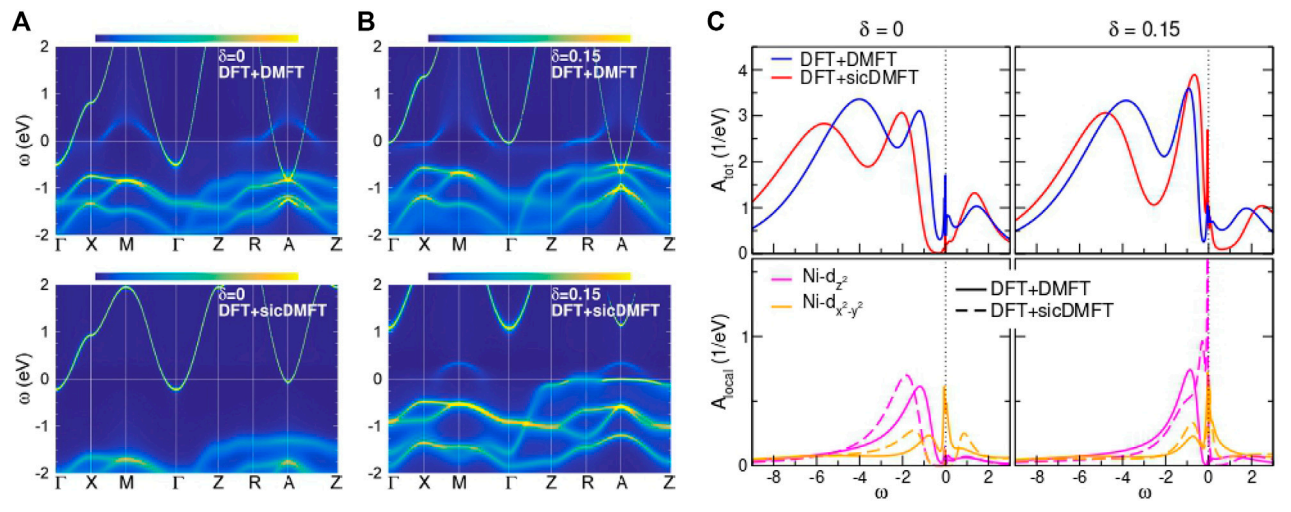

FIGURE 8 | Comparison between DFT + DMFT and DFT + sicDMFT at $T = 30$ K, using $U_{avg} = 10$ eV, $J_{avg} = 1$ eV and projected-local orbitals on the 12 KS states above the O(2*s*) bands for both schemes, respectively. **(A,B)** *k*-resolved spectral function $A(\mathbf{k}, \omega)$ for **(A)** pristine and **(B)** $\delta = 0.15$ hole-doped $NdNiO_2$. **(C)** Total and Ni-e_g local spectral function for both doping cases. Adapted from [108].

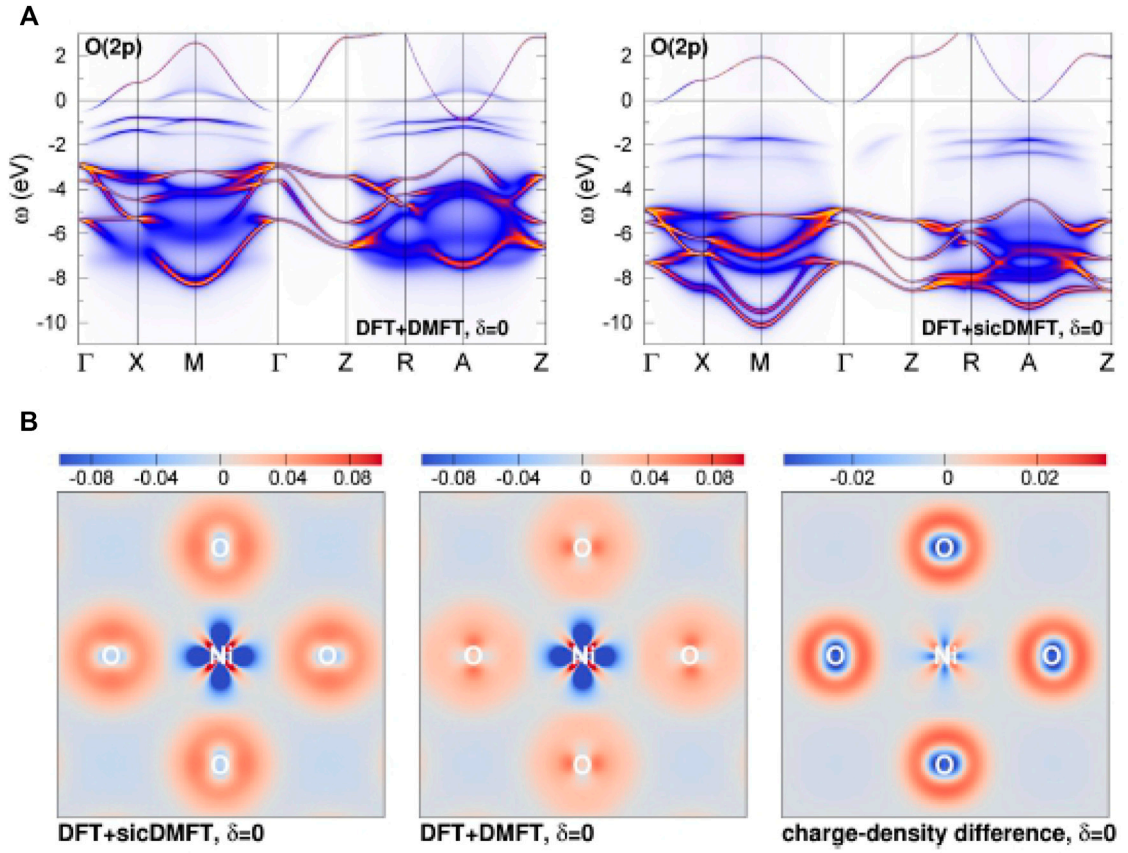

FIGURE 9 | Oxygen 2*p* states in DFT + DMFT and DFT + sicDMFT. **(A)** Orbital weight (i.e., fatbands) in the interacting regime along high symmetry lines. **(B)** Interacting bond charge density $\rho - \rho^{\mathrm{LDA}}_{\mathrm{atom}}$, with right panel displaying the difference between the densities shown in the left and middle panel. F.L. to be published.

occupancy almost unchanged at half filling. Instead, the Ni-$d_{3z^2-r^2}$ orbital takes care of most of the charge doping and becomes significantly further depleted. Therefore within DFT + sicDMFT, the superconducting region is designated by the coexistence of nearly half-filled Ni-$d_{x^2-y^2}$ and a Ni-$d_{3z^2-r^2}$-based flat band crossing the Fermi level. As discussed in Ref. [108], this flat band interacts with the Mott-like state such as to increase coherency within the Ni-$d_{x^2-y^2}$ sector. For even larger hole doping, the system evolves into a bad Hund metal, where coherence is lost again [108]. Let us note that the shift of the Ni-$d_{3z^2-r^2}$-based flat band towards the Fermi level is supported by a full GW + EDMFT investigation [79].

As depicted in **Figure 9**, the increase of correlation strength with SIC inclusion originates from the stronger localization of O(2*p*) electrons. The oxygen states are shifted down in energy, leading to an increase of the *p*-*d* splitting and thus to a value Δ = 5 eV for the charge-transfer energy [106]. **Figure 9B** shows directly in real space, that the SIC-modified pseudopotential of oxygen enhances the 2*p* charge density around the oxygen sites, with additionally further depleting Ni-$d_{x^2-y^2}$. Hence in DFT + sicDMFT an adjustment of the *U vs.* Δ competition takes place, which refines furthermore the various hopping integrals of the system.

These results highlight the basic electronic structure questions: 1) what is the coherence (scattering rate and mass enhancement) of the Ni-$d_{x^2-y^2}$-derived band and 2) how strong are the interactions on the "spectator" bands? 3) what is the energy difference between the O-2*p* and $d_{x^2-y^2}$ orbitals. The different implementations of the DFT + DMFT methodology give different answers to these questions. While most methods, with the exception of the sic method, give a somewhat coherent $d_{x^2-y^2}$ band the estimates of the orbital mass enhancement vary substantially, as shown in **Table 2**. These quantities are experimentally accessible *via* photoemission experiments, and future experiment/theory comparisons will provide valuable methodological guidance. It should be noted that most papers only discuss orbital mass enhancements, which are generally larger than band enhancements, especially for large energy window calculations.

The question of band renormalization in different downfolding choices is tightly coupled with the question of screening (see **Section 3.2.2**). cRPA studies showed that if a seven orbital downfolding model is constructed from five Ni(3*d*) orbitals and two Nd(5*d*) orbitals in a small energy window (not containing any oxygen states), the static part of the onsite Coulomb interaction is $U_{d_{x^2-y^2}} \approx 5$ eV [19, 79]. For a minimal

TABLE 2 | $d_{x^2-y^2}$ orbital mass enhancement from different DMFT results in the literature. n_c refers to the number of correlated orbitals in the impurity problem.

Ref.	Downfolding model	n_c	Interactions (eV)	T (K)	$d_{x^2-y^2}$ m^*/m
[25]	3 MLWF	1	$\mathcal{U}$ = 3.1	290	4.0
[21]	4 MLWF	1	$\mathcal{U}$ = 3.0	116	3.3
[79]	7 MLWF (5 Ni + 2 Nd)	5	full GW + EDMFT	1,160	5.6
[9]	10 MLWF (5 Ni + 5 Nd)	2	$\mathcal{U}$ = 3.1, $\mathcal{J}$ = 0.65	300	4.4
[44]	13 MLWF	2	$\mathcal{U}$ = 7, $\mathcal{J}$ = 0.7	290	7.6
[44]	13 SLWF	2	$\mathcal{U}$ = 7, $\mathcal{J}$ = 0.7	290	3.9
[117]	16 MLWF (Ni, Nd, O)	5	U_{avg} = 6, J_{avg} = 0.95	290	3
[44]	Projectors −10 to 3	2	$\mathcal{U}$ = 7, $\mathcal{J}$ = 0.7	290	5.6
[108]	Projectors −10 to 3	5	U_{avg} = 10, J_{avg} = 1	30	6.4
[108]	Projectors −10 to 3	5	U_{avg} = 10, J_{avg} = 1 (SIC on O)	30	Mott insulating
[44]	Projectors −10 to 10	2	$\mathcal{U}$ = 7, $\mathcal{J}$ = 0.7	290	4.6
[27]	Projectors −10 to 10	5	U_{avg} = 7, J_{avg} = 0.7	390	3.7
[16]	Projectors −10 to 10	5	U_{avg} = 5, J_{avg} = 1	100	2.8
[101]	Projectors −10 to 10	5	U_{avg} = 5, J_{avg} = 0.8	-	2.4
[101]	Projectors −10 to 10	5	U_{avg} = 9, J_{avg} = 0.8	-	4.1
[15]	Projectors −10 to 10	5	U_{avg} = 5, J_{avg} = 1	60	2.6

model containing only the Ni $d_{x^2-y^2}$, the Nd $d_{3z^2-r^2}$, and the interstitial s orbital, $U_{d_{x^2-y^2}}$ is even further reduced to ≈ 3.1 eV [19]. The bare Coulomb interaction is of the order of $V_{d_{x^2-y^2}} \approx 25$ eV, highlighting the strong screening of the low-energy states. The resulting strong frequency dependency, which is usually neglected in DFT + DMFT calculations, plays a crucial role leading to a mass enhancement in GW + EDMFT calculations comparable to that of DFT + DMFT calculations with much larger static $\mathcal{U}$ values (see **Table 2**) [79]. This shows, that the other orbitals close to the Fermi level play an important role in screening processes for the Ni $d_{x^2-y^2}$ correlations, and using static Coulomb interaction parameters from cRPA will lead to a underestimation of correlation effects in a small energy window downfolding scheme. This also raises the importance of inter-site interaction Coulomb matrix elements in a large energy window calculation between the Ni(3d) orbitals and O(2p) and Nd(5d) states.

Finally, we may consider the functional form of the self energy, which is relevant to the issue of Hund's physics. Hund's metal physics is believed to imply a particle-hole asymmetric structure in the self energy leading to an extra peak in the electron spectral function [33, 109]; for materials such as $NdNiO_2$ where the d-shell is more than half filled the peak is on the unoccupied part of the spectrum [33]. Conversely, Mott physics would result in a two peak spectral function and a more symmetric self energy with peaks on both sides. As shown in **Figure 10**, the $d_{x^2-y^2}$ self energy computed in [27] has strong (but broadened, especially on the positive frequency side) peaks at $\omega \approx -0.7eV$ and $\omega \approx 2eV$ and the corresponding spectral function shows two Hubbard peaks and a central quasiparticle feature. These are consistent with expectations of a Mott-Hubbard material. In addition, a weak feature is visible as a change of concavity around $\omega = 0.2eV$; comparison to spectra presented for the Hund's metals Sr_2RuO_4 and Sr_2MoO_4 suggests that this may be a signature of weak Hund's physics [33]. Wang *et al.* report a much larger d^8 weight in the ground state but exhibit a similar $d_{x^2-y^2}$ spectral function, suggesting that the presence of some admixture of high-spin d^8 does not strongly affect the low energy physics. Kang et al. [110] present a spectral function that shows a stronger feature (a peak) at about $\omega = 0.2eV$ on the unoccupied side of the spectral function at low temperatures, which may be a sign of Hund's correlations. They also report a slope inversion on the occupied side which is not expected in the theory of Hund's metals with more than half filled d-shells [33].

4.4 Magnetism

We now discuss briefly the magnetic properties. The stoichiometric cuprates are antiferromagnetic insulators, with a charge gap of approximately 1.5 eV, a Neel temperature ≈ 300 K set by weak interlayer and spin orbit effects, and an intrinsically large magnetic scale evident for example as a zone boundary magnon energy ≈ 0.3 eV. Fitting to a Heisenberg model implies a nearest neighbor exchange coupling $J_{NN} \approx 120$ meV although it must be born in mind that the materials are intermediate coupling, so the magnetism is in a intermediate regime between itinerant and localized. Upon doping the commensurate magnetism vanishes rapidly but evidence of strong magnetic correlations (and in some materials tendency to incommensurate magnetic order) persists to a doping of about 0.15.

A discussion of magnetism in the nickelates is complicated by the self-doping effect. If the physics of the nickelates is directly comparable to that of the cuprates then one would expect the stoichiometric nickelates to be on the boundary of magnetism. Recent resonant inelastic X-ray (RIXS) [92] and nuclear magnetic resonance experiments [91] are consistent with this picture. In particular, Lu *et al.* report no long ranged order but observe a strong zone boundary paramagnon-like excitation implying a $J_{NN} \approx 60$ meV, about half of the cuprate value.

Theoretically a number of DFT + U, hybrid DFT and DFT + DMFT studies have studied magnetism of infinite layer nickelates [17, 21, 24, 25, 84, 99, 101, 108, 111] and reported a wide range of magnetic superexchange [17, 18, 23, 66, 76, 77, 99, 112] from a small value of about 10 meV [23, 99] to an intermediate value of about 30 meV [66] to a large value of about 80–100 meV [17, 18, 76, 77, 112]. DFT + DMFT studies have not examined the Ni

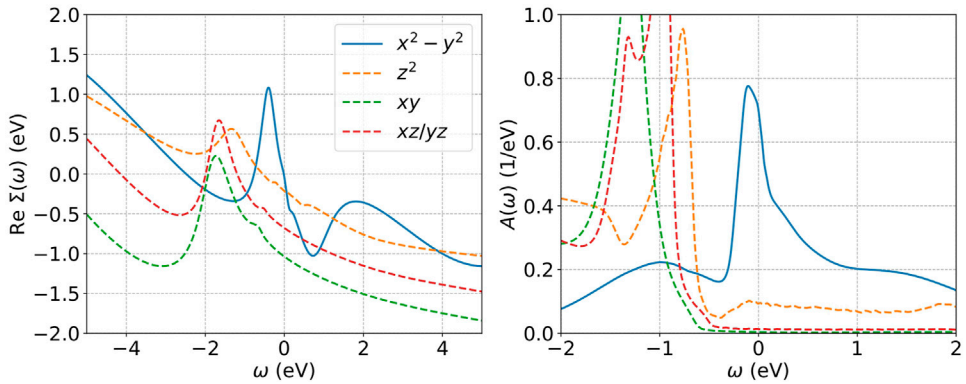

FIGURE 10 | Left: Self energy of the different orbitals in a five orbital fully charge self consistent DFT + DMFT calculation at stoichiometry with projectors in an energy range from −10 to 10 eV around the Fermi level, using a rotationally invariant slater Hamiltonian with U_{avg} = 7 *eV*, J_{avg} = 0.7 *eV*, and T = 290*K*. Right: corresponding momentum integrated spectral function. Adapted from Ref. [27].

exchange coupling systematically. Further investigation of the magnetic properties within this method is likely to provide valuable insights.

5 SUMMARY

DFT and beyond DFT analyses have produced a broadly coherent picture of the electronic structure of the infinite layer d^9 nickelates. Similar to the cuprates there is a rather two dimensional Ni-$d_{x^2-y^2}$-derived band that is moderately to strongly correlated. Differently from the cuprates, at the Fermi surface there is an additional, much more three dimensional, band derived from the rare earth d-orbitals (with some admixture of interstitial charge and of Ni(3d) states). The energy difference between Ni(3d) and O(2p) orbitals is larger in the nickelates than the cuprates, putting the nickelates farther from the charge transfer regime than are the cuprates. Finally, in contrast to the cuprate materials where the only relevant configurations of the transition metal ions are the d^9 and d^{10} states, in the nickelate materials some admixture of the high-spin d^8 configuration occurs, raising the possibility of Hund's metal physics.

Given this broad consensus, the question becomes which of the differences and similarities to the cuprates are important for the low energy physics. It is clear that the additional band "self-dopes" the Ni $d_{x^2-y^2}$ bands, so that the chemistry-doping phase diagram of the infinite layer nickelates is shifted from that of the cuprates by about 0.1 hole/Ni, and that charge transfer to the oxygen orbitals is less relevant in the nickelates than in the cuprates. The important open question is whether the other differences are important for the low energy correlation physics, in other words, whether the low energy physics of the infinite layer nickelates may be understood in terms of a one band Hubbard model or whether richer physics is needed. Answering this question bears directly on the issue of the mechanism for the observed superconductivity. This question is not yet settled, in part because different flavors of the DFT + DMFT have provided different quantitative answers to questions including the fractional weight of high spin d^8 configurations in the ground state, the relative energy positions of the p and d band manifolds and what is the mass enhancement of the different bands near Fermi surface. Some of these differences may be traced to different choices required in the DFT + DMFT approach to correlated materials.

In this article we have explained the different choices and the different results that emerge. Some of the differences in results are experimentally testable. For example, the DFT + (sic)DMFT approach yield significantly more strongly correlated/less coherent $d_{x^2-y^2}$ derived bands and indeed different DFT + DMFT methods produce different mass enhancements. Thus angle-resolved photoemission measurements of the quasiparticle dispersion and linewidth, in combination with higher energy measurements of the p-d energy splitting, can experimentally test the different predictions. Hund's metal physics is an intrinsically multiband effect, which involves characteristic asymmetries in the electron self energy. Even more importantly the known examples of Hund's metals involve multiple strongly correlated bands crossing the Fermi surface. Detailed analyses of the structure of the electron dispersion and the strength of the correlations on the "spectator" bands will provide insight. There are also interesting differences in the theoretical predictions for magnetic properties and superconducting pairing [9, 14, 18, 64, 88, 113, 114], which future experiments may test. Finally, we note that our discussion is based on the single-site version of dynamical mean field theory. While model-system studies have shown that this approximation captures the main features of the wide energy range many-body electronic structure, the single-site approximation does not capture important aspects of the low energy physics, such as superconductivity or pseudogap physics. "Cluster" and related extensions (e.g., DΓA) of the theory are an important directions for future research [9].

We hope that our work will motivate comparisons to experiment and to more fundamental theoretical approaches

that will help resolve some of the methodological questions relating to the DFT + DMFT approach to correlated materials.

AUTHOR CONTRIBUTIONS

All authors listed have made a substantial, direct, and intellectual contribution to the work and approved it for publication.

FUNDING

HC is supported by the National Natural Science Foundation of China under project number 11 774 236, the Ministry of Science and Technology of China under project number SQ2020YFE010418, and NYU University Research Challenge Fund. FL and JK were supported by grants from the Simons Foundation. The Flatiron Institute is a division of the Simons Foundation.

ACKNOWLEDGMENTS

HC acknowledges useful discussions with Yuhao Gu, Mi Jiang, Danfeng Li, Jiawei Mei, Xiangang Wan, Tao Wu, Xianxin Wu, Yifeng Yang, Guangming Zhang, Zhicheng Zhong, Wei Zhu, and in particular, Chengliang Xia for his help in making part of the figures.

REFERENCES

1. Bednorz JG, Miller KA. Possible highT C Superconductivity in the Ba-La-Cu-O System. *Z Physik B - Condensed Matter* (1986) 64:189–93. doi:10.1007/BF01303701
2. Wu MK, Ashburn JR, Torng CJ, Hor PH, Meng RL, Gao L, et al. Superconductivity at 93 K in a New Mixed-phase Y-Ba-Cu-O Compound System at Ambient Pressure. *Phys Rev Lett* (1987) 58:908–10. doi:10.1103/PhysRevLett.58.908
3. Orenstein J, Millis AJ. Advances in the Physics of High-Temperature Superconductivity. *Science* (2000) 288:468–74. doi:10.1126/science.288.5465.468
4. Li D, Lee K, Wang BY, Osada M, Crossley S, Lee HR, et al. Superconductivity in an Infinite-Layer Nickelate. *Nature* (2019) 572:624–7. doi:10.1038/s41586-019-1496-5
5. Anisimov VI, Bukhvalov D, Rice TM. Electronic Structure of Possible Nickelate Analogs to the Cuprates. *Phys Rev B* (1999) 59:7901–6. doi:10.1103/PhysRevB.59.7901
6. LeBlanc JPF, Antipov AE, Becca F, Bulik IW, Chan GK-L, Chung C-M, et al. Solutions of the Two-Dimensional hubbard Model: Benchmarks and Results from a Wide Range of Numerical Algorithms. *Phys Rev X* (2015) 5:041041. doi:10.1103/PhysRevX.5.041041
7. Zheng B-X, Chung C-M, Corboz P, Ehlers G, Qin M-P, Noack RM, et al. Stripe Order in the Underdoped Region of the Two-Dimensional hubbard Model. *Science* (2017) 358:1155–60. doi:10.1126/science.aam7127
8. Jiang H-C, Devereaux TP. Superconductivity in the Doped Hubbard Model and its Interplay with Next-Nearest Hopping T ′. *Science* (2019) 365:1424–8. doi:10.1126/science.aal5304
9. Kitatani M, Si L, Janson O, Arita R, Zhong Z, Held K. Nickelate Superconductors-A Renaissance of the One-Band Hubbard Model. *Npj Quan Mater.* (2020) 5:59. doi:10.1038/s41535-020-00260-y
10. Hepting M, Li D, Jia CJ, Lu H, Paris E, Tseng Y, et al. Electronic Structure of the Parent Compound of Superconducting Infinite-Layer Nickelates. *Nat Mater* (2020) 19:381–5. doi:10.1038/s41563-019-0585-z
11. Been E, Lee WS, Hwang HY, Cui Y, Zaanen J, Devereaux T, et al. Electronic Structure Trends across the Rare-Earth Series in Superconducting Infinite-Layer Nickelates. *Phys Rev X* (2021) 11:011050. doi:10.1103/physrevx.11.011050
12. Hu L-H, Wu C. Two-band Model for Magnetism and Superconductivity in Nickelates. *Phys Rev Res* (2019) 1:032046. doi:10.1103/PhysRevResearch.1.032046
13. Werner P, Hoshino S. Nickelate Superconductors: Multiorbital Nature and Spin Freezing. *Phys Rev B* (2020) 101:041104. doi:10.1103/PhysRevB.101.041104
14. Zhang Y-H, Vishwanath A. Type-II t–J Model in Superconducting Nickelate Nd1−xSrxNiO2. *Phys Rev Res* (2020) 2:023112. doi:10.1103/PhysRevResearch.2.023112
15. Kang C-J, Kotliar G. Optical Properties of the Infinite-Layer La1−xSrxNiO2 and Hidden Hund's Physics. *Phys Rev Lett* (2021) 126:127401. doi:10.1103/PhysRevLett.126.127401
16. Wang Y, Kang C-J, Miao H, Kotliar G. Hund's Metal Physics: From SrNiO2 to LaNiO2. *Phys Rev B* (2020) 102:161118. doi:10.1103/PhysRevB.102.161118
17. Wan X, Ivanov V, Resta G, Leonov I, Savrasov SY. Exchange Interactions and Sensitivity of the Ni Two-Hole Spin State to Hund's Coupling in Doped NdNiO2. *Phys Rev B* (2021) 103:075123. doi:10.1103/PhysRevB.103.075123
18. Wu X, Di Sante D, Schwemmer T, Hanke W, Hwang HY, Raghu S, et al. Robust Dx2−y2 -wave Superconductivity of Infinite-Layer Nickelates-Wave Superconductivity of Infinite-Layer Nickelates$d_{x{2}-Y{2}}$fx169. *Phys Rev B* (2020) 101:060504. doi:10.1103/PhysRevB.101.060504
19. Nomura Y, Hirayama M, Tadano T, Yoshimoto Y, Nakamura K, Arita R. Formation of a Two-Dimensional Single-Component Correlated Electron System and Band Engineering in the Nickelate Superconductor NdNiO2. *Phys Rev B* (2019) 100:205138. doi:10.1103/PhysRevB.100.205138
20. Lechermann F. Multiorbital Processes Rule the Nd1−xSrxNiO2 Normal State. *Phys Rev X* (2020) 10:041002. doi:10.1103/PhysRevX.10.041002
21. Gu Y, Zhu S, Wang X, Hu J, Chen H. A Substantial Hybridization between Correlated Ni-*D* Orbital and Itinerant Electrons in Infinite-Layer Nickelates. *Commun Phys* (2020) 3:84. doi:10.1038/s42005-020-0347-x
22. Gao J, Peng S, Wang Z, Fang C, Weng H. Electronic Structures and Topological Properties in Nickelates Ln n+1NinO2n+2. *Natl Sci Rev* (2021) 8. doi:10.1093/nsr/nwaa218
23. Jiang M, Berciu M, Sawatzky GA. Critical Nature of the Ni Spin State in Doped NdNiO2. *Phys Rev Lett* (2020) 124:207004. doi:10.1103/PhysRevLett.124.207004
24. Botana AS, Norman MR. Similarities and Differences between LaNiO2 and CaCuO2 and Implications for Superconductivity. *Phys Rev X* (2020) 10:011024. doi:10.1103/PhysRevX.10.011024
25. Karp J, Botana AS, Norman MR, Park H, Zingl M, Millis A. Many-body Electronic Structure of NdNiO2 and CaCuO2. *Phys Rev X* (2020) 10:021061. doi:10.1103/PhysRevX.10.021061
26. Kapeghian J, Botana AS. Electronic Structure and Magnetism in Infinite-Layer Nickelates RNiO2 (R=La−Lu). *Phys Rev B* (2020) 102:205130. doi:10.1103/PhysRevB.102.205130
27. Karp J, Hampel A, Zingl M, Botana AS, Park H, Norman MR, et al. Comparative many-body Study of Pr4Ni3O8 and NdNiO2. *Phys Rev B* (2020) 102:245130. doi:10.1103/PhysRevB.102.245130
28. Park H, Millis AJ, Marianetti CA. Site-selective mott Transition in Rare-Earth-Element Nickelates. *Phys Rev Lett* (2012) 109:156402. doi:10.1103/PhysRevLett.109.156402

29. Mizokawa T, Khomskii DI, Sawatzky GA. Spin and Charge Ordering in Self-Doped mott Insulators. *Phys Rev B* (2000) 61:11263–6. doi:10.1103/PhysRevB.61.11263
30. Georges A. Strongly Correlated Electron Materials: Dynamical Mean-Field Theory and Electronic Structure. *AIP Conf Proc* (2004) 715:3–74. doi:10.1063/1.1800733
31. Kotliar G, Savrasov SY, Haule K, Oudovenko VS, Parcollet O, Marianetti CA. Electronic Structure Calculations with Dynamical Mean-Field Theory. *Rev Mod Phys* (2006) 78:865–951. doi:10.1103/RevModPhys.78.865
32. Tamai A, Zingl M, Rozbicki E, Cappelli E, Riccò S, de la Torre A, et al. High-Resolution Photoemission on Sr2RuO4 Reveals Correlation-Enhanced Effective Spin-Orbit Coupling and Dominantly Local Self-Energies. *Phys Rev X* (2019) 9:021048. doi:10.1103/PhysRevX.9.021048
33. Karp J, Bramberger M, Grundner M, Schollwöck U, Millis AJ, Zingl M. Sr2MoO4 and Sr2RuO4 : Disentangling the Roles of Hund's and Van Hove Physics. *Phys Rev Lett* (2020) 125:166401. doi:10.1103/physrevlett.125.166401
34. Perdew JP, Zunger A. Self-interaction Correction to Density-Functional Approximations for many-electron Systems. *Phys Rev B* (1981) 23:5048–79. doi:10.1103/PhysRevB.23.5048
35. Burke K, Wagner LO. Dft in a Nutshell. *Int J Quan Chem.* (2013) 113:96–101. doi:10.1002/qua.24259
36. Hampel A, Beck S, Ederer C. Effect of Charge Self-Consistency in DFT+DMFT Calculations for Complex Transition Metal Oxides. *Phys Rev Res* (2020) 2:033088. doi:10.1103/PhysRevResearch.2.033088
37. Anisimov VI, Kondakov DE, Kozhevnikov AV, Nekrasov IA, Pchelkina ZV, Allen JW, et al. Full Orbital Calculation Scheme for Materials with Strongly Correlated Electrons. *Phys Rev B* (2005) 71:125119. doi:10.1103/physrevb.71.125119
38. Amadon B, Lechermann F, Georges A, Jollet F, Wehling TO, Lichtenstein AI. Plane-wave Based Electronic Structure Calculations for Correlated Materials Using Dynamical Mean-Field Theory and Projected Local Orbitals. *Phys Rev B* (2008) 77:205112. doi:10.1103/PhysRevB.77.205112
39. Aichhorn M, Pourovskii L, Vildosola V, Ferrero M, Parcollet O, Miyake T, et al. Dynamical Mean-Field Theory within an Augmented Plane-Wave Framework: Assessing Electronic Correlations in the Iron Pnictide Lafeaso. *Phys Rev B* (2009) 80:085101. doi:10.1103/PhysRevB.80.085101
40. Marzari N, Vanderbilt D. Maximally Localized Generalized Wannier Functions for Composite Energy Bands. *Phys Rev B* (1997) 56:12847–65. doi:10.1103/PhysRevB.56.12847
41. Wang R, Lazar EA, Park H, Millis AJ, Marianetti CA. Selectively Localized Wannier Functions. *Phys Rev B* (2014) 90:165125. doi:10.1103/PhysRevB.90.165125
42. Marzari N, Mostofi AA, Yates JR, Souza I, Vanderbilt D. Maximally Localized Wannier Functions: Theory and Applications. *Rev Mod Phys* (2012) 84:1419–75. doi:10.1103/RevModPhys.84.1419
43. Souza I, Marzari N, Vanderbilt D. Maximally Localized Wannier Functions for Entangled Energy Bands. *Phys Rev B* (2001) 65:035109. doi:10.1103/PhysRevB.65.035109
44. Karp J, Hampel A, Millis AJ. Dependence of DFT+DMFT Results on the Construction of the Correlated Orbitals. *Phys Rev B* (2021) 103:195101. doi:10.1103/PhysRevB.103.195101
45. Haule K. Exact Double Counting in Combining the Dynamical Mean Field Theory and the Density Functional Theory. *Phys Rev Lett* (2015) 115:196403. doi:10.1103/PhysRevLett.115.196403
46. Beck S, Hampel A, Parcollet O, Ederer C, Georges A. Charge Self-Consistent Electronic Structure Calculations with Dynamical Mean-Field Theory Using Quantum Espresso, Wannier90 and Triqs. arXiv (2021) 2111–10289.
47. Park H, Millis AJ, Marianetti CA. Density Functional versus Spin-Density Functional and the Choice of Correlated Subspace in Multivariable Effective Action Theories of Electronic Structure. *Phys Rev B* (2015) 92:035146. doi:10.1103/physrevb.92.035146
48. Pavarini E, Koch E, Lichtenstein A, Vollhardt DE. The LDA+DMFT Approach to Strongly Correlated Materials. *Schriften des Forschungszentrums Jülich : Model Simulation* (2011) 1. Record converted from VDB: 12.11.2012.
49. Slater LJ. *Confluent Hypergeometric Functions*. Cambridge, United Kingdom: Cambridge Univ. Press (1960).
50. Vaugier L, Jiang H, Biermann S. HubbardUand Hund exchangeJin Transition Metal Oxides: Screening versus Localization Trends from Constrained Random Phase Approximation. *Phys Rev B* (2012) 86:165105. doi:10.1103/PhysRevB.86.165105
51. Castellani C, Natoli CR, Ranninger J. Magnetic Structure ofV2O3in the Insulating Phase. *Phys Rev B* (1978) 18:4945–66. doi:10.1103/PhysRevB.18.4945
52. Kanamori J. Electron Correlation and Ferromagnetism of Transition Metals. *Prog Theor Phys* (1963) 30:275–89. doi:10.1143/PTP.30.275
53. Anisimov VI, Gunnarsson O. Density-functional Calculation of Effective Coulomb Interactions in Metals. *Phys Rev B* (1991) 43:7570–4. doi:10.1103/PhysRevB.43.7570
54. Aryasetiawan F, Imada M, Georges A, Kotliar G, Biermann S, Lichtenstein AI. Frequency-dependent Local Interactions and Low-Energy Effective Models from Electronic Structure Calculations. *Phys Rev B* (2004) 70:195104. doi:10.1103/physrevb.70.195104
55. Aryasetiawan F, Miyake T, Sakuma R. *The LDA+DMFT approach to strongly correlated materials (Schriften des Forschungszentrums Jülich), chap. The Constrained RPA Method for Calculating the Hubard U from First-Principles* (2011). p. 71–726.
56. Kaltak M. *Merging GW with DMFT*. Ph.D. thesis. Vienna: University of Vienna (2015).
57. Vogel D, Krüger P, Pollmann J. Self-interaction and Relaxation-Corrected Pseudopotentials for II-VI Semiconductors. *Phys Rev B* (1996) 54:5495–511. doi:10.1103/physrevb.54.5495
58. Filippetti A, Spaldin NA. Self-interaction-corrected Pseudopotential Scheme for Magnetic and Strongly-Correlated Systems. *Phys Rev B* (2003) 67:125109. doi:10.1103/PhysRevB.67.125109
59. Puphal P, Wu M, Fürsich K, Lee H, Pakdaman M, Bruin JAN, et al. Synthesis and Characterization of Ca-Substituted Infinite-Layer Nickelate 2121 Crystals. *Sci Adv* (2021) 7:eabl8091.
60. Lechermann F, Körner W, Urban DF, Elsässer C. Interplay of Charge-Transfer and mott-hubbard Physics Approached by an Efficient Combination of Self-Interaction Correction and Dynamical Mean-Field Theory. *Phys Rev B* (2019) 100:115125. doi:10.1103/physrevb.100.115125
61. Wang BX, Zheng H, Krivyakina E, Chmaissem O, Lopes PP, Lynn JW, et al. Synthesis and Characterization of Bulk $Nd_{1-x}Sr_xNiO_2$ and $Nd_{1-x}Sr_xNiO_3$. *Phys Rev Mater* (2020) 4:084409. doi:10.1103/physrevmaterials.4.084409
62. Si L, Xiao W, Kaufmann J, Tomczak JM, Lu Y, Zhong Z, et al. Topotactic Hydrogen in Nickelate Superconductors and Akin Infinite-Layer Oxides ABO2. *Phys Rev Lett* (2020) 124:166402. doi:10.1103/physrevlett.124.166402
63. Geisler B, Pentcheva R. Fundamental Difference in the Electronic Reconstruction of Infinite-Layer versus Perovskite Neodymium Nickelate Films on $SrTiO_3$ (001). *Phys Rev B* (2020) 102:020502. doi:10.1103/physrevb.102.020502
64. Sakakibara H, Usui H, Suzuki K, Kotani T, Aoki H, Kuroki K. Model Construction and a Possibility of Cupratelike Pairing in a New D9 Nickelate Superconductor (Nd,Sr)NiO2. *Phys Rev Lett* (2020) 125:077003. doi:10.1103/PhysRevLett.125.077003
65. He R, Jiang P, Lu Y, Song Y, Chen M, Jin M, et al. Polarity-induced Electronic and Atomic Reconstruction at NdNiO2/SrTiO3 Interfaces. *Phys Rev B* (2020) 102:035118. doi:10.1103/PhysRevB.102.035118
66. Zhang H, Jin L, Wang S, Xi B, Shi X, Ye F, et al. Effective Hamiltonian for Nickelate Oxides Nd1−xSrxNiO2. *Phys Rev Res* (2020) 2:013214. doi:10.1103/PhysRevResearch.2.013214
67. Zhang J, Zheng H, Chen Y-S, Ren Y, Yonemura M, Huq A, et al. High Oxygen Pressure Floating Zone Growth and crystal Structure of the Metallic Nickelates R4Ni3O10 (R=La,Pr). *Phys Rev Mater* (2020) 4:083402. doi:10.1103/PhysRevMaterials.4.083402
68. Bernardini F, Olevano V, Blase X, Cano A. Infinite-layer Fluoro-Nickelates as D 9 Model Materials. *J Phys Mater* (2020) 3:035003. doi:10.1088/2515-7639/ab885d
69. Bernardini F, Cano A. Stability and Electronic Properties of LaNiO2/SrTiO3 Heterostructures. *J Phys Mater* (2020) 3:03LT01. doi:10.1088/2515-7639/ab9d0f
70. Liu Z, Xu C, Cao C, Zhu W, Wang ZF, Yang J. Doping Dependence of Electronic Structure of Infinite-Layer NdNiO2. *Phys Rev B* (2021) 103:045103. doi:10.1103/PhysRevB.103.045103

71. Plienbumrung T, Daghofer M, Oleś AM. Interplay between Zhang-Rice Singlets and High-Spin States in a Model for Doped NiO2 Planes. *Phys Rev B* (2021) 103:104513. doi:10.1103/PhysRevB.103.104513
72. Malyi OI, Varignon J, Zunger A. Bulk NdNiO2 Is Thermodynamically Unstable with Respect to Decomposition while Hydrogenation Reduces the Instability and Transforms it from Metal to Insulator. arXiv (2021) 2107–01790.
73. Peng C, Jiang HC, Moritz B, Devereaux TP, Jia C. Superconductivity in a Minimal Two-Band Model for Infinite-Layer Nickelates. arXiv (2021) 2110.07593. (2021).
74. Choubey P, Eremin IM. Electronic Theory for Scanning Tunneling Microscopy Spectra in Infinite-Layer Nickelate Superconductors. *Phys Rev B* (2021) 104:144504. doi:10.1103/PhysRevB.104.144504
75. Sawatzky GA. Superconductivity Seen in a Non-magnetic Nickel Oxide. *Nature* (2019) 572:592–3. doi:10.1038/d41586-019-02518-3
76. Nomura Y, Nomoto T, Hirayama M, Arita R. Magnetic Exchange Coupling in Cuprate-Analog D9 Nickelates. *Phys Rev Res* (2020) 2:043144. doi:10.1103/PhysRevResearch.2.043144
77. Hirayama M, Tadano T, Nomura Y, Arita R. Materials Design of Dynamically Stable D9 Layered Nickelates. *Phys Rev B* (2020) 101:075107. doi:10.1103/PhysRevB.101.075107
78. Jin H-S, Pickett WE, Lee K-W. Proposed Ordering of Textured Spin Singlets in a Bulk Infinite-Layer Nickelate. *Phys Rev Res* (2020) 2:033197. doi:10.1103/PhysRevResearch.2.033197
79. Petocchi F, Christiansson V, Nilsson F, Aryasetiawan F, Werner P. Normal State of Nd1−xSrxNiO2 from Self-Consistent GW+EDMFT. *Phys Rev X* (2020) 10:041047. doi:10.1103/PhysRevX.10.041047
80. Higashi K, Winder M, Kuneš J, Hariki A. Core-Level X-Ray Spectroscopy of Infinite-Layer Nickelate: LDA+DMFT Study. *Phys Rev X* (2021) 11:041009. doi:10.1103/PhysRevX.11.041009
81. Leonov I. Effect of Lattice Strain on the Electronic Structure and Magnetic Correlations in Infinite-Layer (Nd,Sr)NiO2. *J Alloys Compounds* (2021) 883:160888. doi:10.1016/J.JALLCOM.2021.160888
82. Lin H, Gawryluk DJ, Klein YM, Huangfu S, Pomjakushina E, von Rohr F, et al. Universal Spin-Glass Behaviour in Bulk LaNiO2, PrNiO2 and NdNiO2. arXiv (2021) 2104–14324.
83. Lee K-W, Pickett WE. Infinite-layerLaNiO2: Ni1+is notCu2+. *Phys Rev B* (2004) 70:165109. doi:10.1103/PhysRevB.70.165109
84. Choi M-Y, Pickett WE, Lee K-W. Fluctuation-frustrated Flat Band Instabilities in NdNiO2. *Phys Rev Res* (2020) 2:033445. doi:10.1103/PhysRevResearch.2.033445
85. Choi M-Y, Lee K-W, Pickett WE. Role of 4f States in Infinite-Layer NdNiO2. *Phys Rev B* (2020) 101:020503. doi:10.1103/PhysRevB.101.020503
86. Zeng S, Tang CS, Yin X, Li C, Li M, Huang Z, et al. Phase Diagram and Superconducting Dome of Infinite-Layer Nd1−xSrxNiO2 Thin Films. *Phys Rev Lett* (2020) 125:147003. doi:10.1103/PhysRevLett.125.147003
87. Li D, Wang BY, Lee K, Harvey SP, Osada M, Goodge BH, et al. Superconducting Dome in Nd1−xSrxNiO2 Infinite Layer Films. *Phys Rev Lett* (2020) 125:027001. doi:10.1103/PhysRevLett.125.027001
88. Gu Q, Li Y, Wan S, Li H, Guo W, Yang H, et al. Single Particle Tunneling Spectrum of Superconducting Nd1-xSrxNiO2 Thin Films. *Nat Commun* (2020) 11. doi:10.1038/s41467-020-19908-1
89. Goodge BH, Li D, Lee K, Osada M, Wang BY, Sawatzky GA, et al. Doping Evolution of the Mott-Hubbard Landscape in Infinite-Layer Nickelates. *Proc Natl Acad Sci USA* (2021) 118:e2007683118. doi:10.1073/pnas.2007683118
90. Wang BY, Li D, Goodge BH, Lee K, Osada M, Harvey SP, et al. Isotropic Pauli-Limited Superconductivity in the Infinite-Layer Nickelate Nd0.775Sr0.225NiO2. *Nat Phys* (2021) 17:473–7. doi:10.1038/s41567-020-01128-5
91. Zhao D, Zhou YB, Fu Y, Wang L, Zhou XF, Cheng H, et al. Intrinsic Spin Susceptibility and Pseudogaplike Behavior in Infinite-Layer LaNiO2. *Phys Rev Lett* (2021) 126:197001. doi:10.1103/PhysRevLett.126.197001
92. Lu H, Rossi M, Nag A, Osada M, Li DF, Lee K, et al. Magnetic Excitations in Infinite-Layer Nickelates. *Science* (2021) 373:213–6. doi:10.1126/science.abd7726
93. Osada M, Wang BY, Goodge BH, Lee K, Yoon H, Sakuma K, et al. A Superconducting Praseodymium Nickelate with Infinite Layer Structure. *Nano Lett* (2020) 20:5735–40. doi:10.1021/acs.nanolett.0c01392
94. Osada M, Wang BY, Lee K, Li D, Hwang HY. Phase Diagram of Infinite Layer Praseodymium Nickelate Pr1−xSrxNiO2 Thin Films. *Phys Rev Mater* (2020) 4:121801. doi:10.1103/PhysRevMaterials.4.121801
95. Osada M, Wang BY, Goodge BH, Harvey SP, Lee K, Li D, et al. Nickelate Superconductivity without Rare-Earth Magnetism: (La,Sr)NiO 2. *Adv Mater* (2021) 33:2104083. doi:10.1002/adma.202104083
96. Ren X, Gao Q, Zhao Y, Luo H, Zhou X, Zhu Z. Superconductivity in Infinite-Layer Pr0.8Sr0.2NiO2 Films on Different Substrates. arXiv (2021) 2109.05761. (2021).
97. Zeng SW, Li CJ, Chow LE, Cao Y, Zhang ZT, Tang CS, et al. Superconductivity in Infinite-Layer Lanthanide Nickelates. arXiv (2021) 2105.13492. (2021).
98. Puphal P, Wu YM, Fürsich K, Lee H, Pakdaman M, Bruin JAN, et al. Synthesis and Characterization of Ca-Substituted Infinite-Layer Nickelate Crystals. arXiv (2021) 2106–13171.
99. Liu Z, Ren Z, Zhu W, Wang Z, Yang J. Electronic and Magnetic Structure of Infinite-Layer NdNiO2: Trace of Antiferromagnetic Metal. *Npj Quan Mater.* (2020) 5. doi:10.1038/s41535-020-0229-1
100. Jiang P, Si L, Liao Z, Zhong Z. Electronic Structure of Rare-Earth Infinite-Layer RNiO2(R=La,Nd). *Phys Rev B* (2019) 100:201106. doi:10.1103/PhysRevB.100.201106
101. Ryee S, Yoon H, Kim TJ, Jeong MY, Han MJ. Induced Magnetic Two-Dimensionality by Hole Doping in the Superconducting Infinite-Layer Nickelate $Nd_{1-x}Sr_xNiO_2$. *Phys Rev B* (2020) 101:064513. doi:10.1103/physrevb.101.064513
102. Zhang G-M, Yang Y-f., Zhang F-C. Self-doped Mott Insulator for Parent Compounds of Nickelate Superconductors. *Phys Rev B* (2020) 101:020501. doi:10.1103/PhysRevB.101.020501
103. Yang Y, Zhang GM. Self-doping and the Mott-Kondo Scenario for Infinite-Layer Nickelate Superconductors. arXiv (2021) 2110.11089. (2021).
104. Xia C, Wu J, Chen Y, Chen H. Dynamical Structural Instability and a New crystal-electronic Structure of Infinite-Layer Nickelates. arXiv (2021) 2110–12405.
105. Zaanen J, Sawatzky GA, Allen JW. Band Gaps and Electronic Structure of Transition-Metal Compounds. *Phys Rev Lett* (1985) 55:418–21. doi:10.1103/physrevlett.55.418
106. Lechermann F. Late Transition Metal Oxides with Infinite-Layer Structure: Nickelates versus Cuprates. *Phys Rev B* (2020) 101:081110. doi:10.1103/PhysRevB.101.081110
107. Shen Y, Sears J, Fabbris G, Li J, Pelliciari J, Jarrige I, et al. Role of Oxygen States in Square Planar D9−δ Nickelates arXiv:2110.08937. (2021).
108. Lechermann F. Doping-dependent Character and Possible Magnetic Ordering of $NdNiO_2$. *Phys Rev Mater* (2021) 5:044803. doi:10.1103/physrevmaterials.5.044803
109. Stadler KM, Kotliar G, Weichselbaum A, von Delft J. Hundness versus Mottness in a Three-Band Hubbard-Hund Model: On the Origin of strong Correlations in Hund Metals. *Ann Phys* (2019) 405:365–409. doi:10.1016/j.aop.2018.10.017
110. Kang B, Melnick C, Semon P, Kotliar G, Choi S (2020).
111. Zhang R, Lane C, Singh B, Nokelainen J, Barbiellini B, Markiewicz RS, et al. Magnetic and F-Electron Effects in LaNiO2 and NdNiO2 Nickelates with Cuprate-like $$3{d}$3d_{x{2}-Y{2}}$fx170_{{x}{2}-{y}{2}}$$ Band Band. *Commun Phys* (2021) 4. doi:10.1038/s42005-021-00621-4
112. Katukuri VM, Bogdanov NA, Weser O, van den Brink J, Alavi A. Electronic Correlations and Magnetic Interactions in Infinite-Layer NdNiO2. *Phys Rev B* (2020) 102:241112. doi:10.1103/PhysRevB.102.241112
113. Wang Z, Zhang G-M, Yang Y-f., Zhang F-C. Distinct Pairing Symmetries of Superconductivity in Infinite-Layer Nickelates. *Phys Rev B* (2020) 102:220501. doi:10.1103/PhysRevB.102.220501
114. Adhikary P, Bandyopadhyay S, Das T, Dasgupta I, Saha-Dasgupta T. Orbital-selective Superconductivity in a Two-Band Model of Infinite-Layer Nickelates. *Phys Rev B* (2020) 102:100501. doi:10.1103/PhysRevB.102.100501
115. Momma K, Izumi F. VESTA 3for Three-Dimensional Visualization of crystal, Volumetric and Morphology Data. *J Appl Cryst* (2011) 44:1272–6. doi:10.1107/S0021889811038970
116. Lechermann F. From Basic Properties to the Mott Design of Correlated Delafossites. *Npj Comput Mater* (2021) 7:120. doi:10.1038/s41524-021-00586-6

117. Leonov I, Skornyakov SL, Savrasov SY. Lifshitz Transition and Frustration of Magnetic Moments in Infinite-Layer NdNiO2 upon Hole Doping. *Phys Rev B* (2020) 101:241108. doi:10.1103/PhysRevB.101.241108

Conflict of Interest: The authors declare that the research was conducted in the absence of any commercial or financial relationships that could be construed as a potential conflict of interest.

Publisher's Note: All claims expressed in this article are solely those of the authors and do not necessarily represent those of their affiliated organizations, or those of the publisher, the editors and the reviewers. Any product that may be evaluated in this article, or claim that may be made by its manufacturer, is not guaranteed or endorsed by the publisher.

frontiers in Physics

MINI REVIEW
published: 02 February 2022
doi: 10.3389/fphy.2021.813532

Low Valence Nickelates: Launching the Nickel Age of Superconductivity

Antia S. Botana[1]*, *Kwan-Woo Lee*[2], *Michael R. Norman*[3], *Victor Pardo*[4,5] and *Warren E. Pickett*[6]

[1]Department of Physics, Arizona State University, Tempe, AZ, United States, [2]Division of Display and Semiconductor Physics, Korea University, Sejong, South Korea, [3]Materials Science Division, Argonne National Laboratory, Lemont, IL, United States, [4]Departamento de Física Aplicada, Facultade de Física, Universidade de Santiago de Compostela, Santiago de Compostela, Spain, [5]Instituto de Materiais (iMATUS), Universidade de Santiago de Compostela, Santiago de Compostela, Spain, [6]Department of Physics and Astronomy, University of California, Davis, Davis, CA, United States

The discovery of superconductivity in thin films (~10 nm) of infinite-layer hole-doped $NdNiO_2$ has invigorated the field of high temperature superconductivity research, reviving the debate over contrasting views that nickelates that are isostructural with cuprates are either 1) sisters of the high temperature superconductors, or 2) that differences between nickel and copper at equal band filling should be the focus of attention. Each viewpoint has its merits, and each has its limitations, suggesting that such a simple picture must be superseded by a more holistic comparison of the two classes. Several recent studies have begun this generalization, raising a number of questions without suggesting any consensus. In this paper, we organize the findings of the electronic structures of n-layered NiO_2 materials (n = 1 to ∞) to outline (ir) regularities and to make comparisons with cuprates, with the hope that important directions of future research will emerge.

Keywords: superconductivity, electronic structure ab-initio calculations, nickelates, magnetism, cuprates electronic structure

OPEN ACCESS

Edited by:
Matthias Eschrig,
University of Greifswald, Germany

Reviewed by:
Andrzej M. Oles,
Jagiellonian University, Poland

****Correspondence:***
Antia S. Botana
antia.botana@asu.edu

Specialty section:
This article was submitted to Condensed Matter Physics, a section of the journal Frontiers in Physics

Received: *11 November 2021*
Accepted: *14 December 2021*
Published: *02 February 2022*

Citation:
Botana AS, Lee K-W, Norman MR, Pardo V and Pickett WE (2022) Low Valence Nickelates: Launching the Nickel Age of Superconductivity. Front. Phys. 9:813532. doi: 10.3389/fphy.2021.813532

1 BACKGROUND

After much synthesis and characterization of low-valence layered nickelates over three decades [1–7], superconductivity was finally observed [8] in hole-doped $\mathcal{R}NiO_2$ (initially for rare earth $\mathcal{R}$ = Nd, later for $\mathcal{R}$ = La [9, 10] and Pr [11]) with T_c exhibiting a dome-like dependence [12, 13] being maximal (10–15 K) near 20% doping. This series of discoveries in $\mathcal{R}NiO_2$ materials marked the beginning of a new, nickel age of superconductivity [14, 15] launching a plethora of experimental [16–22] and theoretical [23–43] work.

$\mathcal{R}NiO_2$ materials are the $n = \infty$ member of a larger series of layered nickelates with chemical formula $(\mathcal{R}O_2)^-[\mathcal{R}(NiO_2)_n]^+$ ($\mathcal{R}$ = La, Pr, and Nd; $n = 2, 3, \ldots, \infty$) that possess n cuprate-like NiO_2 planes in a square-planar coordination. Except for the $n = \infty$ case, groups of n-NiO_2 layers are separated by $\mathcal{R}_2O_2$ blocking layers that severely limit coupling between adjacent units (see **Figure 1**). These layered square-planar compounds are obtained via oxygen deintercalation from the corresponding parent perovskite $\mathcal{R}NiO_3$ ($n = \infty$) [2] and Ruddlesden-Popper $\mathcal{R}_{n+1}Ni_nO_{3n+1}$ ($n \neq \infty$) phases [1]. As shown in **Figure 1**, the $(\mathcal{R}O_2)^-[(\mathcal{R}NiO_2)_n]^+$ series can be mapped onto the cuprate phase diagram in terms of the nickel 3d-electron count, with nominal fillings running from d^9 ($n = \infty$) to d^8 (for n = 1). That superconductivity arises in this series suggests that a new family of superconductors has been uncovered, currently with two members, $n = \infty$ and n = 5 [44], the only ones (so far) where an optimal Ni valence near $d^{8.8}$ has been attained.

Some overviews on experimental and theoretical findings in this family of materials have been recently published [45–48]. In this paper, we focus on the electronic structure of layered nickelates,

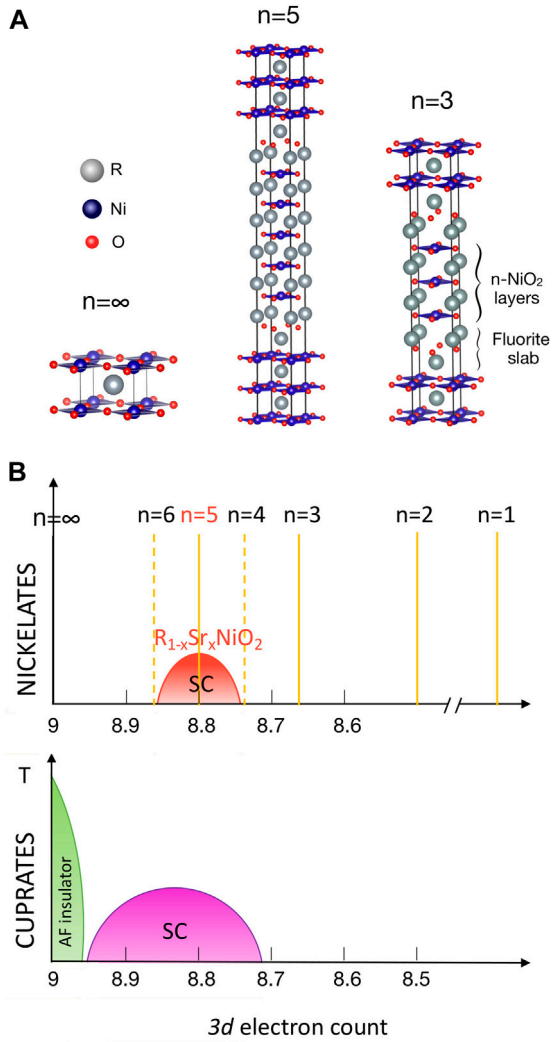

FIGURE 1 | (A) Crystal structures of the $n = \infty$, $n = 5$, and $n = 3$ layered nickelates highlighting the presence of the n-NiO_2 layers and the fluorite blocking slabs present in the $n \neq \infty$ materials. $\mathcal{R}$, Ni and O atoms are shown in gray, blue, and red, respectively. **(B)** Schematic phase diagram as a function of nominal d filling for layered nickelates (top) and cuprates (bottom), highlighting the regions where superconducting domes have been experimentally reported. The members of the $\mathcal{R}_{n+1}Ni_nO_{2n+2}$ series are marked with lines (dashed lines correspond to materials that have not been synthesized yet). The $n = 5$ member falls close to the optimal doping value for both cuprates and the infinite-layer nickelate.

confining ourselves to materials with the basic infinite-layer structure: n square planar NiO_2 layers each separated by an $\mathcal{R}^{3+}$ ion without the apical oxygen ion(s) that are common in most cuprates and nickelates.

2 FROM ∞ TO ONE

2.1 "Infinite-Layer" $n = \infty$ Nickelate: $\mathcal{R}NiO_2$

In parent $\mathcal{R}NiO_2$ materials, Ni has the same formal $3d^9$ electronic configuration as in cuprates. As mentioned above, superconductivity in $\mathcal{R}NiO_2$ materials emerges via hole doping, with T_c exhibiting a dome-like dependence [12, 13, 49] akin to cuprates, as shown in **Figure 1**. However, in parent infinite-layer nickelates the resistivity shows a metallic T-dependence (but with a low temperature upturn) [7, 8] and there is no signature of long-range magnetic order, even though the presence of strong antiferromagnetic (AFM) correlations has recently been reported via resonant inelastic x-ray scattering (RIXS) experiments [50]. This is in contrast to cuprates, where the parent phase is an AFM charge-transfer insulator.

Noteworthy differences from cuprates were already reflected in early electronic structure calculations as well [51, 52]. For the parent material $\mathcal{R}NiO_2$, non-magnetic density functional theory (DFT) calculations show that besides the Ni-$d_{x^2-y^2}$ band, additional bands of $\mathcal{R}$-5d character cross the Fermi level. The electronic structure of $\mathcal{R}NiO_2$ is three-dimensional-like, with a large c-axis dispersion of both (occupied) Ni and (nearly empty) $\mathcal{R}$-5d_{z^2} bands (see **Figure 2**) due to the close spacing of successive NiO_2 planes along the c-axis. The $\mathcal{R}$-5d_{z^2} dispersion leads to the appearance of electron pockets at the Γ and A points of the Brillouin zone which display mainly $\mathcal{R}$-5d_{z^2} and $\mathcal{R}$-5d_{xy} character, respectively, that self-dope the large hole-like Ni-$d_{x^2-y^2}$ Fermi surface. This self-doping effect (absent in the cuprates) introduces a substantial difference between nominal and actual filling of the Ni-d bands, accounting for conduction and possibly also disrupting AFM order. The presence of the 5d electrons is consistent with experimental data, which reveal not only metallic behavior but also evidence for negative charge carriers as reflected in the negative Hall coefficient [8, 12, and 13]. However, as the material becomes doped with Sr, the $\mathcal{R}$-5d pockets become depopulated, the Hall coefficient changes sign [8], and the electronic structure becomes more single-band, cuprate-like [39, 53].

Besides the presence of $\mathcal{R}$-5d electrons, infinite-layer nickelates have some other relevant differences from the cuprates, particularly their much larger charge-transfer energy between the metal 3d, and oxygen 2p states. In cuprates, the charge-transfer energy ε_{3d}-ε_{2p} is as small as 1–2 eV [54], indicative of a large p-d hybridization, and enabling Zhang-Rice singlet formation. In $NdNiO_2$, the charge-transfer energy is much larger, ~4.4 eV, as obtained from the on-site energies derived from a Wannier analysis [39]. The lack of a pre-peak in x-ray absorption (XAS) data at the oxygen K-edge [18] in $NdNiO_2$ has indeed been associated to the presence of a large charge-transfer energy. Because of this increase in charge transfer energy, the nickelate is more Mott-like, whereas the cuprate is more charge-transfer-like, in the scheme of Zaanen, Sawatzky, and Allen [35, 38]. In addition, theoretical investigations of $\mathcal{R}NiO_2$ find decreasing oxygen content as one traverses from La to Lu [55].

The doped holes tend to be on the Ni sites, as opposed to cuprates where they tend to reside on the oxygen sites. Recent DFT + DMFT Ni $2p_{3/2}$ core-level XPS, XAS, and RIXS calculations (consistent with available core-level spectroscopies) indeed confirm that the Ni-O hybridization does not play an important role in connection with doping, implying that the physics of $NdNiO_2$ is well described by a single-band Hubbard model [56]. This in turn brings up the issue of the nature of the doped holes on the Ni sites. That is, do

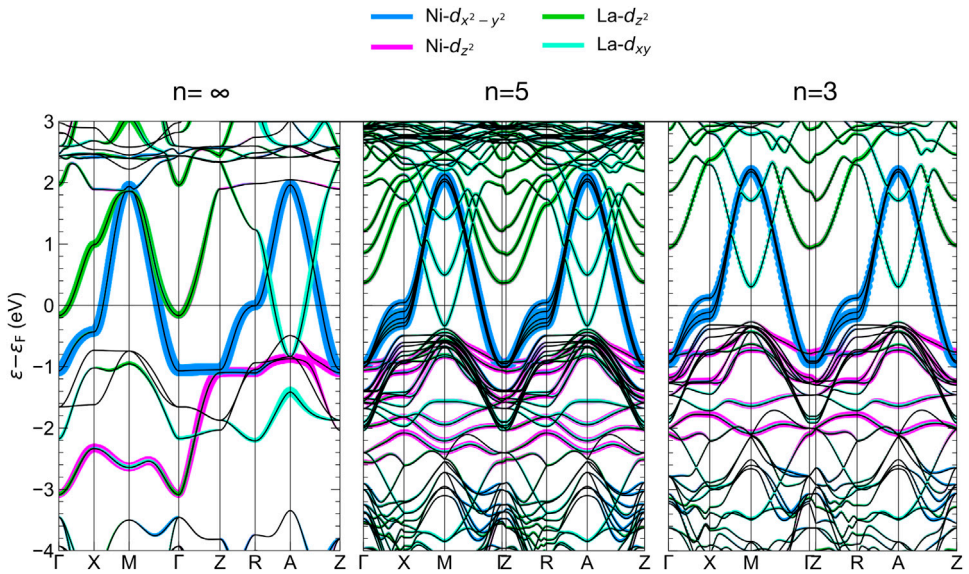

FIGURE 2 | DFT band structures in the paramagnetic state for the $n = \infty$, $n = 5$, and $n = 3$ layered nickelates. The two types of Ni e_g bands are highlighted, as well as the two relevant $\mathcal{R}$-5*d* bands (La is used as an example). It can be observed how the involvement of $\mathcal{R}$-d bands around the Fermi level is reduced with decreasing *n*.

they behave as effective d^8 dopants, and if so, is d^8 high-spin (S = 1) or low-spin (S = 0)? If the former, then these materials would fall in the category of Hund's metals, and thus would deviate substantially from cuprates. DMFT calculations are consistent with this picture as they systematically favor high-spin d^8 (S = 1) states [40, 57–60]. DFT calculations point instead towards a cuprate-like low-spin (S = 0) picture due to the large crystal-field splitting of the e_g states in a square planar environment [53]. Along these lines, impurity calculations show that in the NiO_2 layers a Zhang-Rice singlet (like in CuO_2) is indeed favored upon hole-doping [35]. Further, cluster calculations find that hole doping distributes over the entire cluster, in contrast to local S = 1 states [61].

Because of their lower degree of $p - d$ hybridization, the superexchange in $\mathcal{R}NiO_2$, as determined by resonant inelastic x-ray scattering experiments [50], is about half that of the cuprates. Still, its value (J = 64 meV) confirms the existence of significant AFM correlations [30, 50]. Long-range AFM order has however not been reported, with NMR data suggesting the ground state is paramagnetic [62], and susceptibility data interpreted as spin-glass behavior [63]. Neél type order is consistently obtained in DFT studies [24, 27, 29, and 51], as in d^9 insulating cuprates. The predicted AFM ground state in DFT + U calculations [64] is characterized by the involvement of both $d_{x^2-y^2}$ and d_{z^2} Ni bands [65]. This state is peculiar in that it displays a flat-band one-dimensional-like van Hove singularity of d_{z^2} character pinned at the Fermi level. These flat-band instabilities should inhibit but not eliminate incipient AFM tendencies [65].

Discussing the origin of superconductivity in $\mathcal{R}NiO_2$, as in the cuprates, is a controversial topic. But certainly the reduced T_c of the nickelate compared to the cuprates is consistent with the reduced value of the superexchange, and the larger charge-transfer energy. *t-J* model and RPA calculations building from tight-binding parameters derived from DFT calculations show that the dominant pairing instability is in the $d_{x^2-y^2}$ channel, as in cuprates [66]. Indeed, single-particle tunneling measurements on the superconducting infinite-layer nickelate have revealed a V-shape feature indicative of a *d*-wave gap [67]. On a broader level, several theoretical papers have speculated that the superconductivity is instead an interfacial effect of the infinite-layer film with the $SrTiO_3$ substrate [68–71], though recently superconductivity has been observed when other substrates are used [72]. In this context, it should be noted that superconductivity has not been observed in bulk samples yet; since the precursor is cubic, there is no set orientation for the *c*-axis, meaning the bulk is far less ordered than the film [20, 21].

2.2 The Superconducting $n = 5$ Material

Recently, a second superconducting member has been found in the $(\mathcal{R}O_2)^-[(\mathcal{R}NiO_2)_n]^+$ family: the $n = 5$ layered nickelate $Nd_6Ni_5O_{12}$, also synthesized in thin-film form [44]. As schematically shown in **Figure 1**, this material has a nominal valence near that of the optimally-doped infinite-layer material (that is, $Ni^{1.2+}$: $d^{8.8}$ nominal filling) and so, in contrast to its infinite-layer counterpart, it is superconducting without the need for chemical doping. While $\mathcal{R}NiO_2$ displays NiO_2 layers separated by $\mathcal{R}$ ions, this quintuple-layer material (with five NiO_2 layers per formula unit) has an additional fluorite $\mathcal{R}_2O_2$ slab separating successive five-layer units. Further, each successive five-layer group is displaced by half a lattice constant along the *a* and *b* directions (i.e., the body centered translation of the *I*4/*mmm* space group). These additional structural features effectively decouple the five-layer blocks, so the *c*-axis dispersion of this material is much weaker than its infinite-layer counterpart. Despite these significant structural

differences, T_c is similar to that of the doped infinite-layer materials (with the onset of the superconducting transition taking place at ~ 15 K), reducing the chances that yet to be synthesized low valence nickelates will have substantially higher transition temperatures.

In terms of its electronic structure [73], the $n = 5$ material is intermediate between cuprate-like and $n = \infty$-like behavior. From DFT calculations, the charge-transfer energy of $Nd_6Ni_5O_{12}$ is ~ 4.0 eV. This reduced energy compared to the undoped infinite-layer material means that the Ni-3*d* states are not as close in energy to the Nd-5*d* states, consistent with the presence of a pre-peak in the oxygen K-edge (similar to what happens with Sr-doped $NdNiO_2$ [53]). As a consequence, the electron pockets arising from the Nd-5*d* states are significantly smaller than those in the infinite-layer material (see **Figure 2**). This reduced pocket size along with the large hole-like contribution from the Ni-3*d* states is consistent with experiment in that the Hall coefficient remains positive at all temperatures, with a semiconductor-like temperature dependence reminiscent of under- and optimally-doped layered cuprates. Aside from the appearance of these small Nd-derived pockets at the zone corners, the Fermi surface of $Nd_6Ni_5O_{12}$ is analogous to that of multilayer cuprates with one electron-like and four hole-like $d_{x^2-y^2}$ Fermi surface sheets. Importantly, the Fermi surface of the quintuple-layer nickelate is much more two-dimensional-like compared to the infinite-layer nickelate material, as the presence of the fluorite blocking slab reduces the *c*-axis dispersion, as mentioned above.

2.3 The $n = 3$ Material, the Next Superconducting Member of the Series?

The materials discussed above can be put into the context of earlier studies of bulk reduced RP phases with $n = 2, 3$ NiO_2 layers [5, 74–76], separated by fluorite $\mathcal{R}_2O_2$ blocking slabs that enforce quasi-2D electronic and magnetic behavior.

The $n = 3$ member of the series, $\mathcal{R}_4Ni_3O_8$ (with $Ni^{1.33+}$: $d^{8.67}$ filling), has been studied extensively over the past decade (both single crystal and polycrystralline samples) [74]. Since the charge-transfer energy decreases with decreasing n [73], the $n = 3$ class is more cuprate-like than its $n = \infty$ and $n = 5$ counterparts. Both La and Pr materials are rather similar regarding their high-energy physics, with a large orbital polarization of the Ni-e_g states, so that the d^8 admixture is low spin [75, 77] (but see Ref. [78]). The primary difference is that $La_4Ni_3O_8$ exhibits long-range stripe order [76, 79] (similar to that seen in 1/3 hole-doped La_2NiO_4), consisting of diagonal rows of Ni^{1+} (S = 1/2) and Ni^{2+} (S = 0) in a two to one ratio [80]. In contrast, the Pr counterpart appears to have short-range order instead [81]. This results in the La material being insulating [82] in its low-temperature charge-ordered phase [80], whereas $Pr_4Ni_3O_8$ remains metallic at all temperatures [75], with an intriguing linear *T* behavior in its resistivity for intermediate temperatures (similar to that of cuprates at a comparable hole doping). Nd samples have also been studied [83], but the degree of insulating/metallic behavior seems to be sample dependent.

The difference between La and Pr trilayer materials could be due to the reduced volume associated with Pr (one of the motivations for the authors of Ref. [8] to study Sr-doped $NdNiO_2$ rather than Sr-doped $LaNiO_2$). The Ni spin state and metal versus insulator character have indeed been calculated to be sensitive to modest pressure [77]. Another factor is possible mixed valency of Pr as observed in cuprates (though Pr-M edge data on $Pr_4Ni_3O_8$ did not indicate mixed valent behavior [75]). Because of its decreased charge-transfer energy relative to $n = 5$, the rare-earth derived pockets no longer occur [84] (see **Figure 2**). This lack of $\mathcal{R}$-5*d* involvement is confirmed by the Hall coefficient that stays positive at all temperatures [44], (it remains to be understood why the thermopower in the case of $La_4Ni_3O_8$ is always negative [82], also seen in the metallic phase). In addition, these trilayer nickelates show a reduced charge-transfer energy (~ 3.5 eV as obtained from a Wannier analysis [73]) that, along with the larger effective doping level, is consistent with the strong oxygen K edge pre-peak seen in x-ray absorption data [75]. Oxygen K edge RIXS data indicate a significant contribution of oxygen 2*p* states to the doped holes [85]. As the effective hole doping level is 1/3, these materials are outside the range where superconductivity would be expected (see **Figure 1**). Reaching the desired doping range for superconductivity might be possible via electron doping. This could be achieved by replacing the rare earth with a 4 + ion (such as Ce,Th, or Zr) [86], intercalating with lithium, or gating the material with an ionic liquid.

If superconductivity were to occur, one might hope for a higher T_c as has indeed been predicted via $t - J$ model calculations [87]. Recent RIXS measurements [81], though, and find a superexchange value for $n = 3$ nearly the same as that reported for the infinite-layer material. This suggests the possibility that T_c in the whole nickelate family may be confined to relatively low temperatures compared to the cuprates. The similar value of the superexchange for $n = \infty$ and $n = 3$ is somewhat of a puzzle. Though their t_{pd} hoppings are very similar, the difference in the charge-transfer energy should have resulted in a larger superexchange for $n = 3$. The fact that it is not larger is one of the intriguing questions to be resolved in these low valence layered nickelates.

2.4 The $n = 2$ Material

The $n = 2$ member of the series, $La_3Ni_2O_6$, has been synthesized and studied as well [5, 88]. In terms of filling, it lies further away from optimal *d*-filling, being nominally $Ni^{1.5+}$: $d^{8.5}$. Experimentally, it is a semiconductor with no trace of a transition occurring at any temperature, although NMR data suggest that the AFM correlations are similar to those of the $n = 3$ material. Electronic structure studies [80] have predicted its ground state to have a charge-ordered pattern with Ni^{2+} cations in a low-spin state and the Ni^{1+}: d^9 cations forming a S = 1/2 checkerboard pattern. This charge-ordering between S = 1/2 Ni^{1+}: d^9 and non-magnetic Ni^{2+}: d^8 cations is similar to the situation in the $n = 3$ material [80]. Calculations suggest that it is quite general in these layered nickelates that the Ni^{2+} cations in this square-planar environment are non-magnetic. This has been shown by *ab* initio calculations to be the case also with the Ni^{2+} dopants in the $\mathcal{R}NiO_2$ materials [53].

2.5 The $n = 1$ Case

The long-known $\mathcal{R}_2NiO_4$ materials, with the $n = 1$ formula as above, contain Ni ions with octahedral coordination. We instead consider $Ba_2NiO_2(AgSe)_2$ (BNOAS) [89], as it represents the extreme opposite of the $n = \infty$ member, not only in regards to its d^8 valence, but also because its square planar coordination with long Ni-O bond is thought to promote "high-spin" (magnetic) behavior, that is, one hole in $d_{x^2-y^2}$, and one hole in d_{z^2}. Unlike the other n cases, the charge balanced formula is $(BaAg_2Se_2)^0(BaNiO_2)^0$; both blocking and active layers are formally neutral. BNOAS is insulating, distinguished by a magnetic susceptibiliy that is constant, thus non-magnetic, above and below a peak at T* ~130 K. This increase from and subsequent decrease to its high-T value reflects some kind of magnetic reconstruction at T* that was initially discussed in terms of canting of high-spin moments. That interpretation does not account for the constant susceptibility above and below the peak.

Valence counting indicates Ni^{2+}: d^8, so a half-filled e_g manifold. Conventional expectations are either 1) both $3d$ holes are in the $d_{x^2-y^2}$ orbital–a magnetically dead singlet that cannot account for the behavior around T*, or 2) a Hund's rule $S = 1$ triplet, which would show a Curie-Weiss susceptibility above the ordering temperature, but that is not seen in experiment. Correlated DFT calculations [90] predict an unusual Ni d^8 singlet: a singly occupied d_{z^2} orbital anti-aligned with a $d_{x^2-y^2}$ spin. This "off-diagonal singlet" consists of two fully spin-polarized $3d$ orbitals singlet-coupled, giving rise to a "non-magnetic" ion, however one having an internal orbital texture. Such tendencies were earlier noted [51] in $LaNiO_2$, and related Ni spin states were observed to be sensitive to modest pressure in the $n = 2$ and $n = 3$ classes [77]. Attempts are underway [91, 92] to understand this "magnetic transition in a non-magnetic insulator".

3 OUTLOOK

While this new nickelate family seems to be emerging as its own class of superconductors, its connections to cuprates (crystal and electronic structures, formal d count in the superconducting region, and AFM correlations) retain a focus on similarities between the two classes. Apart from the obvious structural analogy, the cuprate-motivated prediction of optimal $d^{8.8}$ filling has been realized in two nickelate materials, one achieved through chemical doping, and the other by layering dimensionality. In this context, the (so far) little studied $n = 6$ and $n = 4$ members of the series [73] may provide some prospect for superconductivity. Oxygen-reduced samples of these materials are so far lacking (though the $n = 4$ member of the RP series has been epitaxially grown [93]), and even if they are synthesized, they might require additional chemical tuning to achieve superconductivity. They share a similar electronic structure to the $n = 5$ material, but with slightly different nominal filling of the $3d$ bands [73]. Calculations show that as n decreases from $n = \infty$ to $n = 3$, the cuprate-like character increases, with the charge-transfer energy decreasing along with the self-doping effect from the rare earth $5d$ states. In contrast, the particular $n = 1$ member discussed above seems distinct from other nickelates, and provides a different set of questions in the context of quantum materials [91, 92].

AUTHOR CONTRIBUTIONS

All authors listed have made a substantial, direct, and intellectual contribution to the work and approved it for publication.

FUNDING

AB was supported by the United States National Science Foundation, Grant No. DMR 2045826. K-WL was supported by the National Research Foundation of Korea, and Grant No. NRF2019R1A2C1009588. MN was supported by the Materials Sciences and Engineering Division, Basic Energy Sciences, Office of Science, United States Department of Energy. VP acknowledges support from the MINECO of Spain through the project PGC2018-101 334-BC21. WP acknowledges support from United States National Science Foundation, Grant No. DMR 1607139.

REFERENCES

1. Greenblatt M. Ruddlesden-Popper $Ln_{n+1}Ni_nO_{3n+1}$ Nickelates: Structure and Properties. *Curr Opin Solid State Mater Sci* (1997) 2:174–83. doi:10.1016/s1359-0286(97)80062-9
2. Hayward MA, Green MA, Rosseinsky MJ, Sloan J. Sodium Hydride as a Powerful Reducing Agent for Topotactic Oxide Deintercalation: Synthesis and Characterization of the Nickel(I) Oxide $LaNiO_2$. *J Am Chem Soc* (1999) 121:8843–54. doi:10.1021/ja991573i
3. Crespin M, Levitz P, Gatineau L. Reduced Forms of $LaNiO_3$ perovskite. Part 1.-Evidence for New Phases: $La_2Ni_2O_5$ and $LaNiO_2$. *J Chem Soc Faraday Trans 2* (1983) 79:1181–94. doi:10.1039/f29837901181
4. Crespin M, Isnard O, Dubois F, Choisnet J, Odier P. $LaNiO_2$: Synthesis and Structural Characterization. *J Solid State Chem* (2005) 178:1326–34. doi:10.1016/j.jssc.2005.01.023
5. Poltavets VV, Lokshin KA, Dikmen S, Croft M, Egami T, Greenblatt M. $La_3Ni_2O_6$: A New Double T'-type Nickelate with Infinite $Ni^{1+/2+}O_2$ Layers. *J Am Chem Soc* (2006) 128:9050–1. doi:10.1021/ja063031o
6. Kawai M, Matsumoto K, Ichikawa N, Mizumaki M, Sakata O, Kawamura N, et al. Orientation Change of an Infinite-Layer Structure $LaNiO_2$ Epitaxial Thin Film by Annealing with CaH_2. *Cryst Growth Des* (2010) 10:2044–6. doi:10.1021/cg100178y
7. Ikeda A, Manabe T, Naito M. Improved Conductivity of Infinite-Layer $LaNiO_2$ Thin Films by Metal Organic Decomposition. *Physica C: Superconductivity* (2013) 495:134–40. doi:10.1016/j.physc.2013.09.007
8. Li D, Lee K, Wang BY, Osada M, Crossley S, Lee HR, et al. Superconductivity in an Infinite-Layer Nickelate. *Nature* (2019) 572:624–7. doi:10.1038/s41586-019-1496-5
9. Zeng SW, Li CJ, Chow LE, Cao Y, Zhang ZT, Tang CS, et al. Superconductivity In Infinite-Layer Lanthanide Nickelates. *arXiv:2105.13492* (2021).
10. Osada M, Wang BY, Goodge BH, Harvey SP, Lee K, Li D, et al. Nickelate Superconductivity without Rare-Earth Magnetism: $(La,Sr)NiO_2$. *Adv Mater* (2021) 33:2104083. doi:10.1002/adma.202104083
11. Osada M, Wang BY, Goodge BH, Lee K, Yoon H, Sakuma K, et al. A Superconducting Praseodymium Nickelate with Infinite Layer Structure. *Nano Lett* (2020) 20:5735–40. doi:10.1021/acs.nanolett.0c01392

12. Li D, Wang BY, Lee K, Harvey SP, Osada M, Goodge BH, et al. Superconducting Dome in $Nd_{1-x}Sr_xNiO_2$ Infinite Layer Films. *Phys Rev Lett* (2020) 125:027001. doi:10.1103/physrevlett.125.027001
13. Zeng S, Tang CS, Yin X, Li C, Li M, Huang Z, et al. Phase Diagram and Superconducting Dome of Infinite-Layer $Nd_{1-x}Sr_xNiO_2$ Thin Films. *Phys Rev Lett* (2020) 125:147003. doi:10.1103/physrevlett.125.147003
14. Norman MR. Entering the Nickel Age of Superconductivity. *Physics* (2020) 13: 85. doi:10.1103/physics.13.85
15. Pickett WE. The Dawn of the Nickel Age of Superconductivity. *Nat Rev Phys* (2021) 3:7–8. doi:10.1038/s42254-020-00257-3
16. Lee K, Goodge BH, Li D, Osada M, Wang BY, Cui Y, et al. Aspects of the Synthesis of Thin Film Superconducting Infinite-Layer Nickelates. *APL Mater* (2020) 8:041107. doi:10.1063/5.0005103
17. Goodge BH, Li D, Lee K, Osada M, Wang BY, Sawatzky GA, et al. Doping Evolution of the Mott-Hubbard Landscape in Infinite-Layer Nickelates. *Proc Natl Acad Sci USA* (2021) 118:e2007683118. doi:10.1073/pnas.2007683118
18. Hepting M, Li D, Jia CJ, Lu H, Paris E, Tseng Y, et al. Electronic Structure of the Parent Compound of Superconducting Infinite-Layer Nickelates. *Nat Mater* (2020) 19:381–5. doi:10.1038/s41563-019-0585-z
19. Fu Y, Wang L, Cheng H, Pei S, Zhou X, Chen J, et al. Core-Level X-Ray Photoemission And Raman Spectroscopy Studies On Electronic Structures In Mott-Hubbard Type Nickelate Oxide $NdNiO_2$. *arXiv:1911.03177* (2019).
20. Li Q, He C, Si J, Zhu X, Zhang Y, Wen H-H. Absence of Superconductivity in Bulk $Nd_{1-x}Sr_xNiO_2$. *Commun Mater* (2020) 1:16. doi:10.1038/s43246-020-0018-1
21. Wang B-X, Zheng H, Krivyakina E, Chmaissem O, Lopes PP, Lynn JW, et al. Synthesis and characterization of bulk $Nd_{1-x}Sr_xNiO_2$ and $Nd_{1-x}Sr_xNiO_3$. *Phys Rev Mater* (2020) 4:084409. doi:10.1103/physrevmaterials.4.084409
22. Gu Q, Li Y, Wan S, Li H, Guo W, Yang H, et al. Single Particle Tunneling Spectrum of Superconducting $Nd_{1-x}Sr_xNiO_2$ Thin Films. *Nat Commun* (2020) 11:6027. doi:10.1038/s41467-020-19908-1
23. Jiang P, Si L, Liao Z, Zhong Z. Electronic Structure of Rare-Earth Infinite-Layer $RNiO_2$(R=La,Nd). *Phys Rev B* (2019) 100:201106. doi:10.1103/physrevb.100.201106
24. Liu Z, Ren Z, Zhu W, Wang Z, Yang J. Electronic and Magnetic Structure of Infinite-Layer $NdNiO_2$: Trace of Antiferromagnetic Metal. *Npj Quan Mater.* (2020) 5:31. doi:10.1038/s41535-020-0229-1
25. Nomura Y, Hirayama M, Tadano T, Yoshimoto Y, Nakamura K, Arita R. Formation of a Two-Dimensional Single-Component Correlated Electron System and Band Engineering in the Nickelate Superconductor $NdNiO_2$. *Phys Rev B* (2019) 100:205138. doi:10.1103/physrevb.100.205138
26. Wu X, Di Sante D, Schwemmer T, Hanke W, Hwang HY, Raghu S, et al. Robust $d_{x^2-y^2}$-wave Superconductivity Of Infinite-Layer Nickelates. *Phys Rev B* (2020) 101:060504. doi:10.1103/physrevb.101.060504
27. Choi M-Y, Lee K-W, Pickett WE. Role of 4f States in Infinite-Layer $NdNiO_2$. *Phys Rev B* (2020) 101:020503. doi:10.1103/physrevb.101.020503
28. Ryee S, Yoon H, Kim TJ, Jeong MY, Han MJ. Induced Magnetic Two-Dimensionality By Hole Doping In The Superconducting Infinite-Layer Nickelate $Nd_{1-x}Sr_xNiO_2$. *Phys Rev B* (2020) 101:064513. doi:10.1103/physrevb.101.064513
29. Gu Y, Zhu S, Wang X, Hu J, Chen H. A Substantial Hybridization between Correlated Ni-D Orbital and Itinerant Electrons in Infinite-Layer Nickelates. *Commun Phys* (2020) 3:84. doi:10.1038/s42005-020-0347-x
30. Leonov I, Skornyakov SL, Savrasov SY. Lifshitz Transition and Frustration of Magnetic Moments in Infinite-Layer $NdNiO_2$ upon Hole Doping. *Phys Rev B* (2020) 101:241108. doi:10.1103/physrevb.101.241108
31. Lechermann F. Late Transition Metal Oxides with Infinite-Layer Structure: Nickelates versus Cuprates. *Phys Rev B* (2020) 101:081110. doi:10.1103/physrevb.101.081110
32. Lechermann F. Multiorbital Processes Rule the $Nd_{1-x}Sr_xNiO_2$ normal State. *Phys Rev X* (2020) 10:041002. doi:10.1103/physrevx.10.041002
33. Hu Y, Liu G, Hao W, Liu Y, Liu Z. Experimental Study on Regression Model of Ultraviolet Laser Processing Thermal Barrier Coating Based on Response Surface Method. *J Phys Conf Ser* (2019) 1187:032046. doi:10.1088/1742-6596/1187/3/032046
34. Sakakibara H, Usui H, Suzuki K, Kotani T, Aoki H, Kuroki K. Model Construction and a Possibility of Cupratelike Pairing in a New d^9 Nickelate Superconductor (Nd, Sr)NiO_2. *Phys Rev Lett* (2020) 125:077003. doi:10.1103/physrevlett.125.077003
35. Jiang M, Berciu M, Sawatzky GA. Critical Nature of the Ni Spin State in Doped $NdNiO_2$. *Phys Rev Lett* (2020) 124:207004. doi:10.1103/physrevlett.124.207004
36. Werner P, Hoshino S. Nickelate Superconductors: Multiorbital Nature and Spin Freezing. *Phys Rev B* (2020) 101:041104. doi:10.1103/physrevb.101.041104
37. Zhang H, Jin L, Wang S, Xi B, Shi X, Ye F, et al. Effective Hamiltonian for Nickelate Oxides $Nd_{1-x}Sr_xNiO_2$. *Phys Rev Res* (2020) 2:013214. doi:10.1103/physrevresearch.2.013214
38. Karp J, Botana AS, Norman MR, Park H, Zingl M, Millis A. Many-Body Electronic Structure of $NdNiO_2$ and $CaCuO_2$. *Phys Rev X* (2020) 10:021061. doi:10.1103/physrevx.10.021061
39. Botana AS, Norman MR. Similarities and Differences between $LaNiO_2$ and $CaCuO_2$ and Implications for Superconductivity. *Phys Rev X* (2020) 10:011024. doi:10.1103/physrevx.10.011024
40. Wang Y, Kang C-J, Miao H, Kotliar G. Hund's Metal Physics: From $SrNiO_2$ to $LaNiO_2$. *Phys Rev B* (2020) 102:161118. doi:10.1103/physrevb.102.161118
41. Olevano V, Bernardini F, Blase X, Cano A. Ab Initio many-body GW Correlations in the Electronic Structure of $LaNiO_2$. *Phys Rev B* (2020) 101: 161102(R). doi:10.1103/physrevb.101.161102
42. Zhang Y-H, Vishwanath A. Type-II t-J model in Superconducting Nickelate $Nd_{1-x}Sr_xNiO_2$. *Phys Rev Res* (2020) 2:023112. doi:10.1103/physrevresearch.2.023112
43. Petocchi F, Christiansson V, Nilsson F, Aryasetiawan F, Werner P. Normal State of $Nd_{1-x}Sr_xNiO_2$ from Self-Consistent GW+EDMFT. *Phys Rev X* (2020) 10:041047. doi:10.1103/physrevx.10.041047
44. Pan GA, Segedin DF, LaBollita H, Song Q, Nica EM, Goodge BH, et al. Superconductivity in a Quintuple-layer Square-planar Nickelate. *Nat Mater (published online)* (2021). doi:10.1038/s41563-021-01142-9
45. Zhang J, Tao X. Review on quasi-2D Square Planar Nickelates. *CrystEngComm* (2021) 23:3249–64. doi:10.1039/d0ce01880e
46. Nomura Y, Arita R. Superconductivity In Infinite-Layer Nickelates. *arXiv: 2107.12923* (2021).
47. Gu Q, Wen H-H. Superconductivity In Nickel Based 112 Systems. *arXiv: 2109.07654* (2021).
48. Botana AS, Bernardini F, Cano A. Nickelate Superconductors: An Ongoing Dialog between Theory and Experiments. *J Exp Theor Phys* (2021) 132:618–27. doi:10.1134/s1063776121040026
49. Osada M, Wang BY, Lee K, Li D, Hwang HY. Phase Diagram of Infinite Layer Praseodymium Nickelate $Pr_{1-x}Sr_xNiO_2$ Thin Films. *Phys Rev Mater* (2020) 4: 121801. doi:10.1103/physrevmaterials.4.121801
50. Lu H, Rossi M, Nag A, Osada M, Li DF, Lee K, et al. Magnetic Excitations in Infinite-Layer Nickelates. *Science* (2021) 373:213–6. doi:10.1126/science.abd7726
51. Lee K-W, Pickett WE. Infinite-layer $LaNiO_2$: Ni^{1+} is not Cu^{2+}. *Phys Rev B* (2004) 70:165109. doi:10.1103/physrevb.70.165109
52. Anisimov VI, Bukhvalov D, Rice TM. Electronic Structure of Possible Nickelate Analogs to the Cuprates. *Phys Rev B* (1999) 59:7901–6. doi:10.1103/physrevb.59.7901
53. Krishna J, LaBollita H, Fumega AO, Pardo V, Botana AS. Effects of Sr Doping on the Electronic and Spin-State Properties of Infinite-Layer Nickelates: Nature of Holes. *Phys Rev B* (2020) 102:224506. doi:10.1103/physrevb.102.224506
54. Weber C, Yee C, Haule K, Kotliar G. Scaling of the Transition Temperature of Hole-Doped Cuprate Superconductors with the Charge-Transfer Energy. *Epl* (2012) 100:37001. doi:10.1209/0295-5075/100/37001
55. Been E, Lee WS, Hwang HY, Cui Y, Zaanen J, Deveraux T, et al. Electronic Structure Trends Across the Rare-Earth Series in Superconducting Infinite-Layer Nickelates. *Phys Rev X* (2021) 11:011050. doi:10.1103/physrevx.11.011050
56. Higashi K, Winder M, Kunes J, Hariki A. Core-Level X-Ray Spectroscopy of Infinite-Layer Nickelate: LDA + DMFT Study. *Phys Rev X* (2021) 11:041009. doi:10.1103/physrevx.11.041009
57. Kang B, Melnick C, Semon P, Ryee S, Han MJ, Kotliar G, et al. Infinite-Layer Nickelates As Ni-e_g Hund's Metals *arXiv:2007.14610* (2021).
58. Ryee S, Han MJ, Choi S. Hund Physics Landscape of Two-Orbital Systems. *Phys Rev Lett* (2021) 126:206401. doi:10.1103/physrevlett.126.206401

59. Liu Z, Xu C, Cao C, Zhu W, Wang ZF, Yang J. Doping Dependence of Electronic Structure of Infinite-layer $NdNiO_2$. *Phys Rev B* (2021) 103:045103. doi:10.1103/physrevb.103.045103
60. Kang C-J, Kotliar G. Optical Properties of the Infinite-Layer $La_{1-x}Sr_xNiO_2$ and Hidden Hund's Physics. *Phys Rev Lett* (2021) 126:127401. doi:10.1103/physrevlett.126.127401
61. Plienbumrung T, Daghofer M, Oleś AM. Interplay between Zhang-Rice Singlets and High-Spin States in a Model for Doped NiO_2 Planes. *Phys Rev B* (2021) 103:104513. doi:10.1103/physrevb.103.104513
62. Zhao D, Zhou YB, Fu Y, Wang L, Zhou XF, Cheng H, et al. Intrinsic Spin Susceptibility and Pseudogaplike Behavior in Infinite-Layer $LaNiO_2$. *Phys Rev Lett* (2021) 126:197001. doi:10.1103/physrevlett.126.197001
63. Lin H, Gawryluk DJ, Klein YM, Huangfu S, Pomjakushina E, von Rohr F, et al. Universal Spin-Glass Behaviour In Bulk $LaNiO_2$, $PrNiO_2$, and $NdNiO_2$. *arXiv: 2104.14324* (2021).
64. Zhang R, Lane C, Singh B, Nokelainen J, Barbiellini B, Markiewicz RS, et al. Magnetic and F-Electron Effects in $LaNiO_2$ and $NdNiO_2$ Nickelates with Cuprate-like $3d_{x^2-y^2}$ Band. *Commun Phys* (2021) 4:118. doi:10.1038/s42005-021-00621-4
65. Choi M-Y, Pickett WE, Lee K-W. Fluctuation-frustrated Flat Band Instabilities in $NdNiO_2$. *Phys Rev Res* (2020) 2:033445. doi:10.1103/physrevresearch.2.033445
66. Wu X, Di Sante D, Schwemmer T, Hanke W, Hwang HY, Raghu S, et al. Robust $d_{x^2-y^2}$ -wave Superconductivity of Infinite-layer Nickelates. *Phys Rev B* (2020) 101:060504. doi:10.1103/physrevb.101.060504
67. Gu Q, Li Y, Wan S, Li H, Guo W, Yang H, et al. Single Particle Tunneling Spectrum of Superconducting $Nd_{1-x}Sr_xNiO_2$ Thin Films. *Nat Commun* (2020) 11:6027. doi:10.1038/s41467-020-19908-1
68. He R, Jiang P, Lu Y, Song Y, Chen M, Jin M, et al. Polarity-Induced Electronic and Atomic Reconstruction at $NdNiO_2/SrTiO_3$ Interfaces. *Phys Rev B* (2020) 102:035118. doi:10.1103/physrevb.102.035118
69. Bernardini F, Cano A. Stability and Electronic Properties of $LaNiO_2/SrTiO_3$ Heterostructures. *J Phys Mater* (2020) 3:03LT01. doi:10.1088/2515-7639/ab9d0f
70. Geisler B, Pentcheva R. Correlated Interface Electron gas in Infinite-Layer Nickelate Versus Cuprate Films on $SrTiO_3$(001). *Phys Rev Res* (2021) 3:013261. doi:10.1103/physrevresearch.3.013261
71. Ortiz RA, Menke H, Misják F, Mantadakis DT, Fürsich K, Schierle E, et al. Superlattice Approach to Doping Infinite-Layer Nickelates. *Phys Rev B* (2021) 104:165137. doi:10.1103/physrevb.104.165137
72. Ren X, Gao Q, Zhao Y, Hailan Luo XZ, Zhu Z. Superconductivity in Infinite-Layer $Pr_{\{0.8\}}Sr_{\{0.2\}}NiO_2$ Films on Different Substrates. *arXiv:2109.05761* (2021).
73. LaBollita H, Botana AS. Tuning the Van Hove Singularities in AV_3Sb_5 (A=K, Rb, Cs) via Pressure and Doping. *Phys Rev B* (2021) 104:035148. doi:10.1103/physrevb.104.205129
74. Poltavets VV, Lokshin KA, Croft M, Mandal TK, Egami T, Greenblatt M. Crystal Structures of $Ln_4Ni_3O_8$ (Ln = La, Nd) Triple Layer T'-type Nickelates. *Inorg Chem* (2007) 46:10887–91. doi:10.1021/ic701480v
75. Zhang J, Botana AS, Freeland JW, Phelan D, Zheng H, Pardo V, et al. Large Orbital Polarization in a Metallic Square-Planar Nickelate. *Nat Phys* (2017) 13: 864–9. doi:10.1038/nphys4149
76. Zhang J, Chen Y-S, Phelan D, Zheng H, Norman MR, Mitchell JF. Stacked Charge Stripes in the quasi-2D Trilayer Nickelate $La_4Ni_3O_8$. *Proc Natl Acad Sci USA* (2016) 113:8945–50. doi:10.1073/pnas.1606637113
77. Pardo V, Pickett WE. Pressure-Induced Metal-Insulator and Spin-State Transition in Low-Valence Layered Nickelates. *Phys Rev B* (2012) 85:045111. doi:10.1103/physrevb.85.045111
78. Karp J, Hampel A, Zingl M, Botana AS, Park H, Norman MR, et al. Comparative many-body Study of $Pr_4Ni_3O_8$ and $NdNiO_2$. *Phys Rev B* (2020) 102:245130. doi:10.1103/physrevb.102.245130
79. Zhang J, Pajerowski DM, Botana AS, Zheng H, Harriger L, Rodriguez-Rivera J, et al. Spin Stripe Order in a Square Planar Trilayer Nickelate. *Phys Rev Lett* (2019) 122:247201. doi:10.1103/physrevlett.122.247201
80. Botana AS, Pardo V, Pickett WE, Norman MR. Charge Ordering in Ni^{1+}/Ni^{2+} Nickelates: $La_4Ni_3O_8$ and $La_3Ni_2O_6$. *Phys Rev B* (2016) 94:081105. doi:10.1103/physrevb.94.081105
81. Lin JQ, Villar Arribi P, Fabbris G, Botana AS, Meyers D, Miao H, et al. Strong Superexchange in a $d^{9-\delta}$ Nickelate Revealed by Resonant Inelastic X-Ray Scattering. *Phys Rev Lett* (2021) 126:087001. doi:10.1103/physrevlett.126.087001
82. Cheng J-G, Zhou J-S, Goodenough JB, Zhou HD, Matsubayashi K, Uwatoko Y, et al. Pressure Effect on the Structural Transition and Suppression of the High-Spin State in the Triple-LayerT'–$La_4Ni_3O_8$. *Phys Rev Lett* (2012) 108:236403. doi:10.1103/physrevlett.108.236403
83. Retoux R, Rodriguez-Carvajal J, Lacorre P. Neutron Diffraction and TEM Studies of the Crystal Structure and Defects of $Nd_4Ni_3O_8$. *J Solid State Chem* (1998) 140:307–15. doi:10.1006/jssc.1998.7892
84. Pardo V, Pickett WE. Quantum Confinement Induced Molecular Correlated Insulating State in $La_4Ni_3O_8$. *Phys Rev Lett* (2010) 105:266402. doi:10.1103/physrevlett.105.266402
85. Shen Y, Sears J, Fabbris G, Li J, Pelliciari J, Jarrige I, et al. Role of Oxygen States in Square Planar d^9-Delta Nickelates. *arXiv:2110.08937* (2021).
86. Botana AS, Pardo V, Norman MR. Electron Doped Layered Nickelates: Spanning the Phase Diagram of the Cuprates. *Phys Rev Mater* (2017) 1: 021801. doi:10.1103/physrevmaterials.1.021801
87. Nica EM, Krishna J, Yu R, Si Q, Botana AS, Erten O. Theoretical Investigation of Superconductivity in Trilayer Square-Planar Nickelates. *Phys Rev B* (2020) 102:020504. doi:10.1103/physrevb.102.020504
88. Crocker J, Dioguardi A, Shirer K, Poltavets V, Greenblatt M, Klavins P, et al. NMR Evidence for Spin Fluctuations in the Bilayer Nickelate $La_3Ni_2O_6$. *Phys Rev B* (2013) 88:075124.
89. Matsumoto Y, Yamamoto T, Nakano K, Takatsu H, Murakami T, Hongo K, et al. High-Pressure Synthesis of $A_2NiO_2Ag_2Se_2$ (A=Sr, Ba) with a High-Spin Ni^{2+} in Square-Planar Coordination. *Angew Chem Int Ed* (2019) 58:756–9. doi:10.1002/anie.201810161
90. Jin H-S, Pickett WE, Lee K-W. Proposed Ordering of Textured Spin Singlets in a Bulk Infinite-Layer Nickelate. *Phys Rev Res* (2020) 2:033197. doi:10.1103/physrevresearch.2.033197
91. Tu W-L, Moon E-G, Lee K-W, Pickett WE, Lee H-Y Field-Induced Bose-Einstein Condensation and Supersolid in the Two-Dimensional Kondo Necklace. *arXiv:2107.11936* (2021).
92. Singh RRP Magnetism of Competing High-Spin/Low-Spin States in $Ba_2NiO_2(AgSe)_2$ and Related Two-Orbital Two-Electron Systems. *arXiv: 2108.09706* (2021).
93. Li Z, Guo W, Zhang TT, Song JH, Gao TY, Gu ZB, et al. Epitaxial Growth and Electronic Structure of Ruddlesden-Popper Nickelates ($Ln_{n+1}Ni_nO_{3n+1}$, n = 1-5). *APL Mater* (2020) 8:091112. doi:10.1063/5.0018934

Conflict of Interest: The authors declare that the research was conducted in the absence of any commercial or financial relationships that could be construed as a potential conflict of interest.

Publisher's Note: All claims expressed in this article are solely those of the authors and do not necessarily represent those of their affiliated organizations, or those of the publisher, the editors and the reviewers. Any product that may be evaluated in this article, or claim that may be made by its manufacturer, is not guaranteed or endorsed by the publisher.

frontiers in Physics

MINI REVIEW
published: 09 February 2022
doi: 10.3389/fphy.2022.828007

Thin-Film Aspects of Superconducting Nickelates

F. Bernardini[1], *L. Iglesias*[2], *M. Bibes*[2] *and A. Cano*[3]*

[1]Dipartimento di Fisica, Università di Cagliari, Monserrato, Italy, [2]Unité Mixte de Physique, CNRS, Thales, Université Paris-Saclay, Palaiseau, France, [3]Universite Grenoble Alpes, CNRS, Grenoble INP, Institut Néel, Grenoble, France

The discovery of superconductivity in infinite-layer nickelates has attracted much attention due to their association to the high-T_c cuprates. Cuprate superconductivity was first demonstrated in bulk samples and subsequently in thin films. In the nickelates, however, the situation has been reversed: although surging as a bulk phenomenon, nickelate superconductivity has only been reported in thin films so far. At the same time, the specifics of infinite-layer nickelates yield distinct interface and surface effects that determine their bulk vs thin-film behavior. In this paper, we provide an overview on these important aspects.

Keywords: superconductivity, strongly correlated, first principles calculations, thin films, interfaces and surfaces, nickelates, cuprates

1 INTRODUCTION

The infinite-layer nickelates RNiO$_2$ (R = rare-earth element) have long been discussed as potential cuprate-like high-T_c superconductors [1–4]. This idea can now be scrutinized experimentally after the discovery of superconductivity in hole-doped NdNiO$_2$ [5] and its subsequent verification in hole-doped PrNiO$_2$ and LaNiO$_2$ as well [6–13]. To date, however, this breakthrough remains limited to thin films (see e.g. [14–16]). This circumstance is apparently related to the thermodynamic fragility of these special phases, in which the interesting electronic properties require an unfavorably low valence of the nickel atom. Thus, the simultaneous control of both sample quality and doping necessary to promote superconductivity in these nickelates turns out to be a real experimental challenge. In this respect, the thin-film approach has proven its advantages. At the same time, superconductivity has been reported for thicknesses as large as 17 nm (i.e., ~ 50 unit cells), with relatively large critical currents ($\gtrsim$ 200 kA/cm^2), and also for thin films on different substrates. Consequently, there is consensus in that nickelate superconductivity is a genuine bulk phenomenon.

The verification and further investigation of nickelate superconductivity in actual bulk samples (ideally single-crystals) has therefore emerged as an important goal in the field. In parallel, the efforts made along the thin-film route have very recently enabled the observation of nickelate superconductivity in a quintuple layer system that is hardly realizable in its bulk form [17]. Thus, the thin-film approach continues to be the favoured option to gain further insight about nickelate superconductivity. At the same time, the specific effects that may be at play in thin-film vs bulk samples need to be better understood. In the following we provide an overview of the current research along this line.

2 EPITAXIAL-GROWTH ASPECTS

The synthesis of rare-earth infinite-layer nickelate thin films requires the epitaxial growth of the perovskite precursors RNiO$_3$ in the first place. These perovskite nickelates have been grown by various techniques. The most popular is pulsed laser deposition (PLD) [18–21], but sputtering

OPEN ACCESS

Edited by:
Antia Botana,
Arizona State University, United States

Reviewed by:
Kwan-Woo Lee,
Korea University, South Korea

***Correspondence:**
A. Cano
andres.cano@neel.cnrs.fr

Specialty section:
This article was submitted to Condensed Matter Physics, a section of the journal Frontiers in Physics

Received: *02 December 2021*
Accepted: *17 January 2022*
Published: *09 February 2022*

Citation:
Bernardini F, Iglesias L, Bibes M and Cano A (2022) Thin-Film Aspects of Superconducting Nickelates. Front. Phys. 10:828007. doi: 10.3389/fphy.2022.828007

[22, 23] and molecular beam epitaxy [24] have also been used. At this stage, the main difficulty lies in the stabilization of the unfavorable high 3+ valence of Ni (instead of its most preferred 2+), reproducibility and off-stoichiometry issues have been reported in the literature [25]. This difficulty increases for Ca- or Sr-doped films, as required to obtain the subsequent infinite-layer phases in the appropriate regime of Ni 3*d*-electron filling for superconductivity (i.e., $\sim d^{8.8}$). In PLD this is typically achieved by starting from a mixed-phase polycrystalline target and using a highly oxygen rich atmosphere (on the order of 0.15–0.3 mbar), temperature around 600–650°C and a laser fluence ranging from 0.9 to 2 J cm^{-2}. It was also shown that parameters such as the laser spot size or the target history could also play an important role in obtaining single phase perovskite films. However, the synthesis of hole doped nickelates is particularly challenging, not only due to the instability of high-valence Ni itself but also because of the competition between the perovskite phase and Ruddelsden-Popper phases [26, 27]. These two factors are the main obstacles to obtain single-phase perovskite films. The fraction of perovskite phase present in the film can be optimized by monitoring the intensity of the (001) diffraction peak (which is absent in the Ruddelsden-Popper compound) and the position of the (002) peak, which exists in both the perovskite and Ruddelsden-Popper phases but appears at a larger angle for the perovskite (above 48°). Lee et al [28] have shown that to optimize both criteria it is preferable to work with relatively high laser fluence and very small laser spot size (on the order of 2 mm^2 or less).

Even if single-phase perovskite thin films are obtained, it is important to keep in mind that the quality of the samples may be limited by the presence of additional atoms or defects. At the interfaces, in particular, epitaxial strain may favor the presence of oxygen or even *A*-site vacancies (see e.g., [29, 30]). What is more, achieving a single termination is difficult in many substrates and different interfacial configurations are generally possible in these systems (see e.g., [31, 32]). Consequently, the Ni atom may be embedded in multiple interfacial environments already at this stage.

After the precursor perovskite phase has been obtained, the samples are reduced by thermal annealing in a vacuum-sealed tube containing a small amount of a highly reducing agent (CaH_2). The goal is to selectively remove one-third of oxygens (i.e., one full plane of apical oxygens) and thereby stabilize the oxygen poorer infinite-layer phase. The literature diverges regarding the exact conditions for this process, but it typically has to be performed between 200 and 360°C for several hours [6, 7, 10, 27, 28]. In the ideal case, X-ray diffraction then reveals the complete transformation of the perovskite phase into the infinite-layer phase, with a characteristic shift of the (002) peak position to higher angles (~54°) signalling the contraction of the out-of-plane lattice constant, an intense (001) peak (its absence or reduced intensity is again the signature of spurious phases) and Laue fringes, attesting of the good structural coherence of the infinite-layer phase in the growth direction [9, 27, 28].

3 EPITAXIAL STRAIN

The most obvious additional ingredient that appears in thin films is the epitaxial—or biaxial—strain associated to the lattice mismatch between the nickelate and the substrate. For instance, the lattice parameter of the common substrate $SrTiO_3$ is 3.905 Å while the lattice parameters of bulk $LaNiO_2$ have been reported to be $a = 3.96$ Å and $c = 3.37$ Å [1]. Thus, for *c*-axis oriented thin films of $LaNiO_2$ grown on $SrTiO_3$(001) the epitaxial strain, which is defined as $(a_{substrate} - a)/a$, will be −1.4%. In general, this reduction of the *a* parameter is accompanied with an increase in *c* since the system is free to relax the stress in that direction. That is, imposing an in-plane compression at the interface results in out-of-plane tensile strain. Conversely, in-plane tensile strain—due to a different substrate for example—can be expected to produce an out-of-plane compression.

By means of these changes in the cell parameters, epitaxial strain can further modify the key features of the corresponding electronic structure (see e.g., [33]). The "cuprateness" of this structure, in particular, is generally defined from the nature of the states at the Fermi level and the so-called charge-transfer energy (see e.g., [3, 34–37]). In this respect, in-plane compressive strain increases both the bandwidth of the main Ni-3$d_{x^2-y^2}$ band crossing the Fermi level and its self-doping with the *R*-5*d* states. At the same time, the O-2*p* states are pushed further below the Fermi level, thereby increasing the corresponding charge-transfer energy. These changes that can be obtained locally due to epitaxial strain have been argued to mimic the trends across the $RNiO_2$ series, including the corresponding tendency towards magnetic order [33]. Furthermore, epitaxial strain can also induce changes in the crystal structure itself and promote a $P4/mmm \rightarrow I4/mcm$ transition associated with an A_3^+ soft mode in which the NiO_4 squares undergo antiphase in-plane rotations [38, 39].

If the film relaxes, epitaxial strain will typically decrease with the distance to the interface and the lattice parameters should eventually recover their bulk values as the thickness of the film increases. This overall relaxation should occur following a power-law behavior—rather than an exponential one—due to the long-range nature of the strain field. This has been quantified for (Nd,Sr)NiO_2/$SrTiO_3$ in [11]. Specifically, the *c* lattice parameter is found to decrease from 3.42 Å for their 5.1 nm thick sample to 3.36 Å whenever the thickness is larger than 7 nm. At the same time, the superconducting T_c is found to correlate with such a decrease in the strain as it displays an increase from 6 to 13 K. On the other hand, the T_c has been reported to increase in (Pr,Sr)NiO_2 grown on $(LaAlO_3)_{0.3}(Sr_2AlTaO_6)_{0.7}$ (LSAT) as compared to the original $SrTiO_3$ substrate, for 8 nm-thick thin films in both cases [12]. This increase has been interpreted as due to the additional strain induced by the LSAT substrate. However, in contrast to the above, a higher degree of in-plane compressive (out-of-plane tensile) strain would seem to enhance the T_c in this case.

The apparent contradiction between these observations may be resolved due to different factors. Two of them may be just stoichiometry and sample quality. The *R*:Ni flux ratio used during the growth of the perovskite films, for example, has been reported to be an important factor for their subsequent reduction into the infinite-layer phase and hence for the observation superconductivity [40]. Beyond that, samples synthesized in

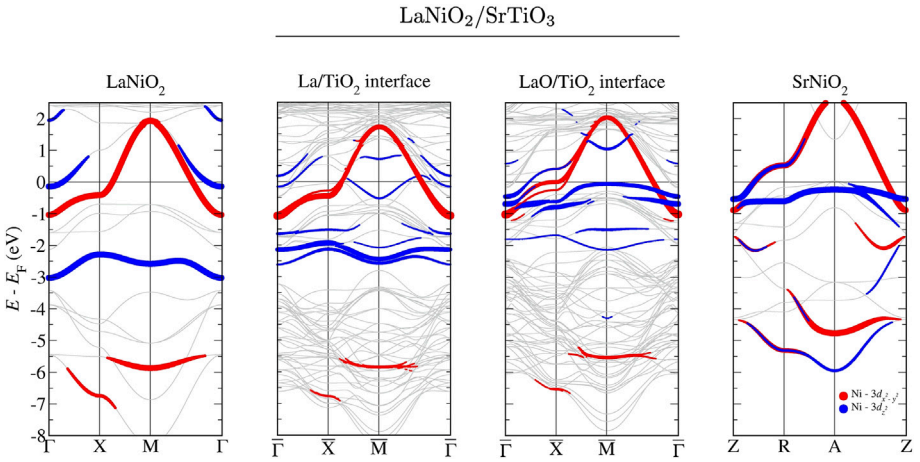

FIGURE 1 | Electronic band structure of the $LaNiO_2/SrTiO_3$ heterostructure for different interfacial configurations compared to bulk $LaNiO_2$ and $SrNiO_2$ with the same crystal structure and lattice parameters (the Γ-X-M-Γ and Z-R-A-Z paths fold to $\bar{\Gamma}$-$\bar{X}$-$\bar{M}$-$\bar{\Gamma}$). The presence of interfacial apical oxygens introduces an effective hole doping that locally changes the occupation of the Ni-3*d* states, so that oxidation state of the Ni atom increases from +1 towards +2. Adapted from [44].

nominally similar conditions can easily show substantial variations in the superconducting T_c and even stay non-superconducting [5]. In this respect, the recent report of superconductivity in (La,Sr)NiO_2 emphasizes the importance of sufficiently low disorder and high crystallinity [9, 10]. Consequently, the quantification of the T_c as a function of the structure may be taken with a grain of salt (in the sense that the actual error bars may be quite large).

4 CHEMICAL RECONSTRUCTIONS

4.1. Topotatic Hydrogen

Another factor that convolutes with the above is the composition itself. As mentioned above, infinite-layer nickelates are synthesized by topotactic reduction of perovskite precursors using reducing agents such as CaH_2. This process, however, may result in the formation of oxide-hydrides $RNiO_2H$. This possibility has been argued to correlate with both the *R* element and epitaxial strain [38, 41, 42]. Specifically, while the parent phases are prone to topotactically incorporate H, both *R*-element substitution and compressive epitaxial strain can limit this possibility. The latter is consistent with the transformation of the infinite-layer $NdNiO_2$ phase into a fluorite-defect structure $NdNiO_xH_y$ as a function of the distance to the interface with (001) $SrTiO_3$ reported in [43].

4.2 Apical Oxygens

Beyond that, even without insertion of topotactic hydrogen, the reduction process can be different at the interface and further away from it and may result, in particular, in the presence of apical oxygens. This question was first addressed by means of DFT calculations in [44, 45]. Both these works predicted the presence of these interfacial apical oxygens, which have recently been confirmed in an *ad hoc* experimental study supplemented with DMFT calculations [46].

The presence of apical oxygens at the interfaces can be seen as a sort of "chemical" reconstruction of the nickelate that locally introduces hole doping. This is illustrated in **Figure 1**. Without reconstruction, the characteristic band structure of the bulk would be essentially preserved at the interface. Accordingly, the Ni atom would display the same oxidation state everywhere. However, if the apical oxygen remains at the interface, then the local band structure changes towards the $RNiO_3$ —or rather $RNiO_{2.5}$— case. This implies that the Ni oxidation state locally approaches +2 rather than +1. This is a very interesting possibility since it may emulate the hole doping obtained by means of the $R \rightarrow$ Sr or Ca substitution, necessary to further promote superconductivity. However, the additional charge introduced in this way may be distributed over a distance in the film. Thus, in the ultrathin limit, the effective degree of doping would eventually be controlled by the thickness of the film. In fact, a gradual increase of the Ni oxidation state as the thickness of the superconducting films decreases has been inferred from XAS data in [11]. These carriers, however, have been argued to be self-trapped at the interfaces due to Hund's coupling according to DMFT calculations [46]. We note that this may be reminiscent of the metal-insulator transition that takes place in the perovskite counterparts. At the same time, carriers from *B*-site atom of the substrate—Ti in $SrTiO_3$ vs Ga in $LaGaO_3$ for example—also participate in the overall process so that the self-trapping may be surface specific.

4.3 Additional Thin Film/Substrate Terminations

The situation may be even more complex since, depending on the actual synthesis conditions, additional chemical reconstructions have been shown to be possible at the interface [44]. In particular, the most likely RO/TiO_2 configuration may be replaced by the NiO_2/SrO one. That is, the termination may be different. In that case, there would be an extra local doping associated to the

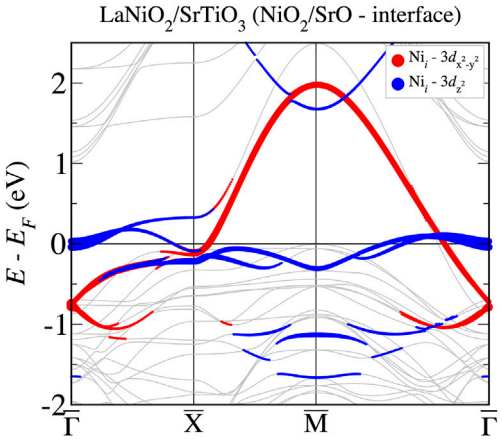

FIGURE 2 | Electronic band structure of the $LaNiO_2/SrTiO_3$ heterostructure for the NiO_2/SrO interfacial configuration (the colors highlight the main contributions of the interfacial Ni-3*d* states near the Fermi level and a 3/3 superlattice is considered). The effective interfacial doping for this configuration depletes the self-doping from the *R*-5*d* states characteristic of the bulk and places the Ni-$3d_{z^2}$ states at the Fermi level introducing flatband features. Adapted from [44].

interfacial Sr, superimposed to the one from the apical oxygen. In fact, the interfacial cell would be $La_{0.5}Sr_{0.5}NiO_{2.5}$ so that the oxidation state of the Ni atom would increase to +2.5. This overdoping again may be distributed over a distance so that the actual occupation of the Ni-3*d* states may be determined by the thickness of the film. In the ultrathin limit, in particular, the corresponding electronic structure has been shown to undergo drastic changes (see **Figure 2**). Specifically, the initial self-doping effect provided by the *R*-5*d* states in the bulk will be completely depleted by the local SrO overdoping at the interface. At the same time, the intefacial Ni-$3d_{z^2}$ states are driven even closer to the Fermi energy so that they will manifestly participate in the low-energy physics. The Ni-e_g sector then can be expected to be fully active, and supplemented with a markedly flatband character of the interfacial Ni-$3d_{z^2}$ states. In addition, the charge-transfer energy also decreases. As a result of these local changes, both Hubbard's and Hund's couplings may be equally important for quantifying the corresponding correlation effects and/or distinct interface-specific instabilities may appear.

4.4 Surface

The above changes with respect to the bulk may also happen in thin films with asymmetric boundaries where the effective built-in electric field that appears due to the corresponding polar discontinuities play a role. Specifically, the screening of this field implies a charge transfer that adds to the aforementioned effects. In the case of asymmetric boundaries, polar layers can be formed at both the surface and the interface [47, 48]. These layers display antiparallel NiO_2 displacements, but otherwise are decoupled. Further, the aforementioned depletion of the *R*-5*d* states can also be obtained at the surface while a two-dimensional electron gas extending over several layers can be formed at the interface [45, 47]. Besides, the combined effect of magnetism—*G*-type antiferromagnetic order—and correlations at the DFT + *U* level has been found to enhance the itineracy of the Ni-$3d_{z^2}$ orbitals at the interface with the substrate, while the magnetism is essentially suppressed at the surface to vacuum [47].

The focus has been put on the surface properties in [49] taking into account the possibility of apical oxygens anticipated in [44, 45]. Thus, it has been confirmed that different terminations yield different electronic structures also at the surface (see **Figure 1**). This is further shown to modify qualitatively the corresponding Fermi surface. As a result of this modification, it is argued that the *d*-wave superconducting gap expected for the bulk may transform into a $s_{\pm}$-wave one at the NiO_2-terminated surface. This provides a rather natural explanation to the local changes in the tunneling spectrum observed in [13]. Further, it suggests that a surface *s* + *id*-wave state may also be realized under the appropriate conditions.

5 OUTLOOK

The thin-film approach has proven its advantages to overcome the thermodynamic fragility of the infinite-layer nickelates, thereby demonstrating the emergence of unconventional superconductivity in these systems. Besides, this approach offers additional degrees of flexibility to further investigating this phenomenon.

Epitaxial strain can be used not only to fine tune the electronic structure of these nickelates and hence their "cuprateness", but also the underlying crystal structure itself. Beyond that, the presence of apical oxygens at the interfaces/surfaces enables a local control of the effective doping without the need of rare-earth-element substitution. This apical-oxygen doping can be further supplemented with an extra contribution from the interfacial terminations themselves. This may be useful to bypass the sample-quality issues associated with doping at the rare-earth site. In fact, the overall local doping obtained in that way may be a particularly effective control parameter in the ultrathin limit.

Another route yet to be explored experimentally is the engineering of the electronic properties via nickelate-based superlattices. This idea was put forward some time ago with the perovskite phases as building blocks [50]. This concept can now be supplemented with the possibility reducing these phases, thereby mimicking higher-order layered nickelates. The $(RNiO_2)_3/(SrTiO_3)_3$ superlattices, for example, have been shown to display many analogies with the trilayer systems $R_4Ni_3O_8$ [or RO_2 $(RNiO_2)_3$] [44]. Conceptually, the superconducting pentalayer nickelate can also be simulated in this way. This meta-material approach may enable to bypass the thermodynamic instability of these higher-order phases and, at the same time, exploit the interfaces—rather than the spacers of layered bulk materials—as reservoirs for charge doping. In addition, it can also help to clarify the interplay between superconductivity and other degrees of freedom. Charge density waves, in particular, have very recently been reported to display an intriguing dependence on the presence of capping

layers in infinite-layer nickelate thin films calling for further investigations [51–53].

AUTHOR CONTRIBUTIONS

All authors listed have made a substantial, direct, and intellectual contribution to the work and approved it for publication.

ACKNOWLEDGMENTS

LI acknowledges the support and funding from the Île de France region and the European Union's Horizon 2020 research and innovation programme under the Marie Sklodowska-Curie grant agreement N°21 004 513 (DOPNICKS project). AC was supported by ANR, Grant ANR-18-CE30-0018.

REFERENCES

1. Hayward MA, Green MA, Rosseinsky MJ, Sloan J Sodium Hydride as a Powerful Reducing Agent for Topotactic Oxide Deintercalation: Synthesis and Characterization of the Nickel(I) Oxide LaNiO2. *J Am Chem Soc* (1999) 121: 8843–54. doi:10.1021/ja991573i
2. Anisimov VI, Bukhvalov D, Rice TM Electronic Structure of Possible Nickelate Analogs to the Cuprates. *Phys Rev B* (1999) 59:7901–6. doi:10.1103/physrevb.59.7901
3. Lee K-W, Pickett WE Infinite-layerLaNiO2: Ni1+is notCu2+. *Phys Rev B* (2004) 70:165109. doi:10.1103/physrevb.70.165109
4. Norman MR Entering the Nickel Age of Superconductivity. *Physics* (2020) 13: 85. doi:10.1103/physics.13.85
5. Li D, Lee K, Wang BY, Osada M, Crossley S, Lee HR, et al. Superconductivity in an Infinite-Layer Nickelate. *Nature* (2019) 572:624–7. doi:10.1038/s41586-019-1496-5
6. Zeng S, Tang CS, Yin X, Li C, Li M, Huang Z, et al. Phase Diagram and Superconducting Dome of Infinite-Layer Nd1−xSrxNiO2 Thin Films. *Phys Rev Lett* (2020) 125:147003. doi:10.1103/physrevlett.125.147003
7. Osada M, Wang BY, Goodge BH, Lee K, Yoon H, Sakuma K, et al. A Superconducting Praseodymium Nickelate with Infinite Layer Structure. *Nano Lett* (2020) 20:5735–40. doi:10.1021/acs.nanolett.0c01392
8. Osada M, Wang BY, Lee K, Li D, Hwang HY Phase Diagram of Infinite Layer Praseodymium Nickelate Pr1−xSrxNiO2 Thin Films. *Phys Rev Mater* (2020) 4: 121801. doi:10.1103/physrevmaterials.4.121801
9. Osada M, Wang BY, Goodge BH, Harvey SP, Lee K, Li D, et al. Nickelate Superconductivity without Rare-Earth Magnetism: (La,Sr)NiO 2. *Adv Mater* (2021) 33:2104083. doi:10.1002/adma.202104083
10. Zeng SW, Li CJ, Chow LE, Cao Y, Zhang ZT, Tang CS, et al. *arXiv:2105.13492* (2021).
11. Zeng SW, Yin XM, Li CJ, Tang CS, Han K, Huang Z, et al. *arXiv:2104.14195* (2021).
12. Ren X, Gao Q, Zhao Y, Luo H, Zhou X, Zhu Z *arXiv:2109.05761* (2021).
13. Gu QQ, Li YY, Wan SY, Li HZ, Guo W, Yang H, et al. *Nat Commun* (2020) 11: 7. doi:10.1038/s41467-020-19908-1
14. Botana AS, Bernardini F, Cano A Nickelate Superconductors: an Ongoing Dialog between Theory and Experiments. *Zh Eksp Teor Fiz* (2021) 159:711–8. arXiv:2012.02764. doi:10.31857/s0044451021040131
15. Zhang J, Tao X *arXiv:2103.06674* (2021).
16. Nomura Y, Arita R *arXiv:2107.12923* (2021).
17. Pan GA, Ferenc Segedin D, LaBollita H, Song Q, Nica EM, Goodge BH, et al. *arXiv:2109.09726* (2021).
18. Preziosi D, Sander A, Barthélémy A *AIP Adv* (2017) 11.
19. Guo Q, Farokhipoor S, Magén C, Rivadulla F, Noheda B Tunable Resistivity Exponents in the Metallic Phase of Epitaxial Nickelates. *Nat Commun* (2020) 11:2949. arXiv: 1909.06256. doi:10.1038/s41467-020-16740-5
20. Frano A, Benckiser E, Lu Y, Wu M, Castro-Colin M, Reehuis M, et al. Layer Selective Control of the Lattice Structure in Oxide Superlattices. *Adv Mater* (2014) 26:258–62. doi:10.1002/adma.201303483
21. Liu J, Kargarian M, Kareev M, Gray B, Ryan PJ, Cruz A, et al. Heterointerface Engineered Electronic and Magnetic Phases of NdNiO3 Thin Films. *Nat Commun* (2013) 4:2714. doi:10.1038/ncomms3714
22. Scherwitzl R, Zubko P, Lezama IG, Ono S, Morpurgo AF, Catalan G, et al. Electric-Field Control of the Metal-Insulator Transition in Ultrathin NdNiO3 Films. *Adv Mater* (2010) 22:5517–20. doi:10.1002/adma.201003241
23. Mikheev E, Hauser AJ, Himmetoglu B, Moreno NE, Janotti A, Van de Walle CG, et al. *Sci Adv* (2015) 1:e1500797. doi:10.1126/sciadv.1500797
24. King PDC, Wei HI, Nie YF, Uchida M, Adamo C, Zhu S, et al. Atomic-scale Control of Competing Electronic Phases in Ultrathin LaNiO3. *Nat Nanotech* (2014) 9:443–7. doi:10.1038/nnano.2014.59
25. Preziosi D, Sander A, Barthélémy A, Bibes M Reproducibility and Off-Stoichiometry Issues in Nickelate Thin Films Grown by Pulsed Laser Deposition. *AIP Adv* (2017) 7:015210. doi:10.1063/1.4975307
26. Lee K, Goodge BH, Li D, Osada M, Wang BY, Cui Y, et al. Aspects of the Synthesis of Thin Film Superconducting Infinite-Layer Nickelates. *APL Mater* (2020) 8:041107. doi:10.1063/5.0005103
27. Gao Q, Zhao Y, Zhou X-J, Zhu Z Preparation of Superconducting Thin Films of Infinite-Layer Nickelate Nd0.8Sr0.2NiO2. *Chin Phys. Lett.* (2021) 38: 077401. doi:10.1088/0256-307x/38/7/077401
28. Lee K, Goodge BH, Li D, Osada M, Wang BY, Cui Y, et al. Aspects of the Synthesis of Thin Film Superconducting Infinite-Layer Nickelates. *APL Mater* (2020) 8:041107. doi:10.1063/5.0005103
29. Aschauer U, Pfenninger R, Selbach SM, Grande T, Spaldin NA *Phys Rev B* (2013) 88:054111. doi:10.1103/physrevb.88.054111
30. Petrie JR, Mitra C, Jeen H, Choi WS, Meyer TL, Reboredo FA, et al. *arXiv: Mater Sci* (2016).
31. Kumah DP, Malashevich A, Disa AS, Arena DA, Walker FJ, Ismail-Beigi S, et al. *Phys Rev Appl* (2014) 2:054004. doi:10.1103/physrevapplied.2.054004
32. Li Y, Wrobel F, Yan X, Bhattacharya A, Sun J, Hong H, et al. Interface Creation on a Mixed-Terminated Perovskite Surface. *Appl Phys Lett* (2021) 118:061601. doi:10.1063/5.0036279
33. Kapeghian J, Botana AS Electronic Structure and Magnetism in Infinite-Layer Nickelates RNiO2 (R=La–Lu). *Phys Rev B* (2020) 102:205130. doi:10.1103/physrevb.102.205130
34. Botana AS, Norman MR *Phys Rev X* (2020) 10:011024. doi:10.1103/physrevx.10.011024
35. Olevano V, Bernardini F, Blase X, Cano A Ab Initio many-body GW Correlations in the Electronic Structure of LaNiO2. *Phys Rev B* (2020) 101: 161102. doi:10.1103/physrevb.101.161102
36. Wang Y, Kang C-J, Miao H, Kotliar G Hund's Metal Physics: From SrNiO2 to LaNiO2. *Phys Rev B* (2020) 102:161118. doi:10.1103/physrevb.102.161118
37. Lechermann F *Phys Rev B* (2020) 101:081110. doi:10.1103/physrevb.101.081110
38. Bernardini F, Bosin A, Cano A *arXiv:2110.13580* (2021).
39. Xia C, Wu J, Chen Y, Chen H *arXiv:2110.12405* (2021).
40. Li Y, Sun W, Yang J, Cai X, Guo W, Gu Z, et al. *Front Phys* (2021) 9:443. doi:10.3389/fphy.2021.719534
41. Si L, Xiao W, Kaufmann J, Tomczak JM, Lu Y, Zhong Z, et al. Topotactic Hydrogen in Nickelate Superconductors and Akin Infinite-Layer Oxides ABO2. *Phys Rev Lett* (2020) 124:166402. doi:10.1103/physrevlett.124.166402
42. Malyi OI, Varignon J, Zunger A *arXiv:2107.01790* (2021).
43. Onozuka T, Chikamatsu A, Katayama T, Fukumura T, Hasegawa T Formation of Defect-Fluorite Structured NdNiOxHy Epitaxial Thin Films via a Soft Chemical Route from NdNiO3 Precursors. *Dalton Trans* (2016) 45: 12114–8. doi:10.1039/c6dt01737a
44. Bernardini F, Cano A Stability and Electronic Properties of LaNiO2/SrTiO3 Heterostructures. *J Phys Mater* (2020) 3:03LT01. doi:10.1088/2515-7639/ab9d0f
45. Geisler B, Pentcheva R *Phys Rev B* (2020) 102:020502. doi:10.1103/physrevb.102.020502

46. Ortiz RA, Menke H, Misják F, Mantadakis DT, Fürsich K, Schierle E, et al. Superlattice Approach to Doping Infinite-Layer Nickelates. *Phys Rev B* (2021) 104:165137. doi:10.1103/physrevb.104.165137
47. Zhang Y, Lin L-F, Hu W, Moreo A, Dong S, Dagotto E Similarities and Differences between Nickelate and Cuprate Films Grown on a SrTiO3 Substrate. *Phys Rev B* (2020) 102:195117. doi:10.1103/physrevb.102.195117
48. Geisler B, Pentcheva R *Phys Rev Res* (2021) 3:013261. doi:10.1103/physrevresearch.3.013261
49. Wu X, Jiang K, Di Sante D, Hanke W, Schnyder AP, Hu J, et al. *arXiv: 2008.06009* (2021).
50. Hansmann P, Yang X, Toschi A, Khaliullin G, Andersen OK, Held K *Phys Rev Lett* (2009) 103:016401. doi:10.1103/physrevlett.103.016401
51. Rossi M, Osada M, Choi J, Agrestini S, Jost D, Lee Y, et al. *arXiv e-prints , arXiv: 2112.02484* (2021). arXiv:2112.02484 [cond-mat.supr-con].
52. Krieger G, Martinelli L, Zeng S, Chow LE, Kummer K, Arpaia R, et al. *arXiv e-prints , arXiv:2112.03341* (2021). arXiv:2112.03341 [cond-mat.supr-con].
53. Tam CC, Choi J, Ding X, Agrestini S, Nag A, Huang B, et al. *arXiv e-prints, arXiv:2112.04440* (2021). arXiv:2112.04440 [cond-mat.supr-con].

Conflict of Interest: The authors declare that the research was conducted in the absence of any commercial or financial relationships that could be construed as a potential conflict of interest.

frontiers in Physics

MINI REVIEW
published: 11 February 2022
doi: 10.3389/fphy.2022.834882

Carrier Doping Physics of Rare Earth Perovskite Nickelates $RENiO_3$

Jiarui Li[1]*, *Shriram Ramanathan*[2] *and Riccardo Comin*[1]*

[1]*Department of Physics, Massachusetts Institute of Technology, Cambridge, MA, United States,* [2]*School of Materials Engineering, Purdue University, West Lafayette, IN, United States*

The family of rare earth (RE) nickelate perovskites $RENiO_3$ has emerged over the past two decades as an important platform for quantum matter physics and advanced applications. The parent compounds from this family are strongly correlated insulators or metals, in most cases with long-range spin order. In the past few years, carrier doping has been achieved using different approaches and has been proven to be a powerful tuning parameter for the microscopic properties and collective macroscopic states in $RENiO_3$ compounds. In particular, a series of recent studies has shown that carrier doping can be responsible for dramatic but reversible changes in the long-range electronic and magnetic properties, underscoring the potential for use of nickelates in advanced functional devices. In this review, we discuss the recent advancements in our description, understanding and application of electron-doped rare earth nickelates. We conclude with a discussion of the developments and outlook for harnessing the quantum functional properties of nickelates in novel devices for sensing and neuromorphic computation.

Keywords: rare earth nickelate, carrier doping, resistive switching (RS), antidoping, hydrogenation, oxygen vancany, ion intercalation/de-intercalation

OPEN ACCESS

Edited by:
Matthias Hepting,
Max Planck Institute for Solid State Research, Germany

Reviewed by:
Chun-Gang Duan,
East China Normal University, China

***Correspondence:**
Jiarui Li
jiaruili@mit.edu
Riccardo Comin
rcomin@mit.edu

Specialty section:
This article was submitted to Condensed Matter Physics, a section of the journal Frontiers in Physics

Received: *13 December 2021*
Accepted: *11 January 2022*
Published: *11 February 2022*

Citation:
Li J, Ramanathan S and Comin R (2022) Carrier Doping Physics of Rare Earth Perovskite Nickelates $RENiO_3$. Front. Phys. 10:834882. doi: 10.3389/fphy.2022.834882

INTRODUCTION

Functional materials exhibit properties that can be harnessed for novel technological applications. Control over selected electronic, magnetic, optical, and/or structural properties is often achieved by stabilizing one particular phase of matter over other competing phases or by tuning the material across phase boundaries. A significant fraction of functional materials is found among transition metal oxides (TMOs) characterized by perovskite structures with chemical formula ABO_3. The advantage of the perovskite structure is its flexibility to accommodate atoms of various sizes and its tolerance to stoichiometry variations, making their physical properties highly tunable.

One of the most common ways to modify the physical properties of perovskite-type TMOs is via carrier doping [1]. The latter is typically achieved by partial substitution of atoms with different valence; by creating charged atomic vacancies; or by ion intercalation. Carrier control has been shown to induce emergent properties in the perovskite TMOs including colossal magnetoresistance, unconventional high-temperature superconductivity, quantum criticality, and charge/spin density wave orders [2–6].

This review focuses on the TMO family of rare earth nickelates ($RENiO_3$; RE = rare earth ion), which have for many years attracted the attention of the scientific community owing to their highly tunable electronic properties. The electronic, magnetic, optical, and structural tunability of these systems not only leads to potential applications but also provides new opportunities to realize and understand quantum matter phenomena.

Before discussing the physical properties of doped $RENiO_3$, we review the complex electronic properties of undoped nickelates. $RENiO_3$ has a distorted $GdFeO_3$-perovskite-like structure where the Ni-O-Ni bond angle can be continuously varied by rare earth substitution. The bond angle has been shown to have a profound impact on their electronic properties [7, 8]. In the rare earth series (except La), $RENiO_3$ first undergo a metal (or semiconductor) to insulator transitions and subsequently a paramagnet to antiferromagnet transition. The transition points vary with the size of the rare earth atoms and are concurrent for RE = Nd, Pr. In terms of local electronic configuration, Ni has a nominal electron filling d^7 (Ni^{3+}). However, a series of experimental and theoretical studies have identified $RENiO_3$ as a negative charge transfer insulator, with the electronic ground state exhibiting a significant projection onto a $3d^8\underline{L}$ configuration ($\underline{L}$ denotes a ligand hole in oxygen orbital) [9–12]. Therefore, $RENiO_3$ has rather unique ground state properties among charge transfer insulators.

Upon entering the insulating state, a disproportionated state emerges where neighboring Ni-O_6 octahedra alternately compress and expand, forming a 3D period-2 checkerboard arrangement. In the antiferromagnetically ordered phase, the Ni spins are close to S = 1/2 and order at the wavevector (1/4, 1/4, 1/4) in the pseudocubic cell [13–16]. Since $RENiO_3$ could be hardly synthesized in single crystalline form until recently [17], most earlier studies focused on polycrystalline $RENiO_3$ with varying chemical compositions. Since the development of epitaxial synthesis in the last two decades, many studies of $RENiO_3$ have focused on thin films, whose physical properties can be altered not only via chemical composition, but also by strain, dimensionality, and superlattice engineering [18].

Due to strong on-site Coulomb interactions, the electronic properties of $RENiO_3$ are extremely sensitive to the electron filling of the Ni-O bands. Therefore, carrier doping is another effective and well-established practice of controlling the physical properties of $RENiO_3$. In the following, we will review the recent progress on carrier-doped nickelates. We will focus on recent advances in understanding the physics of rare earth nickelates as a function of carrier doping and the potential functional applications enabled by the latter.

INTERSTITIAL ION DOPING

It has been recently demonstrated that pseudocubic $RENiO_3$ can conduct and incorporate large amounts of dopant ions such as hydrogen, alkali (Li, Na) or alkali-earth metals [19–22]. The ion dopants have been shown to preferentially bond with oxygen and can undergo frequent diffusive hopping to nearby sites via the Grotthuss mechanism [22, 23]. In presence of an external bias (chemical/electrical), the ions will diffuse in and out of the $RENiO_3$ scaffolding with a relatively high ionic conductivity [20, 24].

The incorporation of interstitial ions with low electron affinity adds extra electrons to the conduction states and can dramatically alter the ground state of $RENiO_3$. It has been shown that the incorporated ion concentration can be as high as ~1:1 ion:Ni ratio [20–22, 25]. Recent studies report that the properties of ion-intercalated nickelates change dramatically: 1) Doping induces a reversible giant resistance switching by eight orders of magnitude at room temperature [19, 20], with accompanying changes from a metallic or semiconducting state (~100 meV) to a large bandgap insulating state (~3 eV) [19, 26]. 2) The doping process alters the nickel valence state from Ni^{3+} to Ni^{2+} and is independent of temperature, a fundamental departure from thermally-driven insulator-metal transitions previously noted in perovskite nickelates. 3) The ligand holes are getting filled upon doping. 4) The lattice constants can increase significantly (~10%, depending on the ion species) upon ion intercalation [27]. 5) The (1/4, 1/4, 1/4) antiferromagnetic order breaks down after some critical doping [28]. Many exciting applications have been proposed and realized in these interstitially-doped nickelates, e.g., electronic devices (phase-change transistor) [19, 29–31], fuel cells [22], bio-electronic interfaces [32, 33], electric field sensor [21], as well as artificial cognitive systems [28, 34, 35].

Most of these studies focused on $SmNiO_3$ for its large resistive switching, faster intercalation dynamics, and facile synthesis. The study by Chen et al. examined the hydrogenation of $RENiO_3$ for RE = La, Nd, Sm, Eu [26]. They showed that for rare earth ions with larger atomic numbers, the resistivity could be tuned over a more extensive range with faster kinetics. This general trend unveils the role of the structure in ionic doping. With the decrease of RE radius, the tolerance factor further deviates from 1, and the structure becomes less stable. Thus, the smaller RE compounds are more prone to incorporate and retain interstitial ions. However, the structural changes during the intercalation process cannot alone explain the very large changes in resistivity. From a structural point of view, the expansion of lattice upon intercalation tends to straighten the Ni-O-Ni bonds and should stabilize the metallic state over the insulating state [36, 37]. Therefore, the electronic contribution must be accounted for to explain the colossal resistive switching effect.

In a semiconductor, carrier doping is generally realized by injecting electron/hole carriers into the conduction/valence band so that electrical conductivity increases proportionally to the number of mobile carriers. Carrier doping in $RENiO_3$ by ion intercalation (and oxygen vacancies as will be discussed in the following section) defies this simple notion as the resistance increases by orders of magnitude. Such a phenomenon is sometimes called antidoping [38]. The large increase of the resistance and the bandgap cannot be explained simply by a Fermi level shift as described in the rigid-band model. The physical origin of the antidoping has recently been unveiled by Ref. [38]. A prerequisite of an antidoping system is the existence of partially filled intermediate side bands consisting of trapped holes (electrons) inside the conduction-to-valence bandgap. The intermediate side bands in $RENiO_3$ are represented by $3d^8\underline{L}$ states consisting of hybridized trapped ligand holes and Ni orbitals. Upon electron doping, the electrons fill the available trapped hole states in the intermediate band and thus significantly alter the Ni-O hybridization. Instead of the shift in the Fermi level, the doping alters the band structure where the density of state of

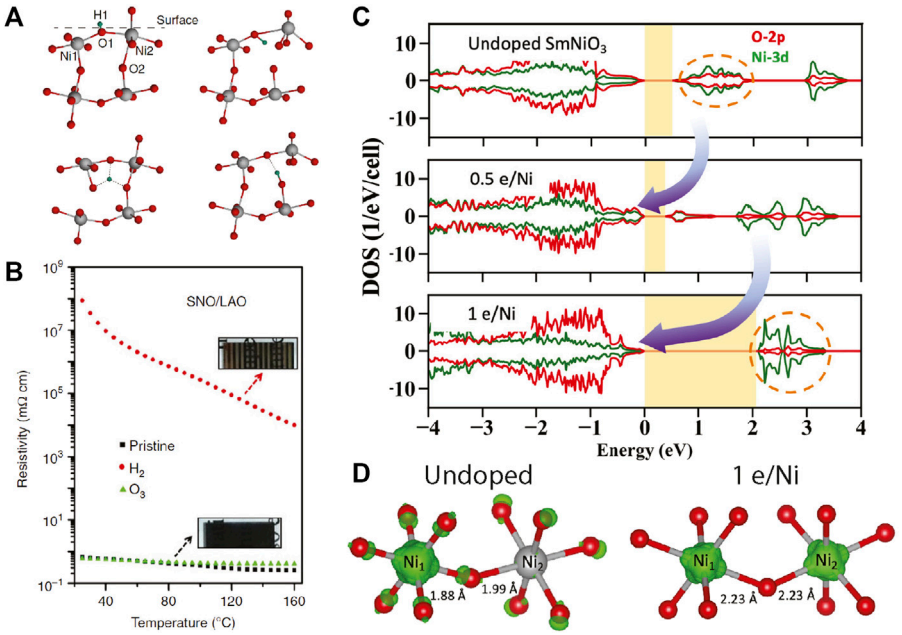

FIGURE 1 | (A) The diffusive ionic intercalation process exemplified by hydrogen. The proton (H+, in green) mainly bonds with oxygen and undergoes diffusive rotation and transfer onto neighboring oxygen ions [35]. **(B)** Resistivity versus temperature for the pristine (black), hydrogen-intercalated (red), and ozone-annealed (green) $SmNiO_3$ thin films grown on $LaAlO_3$ substrates (SNO/LAO). The resistivity increases by eight orders of magnitude upon doping [19]. **(C)** Density of states of undoped and electron-doped $SmNiO_3$. **(D)** The squared modulus of the unoccupied intermediated band wavefunctions (green isosurfaces) [dashed-circles in **(D)**] [38].

the intermediate side band diminishes and restores the pure O-2p and Ni-3d character of the conduction and valence band. This mechanism increases the effective band gap and leads to extraordinary resistive switching [1].

This interpretation was supported by the DFT calculations in electron doped $SmNiO_3$ and $YNiO_3$ by two different groups [38–40]. As shown in **Figure 1**, in the undoped compound, the intermediate band is composed of Ni-3d and O-2p states with a gap size of ~0.5 eV. Upon doping, the doped electrons selectively fill the ligand hole states, transferring the unoccupied intermediate in-gap density of states to the valence band below. The gap is widened to 2–3 eV with no oxygen ligand holes, suggesting a positive charge transfer system upon doping.

DOPING *VIA* OXYGEN VACANCIES

Similar to ion-intercalated nickelates, creating oxygen vacancies is an alternative chemical route to introduce carriers into nickelates *via* charge compensation. Since Ni^{3+} is chemically less stable than Ni^{2+}, the synthesis of stoichiometric $RENiO_3$ polycrystalline ceramics requires high temperatures and high oxygen pressures. Failure to meet the synthesis criteria (whether undoped compound or intentionally oxygen-deficient compounds) often results in cation and oxygen off-stoichiometry issues, manifested by substantial deviations and broadening in the metal-insulator transition temperature and its reproducibility [41–44].

Recently, with the development of the topotactic reduction technique, high-quality $RENiO_3$ thin films with precise-controlled oxygen vacancy concentration could be produced [45, 46]. Studies have shown that the oxygen vacancies can induce novel forms of electronic symmetry breaking including unconventional superconductivity in the infinite-layer nickelates $RENiO_2$ (where Ni is in a 1+ state [45]). Such precise control over the oxygen concentration provides another avenue to tune the physical properties of $RENiO_{3-x}$ in the small x limit.

Studies of oxygen-deficient films have shown phenomena similar to other electron-doped $RENiO_3$, in particular the dramatic increase of the resistance similar to the colossal resistive switching achieved *via* ionic intercalation [46, 47]. Moreover, oxygen-deficient $RENiO_3$ can be used as an ionic voltage-driven switch. By applying a bias voltage, the oxygen vacancies can be driven toward the electrode to realize a high resistance state. With a reversed bias voltage, the oxygen vacancies redistribute and are pushed away from the electrode, and the device returns to the low resistance state [46]. Numerous intermediate states can be achieved by controlling the strength of the electric field. Although the local oxygen defect concentration can be modified by the electric field, it has been shown that the oxygen vacancies do not aggregate into clusters segregating the undoped/doped domains [47].

Unlike ion intercalation, doping through oxygen vacancies more severely alters the local crystal structure. Depending on the density and distribution of the oxygen vacancies, the Ni local symmetry can be lowered to square pyramidal, square planar and tetrahedral, which leads to a dramatic change in the crystal field splitting (**Figure 2A**). DFT calculations on these Ni-O local electronic structures have shown a smaller contribution from

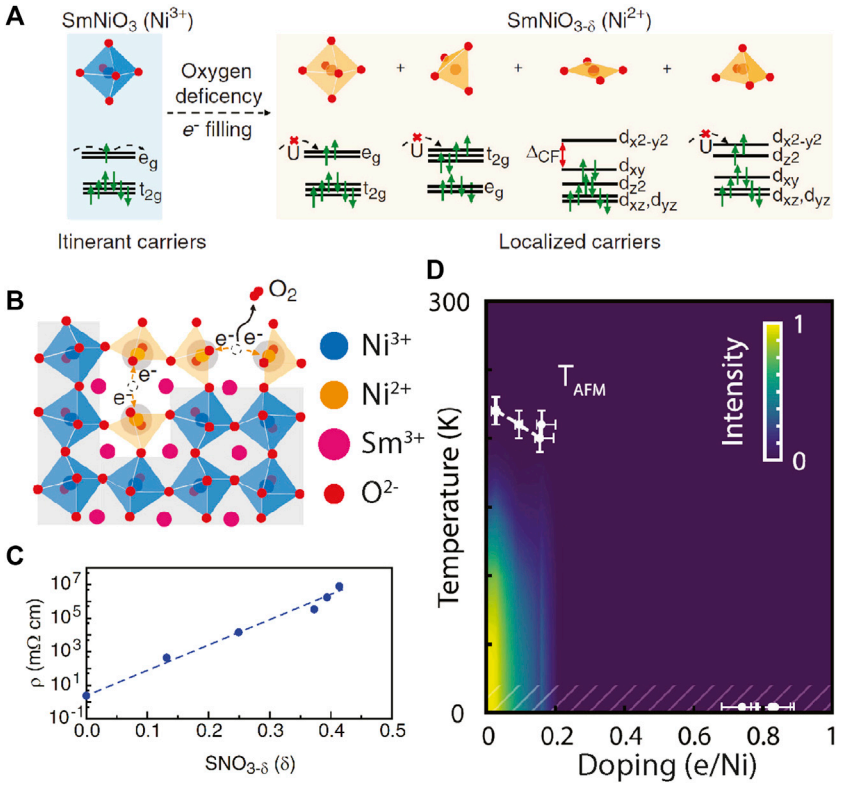

FIGURE 2 | (A) Illustration of how oxygen vacancies modify the local crystal field splitting of Ni 3d orbitals, together with the doping effect, leading to opening of the bandgap and resistive switching [46]. **(B)** Oxygen vacancy formation changes the local symmetry from octahedral to lower-than-cubic. **(C)** Electrical resistivity at room temperature as a function of oxygen deficiency level in SNO_{3-x}. The resistance can be tuned over eight orders of magnitude. **(D)** Temperature-doping plot of the magnetic phase diagram in $SmNiO_{3-x}$. The magnitude of the antiferromagnetic order parameter is color coded in the background [47].

unoccupied Ni-3d and O-2p $3d^8\underline{L}$ hybridized states. These states are transferred from the bottom of the conduction band to the top of the valence band. The unoccupied states with Ni^{2+} are also pushed up in energy, resulting in a 2–3 eV bandgap that characterizes the insulating nature of the doped nickelates [46, 48, 49]. Such a transfer of electronic states was also observed experimentally, where the low-energy density of states near the Fermi energy is continuously shifted to the high energy states in response to the doping changes [50].

The introduction of oxygen vacancies has been shown to also modify the magnetic properties of $RENiO_3$. The latter were recently explored in $SmNiO_{3-x}$ and $NdNiO_{3-x}$ [47]. Despite the fact that doping linearly suppresses the strength of the (1/4, 1/4, 1/4) antiferromagnetic state, the magnetic properties (correlation length, transition temperature, etc.) are remarkably robust to substantial levels of carrier doping up to a doping threshold of x~0.1 where magnetic order collapses without an accompanying structural transition (**Figure 2D**).

There is also evidence of emergent magnetic order in oxygen-deficient nickelates. The parent compound of $LaNiO_3$ stands out as the only member in the $RENiO_3$ family that remains metallic and paramagnetic down to low temperature. The recent reports on the synthesis of the bulk $LaNiO_3$ single crystals have shown an unexpected antiferromagnetic order below 157K with ordering wave vector consistent to (1/4, 1/4, 1/4) as in other $RENiO_3$ [51]. However, it was inconclusive whether this antiferromagnetic order in $LaNiO_3$ discovered by Ref. [51] is intrinsic or resulted from extrinsic oxygen defects, as other studies have shown that magnetic order (ferro- and antiferromagnetic) could arise upon intentional introduction of the oxygen vacancies [52, 53].

CATION DOPING AND OTHERS

Carrier doping can further be obtained by A-site substitution of the 3+ rare earth ions by other divalent (typically Sr^{2+}, Ca^{2+}) or tetravalent elements (Th^{4+}, Ce^{4+}). Divalent doping adds holes while tetravalent doping adds electrons into $RE_{1-x}A_xNiO_3$, changing the formal valence of Ni to (3+x) and (3-x), respectively. Studies have shown that the metal-to-insulator transition temperature is rapidly suppressed upon cation substitution ($x < 0.1$) [54–58], despite the type of dopants.

The goal of cation doping is to separate the genuine electronic carrier doping effect from steric contribution arising from the change of the A-site ionic radius. In the seminal study by García-Muñoz Ref. [54], by accounting for the size changes of the dopants, they have found that both electron and hole doping suppress the insulating phases by cationic doping (Sr, Ca, Th, Ce) with asymmetric suppression rates for the metal-insulator

transition temperature (T_{MI}): hole doping is more effective than electron doping to suppress T_{MI} with the rate:

$$(\partial T_{MI}/x)_{holes} \sim 3 \times (\partial T_{MI}/x)_{electrons}$$

Since both doping routines lead to a suppression of T_{MI}, the doped carriers are more likely to create a new in-gap state rather than causing a rigid-band shift [54]. The origin of the electron-hole asymmetry is naturally attributed to the hybridization of Ni-O bands. Such a trend is in contrast with the tendency towards strong insulating state upon electron doping via ion intercalation or oxygen removal as described in the previous sections. A possible explanation is that the latter doping processes alter the material at a very local scale, drastically altering the electronic potential in the vicinity of the added (or missing) atom and reducing the local symmetry and potentially the bonding environment. Conversely, cation substitution largely preserves the coordination, leading to a less drastic alteration of the local environment. For carriers introduced in a high symmetry environment, the wavefunction can be more extended in space and thus lead to more delocalized, itinerant states, promoting metallic behavior. Charge compensation mechanism studies and local structure analysis should be carried out in future to better understand the doping processes. The magnetic properties of the cation doped $RENiO_3$ are yet to be explored.

It is worth mentioning that there are also other methods of doping the $RENiO_3$, such as electrostatic gating [59, 60], ionic liquid gating [61–63], and fluorine substitution [64], which are capable of changing the charge carrier density, resistance level, and transition temperature of $RENiO_3$.

CONCLUSION AND OUTLOOK

Carrier doping has historically been a powerful tuning parameter in the exploration of the rich physics of strongly correlated quantum material. We have summarized recent studies of carrier doping effects in the rare earth nickelates $RENiO_3$ and the resulting unconventional phenomena, including giant resistive switching, the antidoping mechanism, the fast and reversible switching of the Ni valence and ligand electronic state, the doping evolution of the coupled electronic and magnetic ground state, and emergent quantum states (superconductivity). These phenomena would not be possible without convergent advances in highly controlled synthesis and doping protocols, and in characterization methods and theoretical modelling.

Doped nickelates also represent a promising platform for new functional devices owing to their high sensitivity to external perturbations. A wide range of proof-of-principle applications has been reported based on their novel electronic transport, magnetic, optical, catalytical, and energy storage/conversion properties. Based on these, major areas of application could be electronic/magnetic switching applications such as multistate switching memory devices for neuromorphic computing [28, 29, 34, 35, 63], optical and photonic modulation technologies [65], and high-density hydrogen storage [22].

At the same time, further studies are necessary to develop a deeper mechanistic understanding of the physics of doped nickelates and their practical applications across multiple scales. A major outstanding question is how the local atomic defects contribute to macroscopic transport properties. First principles calculations incorporating defects in large unit cells are necessary to understand how atomic-scale dopants influence the electronic band structure. At a higher scale, spatial cluster simulations can be helpful to understand the percolative nature of electronic conduction and its variable-range hopping nature. Despite limited studies on the magnetic properties in doped nickelates, more research efforts are needed to produce a unified picture of the magnetic properties and their nanoscale underpinnings. Moreover, a broader canvassing of the doping-temperature phase diagram could possibly unveil new collective states of matter, for example superconductivity at the far end of the electron doping axis (Ni d^9 configuration). On the application front, there are many opportunities that can be harnessed by a deeper understanding of the properties of doped nickelates. As an example, various open questions remain to be answered to assess the applicability of doped nickelates for non-Von Neuman architecture computation such as dynamics of multi-state switching; energy landscapes as a function of electron doping and percolation transport physics in inhomogeneous doped films.

AUTHOR CONTRIBUTIONS

All authors listed have made a substantial, direct, and intellectual contribution to the work and approved it for publication.

FUNDING

Work at MIT (JL and RC) was supported by the Air Force Office of Scientific Research Young Investigator Program under grant FA9550-19-1-0063. SR acknowledges AFOSR FA9550-19-1-0351 for support.

ACKNOWLEDGMENTS

We acknowledge Robert Green for many invaluable discussions.

REFERENCES

1. Zunger A, Malyi OI. Understanding Doping of Quantum Materials. *Chem Rev* (2021) 121:3031–60. doi:10.1021/acs.chemrev.0c00608
2. Ramirez AP. Colossal Magnetoresistance. *J Phys Condens Matter* (1997) 9: 8171–99. doi:10.1088/0953-8984/9/39/005
3. Keimer B, Kivelson SA, Norman MR, Uchida S, Zaanen J. From Quantum Matter to High-Temperature Superconductivity in Copper Oxides. *Nature* (2015) 518:179–86. doi:10.1038/nature14165

4. Janod E, Tranchant J, Corraze B, Querré M, Stoliar P, Rozenberg M, et al. Resistive Switching in Mott Insulators and Correlated Systems. *Adv Funct Mater* (2015) 25:6287–305. doi:10.1002/adfm.201500823
5. Dagotto E. Complexity in Strongly Correlated Electronic Systems. *Science* (2005) 309:257–62. doi:10.1126/science.1107559
6. Sleight AW. Bismuthates: $BaBiO_3$ and Related Superconducting Phases. *Physica C: Superconductivity its Appl* (2015) 514:152–65. doi:10.1016/j.physc.2015.02.012
7. Catalano S, Gibert M, Fowlie J, Íñiguez J, Triscone J-M, Kreisel J. Rare-earth Nickelates $RNiO_3$: Thin Films and Heterostructures. *Rep Prog Phys* (2018) 81:046501. doi:10.1088/1361-6633/aaa37a
8. Catalan G. Progress in Perovskite Nickelate Research. *Phase Transitions* (2008) 81:729–49. doi:10.1080/01411590801992463
9. Zaanen J, Sawatzky GA, Allen JW. Band Gaps and Electronic Structure of Transition-Metal Compounds. *Phys Rev Lett* (1985) 55:418–21. doi:10.1103/physrevlett.55.418
10. Bisogni V, Catalano S, Green RJ, Gibert M, Scherwitzl R, Huang Y, et al. Ground-state Oxygen Holes and the Metal-Insulator Transition in the Negative Charge-Transfer Rare-Earth Nickelates. *Nat Commun* (2016) 7:13017. doi:10.1038/ncomms13017
11. Johnston S, Mukherjee A, Elfimov I, Berciu M, Sawatzky GA. Charge Disproportionation without Charge Transfer in the Rare-Earth-Element Nickelates as a Possible Mechanism for the Metal-Insulator Transition. *Phys Rev Lett* (2014) 112:106404. doi:10.1103/physrevlett.112.106404
12. Medarde M, Fontaine A, García-Muñoz JL, Rodríguez-Carvajal J, de Santis M fnm, Sacchi M, et al. $RNiO_3$ Perovskites (R=Pr,Nd): Nickel Valence and the Metal-Insulator Transition Investigated by x-ray-absorption Spectroscopy. *Phys Rev B Condens Matter* (1992) 46:14975–84. doi:10.1103/physrevb.46.14975
13. Scagnoli V, Staub U, Bodenthin Y, García-Fernández M, Mulders AM, Meijer GI, et al. Induced Noncollinear Magnetic Order of Nd^{3+} in $NdNiO_3$ Observed by Resonant Soft X-ray Diffraction. *Phys Rev B* (2008) 77:115138. doi:10.1103/physrevb.77.115138
14. Frano A, Schierle E, Haverkort MW, Lu Y, Wu M, Blanco-Canosa S, et al. Orbital Control of Noncollinear Magnetic Order in Nickel Oxide Heterostructures. *Phys Rev Lett* (2013) 111:106804. doi:10.1103/physrevlett.111.106804
15. Hepting M, Green RJ, Zhong Z, Bluschke M, Suyolcu YE, Macke S, et al. Complex Magnetic Order in Nickelate Slabs. *Nat Phys* (2018) 14:1097–102. doi:10.1038/s41567-018-0218-5
16. Gaecía-Muñoz JL, Rodríguez-Carvajal J, Lacorre P. Sudden Appearance of an Unusual Spin Density Wave at the Metal-Insulator Transition in the Perovskites $RNiO_3$ (R = Pr, Nd). *Epl* (1992) 20:241–7. doi:10.1209/0295-5075/20/3/009
17. Klein YM, Kozłowski M, Linden A, Lacorre P, Medarde M, Gawryluk DJ. $RENiO_3$ Single Crystals (RE = Nd, Sm, Gd, Dy, Y, Ho, Er, Lu) Grown from Molten Salts under 2000 Bar of Oxygen Gas Pressure. *Cryst Growth Des* (2021) 21:4230–41. doi:10.1021/acs.cgd.1c00474
18. Middey S, Chakhalian J, Mahadevan P, Freeland JW, Millis AJ, Sarma DD. Physics of Ultrathin Films and Heterostructures of Rare-Earth Nickelates. *Annu Rev Mater Res* (2016) 46:305–34. doi:10.1146/annurev-matsci-070115-032057
19. Shi J, Zhou Y, Ramanathan S. Colossal Resistance Switching and Band gap Modulation in a Perovskite Nickelate by Electron Doping. *Nat Commun* (2014) 5:4860. doi:10.1038/ncomms5860
20. Sun Y, Kotiuga M, Lim D, Narayanan B, Cherukara M, Zhang Z, et al. Strongly Correlated Perovskite Lithium Ion Shuttles. *Proc Natl Acad Sci USA* (2018) 115:9672–7. doi:10.1073/pnas.1805029115
21. Zhang Z, Schwanz D, Narayanan B, Kotiuga M, Dura JA, Cherukara M, et al. Perovskite Nickelates as Electric-Field Sensors in Salt Water. *Nature* (2017) 553:68–72. doi:10.1038/nature25008
22. Zhou Y, Guan X, Zhou H, Ramadoss K, Adam S, Liu H, et al. Strongly Correlated Perovskite Fuel Cells. *Nature* (2016) 534:231–4. doi:10.1038/nature17653
23. Kreuer K-D. Proton Conductivity: Materials and Applications. *Chem Mater* (1996) 8:610–41. doi:10.1021/cm950192a
24. Sidik U, Hattori AN, Rakshit R, Ramanathan S, Tanaka H. Catalytic Hydrogen Doping of $NdNiO_3$ Thin Films under Electric Fields. *ACS Appl Mater Inter* (2020) 12:54955–62. doi:10.1021/acsami.0c15724
25. Chen J, Mao W, Ge B, Wang J, Ke X, Wang V, et al. Revealing the Role of Lattice Distortions in the Hydrogen-Induced Metal-Insulator Transition of $SmNiO_3$. *Nat Commun* (2019) 10:694–8. doi:10.1038/s41467-019-08613-3
26. Chen J. Self-limited Kinetics of Electron Doping in Correlated Oxides. *Appl Phys Lett* (2015) 107:031905. doi:10.1063/1.4927322
27. Zaluzhnyy IA. Proton Distribution Visualization in Perovskite Nickelate Devices Utilizing Nanofocused X Rays. *Phys Rev Mater* (2021) 5:095003. doi:10.1103/physrevmaterials.5.095003
28. Zuo F, Panda P, Kotiuga M, Li J, Kang M, Mazzoli C, et al. Habituation Based Synaptic Plasticity and Organismic Learning in a Quantum Perovskite. *Nat Commun* (2017) 8:240. doi:10.1038/s41467-017-00248-6
29. Shi J, Ha SD, Zhou Y, Schoofs F, Ramanathan S. A Correlated Nickelate Synaptic Transistor. *Nat Commun* (2013) 4:2676–9. doi:10.1038/ncomms3676
30. Oh C, Heo S, Jang HM, Son J. Correlated Memory Resistor in Epitaxial $NdNiO_3$ Heterostructures with Asymmetrical Proton Concentration. *Appl Phys Lett* (2016) 108:122106. doi:10.1063/1.4944842
31. Ramadoss K. Proton-Doped Strongly Correlated Perovskite Nickelate Memory Devices. *IEEE Electron Device Lett* (2018) 39:1500–3. doi:10.1109/led.2018.2865776
32. Zhang HT, Zuo F, Li F, Chan H, Wu Q, Zhang Z, et al. Perovskite Nickelates as Bio-Electronic Interfaces. *Nat Commun* (2019) 10:1651–7. doi:10.1038/s41467-019-09660-6
33. Sun Y, Nguyen TNH, Anderson A, Cheng X, Gage TE, Lim J, et al. *In Vivo* Glutamate Sensing inside the Mouse Brain with Perovskite Nickelate-Nafion Heterostructures. *ACS Appl Mater Inter* (2020) 12:24564–74. doi:10.1021/acsami.0c02826
34. Zhang HT. Organismic materials for beyond von Neumann machines. *Appl Phys Rev* (2020) 7:011309. doi:10.1063/1.5113574
35. Zhang HT, Park TJ, Zaluzhnyy IA, Wang Q, Wadekar SN, Manna S, et al. Perovskite Neural Trees. *Nat Commun* (2020) 11:2245–9. doi:10.1038/s41467-020-16105-y
36. Catalano S, Gibert M, Fowlie J, Íñiguez J, Triscone JM, Kreisel J. Rare-earth Nickelates $RNiO_3$: Thin Films and Heterostructures. *Rep Prog Phys* (2018) 81:046501. doi:10.1088/1361-6633/aaa37a
37. Torrance J, Lacorre P, Nazzal A, Ansaldo E, Niedermayer C. Systematic Study of Insulator-Metal Transitions in Perovskites RNiO3 (R=Pr,Nd,Sm,Eu) Due to Closing of Charge-Transfer gap. *Phys Rev B* (1992) 45:8209–12. doi:10.1103/physrevb.45.8209
38. Liu Q, Dalpian GM, Zunger A. Antidoping in Insulators and Semiconductors Having Intermediate Bands with Trapped Carriers. *Phys Rev Lett* (2019) 122:106403. doi:10.1103/physrevlett.122.106403
39. Kotiuga M, Rabe KM. High-density Electron Doping of $SmNiO_3$ from First Principles. *Phys Rev Mater* (2019) 3:115002. doi:10.1103/physrevmaterials.3.115002
40. Malyi OI, Zunger A. Hole Antidoping of Oxides. *Phys Rev B* (2020) 101:235202. doi:10.1103/physrevb.101.235202
41. Preziosi D, Sander A, Barthélémy A, Bibes M. Reproducibility and Off-Stoichiometry Issues in Nickelate Thin Films Grown by Pulsed Laser Deposition. *AIP Adv* (2017) 7:015210. doi:10.1063/1.4975307
42. Breckenfeld E, Chen Z, Damodaran AR, Martin LW. Effects of Nonequilibrium Growth, Nonstoichiometry, and Film Orientation on the Metal-To-Insulator Transition in $NdNiO_3$ Thin Films. *ACS Appl Mater Inter* (2014) 6:22436–44. doi:10.1021/am506436s
43. Nikulin IV, Novojilov MA, Kaul AR, Mudretsova SN, Kondrashov SV. Oxygen Nonstoichiometry of $NdNiO_{3-\delta}$ and $SmNiO_{3-\delta}$. *Mater Res Bull* (2004) 39:775–91. doi:10.1016/j.materresbull.2004.02.005
44. Hauser AJ. Correlation between Stoichiometry, Strain, and Metal-Insulator Transitions of $NdNiO_3$ Films. *Appl Phys Lett* (2015) 106:092104. doi:10.1063/1.4914002
45. Li D, Lee K, Wang BY, Osada M, Crossley S, Lee HR, et al. Superconductivity in an Infinite-Layer Nickelate. *Nature* (2019) 572:624–7. doi:10.1038/s41586-019-1496-5
46. Kotiuga M, Zhang Z, Li J, Rodolakis F, Zhou H, Sutarto R, et al. Carrier Localization in Perovskite Nickelates from Oxygen Vacancies. *Proc Natl Acad Sci USA* (2019) 116:21992–7. doi:10.1073/pnas.1910490116
47. Li J, Green RJ, Zhang Z, Sutarto R, Sadowski JT, Zhu Z, et al. Sudden Collapse of Magnetic Order in Oxygen-Deficient Nickelate Films. *Phys Rev Lett* (2021) 126:187602. doi:10.1103/physrevlett.126.187602
48. Iglesias L, Bibes M, Varignon J. First-principles Study of Electron and Hole Doping Effects in Perovskite Nickelates. *Phys Rev B* (2021) 104:035123. doi:10.1103/physrevb.104.035123

49. Espinosa-García WF, Dalpian GM. Influence of Defects on Antidoping Behavior in $SmNiO_3$. *Phys Rev B* (2021) 104:205106. doi:10.1103/PhysRevB.104.205106
50. Jaramillo R, Ha SD, Silevitch DM, Ramanathan S. Origins of Bad-Metal Conductivity and the Insulator-Metal Transition in the Rare-Earth Nickelates. *Nat Phys* (2014) 10:304–7. doi:10.1038/nphys2907
51. Guo H, Li ZW, Zhao L, Hu Z, Chang CF, Kuo CY, et al. Antiferromagnetic Correlations in the Metallic Strongly Correlated Transition Metal Oxide $LaNiO_3$. *Nat Commun* (2018) 9:43. doi:10.1038/s41467-017-02524-x
52. Wang BX. Antiferromagnetic Defect Structure in $LaNiO_{3-\delta}$ Single Crystals. *Phys Rev Mater* (2018) 2:064404. doi:10.1103/physrevmaterials.2.064404
53. Sânchez RD. Metal-insulator Transition in Oxygen-Deficient $LaNiO_{3-x}$. Perovskites. *Phys Rev B-condensed Matter* (1996) 54:16574–8. doi:10.1103/physrevb.54.16574
54. García-Muñoz JL, Suaaidi M, Martínez-Lope MJ, Alonso JA. Influence of Carrier Injection on the Metal-Insulator Transition in Electron- and Hole-Doped $R_{1-x}A_xNiO_3$ Perovskites. *Phys Rev B* (1995) 52:13563–9. doi:10.1103/physrevb.52.13563
55. Xiang PH. Room Temperature Mott Metal-Insulator Transition and its Systematic Control in $Sm_{1-x}Ca_xNiO_3$ Thin Films. *Appl Phys Lett* (2010) 97:032114. doi:10.1063/1.3467199
56. Wang L, Chang L, Yin X, Rusydi A, You L, Zhou Y, et al. Localization-driven Metal-Insulator Transition in Epitaxial Hole-Doped $Nd_{1-X}Sr_XNiO_3$ Ultrathin Films. *J Phys Condens Matter* (2017) 29:025002–6. doi:10.1088/0953-8984/29/2/025002
57. Wang BX. Synthesis and Characterization of Bulk $Nd_{1-x}Sr_xNiO_2$ and $Nd_{1-x}Sr_xNiO_3$. *Phys Rev Mater* (2020) 4:084409. doi:10.1103/physrevmaterials.4.084409
58. Yang H, Wen Z, Cui Y, Chen Y, Zhao Y. The Preparation, Structure, and Metal-Insulator Transition in Bulk $Nd_{1-x}Ca_xNiO_3$ (X = 0 ~ 0.3). *J Supercond Nov Magn* (2021) 34:2339–47. doi:10.1007/s10948-021-05929-4
59. Ha SD, Vetter U, Shi J, Ramanathan S. Electrostatic Gating of Metallic and Insulating Phases in $SmNiO_3$ Ultrathin Films. *Appl Phys Lett* (2013) 102:183102. doi:10.1063/1.4804142
60. Son J. Probing the Metal-Insulator Transition of $NdNiO_3$ by Electrostatic Doping. *Appl Phys Lett* (2011) 99:192107. doi:10.1063/1.3659310
61. Asanuma S. Tuning of the Metal-Insulator Transition in Electrolyte-Gated $NdNiO_3$ Thin Films. *Appl Phys Lett* (2010) 97:142110. doi:10.1063/1.3496458
62. Scherwitzl R, Zubko P, Lezama IG, Ono S, Morpurgo AF, Catalan G, et al. Electric-field Control of the Metal-Insulator Transition in Ultrathin $NdNiO_3$ Films. *Adv Mater* (2010) 22:5517–20. doi:10.1002/adma.201003241
63. Zhang HT. Beyond Electrostatic Modification: Design and Discovery of Functional Oxide Phases via Ionic-Electronic Doping. *Adv Phys X* (2019) 4:1523686. doi:10.1080/23746149.2018.1523686
64. Onozuka T, Chikamatsu A, Katayama T, Hirose Y, Harayama I, Sekiba D, et al. Reversible Changes in Resistance of Perovskite Nickelate $NdNiO_3$ Thin Films Induced by Fluorine Substitution. *ACS Appl Mater Inter* (2017) 9:10882–7. doi:10.1021/acsami.7b00855
65. Shahsafi A, Roney P, Zhou Y, Zhang Z, Xiao Y, Wan C, et al. Temperature-independent thermal Radiation. *Proc Natl Acad Sci USA* (2019) 116:26402–6. doi:10.1073/pnas.1911244116

Conflict of Interest: The authors declare that the research was conducted in the absence of any commercial or financial relationships that could be construed as a potential conflict of interest.

Publisher's Note: All claims expressed in this article are solely those of the authors and do not necessarily represent those of their affiliated organizations, or those of the publisher, the editors and the reviewers. Any product that may be evaluated in this article, or claim that may be made by its manufacturer, is not guaranteed or endorsed by the publisher.

frontiers in Physics

ORIGINAL RESEARCH
published: 21 February 2022
doi: 10.3389/fphy.2022.834682

Magnetic Properties and Pseudogap Formation in Infinite-Layer Nickelates: Insights From the Single-Band Hubbard Model

Marcel Klett[1]*, *Philipp Hansmann*[2] *and Thomas Schäfer*[1]

[1]Max-Planck-Institut für Festkörperforschung, Stuttgart, Germany, [2]Department of Physics, Friedrich-Alexander-University (FAU) Erlangen-Nürnberg, Erlangen, Germany

We study the magnetic and spectral properties of a single-band Hubbard model for the infinite-layer nickelate compound $LaNiO_2$. As spatial correlations turn out to be the key ingredient for understanding its physics, we use two complementary extensions of the dynamical mean-field theory to take them into account: the cellular dynamical mean-field theory and the dynamical vertex approximation. Additionally to the systematic analysis of the doping dependence of the non-Curie-Weiss behavior of the uniform magnetic susceptibility, we provide insight into its relation to the formation of a pseudogap regime by the calculation of the one-particle spectral function and the magnetic correlation length. The latter is of the order of a few lattice spacings when the pseudogap opens, indicating a strong-coupling pseudogap formation in analogy to cuprates.

Keywords: nickelates, magnetism, pseudogap, hubbard model, dynamical mean-field theory (DMFT), dynamical vertex approximation, cellular dynamical mean field theory

OPEN ACCESS

Edited by:
Danfeng Li,
City University of Hong Kong, Hong Kong SAR, China

Reviewed by:
Sergio Ciuchi,
University of L'Aquila, Italy
Heron Carlos De Godoy Caldas,
Universidade Federal de São João del-Rei, Brazil

***Correspondence:**
Marcel Klett
m.klett@fkf.mpg.de

Specialty section:
This article was submitted to Condensed Matter Physics, a section of the journal Frontiers in Physics

Received: *13 December 2021*
Accepted: *14 January 2022*
Published: *21 February 2022*

Citation:
Klett M, Hansmann P and Schäfer T (2022) Magnetic Properties and Pseudogap Formation in Infinite-Layer Nickelates: Insights From the Single-Band Hubbard Model. Front. Phys. 10:834682. doi: 10.3389/fphy.2022.834682

INTRODUCTION

With the discovery of superconductivity in Sr-doped $NdNiO_2$ in 2018 [1] it is likely that a new branch of the family of unconventional superconductors (i.e. with non-phonon mediated pairing) was revealed. At this time nickelates, as bulk materials and heterostructures, have already been in the focus of an intense search for high-T_c cuprate anaolgue oxides for a while (see e.g. [2–9]). One of the current challenges is therefore to understand similarities and/or differences between nickelate and other unconventional superconductors like, e.g., cuprate-, organic-, iron pnictide-, and heavy-fermion compounds. While there is currently no consensus if these materials could be covered by a single theory, there are strong indications that for all of them purely electronic (in particular magnetic) fluctuations are at least part of the key to understand their pairing mechanism. Such fluctuations are also expected to be responsible for unusual observations above the critical temperature which for the high-T_c cuprates include non-Fermi liquid behaviour in 1) temperature dependence of resistivity (universal in all cuprates, e.g. [10, 11], and found also in organic- and iron pnictide-SC [12, 13] 2) magnetic susceptibilities which are neither Pauli- nor Curie-like but exhibit sharp drops at a new temperature scale commonly denoted T^* [14], and 3) partially (i.e. momentum dependently) gapped quasi-particle Fermi surfaces [15–17]. The region of these phenomena in the temperature/hole-doping phase diagram is commonly referred to as the "pseudogap" region.

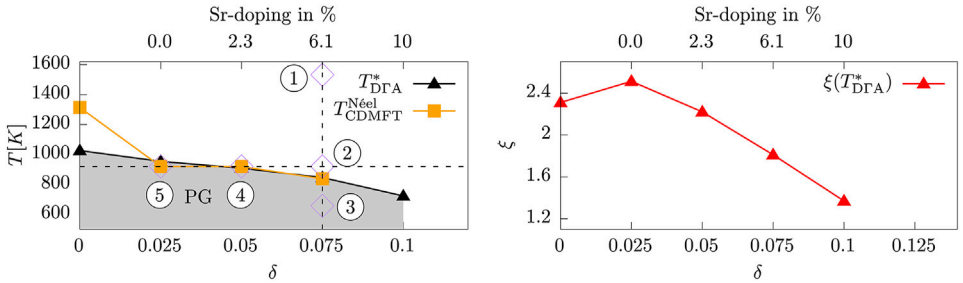

FIGURE 1 | Left: phase diagram of the Hubbard model given by **Eq. 1** as a function of temperature T and doping δ. T^* indicates the maximum of χ calculated in DΓA (black triangles). The orange squares indicate the magnetic ordering temperature in CDMFT $T^{Néel}_{CDMFT}$, signalling the onset of non-local correlations. The points—(diamonds) refer to **Figures 3**, **4**. Right: The correlation length ξ in units of lattice spacings is shown for the temperatures T^*.

Motivated by our recent combined experiment/theory multi-method study of the static uniform magnetic susceptibility χ in $LaNiO_2$ [18] and other recent experimental studies [19–21], in this manuscript we investigate deeper how the two-particle magnetic response is linked to one-particle spectra $A(\mathbf{k}, \omega)$ for different temperatures and different doping levels. With the help of complementary quantum many-body techniques, we show that the emergence of a maximum in χ is concomitant with a significant drop in the antinodal weight of $A(\mathbf{k} \approx (\pi, 0), \omega = \varepsilon_F)$ at the Fermi level. On the basis of these results we argue that - like cuprates - also nickelate superconductors feature a pseudogap region in their phase diagram.

The paper is organized as follows: in **Section 2** we introduce the effective single-band model of infinite-layer nickelates and a brief overview of the numerical methods used to analyze it. In **Section 3** we present our results starting with the temperature/doping phase diagram obtained from the maxima of χ (**Section 3.1**). Afterwards we show the one-particle spectral functions (**Section 3.2**) and provide magnetic correlation lengths as a function of temperature (**Section 3.3**). We conclude the paper in **Section 4** by commenting on the relevance of our findings to infinite-layer nickelates and their cuprate analogues.

MODEL AND METHODS

For our study we use the single-band repulsive Hubbard model [22–27] on a two-dimensional square lattice:

$$H = -\sum_{\langle i,j \rangle} \sum_{\sigma} t_{i,j}\, \hat{c}^{\dagger}_{i,\sigma} \hat{c}_{j,\sigma} - \mu \sum_{i} \sum_{\sigma} \hat{n}_{i,\sigma} + U \sum_{i} \hat{n}_{i,\uparrow} n_{i,\downarrow}, \qquad (1)$$

where σ is the spin of the electron, $\hat{c}^{\dagger}_{i,\sigma}$ ($\hat{c}_{i,\sigma}$) creates (annihilates) an electron on lattice site i with spin σ and $\hat{n}_{i,\sigma}$ is the number operator.

Such models has already been successfully applied in the description of the superconducting phase in $NdNiO_2$ [28–30] and the non-Curie-Weiss behavior of the magnetic susceptibility in $LaNiO_2$ [18]. The material realistic hopping parameters, resulting from a Wannier- and tight-binding projection are t = 395meV, $t' = -0.25t = -95$ meV, and $t'' = 0.12t = 47$ meV as well as the local Hubbard interaction $U = 8t = 3.16$ eV from a cRPA calculation [28]. All energies are given in units of eV except for temperatures, which are given in Kelvin. The chemical potential μ is adjusted to an average filling of $n = 1 - \delta$, where δ indicates the hole-doping of the single $d_{x^2-y^2}$ band. When relevant we will also give the corresponding level of Sr-doping.

We investigate the properties of the model in **Eq. 1** as a function of temperature T and doping δ by applying three numerical methods. Besides dynamical mean-field theory (DMFT) [31–34], which includes all temporal onsite-correlations of the lattice problem, we use two complementary extensions of it: cellular dynamical mean-field theory (CDMFT) [35] and the dynamical vertex approximation (DΓA) [36, 37], a diagrammatic extension of DMFT [38]. The combination of complementary numerical methods ("multi-method approach" [39, 40]) turned out to be very useful and versatile recently for both purely model- [39, 41] and material-based [18] studies.

For the present work we make use of this approach in order to study the influence of (non-local) magnetic fluctuations captured by the different approximations on different length scales. CDMFT is a conceptually simple real-space cluster extension of DMFT and controlled in the sense that it recovers the exact solution for infinite cluster sizes ($N_c \to \infty$). For finite N_c (for the present study we use $N_c = 4 \times 4$) it captures correlations up to the characteristic length scale of the cluster. For the DΓA we employ its ladder-version in the particle-hole (magnetic) channel with Moriyaesque λ-corrections in the spin channel [42–44]. This choice of the scattering channel greatly simplifies the algorithm (as it bypasses the general, but complicated, parquet treatment) and is justified in the pseudogap regime of the Hubbard model, where fluctuation diagnostics methods could demonstrate unequivocally the dominance of the spin channel on the single-particle spectrum [45–48].

Different from CDMFT, DΓA captures short- and long-range fluctuations in the magnetic channel on equal footing which, as previous studies have shown, is indispensable in the vicinity of second order phase transitions [49–52]. Moreover, DΓA respects the Mermin-Wagner theorem [53, 54] and shows no ordering instability at finite temperatures for our two-dimensional model **Eq. 1**. This is not the case for DMFT and CDMFT where the finite cluster size (for DMFT $N_c = 1$) leads to an antiferromagnetic phase transition at a finite Néel temperature $T^{Néel}$. We therefore

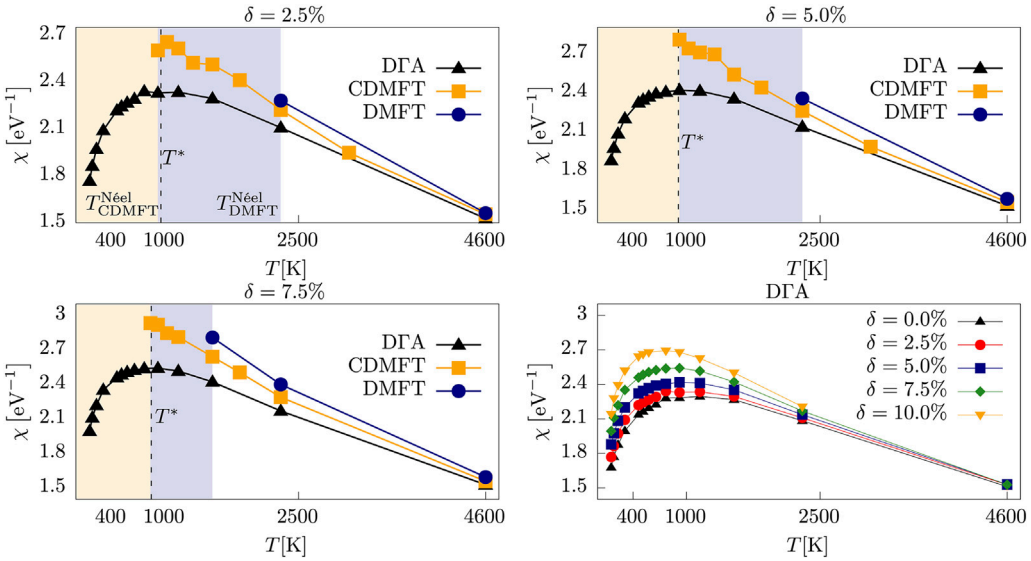

FIGURE 2 | Static uniform magnetic susceptibilities χ as a function of T for 2.5% (upper left panel), 5% (upper right panel) and 7.5% (lower left panel) hole doping. The transition temperature of DMFT $T^{\text{Néel}}_{\text{DMFT}}$ is indicated in blue and the DMFT-ordered regime in blue shadings (for CDMFT $T^{\text{Néel}}_{\text{CDMFT}}$ in orange). The lower right panel summarizes χ from DΓA for different hole dopings.

restrict ourselves to results obtained at temperatures above $T^{\text{Néel}}$ for these methods.

As impurity solver we use the latest generation of a continuous time quantum Monte-Carlo solver in its interaction expansion (CT-INT [55]) which is an application of the TRIQS package [56].

RESULTS

Phase Diagram and Uniform Susceptibilities

We start the presentation of our results by discussing the phase diagram of **Figure 1**, a summary of the data obtained by our different numerical techniques applied to **Eq. 1** as a function of doping (δ as the bottom horizontal axis, Sr-doping as the top one). In the left panel the black triangles represent the temperatures T^* where the static uniform magnetic susceptibility $\chi := \text{Re}\,\chi_{\text{m}}$ ($\mathbf{q} = (0, 0)$, $i\Omega_n = 0$) displays a maximum in DΓA. This temperature scale T^* is highest in the half-filled case and monotonously decreases with increasing doping. Interestingly, for the doped system, this line follows to very good agreement the magnetic ordering temperature of CDMFT $T^{\text{NeCel}}_{\text{CDMFT}}$, indicating the increased importance of non-local correlations. In the right panel we show the magnetic correlation length ξ (red triangles) calculated with DΓA for varying doping levels at the respective temperature T^*. $\xi(T^*)$ varies from around 1.2 to 2.5 lattice spacings (see also **Section 3.3**).

For the determination of T^* we turn to **Figure 2**, which shows χ calculated by DMFT (blue circles), CDMFT (orange squares) and DΓA (black triangles) for three representative levels of doping. The shaded areas indicate magnetically ordered phases of DMFT (below $T^{\text{Néel}}_{\text{DMFT}}$) and CDMFT (below $T^{\text{Néel}}_{\text{CDMFT}} < T^{\text{Néel}}_{\text{DMFT}}$), at the boundary of which the respective antiferromagnetic susceptibility diverges, indicating a second order phase transition. In contrast, as $T^{\text{Néel}}_{D\Gamma A} = 0$ we can trace χ obtained by DΓA down to the lowest temperatures allowed by the impurity solver. Here, we determine its maximum at $T^*_{D\Gamma A}$ (shown as a black dashed line) by a third order polynomial fit of the numerical data. Please note that an additional hopping in c-direction would lift the constraint of the Mermin-Wagner theorem also for DΓA and lead to long-range order [49, 50]. Also please note that disorder [18], affecting the transition temperature, is neglected in this study. Overall we see that $\chi_{\text{DMFT}} > \chi_{\text{CDMFT}} > \chi_{D\Gamma A}$ which can be attributed to the increasing consideration of longer-ranged correlations in the approximation. Next we observe that hole-doping away from half-filling reduces $T^{\text{Néel}}_{\text{DMFT}}$ [50] and $T^{\text{Néel}}_{\text{CDMFT}}$ [57, 58] (for the cluster size dependence of $T^{\text{Néel}}_{\text{CDMFT}}$ see [59]). In DΓA, instead, the doping leads to a reduction of $T^*_{D\Gamma A}$ as highlighted in the bottom right panel of **Figure 2**.

For all hole dopings considered in our nickelate model the flat maximum $\chi_{\text{max}} := \chi(T^*)$ is a clear indicator of non-Curie-Weiss (and non-Pauli) behavior [18, 58, 60–62]. In high-T_c cuprates such behavior is also seen in the suppression of the nuclear magnetic resonance (NMR) Knight shift [63], which is the original hallmark of the onset of the pseudogap phase [14]. Its second hallmark, observed in angle-resolved photoemission spectroscopy (ARPES [17]) is the non-isotropic suppression of spectral weight and emergence of Fermi arcs in the one-particle spectrum, which we investigate in the next section.

Spectral Functions

For the analysis of the one-particle spectral function $A(\mathbf{k}, \omega = 0) = -\frac{1}{\pi}\text{Im}\,G(\mathbf{k}, i\omega_n \to 0)$ in the paramagnetic phase we

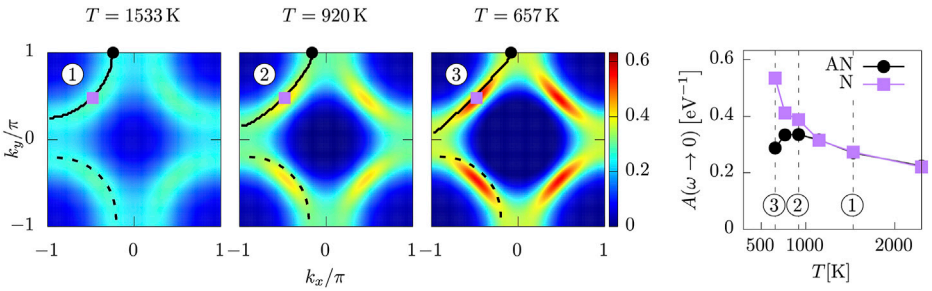

FIGURE 3 | Spectral intensities $A(\mathbf{k}, \omega = 0)$ for a constant doping of 7.5% and temperatures of 1533K, 920K, and 657K, calculated by DΓA. The black lines indicate the Fermi surfaces of the non-interacting case (dashed) and interacting case (solid) [for increased readability, these are only shown for one quadrant of the Brillouin zone]. The nodal (purple square)-antinodal (black circle) differentiation of the spectral weight together with the suppression of it at the antinode (right-hand panel) is a clear indication of a pseudogap.

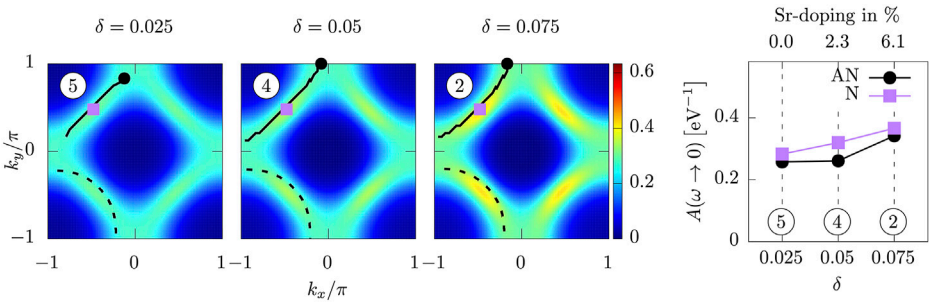

FIGURE 4 | Analogous plots to **Figure 3** at fixed T = 920 K for dopings 2.5%, 5%, and 7.5%.

restrict ourselves to a DΓA analysis. **Figure 3** shows the temperature evolution of $A(\mathbf{k}, \omega = 0)$ obtained by a linear fit of the first two Matsubara frequencies of the lattice Green function and extrapolation to zero frequency. Starting at the high-temperature point o at T = 1533 K we follow the *vertical* dashed line (i.e. at fixed 7.5% hole doping) in the T/δ phase diagram of **Figure 1**. At the highest temperature o both the spectral intensity (indicated by the color scale) as well as the interacting Fermi surface (solid black line) follow the (hole-like) shape of the non-interacting Fermi surface (dashed black line). The locations of the Fermi surface points have been obtained from the roots of the quasi-particle equation (QPE)

$$\tilde{\varepsilon}(\mathbf{k}) := \varepsilon(\mathbf{k}) - \mu + \mathrm{Re}\Sigma(\mathbf{k}, i\omega_n \to 0), \tag{2}$$

where $\varepsilon(\mathbf{k})$ is the non-interacting dispersion relation and $\Sigma(\mathbf{k}, i\omega_n)$ the self-energy from DΓA (which is zero in the non-interacting case).

Cooling the system across T^*, and passing 920 and 657 K, one first notices that the shape of the Fermi surface starts to deviate strongly from the non-interacting case. This can be attributed to self-energy effects stemming from non-local correlations. This behaviour is also in qualitative agreement with recent numerically exact diagrammatic Monte Carlo calculations [64] for smaller interactions. Second, at low temperatures, one can observe a clear Fermi arc structure of the spectral intensity. Third, the temperature dependence of the spectral weight at the antinode (black circle) starts to differ strongly from that of the node (purple square): At high temperatures, both values increase when the system is cooled. After reaching T^*, however, only the spectral weight at the node continues to grow, whereas at the antinode it starts to decrease. Together with the decrease in the uniform static magnetic susceptibility (see **Section 3.1**) this is an unequivocal indication of the onset of a pseudogap regime. Topologically at T^* the Fermi surface is hole-like, i.e. $\tilde{\varepsilon}(\mathbf{k} = (\pi, 0)) < 0$ in **Eq. 2**, in accordance with the finding of [65] that a pseudogap develops only for hole-like Fermi surface topologies. We also note that our results for T^* agree for small dopings with the ones obtained within the dynamical cluster approximation (DCA) on eight sites with similar model parameters [65], however, the drop with doping is less pronounced within the compared doping range for our data. We sense that this is an effect of both, slightly different model parameters and the DCA momentum patching, which for this model and small cluster sizes is not able to resolve the exact location of the antinode away from $\mathbf{k} = (\pi, 0)$. This resolution, however, is possible within DΓA so that the location of antinode and node can be precisely determined within the Brillouin zone [e.g. $\mathbf{k}_{\mathrm{AN}} = (\pi, 0.51)$ and $\mathbf{k}_{\mathrm{N}} = (1.51, 1.51)$ for].

In **Figure 4** we show the complementary evolution of the spectral intensity across the T^* line at fixed T = 920 K following the *horizontal* dashed line in phase diagram **Figure 1**. On can observe here that the progressive reduction of the doping from 7.5 to 2.5% leads to a significant drop of spectral intensity at both the node and the antinode and, eventually, to a mitigation of the nodal-antinodal differentiation. Furthermore, there is a strong

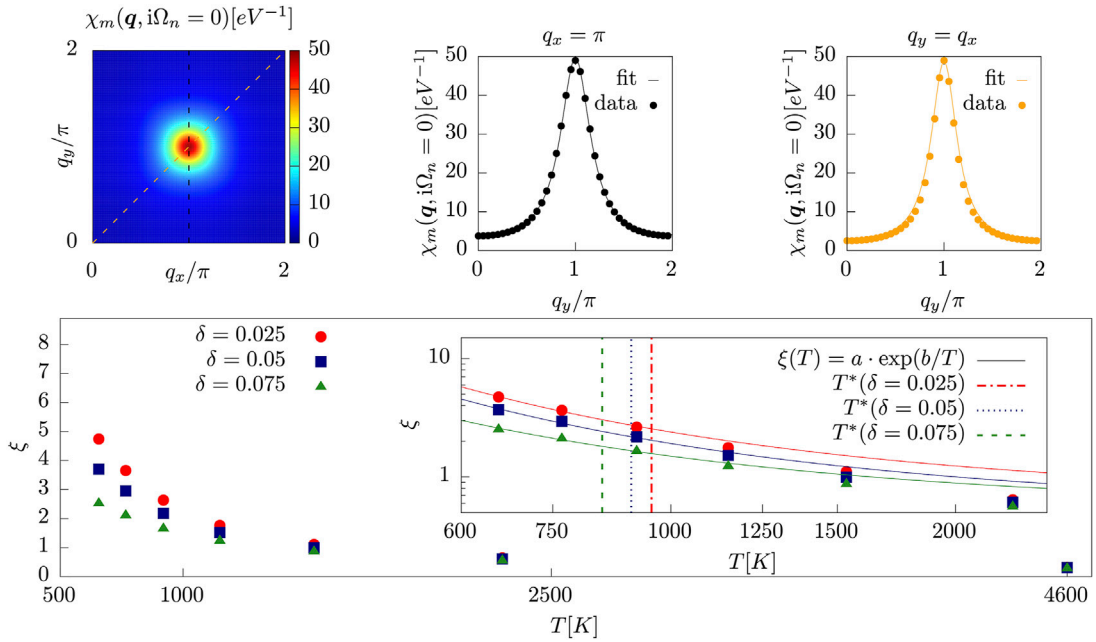

FIGURE 5 | Top, from left to right: $\chi_m(\mathbf{q}, i\Omega_n = 0)$, $\chi_m(\mathbf{q} = (q_x, \pi), i\Omega_n = 0)$, and $\chi_m(\mathbf{q} = (q_x, q_x), i\Omega_n = 0)$ for a doping of $\delta = 7.5\%$ and a temperature of 960K, calculated by DΓA. Circles denote calculated points, the solid line an Ornstein-Zernike fit by **Eq. 3**. Bottom: Correlation lengths ξ of DΓA plotted over the temperature for different dopings. The insets shows a double-logarithmic plot and temperature fits [see text and **Eq. 4**].

tendency visible toward a reconstruction of the topology of the Fermi surface from hole-like [$\tilde{\varepsilon}(\mathbf{k} = (\pi, 0)) < 0$, within the pseudogap regime] to electron-like [$\tilde{\varepsilon}(\mathbf{k} = (\pi, 0)) > 0$, at small dopings [65, 66]], what can be attributed to strong non-local spin fluctuations approaching half-filling, where the magnetic correlation length is increased (see also **Figure 1**, right-hand panel).

In order to investigate more closely the nature of the emerging pseudogap, in the next section we analyse the magnetic correlation length and the momentum-dependent magnetic response.

Momentum-dependent Susceptibility and Correlation Lengths

We first calculate the fully momentum-dependent static magnetic susceptibility $\chi_m(\mathbf{q}, i\Omega_n = 0)$ within DΓA. The top leftmost panel of **Figure 5** shows results for ($\delta = 7.5\%$ and $T = 960$ K), which is slightly above T^* for this doping. The maximum value of $\chi_m(\mathbf{q}, i\Omega_n = 0)$ is assumed at $\mathbf{q} = \mathbf{Q} = (\pi, \pi)$ at T^*. We note in passing that also incommensurate Néel order with $\mathbf{Q} \neq (\pi, \pi)$ may occur in different parameter regimes of the model [50, 62, 67, 68]. For obtaining the correlation length ξ we perform an Ornstein-Zernike fit with [39, 49, 69, 70].

$$\chi_m(\mathbf{q}, i\Omega_n = 0) = \frac{A}{4\sin^2\left(\frac{q_x - Q_x}{2}\right) + 4\sin^2\left(\frac{q_y - Q_y}{2}\right) + \xi^{-2}} \overset{\mathbf{q}\to\mathbf{Q}}{\to} \mathbf{q} \to \mathbf{Q} \frac{A}{(\mathbf{q} - \mathbf{Q})^2 + \xi^{-2}}, \quad (3)$$

where $\mathbf{Q}$ denotes the momentum vector where the susceptibility assumes its maximum value. Assuming this functional form for the fit is justified by two exemplary fits in the momentum directions $\mathbf{q} = (q_x, \pi)$ and $\mathbf{q} = (q_x, q_x)$ shown in the upper center and right panels of **Figure 5**. The so-obtained temperature dependence of ξ for several dopings is plotted in the lower panel of **Figure 5**. For small dopings we fit this dependence with

$$\xi = \xi_0 e^{2\pi\rho_S/T} \quad (4)$$

(with ρ_S being the spin stiffness), characteristic of a low-T gapped regime in two dimensions. The fit works reasonably well for temperatures $T < T^*$, hinting towards a magnetically ordered ground state in DΓA for the dopings investigated.

As already commented in the discussion of **Figure 1**, the correlation lengths at the pseudogap temperature T^* range from 1.2 to about 2 lattice spacings. This is a clear indicator that the pseudogap mechanism in our case is not the one observed in the weak coupling regime of the Hubbard model [39, 70–76]: there, in contrast, the pseudogap is opened when the magnetic correlation length exceeds the thermal de Broglie wavelength of the quasiparticles $\xi \gg v_F/(\pi T)$ (Vilk criterion), where v_F is the Fermi velocity. Hence, in the weak coupling regime, large correlation lengths have to be present for opening the (pseudo-)gap. This, however, does not need to be the case for stronger coupling: here, already the treatment of short-ranged (spin) fluctuations allows for the development of a pseudogap as momentum-differentiated gap, which is the reason for the successful description of this regime by cluster extensions of DMFT (like CDMFT and DCA [45, 60, 61, 77–79]).

DISCUSSION AND CONCLUSION

To summarize, we analyzed a material-realistic single-band Hubbard model for the infinite-layer nickelate compound $LaNiO_2$. By a combination of cellular dynamical mean-field theory and dynamical vertex approximation calculations we could trace the temperatures sufficiently low to determine a flat maximum in the uniform static magnetic susceptibility for the hole-doped system at T^*. This temperature marks the onset of the pseudogap regime which manifests on the one-particle level as Fermi arcs in the spectral function. Concomitant on the two-particle level, the momentum-resolved magnetic susceptibility shows short-ranged magnetic fluctuations, which is characteristic of a strong coupling pseudogap. The exact location of the change from a weak-coupling to a strong-coupling pseudogap regime is a matter of current debate. Three indicators for this change can be mentioned: 1) a sudden increase in electronic correlations leading to a change in Fermi surface topology [65], 2) this strong correlation regime hosts relatively short-ranged correlations with the occurrence of (partial) localization [45, 68] and 3) the electron-boson coupling vertex develops a significant imaginary part [80, 81]. Our investigations of 1) and 2) in this manuscript by means of the DΓA, hence, allow us to characterize the found pseudogap as driven by strong coupling (Mott) physics.

In conclusion, our results for $LaNiO_2$ support the idea that the infinite-layer nickelates and new nickelate superconductors are indeed close relatives of other unconventional superconductors and, in particular, high-T_c cuprates. This is a most promising perspective as contrasting nickelates with cuprates might lead to a much deeper understanding of non-phonon mediated pairing. Indeed future research should focus on apparent differences between the two material classes. Specifically, the absence of magnetic order in the infinite-layer nickelate compounds as well as their reduced covalency with oxygen [3, 82] compared to the cuprates is remarkable. Whether this means that also pairing mechanisms are distinct remains to be investigated.

COMPUTATIONAL DETAILS

For applying DΓA with Moriyaesque λ-corrections we solve the Bethe-Salpeter equations in Matsubara frequency space with $N_{i\omega}$ = 90 positive fermionic and $N_{i\Omega}$ = 89 positive bosonic Matsubara frequencies for the two-particle Green function at all temperature shown, as well as 200 linear momentum grid points. To converge the DMFT calculation self-consistently we used the continuous-time quantum Monte Carlo solver in an interaction expansion (CT-INT) as part of an application of the TRIQS package. Every iteration was done using $256 \cdot 10^5$ cycles and roughly 6,200 core hours per temperature. For all shown spectral function plots over the Brillouin Zone we used a momentum resolution of 3,000 k-points.

In order to extract the magnetic susceptibility in a CDMFT approach we apply a ferromagnetic field on each lattice site with field strengths H_F = 0.02, 0.04, 0.06 to get the slope of a linear fit which enables us to calculate the magnetic susceptibility:

$$\mathrm{Re}\,\chi_m\left(\mathbf{q} = (0,0), i\Omega_n = 0\right) = \left.\frac{\partial m}{\partial H}\right|_{H=0} \approx \frac{m}{H_F}. \tag{5}$$

For each doping/temperature point we checked that all the applied fields are still within the linear response regime. All CDMFT calculations are again performed using the CT-INT quantum Monte Carlo solver in a continuous-time approach. For every data point we used twenty self-consistency steps, each using 6.4 million Monte Carlo cycles.

DATA AVAILABILITY STATEMENT

The raw data supporting the conclusion of this article will be made available by the authors, without undue reservation.

AUTHOR CONTRIBUTIONS

MK performed the numerical calculations and the post-processing of the data. The manuscript has been written by MK, PH, and TS. TS initiated and supervised the project. All authors provided critical feedback and shaped the research, analysis and manuscript.

FUNDING

The Max Planck Society is acknowledged for funding of the open access fee.

ACKNOWLEDGMENTS

We thank K. Held, M. Kitatani, L. Si, P. Worm, M. Hepting, M. Ferrero, A. Georges, F. Šimkovic, and A. Toschi for insightful discussions and F. Šimkovic and E. König for critically reading the manuscript. We thank the computing service facility of the MPI-FKF for their support and we gratefully acknowledge use of the computational resources of the Max Planck Computing and Data Facility.

REFERENCES

1. Li D, Lee K, Wang BY, Osada M, Crossley S, Lee HR, et al. Superconductivity in an Infinite-Layer Nickelate. *Nature* (2019) 572:624–7. doi:10.1038/s41586-019-1496-5
2. Anisimov VI, Bukhvalov D, Rice TM Electronic Structure of Possible Nickelate Analogs to the Cuprates. *Phys Rev B* (1999) 59:7901–6. doi:10.1103/physrevb.59.7901
3. Lee K-W, Pickett WE Infinite-layerLaNiO2: Ni1+is notCu2+. *Phys Rev B* (2004) 70:165109. doi:10.1103/physrevb.70.165109
4. Chaloupka Jc. v., Khaliullin G *Phys Rev Lett* (2008) 100:016404. doi:10.1103/physrevlett.100.016404

5. Hansmann P, Yang X, Toschi A, Khaliullin G, Andersen OK, Held K *Phys Rev Lett* (2009) 103:016401. doi:10.1103/physrevlett.103.016401
6. Hansmann P, Toschi A, Yang X, Andersen OK, Held K Electronic Structure of Nickelates: From Two-Dimensional Heterostructures to Three-Dimensional Bulk Materials. *Phys Rev B* (2010) 82:235123. doi:10.1103/physrevb.82.235123
7. Benckiser E, Haverkort MW, Brück S, Goering E, Macke S, Frañó A, et al. Orbital Reflectometry of Oxide Heterostructures. *Nat Mater* (2011) 10:189–93. doi:10.1038/nmat2958
8. Han MJ, Wang X, Marianetti CA, Millis AJ Dynamical Mean-Field Theory of Nickelate Superlattices. *Phys Rev Lett* (2011) 107:206804. doi:10.1103/physrevlett.107.206804
9. Disa AS, Kumah DP, Malashevich A, Chen H, Arena DA, Specht ED, et al. *Phys Rev Lett* (2015) 114:026801. doi:10.1103/physrevlett.114.026801
10. Takagi H, Batlogg B, Kao HL, Kwo J, Cava RJ, Krajewski JJ, et al. Systematic Evolution of Temperature-dependent Resistivity inLa2−xSrxCuO4. *Phys Rev Lett* (1992) 69:2975–8. doi:10.1103/physrevlett.69.2975
11. Daou R, Doiron-Leyraud N, LeBoeuf D, Li SY, Laliberté F, Cyr-Choinière O, et al. Linear Temperature Dependence of Resistivity and Change in the Fermi Surface at the Pseudogap Critical point of a High-Tc Superconductor. *Nat Phys* (2009) 5:31–4. doi:10.1038/nphys1109
12. Doiron-Leyraud N, Auban-Senzier P, René de Cotret S, Bourbonnais C, Jérome D, Bechgaard K, et al. Correlation between Linear Resistivity andTcin the Bechgaard Salts and the Pnictide superconductorBa(Fe1−xCox)2As2. *Phys Rev B* (2009) 80:214531. doi:10.1103/physrevb.80.214531
13. Taillefer L Scattering and Pairing in Cuprate Superconductors. *Annu Rev Condens Matter Phys* (2010) 1:51–70. doi:10.1146/annurev-conmatphys-070909-104117
14. Alloul H, Ohno T, Mendels P Y89NMR Evidence for a Fermi-Liquid Behavior inYBa2Cu3O6+x. *Phys Rev Lett* (1989) 63:1700–3. doi:10.1103/physrevlett.63.1700
15. Shen KM, Ronning F, Lu DH, Baumberger F, Ingle NJC, Lee WS, et al. Nodal Quasiparticles and Antinodal Charge Ordering in Ca 2-x Na X CuO 2 Cl 2. *Science* (2005) 307:901–4. doi:10.1126/science.1103627
16. Kanigel A, Norman MR, Randeria M, Chatterjee U, Souma S, Kaminski A, et al. Evolution of the Pseudogap from Fermi Arcs to the Nodal Liquid. *Nat Phys* (2006) 2:447–51. doi:10.1038/nphys334
17. Damascelli A, Hussain Z, Shen Z-X Angle-resolved Photoemission Studies of the Cuprate Superconductors. *Rev Mod Phys* (2003) 75:473–541. doi:10.1103/revmodphys.75.473
18. Ortiz RA, Puphal P, Klett M, Hotz F, Kremer RK, Trepka H, et al. *Magnetic Correlations in Infinite-Layer Nickelates: An Experimental and Theoretical Multi-Method Study* (2021). arXiv:2111.13668 [cond-mat.str-el].
19. Zhao D, Zhou YB, Fu Y, Wang L, Zhou XF, Cheng H, et al. Intrinsic Spin Susceptibility and Pseudogaplike Behavior in Infinite-Layer LaNiO2. *Phys Rev Lett* (2021) 126:197001. doi:10.1103/physrevlett.126.197001
20. Lu H, Rossi M, Nag A, Osada M, Li DF, Lee K, et al. Magnetic Excitations in Infinite-Layer Nickelates. *Science* (2021) 373:213–6. doi:10.1126/science.abd7726
21. Fowlie J, Hadjimichael M, Martins MM, Li D, Osada M, Wang BY, et al. Intrinsic Magnetism in Superconducting Infinite-Layer Nickelates. *arXiv* (2022). arXiv:2201.11943.
22. Hubbard J, Flowers BH *Proc R Soc London, Sect A* (1963) 276:238.
23. Hubbard J, Flowers BH *Proc R Soc London, Sect A* (1964) 281:401.
24. Kanamori J Electron Correlation and Ferromagnetism of Transition Metals. *Prog Theor Phys* (1963) 30:275–89. doi:10.1143/ptp.30.275
25. Gutzwiller MC Effect of Correlation on the Ferromagnetism of Transition Metals. *Phys Rev Lett* (1963) 10:159–62. doi:10.1103/physrevlett.10.159
26. Qin M, Schäfer T, Andergassen S, Corboz P, Gull E The Hubbard Model: A Computational Perspective. *Annu Rev Condens Matter Phys* (2022) 13:033948. doi:10.1146/annurev-conmatphys-090921-033948
27. Arovas DP, Berg E, Kivelson SA, Raghu S The Hubbard Model. *Annu Rev Condens Matter Phys* (2022) 13:null. doi:10.1146/annurev-conmatphys-031620-102024
28. Kitatani M, Si L, Janson O, Arita R, Zhong Z, Held K Nickelate Superconductors-A Renaissance of the One-Band Hubbard Model. *Npj Quan Mater.* (2020) 5:59. doi:10.1038/s41535-020-00260-y
29. Held K, Si L, Worm P, Janson O, Arita R, Zhong Z, et al. Phase Diagram of Nickelate Superconductors Calculated by Dynamical Vertex Approximation. *Front Phys* (2022) 9:810394. doi:10.3389/fphy.2021.810394
30. Karp J, Hampel A, Millis AJ Superconductivity and Antiferromagnetism in $NdNiO_2$ and $CaCuO_2$: A Cluster DMFT Study. *arXiv* (2022). arXiv:2201.10481.
31. Georges A, Kotliar G, Krauth W, Rozenberg MJ Dynamical Mean-Field Theory of Strongly Correlated Fermion Systems and the Limit of Infinite Dimensions. *Rev Mod Phys* (1996) 68:13–125. doi:10.1103/revmodphys.68.13
32. Georges A, Kotliar G Hubbard Model in Infinite Dimensions. *Phys Rev B* (1992) 45:6479–83. doi:10.1103/physrevb.45.6479
33. Metzner W, Vollhardt D Correlated Lattice Fermions ind=∞Dimensions. *Phys Rev Lett* (1989) 62:324–7. doi:10.1103/physrevlett.62.324
34. Chen H, Hampel A, Karp J, Lechermann F, Millis AJ Dynamical Mean Field Studies of Infinite Layer Nickelates: Physics Results and Methodological Implications. *Front Phys* (2022) 10:835942. doi:10.3389/fphy.2022.835942
35. Maier T, Jarrell M, Pruschke T, Hettler MH Quantum Cluster Theories. *Rev Mod Phys* (2005) 77:1027–80. doi:10.1103/revmodphys.77.1027
36. Toschi A, Katanin AA, Held K *Phys Rev B* (2007) 75:045118. doi:10.1103/physrevb.75.045118
37. Katanin AA, Toschi A, Held K *Phys Rev B* (2009) 80:075104. doi:10.1103/physrevb.80.075104
38. Rohringer G, Hafermann H, Toschi A, Katanin AA, Antipov AE, Katsnelson MI, et al. *Rev Mod Phys* (2018) 90:025003. doi:10.1103/revmodphys.90.025003
39. Schäfer T, Wentzell N, Šimkovic F, He Y-Y, Hille C, Klett M, et al. *Phys Rev X* (2021) 11:011058. doi:10.1103/physrevx.11.011058
40. LeBlanc JPF, Antipov AE, Becca F, Bulik IW, Chan GK-L, Chung C-M, et al. Simons Collaboration on the Many-Electron Problem. *Phys Rev X* (2015) 5:041041. doi:10.1103/physrevx.5.041041
41. Wietek A, Rossi R, Šimkovic F, Klett M, Hansmann P, Ferrero M, et al. *Phys Rev X* (2021) 11:041013. doi:10.1103/physrevx.11.041013
42. Rohringer G, Katanin A, Schäfer T, Hausoel A, Held K, Toschi A, ladderDGA. Available from: github.com/ladderDGA (2018).
43. Rohringer G *New Routes towards a Theoretical Treatment of Nonlocal Electronic Correlations*. Ph.D. thesis. Vienna, Austria: TU Wien (2013).
44. Schäfer T *Classical and Quantum Phase Transitions in Strongly Correlated Electron Systems*. Ph.D. thesis. Vienna, Austria: TU Wien (2016).
45. Gunnarsson O, Schäfer T, LeBlanc JPF, Gull E, Merino J, Sangiovanni G, et al. Fluctuation Diagnostics of the Electron Self-Energy: Origin of the Pseudogap Physics. *Phys Rev Lett* (2015) 114:236402. doi:10.1103/physrevlett.114.236402
46. Wu W, Ferrero M, Georges A, Kozik E *Phys Rev B* (2017) 96:041105. doi:10.1103/physrevb.96.041105
47. Rohringer G Spectra of Correlated many-electron Systems: From a One- to a Two-Particle Description. *J Electron Spectrosc Relat Phenomena* (2020) 241:146804. doi:10.1016/j.elspec.2018.11.003
48. Schäfer T, Toschi A *J Phys Condens Matter* (2021).
49. Rohringer G, Toschi A, Katanin A, Held K Critical Properties of the Half-Filled Hubbard Model in Three Dimensions. *Phys Rev Lett* (2011) 107:256402. doi:10.1103/physrevlett.107.256402
50. Schäfer T, Katanin AA, Held K, Toschi A *Phys Rev Lett* (2017) 119:046402. doi:10.1103/physrevlett.119.046402
51. Schäfer T, Katanin AA, Kitatani M, Toschi A, Held K Quantum Criticality in the Two-Dimensional Periodic Anderson Model. *Phys Rev Lett* (2019) 122:227201. doi:10.1103/physrevlett.122.227201
52. Kitatani M, Schäfer T, Aoki H, Held K *Phys Rev B* (2019) 99:041115(R). doi:10.1103/physrevb.99.041115
53. Mermin ND, Wagner H Absence of Ferromagnetism or Antiferromagnetism in One- or Two-Dimensional Isotropic Heisenberg Models. *Phys Rev Lett* (1966) 17:1307. doi:10.1103/physrevlett.17.1307
54. Hohenberg PC Existence of Long-Range Order in One and Two Dimensions. *Phys Rev* (1967) 158:383–6. doi:10.1103/physrev.158.383
55. Gull E, Millis AJ, Lichtenstein AI, Rubtsov AN, Troyer M, Werner P Continuous-time Monte Carlo Methods for Quantum Impurity Models. *Rev Mod Phys* (2011) 83:349–404. doi:10.1103/revmodphys.83.349
56. Parcollet O, Ferrero M, Ayral T, Hafermann H, Krivenko I, Messio L, et al. TRIQS: A Toolbox for Research on Interacting Quantum Systems. *Comput Phys Commun* (2015) 196:398–415. doi:10.1016/j.cpc.2015.04.023
57. Fratino L, Charlebois M, Sémon P, Sordi G, Tremblay A-MS Effects of Interaction Strength, Doping, and Frustration on the Antiferromagnetic Phase of the Two-Dimensional Hubbard Model. *Phys Rev B* (2017) 96:241109. doi:10.1103/physrevb.96.241109
58. Mußhoff J, Kiani A, Pavarini E *Phys Rev B* (2021) 103:075136. doi:10.1103/physrevb.103.075136

59. Klett M, Wentzell N, Schäfer T, Šimkovic F, Parcollet O, Andergassen S, et al. *Phys Rev Res* (2020) 2:033476. doi:10.1103/physrevresearch.2.033476
60. Huscroft C, Jarrell M, Maier T, Moukouri S, Tahvildarzadeh AN Pseudogaps in the 2D Hubbard Model. *Phys Rev Lett* (2001) 86:139–42. doi:10.1103/physrevlett.86.139
61. Macridin A, Jarrell M, Maier T, Kent PRC, D'Azevedo E *Phys Rev Lett* (2006) 97:036401. doi:10.1103/physrevlett.97.036401
62. Wietek A, He Y-Y, White SR, Georges A, Stoudenmire EM *Phys Rev X* (2021) 11:031007. doi:10.1103/physrevx.11.031007
63. Chen X, Leblanc JPF, Gull E Simulation of the NMR Response in the Pseudogap Regime of the Cuprates. *Nat Commun* (2017) 8:14986. doi:10.1038/ncomms14986
64. Rossi R, Šimkovic F, Ferrero M Renormalized Perturbation Theory at Large Expansion Orders. *Epl* (2020) 132:11001. doi:10.1209/0295-5075/132/11001
65. Wu W, Scheurer MS, Chatterjee S, Sachdev S, Georges A, Ferrero M *Phys Rev X* (2018) 8:021048. doi:10.1103/physrevx.8.021048
66. Scheurer MS, Chatterjee S, Wu W, Ferrero M, Georges A, Sachdev S Topological Order in the Pseudogap Metal. *Proc Natl Acad Sci USA* (2018) 115:E3665–E3672. doi:10.1073/pnas.1720580115
67. Huang EW, Mendl CB, Jiang H-C, Moritz B, Devereaux TP Stripe Order from the Perspective of the Hubbard Model. *Npj Quant Mater* (2018) 3:22. doi:10.1038/s41535-018-0097-0
68. Šimkovic F, IV, Rossi R, Ferrero M *The Weak, the Strong and the Long Correlation Regimes of the Two-Dimensional Hubbard Model at Finite Temperature* (2021). arXiv:2110.05863 [cond-mat.str-el].
69. Ornstein LS, Zernike F *Proc Roy Acad Amsterdam* (1916) 17:793.
70. Schäfer T, Geles F, Rost D, Rohringer G, Arrigoni E, Held K, et al. Fate of the False Mott-Hubbard Transition in Two Dimensions. *Phys Rev B* (2015) 91:125109. doi:10.1103/physrevb.91.125109
71. Vilk YM, Tremblay A-MS Destruction of Fermi-Liquid Quasiparticles in Two Dimensions by Critical Fluctuations. *Europhys Lett* (1996) 33:159–64. doi:10.1209/epl/i1996-00315-2
72. Vilk YM, Tremblay A-MS Non-Perturbative Many-Body Approach to the Hubbard Model and Single-Particle Pseudogap. *J Phys France* (1997) 7:1309–68. doi:10.1051/jp1:1997135
73. Schäfer T, Toschi A, Held K Dynamical Vertex Approximation for the Two-Dimensional Hubbard Model. *J Magnetism Magn Mater* (2016) 400:107–11. doi:10.1016/j.jmmm.2015.07.103
74. Šimkovic F, LeBlanc JPF, Kim AJ, Deng Y, Prokof'ev NV, Svistunov BV, et al. *Phys Rev Lett* (2020) 124:017003.
75. Kim AJ, Šimkovic F, Kozik E Spin and Charge Correlations across the Metal-To-Insulator Crossover in the Half-Filled 2D Hubbard Model. *Phys Rev Lett* (2020) 124. doi:10.1103/physrevlett.124.117602
76. Hille C, Rohe D, Honerkamp C, Andergassen S *Phys Rev Res* (2020) 2:033068. doi:10.1103/physrevresearch.2.033068
77. Kyung B, Kancharla SS, Sénéchal D, Tremblay A-MS, Civelli M, Kotliar G Pseudogap Induced by Short-Range Spin Correlations in a Doped Mott Insulator. *Phys Rev B* (2006) 73:165114. doi:10.1103/physrevb.73.165114
78. Gull E, Parcollet O, Millis AJ Superconductivity and the Pseudogap in the Two-Dimensional Hubbard Model. *Phys Rev Lett* (2013) 110:216405. doi:10.1103/physrevlett.110.216405
79. Fratino L, Bag S, Camjayi A, Civelli M, Rozenberg MJ *Doping-driven Pseudogap-Metal-To-Metal Transition in Correlated Electron Systems* (2021). arXiv:2109.06572 [cond-mat.str-el].
80. Krien F, Worm P, Chalupa P, Toschi A, Held K *Spin Scattering Turns Complex at strong Coupling: The Key to Pseudogap and Fermi Arcs in the Hubbard Model* (2021). arXiv:2107.06529 [cond-mat.str-el].
81. van Loon EGCP, Krien F, Hafermann H, Lichtenstein AI, Katsnelson MI Fermion-boson Vertex within Dynamical Mean-Field Theory. *Phys Rev B* (2018) 98:205148. doi:10.1103/physrevb.98.205148
82. Hepting M, Li D, Jia CJ, Lu H, Paris E, Tseng Y, et al. Electronic Structure of the Parent Compound of Superconducting Infinite-Layer Nickelates. *Nat Mater* (2020) 19:381–5. doi:10.1038/s41563-019-0585-z

Conflict of Interest: The authors declare that the research was conducted in the absence of any commercial or financial relationships that could be construed as a potential conflict of interest.

Publisher's Note: All claims expressed in this article are solely those of the authors and do not necessarily represent those of their affiliated organizations, or those of the publisher, the editors and the reviewers. Any product that may be evaluated in this article, or claim that may be made by its manufacturer, is not guaranteed or endorsed by the publisher.

frontiers in Physics

ORIGINAL RESEARCH
published: 23 February 2022
doi: 10.3389/fphy.2022.824144

Ab Initio Downfolding Based on the GW Approximation for Infinite-Layer Nickelates

Motoaki Hirayama[1,2]*, *Yusuke Nomura*[2] *and Ryotaro Arita*[2,3]

[1]QPEC, The University of Tokyo, Tokyo, Japan, [2]RIKEN Center for Emergent Matter Sciences (CEMS), Saitama, Japan, [3]Department of Applied Physics, The University of Tokyo, Tokyo, Japan

We derive an effective three-orbital model for the infinite-layer nickelates based on the band structure obtained by the GW approximation (GWA), where we consider the Ni $3d_{x^2-y^2}$ and O $2p$ orbitals forming the σ-bond. In the GWA, the self-energy correction to the local density approximation (LDA) increases the energy difference between Ni $3d_{x^2-y^2}$ and O $2p$, which reduces the bandwidth of the antibonding $3d_{x^2-y^2}$ orbitals. The isolation of the Ni $3d_{x^2-y^2}$ around the Fermi level suppresses the screening effect. As a result, the correlation effect becomes more significant than that in the model constructed by the LDA-based downfolding. Furthermore, the Mott-Hubbard type character is enhanced in the GWA-based effective model, because the charge-transfer energy increases more rapidly compared to the increase in the interaction parameters.

Keywords: nickelate superconductivity, density functional theory, GW approximation, ab initio downfolding, multi-orbital Hubbard model

OPEN ACCESS

Edited by:
Junjie Zhang,
Shandong University, China

Reviewed by:
Atsushi Fujimori,
Waseda University, Japan
Liviu Chioncel,
University of Augsburg, Germany

***Correspondence:**
Motoaki Hirayama
hirayama@ap.t.u-tokyo.ac.jp

Specialty section:
This article was submitted to Condensed Matter Physics, a section of the journal Frontiers in Physics

Received: *29 November 2021*
Accepted: *17 January 2022*
Published: *23 February 2022*

Citation:
Hirayama M, Nomura Y and Arita R (2022) Ab Initio *Downfolding Based on the GW Approximation for Infinite-Layer Nickelates. Front. Phys. 10:824144. doi: 10.3389/fphy.2022.824144*

INTRODUCTION

The discovery of nickel superconductors [1] has attracted renewed attention to superconductivity in strongly correlated electron systems [2–7]. So far, superconductivity has been found in film samples of doped infinite-layer nickelates $R\mathrm{NiO}_2$ (R = Nd, Pr, and La) [1, 8–16] and a quintuple-layer nickelate $\mathrm{Nd}_6\mathrm{Ni}_5\mathrm{O}_{12}$ [17]. Although the nature of the superconductivity is largely unknown, the pairing mechanism is likely to be unconventional: Theoretically, a phonon calculation for NdNiO_2 has shown that the electron-phonon coupling is too weak to explain the superconductivity with a transition temperature on the order of 10 K [18]. Experimentally, both U- and V-shaped spectra have been observed using the scanning tunneling microscopy, depending on the location of the inhomogeneous surface of the doped NdNiO_2 film [9]. Although the origin of the coexistence of the two different signals is controversial [19–23], the presence of the V-shape spectrum is consistent with an unconventional d-wave pairing. In fact, unconventional pairing mechanisms have been discussed since the early stages of the research [24–26].

In contrast with the conventional phonon-mediated superconductivity for which *ab initio* calculation based on density functional theory (DFT) plays a crucial role [27, 28], construction of low-energy models with few degrees of freedom is critically important for unconventional superconductivity since a detailed analysis of the correlation effects is mandatory. In the standard approach to derive a low-energy effective model from first principles, we first calculate the electronic structure with the local density approximation (LDA) or the generalized gradient approximation (GGA) in the framework of DFT. We then construct the maximally localized Wannier function (MLWF) [29, 30] for the low-energy states around the

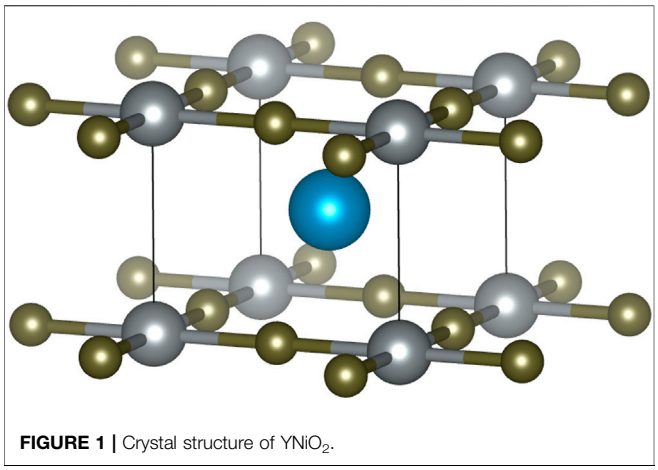

FIGURE 1 | Crystal structure of $YNiO_2$.

Fermi level and derive a tight-binding model. Next, we calculate the effective Coulomb interaction by the constrained random phase approximation (cRPA) [31, 32]. The matrix elements of the (partially) screened interaction are calculated for the Wannier basis, from which we estimate the Hubbard U and Hund coupling J in the multi-orbital Hubbard model [18, 24, 33, 34]. The cRPA is formulated in such a way that RPA calculation for the derived low-energy effective model reproduces a one-shot GW (G_0W_0) result [31, 32, 35].

To improve the accuracy of the parameters in the low-energy model, we can replace the Green's function (G_0) constructed from the DFT/LDA eigenenergies with the dressed Green's function in the GW approximation (GWA).[1] Such a derivation based on the GWA has been recently performed for the celebrated cuprate superconductors [37, 38]. While two types of orbitals, i.e., the Cu 3*d* and O 2*p* orbitals, form low-energy bands near the Fermi level, the GW self-energy correction increases the energy difference between the *d* and *p* orbitals and reduce the bandwidth of the *d* band. With these modifications, it has been shown with an extensive variational Monte Carlo (VMC) calculation that the experimental values of the Mott gap and magnetic moment of La_2CuO_4 are successfully reproduced [38, 39]. Given that the differences in the band structure between the DFT/LDA and that in the GWA are commonly seen in transition metal oxides where 3*d* and 2*p* orbitals with different correlation strengths coexist near the Fermi level, it would be of great interest to derive an effective low-energy model for infinite-layer nickelates based on the GWA.

In this study, we perform a first-principles derivation of the effective model for infinite-layer nickelates. In particular, we mainly focus on the *dpp* three-orbital models (single-orbital model is discussed in **Appendix**) because it is interesting to investigate how the GWA modifies the charge-transfer energy and correlation strength compared to the LDA-based downfolding.[2] First, we calculate the band structure in the DFT/LDA and estimate the parameter of the effective model using the MLWF and cRPA technique. Next, we calculate the band structure in the GWA using the Green's function of the LDA. We derive the effective model from the GW band structure and compare the results with those obtained from the LDA. We find that the GWA-based effective model is predicted to be more strongly-correlated with enhanced Mott-Hubbard type character. The model offers an interesting reference to be compared with that of the cuprates with the charge-transfer type character.

METHODS

In this study, we calculate the parameter of the Hubbard Hamiltonian for the low-energy degree of freedom,

$$\begin{aligned}\mathcal{H}^{\mathrm{eff}} &= \sum_{ij}\sum_{\ell_1\ell_2\sigma} t_{\ell_1\ell_2\sigma}\left(\boldsymbol{R}_i-\boldsymbol{R}_j\right) d^{\dagger}_{i\ell_1\sigma} d_{j\ell_2\sigma} \\ &+\frac{1}{2}\sum_{i_1i_2i_3i_4}\sum_{\ell_1\ell_2\ell_3\ell_4\sigma\eta\rho\tau}\Big\{W^{\mathrm{H}}_{\ell_1\ell_2\ell_3\ell_4\sigma\eta\rho\tau}\left(\boldsymbol{R}_{i_1},\boldsymbol{R}_{i_2},\boldsymbol{R}_{i_3},\boldsymbol{R}_{i_4}\right) \\ &\quad d^{\dagger}_{i_1\ell_1\sigma} d_{i_2\ell_2\eta} d^{\dagger}_{i_3\ell_3\rho} d_{i_4\ell_4\tau}\Big).\end{aligned} \tag{1}$$

Here, the hopping term is represented by

$$t_{\ell_1\ell_2\sigma}(\boldsymbol{R}) = \langle\phi_{\ell_1\boldsymbol{0}}|H|\phi_{\ell_2\boldsymbol{R}}\rangle, \tag{2}$$

where H is the Hamiltonian in the LDA or GWA and $\phi_{\ell\boldsymbol{R}}$ is the MLWF of the ℓth orbital localized at the unit cell $\boldsymbol{R}$. The interaction term is given by

$$W^{\mathrm{H}}_{\ell_1\ell_2\ell_3\ell_4\sigma\eta\rho\tau}\left(\boldsymbol{R}_{i_1},\boldsymbol{R}_{i_2},\boldsymbol{R}_{i_3},\boldsymbol{R}_{i_4}\right) = \langle\phi_{\ell_1\boldsymbol{R}_{i_1}}\phi_{\ell_2\boldsymbol{R}_{i_2}}|W^{\mathrm{H}}|\phi_{\ell_3\boldsymbol{R}_{i_3}}\phi_{\ell_4\boldsymbol{R}_{i_4}}\rangle, \tag{3}$$

where W^{H} is the effective interaction for the low-energy degree of freedom,

$$W^{\mathrm{H}}(q,\omega) = \frac{v(q)}{1-P^{\mathrm{H}}(q,\omega)v(q)}. \tag{4}$$

We calculate the effective interaction from the one-shot GWA band. In the one-shot GWA, we calculate the self-energy from the Green's function G and the fully-screened interaction W,

$$\Sigma = GW, \tag{5}$$

where W is calculated from all the polarizations in the RPA P as follows,

$$W(q,\omega) = \frac{v(q)}{1-P(q,\omega)v(q)}. \tag{6}$$

[1]It should be noted that although the cRPA method is free from the double counting problem for the interaction parameters, we have to apply the constrained GW (cGW) method to avoid the double counting in the self-energy [36].

[2]We note that there are several other effective models for infinite-layer nickelates that have been discussed, including a multi-band model that includes 3*d* orbitals other than the $3d_{x^2-y^2}$ orbital [40–52], a model that includes the contribution of rare-earth 4*f* electrons [53–56], and a model that includes the self-doping bands [57–59]. Here, we focus on the debate [40, 57, 60–67] on the classification of the Mott-Hubbard or charge-transfer regimes in Zaanen-Sawatzky-Allen phase diagram [68].

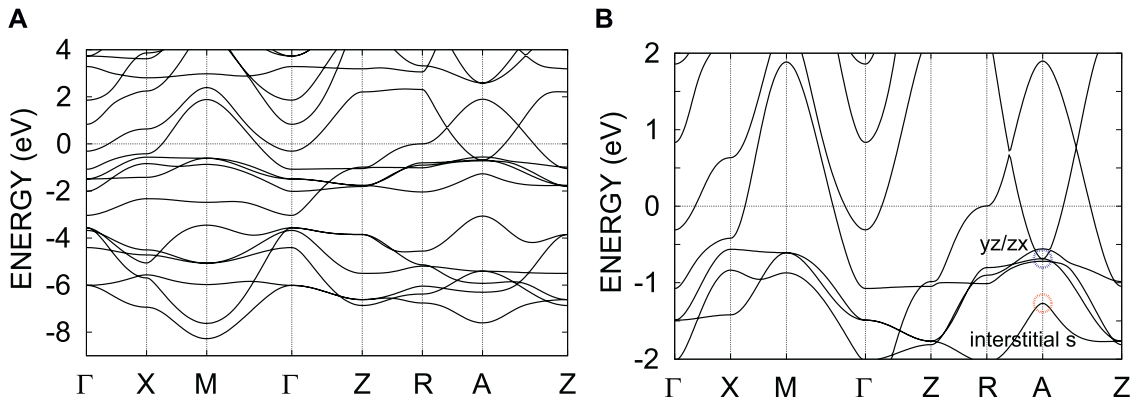

FIGURE 2 | (A) DFT/LDA band structure for $YNiO_2$ and **(B)** its magnified figure. The zero energy corresponds to the Fermi level.

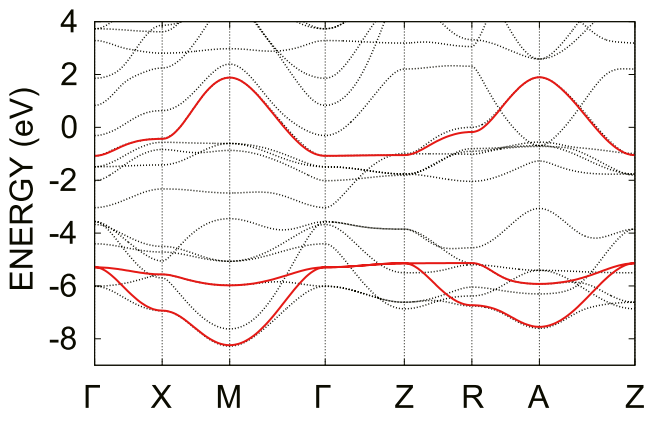

FIGURE 3 | Electronic band structure of the three-orbital model in the LDA (solid lines). The zero energy corresponds to the Fermi level. For comparison, the band structures in the LDA is also given (dotted lines).

The quasiparticle approximation of the Hamiltonian in the GWA is expressed as

$$H^{\mathrm{GW}} = H^{\mathrm{LDA}} + Z\left(\epsilon^{\mathrm{LDA}}\right)\left(-V^{\mathrm{xc}} + \Sigma\left(\epsilon^{\mathrm{LDA}}\right)\right), \tag{7}$$

where H^{LDA} is the Hamiltonian in the LDA, V^{xc} is the exchange correlation potential in the LDA, and $Z(\epsilon^{\mathrm{LDA}})$ is the renormalization factor of Σ at the eigenenergy ϵ^{LDA}:

$$Z(\epsilon) = \left\{1 - \frac{\partial \mathrm{Re}\Sigma}{\partial \omega}\bigg|_{\omega=\epsilon}\right\}^{-1}. \tag{8}$$

We calculate the electronic band structure of the $YNiO_2$ using the experimental lattice parameters of $LaNiO_2$, where a = 3.959 Å and c = 3.375 Å [69]. To exclude the contribution of the 4*f* orbital, here we use Y as the cation. The computational conditions for the DFT/LDA and GW are as follows. The calculation is based on the full-potential linear muffin-tin orbital implementation [70]. The exchange correlation functional is obtained by the local density approximation of the Ceperley-Alder type [71]. We neglect the spin-polarization. The self-consistent LDA calculation is done for the 12 × 12 × 12 *k*-mesh. The muffintin (MT) radii are as follows: $R_{\mathrm{Y}}^{\mathrm{MT}}$ = 2.9 bohr, $R_{\mathrm{Ni}}^{\mathrm{MT}}$ = 2.15 bohr, $R_{\mathrm{O}}^{\mathrm{MT}}$ = 1.5 bohr, The angular momentum of the atomic orbitals is taken into account up to l = 4 for all the atoms.

The cRPA and GW calculations use a mixed basis consisting of products of two atomic orbitals and interstitial plane waves [72]. In the cRPA and GW calculation, the 6 × 6 × 6 *k*-mesh is employed for $YNiO_2$. we interpolate the mesh using the tetrahedron method to treat the screening effect accurately [73, 74]. We disentangle the target band from other bands when the target band crosses another band and construct orthogonalized two separated Hilbert spaces [75]. We include bands about from −25 to 120 eV for calculation of the screened interaction and the self-energy.

RESULT

Figure 1 shows the crystal structure of the infinite-layer nickelates. The block layer is a single lanthanide cation and has large interstitial regions surrounded by cations. This is one of the reasons for the formation of electron pockets originating from the block layer, as described below.

Figure 2 shows the band structure of $YNiO_2$ in the LDA. The band structure of $YNiO_2$ is very similar to that of $NdNiO_2$ if we eliminate the Nd 4*f* bands. The $3d_{x^2-y^2}$ antibonding state mainly forms the Fermi surface, which is a feature commonly seen in the cuprate superconductors. Reflecting the square planar crystal field of oxygen around the nickel site, the other *d* bands are almost fully occupied. However, differently from the cuprates, the infinite-layer nickelates have additional small electron pockets around the Γ and A points. These electron pockets originate from the *d*-orbital and the interstitial state in the block layer, respectively. The energy difference between the 3*d* bands of Ni^{1+} and the 2*p* bands of O^{2-} is larger than that between Cu^{2+} and O^{2-} in copper oxides, and they are energetically separated near −3 eV.

The interstitial state is located at − 1.4 eV at the *A* point, and has a band inversion between *yz*/*zx* orbitals around the *A* point. Because of the inversion between bands with different numbers of degeneracies, the bands of the interstitial *s* and the *yz*/*zx* are continuously connected from the conduction band to the valence band. Since

TABLE 1 | Transfer integrals and effective interactions in the three-orbital Hamiltonian for $YNiO_2$ (in eV). Both the one- and two-body part of the Hamiltonian are constructed based on the LDA band structure. v, U (0), J_v, and J (0) represent the bare Coulomb, the static values of the effective Coulomb, bare exchange interactions, and exchange interactions, respectively (at ω =0). The index "n" and "nn" represent the nearest unit cell (1,0,0) and the next-nearest unit cell (1,1,0), respectively.

t (LDA)		(0, 0, 0)			(1, 0, 0)			(1, 1, 0)			(2, 0, 0)	
	x^2-y^2	p_1	p_2	x^2-y^2	p_1	p_2	x^2-y^2	p_1	p_2	x^2-y^2	p_1	p_2
x^2-y^2	−1.377	−1.327	1.327	0.062	−0.018	−0.027	0.024	−0.006	0.006	−0.005	0.001	0.000
p_1	−1.327	−5.355	−0.671	1.327	0.043	0.671	−0.027	0.037	0.002	0.018	−0.006	0.002
p_2	1.327	−0.671	−5.355	−0.027	−0.002	−0.043	0.027	0.002	0.037	0.000	0.000	0.000
		v			U (0)			J_v			J (0)	
	x^2-y^2	p_1	p_2	x^2-y^2	p_1	p_2	x^2-y^2	p_1	p_2	x^2-y^2	p_1	p_2
x^2-y^2	26.406	7.886	7.886	4.599	0.763	0.763		0.116	0.116		0.066	0.066
p_1	7.886	17.231	5.278	0.763	4.127	0.499	0.116		0.040	0.066		0.019
p_2	7.886	5.278	17.231	0.763	0.499	4.127	0.116	0.040		0.066	0.019	
		v_n			V_n(0)			v_{nn}			V_{nn} (0)	
	x^2-y^2	p_1	p_2	x^2-y^2	p_1	p_2	x^2-y^2	p_1	p_2	x^2-y^2	p_1	p_2
x^2-y^2	3.730	7.886	3.286	0.157	0.763	0.124	2.644	3.286	3.286	0.061	0.124	0.124
p_1	2.530	3.841	2.379	0.080	0.250	0.059	2.124	2.643	2.379	0.035	0.086	0.059
p_2	3.286	5.278	3.566	0.124	0.499	0.155	2.124	2.379	2.643	0.035	0.059	0.086

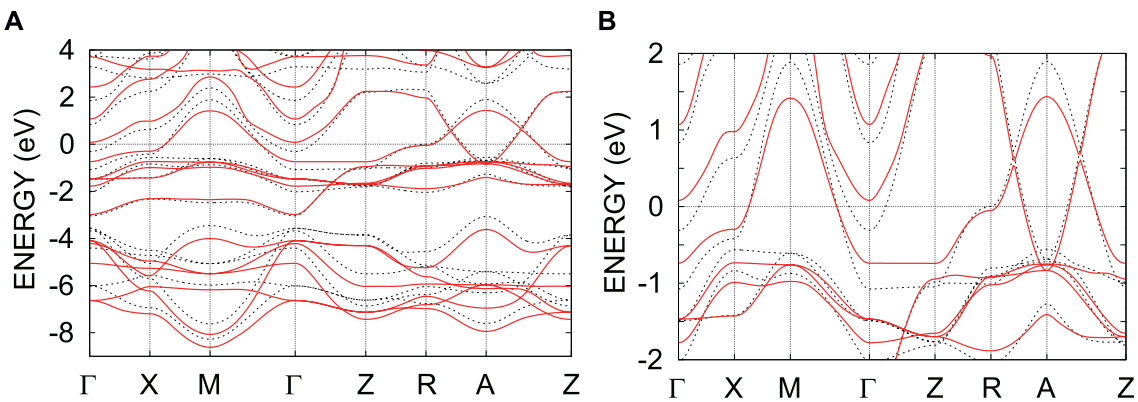

FIGURE 4 | (A) GW band structure for $YNiO_2$ and **(B)** its magnified figure (solid lines). For comparison, the band structures in the LDA is also given (dotted lines). The zero energy corresponds to the Fermi level.

this band inversion is buried in the metallic band, it will be difficult to observe the surface state associated with the band inversion.

In this paper, we derive a three-orbital effective model consisting of the Ni $3d_{x^2-y^2}$ orbital and two O $2p$ orbitals forming a σ-bonding. We first construct the maximally localized Wannier functions [29, 30] for these orbitals and evaluate the parameters in the tight-binding model (see **Table 1** and **Figure 3**). The obtained model has a larger energy difference between the $3d_{x^2-y^2}$ and $2p$ orbitals than that of the cuprate, and is closer to the Mott-Hubbard type.

We then calculate the effective interaction for the three-orbital model by the cRPA method. The obtained effective interactions are summarized in **Table 1**. The bare Coulomb interaction v is slightly smaller than that of the copper oxides (Ni $3d_{x^2-y^2}$: ~ 26 eV, Cu $d_{x^2-y^2}$: ~ 29 eV in Refs. [37, 38]), and the dielectric constant U/v is smaller than that of the copper oxides partially due to the metallic screening from the block layer.

We next show the band structure in the GWA in **Figure 4**. In the GWA, the energy difference between the strongly correlated Ni $3d$ orbitals and the weakly correlated O $2p$ orbitals is enhanced [33, 76]. Thereby, the energy gap between the d- and p-bands around −3 eV is increased. On the other hand, the bandwidth of the antibonding orbitals of the $3d_{x^2-y^2}$ orbital decreases. The contribution of the O $2p$ orbitals to the antibonding orbitals decreases due to the increase in the energy difference between the d- and p-orbitals. The bandwidth of the strongly correlated orbitals in the GWA is also reduced compared to that in the LDA due to the effect of the frequency dependence of the self-energy. The bandwidth of the O $2p$ orbitals remains approximately the same as that in the LDA.

In the GWA, the position of the valence band is lifted up from that in the LDA. In particular, the electron pocket originating from the d orbital in the block layer near the Γ point disappears. On the other hand, the bottom of the band originating from the

TABLE 2 | Transfer integrals and effective interactions in the three-band Hamiltonian for $YNiO_2$ (in eV). The one-body part is obtained from the GW band structure, and the effective interaction is the result of the cRPA calculation for the GW bands. v, U (0), J_v, and J (0) represent the bare Coulomb, the static values of the effective Coulomb, bare exchange interactions, and exchange interactions, respectively (at ω =0). The index "n" and "nn" represent the nearest unit cell [1,0,0] and the next-nearest unit cell [1,1,0] respectively.

t (GW)		(0, 0, 0)			(1, 0, 0)			(1, 1, 0)			(2, 0, 0)	
	x^2-y^2	p_1	p_2	x^2-y^2	p_1	p_2	x^2-y^2	p_1	p_2	x^2-y^2	p_1	p_2
x^2-y^2	−1.204	−1.288	1.288	0.094	−0.025	−0.021	0.015	−0.005	0.005	−0.002	0.001	0.001
p_1	−1.288	−5.802	−0.640	1.288	0.037	0.640	−0.021	0.031	0.007	0.025	−0.004	0.007
p_2	1.288	−0.640	−5.802	−0.021	−0.007	−0.022	0.021	0.007	0.031	0.001	0.000	−0.003
		v			U (0)			J_v			J (0)	
	x^2-y^2	p_1	p_2	x^2-y^2	p_1	p_2	x^2-y^2	p_1	p_2	x^2-y^2	p_1	p_2
x^2-y^2	26.596	7.901	7.901	5.019	0.932	0.932		0.114	0.114		0.066	0.066
p_1	7.901	17.383	5.280	0.932	4.510	0.624	0.114		0.038	0.066		0.019
p_2	7.901	5.280	17.382	0.932	0.624	4.510	0.114	0.038		0.066	0.019	
		v_n			V_n(0)			v_{nn}			V_{nn} (0)	
	x^2-y^2	p_1	p_2	x^2-y^2	p_1	p_2	x^2-y^2	p_1	p_2	x^2-y^2	p_1	p_2
x^2-y^2	3.727	7.901	3.285	0.223	0.932	0.181	2.643	3.285	3.285	0.094	0.181	0.181
p_1	2.528	3.840	2.379	0.116	0.332	0.094	2.123	2.641	2.379	0.057	0.130	0.094
p_2	3.285	5.280	3.567	0.181	0.624	0.230	2.123	2.379	2.641	0.057	0.094	0.13

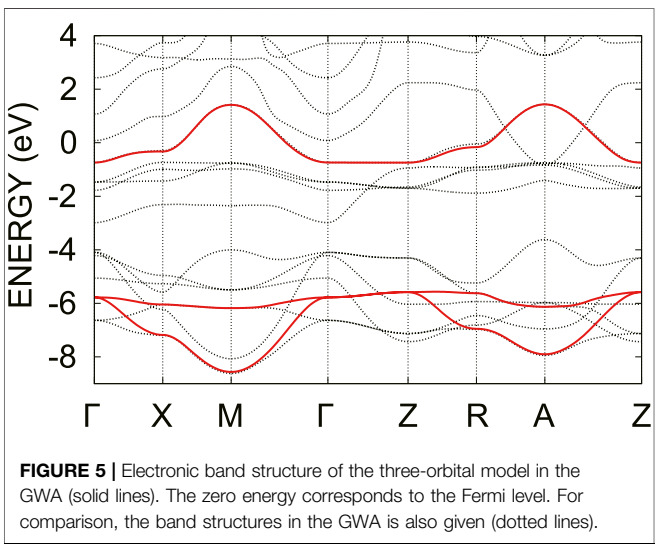

FIGURE 5 | Electronic band structure of the three-orbital model in the GWA (solid lines). The zero energy corresponds to the Fermi level. For comparison, the band structures in the GWA is also given (dotted lines).

interstitial state still creates the electron pocket around the A point even in the GWA.

We derive the three-orbital model (see **Figure 5**) and summarize the hopping parameters in **Table 2**. The difference in the on-site potential between the $3d_{x^2-y^2}$ and $2p$ orbitals increase from 3.98 to 4.60 eV. The nearest-neighbor hopping between the $3d_{x^2-y^2}$ and $2p$ orbitals is almost the same (~ − 1.3 eV), but slightly reduced due to the renormalization factor in the GWA. The increase of the onsite potential deference between the atomic $3d_{x^2-y^2}$ and $2p$ orbitals results in an decrease of the oxygen contribution to the antibonding $3d_{x^2-y^2}$ orbitals and decrease of the hopping between the antibonding $3d_{x^2-y^2}$ orbitals.

The screening effect of the system is reduced compared to that in the LDA mainly due to the increase of the charge-transfer energy, which increases the bare Coulomb interaction of the $3d_{x^2-y^2}$ band and reduces the screening effect from the $2p$ bands. The bands originating from the block layer as well as the O $2p$ orbitals in the GWA move away from the Fermi level compared to the LDA, which makes the screening effect weaker. The disappearance of the metallic screening from the electron pocket at the Γ point also partially contribute to the reduction of the correlation. Therefore, the value of the effective interaction is increased from that in the LDA. For example, while the on-site interaction is 4.6 eV for the $3d_{x^2-y^2}$ orbital and 4.1 eV for the $2p$ orbital in the LDA-based cRPA calculation, the GWA-based cRPA gives 5.0 eV for the $3d_{x^2-y^2}$ orbital and 4.5 eV for the $2p$ orbital. The nearest-neighbor interactions also increase from 0.16 to 0.22 eV for the $3d_{x^2-y^2}$ orbital. Note that the metallic screening from the electron pocket near the A point still remains even in the GWA.[3]

CONCLUSION

We derived a three-orbital low-energy model for the infinite-layer nickelates based on the GWA. In the GWA, the O $2p$ bands locate deeper below the Fermi level, and the bandwidth of the Ni $3d_{x^2-y^2}$ band is narrower than that in the LDA calculation. Due to the isolation of the low-energy Ni $3d_{x^2-y^2}$ band, the screening effect

[3]We note that there is a proposal that the electron pocket at the A point can be eliminated by designing a different type of the block layer [33].

becomes less effective, leading to larger interaction parameters in the Hamiltonian. Thus the GW-based *ab initio* downfolding gives a more correlated model than the LDA-based downfolding.

DATA AVAILABILITY STATEMENT

The original contributions presented in the study are included in the article/Supplementary Material, further inquiries can be directed to the corresponding author.

AUTHOR CONTRIBUTIONS

MH conducted calculations. All authors contributed to writing the article.

FUNDING

We acknowledge funding through Grant-in-Aids for Scientific Research (JSPS KAKENHI) (Grant Nos 20K14423 (YN), 21H01041 (YN), and 19H05825 (RA)) and "Program for Promoting Researches on the Supercomputer Fugaku" (Basic Science for Emergence and Functionality in Quantum Matter —Innovative Strongly-Correlated Electron Science by Integration of "Fugaku" and Frontier Experiments) (Grant No. JPMXP1020200104) from MEXT.

ACKNOWLEDGMENTS

We thank Terumasa Tadano and Motoharu Kitatani for valuable discussions.

REFERENCES

1. Li D, Lee K, Wang BY, Osada M, Crossley S, Lee HR, et al. Superconductivity in an Infinite-Layer Nickelate. *Nature* (2019) 572:624–7. doi:10.1038/s41586-019-1496-5
2. Norman MR. Entering the Nickel Age of Superconductivity. *Physics* (2020) 13: 85. doi:10.1103/physics.13.85
3. Pickett WE. The Dawn of the Nickel Age of Superconductivity. *Nat Rev Phys* (2021) 3:7–8. doi:10.1038/s42254-020-00257-3
4. Zhang J, Tao X. Review on quasi-2D Square Planar Nickelates. *CrystEngComm* (2021) 23:3249–64. doi:10.1039/d0ce01880e
5. Botana AS, Bernardini F, Cano A. Nickelate Superconductors: An Ongoing Dialog between Theory and Experiments. *J Exp Theor Phys* (2021) 132:618–27. doi:10.1134/s1063776121040026
6. Nomura Y, Arita R. *Superconductivity in Infinite-Layer Nickelates* (2021). arXiv:2107.12923.
7. Gu Q, Wen H. H. *Superconductivity in Nickel Based 112 Systems* (2021). arXiv: 2109.07654.
8. Zeng S, Tang CS, Yin X, Li C, Li M, Huang Z, et al. Phase Diagram and Superconducting Dome of Infinite-Layer Nd1−xSrxNiO2 Thin Films. *Phys Rev Lett* (2020) 125:147003. doi:10.1103/PhysRevLett.125.147003
9. Gu Q, Li Y, Wan S, Li H, Guo W, Yang H, et al. Single Particle Tunneling Spectrum of Superconducting Nd1-xSrxNiO2 Thin Films. *Nat Commun* (2020) 11:6027. doi:10.1038/s41467-020-19908-1
10. Gao Q, Zhao Y, Zhou X-J, Zhu Z. Preparation of Superconducting Thin Films of Infinite-Layer Nickelate Nd0.8Sr0.2NiO2. *Chin Phys. Lett.* (2021) 38: 077401. doi:10.1088/0256-307X/38/7/077401
11. Zhou XR, Feng ZX, Qin PX, Yan H, Wang XN, Nie P, et al. *Negligible Oxygen Vacancies, Low Critical Current Density, Electric-Field Modulation, In-Plane Anisotropic and High-Field Transport of a Superconducting* $Nd_{0.8}Sr_{0.2}NiO_2$/$SrTiO_3$ *Heterostructure*. Rare Metals (2021) 40:2847.
12. Li Y, Sun W, Yang J, Cai X, Guo W, Gu Z, et al. Impact of Cation Stoichiometry on the Crystalline Structure and Superconductivity in Nickelates. *Front Phys* (2021) 9:443. doi:10.3389/fphy.2021.719534
13. Osada M, Wang BY, Goodge BH, Lee K, Yoon H, Sakuma K, et al. A Superconducting Praseodymium Nickelate with Infinite Layer Structure. *Nano Lett* (2020) 20:5735–40. doi:10.1021/acs.nanolett.0c01392
14. Osada M, Wang BY, Lee K, Li D, Hwang HY. Phase Diagram of Infinite Layer Praseodymium Nickelate Pr1−xSrxNiO2 Thin Films. *Phys Rev Mater* (2020) 4: 121801. doi:10.1103/PhysRevMaterials.4.121801
15. Osada M, Wang BY, Goodge BH, Harvey SP, Lee K, Li D, et al. Nickelate Superconductivity without Rare-Earth Magnetism: (La,Sr)NiO 2. *Adv Mater* (2021) 33:2104083. doi:10.1002/adma.202104083
16. Zeng SW, Li CJ, Chow LE, Cao Y, Zhang ZT, Tang CS, et al. *Superconductivity in Infinite-Layer Lanthanide Nickelates* (2021). arXiv:2105.13492.
17. Pan GA, Ferenc Segedin D, LaBollita H, Song Q, Nica EM, Goodge BH, et al. Superconductivity in a Quintuple-Layer Square-Planar Nickelate. *Nat Mater* (2021). doi:10.1038/s41563-021-01142-9
18. Nomura Y, Hirayama M, Tadano T, Yoshimoto Y, Nakamura K, Arita R. Formation of a Two-Dimensional Single-Component Correlated Electron System and Band Engineering in the Nickelate Superconductor NdNiO2. *Phys Rev B* (2019) 100:205138. doi:10.1103/PhysRevB.100.205138
19. Adhikary P, Bandyopadhyay S, Das T, Dasgupta I, Saha-Dasgupta T. Orbital-selective Superconductivity in a Two-Band Model of Infinite-Layer Nickelates. *Phys Rev B* (2020) 102:100501. doi:10.1103/PhysRevB.102.100501
20. Wang Z, Zhang G-M, Yang Y-f., Zhang F-C. Distinct Pairing Symmetries of Superconductivity in Infinite-Layer Nickelates. *Phys Rev B* (2020) 102:220501. doi:10.1103/PhysRevB.102.220501
21. Kitamine N, Ochi M, Kuroki K. Designing Nickelate Superconductors with D8 Configuration Exploiting Mixed-Anion Strategy. *Phys Rev Res* (2020) 2: 042032. doi:10.1103/PhysRevResearch.2.042032
22. Wu X, Jiang K, Sante DD, Hanke W, Schnyder AP, Hu J, et al. *Surface* S-*Wave Superconductivity for Oxide-Terminated Infinite-Layer Nickelates* (2020). arXiv:2008.06009.
23. Choubey P, Eremin IM. Electronic Theory for Scanning Tunneling Microscopy Spectra in Infinite-Layer Nickelate Superconductors. *Phys Rev B* (2021) 104:144504. doi:10.1103/PhysRevB.104.144504
24. Sakakibara H, Usui H, Suzuki K, Kotani T, Aoki H, Kuroki K. Model Construction and a Possibility of Cupratelike Pairing in a New D9 Nickelate Superconductor (Nd,Sr)NiO2. *Phys Rev Lett* (2020) 125:077003. doi:10.1103/PhysRevLett.125.077003
25. Hirsch JE, Marsiglio F. Hole Superconductivity in Infinite-Layer Nickelates. *Physica C: Superconductivity its Appl* (2019) 566:1353534. doi:10.1016/j.physc.2019.1353534
26. Wu X, Di Sante D, Schwemmer T, Hanke W, Hwang HY, Raghu S, et al. Robust Dx2−y2 -wave Superconductivity of Infinite-Layer Nickelates. *Phys Rev B* (2020) 101:060504. doi:10.1103/PhysRevB.101.060504
27. Giustino F. Electron-phonon Interactions from First Principles. *Rev Mod Phys* (2017) 89:015003. doi:10.1103/RevModPhys.89.015003
28. Flores-Livas JA, Boeri L, Sanna A, Profeta G, Arita R, Eremets M. A Perspective on Conventional High-Temperature Superconductors at High Pressure: Methods and Materials. *Phys Rep* (2020) 856:1–78. doi:10.1016/j.physrep.2020.02.003.A
29. Marzari N, Vanderbilt D. Maximally Localized Generalized Wannier Functions for Composite Energy Bands. *Phys Rev B* (1997) 56:12847–65. doi:10.1103/PhysRevB.56.12847
30. Souza I, Marzari N, Vanderbilt D. Maximally Localized Wannier Functions for Entangled Energy Bands. *Phys Rev B* (2001) 65:035109. doi:10.1103/PhysRevB.65.035109

31. Aryasetiawan F, Imada M, Georges A, Kotliar G, Biermann S, Lichtenstein AI. Frequency-dependent Local Interactions and Low-Energy Effective Models from Electronic Structure Calculations. *Phys Rev B* (2004) 70:195104. doi:10.1103/PhysRevB.70.195104
32. Imada M, Miyake T. Electronic Structure Calculation by First Principles for Strongly Correlated Electron Systems. *J Phys Soc Jpn* (2010) 79:2001. doi:10.1143/jpsj.79.112001
33. Hirayama M, Tadano T, Nomura Y, Arita R. Materials Design of Dynamically Stable D9 Layered Nickelates. *Phys Rev B* (2020) 101:075107. doi:10.1103/PhysRevB.101.075107
34. Nomura Y, Nomoto T, Hirayama M, Arita R. Magnetic Exchange Coupling in Cuprate-Analog D9 Nickelates. *Phys Rev Res* (2020) 2:043144. doi:10.1103/PhysRevResearch.2.043144
35. Hirayama M, Miyake T, Imada M, Biermann S. Low-energy Effective Hamiltonians for Correlated Electron Systems beyond Density Functional Theory. *Phys Rev B* (2017) 96:075102. doi:10.1103/physrevb.96.075102
36. Hirayama M, Miyake T, Imada M. Derivation of Static Low-Energy Effective Models by Anab Initiodownfolding Method without Double Counting of Coulomb Correlations: Application to SrVO3, FeSe, and FeTe. *Phys Rev B* (2013) 87:195144. doi:10.1103/PhysRevB.87.195144
37. Hirayama M, Yamaji Y, Misawa T, Imada M. Ab Initio effective Hamiltonians for Cuprate Superconductors. *Phys Rev B* (2018) 98:134501. doi:10.1103/PhysRevB.98.134501
38. Hirayama M, Misawa T, Ohgoe T, Yamaji Y, Imada M. Effective Hamiltonian for Cuprate Superconductors Derived from Multiscale Ab Initio Scheme with Level Renormalization. *Phys Rev B* (2019) 99:245155. doi:10.1103/PhysRevB.99.245155
39. Ohgoe T, Hirayama M, Misawa T, Ido K, Yamaji Y, Imada M. Ab Initio study of Superconductivity and Inhomogeneity in a Hg-Based Cuprate Superconductor. *Phys Rev B* (2020) 101:045124. doi:10.1103/PhysRevB.101.045124
40. Jiang M, Berciu M, Sawatzky GA. Critical Nature of the Ni Spin State in Doped NdNiO2. *Phys Rev Lett* (2020) 124:207004. doi:10.1103/PhysRevLett.124.207004
41. Zhang Y-H, Vishwanath A. Type-II t–J Model in Superconducting Nickelate Nd1−xSrxNiO2. *Phys Rev Res* (2020) 2:023112. doi:10.1103/PhysRevResearch.2.023112
42. Werner P, Hoshino S. Nickelate Superconductors: Multiorbital Nature and Spin Freezing. *Phys Rev B* (2020) 101:041104. doi:10.1103/PhysRevB.101.041104
43. Petocchi F, Christiansson V, Nilsson F, Aryasetiawan F, Werner P. Normal State of Nd1−xSrxNiO2 from Self-Consistent GW+EDMFT. *Phys Rev X* (2020) 10:041047. doi:10.1103/PhysRevX.10.041047
44. Hu L-H, Wu C. Two-band Model for Magnetism and Superconductivity in Nickelates. *Phys Rev Res* (2019) 1:032046. doi:10.1103/PhysRevResearch.1.032046
45. Lechermann F. Late Transition Metal Oxides with Infinite-Layer Structure: Nickelates versus Cuprates. *Phys Rev B* (2020) 101:081110. doi:10.1103/PhysRevB.101.081110
46. Lechermann F. Multiorbital Processes Rule the Nd1−xSrxNiO2 Normal State. *Phys Rev X* (2020) 10:041002. doi:10.1103/PhysRevX.10.041002
47. Lechermann F. Doping-dependent Character and Possible Magnetic Ordering of NdNiO2. *Phys Rev Mater* (2021) 5:044803. doi:10.1103/PhysRevMaterials.5.044803
48. Chang J, Zhao J, Ding Y. Hund-Heisenberg Model in Superconducting Infinite-Layer Nickelates. *Eur Phys J B* (2020) 93:220. doi:10.1140/epjb/e2020-10343-7
49. Wang Y, Kang C-J, Miao H, Kotliar G. Hund's Metal Physics: From SrNiO2 to LaNiO2. *Phys Rev B* (2020) 102:161118. doi:10.1103/PhysRevB.102.161118
50. Liu Z, Xu C, Cao C, Zhu W, Wang ZF, Yang J. Doping Dependence of Electronic Structure of Infinite-Layer NdNiO2. *Phys Rev B* (2021) 103:045103. doi:10.1103/PhysRevB.103.045103
51. Kang B, Melnick C, Semon P, Ryee S, Han MJ, Kotliar G, et al. *Infinite-layer Nickelates as Ni-*E_g *Hund's Metals* (2021). arXiv:2007.14610.
52. Choi M-Y, Pickett WE, Lee K-W. Fluctuation-frustrated Flat Band Instabilities in NdNiO2. *Phys Rev Res* (2020) 2:033445. doi:10.1103/PhysRevResearch.2.033445
53. Jiang P, Si L, Liao Z, Zhong Z. Electronic Structure of Rare-Earth Infinite-Layer RNiO2(R=La,Nd). *Phys Rev B* (2019) 100:201106. doi:10.1103/PhysRevB.100.201106
54. Choi M-Y, Lee K-W, Pickett WE. Role of 4f States in Infinite-Layer NdNiO2. *Phys Rev B* (2020) 101:020503. doi:10.1103/PhysRevB.101.020503
55. Zhang R, Lane C, Singh B, Nokelainen J, Barbiellini B, Markiewicz RS, et al. Magnetic and F-Electron Effects in LaNiO2 and NdNiO2 Nickelates with Cuprate-like $$3{d}_{{x}^{2}-{y}^{2}}$$ Band. *Commun Phys* (2021) 4:118. doi:10.1038/s42005-021-00621-4
56. Bandyopadhyay S, Adhikary P, Das T, Dasgupta I, Saha-Dasgupta T. Superconductivity in Infinite-Layer Nickelates: Role of *F* Orbitals. *Phys Rev B* (2020) 102:220502. doi:10.1103/PhysRevB.102.220502
57. Hepting M, Li D, Jia CJ, Lu H, Paris E, Tseng Y, et al. Electronic Structure of the Parent Compound of Superconducting Infinite-Layer Nickelates. *Nat Mater* (2020) 19:381–5. doi:10.1038/s41563-019-0585-z
58. Zhang G-M, Yang Y-f., Zhang F-C. Self-doped Mott Insulator for Parent Compounds of Nickelate Superconductors. *Phys Rev B* (2020) 101:020501. doi:10.1103/PhysRevB.101.020501
59. Gu Y, Zhu S, Wang X, Hu J, Chen H. A Substantial Hybridization between Correlated Ni-*D* Orbital and Itinerant Electrons in Infinite-Layer Nickelates. *Commun Phys* (2020) 3:84. doi:10.1038/s42005-020-0347-x
60. Fu Y, Wang L, Cheng H, Pei S, Zhou X, Chen J, et al. *Core-level X-ray Photoemission and Raman Spectroscopy Studies on Electronic Structures in Mott-Hubbard Type Nickelate Oxide* $NdNiO_2$ (2019). arXiv:1911.03177.
61. Goodge BH, Li D, Lee K, Osada M, Wang BY, Sawatzky GA, et al. Doping Evolution of the Mott–Hubbard Landscape in Infinite-Layer Nickelates. *Proc Natl Acad Sci* (2021) 118. doi:10.1073/pnas.2007683118
62. Kitatani M, Si L, Janson O, Arita R, Zhong Z, Held K. Nickelate Superconductors-A Renaissance of the One-Band Hubbard Model. *Npj Quan Mater.* (2020) 5:59. doi:10.1038/s41535-020-00260-y
63. Karp J, Hampel A, Zingl M, Botana AS, Park H, Norman MR, et al. Comparative many-body Study of Pr4Ni3O8 and NdNiO2. *Phys Rev B* (2020) 102:245130. doi:10.1103/PhysRevB.102.245130
64. Higashi K, Winder M, Kuneš J, Hariki A. Core-Level X-Ray Spectroscopy of Infinite-Layer Nickelate: LDA+DMFT Study. *Phys Rev X* (2021) 11:041009. doi:10.1103/PhysRevX.11.041009
65. Karp J, Botana AS, Norman MR, Park H, Zingl M, Millis A. Many-body Electronic Structure of NdNiO2 and CaCuO2. *Phys Rev X* (2020) 10:021061. doi:10.1103/PhysRevX.10.021061
66. Lang Z-J, Jiang R, Ku W. Strongly Correlated Doped Hole Carriers in the Superconducting Nickelates: Their Location, Local many-body State, and Low-Energy Effective Hamiltonian. *Phys Rev B* (2021) 103:L180502. doi:10.1103/PhysRevB.103.L180502
67. Worm P, Si L, Kitatani M, Arita R, Tomczak JM, Held K. *Correlations Turn Electronic Structure of Finite-Layer Nickelates Upside Down* (2021). arXiv:2111.12697.
68. Zaanen J, Sawatzky GA, Allen JW. Band Gaps and Electronic Structure of Transition-Metal Compounds. *Phys Rev Lett* (1985) 55:418–21. doi:10.1103/PhysRevLett.55.418
69. Crespin M, Isnard O, Dubois F, Choisnet J, Odier P. Lanio2: Synthesis and Structural Characterization. *J Solid State Chem* (2005) 178:1326–34. doi:10.1016/j.jssc.2005.01.023
70. Methfessel M, van Schilfgaarde M, Casali RA. *Lecture Notes in Physics*. editorH Dreysse 535. Berlin): Springer-Verlag (2000).
71. Ceperley DM, Alder BJ. Ground State of the Electron Gas by a Stochastic Method. *Phys Rev Lett* (1980) 45:566–9. doi:10.1103/PhysRevLett.45.566
72. van Schilfgaarde M, Kotani T, Faleev SV. Adequacy of Approximations inGWtheory. *Phys Rev B* (2006) 74:245125. doi:10.1103/physrevb.74.245125

73. Fujiwara T, Yamamoto S, Ishii Y. Generalization of the Iterative Perturbation Theory and Metal-Insulator Transition in Multi-Orbital Hubbard Bands. *J Phys Soc Jpn* (2003) 72:777–80. doi:10.1143/jpsj.72.777
74. Nohara Y, Yamamoto S, Fujiwara T. Electronic Structure of Perovskite-type Transition Metal oxidesLaMO3(M=Ti~Cu)byU+GWapproximation. *Phys Rev B* (2009) 79:195110. doi:10.1103/physrevb.79.195110
75. Miyake T, Aryasetiawan F, Imada M. Ab Initioprocedure for Constructing Effective Models of Correlated Materials with Entangled Band Structure. *Phys Rev B* (2009) 80:155134. doi:10.1103/physrevb.80.155134
76. Olevano V, Bernardini F, Blase X, Cano A. Ab Initio many-body GW Correlations in the Electronic Structure of LaNiO2. *Phys Rev B* (2020) 101: 161102. doi:10.1103/PhysRevB.101.161102

Conflict of Interest: The authors declare that the research was conducted in the absence of any commercial or financial relationships that could be construed as a potential conflict of interest.

The reviewer AF declared a shared affiliation, with no collaboration, with the authors, RA, MH, to the handling editor at time of review.

Publisher's Note: All claims expressed in this article are solely those of the authors and do not necessarily represent those of their affiliated organizations, or those of the publisher, the editors, and the reviewers. Any product that may be evaluated in this article, or claim that may be made by its manufacturer, is not guaranteed or endorsed by the publisher.

APPENDIX

For reference, we summarize the parameters in the single-orbital model in **Tables A1** and **A2**. Special attention should be paid to the strength of the interaction in the GWA-based effective single-orbital model (see Ref. [38]). In the copper oxides, the correlation effect beyond the RPA between the d and p orbitals in the three-orbital model is not small. Therefore, in order to calculate the single-orbital model accurately, it is necessary to treat the screening effect originating from the bonding and nonbonding bands beyond the RPA. To do so, we need to solve the three-orbital model once with a low-energy solver such as the VMC and estimate the energy corrections between the d and p orbitals beyond the GWA. By combining such a correction with the GW self-energy correction, we can calculate the band structure beyond the GWA, and can estimate a single-orbital model with high accuracy (See Ref. [38] for details of the method). Because the nickelates have a qualitatively similar band structure to the cuprates, the reliability of the GWA-based single-orbital model for the nickelates also needs to be carefully examined: in particular, the correlation strength $|U/t|$ might be overestimated.

TABLE A1 | Transfer integral and effective interaction in the one-band Hamiltonian for $YNiO_2$ (in eV). Both the one-body and two-body parts in the Hamiltonian are derived based on the LDA band structure. v and U (0) represent the bare Coulomb interaction and the static value of the effective Coulomb interaction, respectively (at ω =0). The index "n" and "nn" represent the nearest unit cell [1,0,0] and the next-nearest unit cell [1,1,0], respectively.

t (LDA)	(0, 0, 0)	(1, 0, 0)	(1, 1, 0)	(2, 0, 0)	U/v	$\|U/t\|$
$x^2 - y^2$	0.211	–0.357	0.093	–0.046	0.149	8.15
	v	U (0)	v_n	V_n(0)	v_{nn}	V_{nn} (0)
$x^2 - y^2$	19.578	2.910	3.981	0.229	2.685	0.091

TABLE A2 | Transfer integral and effective interaction in the one-band Hamiltonian for $YNiO_2$ (in eV). The one-body part is derived based on the GW band structure, and the effective interaction is the result of the cRPA calculation for the GW bands. v and U (0) represent the bare Coulomb interaction and the static value of the effective Coulomb interaction, respectively (at ω =0). The index "n" and "nn" represent the nearest unit cell [1,0,0] and the next-nearest unit cell [1,1,0] respectively.

t (GW)	(0, 0, 0)	(1, 0, 0)	(1, 1, 0)	(2, 0, 0)	U/v	$\|U/t\|$
$x^2 - y^2$	0.172	–0.271	0.075	–0.033	0.167	12.94
	v	U (0)	v_n	V_n(0)	v_{nn}	V_{nn} (0)
$x^2 - y^2$	20.948	3.508	3.957	0.300	2.677	0.131

frontiers in Physics

ORIGINAL RESEARCH
published: 28 February 2022
doi: 10.3389/fphy.2022.836959

On the Nature of Valence Charge and Spin Excitations *via* Multi-Orbital Hubbard Models for Infinite-Layer Nickelates

Emily M. Been[1,2], *Kuan H. Hsu*[1,3], *Yi Hu*[1,3], *Brian Moritz*[1], *Yi Cui*[3], *Chunjing Jia*[1] *and Thomas P. Devereaux*[1,3]*

[1]SLAC National Accelerator Laboratory, Stanford Institute for Materials and Energy Sciences, Menlo Park, CA, United States, [2]Department of Physics, Stanford University, Stanford, CA, United States, [3]Department of Materials Science and Engineering, Stanford University, Stanford, CA, United States

Building upon the recent progress on the intriguing underlying physics for the newly discovered infinite-layer nickelates, in this article we review an examination of valence charge and spin excitations via multi-orbital Hubbard models as way to determine the fundamental building blocks for Hamiltonians that can describe the low energy properties of infinite-layer nickelates. We summarize key results from density-functional approaches, and apply them to the study of x-ray absorption to determine the valence ground states of infinite-layer nickelates in their parent form, and show that a fundamental d^9 configuration as in the cuprates is incompatible with a self-doped ground state having holes in both $d_{x^2-y^2}$ and a rare-earth-derived axial orbital. When doped, we determine that the rare-earth-derived orbitals empty and additional holes form low spin ($S = 0$) d^8 Ni states, which can be well-described as a doped single-band Hubbard model. Using exact diagonalization for a 2-orbital model involving Ni and rare-earth orbitals, we find clear magnons at 1/2 filling that persist when doped, albeit with larger damping, and with a dependence on the precise orbital energy separation between the Ni- and rare-earth-derived orbitals. Taken together, a full two-band model for infinite-layer nickelates can well describe the valence charge and spin excitations observed experimentally.

Keywords: nickelate, superconductor, exact diagonalization, dynamic spin structure factor, spectroscopy, x-ray absorption spectroscopy, XAS

OPEN ACCESS

Edited by:
Antia Botana,
Arizona State University, United States

Reviewed by:
Atsushi Fujimori,
Waseda University, Japan
Franca Manghi,
University of Modena and Reggio Emilia, Italy

***Correspondence:**
Thomas P. Devereaux
tpd@stanford.edu

Specialty section:
This article was submitted to Condensed Matter Physics, a section of the journal Frontiers in Physics

Received: *16 December 2021*
Accepted: *17 January 2022*
Published: *28 February 2022*

Citation:
Been EM, Hsu KH, Hu Y, Moritz B, Cui Y, Jia C and Devereaux TP (2022) On the Nature of Valence Charge and Spin Excitations via Multi-Orbital Hubbard Models for Infinite-Layer Nickelates. Front. Phys. 10:836959. doi: 10.3389/fphy.2022.836959

1 INTRODUCTION

The discovery of experimental superconductivity in infinite-layer nickelates [1], 20 years after they were theoretically proposed [2], has unveiled new territory to probe the unknowns of unconventional superconductivity. The comparison between the superconducting nickelates to the cuprates has proven to be a rich area of inquiry. Significant progress has been made in the last 2 years, but many mysteries about this novel superconducting family remain unsolved. As pointed out early on [3], the bandstructure for $LaNiO_2$ while being primarily $3d^9$ Ni near the Fermi level has additional small Fermi pockets of largely axial character involving Ni $3d_{z^2}$ and La $5d_{z^2}$ orbitals. Including a Hubbard U on nickel splits the d^9 states but still leaves itinerant states at the Fermi level, indicating that the parent compound for infinite-layer nickelate is not analogous to undoped CuO_2 as an antiferromagnetic Mott insulator. Moreover, the location of the centroid of the oxygen states in

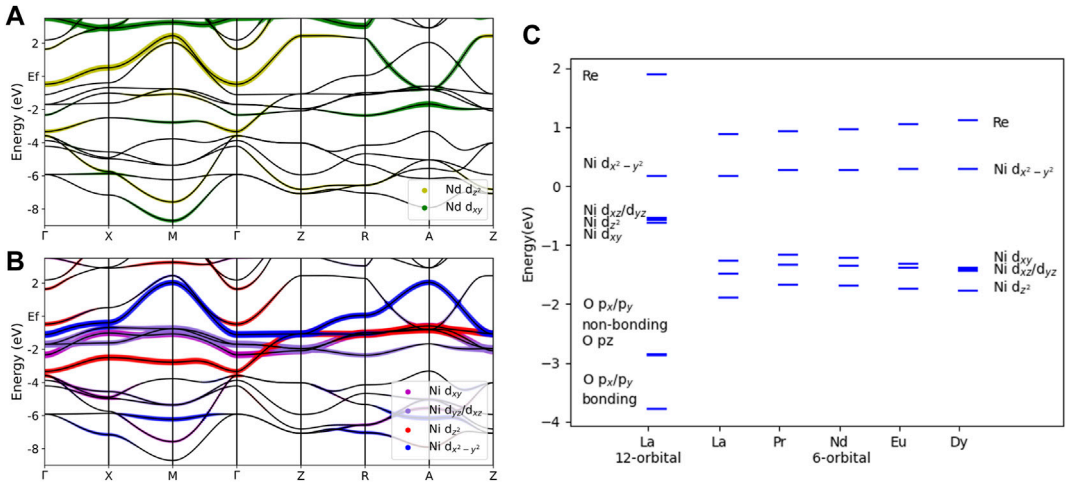

FIGURE 1 | (A) DFT calculated band structure and projected Nd 5*d* orbital content for infinite-layer nickelate $NdNiO_2$. **(B)** DFT calculated band structure and projected Ni 3*d* orbital content for $NdNiO_2$. **(C)** Atomic energy level diagram for infinite-layer nickelates $RNiO_2$, where *R* = La, Pr, Nd, Eu, and Dy. On-site energies are obtained by 6-orbital and 12-orbital Wannier downfolding from DFT calculated band structures. All energy levels are relative to the Fermi level of the corresponding material.

$LaNiO_2$ lies at lower energies than CuO_2 compounds, moving them closer to the boundary between Mott-Hubbard systems and charge-transfer insulators in the Zaanen-Sawatzky-Allen scheme [4]. While there is scant evidence that $LaNiO_2$ is antiferromagnetic, resonant inelastic x-ray scattering (RIXS) has clearly revealed propagating magnons, yielding a spin exchange energy ~ 60 meV in the parent compound [5]. These excitations persist when doped, albeit with larger damping [5], in a way that is not too disimilar to paramagnon excitations in doped cuprates [6–8].

Thus there already is a rich amount of information from which an estimate for a fundamental low energy model Hamiltonian can be obtained and used to model the phase diagram of infinite-layer nickelates. In this article we review efforts to combine density functional approaches with cluster exact diagonalization to determine such a model. Specifically we utilize x-ray absorption (XAS) as a tool to determine valence charge states in the undoped and doped infinite-layer nickelates, arriving at a low-energy 2-orbital model Hamiltonian. We then perform calculations on finite-sized clusters to determine the dynamic spin structure factor in undoped and doped systems. Our results yield a consistent description of charge valence and spin excitation states in the infinite-layer nickelates, indicating that a 2-orbital model likely contains the fundamental ingredients needed to explore superconductivity and the rich phase diagram in these compounds.

2 METHODS

2.1 Density Functional Theory

The electronic structure of the infinite-layer nickelates $RNiO_2$ have been evaluated using density functional theory (DFT) in the generalized gradient approximation (GGA) for the exchange-correlation functional as implemented in Quantum Espresso [9, 10]. The band structure near the Fermi energy that was obtained for $NdNiO_2$ is shown in **Figures 1A, B**.

To obtain a microscopic Hamiltonian and understand the atomic energy levels, we downfolded the bandstructure as implemented in Wannier90 [11] to obtain the tight-binding model parameters $t_{i,j}^{\mu,\nu}$ as shown in **Eq. 2** below. Two types of Wannier downfolding have been calculated: **(Eq. 1)** a 12-orbital model downfolding, which includes five Ni 3*d* orbitals, one *R* 5*d* orbital and six O 2*p* orbitals; and **(Eq. 2)** a 6-orbital model downfolding, which includes five Ni 3*d* orbitals and one *R* 5*d* orbital. For $NdNiO_2$, the bandstructure corresponding to the 6-orbital model spans an energy range from ~ −3.5 eV to ~ 2 eV, covering the most prominent low energy features. The bands below ~ −3.5 eV for $NdNiO_2$ have predominantly oxygen orbital content. **Figure 1C** summarizes the atomic energy level diagram, which shows the on-site energies from the Wannier downfolding for a series of $RNiO_2$ materials (*R* = La, Pr, Nd, Eu or Dy).

2.2 X-Ray Absorption from Multi-Orbital Hubbard Hamiltonians

We focus on the Ni *L*-edge ($2p \rightarrow 3d$) XAS utilizing a cluster model for monovalent NiO_2 containing five Ni 3*d* orbitals and six O 2*p* orbitals in a square-planar geometry, and three Ni 2*p* orbitals per unit cell in the atomic core, with hybridization parameters obtained from Wannier downfolding as described in the previous section. We evaluate the XAS κ for the absorption of a photon having momentum and polarization $\mathbf{k}_i$, e_i, respectively, as

$$\kappa_{\mathbf{e}_i,\mathrm{k}_i}(\omega) = \frac{1}{\pi Z}\sum_{i,\nu} e^{-\beta E_i}|\langle\nu|\hat{D}_{\mathbf{k}_i}(\mathbf{e}_i)|i\rangle|^2\delta(\omega-(E_\nu-E_i)), \quad (1)$$

Here, Z is the partition function, $E_{\{i,\nu\}}$, $|\{i,\nu\}\rangle$ are the energies and eigenstates of the initial (ground state) and XAS final states, respectively, obtained from exact diagonalization of the

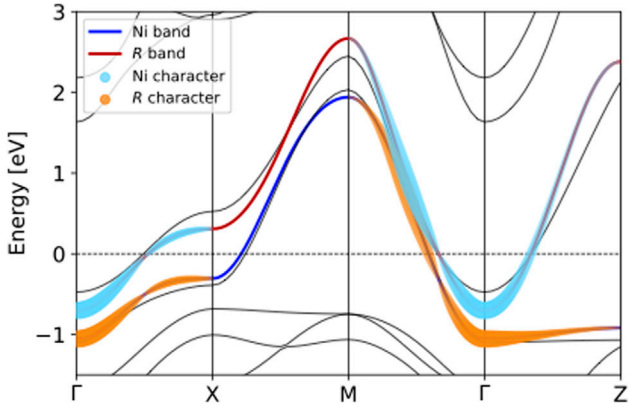

FIGURE 2 | Hybridization of the 2-orbital model for $NdNiO_2$, as described in **Eq. 4**, showing subdominant Ni and *R* band character, respectively.

multi-orbital Hubbard model in the cluster Hilbert space. The multi-orbital Hubbard model can be compactly written as

$$H = \sum_{i,j,\sigma} \sum_{\mu,\nu} t_{i,j}^{\mu,\nu} d_{i,\mu,\sigma}^{\dagger} d_{j,\nu,\sigma}$$

$$+\frac{1}{2} \sum_{i} \sum_{\mu,\nu,\mu',\nu'} \sum_{\sigma,\sigma'} U_{\mu,\nu,\mu',\nu'} d_{i,\mu,\sigma}^{\dagger} d_{i,\nu,\sigma'}^{\dagger} d_{i,\mu',\sigma'} d_{i,\nu',\sigma}. \quad (2)$$

Here i, j denote sites, σ, σ' denote spin, and μ, ν, μ', ν' denote orbital indices. The operators $d_{i,\mu,\sigma}^{\dagger}, d_{i,\mu,\sigma}$ create, annihilate holes having spin σ in orbital μ at site i, and can represent valence, ligand, or core holes. The Coulomb matrix elements U are written in terms of Slater-Condon parameters pertaining to the valence hole and core hole states, which can be determined via a variety of methods or simply used as fitting parameters to x-ray spectra. Lastly $\hat{D}$ is the dipole operator connecting Ni $2p$ core levels to Ni $3d$ states. Additional details about XAS can be found in various textbooks, *i.e.* Ref. [12]. As the Hilbert space scales exponentially with the number of orbitals in the unit cell, this technique is amenable to only small clusters. However, since XAS is a local probe of electronic structure, our computational approach is well suited to determine the effective low energy valence and spin states of Ni, as is well known in many other contexts.

2.3 Dynamic Spin Structure Factor

The dynamic spin structure factor has been shown to be an accurate approximation of the RIXS cross section of both Mott insulators and doped systems [6, 13]. The dynamical spin structure factor is defined as

$$S(\mathbf{q},\omega) = \frac{1}{\pi} \mathrm{Im} \langle G \left| \rho_{\mathbf{q}}^{(s)\dagger} \frac{1}{\mathcal{H} - E_G - \omega - i\Gamma} \rho_{\mathbf{q}}^{(s)} \right| G \rangle, \quad (3)$$

where the spin density operator is given by $\rho_{\mathbf{q}}^{(s)} = \sum_{\mathbf{i},\sigma} s_{\mathbf{i}\sigma} e^{i\mathbf{q}\cdot\mathbf{r}_{\mathbf{i}}} = \sum_{\mathbf{k},\sigma} \sigma c_{\mathbf{k}+\mathbf{q},\sigma}^{\dagger} c_{\mathbf{k}\sigma}$, and the 2-orbital nickelate model Hamiltonian is given by

$$\mathcal{H} = \sum_{\mathbf{k},\sigma} \left(\varepsilon_{\mathbf{k}}^{R} c_{\mathbf{k}\sigma}^{\dagger} c_{\mathbf{k}\sigma} + \varepsilon_{\mathbf{k}}^{\mathrm{Ni}} d_{\mathbf{k}\sigma}^{\dagger} d_{\mathbf{k}\sigma} \right) + \frac{U}{N} \sum_{\mathbf{k}_1,\mathbf{k}_2,\mathbf{q}} d_{\mathbf{k}_1+\mathbf{q},\uparrow}^{\dagger} d_{\mathbf{k}_2-\mathbf{q},\downarrow}^{\dagger} d_{\mathbf{k}_2,\downarrow} d_{\mathbf{k}_1,\uparrow}$$

$$+ \sum_{\mathbf{k},\sigma} \left(\varepsilon_{\mathbf{k}}^{R-Ni} c_{\mathbf{k},\sigma}^{\dagger} d_{\mathbf{k},\sigma} + \mathrm{H.c.} \right), \quad (4)$$

where $c_{\mathbf{k}}$ ($c_{\mathbf{k}}^{\dagger}$) operators represent the dispersive R $5d$ band and the $d_{\mathbf{k}}$ ($d_{\mathbf{k}}^{\dagger}$) operators represent the Hubbard-like Ni $3d$ band. The details of $\varepsilon_{\mathbf{k}}^{R}$, $\varepsilon_{\mathbf{k}}^{\mathrm{Ni}}$, and $\varepsilon_{\mathbf{k}}^{\mathrm{R-Ni}}$ are defined in Ref. [14] which proposed this form of the 2-orbital model. The hybridization between Ni and R in this 2-orbital model is shown visually by plotting only the subdominant orbital character in **Figure 2**. This hybridization results in the "self-doped" nature of the nickelates.

We evaluate the dynamic spin structure factor, S ($\mathbf{q}$, ω), for the 2-orbital nickelate model using exact diagonalization (ED) on an 8-site (diamond-shaped) Betts cluster [15] with periodic boundary conditions, which suffers from finite-size effects but is sufficient for determining the magnon spectrum on the antiferromagnetic Brillouin zone boundary at (π/2, π/2). We take the value of the Hubbard U = 8 eV so that we get a reasonable estimate of J ~ 80 meV. The eigenvalues and eigenvectors of the ED calculations were found using the Implicitly Restarted Lanczos Method from the ARnoldi PACKage (ARPACK), as implemented in SciPy Linalg library ([16], RRID: SCR_008058). The biconjugate gradient stabilized method was used to calculate S ($\mathbf{q}$, ω).

3 RESULTS

3.1 X-Ray Absorption Spectroscopy

3.1.1 Single-Site

The single site XAS is simulated using techniques mentioned in **Sec. 2.2**, where the Hilbert space is determined using only the $3d$ (valence) and $2p$ (core) orbitals of the Ni transition metal ion, without ligand $2p$ orbitals, and with open boundary conditions. The eigenenergies are obtained by diagonalizing the Hamiltonian and the XAS cross section is evaluated using **Eq. (1)**.

We first calculate the multiplet XAS of the d^9 electronic configuration of the Ni ion where the Slater-Condon, spin orbit coupling and crystal-field splitting parameters are taken from Ref. [17]. The results are plotted in **Figure 3**. Since the single site calculation does not include ligand orbitals in the Hilbert space, direct measurements of crystal field splitting of d orbitals energy levels are used without hybridization parameters obtained by Wannier downfolding from Ref. [18]. Although hybridization with ligands is not considered in this single-site calculation, it can still capture the difference in XAS between high-spin and low-spin ground state as described below. The Coulomb interaction for d^9 ions is less relevant and the spectral lineshape is dominated by the spin orbit coupling of the core levels, showing a single peak for both the L_3 and L_2 edges with light polarization along the x-direction, and no absorption with light polarization along the z-direction, due to the orbital $d_{x^2-y^2}$ character of the holes in the d^9 configuration. We then

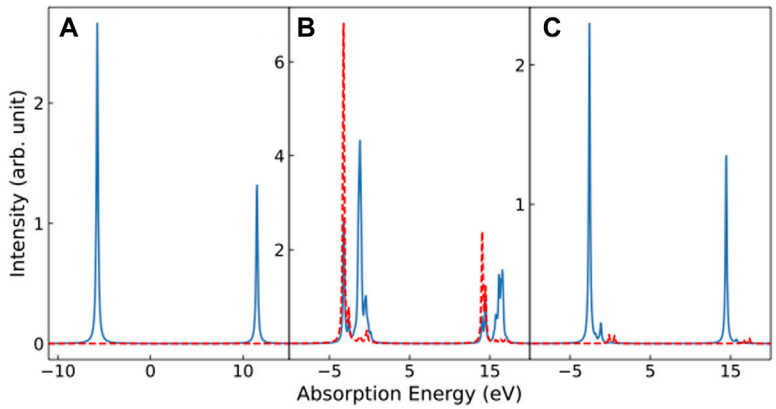

FIGURE 3 | Multiplet XAS calculations for the single-site nickel ion. The absorption energy is measured with respect to the ground state of d^9 ion. The solid line is the spectra measured with *x*-polarized light, and the dashed line is the spectra measured with *z*-polarized light. From left to right are spectra of **(A)** the d^9 ion, **(B)** the d^8 high-spin ion, and **(C)** the d^8 low-spin ion.

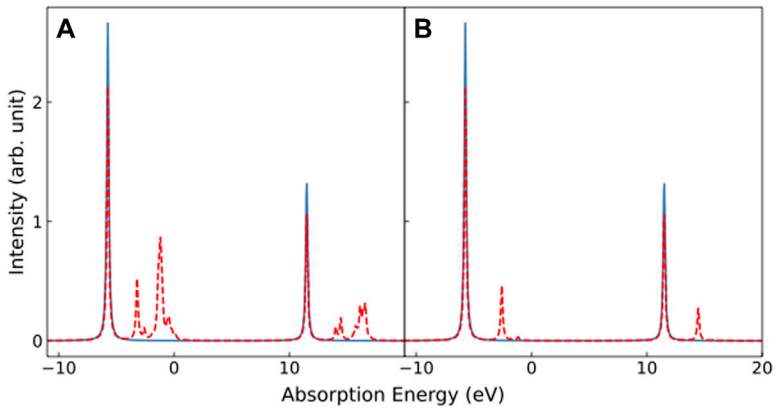

FIGURE 4 | XAS spectra for the undoped d^9 ion (solid line) and with 20% of the hole-doped d^8 ion (dashed line) calculated for *x*-polarization. Panel **(A)** shows the results for doping with the d^8 high-spin state, and panel **(B)** shows the results for doping with the d^8 low-spin state.

calculated the multiplet XAS on the d^8 ion using the same parameters for a spin singlet ($S = 0$) and a spin triplet ($S = 1$) ground state. Similar to previous reports by Ref. [17], with light polarized along the *z*-direction, the intensity of the XAS peaks decrease in the low spin state, while the intensity remains the same order of magnitude for the high spin state. With light polarized along the *x*-direction, the high-spin ground state displays stronger intensity across a wide range of absorption energies, with more dipole-allowed transitions to excited states, compared to the singly degenerate, low-spin ground state.

We also simulated doped spectra as a linear combination of the d^8 and d^9 spectra, with the results plotted in **Figure 4**. Clearly, the high-spin d^8 state produces spectra with a wide energy spread and additional multiplet peaks. A better comparison to experiment [17] can be made if the d^8 ion is in the low-spin configuration, producing a less pronounced shoulder in addition to the main absorption peak from the dominant d^9 configuration.

3.1.2 Two-Site

The two-site XAS is simulated with a two-site, multi-orbital Hubbard model as described in **Sec. 2.2** with periodic boundary conditions in contrast to section **Sec. 3.1.1**, with 11 orbitals for each site (unit cell NiO_2) in the initial state that includes six oxygen 2*p* orbitals and the five nickel 3*d* orbitals, and 14 orbitals for one of the cells in the final state, which includes an additional three core-level nickel 2*p* orbitals for the target atom. The eigenenergies and eigenstates are obtained by exact diagonalization of the model Hamiltonian and the XAS spectra are calculated using **Eq. (1)**. Including the oxygen ligand orbitals in the model allows hybridization and charge transfer effects between oxygen 2*p* and Nickel 3*d* orbitals. The Ni-O hybridization will affect not only the effective energy levels of the Nickel 3*d* orbitals, but this also changes the effective band character, with oxygen ligand *p* orbital contributions to the valance and conduction bands, which will result in changes to the XAS lineshape compared to the single-site calculation in **Sec. 3.1.1**.

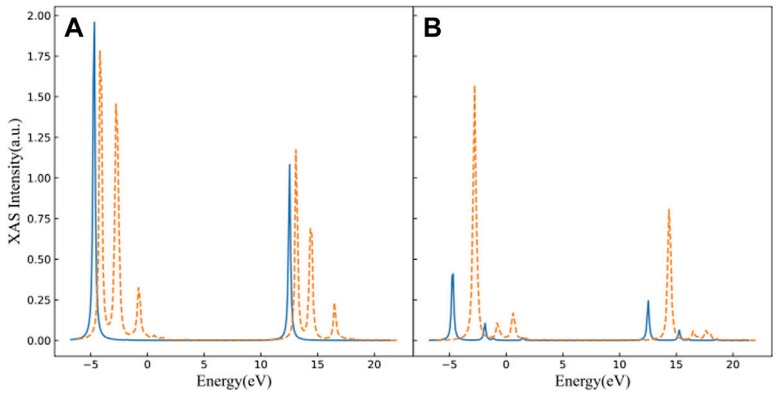

FIGURE 5 | Multiplet calculations for two-site, two-hole (solid, blue line) and two-site, three-hole (dashed, orange) NiO_2 clusters. The absorption energy is measured from the ground state of the two-site, two-hole calculation. Panel **(A)** shows the XAS spectra in *x*-polarization; and panel **(B)** shows the XAS spectra in *z*-polarization.

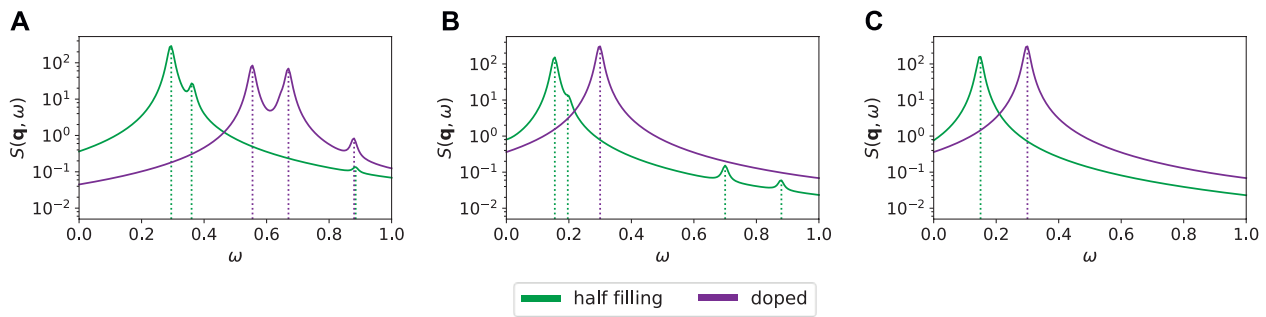

FIGURE 6 | Comparison of S ($\mathbf{q}$, ω) at $\mathbf{q} = (\frac{\pi}{2}, \frac{\pi}{2})$ between **(A)** the 2-orbital model with $\varepsilon^R_{\mathbf{k}} - \varepsilon^{Ni}_{\mathbf{k}} \equiv \Delta \sim 1$ eV, **(B)** the 2-orbital model with $\Delta \rightarrow \Delta + U/2$, and **(C)** the 1-orbital model that only includes the Ni layer. The dotted vertical lines in each plot show positions of energy eigenvalues (differences) broadened by Lorentzian convolution in the final spectrum. All energies are in eV with S ($\mathbf{q}$, ω) shown on a log scale to enhance weaker features. The half-filling curve (green) in panel **(A)** aligns with the doped curves (purple) in panels **(B)** and **(C)** which correspond to 25% doping of the nickel layer, highlighting the "self-doping" influence of the rare-earth layer when Δ is small.

We performed multiplet calculations for a two-site, two-hole (nominally d^9 nickel) and a two-site, three-hole (doped NiO_2 planes) cluster using effective parameters described in **Sec. 3.1.1**, and hopping parameters (t_{pd}, t_{pdz}, t_{pdxy}, t_{pdxz}, t_{pdyz} are 1.2, 0.3, 0.7, 0.8 and 0.8 eV, respectively) obtained by Wannier downfolding as described in **Sec. 2.1**. The inclusion of hybridization parameters allow us to modulate the strength of electron hopping between each orbital and the onsite energy, with the electrons distributed between the different orbitals based on the model Hamiltonian as described in Ref. [18]. These XAS spectra are shown in **Figure 5**. The two-site, two-hole XAS spectrum with *x*-polarization is similar to the single-site, d^9 model, which was described in the previous section. When doped with one hole, the L_3 and L_2 edges split into three peaks due to Ni-O hybridization. These results are consistent with both the single-site calculation and the experimental results [17].

3.2 Spin Structure Factor

Results for the dynamical spin structure factor calculated via exact diagonalization are plotted in **Figure 6**, showing a comparison of the 2-orbital model with two different values of the energy difference between Ni and R orbitals $\varepsilon^R_{\mathbf{k}} - \varepsilon^{Ni}_{\mathbf{k}} \equiv \Delta$, and also results from a single-orbital model for the nickel oxide layer. "Half-filling" corresponds to eight electrons distributed among the 16 orbitals of the 2-orbital, 8A Betts cluster, or the eight orbitals of the 8A Betts cluster in the 1-orbital model for the Ni-O layer. The Ni-R energy difference and hybridization dictate the effective filling of the Ni band in the 2-orbital model. The doped calculation is performed with six electrons, corresponding to a nominal doping of ~ 25%.

For the 2-orbital model, tuning the energy difference between Ni and R sites, Δ, plays a major role in the occupation of the R orbital, and hence the "self-doping" of the Ni layer. In **Figure 6A**, $\Delta \sim 1$ eV results in approximately two electrons occupying the R-sites at both overall half-filling and ~25% doping, meaning the Ni layer retains a 25% "self-doping" offset. In contrast, panel **Figure 6B** shows the results for the 2-orbital model with a large offset of $U/2 = 4$ eV added to Δ, resulting in $\Delta \sim 5$ eV. Here, the R-site is almost completely empty and S ($\mathbf{q}$, ω) looks very similar to results from the 1-orbital calculation shown in **Figure 6C**.

Obviously, the infinite-layer nickelates live between these two extremes and **Figure 6** gives us some clues as to how S ($\mathbf{q}$, ω) is affected by the occupation of the R sites, with $S(\mathbf{q}, \omega)$ extremely sensitive to the R and Ni occupations.

4 DISCUSSION

In this paper we explored numerical simulations using DFT and ED to determine the underlying band structure, valence configuration, and dynamical spin response of model Hamiltonians aimed to describe infinite-layer nickelates. DFT for various R substituted nickelates was used to determine the parameters of an effective 2-orbital model including Ni $3d_{x^2-y^2}$ and R $5d$ "axial" orbitals, where the effect of lower-lying oxygen orbitals is to modify the inter-orbital hybridizations. Cluster multiplet ED was used to determine that undoped nickelate has predominantly $3d^9$ valence which upon doping involves low-spin nickel $3d^8$ valence holes. These results indicate that undoped infinite-layer nickelate is "self-doped" away from half-filling Ni $3d^9$ via the presence of a finite electron concentration in the R layer compensating the holes in the Ni layer, the physics of doped nickelates may be described simply from the point of view of a one-band Hubbard-like model. Our consideration of the spin response indicates a close similarity of the paramagnon energies and intensities to one-band systems, in close analogy with the behavior seen in the cuprates.

Our ED calculations are limited to small clusters and therefore the effect of long-wavelength physics remains beyond our level of investigation. This may be particularly relevant to a discussion of the root cause of superconductivity and the competition between superconductivity and other intertwined phases, such as spin and/or charge stripes that are prevalent in both cuprate phase diagrams and numerical simulations of the single-band Hubbard model [19, 20]. Reference [21] reports density matrix renormalization group (DMRG) simulations of a similar 2-orbital model, and finds Luther-Emery behavior - coexistence of long-range superconducting and charge-density wave order - away from half-filling as in the 1D Hubbard model, while the undoped model does not contain long-range antiferromagnetic order, different than single-band Hubbard and more closely in-line with infinite-layer nickelates. The spin dynamics may be investigated using t-DMRG or other techniques, such as determinant quantum Monte Carlo [22]. This remains a topic of future interest.

DATA AVAILABILITY STATEMENT

The original contributions presented in the study are included in the article/Supplementary Material, further inquiries can be directed to the corresponding author.

AUTHOR CONTRIBUTIONS

EB performed ED calculations for S (q, ω), YH and KH performed ED calculations for XAS, CJ and EB performed DFT calculations for the nickelate bandstructure. BM, CJ, YC, and TD conceived the project. All authors contributed to the writing of the manuscript.

FUNDING

This work was supported by the U.S. Department of Energy (DOE), Office of Basic Energy Sciences, Division of Materials Sciences and Engineering. Computational work was performed on the Sherlock cluster at Stanford University and on resources of the National Energy Research Scientific Computing Center, supported by the U.S. DOE, Office of Science, under Contract no. DE-AC02-05CH11231.

ACKNOWLEDGMENTS

We would like to thank Yao Wang from Clemson University for helpful discussions about exact diagonalization and the 2-orbital nickelate model.

REFERENCES

1. Li D, Lee K, Wang BY, Osada M, Crossley S, Lee HR, et al. Superconductivity in an Infinite-Layer Nickelate. *Nature* (2019) 572:624–7. doi:10.1038/s41586-019-1496-5
2. Anisimov VI, Bukhvalov D, Rice TM. Electronic Structure of Possible Nickelate Analogs to the Cuprates. *Phys Rev B* (1999) 59:7901–6. doi:10.1103/PhysRevB.59.7901
3. Lee K-W, Pickett WE. Infinite-layerLaNiO2: Ni1+is notCu2+. *Phys Rev B* (2004) 70:165109. doi:10.1103/PhysRevB.70.165109
4. Zaanen J, Sawatzky GA, Allen JW. Band Gaps and Electronic Structure of Transition-Metal Compounds. *Phys Rev Lett* (1985) 55:418–21. doi:10.1103/PhysRevLett.55.418
5. Lu H, Rossi M, Nag A, Osada M, Li DF, Lee K, et al. Magnetic Excitations in Infinite-Layer Nickelates. *Science* (2021) 373:213–6. doi:10.1126/science.abd7726
6. Jia CJ, Nowadnick EA, Wohlfeld K, Kung YF, Chen C-C, Johnston S, et al. Persistent Spin Excitations in Doped Antiferromagnets Revealed by Resonant Inelastic Light Scattering. *Nat Commun* (2014) 5:3314. doi:10.1038/ncomms4314
7. Le Tacon M, Ghiringhelli G, Chaloupka J, Sala MM, Hinkov V, Haverkort MW, et al. Intense Paramagnon Excitations in a Large Family of High-Temperature Superconductors. *Nat Phys* (2011) 7:725–30. doi:10.1038/nphys2041
8. Dean MPM, Dellea G, Springell RS, Yakhou-Harris F, Kummer K, Brookes NB, et al. Persistence of Magnetic Excitations in La2−xSrxCuO4 from the Undoped Insulator to the Heavily Overdoped Non-superconducting Metal. *Nat Mater* (2013) 12:1019–23. doi:10.1038/nmat3723
9. Giannozzi P, Baseggio O, Bonfà P, Brunato D, Car R, Carnimeo I, et al. QuantumESPRESSO toward the Exascale. *J Chem Phys* (2020) 152:154105. doi:10.1063/5.0005082
10. Perdew JP, Burke K, Ernzerhof M. Generalized Gradient Approximation Made Simple. *Phys Rev Lett* (1996) 77:3865–8. doi:10.1103/PhysRevLett.77.3865
11. Mostofi AA, Yates JR, Pizzi G, Lee Y-S, Souza I, Vanderbilt D, et al. An Updated Version of Wannier90: A Tool for Obtaining Maximally-Localised Wannier Functions. *Comp Phys Commun* (2014) 185:2309–10. doi:10.1016/j.cpc.2014.05.003
12. de Groot F, Kotani A. *Advances in Condensed Matter Science*. Boca Raton: CRC Press (2008). doi:10.1201/9781420008425 Core Level Spectroscopy of Solids.

13. Jia C, Wohlfeld K, Wang Y, Moritz B, Devereaux TP. Using RIXS to Uncover Elementary Charge and Spin Excitations. *Phys Rev X* (2016) 6:021020. doi:10.1103/PhysRevX.6.021020
14. Been E, Lee W-S, Hwang HY, Cui Y, Zaanen J, Devereaux T, et al. Electronic Structure Trends across the Rare-Earth Series in Superconducting Infinite-Layer Nickelates. *Phys Rev X* (2021) 11:011050. doi:10.1103/physrevx.11.011050
15. Betts DD, Lin HQ, Flynn JS. Improved Finite-Lattice Estimates of the Properties of Two Quantum Spin Models on the Infinite Square Lattice. *Can J Phys* (1999) 77:353–69. doi:10.1139/p99-041
16. Virtanen P, Gommers R, Oliphant TE, Haberland M, Reddy T, Cournapeau D, et al. SciPy 1.0: Fundamental Algorithms for Scientific Computing in Python. *Nat Methods* (2020) 17:261–72. doi:10.1038/s41592-019-0686-2
17. Rossi M, Lu H, Nag A, Li D, Osada M, Lee K, et al. Orbital and Spin Character of Doped Carriers in Infinite-Layer Nickelates. *Phys Rev B* (2021) 104:L220505. doi:10.1103/PhysRevB.104.L220505
18. Hepting M, Li D, Jia CJ, Lu H, Paris E, Tseng Y, et al. Electronic Structure of the Parent Compound of Superconducting Infinite-Layer Nickelates. *Nat Mater* (2020) 19:381–5. doi:10.1038/s41563-019-0585-z
19. Arovas DP, Berg E, Kivelson S, Raghu S. *The Hubbard Model* (2021). arXiv e-prints , arXiv:2103.12097.
20. Huang EW, Wang WO, Ding JK, Liu T, Liu F, Huang X-X, et al. Intertwined States at Finite Temperatures in the Hubbard Model. *J Phys Soc Jpn* (2021) 90:111010. doi:10.7566/JPSJ.90.111010
21. Peng C, Jiang H-C, Moritz B, Devereaux TP, Jia C. *Superconductivity in a Minimal Two-Band Model for Infinite-Layer Nickelates* (2021). arXiv e-printsarXiv:2110.07593.
22. Liu F, Peng C, Huang EW, Moritz B, Jia C, Devereaux T (2021). Spin excitations and stripes in the failed antiferromagnetic infinite-layer nickelates. unpublished

Conflict of Interest: The authors declare that the research was conducted in the absence of any commercial or financial relationships that could be construed as a potential conflict of interest.

Publisher's Note: All claims expressed in this article are solely those of the authors and do not necessarily represent those of their affiliated organizations, or those of the publisher, the editors and the reviewers. Any product that may be evaluated in this article, or claim that may be made by its manufacturer, is not guaranteed or endorsed by the publisher.

frontiers in Physics

PERSPECTIVE
published: 03 March 2022
doi: 10.3389/fphy.2022.834658

Infinite-Layer Nickelate Superconductors: A Current Experimental Perspective of the Crystal and Electronic Structures

L. E. Chow and A. Ariando *

Department of Physics, Faculty of Science, National University of Singapore, Singapore

After the reward of more than 2 decades of pursuit on the high-T_c cuprate analog with the hope to obtain a better understanding of the mechanism of high-T_c superconductivity, the discovery of superconductivity in the infinite-layer nickelate brings more mystery to the picture than expected. Tops in the list of questions are perhaps 1) absence of superconductivity in the bulk nickelate and limited thickness of the infinite-layer phase in thin film, 2) absence of superconductivity in the La-nickelate despite it being the earliest studied rare-earth nickelate, and the role of 4 *f* orbital in the recipe of superconductivity, 3) absence of Meissner effect and suspect of the origin of superconductivity from the interface, 4) whether nickelate hosts similar pairing symmetry to the single-band high-T_c cuprates or multiband iron-based superconductor. In this perspective article, we will discuss the following aspects: 1) stabilization of the infinite-layer phase on the $SrTiO_3$(001) substrate and the thickness dependency of observables; 2) rare-earth dependence of the superconducting dome and phase diagram of the (La/Pr/Nd)- infinite-layer nickelate thin film; 3) experimental aspects of the measurement of Meissner effect; 4) theoretical framework and experimental study of the pairing symmetry of infinite-layer nickelate superconductor.

Keywords: infinite-layer nickelates, nickelate superconductivity, pairing symmetry, meissner effect, lanthanide nickelate, thickness dependence, rare earth magnetism

OPEN ACCESS

Edited by:
Junjie Zhang,
Shandong University, China

Reviewed by:
Xingjiang Zhou,
Institute of Physics (CAS), China

***Correspondence:**
A. Ariando
ariando@nus.edu.sg

Specialty section:
This article was submitted to Condensed Matter Physics, a section of the journal Frontiers in Physics

Received: *13 December 2021*
Accepted: *10 January 2022*
Published: *03 March 2022*

Citation:
Chow LE and Ariando A (2022) Infinite-Layer Nickelate Superconductors: A Current Experimental Perspective of the Crystal and Electronic Structures. Front. Phys. 10:834658. doi: 10.3389/fphy.2022.834658

MAIN TEXT

Around 4 decades ago, the witness of superconductivity above 30 K redefined preexisting knowledge on the mechanism of superconductivity and restructured the landscape of the playground on superconductor materials [1, 2]. Understanding the high-temperature (high-T_c) superconductivity has since been one of the holy grails in physics. Several characteristic properties were discussed in the cuprate superconductor: 1) quasi-2D CuO_2 square-planar lattice, 2) antiferromagnetic order and superexchange interaction, 3) spin $S = \frac{1}{2}$ half-filling state, 4) Cu^{2+} of 3 d^9 electronic configurations [3–7]. To identify which parameters are the key ingredients which drive the high-T_c superconductivity in cuprate, searching for isostructural compounds with some of these properties and comparing them to the cuprate were motivated [8]. Among all the cuprate analogs [9], nickelate of Ni^{1+} with the same 3 d^9 electronic configurations was identified as the closest cousin to the cuprate [7, 10]. For decades, theoretical and experimental efforts have been made to explore the lead [11–13]. Unlike cuprate, which was first synthesized in the bulk form, superconducting nickelate was only realized recently in the thin-film form [14–21], with Ni^{1+} in the

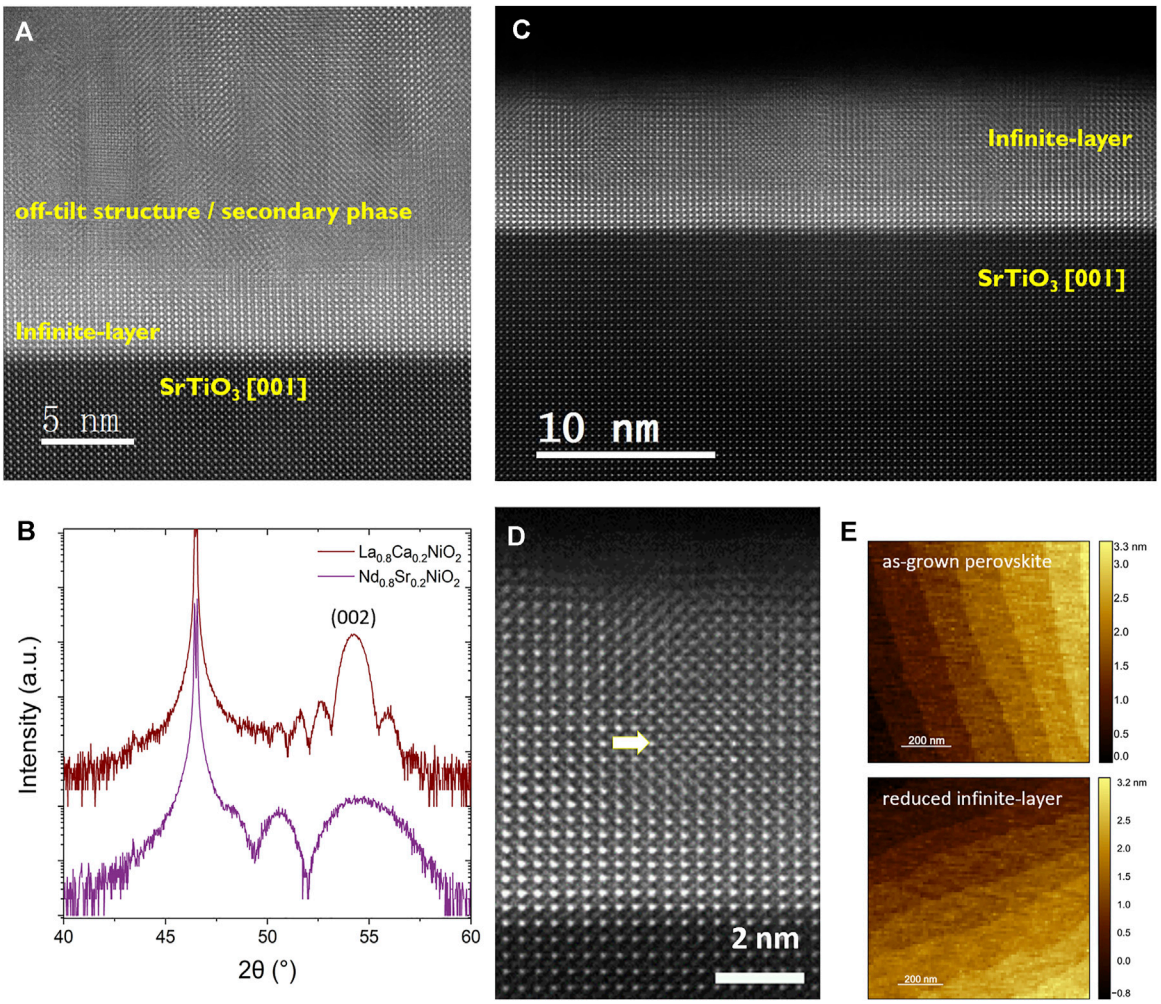

FIGURE 1 | Structural properties of the reduced infinite-layer nickelate thin film. **(A,C,D)** STEM HAADF images. **(B)** XRD (002) pattern. **(A)** A thick 30 nm $Nd_{0.85}Sr_{0.15}NiO_2$ film has infinite-layer phase stabilized up to ~5 nm from the substrate interface. Above 5 nm, secondary phase or off-tilt structure can be seen, data is adapted from [26]. Entire $Nd_{0.8}Sr_{0.2}NiO_2$ film of thinner <10 nm can be reduced to infinite-layer phase with perfect crystallinity **(C,D)** up to the surface, with no sign of secondary phase except for possible RP stacking fault occurs at some part of the film **(D)**. **(B)** A clear Laue fringes can be observed for 8 nm $Nd_{0.8}Sr_{0.2}NiO_2$ and 15 nm $La_{0.8}Ca_{0.2}NiO_2$ thin films, indicating coherent infinite-layer phase. **(E)** Atomic-force-microscopy (AFM) images show the atomically flat terrace-like surface topography in $Nd_{0.8}Sr_{0.2}NiO_2$ (6.5 nm) film surfaces before (top) and after (bottom) topotactic reduction done in the PLD chamber.

infinite-layer phase that can be achieved through topotactic reduction from the perovskite compound. Missing superconductivity in the bulk nickelate [22, 23] and limitation in stabilizing the infinite-layer phase above ~10 nm from the substrate [24–26] demands answers on the thickness-dependent crystallinity and electronic structure of the infinite-layer nickelate film. While lanthanide-cuprate La-Ba-Cu-O was the first superconducting compound synthesized [27], lanthanide-nickelate was initially reported to not host superconductivity, but superconductivity was only realized in the neodymium-based counterpart, a rare-earth element with 4 f magnetism [14]. The possible roles of rare-earth magnetism in the early observation of nickelate's superconductivity added layers of mystery to the newfound sister of cuprate [6, 28, 29]. In addition to the bulk nickelate not being reported to show superconductivity, concrete evidence of the Meissner effect in the superconducting nickelate thin film was missing [14], leading to the suspect whether the phenomenon was interfacial in nature. High-T_c cuprate is uniquely identified with a dominant $d_{x^2-y^2}$-wave gap which is believed to be mediated by the antiferromagnetic superexchange interaction, that poses as a crucial factor in the high-T_c superconductivity [3]. Hence, answering the superconducting order parameter in the nickelate is the top priority. However, the challenge in the fabrication of high-quality infinite-layer nickelate films obstructed the experimental means to investigate, especially with those surface-sensitive techniques are not applicable when bad crystallinity or secondary phases are prone to form at the surface of nickelate superconducting thin-film [25]. Overall, while the discovery of superconductivity in the nickelate provided an exciting playground to study the highly correlated system, the newfound superconductor family also ignited controversial debates that will reshape high-T_c

framework [4–6, 30–37]. In this article, we provided a contemporary experimental perspective on the topics.

THICKNESS DEPENDENCE

Stabilization of Infinite-Layer Phase

Since the observation of superconductivity in the infinite-layer nickelate $Nd_{0.8}Sr_{0.2}NiO_2$ thin film [14], apparent challenges have emerged in material synthesis [25]. On top of low reproducibility and difficulty in the fabrication of superconducting doped infinite-layer structure by many experimental groups [38, 39], a hard-nut-to-crack issue is a limited thickness from the substrate interface, which the infinite-layer phase can be stabilized [25, 26, 40]. Above ~10 nm from the substrate interface, obvious secondary phases or off-tilt structures form instead of the infinite-layer or partially reduced perovskite phase [25]. In many cases, growing a thick film will lead to the formation of a secondary phase even at just ~5 nm from the substrate (**Figure 1A**) [26]. On the other hand, if a thinner <10 nm film is grown, the entire film can be fully reduced with no observation of secondary phase even at the film surface (**Figures 1C,D**), except for possibly Ruddlesden-Popper (RP) stacking fault at some regions of the film (**Figure 1D**). The obvious strategy for obtaining the purest possible infinite-layer phase is fabricating thin films below 10 nm. In addition to the absence of secondary phases as shown in the STEM image, atomically flat surfaces with terrace-like topography can be observed on the film surface before and after topotactic reduction, as shown in the atomic-force-microscopy images in **Figure 1E**. Some reports suggested using $SrTiO_3$ (STO) capping layer on top of the nickelate thin film prior to a topotactic reduction that can serve as a "backbone" to help stabilize the infinite-layer phase during topotactic reduction from the perovskite phase [25, 41]. However, such a method has not led to a thicker infinite-layer phase of >10 nm. Lattice coherency of a crystalline thin film can be seen from the X-ray diffraction (XRD) Laue fringes which originate from the constructive interference between perfect lattice layers of the thin film. To date, most reported XRD data of the perovskite phase of the doped nickelate thin film has clear Laue fringes in the vicinity of the (002) peak; however, Laue fringes are typically absent for the reduced doped infinite-layer nickelate (002) peak [16, 26, 41–43]. This may suggest the presence of nonstoichiometric oxygen at random parts of the reduced infinite-layer thin film. Significant development of secondary or perovskite phases is typically avoided after optimization in film growth conditions since no perovskite peak or defect phase peak is seen in the XRD curve.

The challenge of obtaining a coherent infinite-layer phase does not affect transport-related study since zero resistance can be observed even when only a small part of the film is superconducting. Unfortunately, the same cannot be said for measurements requiring a pure phase with coherent crystallinity, especially at the film surface, such as the Angle-resolved Photoemission Spectroscopy (ARPES) or Scanning Tunneling Spectroscopy (STS). Many probing techniques which reveal crucial aspects of the superconductivity in nickelate cannot be carried out because of the lack of coherent lattice and purity in the infinite-layer phase, especially on the top surface. With much effort in optimizing film quality, we recently reported an observation of clear Laue fringes in the vicinity of XRD (002) peak of the infinite-layer phase for $Nd_{1-x}Sr_xNiO_2$ and $La_{1-x}Ca_xNiO_2$ (**Figure 1B**). Especially in the case of superconducting lanthanide infinite-layer nickelate, more than 30 unit-cells (uc) of a coherent infinite-layer lattice can be seen vividly from the XRD Laue fringes.

Thickness Dependency and Role of Strain and Interface

Superconductivity is missing in the bulk infinite-layer nickelate [23, 44–46]. The puzzling limitation in the thickness of the infinite-layer thin film further warrants the importance of investigating the thickness dependency of the physical observables and electronic structure of the infinite-layer nickelate. The zero-resistivity critical temperature , $T_{c,0}$, of $Pr_{0.8}Sr_{0.2}NiO_2$ thin film with thickness from 5.3 to 12 nm has been reported [8], showing a slight decrease from 5.3 to 8 nm and it then increases again up to 12 nm. However, the normal state resistivity of the same samples also shows corresponding change, where high $T_{c,0}$ samples have low resistivity. This implies the stronger correlation between $T_{c,0}$ and normal state resistivity but not the film thickness [25]. On the other hand, the $T_{c,0}$ of $Nd_{0.8}Sr_{0.2}NiO_2$ thin films monotonically increases with film thickness (4.6–10.1 nm) observed from both resistivity and susceptibility measurements [24]. In addition, a systematic evaluation of the thickness-dependent electronic structure has been shown with the change in Hall coefficients and XAS spectra of $Nd_{0.8}Sr_{0.2}NiO_2$ thin film from 4.6 to 10.1 nm [24]. The results imply strain modulation and interface effect in the infinite-layer nickelate.

RARE-EARTH DEPENDENCE

Doping Dependent Phase Diagram

The barium (Ba) hole-doped lanthanide La-cuprate $La_{2-x}Ba_xCuO_4$ was the first high-T_c cuprate synthesized, which kicked off the door to high-temperature superconductivity beyond the BCS paradigm [27]. To mimic cuprate's square-planar structure and 3 d^9 electronic configurations, Ni^{1+} state in nickelate was predicted to be an ideal cuprate analog to assist in the understanding of the origin of high-T_c superconductivity in cuprate [4, 7, 13, 14, 34, 47, 48]. Naturally, lanthanum (La) was the first rare-earth option to be looked for in nickelate. Many experimental attempts were made on La-nickelate to achieve superconductivity with Ni^{1+} state in the form of superlattices, infinite-layer structure for the past 2 decades [12, 14, 49, 50]. Despite the long search, La-nickelate was initially found not to be superconducting and the first observation of nickelate superconductivity was realized by Sr-doped on a smaller neodymium ion Nd-infinite-layer nickelate thin film with 4f magnetism in 2019 [14]. Since then, superconductivity in the infinite-layer nickelate family has been quickly expanded to another neighbor with rare-earth magnetism in the rare-earth series, praseodymium (Pr) [42], and has been successfully reproduced by multiple experimental groups [17, 51]. However, superconductivity in La-nickelate, which has an empty 4f orbital, still seems non-existent for another 2 years until it was successfully realized independently by two different groups in the Ca-doped La_{1-}

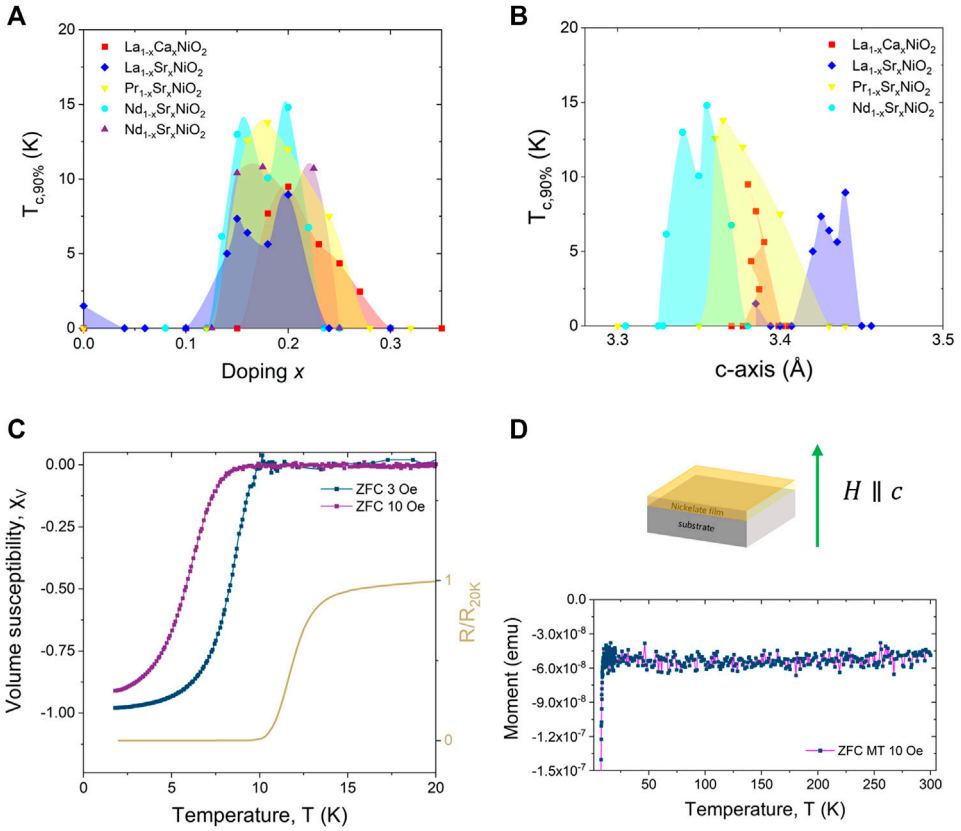

FIGURE 2 | (A,B) Superconducting phase diagram of various hole doped infinite-layer nickelates, plotted as a function of hole doping levels *x* **(A)** and c-axis lattice constant **(B)**. Data are adapted from (La, Ca) [16], (La,Sr) [41], (Pr, Sr) [15], (Nd, Sr) [26, 40]. **(C,D)** Observation of Meissner effect in the superconducting infinite-layer thin film at $H \parallel c$. Superconducting transition observed in resistivity and susceptibility **(C)** measurements for $Nd_{0.8}Sr_{0.2}NiO_2$ thin film. **(D)** The measured moment at above T_c is typically of -10^{-8} emu scale and almost constant at $T_{c,onset} < T < 300K$, correspond to STO substrate diamagnetic signal.

$_xCa_xNiO_2$ [16] and Sr-doped $La_{1-x}Sr_xNiO_2$ [41] infinite-layer thin film. Given the missing report of superconductivity in La-nickelate for almost 2 decades, the role of 4 *f* magnetism and other differences between $LaNiO_2$ and (Pr/Nd)NiO_2 in the recipe of superconductivity become an open question and inspire further investigation on their pairing symmetries, anisotropy and doping dependent phase diagram [16, 26, 28, 29, 40, 41, 52–55].

Figure 2A shows doping-dependent superconducting dome and phase diagram in various Sr-doped and Ca-doped rare-earth (La, Pr, Nd) infinite-layer nickelate synthesized so far [15, 16, 26, 40, 41]. The first eye-catching feature is the presence of "dip" with a lower T_c for a particular doping in the $Nd_{1-x}Sr_xNiO_2$ [26, 40] and $La_{1-x}Sr_xNiO_2$ [41] thin films. Given the lack of consistency of the "dip" feature on a particular doping across different rare-earth nickelates and reports, it is presently unclear whether it is an experimental artifact or a reminiscence of certain quantum critical transitions in the system. The second observation is the expansion of the superconducting dome to a higher doping level from $Nd_{1-x}Sr_xNiO_2$, $Pr_{1-x}Sr_xNiO_2$ to $La_{1-x}Ca_xNiO_2$. Given the increased difficulty in synthesizing infinite-layer nickelate thin film at larger doping [25, 41], such observation may have a certain correlation to film crystallinity. The perovskite nickelate has a smaller in-plane lattice constant than the $SrTiO_3$ (001) substrate, which the lattice mismatches are decreasing from $NdNiO_3$ to $LaNiO_3$. It has been established that a perovskite phase nickelate with good crystallinity is essential to the success in topotactic reduction to the infinite-layer phase [25]. One may suggest that perovskite $La_{1-x}Ca_xNiO_3$ and $Pr_{1-x}Sr_xNiO_3$ can be grown to have better crystallinity than the $Nd_{1-x}Sr_xNiO_3$ at a large doping regime. A similar argument could be made for the difference in superconducting dome between $La_{1-x}Ca_xNiO_2$ and $La_{1-x}Sr_xNiO_2$. The Ca^{2+} ion is of more similar size to the rare-earth La^{3+}, Pr^{3+} and Nd^{3+} ions than the larger Sr^{2+} ion [16]. Regardless, it is also possible that different rare-earth ion and cation doping leads to a slight difference in the electronic band structure of the infinite-layer nickelate, causing a different span of superconducting domes. Another note is, so far, the doping level in the fabricated thin films is expected to follow the stoichiometry of the polycrystalline target used in the pulsed-laser-deposition (PLD) growth. It is not warranted that the doping level is accurate, and further investigation on the stoichiometry of the doped thin film shall be carried out. The third observation is the correlation between the size of the rare-earth ions and superconducting transition temperature T_c. The maximum

onset temperature in resistivity, where resistivity reaches 90% of its value at 20 K, $T_{c,90\%}$ is roughly consistent among various reports, where La-nickelate has $T_{c,90\%}$ ~9–10 K while Pr- and Nd-nickelate has $T_{c,90\%}$ ~12–15 K. It is routinely explained by the increase in electronic bandwidth for a smaller rare-earth ion [14, 16].

In addition to the difference in the superconducting T_c between La- and (Pr/Nd)- infinite-layer nickelate, the Hall coefficient (R_H) sign change temperature across doping levels also exhibits dissimilarity between La- and (Pr/Nd)-nickelate. R_H sign change temperature is monotonically increasing with hole doping in the case of (Pr/Nd)- infinite-layer nickelate [15, 26, 40], which may suggest increased-dominancy in $d_{x^2-y^2}$ hole pocket at Fermi level with increasing hole doping. However, in the case of $La_{1-x}Ca_xNiO_2$, the R_H sign change temperatures are constant at around 35 K between $0.23 \leq x \leq 0.3$ and the difference in R_H at low temperature is small at increasing doping [16]. While preliminary and possibly confounded by the impact of in-plane compressive stress from the substrate, the role of hole doping is likely to be different in modifying the band structure of the Ca-doped La-nickelate as compared to the Sr-doped (Pr/Nd)-nickelate.

Relevance to Lattice Constant

Since superconductivity has not been observed in the bulk infinite-layer nickelate despite that high crystallinity samples were made [44, 45], the ab-axis lattice constants of the superconducting infinite-layer thin film are epitaxially constrained to the substrate in-plane lattice constants. It might be intuitive to look for any correlation between the c-axis lattice dimension and superconducting dome of the infinite-layer nickelate (**Figure 2B**). At first glance, the superconducting dome is generally limited to between 3.32 Å and 3.45 Å. However, the superconducting domes between various rare-earth compounds do not completely overlap. Also, for the case of $La_{1-x}Ca_xNiO_2$, the variation in c-axis lattice constant across doping is small due to a very similar ionic size between Ca^{2+} ion and La^{3+}, and has slight sample-to-sample variation at the same Ca doping [16]. It seems early to suggest any strict correlation between the superconducting dome of infinite-layer nickelate and the c-axis lattice dimension. It is worth noting that an enhancement in onset T_c was realized experimentally by applying external pressure [17], which suggests the likelihood of further increasing T_c by simulating chemical pressure through tuning in-plane lattice constants, rare-earth ions size, or dopant size. In addition, we note that there are recent theoretical calculations on the effect of in-plane lattice constant and epitaxial strain in tuning the *P4/mmm - I4/mcm* phase transition in $RNiO_2$ (R = La, Pr, Nd, Eu-Lu, Y) [56, 57].

OBSERVATION OF MEISSNER EFFECT

Two main phenomena characterize superconductivity: 1) zero electrical resistivity, 2) Meissner effect. The first experimental report of the discovery of superconductivity in $Nd_{0.8}Sr_{0.2}NiO_2$ thin film provided multiple resistivity-temperature ($R-T$) curves with clear zero resistivity data and two-coil mutual inductance measurement to observe the expulsion of the magnetic field in the Meissner state [14]. However, the real part of the pickup voltage $Re(V_p)$ does not go to zero as expected for a superconductor in the Meissner state. Some diamagnetic signal is observed, but the $Re(V_p)$ measured the lowest temperature is far from zero as compared to the change within the transition $Re(V_p) \sim 1.7 \rightarrow 1.25\,\mu V$ [14]. The absence of concrete data to support the presence of Meissner state led to a suspicion that the superconductivity in nickelate arises from the interface with the substrate but is not intrinsic to the bulk material.

Meissner effect is routinely seen in the magnetic susceptibility measurement: 1) a negative slope in the $M-H$ curve which ends at the lower critical field H_{c1}, 2) negative diamagnetic signal below T_c in $M-T$ curve which the volume susceptibility χ_V (in S. I. unit) goes to -1 for Meissner state. The $M-T$ and $M-H$ data were not presented in the early reports of the superconductivity observed in the infinite-layer nickelate thin films. Zeng *et al.* provided a study on the thickness-dependent effect on the film's T_c in both resistivity and susceptibility measurements [24]. The diamagnetic moment in $M-T$ curve (measured at $H \parallel c$) below the superconducting transition is typically of ~ 10^{-5} emu scale for a $2.5 \times 5\,mm^2$ superconducting thin film of 8 nm thick. After demagnetizing field correction, the volume susceptibility at 2 K can be calculated to be $\chi_V < -0.9$ which is fairly close to -1 for perfect diamagnetism (**Figure 2C**). **Figure 2D** presents the raw data for the magnetic moment measured above transition $T > T_{c,onset}$. The infinite-layer thin film on STO substrate has an almost temperature-independent moment for $T_{c,onset} < T < 300K$, which the small ~ 10^{-8} emu negative moment measured shall correspond to the STO substrate diamagnetic signal. In addition, a negative slope in $M-H$ curve was also observed in superconducting $Nd_{0.8}Sr_{0.2}NiO_2$ thin film, resembling the Meissner effect and bulk superconductivity, which is intrinsic to the nickelate thin film but not of the interface. The lower critical field H_{c1} is defined as the magnetic field in the sample which the field penetrates the sample volume and the onset of mixed state for type II superconductor. In the $M-H$ curve, due to the thin-film nature with large demagnetizing factor $N \rightarrow 1$ for $H \parallel c$, the $H_{c1}^{applied}$ before demagnetization factor correction is around and less than 1Oe, which is difficult to be resolved and has a large error in the calculation of actual H_{c1}. After demagnetizing factor correction, the $H_{c1}\,(T = 0K)$ is approximated to be around 79 Oe.

The superconducting transition temperature observed in the $M-T$ curve typically has an onset close to the $T_{c,0}$ in resistivity provided good homogeneity of the entire sample (**Figure 2C**). Lower $T_{c,\,onset}$ in $M-T$ can be measured if the applied field is larger than the lower critical field $H > H_{c1}$. Since the applied $H_{c1}^{applied} \leq 1$ Oe for $Nd_{0.8}Sr_{0.2}NiO_2$ infinite-layer nickelate thin film, a larger measuring field of 10 Oe can lead to lower $T_{c,\,onset}$ and smaller $\chi_V\,(2K)$ as compared to 3 Oe measuring field, for example. In addition, the Meissner effect will not be observable, or only a very small diamagnetic signal is observed if there are inhomogeneity and defect phases in the infinite-layer

nickelate thin film, which can easily present even when a high T_c is observed in the resistivity $R-T$ data.

PAIRING SYMMETRY

Dominant *d*-wave Gap

The infinite-layer nickelate is a sister of the high-T_c cuprate, which hosts a dominant $d_{x^2-y^2}$-wave gap, both sharing a similar crystal structure and 3 d^9 electronic configuration. In the recent resonant inelastic X-ray scattering (RIXS) experiments at Ni L_3-edge on the infinite-layer nickelate thin films, charge order and spin wave of antiferromagnetically coupled spins in a square lattice was observed [43, 58–60]. The antiferromagnetic exchange coupling strength J is estimated to be around 63.6 meV in RIXS. While a different J value can be estimated with different spin model calculation, the general consensus is that the nickelate's J value is smaller than the $J \sim 130$ **meV** of the high-T_c cuprates [58, 61]. In addition, exchange bias effect was observed at a ferromagnet/$Nd_{0.8}Sr_{0.2}NiO_2$(20 nm) interface which could be interpreted as the antiferromagnetic nature at the surface of thick $Nd_{0.8}Sr_{0.2}NiO_2$ film (though exchange bias field is absent for $\leq$ 10 nm film) [18]. Despite the lack of concrete proof on the long-range magnetic order to date, the $t-J$ model used in cuprates is perceived to be suitable to capture nickelate's superconductivity [55] and the general consensus across different theoretical calculations on the superconducting pairing symmetry of nickelate is a dominant $d_{x^2-y^2}$-wave pairing like the cuprate with some pointed out various possibility of multiband superconductivity [35, 52, 55, 62]. In the $t-J-K$ model which accounted for the Kondo coupling in nickelate, an interstitial s-wave gap exists at the large hole doping and small t/K region of the phase diagram [63]. On the other hand, if hopping t/K is large as compared to the Kondo coupling, a dominant d-wave pairing or a transition from $(d+is)$-wave at low doping to d-wave at large doping is expected [63].

Considering the role of nickelate superconductivity in illuminating the origin of high-T_c superconductivity in cuprates, a detailed experimental study on the pairing symmetry of nickelate is crucial. The first experimental report on the superconducting gap symmetry of the infinite-layer nickelate is a single-particle-tunneling experiment on $Nd_{0.8}Sr_{0.2}NiO_2$ film surface which detected signals correspond to s-wave, d-wave or a mixture of both in different parts of the film surface [19]. However, we note here the difficulty in achieving a good crystallinity and high purity of the superconducting phase, especially near the film surface of the reduced infinite-layer thin film. Hence, surface-sensitive techniques which are useful in determining the gap profile like the angle-resolved photoemission spectroscopy (ARPES) may not be feasible to investigate the pairing order of the infinite-layer nickelate thin films until the film quality at the surface is perfected. Furthermore, phase-sensitive experiments are also waiting to be seen [64].

Fully Gapped Pairing and Isotropic Upper Critical Field

While the tunneling experiment did not lead to a complete answer of the nickelate's pairing order, the existence of a fully gapped s-wave signal ignited multiple explanations to the observation [63, 65]. Recently the upper critical field H_{c2} of $Nd_{0.775}Sr_{0.225}NiO_2$ thin film is measured to be mostly isotropic down to the lowest temperature and is smaller than the Pauli limit [66]. The isotropic H_{c2} in the $Nd_{0.775}Sr_{0.225}NiO_2$ infinite-layer nickelate is completely distinct from the cuprate with large anisotropy and other quasi-2D superconductors. On the other hand, this isotropic upper critical field behavior places nickelate to be more similar to the high-T_c multiband iron-based superconductor which is believed to host nodeless $s_{\pm}$-wave multigap pairing [67, 68]. Further investigation on the nickelate's controversial pairing symmetry is warranted [69, 70].

DATA AVAILABILITY STATEMENT

The original contributions presented in the study are included in the article/Supplementary Material, further inquiries can be directed to the corresponding author.

AUTHOR CONTRIBUTIONS

All authors listed have made a substantial, direct, and intellectual contribution to the work and approved it for publication.

FUNDING

This research is supported by the Agency for Science, Technology, and Research (A*STAR) under its Advanced Manufacturing and Engineering (AME) Individual Research Grant (IRG) (A1983c0034) and the Singapore National Research Foundation (NRF) under the Competitive Research Programs (CRP Grant No. NRF-CRP15-2015-01) and by the Ministry of Education, Singapore, under its MOE Tier 2 grant (Grant no. MOE-T2EP50121-0018).

ACKNOWLEDGMENTS

We thank S. W. Zeng for the fruitful discussion and revision of this article. We acknowledge Elbert E. M. Chia, C. Z. Diao, W. Escoffier, M. Goiran, S. K. Goh, J. X. Hu, H. Jani, Z. S. Lim, C. J. Li, P. Nandi, G. J. Omar, M. Pierre, D. Preziosi, S. K. Sudheesh, M. Salluzzo, C. S. Tang, Andrew T. S. Wee, K. Y. Yip, X. M. Yin, P. Yang, Z. T. Zhang for discussions.

REFERENCES

1. Wu MK, Ashburn JR, Torng CJ, Hor PH, Meng RL, Gao L, et al. Superconductivity at 93 K in a New Mixed-phase Y-Ba-Cu-O Compound System at Ambient Pressure. *Phys Rev Lett* (1987) 58:908–10. doi:10.1103/physrevlett.58.908
2. Azuma M, Hiroi Z, Takano M, Bando Y, Takeda Y. Superconductivity at 110 K in the Infinite-Layer Compound (Sr1-xCax)1-yCuO2. *Nature* (1992) 356:775–6. doi:10.1038/356775a0
3. Keimer B, Kivelson SA, Norman MR, Uchida S, Zaanen J. From Quantum Matter to High-Temperature Superconductivity in Copper Oxides. *Nature* (2015) 518:179–86. doi:10.1038/nature14165
4. Botana AS, Bernardini F, Cano A. Nickelate Superconductors: An Ongoing Dialog between Theory and Experiments. *J Exp Theor Phys* (2021) 132:618–27. doi:10.1134/s1063776121040026
5. Jiang M, Berciu M, Sawatzky GA. Critical Nature of the Ni Spin State in Doped NdNiO2. *Phys Rev Lett* (2020) 124:207004. doi:10.1103/physrevlett.124.207004
6. Pickett WE. The Dawn of the Nickel Age of Superconductivity. *Nat Rev Phys* (2021) 3:7–8. doi:10.1038/s42254-020-00257-3
7. Botana AS, Norman MR. Similarities and Differences between LaNiO2 and CaCuO2 and Implications for Superconductivity. *Phys Rev X* (2020) 10:011024. doi:10.1103/physrevx.10.011024
8. Rice TM. Electronic Structure of Possible Nickelate Analogs to the Cuprates. *Phys Rev B - Condens Matter Mater Phys* (1999) 59:7901.
9. Maeno Y, Hashimoto H, Yoshida K, Nishizaki S, Fujita T, Bednorz JG, et al. Superconductivity in a Layered Perovskite without Copper. *Nature* (1994) 372:532–4. doi:10.1038/372532a0
10. Bernardini F, Olevano V, Blase X, Cano A. Infinite-Layer Fluoro-Nickelates as D9 Model Materials. *J Phys Mater* (2020) 3:035003. doi:10.1088/2515-7639/ab885d
11. Lee KW, Pickett WE. Infinite-Layer LaNiO2: Ni1+ Is Not Cu2+ [33]. *Phys Rev B - Condens Matter Mater Phys* (2004) 70:1. doi:10.1103/physrevb.70.165109
12. Chaloupka J, Khaliullin G. Orbital Order and Possible Superconductivity in LaNiO3/LaMO3 Superlattices. *Phys Rev Lett* (2008) 100:016404. doi:10.1103/PhysRevLett.100.016404
13. Zhang J, Botana AS, Freeland JW, Phelan D, Zheng H, Pardo V, et al. Large Orbital Polarization in a Metallic Square-Planar Nickelate. *Nat Phys* (2017) 13:864–9. doi:10.1038/nphys4149
14. Li D, Lee K, Wang BY, Osada M, Crossley S, Lee HR, et al. Superconductivity in an Infinite-Layer Nickelate. *Nature* (2019) 572:624–7. doi:10.1038/s41586-019-1496-5
15. Osada M, Wang BY, Lee K, Li D, Hwang HY. Phase Diagram of Infinite Layer Praseodymium Nickelate Pr1-XSrxNiO2 Thin Films. *Phys Rev Mater* (2020) 4:1. doi:10.1103/physrevmaterials.4.121801
16. Zeng SW, Li CJ, Chow LE, Cao Y, Zhang ZT, Tang CS, et al. Superconductivity in Infinite-Layer Lanthanide Nickelates. *Sci Adv* (2022) 8:eabl9927. doi:10.1126/sciadv.abl9927
17. Wang NN, Yang MW, Chen KY, Yang Z, Zhang H, Zhu ZH, et al. Pressure-Induced Monotonic Enhancement of Tc to over 30 K in the Superconducting Pr0.82Sr0.18NiO2 Thin Films. *arXiv* [Preprint] (2021). Available from: https://arXiv.org/abs/2109.12811.
18. Zhou X, Zhang X, Yi J, Qin P, Feng Z, Jiang P, et al. Antiferromagnetism in Ni-Based Superconductors. *Adv Mater* (2021) 34 2106117. doi:10.1002/adma.202106117
19. Gu Q, Li Y, Wan S, Li H, Guo W, Yang H, et al. Single Particle Tunneling Spectrum of Superconducting Nd1-XSrxNiO2 Thin Films. *Nat Commun* (2020) 11:6027. doi:10.1038/s41467-020-19908-1
20. Pan GA, Segedin DF, LaBollita H, Song Q, Nica EM, Goodge BH, et al. Superconductivity in a Quintuple-Layer Square-Planar Nickelate. *Nat Mater* (2022) 21:160–4. doi:10.1038/s41563-021-01142-9
21. Gao Q, Zhao Y, Zhou XJ, Zhu Z. Preparation of Superconducting Thin Films of Infinite-Layer Nickelate Nd0.8Sr0.2NiO2. *Chin Phys. Lett.* (2021) 38:5. doi:10.1088/0256-307x/38/7/077401
22. Cui Y, Li C, Li Q, Zhu X, Hu Z, Yang YF, et al. NMR Evidence of Antiferromagnetic Spin Fluctuations in Nd0.85Sr0.15NiO2. *Chin Phys. Lett.* (2021) 38. doi:10.1088/0256-307x/38/6/067401
23. Wang BX, Zheng H, Krivyakina E, Chmaissem O, Lopes PP, Lynn JW, et al. Synthesis and Characterization of Bulk Nd1-XSrxNi O2 and Nd1-XSrxNi O3. *Phys Rev Mater* (2020) 4:1. doi:10.1103/physrevmaterials.4.084409
24. Zeng SW, Yin XM, Li CJ, Tang CS, Han K, Huang Z, et al. Observation of Perfect Diamagnetism and Interfacial Effect on the Electronic Structures in Infinite Layer Nd0.8Sr0.2NiO2 Superconductors. *Nat Commun* (2022) 13:743. doi:10.1038/s41467-022-28390-w
25. Lee K, Goodge BH, Li D, Osada M, Wang BY, Cui Y, et al. Aspects of the Synthesis of Thin Film Superconducting Infinite-Layer Nickelates. *APL Mater* (2020) 8:041107. doi:10.1063/5.0005103
26. Zeng S, Tang CS, Yin X, Li C, Li M, Huang Z, et al. Phase Diagram and Superconducting Dome of Infinite-Layer Nd1−xSrxNiO2 Thin Films. *Phys Rev Lett* (2020) 125:147003. doi:10.1103/physrevlett.125.147003
27. Bednorz JG, Müller KA. Possible highT C Superconductivity in the Ba?La?Cu? O System. *Z Physik B - Condensed Matter* (1986) 64:189–93. doi:10.1007/bf01303701
28. Choi M-Y, Lee K-W, Pickett WE. Role of 4f States in Infinite-Layer NdNiO2. *Phys Rev B* (2020) 101:20503. doi:10.1103/physrevb.101.020503
29. Zhang R, Lane C, Singh B, Nokelainen J, Barbiellini B, Markiewicz RS, et al. Magnetic and F-Electron Effects in LaNiO2 and NdNiO2 Nickelates with Cuprate-like 3dx2−y2 Band. *Commun Phys* (2021) 4:1. doi:10.1038/s42005-021-00621-4
30. Norman MR. Entering the Nickel Age of Superconductivity. *Physics (College. Park. Md).* (2020) 13:1. doi:10.1103/physics.13.85
31. Zhang J, Tao X, Review on Quasi-2D Square Planar Nickelates, 23 (n.d.). (2021)
32. Kitatani M, Si L, Janson O, Arita R, Zhong Z, Held K. Nickelate Superconductors—A Renaissance of the One-Band Hubbard Model. *Npj Quan Mater* (2020) 5:6. doi:10.1038/s41535-020-00260-y
33. Liu Z, Xu C, Cao C, Zhu W, Wang ZF, Yang J. Doping Dependence of Electronic Structure of Infinite-Layer NdNiO2. *Phys Rev B* (2021) 103:1. doi:10.1103/physrevb.103.045103
34. Sawatzky GA. Superconductivity Seen in a Non-magnetic Nickel Oxide. *Nature* (2019) 572:592–3. doi:10.1038/d41586-019-02518-3
35. Zhang Y-H, Vishwanath A. Type-II T − J Model in Superconducting Nickelate Nd 1 − X Sr X NiO 2. *Phys Rev Res* (2020) 2:1. doi:10.1103/physrevresearch.2.023112
36. Botana AS, Lee K-W, Norman MR, Pardo V, Pickett WE. Low Valence Nickelates: Launching the Nickel Age of Superconductivity. *Front Phys* (2022) 9:813532. doi:10.3389/fphy.2021.813532
37. Nomura Y, Arita R. Superconductivity in Infinite-Layer Nickelates. *arXiv* [Preprint] (2021). Available from: https://arXiv.org/abs/2107.12923.
38. Si L, Xiao W, Kaufmann J, Tomczak JM, Lu Y, Zhong Z, et al. Topotactic Hydrogen in Nickelate Superconductors and Akin Infinite-Layer Oxides ABO_{2}. *Phys Rev Lett* (2020) 124:166402. doi:10.1103/PhysRevLett.124.166402
39. Li Y, Sun W, Yang J, Cai X, Guo W, Gu Z, et al. Impact of Cation Stoichiometry on the Crystalline Structure and Superconductivity in Nickelates. *Front Phys* (2021) 9:1. doi:10.3389/fphy.2021.719534
40. Li D, Wang BY, Lee K, Harvey SP, Osada M, Goodge BH, et al. Superconducting Dome in Nd 1- X Sr X NiO 2 Infinite Layer Films. *Phys Rev. Lett* (2020) 1.
41. Osada M, Wang BY, Goodge BH, Harvey SP, Lee K, Li D, et al. Nickelate Superconductivity without Rare-Earth Magnetism: (La,Sr)NiO2. *Adv Mater* (2021) 33:1. doi:10.1002/adma.202104083
42. Osada M, Wang BY, Goodge BH, Lee K, Yoon H, Sakuma K, et al. A Superconducting Praseodymium Nickelate with Infinite Layer Structure. *Nano Lett* (2020) 20:5735–40. doi:10.1021/acs.nanolett.0c01392
43. Tam CC, Choi J, Ding X, Agrestini S, Nag A, Huang B, et al. Charge Density Waves in Infinite-Layer NdNiO$_2$ Nickelates. *arXiv* [Preprint] (2021). Available from: https://arXiv.org/abs/2112.04440.
44. Li Q, He C, Si J, Zhu X, Zhang Y, Wen HH. Absence of Superconductivity in Bulk Nd1-XSrxNiO2. *Commun Mater* (2020) 1:16. doi:10.1038/s43246-020-0018-1
45. Puphal P, Wu Y, Fürsich K, Lee H, Pakdaman M, Bruin JAN, et al. Topotactic Transformation of Single Crystals : From Perovskite to Infinite-Layer Nickelates. *Sci Adv* (2021) 7:eabl8091. doi:10.1126/sciadv.abl8091
46. He C, Ming X, Li Q, Zhu X, Si J, Wen H-H. Synthesis and Physical Properties of Perovskite Sm1−x Sr X NiO3 (X = 0, 0.2) and Infinite-Layer Sm0.8Sr0.2NiO2

Nickelates. *J Phys Condens Matter* (2021) 33:265701. doi:10.1088/1361-648x/abfb90
47. Goodge BH, Li D, Lee K, Osada M, Wang BY, Sawatzky GA, et al. Doping Evolution of the Mott-Hubbard Landscape in Infinite-Layer Nickelates. *Proc Natl Acad Sci U S A* (2021) 118:1. doi:10.1073/pnas.2007683118
48. Miller C, Botana AS. Cupratelike Electronic and Magnetic Properties of Layered Transition-Metal Difluorides from First-Principles Calculations. *Phys Rev B*(2020) 101:195116. doi:10.1103/physrevb.101.195116
49. Takamatsu T, Kato M, Noji T, Koike Y. Low-Temperature Synthesis of the Infinite-Layer Compound LaNiO2 Using CaH2 as Reductant. *Phys C Supercond Its Appl* (2010) 470:2009. doi:10.1016/j.physc.2009.10.132
50. Ikeda A, Manabe T, Naito M. Improved Conductivity of Infinite-Layer LaNiO2 Thin Films by Metal Organic Decomposition. *Physica C: Superconductivity* (2013) 495:134–40. doi:10.1016/j.physc.2013.09.007
51. Ren X, Gao Q, Zhao Y, Luo H, Zhou X, Zhu Z. Superconductivity in Infinite-Layer Pr$_{0.8}$Sr$_{0.2}$NiO$_2$ Films on Different Substrates. *arXiv* [Preprint] (2021). Available from: https://arXiv.org/abs/2109.05761.
52. Adhikary P, Bandyopadhyay S, Das T, Dasgupta I, Saha-Dasgupta T. Orbital-Selective Superconductivity in a Two-Band Model of Infinite-Layer Nickelates. *Phys Rev B* (2020) 102:1. doi:10.1103/physrevb.102.100501
53. Hepting M, Li D, Jia CJ, Lu H, Paris E, Tseng Y, et al. Electronic Structure of the Parent Compound of Superconducting Infinite-Layer Nickelates. *Nat Mater* (2020) 19:381–5. doi:10.1038/s41563-019-0585-z
54. Jiang P, Si L, Liao Z, Zhong Z. Electronic Structure of Rare-Earth Infinite-Layer RNi O2(R=La,Nd). *Phys Rev B* (2019) 100:1. doi:10.1103/physrevb.100.201106
55. Wu X, Di Sante D, Schwemmer T, Hanke W, Hwang HY, Raghu S, et al. Robust Dx2-Y2-Wave Superconductivity of Infinite-Layer Nickelates. *Phys Rev B* (2020) 101:1. doi:10.1103/physrevb.101.060504
56. Bernardini F, Bosin A, Cano A. Geometric Effects in the Infinite-Layer Nickelates. *arXiv* [Preprint] (2021). Available from: https://arXiv.org/abs/2110.13580.
57. Xia C, Wu J, Chen Y, Chen H. Dynamical Structural Instability and a New Crystal-Electronic Structure of Infinite-Layer Nickelates. *arXiv* [Preprint] (2021). Available from: https://arXiv.org/abs/2110.12405.
58. Lu H, Rossi M, Nag A, Osada M, Li DF, Lee K, et al. Magnetic Excitations in Infinite-Layer Nickelates. *Science* (2021) 373:213–6. doi:10.1126/science.abd7726
59. Krieger G, Martinelli L, Zeng S, Chow LE, Kummer K, Arpaia R, et al. Charge and Spin Order Dichotomy in $NdNiO_2$ Driven by $SrTiO_3$ Capping Layer. *arXiv* [Preprint] (2021). Available from: https://arXiv.org/abs/2112.03341.
60. Rossi M, Osada M, Choi J, Agrestini S, Jost D, Lee Y, et al. A Broken Translational Symmetry State in an Infinite-Layer Nickelate. *arXiv* [Preprint] (2021). Available from: https://arXiv.org/abs/2112.02484.
61. Lin JQ, Villar Arribi P, Fabbris G, Botana AS, Meyers D, Miao H, et al. Strong Superexchange in a D9-δ Nickelate Revealed by Resonant Inelastic X-Ray Scattering. *Phys Rev Lett* (2021) 126:1. doi:10.1103/physrevlett.126.087001
62. Zhang GM, Yang YF, Zhang FC. Self-Doped Mott Insulator for Parent Compounds of Nickelate Superconductors. *Phys Rev B* (2020) 101:1. doi:10.1103/physrevb.101.020501
63. Wang Z, Zhang GM, Yang YF, Zhang FC. Distinct Pairing Symmetries of Superconductivity in Infinite-Layer Nickelates. *Phys Rev B* (2020) 102:1. doi:10.1103/physrevb.102.220501
64. Tsuei CC, Kirtley JR. Pairing Symmetry in Cuprate Superconductors. *Rev Mod Phys* (2000) 72:969–1016. doi:10.1103/revmodphys.72.969
65. Wu X, Jiang K, Di Sante D, Hanke W, Schnyder AP, Hu J, et al. Surface S-Wave Superconductivity for Oxide-Terminated Infinite-Layer Nickelates. *arXiv* [Preprint] (2020). Available from: https://arXiv.org/abs/2008.06009.
66. Wang BY, Li D, Goodge BH, Lee K, Osada M, Harvey SP, et al. Isotropic Pauli-Limited Superconductivity in the Infinite-Layer Nickelate Nd0.775Sr0.225NiO2. *Nat Phys* (2021) 17:473–7. doi:10.1038/s41567-020-01128-5
67. Yuan HQ, Singleton J, Balakirev FF, Baily SA, Chen GF, Luo JL, et al. Nearly Isotropic Superconductivity in (Ba,K)Fe2As2. *Nature* (2009) 457:565–8. doi:10.1038/nature07676
68. Martin C, Tillman ME, Kim H, Tanatar MA, Kim SK, Kreyssig A, et al. Nonexponential London Penetration Depth of FeAs-Based Superconducting RFeAsO(0.9)F(0.1) (R = La, Nd) Single Crystals. *Phys Rev Lett* (2009) 102:247002. doi:10.1103/PhysRevLett.102.247002
69. Chow LE, Kunniniyil Sudheesh S, Nandi P, Zeng SW, Zhang ZT, Du XM, et al. Pairing Symmetry in Infinite-Layer Nickelate Superconductor. *arXiv* [Preprint] (2022). Available from: https://arxiv.org/abs/2201.10038.
70. Harvey SP, Wang BY, Fowlie J, Osada M, Lee K, Lee Y, et al. Evidence for Nodal Superconductivity in Infinite-lLyer Nickelates. *arXiv* [Preprint] (2022). Available from: https://arxiv.org/abs/2201.12971.

Conflict of Interest: The authors declare that the research was conducted in the absence of any commercial or financial relationships that could be construed as a potential conflict of interest.

Publisher's Note: All claims expressed in this article are solely those of the authors and do not necessarily represent those of their affiliated organizations, or those of the publisher, the editors and the reviewers. Any product that may be evaluated in this article, or claim that may be made by its manufacturer, is not guaranteed or endorsed by the publisher.

frontiers in Physics

ORIGINAL RESEARCH
published: 14 March 2022
doi: 10.3389/fphy.2022.842578

Investigation of Hydrogen Incorporations in Bulk Infinite-Layer Nickelates

P. Puphal[1], V. Pomjakushin[2], R. A. Ortiz[1], S. Hammoud[3], M. Isobe[1], B. Keimer[1] and M. Hepting[1]*

[1]Max-Planck-Institute for Solid State Research, Stuttgart, Germany, [2]Laboratory for Neutron Scattering and Imaging (LNS), Paul Scherrer Institute (PSI), Villigen, Switzerland, [3]Max-Planck-Institute for Intelligent Systems, Stuttgart, Germany

Infinite-layer (IL) nickelates are an emerging class of superconductors, where the Ni^{1+} valence state in a square planar NiO_2 coordination can only be reached *via* topotactic reduction of the perovskite phase. However, this topotactic soft chemistry with hydrogenous reagents is still at a stage of rapid development, and there are a number of open issues, especially considering the possibility of hydrogen incorporation. Here, we study the time dependence of the topotactic transformation of $LaNiO_3$ to $LaNiO_2$ for powder samples with x-ray diffraction and gas extraction techniques. While the hydrogen content of the powder increases with time, neutron diffraction shows no negative scattering of hydrogen in the $LaNiO_2$ crystal lattice. The extra hydrogen appears to be confined to grain boundaries or secondary-phase precipitates. The average crystal structure, and possibly also the physical properties, of the primary $LaNiO_2$ phase are, therefore, not noticeably affected by hydrogen residues created by the topotactic transformation.

Keywords: infinite-layer nickelates, topotactic reduction, superconductivity, neutron diffraction, gas extraction, x-ray diffraction, hydrogen

OPEN ACCESS

Edited by:
Veerpal Singh Awana, National Physical Laboratory (CSIR), India

Reviewed by:
Andrés Cano, UPR2940 Institut Neel (NEEL), France
Atsushi Fujimori, Waseda University, Japan

****Correspondence:***
P. Puphal
puphal@fkf.mpg.de

Specialty section:
This article was submitted to Condensed Matter Physics, a section of the journal Frontiers in Physics

Received: *23 December 2021*
Accepted: *01 February 2022*
Published: *14 March 2022*

Citation:
Puphal P, Pomjakushin V, Ortiz RA, Hammoud S, Isobe M, Keimer B and Hepting M (2022) Investigation of Hydrogen Incorporations in Bulk Infinite-Layer Nickelates. Front. Phys. 10:842578. doi: 10.3389/fphy.2022.842578

1 INTRODUCTION

Superconductivity exists in various hydrogen-containing compounds, highlighted by the recent discoveries of critical temperatures T_c as high as room temperature for hydride compounds formed under extreme pressures [1, 2]. Metal hydroxide–intercalated iron chalcogenides, such as $(Li_{0.8}Fe_{0.2})OHFeSe$ [3], show coexistence of antiferromagnetic order and superconductivity, a feature known from some high-T_c superconductors [4]. Electron-doped 1111 iron pnictides, such as $RFeAsO_{1-x}H_x$ [5, 6], $CeFeAsO_{1-x}H_x$ [7], and the pnictogen-free LaFeSiH [8] are a class, where the introduction of charge carriers *via* doping with hydrogen drives the system from an antiferromagnetically ordered state toward superconductivity. In layered sodium cobalt oxyhydrate, $Na_xCoO_2{\cdot}H_2O$ [9], superconductivity with a similar hole/electron-doping behavior by chemical substitution is observed as in the cuprate high-T_c superconductors [10].

For IL nickelates, a close relation and possible analogy to cuprate superconductors was suggested already in 1999 [11], and since the first discovery of superconductivity in the IL nickelate $(Nd,Sr)NiO_2$ [12], the observation of superconductivity has been confirmed [13–15] and extended to $(Pr,Sr)NiO_2$ [16], $(La,Sr)NiO_2$ [17], $(La,Ca)NiO_2$ [18], and $Nd_6Ni_5O_{12}$ [19]. Furthermore, a recent work reported superconductivity not only for films grown on $SrTiO_3$ substrates but also on LSAT [20], which provides enough evidence to consider thin-film nickelates as a novel class of superconductors. The possible

presence of topotactic hydrogen in IL nickelates, which depends on the rare-earth ion and/or epitaxial strain [21, 22], was proposed in theoretical studies [23, 24] and might have substantial influence on the electronic and magnetic properties of the IL nickelates, as $LaNiO_2H$ would realize a two-orbital Mott insulator [23]. A hint toward the possibility of hydrogen incorporation was provided by an early study of topotactically reduced $NdNiO_3$ films, which showed an oxyhydride $NdNiO_{3-x}H_y$ phase with a defect-fluorite structure in the surface region [25]. Furthermore, topotactic hydrogen can be found in $SrTiO_3$ thin films [26], that is, the material that is commonly used as a substrate and capping layer for IL nickelate films, which again provides a possible route for inclusion of hydrogen in infinite-layer nickelate thin films. While superconductivity has remained elusive in IL nickelates in bulk form, with studies on powder samples reporting insulating behavior [27, 28], a first step toward superconductivity was taken by our recent investigation of $(La,Ca)NiO_2$ single crystals [29], where metallicity was observed.

In this study, we address the issue of possible hydrogen incorporations in IL nickelates by examining bulk $LaNiO_{3-x}H_y$ powder samples with a combination of x-ray and neutron diffraction studies, gas extraction, and complementary high-pressure synthesis attempts of $LaNiO_2H$.

2 METHODS

$LaNiO_3$ powder samples with grain sizes of 0.5 μm were synthesized *via* the citrate–nitrate method as described in Ref. [30]. The method is optimal as the relatively small grains enhance the surface to bulk ratio, reducing reduction times. Moreover, higher purity can be reached than by high-pressure powder synthesis. The IL phase $LaNiO_2$ can be obtained solely through topotactic reduction of the perovskite $LaNiO_3$ phase, which is here achieved by using CaH_2 as the reducing agent [27, 28]. We reduced 50 mg of $LaNiO_3$ powder wrapped in aluminum foil, spatially separated from 250 mg CaH_2 powder at 280°C, as described in detail in Ref. [30], for various times.

We measured the stoichiometry including the hydrogen content with a combination of inductively coupled plasma mass spectroscopy (ICP-OES) and gas extraction; the former with a SPECTRO CIROS CCD and the latter with an Eltra ONH-2000 analyzer. For the determination of oxygen and hydrogen content, the powder samples were placed in a Ni crucible and clipped and heated, where the carrier gas takes the oxygen and hydrogen out of the sample. The oxygen reacts with carbon, and CO_2 is detected in an infrared cell, while hydrogen is detected by a thermal conductivity cell. Each measurement is repeated three times and compared to a standard. The quoted error bars provide the statistical error.

Powder x-ray diffraction (PXRD) data were collected using a Rigaku MiniFlex with a Cu K_α tube at room temperature. Neutron diffraction was performed at the high-resolution powder neutron diffractometer HRPT [31] at the Spallation Neutron Source SINQ at the Paul Scherrer Institute in Villigen. For the HRPT experiments, an amount of 340 mg of $LaNiO_2$ was enclosed into a vanadium can with an inner diameter of 6 mm, where the remaining space of the vanadium can was shielded with Cd foil, and the measurement was carried out at 1.5 K in a ^{4}He bath cryostat with a neutron wavelength of 1.15 Å.

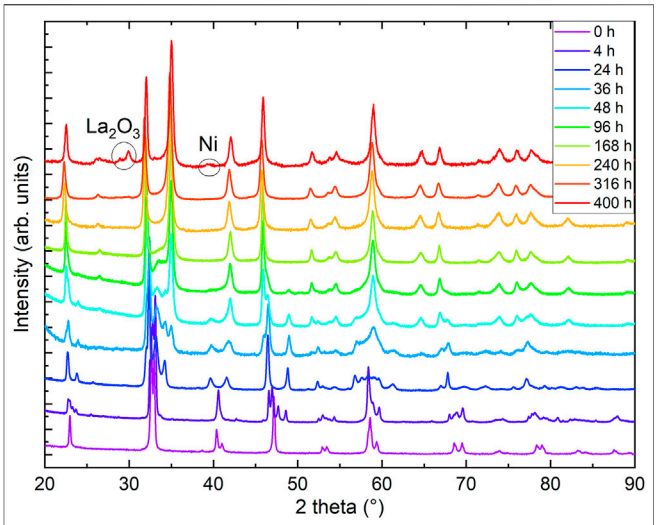

FIGURE 1 | Powder x-ray diffraction (PXRD) of reduced $LaNiO_3$ after different reduction times. Data were measured at T = 300 K with Cu K_α radiation. Curves are offset in vertical direction for clarity. The 0- and 316-h data are reproduced from Ref. [30].

3 RESULTS

As a first step, we checked the purity and stoichiometry of our starting material in the perovskite phase. In PXRD, we found no detectable impurities, and ICP combined with measurements of gas extraction indicated a starting stoichiometry of $La_{0.99(1)}Ni_{0.99(1)}O_{2.99(3)}H_{0.005(2)}$. We studied the reduction progress with time in detail by preparation of several ampules and extracting samples after varying reduction times and analyzed all the products with PXRD. We noticed that the progress of the reduction depends on the purity and sample amount and grain size for a given time as the reduction process is surface-dependent. Motivated by these observations, we carried out a standardized reduction on the same batch of perovskite precursors. After 1 day of reduction in the described process (see **Section 2**) we found a full structural transition to $LaNiO_{2.5}$ (see **Figure 1**). Our Rietveld refinement of the $LaNiO_{2.5}$ crystal structure is in good agreement with previous reports on reduced powder [32–34]. Notably, reduction times of 1 day and longer are in stark contrast to thin-film samples, which can be fully reduced to the IL phase within hours [12–18, 35, 36], presumably due to the enhanced thickness of our grains, with sizes of 0.5 μm as extracted from scanning electron microscopy (SEM) images. The reduction appears to be happening in domains, as we found cluster spin glass behavior in a detailed magnetic characterization [30], and thus after longer reduction times than 1 day, we observe phase mixtures of $LaNiO_{2.5}$ in $P2_1/n$ (#14) [33] and $LaNiO_2$ in $P4/mmm$ (#123) [37], with a slowly increasing fraction of the $LaNiO_2$

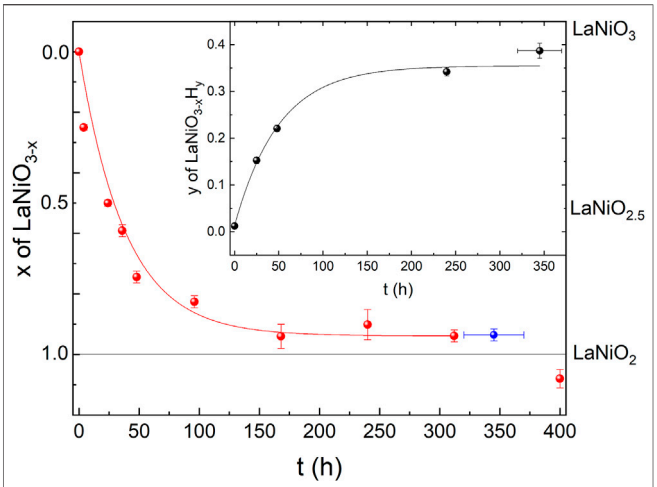

FIGURE 2 | Oxygen and hydrogen content of reduced $LaNiO_3$ after different reduction times. Red symbols correspond to the oxygen content *x* in $LaNiO_{3-x}$, extracted from Rietveld refinements of the PXRD data shown in **Figure 1**. The blue datapoint is extracted from Rietveld refinement of our neutron diffraction data shown in **Figure 3**. The solid red line is a guide to the eye. The black symbols in the inset correspond to the hydrogen content *y* in $LaNiO_{3-x}H_y$, obtained from gas extraction. The solid black line is a guide to the eye.

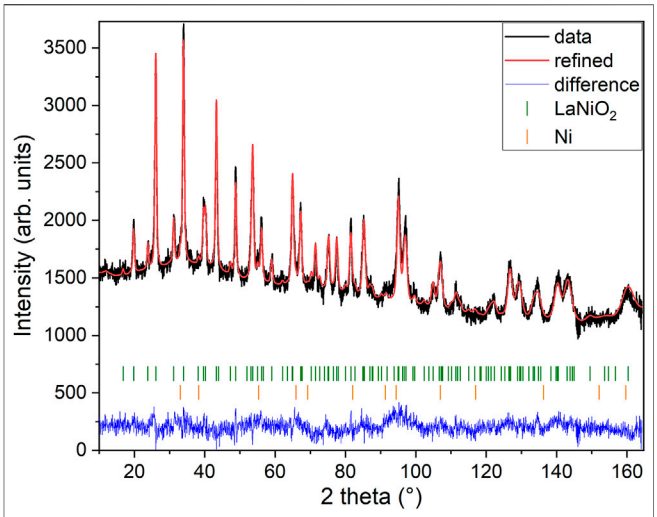

FIGURE 3 | Neutron powder diffraction. The data are taken from mixed samples reduced in the range of 320–376 h. The Rietveld refinement includes the $LaNiO_2$ phase and a Ni minority phase. Data were collected at 1.5 K with a neutron wavelength of 1.15 Å.

phase as a function of time (see **Figure 2**). Extracting the weight percentages from our refinement, we present the reduction progress for the CaH_2 reduction in analogy to a thermogravimetry (TG) curve, which is shown in **Figure 2**. The reduction process follows an exponential decay, which we also observed in thermogravimetry studies in hydrogen gas flow (not shown here). After a reduction time of approximately 316 h, the crystal structure can be refined assuming a single phase of IL $LaNiO_2$ (**Figure 2**, and Ref. [30]). Notably, while the structural transition does not progress further on an exponential time scale, a small amount of apical oxygen remains in the crystal lattice, as will be revealed by neutron diffraction below. However, for even longer reduction times, the sample begins to decompose, forming Ni and La_2O_3, which becomes clearly visible in PXRD after 400 h (**Figures 1**, **2**).

In the inset of **Figure 2**, we plot the hydrogen content in the resulting powder samples versus reduction time, obtained by a gas extraction method. While the initial perovskite nickelate shows a hydrogen content of 0.005(2) wt%, we find increase of hydrogen with time (opposite to the oxygen content), with 0.065(3) wt% for 24 h, 0.094(3) wt% for 38 h, 0.015(5) wt% for 240 h, and finally 0.169(7) wt% after 320–376 h. *Via* gas extraction, we find an oxygen content of 14.1(2) wt% after 316 h and 14.0(2) wt% after 320–376 h of reduction, where 14 wt% corresponds to a full reduction to the $LaNiO_2$ IL phase. If we assume that the amount of hydrogen would be incorporated into the average crystal structure, the corresponding effective stoichiometry of the sample investigated with neutrons would be $La_{0.99(1)}Ni_{0.99(1)}O_{2.00(2)}H_{0.39(2)}$, where La and Ni are determined *via* ICP. However, a first hint that this might not be the case comes from the presence of small amounts of elemental Ni in the PXRD of the 400-h sample (**Figure 1**), which is known to trap hydrogen [38]. The Rietveld refinement of the neutron diffraction data below also indicates a small amount of Ni. Furthermore, signatures of Ni precipitates (below the detection threshold of our PXRD) were also detected in powders after shorter reduction times since they give rise to ferromagnetic contributions in the magnetic signal [30]. The amount of Ni likely increases with reduction time, which could explain the increasing capability of incorporating hydrogen.

TABLE 1 | Refined atomic coordinates of $LaNiO_2$ in tetragonal space group *P4/mmm* with preferred orientation extracted from powder neutron diffraction data at 1.5 K (**Figure 3**).

$LaNiO_2$ | **a, b** = **3.955 0 (3) Å, c** = **3.358 8 (3) Å**					
Atom	***x***	***y***	***Z***	**U[Å^2]**	**Occ**
La (1d)	0.5	0.5	0.5	0.003 6(6)	1
Ni (1a)	0	0	0	0.005 7(5)	1
O (2f)	0	0.5	0	0.009 8(5)	1
O (1b)	0	0	0.5	0.009 8(5)	0.06(1)
Reliability factors	χ^2	R_B	R_f		
	1.89	3.53	2.79		

As a next step, we performed high-resolution neutron diffraction experiments on 340 mg of a sample prepared by mixing batches that had been subject to reduction times of 320, 350, and 376 h, respectively which are all in the range just before the start of the clear decay shown in **Figure 2**. The obtained neutron diffraction pattern can be well refined (see **Figure 3**) assuming $LaNiO_2$ in the IL *P4/mmm* structure (see **Table 1**), with a *c*-axis parameter of 3.3588(3) Å, which is lower than previously reported values [29, 30, 37], and 1.1(2) wt% of elemental Ni was included as a secondary phase.

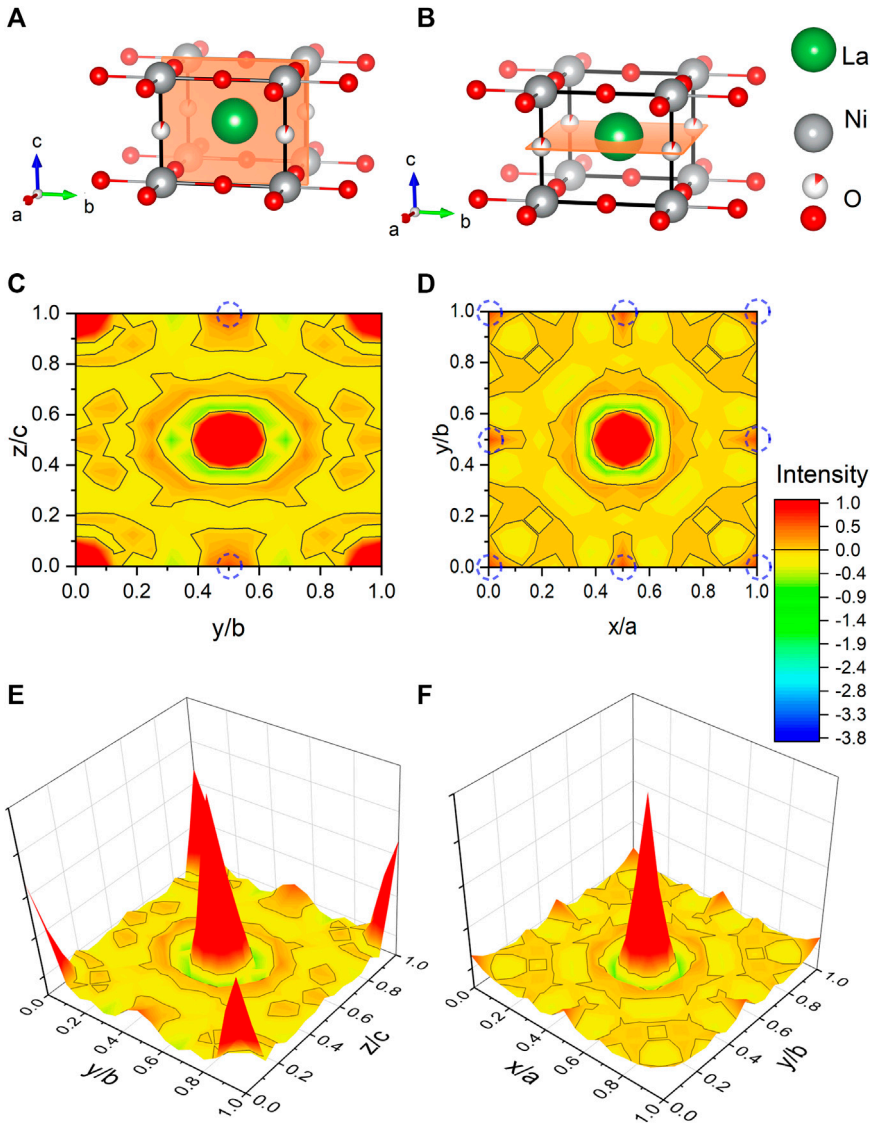

FIGURE 4 | Fourier maps of the scattering length density within the unit cell of $LaNiO_2$ extracted from neutron powder diffraction. **(A,B)** Refined unit cells with cuts corresponding to the Fourier maps in **(C,D)**, with the intensity range focused on the negative scattering length (yellow to blue), with –3.74 fm corresponding to hydrogen [40]. The positive scattering (orange to red) is capped at 1 (with 5.8 fm corresponding to oxygen). The black lines mark the isosurface lines with zero scattering intensity. The theoretically proposed hydrogen positions [23, 24] are highlighted with blue dashed circles. **(E,F)** Fourier maps are shown as a 3D colormap.

Figure 4 shows a Fourier map of the scattering density resulting from the Rietveld refinement of the neutron data, where the range of the color scheme is chosen to focus on the negative scattering length of hydrogen. While the used reduction temperatures (see **Section 2**) are too low to enable significant mobility of the La and Ni ions, the purpose of our topotactic treatment is to reduce oxygen, which becomes mobile and is extracted by reaction with hydrogen. We, therefore, focus on the scattering lengths of the two elements O and H. According to the theoretical prediction of Ref. [23], intercalation of H in IL nickelates is most favorable on the vacant apical oxygen sites with Wyckoff position (1b), or on interstitial positions between the rare-earth ions (Wyckoff positions (2e) and (1c)). Another theoretical work [24] predicts that $NdNiO_2$ is unstable, while $NdNiO_2H$ is not and also proposes the apical oxygen site with Wyckoff position (1b) for hydrogen. However, as shown in the Fourier maps of **Figure 4**, we find no significant negative scattering, which would appear as blue in our plots. The slightly negative scattering realized as a ring around a reflex, here in close proximity to La, is an artifact from the Fourier transformation, typically seen around larger ions [39] due to a signal cutoff from a finite q range. This is best seen in the Fourier maps **Figures 4E,F**. We note that the data can be refined with similar reliability factors as in **Table 1** by putting a mixture of O and H on Wyckoff position (1b) and constraining their occupation. As the positive scattering observed at this site

could be a mixture of negative scattering of H and positive scattering of O, which effectively clouds the negative scattering. Realized in a substitution series with $LaNiO_{3-x}H_x$, which would yield occupations of O: 0.430(8) and H: 0.570(8) in refinements of our data, but this oxygen content is way higher than what can be found in multiple gas extraction experiments ($La_{0.99(1)}Ni_{0.99(1)}O_{2.00(2)}H_{0.39(2)}$). Most importantly, the scenario of $LaNiO_{3-x}H_x$ would hint toward the possibility to synthesize the phase directly, similar as observed in the iron pnictides. However, such synthesis attempts have been carried out as described below and were not successful. Furthermore, in the case of iron pnictides, hydrogen substitution leads to no structural transitions [5–7], contrasting the evolution of the underlying structural transitions in $LaNiO_{3-x}$ according to the PXRD data (see **Figure 1**) and literature [37]. Another possibility to refine mixed occupancy is by constraining an equal occupation of O and H as $LaNiO_2(OH)_x$, which converges to 0.18(4). However, this would rather suggest an OH molecule with typical distances around 0.84 Å, which would realize negative scattering [39] and, thus, reduces the quality of the fit and shifts the occupation again down to 0.06(1). Thus, we conclude that intercalated hydrogen is unlikely in our $LaNiO_{2+\delta}$ powder sample. Nevertheless, we find the presence of a small amount of residual apical oxygen in Wyckoff position (1b), which corresponds to a deviation of $\delta = 0.06(1)$ from the ideal stoichiometry.

In addition, we attempted direct synthesis approaches of $LaNiO_{3-x}H_x$ as, for example, $LaNiO_2H$ *via* a Walker-type high-pressure synthesis in NaCl crucibles. We mixed La_2O_3 and NiO with NaH or CaH_2 and heated it to 650–1000°C under a pressure of 5–7 GPa, but were unable to synthesize any oxyhydride nickelate. Instead, we obtained $La(OH)_3$ and Ni, which is in contrast to related cases, such as $SmFeAsO_{1-x}H_x$ [5], $BaCrO_2H$ [41], $BaScO_2H$ [42], and $SrVO_2H$ [43].

4 CONCLUSION

In summary, we have synthesized high-quality $LaNiO_{2+\delta}$ powders and found some density of residual oxygen ($\delta = 0.06(1)$) even at the final stage of the topotactic reaction, just prior to decomposition of our samples. While our gas extraction method reveals partial hydrogen inclusions in the powder samples, high-resolution neutron diffraction refinements show that there is no clear topotactic hydrogen in $LaNiO_2$, and direct attempts to synthesize $LaNiO_{3-x}H_x$ were unsuccessful. The hydrogen detected by gas extraction could be trapped in Ni impurities that increase with increasing reduction time and/or ascribed to phenomena at surfaces or grain boundaries, such as water adsorption/intercalation [44] on powder surfaces or partial formation of $LaNiO_{3-x}H_x$ on the nanometer scale [25]. Notably, a relatively high density of grain boundaries/crystallographic defects was reported for IL nickelate thin films [45], and also surface effects can play a more decisive role in films. Thus, future studies clarifying the presence and impact of hydrogen in nickelate thin-film samples are highly desirable.

DATA AVAILABILITY STATEMENT

The raw data supporting the conclusion of this article will be made available by the authors, without undue reservation.

AUTHOR CONTRIBUTIONS

PP, MI, BK, and MH conceived the project. RO carried out the topotactic reductions. PP and VP conducted the neutron diffraction experiments. SH executed the ICP and gas extraction measurements. PP analyzed the data and prepared the manuscript with input from all authors.

FUNDING

We acknowledge financial support by the Center for Integrated Quantum Science and Technology (IQ^{ST}) and the Deutsche Forschungsgemeinschaft (DFG, German Research Foundation): Projektnummer 107745057—TRR 80. The Max Planck Society is acknowledged for funding of the open-access fee.

ACKNOWLEDGMENTS

We thank R. Merkle and A. Fuchs for the synthesis of $LaNiO_3$ and H. Hoier for preliminary PXRD characterizations. We acknowledge PXRD measurements by C. Stefani from the X-ray Diffraction Scientific Facility at an early stage of this work. The use of facilities of the Quantum Materials Department of H. Takagi for the attempted high-pressure synthesis of $LaNiO_2H$ is gratefully acknowledged.

REFERENCES

1. Shamp A, Zurek E Superconductivity in Hydrides Doped with Main Group Elements Under Pressure. *Nov Supercond Mater* (2017) 3:14. doi:10.1515/nsm-2017-0003
2. Snider E, Dasenbrock-Gammon N, McBride R, Debessai M, Vindana H, Vencatasamy K, et al. Room-temperature Superconductivity in a Carbonaceous Sulfur Hydride. *Nature* (2020) 586:373–7. doi:10.1038/s41586-020-2801-z
3. Lu XF, Wang NZ, Wu H, Wu YP, Zhao D, Zeng XZ, et al. Coexistence of Superconductivity and Antiferromagnetism in (Li0.8Fe0.2)OHFeSe. *Nat Mater* (2014) 14:325–9. doi:10.1038/nmat4155
4. Kahsay G, Singh P. Coexistence of Superconductivity and Antiferromagnetism in High-T C Gd1+x Ba2−x Cu3O7−δ Superconductor. *J Supercond Nov Magn* (2016) 29:2031–4. doi:10.1007/s10948-016-3549-4
5. Hanna T, Muraba Y, Matsuishi S, Igawa N, Kodama K, Shamoto S-i., et al. Hydrogen in layered iron arsenides: Indirect electron doping to induce superconductivity. *Phys Rev B* (2011) 84:024521. doi:10.1103/physrevb.84.024521
6. Hiraishi M, Iimura S, Kojima KM, Yamaura J, Hiraka H, Ikeda K, et al. Bipartite Magnetic Parent Phases in the Iron Oxypnictide Superconductor. *Nat Phys* (2014) 10:300–3. doi:10.1038/nphys2906
7. Matsuishi S, Hanna T, Muraba Y, Kim SW, Kim JE, Takata M, et al. Structural analysis and superconductivity of $CeFeAsO_{1-x}H_x$. *Phys Rev B* (2012) 85:014514. doi:10.1103/physrevb.85.014514

8. Bernardini F, Garbarino G, Sulpice A, Núñez-Regueiro M, Gaudin E, Chevalier B, et al. Iron-based Superconductivity Extended to the Novel Silicide LaFeSiH. *Phys Rev B* (2018) 97. doi:10.1103/physrevb.97.100504
9. Lynn JW, Huang Q, Brown CM, Miller VL, Foo ML, Schaak RE, et al. Structure and Dynamics of superconductingNaxCoO2hydrate and its Unhydrated Analog. *Phys Rev B* (2003) 68:214516. doi:10.1103/physrevb.68.214516
10. Keimer B, Kivelson SA, Norman MR, Uchida S, Zaanen J. From Quantum Matter to High-Temperature Superconductivity in Copper Oxides. *Nature* (2015) 518:179–86. doi:10.1038/nature14165
11. Anisimov VI, Bukhvalov D, Rice TM. Electronic Structure of Possible Nickelate Analogs to the Cuprates. *Phys Rev B* (1999) 59:7901–6. doi:10.1103/physrevb.59.7901
12. Li D, Lee K, Wang BY, Osada M, Crossley S, Lee HR, et al. Superconductivity in an Infinite-Layer Nickelate. *Nature* (2019) 572:624–7. doi:10.1038/s41586-019-1496-5
13. Zeng S, Tang CS, Yin X, Li C, Li M, Huang Z, et al. Phase Diagram and Superconducting Dome of Infinite-Layer Nd1−xSrxNiO2 Thin Films. *Phys Rev Lett* (2020) 125:147003. doi:10.1103/physrevlett.125.147003
14. Li Y, Sun W, Yang J, Cai X, Guo W, Gu Z, et al. Impact of Cation Stoichiometry on the Crystalline Structure and Superconductivity in Nickelates. *Front Phys* (2021) 9:443. doi:10.3389/fphy.2021.719534
15. Gao Q, Zhao Y, Zhou X-J, Zhu Z. Preparation of Superconducting Thin Films of Infinite-Layer Nickelate Nd0.8Sr0.2NiO2. *Chin Phys. Lett.* (2021) 38: 077401. doi:10.1088/0256-307x/38/7/077401
16. Osada M, Wang BY, Goodge BH, Lee K, Yoon H, Sakuma K, et al. A Superconducting Praseodymium Nickelate with Infinite Layer Structure. *Nano Lett* (2020) 20:5735–40. doi:10.1021/acs.nanolett.0c01392
17. Osada M, Wang BY, Goodge BH, Harvey SP, Lee K, Li D, et al. Nickelate Superconductivity without Rare-Earth Magnetism: (La,Sr)NiO 2. *Adv Mater* (2021) 33:2104083. doi:10.1002/adma.202104083
18. Zeng SW, Li CJ, Chow LE, Cao Y, Zhang ZT, Tang CS, et al. *Superconductivity in Infinite-Layer Lanthanide Nickelates* (2021). arXiv:2105.13492 [cond-mat.supr-con].
19. Pan GA, Ferenc Segedin D, LaBollita H, Song Q, Nica EM, Goodge BH, et al. Superconductivity in a Quintuple-Layer Square-Planar Nickelate. *Nat Mater* (2021) 21:160–4. doi:10.1038/s41563-021-01142-9
20. Ren X, Gao Q, Zhao Y, Luo H, Zhou X, Zhu Z. *Superconductivity in Infinite-Layer* $pr_{0.8}sr_{0.2}nio_2$ *Films on Different Substrates* (2021). arXiv:2109.05761 [cond-mat.supr-con].
21. Bernardini F, Bosin A, Cano A. *Geometric Effects in the Infinite-Layer Nickelates* (2021). arXiv:2110.13580 [cond-mat.supr-con].
22. Alvarez AAC, Petit S, Iglesias L, Prellier W, Bibes M, Varignon J. *Structural Instabilities of Infinite-Layer Nickelates from First-Principles Simulations* (2021). arXiv:2112.02642 [cond-mat.mtrl-sci].
23. Si L, Xiao W, Kaufmann J, Tomczak JM, Lu Y, Zhong Z, et al. Topotactic Hydrogen in Nickelate Superconductors and Akin Infinite-Layer Oxides ABO2. *Phys Rev Lett* (2020) 124:166402. doi:10.1103/physrevlett.124.166402
24. Malyi OI, Varignon J, Zunger A. *Bulk Ndnio2 Is Thermodynamically Unstable with Respect to Decomposition while Hydrogenation Reduces the Instability and Transforms it from Metal to Insulator* (2021). doi:10.1103/PhysRevB.105.014106
25. Onozuka T, Chikamatsu A, Katayama T, Fukumura T, Hasegawa T. Formation of Defect-Fluorite Structured NdNiOxHy Epitaxial Thin Films via a Soft Chemical Route from NdNiO3 Precursors. *Dalton Trans* (2016) 45: 12114–8. doi:10.1039/c6dt01737a
26. Kutsuzawa D, Hirose Y, Chikamatsu A, Nakao S, Watahiki Y, Harayama I, et al. Strain-enhanced Topotactic Hydrogen Substitution for Oxygen in SrTiO3epitaxial Thin Film. *Appl Phys Lett* (2018) 113:253104. doi:10.1063/1.5057370
27. Wang B-X, Zheng H, Krivyakina E, Chmaissem O, Lopes PP, Lynn JW, et al. Synthesis and characterization of bulk Nd_{1-x} Sr_xNi O_2 and Nd_{1-x} Sr_x NiO_3. *Phys Rev Mater* (2020) 4:084409. doi:10.1103/physrevmaterials.4.084409
28. Li Q, He C, Si J, Zhu X, Zhang Y, Wen H-H. Absence of Superconductivity in Bulk Nd1−xSrxNiO2. *Commun Mater* (2020) 1:16. doi:10.1038/s43246-020-0018-1
29. Puphal P, Wu Y-M, Fürsich K, Lee H, Pakdaman M, Bruin JAN, et al. Topotactic transformation of single crystals: From perovskite to infinite-layer nickelates. *Sci Adv* (2021) 7:eabl8091. doi:10.1126/sciadv.abl8091
30. Ortiz RA, Puphal P, Klett M, Hotz F, Kremer RK, Trepka H, et al. *Magnetic Correlations in Infinite-Layer Nickelates: An Experimental and Theoretical Multi-Method Study* (2021). arXiv:2111.13668 [cond-mat.str-el].
31. Fischer P, Frey G, Koch M, Könnecke M, Pomjakushin V, Schefer J, et al. High-resolution Powder Diffractometer HRPT for thermal Neutrons at SINQ. *Physica B: Condensed Matter* (2000) 276-278:146–7. doi:10.1016/s0921-4526(99)01399-x
32. Crespin M, Levitz P, Gatineau L. Reduced Forms of LaNiO3perovskite. Part 1.-Evidence for New Phases: La2Ni2O5and LaNiO2. *J Chem Soc Faraday Trans 2* (1983) 79:1181–94. doi:10.1039/f29837901181
33. Alonso JA, Martínez-Lope MJ. Preparation and crystal Structure of the Deficient Perovskite LaNiO2.5, Solved from Neutron Powder Diffraction Data. *J Chem Soc Dalton Trans* (1995) 2819–24. doi:10.1039/dt9950002819
34. Alonso JA, Martínez-Lope MJ, García-Muñoz JL, Fernández-Díaz MT. A Structural and Magnetic Study of the Defect Perovskite $LaNiO_{2.5}$ from High-Resolution Neutron Diffraction Data. *J Phys Condensed Matter* (1997) 9:6417–6426.
35. Ikeda A, Krockenberger Y, Irie H, Naito M, Yamamoto H. Direct Observation of Infinite NiO2planes in LaNiO2films. *Appl Phys Express* (2016) 9:061101. doi:10.7567/apex.9.061101
36. Hepting M, Li D, Jia CJ, Lu H, Paris E, Tseng Y, et al. Electronic Structure of the Parent Compound of Superconducting Infinite-Layer Nickelates. *Nat Mater* (2020) 19:381–5. doi:10.1038/s41563-019-0585-z
37. Hayward MA, Green MA, Rosseinsky MJ, Sloan J. Sodium Hydride as a Powerful Reducing Agent for Topotactic Oxide Deintercalation: Synthesis and Characterization of the Nickel(I) Oxide LaNiO2. *J Am Chem Soc* (1999) 121: 8843–54. doi:10.1021/ja991573i
38. Louthan MR, Donovan JA, Caskey GR. Hydrogen Diffusion and Trapping in Nickel. *Acta Metallurgica* (1975) 23:745–9. doi:10.1016/0001-6160(75)90057-7
39. Sano-Furukawa A, Hattori T, Komatsu K, Kagi H, Nagai T, Molaison JJ, et al. Direct Observation of Symmetrization of Hydrogen Bond in δ-AlOOH under Mantle Conditions Using Neutron Diffraction. *Sci Rep* (2018) 8. doi:10.1038/s41598-018-33598-2
40. Sears VF. Neutron Scattering Lengths and Cross Sections. *Neutron News* (1992) 3:26–37. doi:10.1080/10448639208218770
41. Higashi K, Ochi M, Nambu Y, Yamamoto T, Murakami T, Yamashina N, et al. Enhanced Magnetic Interaction by Face-Shared Hydride Anions in 6H-BaCrO2H. *Inorg Chem* (2021) 60:11957–63. doi:10.1021/acs.inorgchem.1c00992
42. Goto Y, Tassel C, Noda Y, Hernandez O, Pickard CJ, Green MA, et al. Pressure-Stabilized Cubic Perovskite Oxyhydride BaScO2H. *Inorg Chem* (2017) 56:4840–5. doi:10.1021/acs.inorgchem.6b02834
43. Yamamoto T, Zeng D, Kawakami T, Arcisauskaite V, Yata K, Patino MA, et al. The Role of π-blocking Hydride Ligands in a Pressure-Induced Insulator-To-Metal Phase Transition in SrVO2H. *Nat Commun* (2017) 8. doi:10.1038/s41467-017-01301-0
44. Baeumer C, Li J, Lu Q, Liang AY-L, Jin L, Martins HP, et al. Tuning Electrochemically Driven Surface Transformation in Atomically Flat LaNiO3 Thin Films for Enhanced Water Electrolysis. *Nat Mater* (2021) 20: 674–82. doi:10.1038/s41563-020-00877-1
45. Lee K, Goodge BH, Li D, Osada M, Wang BY, Cui Y, et al. Aspects of the Synthesis of Thin Film Superconducting Infinite-Layer Nickelates. *APL Mater* (2020) 8:041107. doi:10.1063/5.0005103

Conflict of Interest: The authors declare that the research was conducted in the absence of any commercial or financial relationships that could be construed as a potential conflict of interest.

Publisher's Note: All claims expressed in this article are solely those of the authors and do not necessarily represent those of their affiliated organizations, or those of the publisher, the editors, and the reviewers. Any product that may be evaluated in this article, or claim that may be made by its manufacturer, is not guaranteed or endorsed by the publisher.

frontiers in Physics

ORIGINAL RESEARCH
published: 24 March 2022
doi: 10.3389/fphy.2022.846639

Correlated Insulating Behavior in Infinite-Layer Nickelates

Y.-T. Hsu[1], M. Osada[2,3], B. Y. Wang[2,4], M. Berben[1], C. Duffy[1], S. P. Harvey[2,3], K. Lee[2,4], D. Li[2,3,5], S. Wiedmann[1], H. Y. Hwang[2,3] and N. E. Hussey[1,6]*

[1]High Field Magnet Laboratory (HFML-EMFL) and Institute for Molecules and Materials, Radboud University, Nijmegen, Netherlands, [2]SLAC National Accelerator Laboratory, Stanford Institute for Materials and Energy Sciences, Menlo Park, CA, United States, [3]Department of Applied Physics, Stanford University, Stanford, CA, United States, [4]Department of Physics, Stanford University, Stanford, CA, United States, [5]Department of Physics, City University of Hong Kong, Hong Kong, China, [6]H. H. Wills Physics Laboratory, University of Bristol, Bristol, United Kingdom

Unlike their cuprate counterparts, the undoped nickelates are weak insulators without long-range antiferromagnetic order. Identifying the origin of this insulating behavior, found on both sides of the superconducting dome, is potentially a crucial step in the development of a coherent understanding of nickelate superconductivity. In this work, we study the normal-state resistivity of infinite-layer nickelates using high magnetic fields to suppress the superconductivity and examine the impact of disorder and doping on its overall temperature (T) dependence. In superconducting samples, the resistivity of Nd- and La-based nickelates continues to exhibit weakly insulating behavior with a magnitude and functional form similar to that found in underdoped electron-doped cuprates. We find a systematic evolution of the insulating behavior as a function of nominal hole doping across different rare-earth families, suggesting a pivotal role for strong electron interactions, and uncover a correlation between the suppression of the resistivity upturn and the robustness of the superconductivity. By contrast, we find very little correlation between the level of disorder and the magnitude and onset temperature of the resistivity upturn. Combining these experimental observations with previous Hall effect measurements on these two nickelate families, we consider various possible origins for this correlated insulator behavior and its evolution across their respective phase diagrams.

Keywords: superconductivity, nickelates, charge transport, metal-insulator crossover, high magnetic fields

OPEN ACCESS

Edited by:
Veerpal Singh Awana, National Physical Laboratory (CSIR), India

Reviewed by:
Jie Yuan, Institute of Physics (CAS), China
Atsushi Fujimori, Waseda University, Japan

****Correspondence:***
Y.-T. Hsu
yute.hsu@ru.nl

Specialty section:
This article was submitted to Condensed Matter Physics, a section of the journal Frontiers in Physics

Received: *31 December 2021*
Accepted: *11 February 2022*
Published: *24 March 2022*

Citation:
Hsu Y-T, Osada M, Wang BY, Berben M, Duffy C, Harvey SP, Lee K, Li D, Wiedmann S, Hwang HY and Hussey NE (2022) Correlated Insulating Behavior in Infinite-Layer Nickelates. Front. Phys. 10:846639. doi: 10.3389/fphy.2022.846639

INTRODUCTION

The recent discovery of superconductivity in the infinite-layer nickelates (ILN) [1–4] represents the culmination of a three-decade-long search to successfully dope the $3d^9$ (Ni^{1+}) configuration in a square planar geometry as a means of replicating the structural and orbital motif found in high-T_c cuprates. Unlike the cuprates, whose parent ground state is a Mott insulator with long-range antiferromagnetic (AFM) order, the undoped ILN were found to be metallic at elevated temperatures with a crossover to a weakly insulating state below approximately 100 K, at which the resistivity starts to develop a moderate upturn. While static AFM order has thus far remained undetected in the nickelates, recent resonant x-ray scattering [5] and nuclear magnetic resonance (NMR) experiments [6, 7] reported signatures consistent with fluctuating AFM paramagnon excitations. Other NMR studies, however, claimed an absence of magnetic order in the nickelates [8]. The occurrence of weakly insulating behavior at a high hole doping level, beyond the range within which superconductivity is realized, further contrasts with the

correlated but nonetheless metallic ground state found in highly overdoped cuprates [9]. Numerous theoretical calculations [10–22] have indeed pointed out that the 5*d* (and possibly 4*f*) band of the rare-earth (*RE*) elements contributes a finite density of states at the Fermi level, highlighting a fundamental difference between the two $3d^9$ oxides. The sizeable negative Hall coefficient [1, 3] and the finite spectral weight at the Fermi level [23] experimentally found in undoped nickelates appear to corroborate this picture.

Despite the recent progress in understanding the low-energy electronic structure of superconducting nickelates, an understanding of the anomalous insulating behavior that is ubiquitously found in ILN is lacking. Here, we present a systematic study of the normal-state transport of two doped families of ILN—the Nd- and La-based systems—by employing high magnetic fields up to 35 T to fully suppress the superconductivity. The effect of varying the rare-earth (*RE*) element on the functional form of the insulating resistivity, as well as the impact of (hole) doping and disorder level on the transport characteristics are also investigated. By taking into account the evolution of the Hall coefficient in both systems, we arrive at a number of salient points with regards to the origin of the insulating behavior: 1) The resistive upturns at low doping are likely to be due to a partial gapping of the states derived from the *RE* ions. 2) Hole doping *x* is much more effective in suppressing the resistivity upturn than a decrease in disorder (as inferred from the residual resistivity ratio). 3) The upturns, though notably weaker in the superconducting samples, nevertheless persist into the superconducting regime, and show a different functional form depending on the choice of *RE*. 4) In this region of the phase diagram, the insulating behavior is more likely to be associated with the correlated 3*d* states on the Ni. 5) The field dependence of the magnetoresistance in superconducting samples appears to rule out localization or the Kondo effect as the origin of the resistive upturns. 6) The *RE* dependence on the functional form of the low-*T* resistivity, as well as its overall magnitude, are more reminiscent of that seen in electron-doped cuprates than in hole-doped cuprates. 7) Finally, we find that T_c in the nickelates is sensitive to the level of disorder, suggesting that superconductivity in the ILN is unconventional in nature.

MATERIALS AND METHODS

$La_{1-x}Sr_xNiO_2$ and $PrNiO_2$ thin films were grown by pulsed laser technique described in [3, 24], respectively. Electrical resistivity was measured with a four-point configuration using the ac lock-in technique, with an alternating current $I = 10\ \mu$A applied within the *ab*-plane at a frequency between 13 and 30 Hz. Static magnetic fields up to 35 T, applied parallel to the crystalline *c*-axis, were generated using a Bitter magnet at the High Field Magnet Laboratory in Nijmegen, the Netherlands.

RESULTS AND DISCUSSION

Figure 1 shows the *T*-dependent in-plane resistivity $\rho_{ab}(T)$ of a set of undoped $RENiO_2$ films (*RE* = La, Pr, Nd). Several key features of its normal-state resistivity are revealed in these plots. Firstly, for all films, $\rho_{ab}(T)$ undergoes a resistivity minimum (ρ_{min}) at $T = T_{min}$ that delineates the metallic regime from the insulating-like regime at lower temperatures. Secondly, the absolute values of ρ_{ab} show significant variation between samples, with the newer generation exhibiting lower absolute resistivities as well as a reduced level of disorder, as inferred from the higher ρ_{300K}/ρ_{min} ratios. As ρ_{300K}/ρ_{min} increases, T_{min} shifts to lower values, suggesting that disorder plays some role in the insulating behavior, at least in the parent compound(s). (The resistivity of $LaNiO_2$ from an early report [25] was found to be an exceptionally low yet its ρ_{300K}/ρ_{min} ratio is the lowest among all samples investigated, the origin of which is yet unclear). Thirdly, in the high-*T* metallic regime for $PrNiO_2$ and $NdNiO_2$, the slope $d\rho_{ab}/dT$ is found to be very similar despite a large variation in their absolute values. This suggests that the excess disorder, while increasing the impurity scattering rate (and the magnitude of ρ_{ab}), does not significantly affect the intrinsic metallic resistivity. Fourthly, the functional form of the resistive upturn over the accessible temperature range depends on the choice of *RE*. In $LaNiO_2$, for example, $\rho_{ab}(T)$ initially follows a $\log(1/T)$ behavior for $T < T_{min}$ but then tends towards a constant value below 10 K. In contrast, $\rho_{ab}(T)$ in $PrNiO_2$ and $NdNiO_2$ $\rho_{ab}(T) \propto \log(1/T)$ down to the lowest measured temperatures. Whether or not $\rho_{ab}(T)$ in (Pr, Nd) NiO_2 saturates below ≈2 K, however, remains to be seen.

An emerging picture for the electronic structure of undoped ILN, based on recent spectroscopic studies and realistic theoretical calculations with electron interaction taken into account [15, 16, 23, 26, 27], indicates that its Fermi surface comprises a small electron pocket with a dominant character of the *RE* 5*d* band (which hybridizes with the Ni $3d_{z^2}$ band). The Ni $3d_{x^2-y^2}$ band, on the other hand, is split into the upper and lower Hubbard bands and thus does not directly contribute to the Fermi level. The Hall coefficient $R_H(T)$ in both $LaNiO_2$ and $NdNiO_2$ is found to be negative [3, 28], consistent with the notion that the 3*d* states on the Ni sites are Mott localized and that the longitudinal and Hall conductivities are dominated by the electron pocket derived from the *RE* 5*d* states. Hence, it is these states that must be responsible for the resistive upturns in the parent compounds. Secondly, in both systems, T_{min} is found to mark the onset of a marked increase in $R_H(T)$, possibly indicating some form of gap opening below T_{min}. Thirdly, the fact that $\rho_{ab}(T)$ appears to saturate eventually, at least in $LaNiO_2$ (and possibly in $PrNiO_2$ too), implies that this gapping is only partial and that a finite density of states remains on the electron pocket(s) whose low-*T* ground state is ultimately metallic.

According to the conventional Drude transport model, the electrical conductivity σ is given by

$$\sigma = \sum_i n_i e \mu_i = \sum_i \frac{n_i e^2 \tau_i}{m_i^*}, \quad (1)$$

where *i* denotes the distinct channel of conducting carriers, *e* is the elementary charge, and (μ, τ, m^*) denote the associated

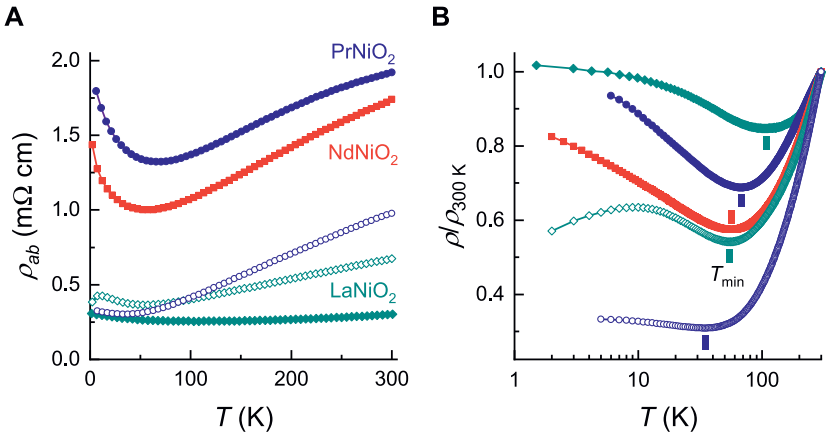

FIGURE 1 | In-plane resistivity versus temperature $\rho_{ab}(T)$ for undoped infinite-layer nickelates with selected rare earth elements. **(A)** Data from a previous generation of samples of $PrNiO_2$ [2], $NdNiO_2$ [28], and $LaNiO_2$ [25] are shown in solid points; data from a new generation of samples of $LaNiO_2$ [3] and $PrNiO_2$ (this work) in open points. **(B)** Normalized resistivity $\rho(T)/\rho_{300\ K}$ in linear-log scale with the same color code as in **(A)**. Vertical bars indicate T_{min}, the temperature at which ρ_{ab} shows a minimum.

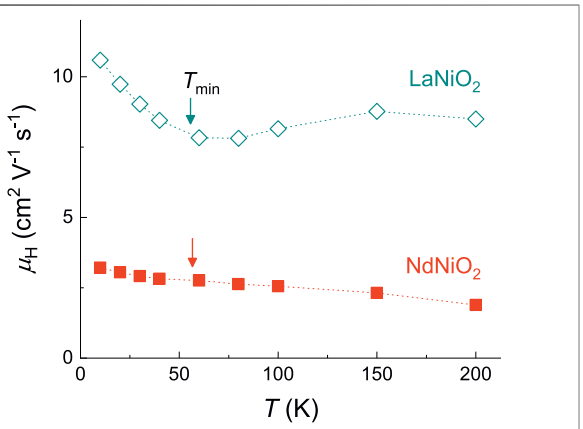

FIGURE 2 | Hall mobility μ_H of undoped $LaNiO_2$ and $NdNiO_2$. μ_H is estimated using $\mu_H = R_H/\rho$ with the Hall coefficient data R_H reported in [3, 28] and ρ as shown in **Figure 1**. The locations of T_{min} are marked by vertical arrows.

mobility, relaxation time, and effective mass, respectively. Consequently, $\rho = 1/(ne\mu) = R_H/\mu$ for a single-band metal, where $R_H = \frac{1}{ne}$ is the Hall coefficient. From **Eq. 1**, it can be seen that a reduction of conductivity (i.e. a metal-insulator transition) can be caused by a reduction of n (loss of carrier) or τ (increased scattering rate), an increase in m^* (effective mass enhancement), or a combination of these factors. For simplicity, here we estimate the carrier mobility using the measured R_H, known as the Hall mobility $\mu_H = R_H/\rho$ for undoped $LaNiO_2$ and $NdNiO_2$, for which the single-band picture is most likely to apply. As shown in **Figure 2**, both $LaNiO_2$ and $NdNiO_2$ show a relatively unchanged μ_H above T_{min}, below which μ_H increases moderately. Crucially, the increase in μ_H below T_{min} indicates that the increase in ρ below T_{min} is not related to a reduction of mobility (i.e. a change in τ/m^*), but is most likely caused by a reduction in n. The minimization of R_H at low T as x approaches 0.20, at which T_{min} and $\rho_0 - \rho_{min}$ are most suppressed (see **Figure 4**) further supports this scenario. Possible candidates responsible for the loss of carriers below T_{min} include the emergence of a secondary order parameter (e.g. magnetic, charge, or stripe order), the opening of a pseudogap that partially depletes the density of states at the Fermi level [29], or a transfer of spectral weight to higher energy [30, 31].

With hole-doping, the situation evolves in a systematic fashion. In $Nd_{1-x}Sr_xNiO_2$, we revealed previously by destroying superconductivity with a large magnetic field, that the resistivity upturn, though persisting throughout the doping range of superconductivity, is progressively suppressed, essentially vanishing as x approaches the edge of the superconducting dome $x_c \approx 0.225$ [32]. Here, we examine the evolution of the low-T resistivity in $La_{1-x}Sr_xNiO_2$ in the field-induced normal state for $0.15 \lesssim x \lesssim 0.20$, i.e. across much of the superconducting doping range [3]. A contrasting behavior manifests in the functional form of $\rho_{ab}(T)$ below T_c, as shown in **Figure 3**. Similar to the undoped compound, $\rho_{ab}(T)$ in the field-induced normal state of superconducting $La_{1-x}Sr_xNiO_2$ exhibits an initial $\log(1/T)$-behavior followed by a leveling off as $T \to 0$. The magnitude of the resistive upturn decreases as x increases from 0.15 to 0.18, after which it again increases at $x = 0.20$.

The overall magnitude of the resistive upturn, on the order of 10% between 0.5 K and T_{min}, is considerably smaller than that observed in the underdoped hole-doped cuprates ($\gtrsim$ 100%) [33, 34, 35] but is comparable with that reported in the electron-doped cuprates $RE_{2-x}Ce_xCuO_4$ below optimal doping [36–38]. A direct comparison of the low-T resistivities in the ILN and $RE_{2-x}Ce_xCuO_4$ is shown in **Figure 3C**. Intriguingly, the functional form of the low-T resistivity in $RE_{2-x}Ce_xCuO_4$ also

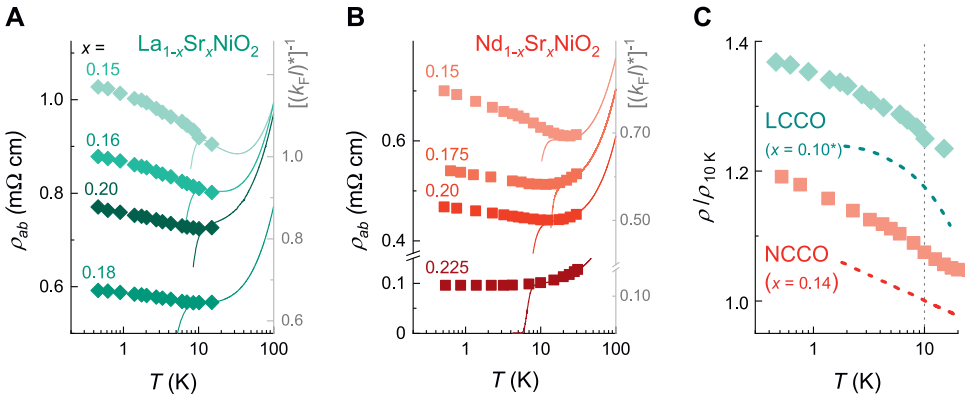

FIGURE 3 | Normal-state resistivity of superconducting nickelates at low temperatures. **(A)** $\rho_{ab}(T)$ of $La_{1-x}Sr_xNiO_2$ and **(B)** $Nd_{1-x}Sr_xNiO_2$ [32] thin films with $0.15 \leq x \leq 0.20$ measured at zero applied magnetic field (lines) and at 35 T (solid points). Magnetic field is applied along the crystalline *c*-axis. Right axis shows the estimates of $(k_F l)^{-1}$ assuming a two-dimensional free electron model (see main text for details). **(C)** Comparison of resistivity normalized by its 10 K value in the field-induced normal state, $\rho/\rho_{10\ K}$, for selected hole-doped nickelates ($x = 0.15$) and electron-doped cuprates below optimal dopings as specified. LCCO: representative rho_{ab}(T) $La_{2-x}Ce_xCuO_4$ measured at $\mu_0 H = 10$ T [38]. NCCO: representative rho_{ab}(T) $Nd_{2-x}Ce_xCuO_4$ measured at $\mu_0 H = 14$ T [37]. Note that the temperature axes are shown in log-scale and a vertical shift is applied to **(C)** for clarity. For LCCO, a rescaling factor of 0.50 is applied to the change in $\rho/\rho_{10\ K}$, which does not affect the functional form of $\rho(T)$.

depends on the *RE* elements in a similar manner to what is seen in the ILN. For $La_{2-x}Ce_xCuO_4$ (LCCO, $x = 0.08$) $\rho_{ab}(T)$ appears to saturate below 4 K, while for $Nd_{2-x}Ce_xCuO_4$ (NCCO, $x = 0.14$), $\rho_{ab}(T) \propto \log(1/T)$ down to the lowest measured temperature. This close alignment to the experimental situation in the *n*-doped cuprates is curious, but may simply be a consequence of the way in which carriers are doped into each system. In the cuprates, doped holes sit preferentially on the O sites while doped electrons reside on the Cu sites [39]. In the ILN, it is thought that the carriers are also introduced directly into the $3d_{x^2-y^2}$ orbital on the Ni sites [40]. At the same time, the similarities found in the low-*T* $\rho_{ab}(T)$ behavior of the ILN (for which no long-range AFM order exists at half-filling) and the *n*-doped cuprates suggests that the resistive upturns in the latter are not necessarily caused by short-range spin correlations, as is believed to be the case for the *p*-doped cuprates.

The evolution of $R_H(T)$ with doping in both ILN families is qualitatively the same, with a gradual reduction in the overall magnitude of R_H culminating in a crossover from negative to positive $R_H(0)$ (the Hall coefficient in the low-*T* limit) around optimal doping [1, 3]. In any two-band metallic system, the sign of $R_H(0)$ reflects the sign of the most mobile carriers. Hence, the observed sign change signals a delocalization of the 3*d* hole states on the Ni sites with hole-doping until eventually, they become the most mobile carriers in each system. Nevertheless, the fact that $\rho_{ab}(T)$ continues to exhibit a logarithmic divergence (at least in $Nd_{1-x}Sr_xNiO_2$) implies that these carriers are also prone to some form of localization, however weak. (Note that $R_H(T)$ exhibits no upturns within the superconducting doping range, and so it is unlikely that the resistive upturns here are due to partial gapping).

It was noted early on that the insulator-to-metal crossover in the cuprates occurs at a threshold value of $k_F \ell > 10$ for both the hole- [35] and electron-doped [36] compounds, far higher than the usual criterion $k_F \ell \approx 1$. Assuming that the suppression of the resistive upturn in $Nd_{0.775}Sr_{0.225}NiO_2$ reflects a metallic ground state and using the two-dimensional free electron model [35]:

$$\rho_{ab}/d = h/(e^2 k_F \ell), \tag{2}$$

where *d* is the *c*-axis lattice spacing, k_F is the Fermi wavevector, and *l* is the electronic mean free path, we find a threshold $k_F l \approx 2 - 10$ for low-*T* metallicity in the ILN. We note, however, that the assumption of a single-band, 2D Fermi surface is likely not valid for the entire series of hole-doped nickelates (due to the expected presence of a 3D electron pocket derived from the 5*d* band of *RE* elements); therefore the estimates of $k_F l$ here should be interpreted with caution.

Several proposals have been put forward to explain the anomalous upturn in the normal-state resistivity in the nickelates [31, 41, 42]. Two well-known mechanisms to produce a logarithmically diverging resistivity at low *T* are weak localization due to disorder [43, 44] and Kondo scatterings due to magnetic impurities [14, 45]. In both circumstances, however, a strong negative magnetic-field dependence of the insulating resistivity is expected, which is not observed in the nickelates. Moreover, a monotonic suppression of the insulating behavior with decreasing residual resistivity, expected for a localization-driven origin, is not seen (**Figure 4**) while the re-entrant insulating behavior found at high dopings also cannot be naturally explained by a Kondo-like mechanism.

In order to gain further insights into the origin of the resistive upturns, we have examined the impact of disorder and doping on the insulating characteristics in the ILN, namely the onset temperature (T_{min}) and the size of the resistivity upturn ($\rho(T \to 0) - \rho(T_{min})$, denoted as $\rho_0 - \rho_{min}$), as shown in **Figure 4**. We find no clear correlations

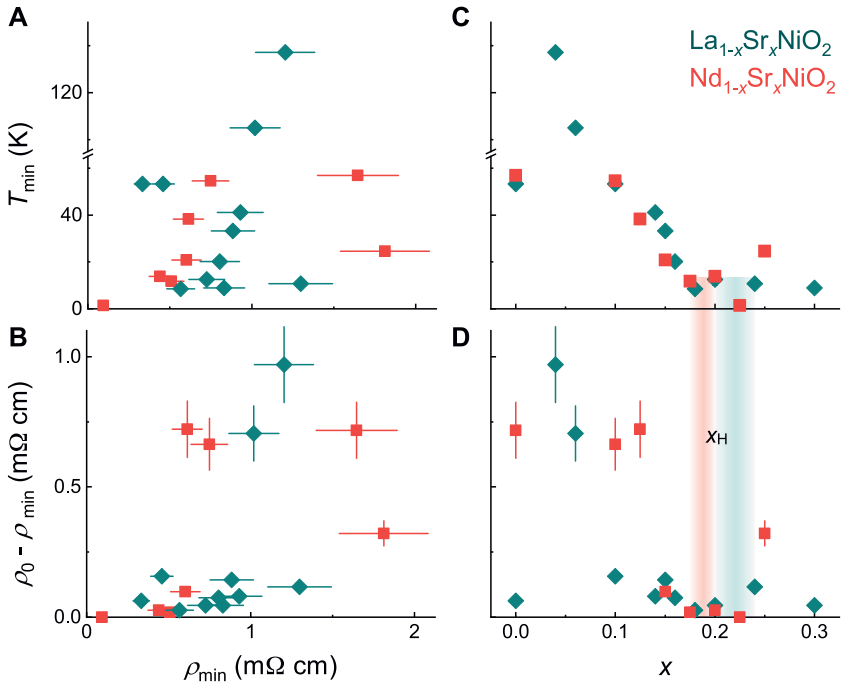

FIGURE 4 | Effect of disorder and hole doping on the insulating characteristics. **(A)** Onset temperature of the resistive upturn (T_{min}) and **(B)** its absolute magnitude ($\rho_0 - \rho_{min}$) versus the normal-state resistivity at its minimum (ρ_{min}) for $La_{1-x}Sr_xNiO_2$ (diamonds) and $Nd_{1-x}Sr_xNiO_2$ (squares). **(C)** T_{min} and **(D)** $\rho_0 - \rho_{min}$ versus the hole doping x given by the nominal Sr level. Color shades indicate the doping levels x_H at which the Hall coefficients change sign at low temperatures (10 K) [3, 28]. Error bars of 15% due to geometric uncertainties are applied to the resistivity data.

between T_{min} and ρ_{min} (**Figure 4A**) nor between $\rho_0 - \rho_{min}$ and ρ_{min} (**Figure 4B**), for both $Nd_{1-x}Sr_xNiO_2$ and $La_{1-x}Sr_xNiO_2$. Meanwhile, T_{min} and $\rho_0 - \rho_{min}$ both appear to collapse near $x = 0.20$ (**Figures 4C,D**), though deviations from the overall trends are visible both at zero doping and at the highest dopings. Notably, while T_{min} and $\rho_0 - \rho_{min}$ are gradually suppressed with improved sample quality (**Figure 1B**), varying x is seen as much more effective in suppressing the insulating behavior, suggesting that it is sensitive to carrier screenings and primarily driven by electron correlation effects. A number of non-Fermi-liquid models have been proposed to explain the anomalous insulating behavior seen in underdoped cuprates, including those based on the marginal Fermi liquid [46], the 2D Luttinger liquid [47] and the polaronic Bose liquid [48] model. The relevance of these more exotic models to the ILN, whose distinction from the (hole-doped) cuprates has become increasingly established, remains to be examined.

Lastly, we examine the impact of disorder on the critical temperature of superconducting nickelates. **Figure 5** shows a compilation of $Nd_{0.8}Sr_{0.2}NiO_2$ resistivity data reported to date [1, 28, 32, 49–53]. A large difference in the absolute values of ρ_{ab} is found, with ρ_{ab}(300 K) ranging from ~ 0.1–6.75 mΩ cm for nominally the same samples. Meanwhile, the agreement in the normalized resistivity $\rho/\rho_{300\ K}$ is much better across different reports, as shown in **Figure 5B**, with a good overlap found in 6 out of 9 traces. This suggests the discrepancy in the absolute resistivities arises from geometric uncertainties. Importantly, we find that T_c depends strongly on the residual resistivity ratio, defined as $\rho_{300\ K}/\rho_{20\ K}$, with T_c increasing from ≈5 K to over 12.5 K as $\rho_{300\ K}/\rho_{20\ K}$ increases. Such a strong dependence of T_c with respect to the level of disorder points to an unconventional nature of the superconductivity in the nickelates, and hints at a possible further increase in T_c with improved sample quality.

CONCLUSION

In summary, by suppressing superconductivity with high magnetic fields, we find the unusual resistivity upturn in the undoped infinite-layer nickelates persists into the superconducting regime and appears to be maximally suppressed near $x = 0.20$ in both La- and Nd-based systems. The resilience of the resistivity upturn against magnetic fields rules out localization and Kondo effect as its origin, and points to a partial gapping of the states with dominant *RE* 5*d* character as its cause at low doping as supported by Hall mobility analysis. In the superconducting doping range, the resistive upturn is found to be highly reminiscent in both its functional form and its overall magnitude to that found in electron-doped cuprates, which suggests the insulating behaviour is associated with the correlated Ni 3*d* states. While disorder has only a minor impact on the insulating behavior, the robustness of

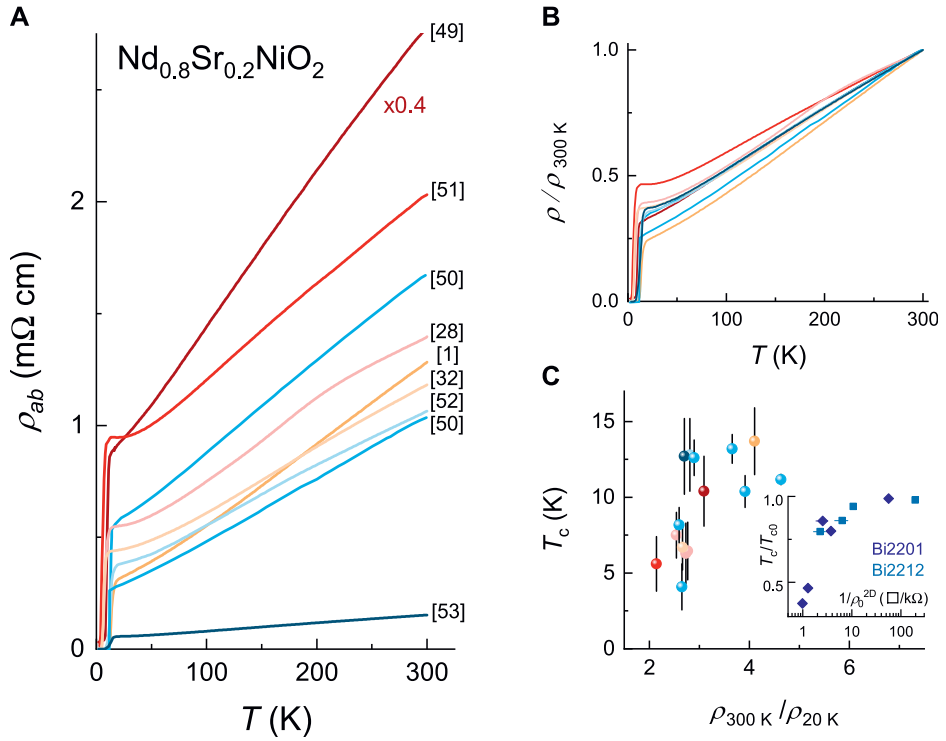

FIGURE 5 | Impact of disorder on the critical temperature T_c of $Nd_{0.8}Sr_{0.2}NiO_2$. **(A)** A compilation of representative resistivity data on $Nd_{0.8}Sr_{0.2}NiO_2$ films reported in [1, 28, 32, 49–53]. Data reported in [49] is rescaled by a factor of 0.4 for clarity. **(B)** Normalized resistivity $\rho/\rho_{300\ K}$ of data shown in **(A)**. **(C)** T_c versus residual resistivity ratio $\rho_{300\ K}/\rho_{20\ K}$. T_c is defined as the midpoint of the resistive superconducting transition and the error bars reflect the 10–90% transition width. The same color code is applied to all panels. Inset: The impact of disorder on T_c of Bi-based cuprates. For both $Bi_2(Sr, La)_2CuO_{6+\delta}$ (Bi2201) and $Bi_2Sr_2CaCu_2O_{8+\delta}$ (Bi2212), T_c is found to be strongly reduced from the optimized value T_{c0} with an increase in residual resistivity per CuO_2 plane (ρ_0^{2D}, similar to that found in $Nd_{0.8}Sr_{0.2}NiO_2$. Data reproduced from [54].

superconductivity is strongly affected by the level of disorder, pointing towards the unconventional nature of nickelate superconductivity.

DATA AVAILABILITY STATEMENT

The original contributions presented in the study are included in the article/Supplementary Material, further inquiries can be directed to the corresponding author.

AUTHOR CONTRIBUTIONS

YTH, HYH and NEH conceived the experiments. MO, BW, SH, KL, and DL grew and prepared the thin-film samples. YTH, MB, CD, and SW performed the resistivity measurements. YTH and NEH analyzed the data and wrote the manuscript with contribution from all authors.

FUNDING

This work was supported by the Netherlands Organisation for Scientific Research (NWO) grant No. 16METL01 “Strange Metals” and the European Research Council (ERC) under the European Union’s Horizon 2020 research and innovation programme (Grant Agreement No. 835279-Catch-22). The work at SLAC/Stanford is supported by the US Department of Energy, Office of Basic Energy Sciences, Division of Materials Sciences and Engineering, under contract number DE-AC02-76SF00515; and the Gordon and Betty Moore Foundations Emergent Phenomena in Quantum Systems Initiative through grant number GBMF9072 (synthesis equipment).

ACKNOWLEDGMENTS

We acknowledge the support of the HFML-RU/NWO, a member of the European Magnetic Field Laboratory (EMFL).

REFERENCES

1. Li D, Lee K, Wang BY, Osada M, Crossley S, Lee HR, et al. Superconductivity in an Infinite-Layer Nickelate. *Nature* (2019) 572:624–7. doi:10.1038/s41586-019-1496-5
2. Osada M, Wang BY, Goodge BH, Lee K, Yoon H, Sakuma K, et al. A Superconducting Praseodymium Nickelate with Infinite Layer Structure. *Nano Lett* (2020) 20:5735–40. doi:10.1021/acs.nanolett.0c01392
3. Osada M, Wang BY, Goodge BH, Harvey SP, Lee K, Li D, et al. Nickelate Superconductivity without Rare-Earth Magnetism: (La,Sr)NiO_2. *Adv Mater* (2021) 33:2104083. doi:10.1002/adma.202104083
4. Zeng SW, Li CJ, Chow LE, Cao Y, Zhang ZT, Tang CS, et al. *Superconductivity in Infinite-Layer Lanthanide Nickelates* (2021). preprints, arXiv:2105.13492.
5. Lu H, Rossi M, Nag A, Osada M, Li DF, Lee K, et al. Magnetic Excitations in Infinite-Layer Nickelates. *Science* (2021) 373:213–6. doi:10.1126/science.abd7726
6. Cui Y, Li C, Li Q, Zhu X, Hu Z, Yang Y-f., et al. NMR Evidence of Antiferromagnetic Spin Fluctuations in Nd 0.85Sr0.15 NiO_2. *Chin Phys. Lett.* (2021) 38:067401. doi:10.1088/0256-307x/38/6/067401
7. Lin H, Gawryluk DJ, Klein YM, Huangfu S, Pomjakushina E, von Rohr F, et al. *Universal Spin-Glass Behavior in Bulk La NiO_2, $PrNiO_2$, and $NdNiO_2$.* Preprints (2021). arXiv:2104.14324.
8. Zhao D, Zhou YB, Fu Y, Wang L, Zhou XF, Cheng H, et al. Intrinsic Spin Susceptibility and Pseudogaplike Behavior in Infinite-Layer $LaNiO_2$. *Phys Rev Lett* (2021) 126:197001. doi:10.1103/physrevlett.126.197001
9. Nakamae S, Behnia K, Mangkorntong N, Nohara M, Takagi H, Yates SJC, et al. Electronic Ground State of Heavily Overdoped nonsuperconducting La_2−xSrx CuO_4. *Phys Rev B* (2003) 68:100502. doi:10.1103/physrevb.68.100502
10. Lee K-W, Pickett WE. Infinite-layer $LaNiO_2$: Ni^{1+} is not Cu^{2+}. *Phys Rev B* (2004) 70:165109. doi:10.1103/physrevb.70.165109
11. Nomura Y, Hirayama M, Tadano T, Yoshimoto Y, Nakamura K, Arita R. Formation of a Two-Dimensional Single-Component Correlated Electron System and Band Engineering in the Nickelate Superconductor Nd NiO_2. *Phys Rev B* (2019) 100:205138. doi:10.1103/physrevb.100.205138
12. Botana AS, Norman MR. Similarities and Differences between $LaNiO_2$ and $CaCuO_2$ and Implications for Superconductivity. *Phys Rev X* (2020) 10:011024. doi:10.1103/physrevx.10.011024
13. Wu X, Di Sante D, Schwemmer T, Hanke W, Hwang HY, Raghu S, et al. Robust-wave Superconductivity of Infinite-Layer Nickelates. *Phys Rev B* (2020) 101:060504. doi:10.1103/physrevb.101.060504
14. Zhang YH, Vishwanath A. Type-II $T - J$ Model in Superconducting Nickelate $Nd_{1-x}Sr_xNiO_2$. *Phys Rev Res* (2020) 2:023112. doi:10.1103/physrevresearch.2.023112
15. Lechermann F. Late Transition Metal Oxides with Infinite-Layer Structure: Nickelates versus Cuprates. *Phys Rev B* (2020) 101:081110. doi:10.1103/physrevb.101.081110
16. Been E, Lee WS, Hwang HY, Cui Y, Zaanen J, Devereaux T, et al. Electronic Structure Trends across the Rare-Earth Series in Superconducting Infinite-Layer Nickelates. *Phys Rev X* (2021) 11:011050. doi:10.1103/physrevx.11.011050
17. Karp J, Botana AS, Norman MR, Park H, Zingl M, Millis A. Many-body Electronic Structure of $NdNiO_2$ and $CaCuO_2$. *Phys Rev X* (2020) 10:021061. doi:10.1103/physrevx.10.021061
18. Sakakibara H, Usui H, Suzuki K, Kotani T, Aoki H, Kuroki K. Model Construction and a Possibility of Cupratelike Pairing in a New D^9 Nickelate Superconductor (Nd, Sr)NiO_2. *Phys Rev Lett* (2020) 125:077003. doi:10.1103/physrevlett.125.077003
19. Adhikary P, Bandyopadhyay S, Das T, Dasgupta I, Saha-Dasgupta T. Orbital-selective Superconductivity in a Two-Band Model of Infinite-Layer Nickelates. *Phys Rev B* (2020) 102:100501. doi:10.1103/physrevb.102.100501
20. Wang Y, Kang CJ, Miao H, Kotliar G. Hund's Metal Physics: From $SrNiO_2$ to $LaNiO_2$. *Phys Rev B* (2020) 102:16118. doi:10.1103/physrevb.102.161118
21. Liu Z, Xu C, Cao C, Zhu W, Wang ZF, Yang J. Doping Dependence of Electronic Structure of Infinite-Layer $NdNiO_2$. *Phys Rev B* (2021) 103:045103. doi:10.1103/physrevb.103.045103
22. Higashi K, Winder M, Kunes J, Hariki A. Core-level X-ray Spectroscopy of Infinite-Layer Nickelate: LDA + DMFT Study. *Phys Rev X* (2021) 11:041009. doi:10.1103/physrevx.11.041009
23. Chen Z, Osada M, Li D, Been EM, Chen SD, Hashimoto M, et al. *Electronic Structure of Superconducting Nickelates Probed by Resonant Photoemission Spectroscopy* (2021). *preprints*, arXiv:2106.03963.
24. Osada M, Wang BY, Lee K, Li D, Hwang HY. Phase Diagram of Infinite Layer Praseodymium Nickelate Pr1−xSrx NiO_2 Thin Films. *Phys Rev Mater* (2020) 4:121801. (R). doi:10.1103/physrevmaterials.4.121801
25. Ikeda A, Krockenberger Y, Irie H, Naito M, Yamamoto H. Direct Observation of Infinite NiO2planes in $LaNiO_2$ films. *Appl Phys Express* (2016) 9:061101. doi:10.7567/apex.9.061101
26. Hepting M, Li D, Jia CJ, Lu H, Paris E, Tseng Y, et al. Electronic Structure of the Parent Compound of Superconducting Infinite-Layer Nickelates. *Nat Mater* (2020) 19:381–5. doi:10.1038/s41563-019-0585-z
27. Goodge BH, Li D, Lee K, Osada M, Wang BY, Sawatzky GA, et al. Doping Evolution of the Mott-Hubbard Landscape in Infinite-Layer Nickelates. *Proc Natl Acad Sci USA* (2021) 118:e2007683118. doi:10.1073/pnas.2007683118
28. Li D, Wang BY, Lee K, Harvey SP, Osada M, Goodge BH, et al. Superconducting Dome in $Nd_{1-x}Sr_xNiO_2$ Infinite Layer Films. *Phys Rev Lett* (2020) 125:027001. doi:10.1103/physrevlett.125.027001
29. Laliberte F, Tabis W, Badoux S, Vignolle B, Destraz D, Momono N, et al. Origin of the Metal-To-Insulator Crossover in Cuprate Superconductors. *preprints* (2016). arXiv:1606.04491.
30. Hussey NE, Takenaka K, Takagi H. Universality of the Mott-Ioffe-Regel Limit in Metals. *Philos Mag* (2004) 84:2847–64. doi:10.1080/14786430410001716944
31. Singh N. *A Road-Map of Nickelate Superconductivity* (2019). preprints, arXiv:1909.07688.
32. Hsu Y-T, Wang BY, Berben M, Li D, Lee K, Duffy C, et al. Insulator-to-metal Crossover Near the Edge of the Superconducting Dome in Nd1−xSrx NiO_2. *Phys Rev Res* (2021) 3:L042015. doi:10.1103/physrevresearch.3.l042015
33. Ando Y, Boebinger GS, Passner A, Kimura T, Kishio K. Logarithmic Divergence of Both In-Plane and Out-Of-Plane Normal-State Resistivities of Super conducting La_2−xSrx CuO_4 in the Zero-Temperature Limit. *Phys Rev Lett* (1995) 75:4662–5. doi:10.1103/physrevlett.75.4662
34. Boebinger GS, Ando Y, Passner A, Kimura T, Okuya M, Shimoyama J, et al. Insulator-to-Metal Crossover in the Normal State of La_2−xSrx CuO_4 Near Optimum Doping. *Phys Rev Lett* (1996) 77:5417–20. doi:10.1103/physrevlett.77.5417
35. Ono S, Ando Y, Murayama T, Balakirev FF, Betts JB, Boebinger GS. Metal-to-Insulator Crossover in the Low-Temperature Normal State of Bi_2 Sr_2−xLax CuO_6+δ. *Phys Rev Lett* (2000) 85:638–41. doi:10.1103/physrevlett.85.638
36. Fournier P, Mohanty P, Maiser E, Darzens S, Venkatesan T, Lobb CJ, et al. Insulator-Metal Crossover Near Optimal Doping in Pr_2−xCex CuO_4: Anomalous Normal-State Low Temperature Resistivity. *Phys Rev Lett* (1998) 81:4720–3. doi:10.1103/physrevlett.81.4720
37. Li SY, Mo WQ, Chen XH, Xiong YM, Wang CH, Luo XG, et al. Low-temperature Transport Properties of Nd_2−xCex CuO_4+δ: Metal-Insulator Crossover in the Overdoped Regime. *Phys Rev B* (2002) 65:224515. doi:10.1103/physrevb.65.224515
38. Sarkar T, Mandal PR, Higgins JS, Zhao Y, Yu H, Jin K, et al. Fermi Surface Reconstruction and Anomalous Low-Temperature Resistivity in Electron-Doped La_2−xCex CuO_4. *Phys Rev B* (2017) 96:155449. doi:10.1103/physrevb.96.155449
39. Armitage NP, Fournier P, Greene RL. Progress and Perspectives on Electron-Doped Cuprates. *Rev Mod Phys* (2010) 82:2421–87. doi:10.1103/revmodphys.82.2421
40. Botana AS, Kwan-Woo Lee KW, Norman MR, Pardo V, Pickett WE. Low Valence Nickelates: Launching the Nickel Age of Superconductivity. *preprints* (2021) 10. arXiv:2111.01296.
41. Zhang GM, Yang YF, Zhang FC. Self-doped Mott Insulator for Parent Compound of Nickelate Superconductors. *Phys Rev B* (2020) 101:020501. doi:10.1103/physrevb.101.020501
42. Wang Z, Zhang G-M, Yang Y-f., Zhang F-C. Distinct Pairing Symmetries of Superconductivity in Infinite-Layer Nickelates. *Phys Rev B* (2020) 102:220501. doi:10.1103/physrevb.102.220501

43. Rullier-Albenque F, Alloul H, Tourbot R, Proust C. Disorder and Transport in Cuprates: Weak Localization and Magnetic Contributions. *Phys Rev Lett* (2001) 87:157001. doi:10.1103/physrevlett.87.157001
44. Rullier-Albenque F, Alloul H, Balakirev F, Proust C. Disorder, Metal-Insulator Crossover and Phase Diagram in High-T C Cuprates. *Europhys Lett* (2008) 81: 37008. doi:10.1209/0295-5075/81/37008
45. Dagan Y, Barr MC, Fisher WM, Beck R, Dhakal T, Biswas A, et al. Origin of the Anomalous Low Temperature Upturn in the Resistivity of the Electron-Doped Cuprate Superconductors. *Phys Rev Lett* (2005) 94:057005. doi:10.1103/PhysRevLett.94.057005
46. Kotliar G, Abrahams E, Ruckenstein AE, Varma CM, Littlewood PB, Schmitt-Rink S. Long-wavelength Behavior, Impurity Scattering and Magnetic Excitations in a Marginal Fermi Liquid. *Europhys Lett* (1991) 15:655–60. doi:10.1209/0295-5075/15/6/016
47. Anderson PW, Ramakrishnan TV, Strong S, Clarke DG. Coherence and Localization in 2D Luttinger Liquids. *Phys Rev Lett* (1996) 77:4241–4. doi:10.1103/physrevlett.77.4241
48. Alexandrov AS. Logarithmic normal State Resistivity of High-Tc Cuprates. *Phys Lett A* (1997) 236:132–6. doi:10.1016/s0375-9601(97)00714-7
49. Zeng S, Tang CS, Yin X, Li C, Li M, Huang Z, et al. Phase Diagram and Superconducting Dome of Infinite-Layer $Nd_{1x}Sr_xNiO_2$ Thin Films. *Phys Rev Lett* (2020) 125:147003. doi:10.1103/physrevlett.125.147003
50. Zeng SW, Yin XM, Li CJ, Tang CS, Han K, Huang Z, et al. *Observation of Perfect Diamagnetism and Interfacial Effect on the Electronic Structures in $Nd_{0.8}Sr_{0.2}NiO_2$ Superconducting Infinite Layers* (2021). arXiv:2104.14195
51. Gao Q, Zhao Y, Zhou X-J, Zhu Z. Preparation of Superconducting Thin Films of Infinite-Layer Nickelate $Nd_{0.8}Sr_{0.2}NiO_2$. *Chin Phys. Lett.* (2021) 38:077401. doi:10.1088/0256-307x/38/7/077401
52. Xiang Y, Li Q, Li Y, Yang H, Nie Y, Wen H-H. Physical Properties Revealed by Transport Measurements for Superconducting $Nd_{0.8}Sr_{0.2}NiO_2$ Thin Films. *Chin Phys. Lett.* (2021) 38:047401. doi:10.1088/0256-307x/38/4/047401
53. Li Y, Sun W, Yang J, Cai X, Guo W, Gu Z, et al. Impact of Cation Stoichiometry on the Crystalline Structure and Superconductivity in Nickelates. *Front Phys* (2021) 9:719534. doi:10.3389/fphy.2021.719534
54. Hobou H, Ishida S, Fujita K, Ishkado M, Kojima KM, Eisaki H, et al. Enhancement of Superconducting Critical Temperature in $Bi_2Sr_2CaCu_2O_{8+\delta}$ by Controlling Disorder outside CuO_2 Planes. *Phys Rev B* (2009) 79:064507. doi:10.1103/physrevb.79.064507

Conflict of Interest: The authors declare that the research was conducted in the absence of any commercial or financial relationships that could be construed as a potential conflict of interest.

Publisher's Note: All claims expressed in this article are solely those of the authors and do not necessarily represent those of their affiliated organizations, or those of the publisher, the editors and the reviewers. Any product that may be evaluated in this article, or claim that may be made by its manufacturer, is not guaranteed or endorsed by the publisher.

frontiers | Frontiers in Physics

ORIGINAL RESEARCH
published: 11 May 2022
doi: 10.3389/fphy.2022.836784

Ab Initio Wavefunction Analysis of Electron Removal Quasi-Particle State of $NdNiO_2$ With Fully Correlated Quantum Chemical Methods

Vamshi M. Katukuri[1]*, *Nikolay A. Bogdanov*[1] and *Ali Alavi*[1,2]

[1]Max Planck Institute for Solid State Research, Stuttgart, Germany, [2]Yusuf Hamied Department of Chemistry, University of Cambridge, Cambridge, United Kingdom

The discovery of superconductivity in hole-doped infinite-layer $NdNiO_2$ — a transition metal (TM) oxide that is both isostructural and isoelectronic to cuprate superconductors—has lead to renewed enthusiasm in the hope of understanding the origin of unconventional superconductivity. Here, we investigate the electron-removal states in infinite-layered Ni^{1+} oxide, $NdNiO_2$, which mimics hole doping, with the state-of-the-art many-body multireference quantum chemistry methods. From the analysis of the many-body wavefunction we find that the hole-doped d^8 ground state of $NdNiO_2$ is very different from the d^8 ground state in isostructural cuprate analog $CaCuO_2$, although the parent d^9 ground states are for the most part identical. We show that the doped hole in $NdNiO_2$ mainly localizes on the Ni $3d_{x^2-y^2}$ orbital to form a closed-shell singlet, and this singlet configuration contributes to ~40% of the wavefunction. In contrast, in $CaCuO_2$ the Zhang-Rice singlet configurations contribute to ~65% of the wavefunction. With the help of the quantum information concept of entanglement entropy, we quantify the different types of electronic correlations in the nickelate and cuprate compounds, and find that the dynamic radial-type correlations within the Ni *d* manifold are persistent in hole-doped $NdNiO_2$. As a result, the d^8 multiplet effects are stronger and the additional hole foot-print is more three-dimensional in $NdNiO_2$. Our analysis shows that the most commonly used three-band Hubbard model employed to express the doped scenario in cuprates represents ~90% of the d^8 wavefunction for $CaCuO_2$, but such a model grossly approximates the d^8 wavefunction for $NdNiO_2$ as it only stands for ~60% of the wavefunction.

Keywords: nickelates, superconductors, wavefunction quantum chemistry, doped-holes, ab initio

OPEN ACCESS

Edited by:
Danfeng Li,
City University of Hong Kong, Hong Kong SAR, China

Reviewed by:
Frank Lechermann,
European X-Ray Free Electron Laser, Germany
BaiYang Wang,
Stanford University, United States

****Correspondence:***
Vamshi M. Katukuri
V.Katukuri@fkf.mpg.de

Specialty section:
This article was submitted to Condensed Matter Physics, a section of the journal Frontiers in Physics

Received: *15 December 2021*
Accepted: *14 March 2022*
Published: *11 May 2022*

Citation:
Katukuri VM, Bogdanov NA and Alavi A (2022) Ab Initio Wavefunction Analysis of Electron Removal Quasi-Particle State of $NdNiO_2$ With Fully Correlated Quantum Chemical Methods. Front. Phys. 10:836784. doi: 10.3389/fphy.2022.836784

1 INTRODUCTION

For more than 3 decades, understanding the mechanism of superconductivity observed at high critical temperature (HTC) in strongly correlated cuprates [1] has been the "holy grail" of many theoretical and experimental condensend matter researchers. In this context, the observation of superconductivity in nickelates $LnNiO_2$, *Ln* = {La, Nd and Pr} [2–4] upon doping with holes is

remarkable. These superconducting nickelates are isostructural as well as isoelectronic to HTC cuprate superconductors and thus enable the comparison of the essential physical features that may be playing a crucial role in the mechanism driving superconductivity.

LnNiO_2 family of compounds are synthesized in the so-called infinite-layer structure, where NiO_2 and *Ln* layers are stacked alternatively [2]. The NiO_2 planes are identical to the CuO_2 planes in HTC cuprates which host much of the physics leading to superconductivity [5]. A simple valence counting of the these nickelates reveals a 1+ oxidation state for Ni (2- for O and 3+ for *Ln*) with nine electrons in the 3*d* manifold. In the cuprates, the Cu^{2+} oxidation state gives rise to the same $3d^9$ electronic configuration. Contrary to many nickel oxides where the Ni atom sits in an octahedral cage of oxygens, in the infinite-layered structure, square planar NiO_4 plaques are formed without the apical oxygens. The crystal field due to square-planar oxygen coordination stabilizes the d_{z^2} orbital of the e_g manifold, making its energy close to the t_{2g} orbitals (the 3*d* orbitals split to 3-fold t_{2g} and 2-fold e_g sub-shells in an octahedral environment). With d^9 occupation, a half-filled $d_{x^2-y^2}$-orbital system is realized as in cuprates. In fact, recent resonant inelastic X-ray scattering (RIXS) experiments [6] as well as the *ab initio* correlated multiplet calculations [7] confirm that the Ni^{1+} *d-d* excitations in $NdNiO_2$ are similar to the Cu^{2+} ions in cuprates [8].

Several electronic structure calculations based on density-functional theory (DFT) have shown that in monovalent nickelates the Ni $3d_{x^2-y^2}$ states sit at the Fermi energy level [9–11]. These calculations further show that the nickelates are more close to the Mott-Hubbard insulating limit with a decreased Ni *3d*- O *2p* hybridization compared to cuprates. The latter are considered to be charge transfer insulators [12] where excitations across the electronic band gap involves O 2*p* to Cu 3*d* electron transfer. Correlated wavefunction-based calculations [7] indeed find that the contribution from the O 2*p* hole configuration to the ground state wavefunction in $NdNiO_2$ is four times smaller than in the cuprate analogue $CaCuO_2$. X-ray absorption and photoemission spectroscopy experiments [13, 14] confirm the Mott behavior of nickelates.

In the cuprate charge-transfer insulators, the strong hybridization of the Cu $3d_{x^2-y^2}$ and O 2*p* orbitals result in O 2*p* dominated bonding and Cu $3d_{x^2-y^2}$ -like antibonding orbitals. As a consequence, the doped holes primarily reside on the bonding O 2*p* orbitals, making them singly occupied. The unpaired electrons on the Cu $d_{x^2-y^2}$ and the O 2*p* are coupled antiferromagnetically resulting in the famous Zhang-Rice (ZR) spin singlet state [15]. In the monovalent nickelates, it is unclear where the doped-holes reside. Do they form a ZR singlet as in cuprates? Instead, if the holes reside on the Ni site, do they form a high-spin local triplet with two singly occupied Ni 3*d* orbitals and aligned ferromagnetically or a low-spin singlet with either both the holes residing in the Ni $3d_{x^2-y^2}$ orbital or two singly occupied Ni 3d orbitals but aligned anti-parallel. While Ni L-edge XAS and RIXS measurements [6] conclude that an orbitally polarized singlet state is predominant, where doped holes reside on the Ni $3d_{x^2-y^2}$ orbital, O K-edge electron energy loss spectroscopy [14] reveal that some of the holes also reside on the O 2*p* orbitals. On the other hand, calculations based on multi-band $d-p$ Hubbard models show that the fate of the doped holes is determined by a subtle interplay of Ni onsite (U_{dd}), Ni *d* - O 2*p* inter-site (U_{dp}) Coulomb interactions and the Hund's coupling along with the charge-transfer gap [16, 17]. However, with the lack of extensive experimental data, it is difficult to identify the appropriate interaction parameters for a model Hamiltonian study, let alone identifying the model that best describes the physics of superconducting nickelates.

Despite the efforts to discern the similarities and differences between the monovalent nickelates and superconducting cuprates, there is no clear understanding on the nature of doped holes in $NdNiO_2$. Particularly, there is no reliable parameter-free *ab initio* analysis of the hole-doped situation. In this work, we investigate the hole-doped ground state in $NdNiO_2$ and draw parallels to the hole-doped ground state of cuprate analogue $CaCuO_2$. We use fully *ab initio* many-body wavefunction-based quantum chemistry methodology to compute the ground state wavefunctions for the hole-doped $NdNiO_2$ and $CaCuO_2$. We find that the doped hole in $NdNiO_2$ mainly localizes on the Ni $3d_{x^2-y^2}$ orbital to form a closed-shell singlet, and this singlet configuration contributes to ~40% of the wavefunction. In contrast, in $CaCuO_2$ the Zhang-Rice singlet configurations contribute to ~65% of the wavefunction. The persistent dynamic radial-type correlations within the Ni *d* manifold result in stronger d^8 multiplet effects than in $CaCuO_2$, and consequently the additional hole foot-print is more three-dimensional in $NdNiO_2$. Our analysis shows that the most commonly used three-band Hubbard model to express the doped scenario in cuprates represents 90% of the d^8 wavefunction for $CaCuO_2$, but such a model grossly approximates the d^8 wavefunction for the $NdNiO_2$ as it only stands for ~60% of the wavefunction.

In what follows, we first describe the computational methodology we use in this work where we highlight the novel features of the methods and provide all the computational details. We then present the results of our calculations and conclude with a discussion.

2 THE WAVEFUNCTION QUANTUM CHEMISTRY METHOD

Ab initio configuration interaction (CI) wavefunction-based quantum chemistry methods, particularly the post Hartree-Fock (HF) complete active space self-consistent field (CASSCF) and the multireference perturbation theory (MRPT), are employed. These methods not only facilitate systematic inclusion of electron correlations, but also enable to quantify different types of correlations, static vs. dynamic [18]. These calculations do not use any *ad hoc* parameters to incorporate electron-electron interactions unlike other many-body methods, instead, they are computed fully *ab initio* from the kinetic and Coulomb integrals. Such *ab initio* calculations provide techniques to systematically analyze electron correlation effects and offer insights into the electronic structure of correlated solids that go substantially beyond standard DFT approaches,

e.g., see Refs. [7, 19–22] for the 3*d* TM oxides and Refs. [23–27] for 5*d* compounds.

2.1 Embedded Cluster Approach

Since strong electronic correlations are short-ranged in nature [28], a local approach for the calculation of the N and $N \pm 1$ –electron wavefunction is a very attractive option for transition metal compounds. In the embedded cluster approach, a finite set of atoms, we call quantum cluster (QC), is cut out from the infinite solid and many-body quantum chemistry methods are used to calculate the electronic structure of the atoms within the QC. The cluster is "embedded" in a potential that accounts for the part of the crystal that is not treated explicitly. In this work, we represent the embedding potential with an array of point charges (PCs) at the lattice positions that are fitted to reproduce the Madelung crystal field in the cluster region [29]. Such procedure enables the use of quantum chemistry calculations for solids involving transition-metal or lanthanide ions, see Refs. [23, 30, 31].

2.2 Complete Active Space Self-Consistent Field

CASSCF method [18] is a specific type of multi-configurational (MC) self-consistent field technique in which a complete set of Slater determinants or configuration state functions (CSFs) that is used in the expansion of the CI wavefunction is defined in a constrained orbital space, called the active space. In the CASSCF(n,m) approach, a subset of n active electrons are fully correlated among an active set of m orbitals, leading to a highly multi-configurational (CAS) reference wavefunction. CASSCF method with a properly chosen active space guarantees a qualitatively correct wavefunction for strongly correlated systems where static correlation [18] effects are taken into account.

We consider active spaces as large as CAS(24,30) in this work. Because the conventional CASSCF implementations based on deterministic CI space (the Hilbert space of all possible configurations within the active space) solvers are limited to active spaces of 18 active electrons in 18 orbitals, we use the full configuration interaction quantum Monte Carlo (FCIQMC) [32–34] and density matrix renormalization group (DMRG) theory [35, 36] algorithms to solve the eigenvalue problem defined within the active space.

2.3 Multireference Perturbation Theory

While the CASSCF calculation provides a qualitatively correct wavefunction, for a quantitative description of a strongly correlated system, dynamic correlations [18] (contributions to the wavefunction from those configurations related to excitations from inactive to active and virtual, and active to virtual orbitals) are also important and must be accounted for. A natural choice is variational multireference CI (MRCI) approach where the CI wavefunction is extended with excitations involving orbitals that are doubly occupied and empty in the reference CASSCF wavefunction [18]. An alternative and computationally less demanding approach to take into account the dynamic correlations is based on perturbation theory in second- and higher-orders. In multireference perturbation theory (MRPT) MC zeroth-order wavefunction is employed and excitations to the virtual space are accounted by means of perturbation theory. If the initial choice of the MC wavefunction is good enough to capture the large part of the correlation energy, then the perturbation corrections are typically small. The most common variations of MRPT are the complete active space second-order perturbation theory (CASPT2) [37] and the n-electron valence second-order perturbation theory (NEVPT2) [38] which differ in the type of zeroth-order Hamiltonian H_0 employed.

TABLE 1 | The different active spaces (CAS) considered in this work. NEL is number of active electrons and NORB is the number of active orbitals. The numbers in parenthesis indicate the orbital numbers in **Figure 2**.

CAS	NEL	NORB
CAS-1	18	24 (1–24)
CAS-2	24	30 (1–30)
CAS-3[a]	12	14 (1, 6, 11, 16 and 21–30)

[a]*The four neighbouring Ni^{1+} (Cu^{2+}) ions in the quantum cluster are treated as closed shell Cu^{1+} (Zn^{2+}) ions.*

3 THE *AB INITIO* MODEL

Before we describe the *ab initio* model we consider, let us summarize the widely used and prominent model Hamiltonian to study the nature of doped hole in HTC cuprates and also employed for monovalent nickelates lately. It is the three-band Hubbard model [39] with three orbital degrees of freedom (bands) which include the d orbital of Cu with x^2-y^2 symmetry and the in-plane oxygen p orbitals aligned in the direction of the nearest Cu neighbours. These belong to the b_1 irreducible representation (irrep) of the D_{4h} point group symmetry realized at the Cu site of the CuO_4 plaque, the other Cu d orbitals belong to a_1 (d_{z^2}), b_2 (d_{xy}) and e ($d_{xz,yz}$) irreps. The parameters in this Hamiltonian include the most relevant hopping and Coulomb interactions within this set of orbitals. More recently, the role of the Cu 3*d* multiplet structure on the hole-doped ground state is also studied [40]. While this model explains certain experimental observations, there is still a huge debate on what is the minimum model to describe the low-energy physics of doped cuprates. Nevertheless, this model has also been employed to investigate the character of the doped hole in monovalent nickelates [16, 17, 41].

Within the embedded cluster approach described earlier, we consider a QC of five NiO_4 (CuO_4) plaques that includes five Ni (Cu) atoms, 16 oxygens and 8 Nd (Ca) atoms, see **Figure 1**. The 10 Ni (Cu) ions neighbouring to the cluster are also included in the QC, however, these are considered as total ion potentials (TIPs). The QC is embedded in point charges that reproduce the electrostatic field of the solid environment. We used the crystal structure parameters for the thin film samples reported in Refs. [2, 42–44].

We used effective core potentials [45] and correlation consistent basis sets of triple-ζ quality with additional

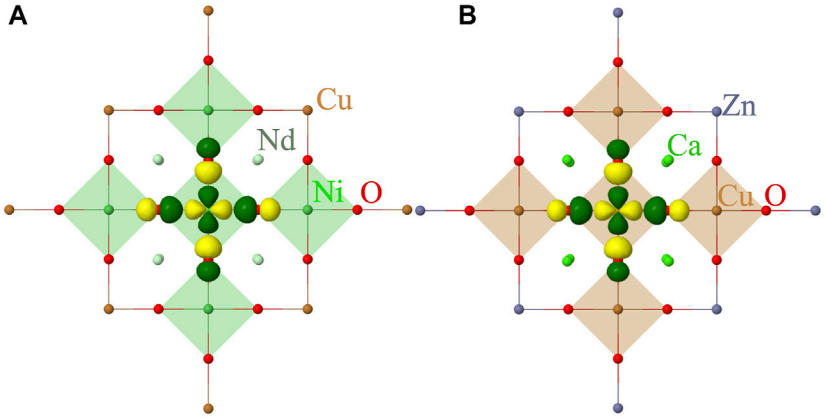

FIGURE 1 | Quantum cluster of five NiO_4 **(A)** and CuO_4 **(B)** plaques considered in our calculations. The point-charge embedding is not shown. The symmetry adapted localized $3d_{x^2-y^2}$ and the oxygen Zhang-Rice-like $2p$ orbitals, the basis in which the wavefunction in **Table 3** is presented are shown in yellow and green color.

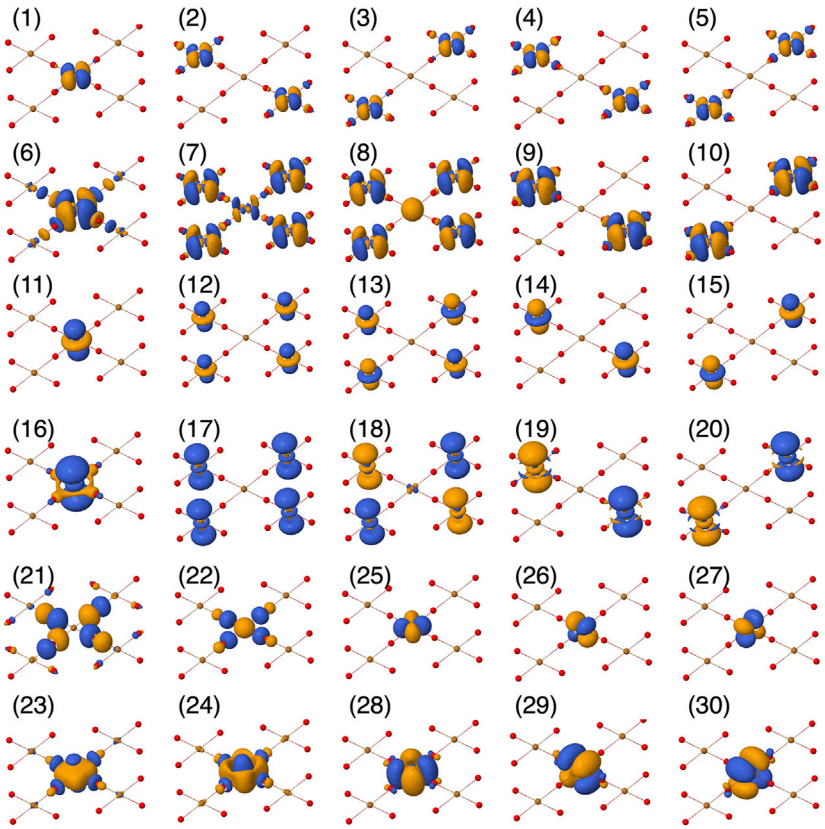

FIGURE 2 | Active orbital basis used in the CASSCF calculations, plotted using Jmol [54].

polarization functions—[4*s*3*p*3*d*1*f*]—for Ni (Cu) [46] and double-ζ quality—[3*s*2*p*1*d*]—for oxygens [47]. For the eight Nd (Ca) atoms large core effective potentials [48–50] and associated [3*s*2*p*2*d*] basis functions were used. In the case of Nd, the *f*-electrons were incorporated in the core. Cu^{1+} (Zn^{2+}) total ion potentials (TIPs) with [2*s*1*p*] functions were used for the 10 Ni^{1+} (Cu^{2+}) [51, 52] peripheral ions of the QC.

To investigate the role of different interactions in the d^8 ground state, two different active spaces were considered. In the first active space, CAS-1 in **Table 1**, only the orbitals in the b_1 and a_1 irreps are active. These are $d_{x^2-y^2}$ and d_{z^2}-like orbitals respectively, and the corresponding double-shell 4*d* orbitals of each of the five Ni (Cu) atoms. CAS-1 also contains the symmetry-adapted ZR-like composite O 2*p* and the double-

TABLE 2 | Relative energies (in eV) of the electron removal d^8 states in $NdNiO_2$ and the iso-structural $CaCuO_2$ obtained from CAS(12,14)SCF and CASSCF + CASPT2 calculations.

State	$NdNiO_2$		$CaCuO_2$	
	CASSCF	+CASPT2	CASSCF	+CASPT2
$^1A_{1g}$	0.00	0.00	0.00	0.00
$^3B_{1g}$	1.35	1.88	2.26	2.50
$^1B_{1g}$	2.98	3.24	3.21	3.33

shell 3*p*-like orbitals, numbers 1–20 and 21–24 in **Figure 2**. At the mean-field HF level of theory, there are 16 electrons within this set of orbitals, resulting in CAS(16,22) active space. In the second active space, CAS-2, orbitals of b_2 and the *e* irreps from the central Ni (Cu) *d* manifold are also included. These are the $3d_{xy}$, $3d_{xz,yz}$-like orbitals and the corresponding 4*d* orbitals and the six electrons, numbers 25–30 in **Figure 2**, resulting in a CAS(24,30) active space. The latter active space takes into account the d^8 multiplet effects within the 3*d* manifold explicitly.

The two active spaces considered in this work not only describe all the physical effects included in the above mentioned three-band Hubbard model but go beyond. More importantly, we do not have any *ad-hoc* input parameters for the calculation as all the physical interactions are implicitly included in the *ab initio* Hamiltonian describing the actual scenario in the real materials. We employed OPENMOLCAS [53] quantum chemistry package for all the calculations.

4 RESULTS

4.1 Ground State of the d^8 Configuration

Starting from the electronic structure of the parent compounds, where each Ni (Cu) is in the d^9 configuration, we compute the electron-removal (in the photoemission terminology) d^8 state to investigate the hole-doped quasiparticle state. Since the parent compounds in d^9 configuration have strong nearest neighbour antiferromagnetic (AF) correlations [7], the total spin of our QC in undoped case, with five Ni (Cu) sites, in the AF ground state is S_{QC} = 3/2. By introducing an additional hole (or removing an electron) from the central Ni (Cu) in our QC, the S_{QC} values range from 0 to 3. To simplify the analysis of the distribution of the additional hole, we keep the spins on the four neighbouring Ni (Cu) sites parallelly aligned in all our calculations and from now on we only specify the spin multiplicity of the central Ni (Cu)O_4 plaque. The multiplet structure of the d^8 configuration thus consists of only spin singlet and triplet states, spanned by the four irreps of the 3*d* manifold. The active spaces we consider in this work allow us to compute accurately the excitations only within the b_1 and a_1 irreps [55] and we address the full multiplet structure elsewhere.

When computing the local excitations, a local singlet state on the central Ni (Cu) corresponds to a total spin on the cluster S_{QC} = 2. However, a local triplet state, with central spin aligned parallel to the neighboring spins, corresponds to S_{QC} = 3 and do not satisfy the AF correlations. To avoid the spin coupling between the central d^8 Ni (Cu) with the neighbouring d^9 Ni (Cu) ions, we replace the latter with closed shell, Cu (Zn) d^{10}, ions and freeze them at the mean-field HF level. Such a simplification is justified, as the local excitation energy we compute is an order of magnitude larger than the exchange interaction [7].

In **Table 2**, the relative energies of the lowest local spin singlets $^1A_{1g}$, $^1B_{1g}$ and spin triplet $^3B_{1g}$ states are shown. These are obtained from CASSCF + CASPT2 calculations with CAS(12,14) active space (CAS-3 in **Table 1**) which includes the 3*d* and 4*d* orbitals of the central Ni (Cu) ion and the in-plane O 2*p* and 3*p* orbitals in the b_1 irrep. In the CASPT2 calculation, the remaining doubly occupied O 2*p*, the central Ni (Cu) 3*s* and 3*p* orbitals and all the unoccupied virtual orbitals are correlated.

It can be seen that the ground state is of $^1A_{1g}$ symmetry and the lowest triplet excited state, with $^3B_{1g}$ symmetry, is around 1.88 and 2.5 eV for $NdNiO_2$ and $CaCuO_2$ respectively. The AF magnetic exchange in these two compounds is 76 and 208 meV respectively [7], and thus we expect that our simplification of making the neighbouring d^9 ions closed shell do not over/underestimate the excitation energies. At the CASSCF level, the $^1A_{1g}$-$^3B_{1g}$ excitation energy is 1.35 eV in $NdNiO_2$ while it is 2.26 eV in $CaCuO_2$. Interestingly, the inclusion of dynamical correlations via the CASPT2 calculation, the $^1A_{1g}$ in $NdNiO_2$ is stabilized by 0.53 eV compared to $^3B_{1g}$ state. However, in $CaCuO_2$, the $^1A_{1g}$ state is stabilized by only 0.24 eV. This indicates that the dynamical correlations are more active in the $^1A_{1g}$ state in $NdNiO_2$ than in $CaCuO_2$. We note that the hole excitations within the 3*d* orbitals in the irreps b_2 and *e*, calculated with this limited active space (CAS-3) results in energies lower than the $^3B_{1g}$ and $^1B_{1g}$ states. However, an accurate description of those states requires an enlarged active space that includes not only the same symmetry oxygen 2*p* and 3*p* orbitals from the central NiO_4 plaque but also the 3*d*, 4*d* manifold of the neighbouring Ni (Cu) ions, making the active space prohibitively large. Here, we concentrate on the analysis of the $^1A_{1g}$ ground state and address the complete d^8 multiplet spectrum elsewhere.

4.2 Wavefunction of the d^8 Ground State

The $^1A_{1g}$ ground wavefunction in terms of the weights of the four leading Slater determinants (SD) (in the case of $CaCuO_2$) is

TABLE 3 | Ni and Cu $3d^8$ $^1A_{1g}$ ground state wavefunction: Weights (%) of the leading configurations in the wavefunction computed for $NdNiO_2$ and $CaCuO_2$ with active spaces CAS-1 and CAS-2 (see **Table 1**). d_{b_1} and p_{b_1} are the localized Ni (Cu) $3d_{x^2-y^2}$ and the oxygen 2*p* ZR-like orbitals (see **Figure 1**) in the b_1 irrep respectively. Arrows in the superscript indicate the spin of the electrons and a $^{\square}$ indicates two holes.

	$NdNiO_2$		$CaCuO_2$	
$^1A_{1g}$	CAS-1	CAS-2	CAS-1	CAS-2
$\|d^{\square}_{b_1} p^{\uparrow\downarrow}_{b_1}\rangle$	51.87	42.40	4.20	20.25
$\|d^{\uparrow}_{b_1} p^{\downarrow}_{b_1}\rangle$	8.27	10.48	42.58	38.52
$\|d^{\downarrow}_{b_1} p^{\uparrow}_{b_1}\rangle$	6.07	7.60	25.00	25.60
$\|d^{\uparrow\downarrow}_{b_1} p^{\square}_{b_1}\rangle$	0.09	0.23	21.56	5.14

TABLE 4 | Dominant ten Slater derterminants and their weights (in %) in the d^8 wavefunction for $NdNiO_2$ (we also show the 11th which is the same as the fourth configuration in **Table 3**). The wavefunction is represented in the same basis as the wavefunction in **Table 3**. However, for convenience we use the orbital numbers from **Figure 2** in the first row to express the basis. These orbitals are visually very close to the actual basis. The doubly occupied orbitals are shown as ↑↓, the singly occupied ones with ↑(↓) for spin $\frac{1}{2}$ ($\frac{-1}{2}$) and an empty box implies that the orbital is unoccupied. The red (electrons removed) and green (electrons added) colors indicate the orbitals involved in the excitation starting from the first configuration. The red box indicates that the orbital becomes empty in this particular excited configuration.

	1	2	3	4	5	6	7	8	9	10	11	12	13	14	15	16	17	18	19	20	21	22	23	24	25	26	27	28	29	30	Wt. (%)
1		↓	↓	↓	↓						↑↓	↑↓	↑↓	↑↓	↑↓						↑↓	↑↓			↑↓	↑↓	↑↓				42.40
2	↓	↓	↓	↓	↓						↑↓	↑↓	↑↓	↑↓	↑↓						↑	↑↓			↑↓	↑↓	↑↓				10.48
3	↑	↓	↓	↓	↓						↑↓	↑↓	↑↓	↑↓	↑↓						↓	↑↓			↑↓	↑↓	↑↓				7.6
4	↓	□	↓	↓	↓						↑↓	↑↓	↑↓	↑↓	↑↓						↑↓	↑↓			↑↓	↑↓	↑↓				2.45
5	↓	↓	□	↓	↓						↑↓	↑↓	↑↓	↑↓	↑↓						↑↓	↑↓			↑↓	↑↓	↑↓				2.38
6	↑↓	↓	↓	↓	↓						□	↑↓	↑↓	↑↓	↑↓						↑↓	↑↓			↑↓	↑↓	↑↓				0.61
7		↓	↓	↓	↓						↑↓	□	↑↓	↑↓	↑↓		↑↓				↑↓	↑↓			↑↓	↑↓	↑↓				0.6
8		↓	↓	↓	↓						↑↓	↑↓	□	↑↓	↑↓			↑↓			↑↓	↑↓			↑↓	↑↓	↑↓				0.6
9	↑↓	↓	↓	↓	↓						↑↓	↑↓	↑↓	↑↓	↑↓						↑↓	↑↓			↑↓	□	↑↓				0.48
10	↑↓	↓	↓	↓	↓						↑↓	↑↓	↑↓	↑↓	↑↓						↑↓	↑↓			↑↓	↑↓	□				0.48
11	↑↓	↓	↓	↓	↓						↑↓	↑↓	↑↓	↑↓	↑↓						□	↑↓			↑↓	↑↓	↑↓				0.23

shown in **Table 3**. The wavefunctions corresponding to the CASSCF calculations with the active spaces CAS-1 and CAS-2 are shown. The basis in which the wavefunctions are represented is constructed in two steps: 1) A set of natural orbitals are generated by diagonalising the CASSCF one-body reduced density matrix. 2) To obtain a set of atomic-like symmetry-adapted localized orbital basis, we localize the Ni (Cu) $3d$ and O $2p$ orbitals on the central NiO_4 (CuO_4) plaque through a unitary transformation. Such partial localization within the active space keeps the total energy unchanged. The resulting $3d_{x^2-y^2}$ and the ZR-like oxygen $2p$ orbital basis is shown in **Figure 1**. FCIQMC calculation was performed in this partial localized basis to obtain the wavefunction as a linear combination of SDs. 10 million walkers were used to converge the FCIQMC energy to within 0.1 mHartree.

From **Table 3** it can be seen that the electron-removal d^8 ground state wavefunction for the two compounds is mostly described by the four configurations spanned by the localized $3d_{x^2-y^2}$ (d_{b_1}) and the symmetry-adapted ZR-like oxygen $2p$ (p_{b_1}) orbitals that are shown in **Figure 1**. Let us first discus the wavefunction obtain from the CAS-1 active space. For $NdNiO_2$, the dominant configuration involves two holes on $3d_{x^2-y^2}$, $|d_{b_1}^{\square} p_{b_1}^{\uparrow\downarrow}\rangle$, and contributes to ~52% of the wavefunction, while the configurations that make up the ZR singlet, $|d_{b_1}^{\uparrow} p_{b_1}^{\downarrow}\rangle$ and $|d_{b_1}^{\downarrow} p_{b_1}^{\uparrow}\rangle$, contributes to only ~14%. On the other hand, the d^8 $^1A_{1g}$ state in $CaCuO_2$ is predominantly the ZR singlet with ~68% weight. In the CASSCF calculation with CAS-2 active space, where all the electrons in the $3d$ manifold are explicitly correlated, we find that the character of the wavefunction remains unchanged in $NdNiO_2$ but weight on the dominant configurations is slightly reduced. On the other hand, in $CaCuO_2$, while the contribution from the ZR singlet is slightly reduced, the contribution from $|d_{b_1}^{\square} p_{b_1}^{\uparrow\downarrow}\rangle$ configuration is dramatically increased at the expense of the weight on $|d_{b_1}^{\uparrow\downarrow} p_{b_1}^{\square}\rangle$. This demonstrates that the additional freedom provided by the d_{xy} and $d_{xz/yz}$ orbitals for the electron correlation helps to accommodate the additional hole on the Cu ion.

We note that the four configurations shown in **Table 3** encompass almost 90% of the d^8 wavefunction (with CAS-2 active space) in $CaCuO_2$. Thus, the use of a three-band Hubbard model [39, 40] to investigate the role of doped holes in CuO_2 planes is a reasonable choice. However, for $NdNiO_2$ these configurations cover only 60% of the d^8 wavefunction, hence a three-band Hubbard model is too simple to describe the hole-doped monovalent nickelates.

In **Table 4** and **Table 5**, we show the first ten dominant SD configurations by weight in the d^8 wavefunction of $NdNiO_2$ and $CaCuO_2$ respectively. Interestingly, the configurations with two holes in the out-of-plane d-orbitals d_{z^2} (configuration 6) and $d_{xz/yz}$ (9 and 10 configurations) is significant in $NdNiO_2$, while such configurations do not exist in the dominant ten for $CaCuO_2$. We also find the additional hole to be more delocalized on to the neighboring Ni ions in $NdNiO_2$ than it is in $CaCuO_2$, however, this observation should be taken with precaution as the oxygen environment around the neighboring Ni/Cu ions is only described at the mean-field level in our calculation setup.

A more intuitive and visual understanding of the distribution of the additional hole can be obtained by plotting the difference of the d^8 and the d^9 ground state electron densities as shown in **Figure 3**. Electron density of a multi-configurational state can be computed as a sum of densities arising from the natural orbitals and corresponding (well-defined) occupation numbers. We used Multiwfn program [56] to perform this summation. The negative values of the heat map of the electron density difference (blue color) and the positive values (in red) represent respectively the extra hole density and additional electron density in d^8 state compared to the d^9 state. From **Figure 3A**/**Figure 3C** that show the density difference in the NiO_2/CuO_2 planes (xy-plane), we conclude the following:

1. The hole density is concentrated on the Ni site (darker blue) with b_1 ($d_{x^2-y^2}$) symmetry in $NdNiO_2$ whereas it is distributed evenly on the four oxygen and the central Cu ions with b_1 symmetry in $CaCuO_2$, a result consistent with the wavefunction reported in **Table 3**.

TABLE 5 | Dominant ten SD configurations and their weights (in %) in the d^8 wavefunction for $CaCuO_2$. See the caption of **Table 4** for details of the wavefunction representation.

	1	2	3	4	5	6	7	8	9	10	11	12	13	14	15	16	17	18	19	20	21	22	23	24	25	26	27	28	29	30	Wt
1	↓	↓	↓	↓	↓						↑↓	↑↓	↑↓	↑↓	↑↓						↑	↑↓			↑↓	↑↓	↑↓				38.52
2	↑	↓	↓	↓	↓						↑↓	↑↓	↑↓	↑↓	↑↓						↓	↑↓			↑↓	↑↓	↑↓				25.60
3	□	↓	↓	↓	↓						↑↓	↑↓	↑↓	↑↓	↑↓						↑↓	↑↓			↑↓	↑↓	↑↓				20.25
4	↑↓	↓	↓	↓	↓						↑↓	↑↓	↑↓	↑↓	↑↓						□	↑↓			↑↓	↑↓	↑↓				5.14
5	↓	□	↓	↓	↓						↑↓	↑↓	↑↓	↑↓	↑↓						↑↓	↑↓			↑↓	↑↓	↑↓				1.30
6	↓	↓	□	↓	↓						↑↓	↑↓	↑↓	↑↓	↑↓						↑↓	↑↓			↑↓	↑↓	↑↓				1.27
7	↓	↑↓	↓	↓	↓						↑↓	↑↓	↑↓	↑↓	↑↓						□	↑↓			↑↓	↑↓	↑↓				0.24
8	↓	↓	↑↓	↓	↓						↑↓	↑↓	↑↓	↑↓	↑↓						□	↑↓			↑↓	↑↓	↑↓				0.23
9	↑↓	↓	↓	↓	↓						↓	↑↓	↑↓	↑↓	↑↓	↑					□	↑↓			↑↓	↑↓	↑↓				0.13
10	↑↓	↓	↓	↓	↓						↑	↑↓	↑↓	↑↓	↑↓	↓					□	↑↓			↑↓	↑↓	↑↓				0.12

2. In $NdNiO_2$, the hole density is spread out around the Ni ion with larger radius, and otherwise in $CaCuO_2$. This demonstrates that the 3*d* manifold in Cu is much more localized than in Ni and therefore the onsite Coulomb repulsion *U* is comparatively smaller for Ni.
3. The darker red regions around the Ni site in $NdNiO_2$ indicate stronger d^8 multiplet effects that result in rearrangement of electron density compared to d^9 configuration.
4. In $CaCuO_2$, we see darker red regions on the oxygen ions instead, which shows that the significant presence of a hole on these ions results in noticeable electron redistribution.

The electron density difference in the xz-plane (which is perpendicular to the NiO_2/CuO_2 planes) is quite different in the two compounds. The hole density in $NdNiO_2$ is spread out up to 2 Å in the *z*-direction, unlike in $CaCuO_2$, where it is confined to within 1 Å. We attribute this to the strong radial-type correlations in $NdNiO_2$. With the creation of additional hole on the $3d_{x^2-y^2}$ orbital, the electron density which is spread out in the d_{z^2} symmetry via the dynamical correlation between $3d_{z^2}$ and $4d_{z^2}$ orbitals [7], becomes more compact in the d_{z^2} symmetry through the reverse breathing. Thus, we see a strong red region with $3d_{z^2}$ profile and a blue region with expanded $4d_{z^2}$ profile.

To obtain a quantitative understanding of the charge density differences for the two compounds, in **Figure 3E** we plot the electron density difference integrated over a sphere centered on the central Ni(Cu) atom as a function of the radius *r* shown in **Figure 3A**. Four features, which we marked A-D, clearly demonstrate the contrast in the charge density differences in the two compounds. From the feature A at *r* close to Ni (Cu), it is evident that the extent of hole density around Ni in $NdNiO_2$ is larger than around Cu in $CaCuO_2$. The features B and C that are on either side of the position of oxygen ions show that the hole density is significantly larger on oxygen atoms in $CaCuO_2$ than in $NdNiO_2$. It is interesting to note that we see a jump (feature D) in the electron density above zero at *r* close to the position of Nd ions in $NdNiO_2$, while in $CaCuO_2$ the curve is flat in the region of Ca ions. This shows that there is some electron redistribution happening around the Nd ions. The hole density within a solid sphere (SS) around the central Ni (Cu) atom obtained by additional integration over the radius *r* is also shown in **Figure 3E** with dashed curves. It can be seen that the total hole density within the SS of *r* ~4 Å, where the neighboring Ni (Cu) ions are located, is only ~0.5 in both the compounds, with slight differences related to the feature D. This is due to the screening of the hole with the electron density pulled in from the farther surroundings. As one would expect, a SS with *r* of the size of the cluster, the total hole density is one in both the compounds.

4.3 Orbital Entanglement Entropy

To analyse the different type of correlations active in the two compounds in d^8 configuration, we compute the entanglement entropy [57–59]. While the single orbital entropy, $s(1)_i$, quantifies the correlation between *i*th orbital and the remaining set of orbitals, the mutual information, $I_{i,j}$ is the two-orbital entropy between *i* and *j* [60, 61], and illustrates the correlation of an orbital with another, in the embedded environment comprising of all other orbitals. We used QCMAQUIS [63] embedded in OPENMOLCAS [54] package to compute the entropies.

In **Figure 4**, $s(1)_i$ and $I_{i,j}$ extracted from the d^8 ground state CASSCF calculations with CAS-2 active space for $NdNiO_2$ and $CaCuO_2$ are shown. The orbital basis for which the entropy is computed is the same as the basis in which the wavefunction presented in **Table 3** is expanded. As mentioned previously, this orbital basis is obtained from partial localization of the natural orbitals in a way that only the $3d_{x^2-y^2}$ and the O 2*p* ZR-like orbitals are localized. Since a large part of electron correlation is compressed in natural orbitals, we see a tiny $s(1)_i$ for all orbitals except for the localized $3d_{x^2-y^2}$ and the O 2*p* ZR-like orbitals where it is significant. This is consistent with the wavefunction in **Table 3**. The mutual orbital entanglement between pairs of orbitals shows strong entanglement between the $3d_{x^2-y^2}$ and the O 2*p* ZR-like orbitals for both $NdNiO_2$ and $CaCuO_2$, a consequence of the dominant weight of the configurations spanned by these two orbitals in the wavefunction. The next strongest entanglement is between the Ni/Cu 3*d* valence and their double-shell 4*d* orbitals. Such strong entanglement also

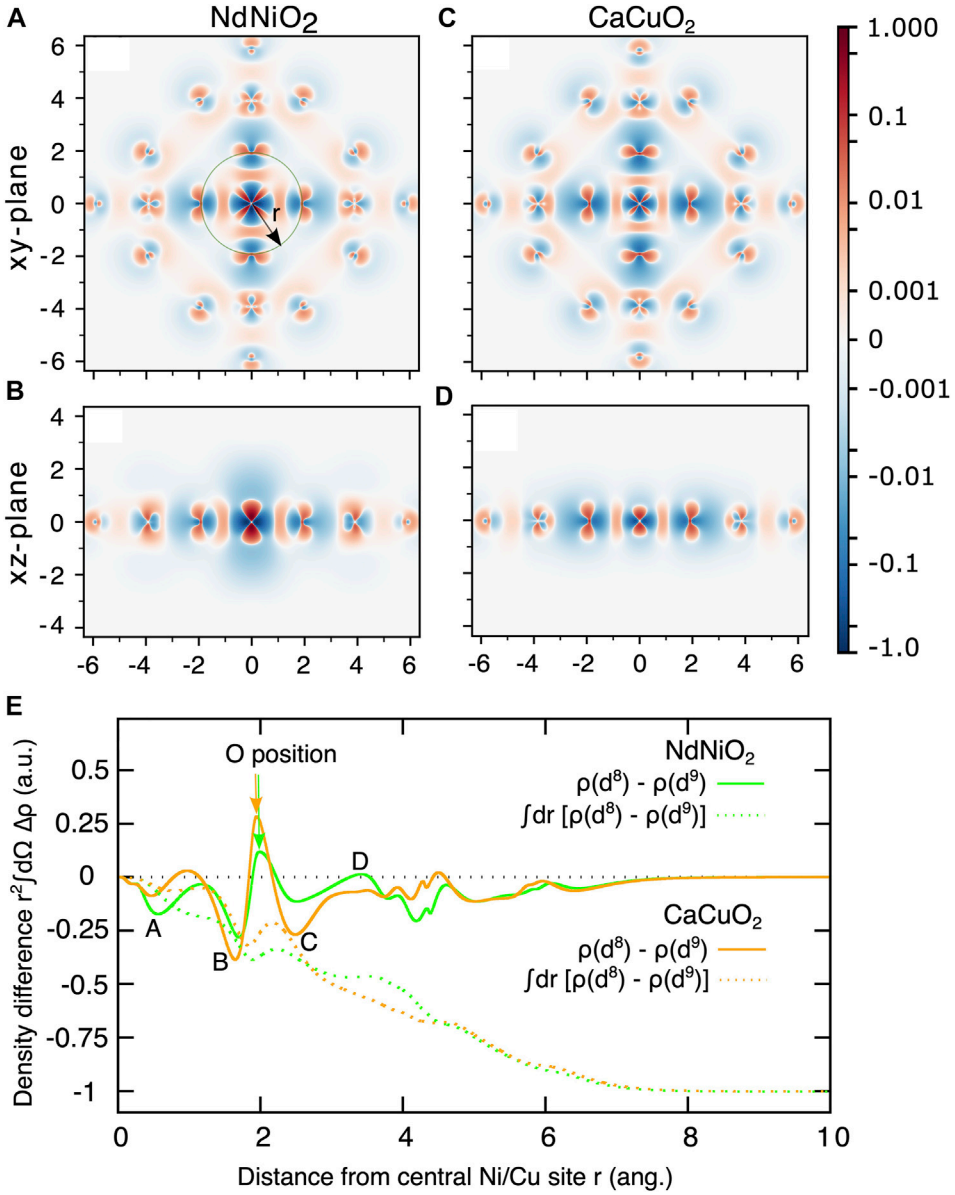

FIGURE 3 | Electron density difference of the d^8 and d^9 ground states ($\rho(d^8) - \rho(d^9)$) for $NdNiO_2$ in the xy-plane **(A)** and xz-plane **(B)**, and for $CaCuO_2$ xy-plane **(C)** and xz-plane **(D)**. The coordinates of the central Ni (Cu) d^8 ion are set to (0,0). The scale of the heat-bar is logarithmic between ±0.001 to ±1.0 and is linear between 0 and ±0.001. **(E)** Electron density difference integrated over a sphere centered on the central Ni(Cu) atoms (full curves) as a function of the radius *r* shown in **(A)**. The result of an additional radial integration (dashed curves) as a function of the upper integration limit.

observed for the undoped d^9 ground state [7], is a result of dynamical radial correlation [18] and orbital breathing effects [63, 64]. Interestingly, the entanglement entropy in the range 0.001–0.01 (green lines) is quite similar in the two compounds, although one sees more entanglement connections in $NdNiO_2$. A comparison of the entropy information between $NdNiO_2$ and $CaCuO_2$ reveals that the Ni 3*d* and 4*d*-like orbitals contribute rather significantly (thicker blue lines) to the total entropy, in contrast to the Cu 3*d* and 4*d*-like orbitals, something that is also seen in the undoped compounds [7].

5 CONCLUSION AND DISCUSSION

In conclusion, our *ab initio* many-body quantum chemistry calculations for the electron removal (d^8) states find a low-spin closed-shell singlet ground state in $NdNiO_2$ and that the additional hole is mainly localized on the Ni $3d_{x^2-y^2}$ orbital, unlike in $CaCuO_2$, where a Zhang-Rice singlet is predominant. We emphasise that the d^8 wavefunction is highly multi-configurational where the dominant closed-shell singlet configuration weight is only ~42%. This result is consistent with the experimental evidence [6, 14] of

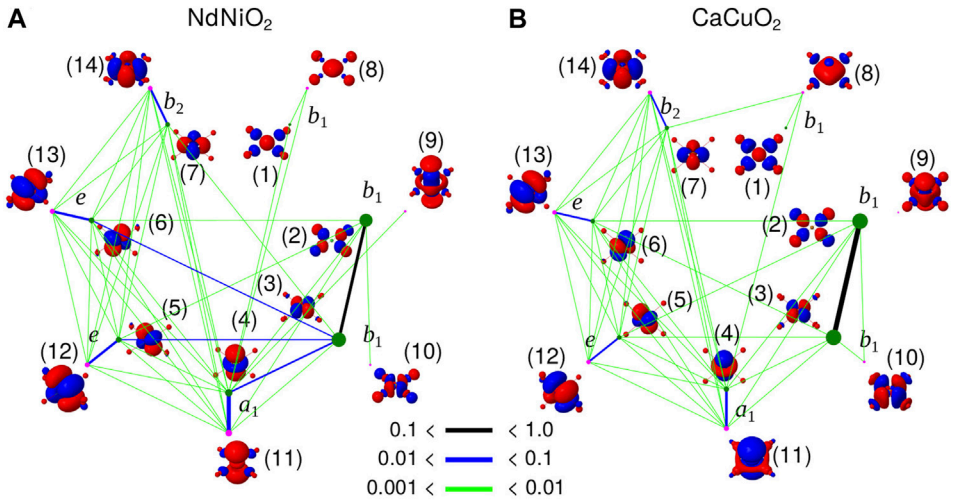

FIGURE 4 | Single orbital entanglement entropy, $s(i)_i$ (dots) and mutual orbital entanglement entropy, $I_{i,j}$ (colored lines) of the orbital basis used to expand the d^8 wavefunction in **Table 3** for $NdNiO_2$ **(A)** and $CaCuO_2$ **(B)**. Entanglement entropy of the orbitals centred on the central NiO_4/CuO_4 plaque are only shown. The irrep to which the orbitals belong to are also shown. The green and magenta colors represent the two different set of orbitals, occupied (at the HF level) and the corresponding double-shell (virtual), respectively. The thickness of the black, blue and green lines denote the strength of $I_{i,j}$, and the size of the dots is proportional to s $(1)_i$. The raw data is presented in **Supplementary Tables S1, S2**.

orbitally polarized singlet state as well as the presence of holes on the O 2*p* orbitals. Importantly, the persistent dynamic radial-type correlations within the Ni *d* manifold result in stronger d^8 multiplet effects in $NdNiO_2$, and consequently the additional hole foot-print is more three dimensional. In $CaCuO_2$, we find that the electron correlations within the d_{xy} and $d_{xz/yz}$ orbitals changes the hole-doped wavefunction significantly. Specifically, the double hole occupation of Cu $d_{x^2-y^2}$ is significantly increased and this can influence the transport properties.

It was recently proposed that nickelates could be a legitimate realization of the single-band Hubbard model [65]. However, our analysis shows that even the three-band Hubbard model [66], which successfully describes the hole-doped scenario in cuprates, falls short to describe hole-doped nickelates and additional orbital degrees of freedom are indeed necessary for the description of the strong multiplet effects we find. Much has been discussed about the importance of rare-earth atoms for the electronic structure of superconducting nickelates, e.g. see [67]. The three-dimensional nature of the hole density we find in $NdNiO_2$ might also be hinting at the importance of out-of-plane Nd ions. It would be interesting to compare the hole density of $NdNiO_2$ with other iso-structural nickelates such as $LaNiO_2$ where La 5*d* states are far from the Fermi energy. Since the infinite-layered monovalent nickelates are thin films that are grown on substrates, one could ask the question of how the electronic structure of the undoped and doped compounds changes with varying Ni-O bond length. Would this influence the role of electronic correlations in d^9 nickelates? We will address these in the near future.

DATA AVAILABILITY STATEMENT

The data supporting the conclusions of this study can be made available upon reasonable request.

AUTHOR CONTRIBUTIONS

VK and AA designed the project. VK and NB performed the calculations. All the authors analysed the data. VK wrote the paper with inputs from NB and AA.

ACKNOWLEDGMENTS

VK would like to acknowledge Giovanni Li Manni and Oskar Weser for fruitful discussions. We gratefully acknowledge the Max Plank Society for financial support.

SUPPLEMENTARY MATERIAL

The Supplementary Material for this article can be found online at: https://www.frontiersin.org/articles/10.3389/fphy.2022.836784/full#supplementary-material

REFERENCES

1. Bednorz JG, Müller KA. Possible High Tc Superconductivity in the Ba-La-Cu-O System. *Z Physik B - Condensed Matter* (1986) 64:189–93. doi:10.1007/bf01303701
2. Li D, Lee K, Wang BY, Osada M, Crossley S, Lee HR, et al. Superconductivity in an Infinite-Layer Nickelate. *Nature* (2019) 572:624–7. doi:10.1038/s41586-019-1496-5
3. Osada M, Wang BY, Goodge BH, Lee K, Yoon H, Sakuma K, et al. A Superconducting Praseodymium Nickelate with Infinite Layer Structure. *Nano Lett* (2020) 20:5735–40. doi:10.1021/acs.nanolett.0c01392
4. Osada M, Wang BY, Goodge BH, Harvey SP, Lee K, Li D, et al. Nickelate Superconductivity without Rare-Earth Magnetism: (La,Sr)NiO_2. *Adv Mater* (2021) 33:2104083. doi:10.1002/adma.202104083
5. Keimer B, Kivelson SA, Norman MR, Uchida S, Zaanen J. From Quantum Matter to High-Temperature Superconductivity in Copper Oxides. *Nature* (2015) 518:179–86. doi:10.1038/nature14165
6. Rossi M, Lu H, Nag A, Li D, Osada M, Lee K, et al. Orbital and Spin Character of Doped Carriers in Infinite-Layer Nickelates. *Phys. Rev. B* (2021). 104: L220505. doi:10.1103/PhysRevB.104.L220505
7. Katukuri VM, Bogdanov NA, Weser O, van den Brink J, Alavi A. Electronic Correlations and Magnetic Interactions in Infinite-Layer $NdNiO_2$. *Phys Rev B* (2020) 102:241112. doi:10.1103/physrevb.102.241112
8. Moretti Sala M, Bisogni V, Aruta C, Balestrino G, Berger H, Brookes NB, et al. Energy and Symmetry of d-d Excitations in Undoped Layered Cuprates Measured by CuL_3 Resonant Inelastic X-ray Scattering. *New J Phys* (2011) 13:043026. doi:10.1088/1367-2630/13/4/043026
9. Lee K-W, Pickett WE. Infinite-Layer $LaNiO_2$: Ni^{1+} is not Cu^{2+}. *Phys Rev B* (2004) 70:165109. doi:10.1103/physrevb.70.165109
10. Liu Z, Ren Z, Zhu W, Wang Z, Yang J. Electronic and Magnetic Structure of Infinite-Layer $NdNiO_2$: Trace of Antiferromagnetic Metal. *Npj Quan Mater* (2020) 5:31. doi:10.1038/s41535-020-0229-1
11. Zhang H, Jin L, Wang S, Xi B, Shi X, Ye F, et al. Effective Hamiltonian for Nickelate Oxides $Nd_{1-x}Sr_xNiO_2$. *Phys Rev Res* (2020) 2:013214. doi:10.1103/physrevresearch.2.013214
12. Zaanen J, Sawatzky GA, Allen JW. Band Gaps and Electronic Structure of Transition-Metal Compounds. *Phys Rev Lett* (1985) 55:418–21. doi:10.1103/physrevlett.55.418
13. Hepting M, Li D, Jia CJ, Lu H, Paris E, Tseng Y, et al. Electronic Structure of the Parent Compound of Superconducting Infinite-Layer Nickelates. *Nat Mater* (2020) 19:381–5. doi:10.1038/s41563-019-0585-z
14. Goodge BH, Li D, Lee K, Osada M, Wang BY, Sawatzky GA, et al. Doping Evolution of the Mott–Hubbard Landscape in Infinite-Layer Nickelates. *Proc Natl Acad Sci* (2021) 118:e2007683118. doi:10.1073/pnas.2007683118
15. Zhang FC, Rice TM. Effective Hamiltonian for the Superconducting Cu Oxides. *Phys Rev B* (1988) 37:3759–61. doi:10.1103/physrevb.37.3759
16. Jiang M, Berciu M, Sawatzky GA. Critical Nature of the Ni Spin State in Doped $NdNiO_2$. *Phys Rev Lett* (2020) 124:207004. doi:10.1103/physrevlett.124.207004
17. Plienbumrung T, Schmid MT, Daghofer M, Oleś AM. Character of Doped Holes in $Nd_{1-x}Sr_xNiO_2$. *Condensed Matter* (2021) 6:33. doi:10.3390/condmat6030033
18. Helgaker T, Jørgensen P, Olsen J. *Molecular Electronic-Structure Theory*. Chichester: Wiley (2000).
19. Muñoz D, Illas F, de P. R. Moreira I. Accurate Prediction of Large Antiferromagnetic Interactions in High-Tc $HgBa_2Ca_{\{n-1\}}Cu_nO_{\{2n+2+\}}$ (n=2,3) Superconductor Parent Compounds. *Phys Rev Lett* (2000) 84: 1579–82. doi:10.1103/physrevlett.84.1579
20. Hozoi L, Siurakshina L, Fulde P, van den Brink J. Ab Initio determination of Cu 3d Orbital Energies in Layered Copper Oxides. *Sci Rep* (2011) 1:65. doi:10.1038/srep00065
21. Hozoi L, Fulde P. *Computational Methods for Large Systems: Electronic Structre Approaches for Biotechnology and Nanotechnology*. Hoboken: John Wiley & Sons (2011). Chap. 6.
22. Bogdanov NA, van den Brink J, Hozoi L. Ab Initio Computation of d-d Excitation Energies in Low-Dimensional Ti and V Oxychlorides. *Phys Rev B* (2011) 84:235146. doi:10.1103/physrevb.84.235146
23. Katukuri VM, Stoll H, van den Brink J, Hozoi L. Ab Initio Determination of Excitation Energies and Magnetic Couplings in Correlated Quasi-Two-Dimensional Iridates. *Phys Rev B* (2012) 85:220402. doi:10.1103/physrevb.85.220402
24. Bogdanov NA, Maurice R, Rousochatzakis I, van den Brink J, Hozoi L. Magnetic State of Pyrochlore $Cd_2Os_2O_7$ Emerging from Strong Competition of Ligand Distortions and Longer-Range Crystalline Anisotropy. *Phys Rev Lett* (2013) 110:127206. doi:10.1103/physrevlett.110.127206
25. Gretarsson H, Clancy JP, Liu X, Hill JP, Bozin E, Singh Y, et al. Crystal-field Splitting and Correlation Effect on the Electronic Structure of A_2IrO_3. *Phys Rev Lett* (2013) 110:076402. doi:10.1103/PhysRevLett.110.076402
26. Katukuri VM, Yushankhai V, Siurakshina L, Brink JVD, Hozoi L, Rousochatzakis I. Mechanism of Basal-Plane Antiferromagnetism in the Spin-Orbit Driven Iridate Ba_2IrO_4. *Phys Rev X* (2014) 4:021051. doi:10.1103/physrevx.4.021051
27. Katukuri VM, Nishimoto S, Yushankhai V, Stoyanova A, Kandpal H, Choi S, et al. Kitaev Interactions Between j= 1/2 Moments in Honeycomb Na_2IrO_3 are Large and Ferromagnetic: Insights From Ab Initio Quantum Chemistry Calculations. *New J Phys* (2014) 16:013056. doi:10.1088/1367-2630/16/1/013056
28. Fulde P. *Correlated Electrons in Quantum Matter*. Singapore: World Scientific (2012).
29. Klintenberg M, Derenzo SE, Weber MJ. Accurate crystal fields for Embedded Cluster Calculations. *Comput Phys Commun* (2000) 131:120–8. doi:10.1016/s0010-4655(00)00071-0
30. Katukuri VM, Roszeitis K, Yushankhai V, Mitrushchenkov A, Stoll H, van Veenendaal M, et al. Electronic Structure of Low-Dimensional $4d^5$ Oxides: Interplay of Ligand Distortions, Overall Lattice Anisotropy, and Spin-Orbit Interactions. *Inorg Chem* (2014) 53:4833–9. doi:10.1021/ic402653f
31. Babkevich P, Katukuri VM, Fåk B, Rols S, Fennell T, Pajić D, et al. Magnetic Excitations and Electronic Interactions in Sr_2CuTeO_6: A Spin-1/2 Square Lattice Heisenberg Antiferromagnet. *Phys Rev Lett* (2016) 117:237203. doi:10.1103/physrevlett.117.237203
32. Booth GH, Thom AJW, Alavi A. Fermion Monte Carlo without Fixed Nodes: a Game of Life, Death, and Annihilation in Slater Determinant Space. *J Chem Phys* (2009) 131:054106. doi:10.1063/1.3193710
33. Cleland D, Booth GH, Alavi A. Communications: Survival of the Fittest: Accelerating Convergence in Full Configuration-Interaction Quantum Monte Carlo. *J Chem Phys* (2010) 132:041103. doi:10.1063/1.3302277
34. Guther K, Anderson RJ, Blunt NS, Bogdanov NA, Cleland D, Dattani N, et al. NECI: N-Electron Configuration Interaction with an Emphasis on State-Of-The-Art Stochastic Methods. *J Chem Phys* (2020) 153:034107. doi:10.1063/5.0005754
35. Chan GK-L, Sharma S. The Density Matrix Renormalization Group in Quantum Chemistry. *Annu Rev Phys Chem* (2011) 62:465–81. doi:10.1146/annurev-physchem-032210-103338
36. Sharma S, Chan GK-L. Spin-adapted Density Matrix Renormalization Group Algorithms for Quantum Chemistry. *J Chem Phys* (2012) 136:124121. doi:10.1063/1.3695642
37. Andersson K, Malmqvist PÅ, Roos BO. Second-order Perturbation Theory with a Complete Active Space Self-consistent Field Reference Function. *J Chem Phys* (1992) 96:1218–26. doi:10.1063/1.462209
38. Angeli C, Cimiraglia R, Evangelisti S, Leininger T, Malrieu J-P. Introduction Of N-Electron Valence States for Multireference Perturbation Theory. *J Chem Phys* (2001) 114:10252–64. doi:10.1063/1.1361246
39. Emery VJ. Theory of High-Tc superconductivity in Oxides. *Phys Rev Lett* (1987) 58:2794–7. doi:10.1103/physrevlett.58.2794
40. Jiang M, Moeller M, Berciu M, Sawatzky GA. Relevance of Cu-3d Multiplet Structure in Models of High-T_c Cuprates. *Phys Rev B* (2020) 101:035151. doi:10.1103/physrevb.101.035151
41. Plienbumrung T, Daghofer M, Oleś AM. Interplay between Zhang-Rice Singlets and High-Spin States in a Model for Doped NiO_2 Planes. *Phys Rev B* (2021) 103:104513. doi:10.1103/physrevb.103.104513

42. Hayward MA, Rosseinsky MJ. Synthesis of the Infinite Layer Ni(I) Phase $NdNiO_{2+x}$ by Low Temperature Reduction of $NdNiO_3$ with Sodium Hydride. *Solid State Sci* (2003) 5:839–50. doi:10.1016/s1293-2558(03)00111-0
43. Kobayashi N, Hiroi Z, Takano M. Compounds and Phase Relations in the SrO-CaO-CuO System under High Pressure. *J Solid State Chem* (1997) 132:274–83. doi:10.1006/jssc.1997.7442
44. Karpinski J, Mangelschots I, Schwer H, Conder K, Morawski A, Lada T, et al. Single crystal Growth of HgBaCaCuO and Infinite Layer $CaCuO_2$ at High Gas Pressure. *Physica C: Superconductivity* (1994) 235-240:917–8. doi:10.1016/0921-4534(94)91683-7
45. Dolg M, Wedig U, Stoll H, Preuss H. Energy-adjusted ab Initio Pseudopotentials for the First Row Transition Elements. *J Chem Phys* (1987) 86:866–72. doi:10.1063/1.452288
46. Martin JML, Sundermann A. Correlation Consistent Valence Basis Sets for Use with the Stuttgart-Dresden-Bonn Relativistic Effective Core Potentials: The Atoms Ga-Kr and In-Xe. *J Chem Phys* (2001) 114:3408–20. doi:10.1063/1.1337864
47. Roos BO, Lindh R, Malmqvist P-Å, Veryazov V, Widmark P-O. Main Group Atoms and Dimers Studied with a New Relativistic ANO Basis Set. *J Phys Chem A* (2004) 108:2851–8. doi:10.1021/jp031064+
48. Dolg M, Stoll H, Savin A, Preuss H. Energy-adjusted Pseudopotentials for the Rare Earth Elements. *Theoret Chim Acta* (1989) 75:173–94. doi:10.1007/bf00528565
49. Dolg M, Stoll H, Preuss H. A Combination of Quasirelativistic Pseudopotential and Ligand Field Calculations for Lanthanoid Compounds. *Theoret Chim Acta* (1993) 85:441–50. doi:10.1007/bf01112983
50. Kaupp M, Schleyer Pv. R, Stoll H, Preuss H. Pseudopotential Approaches to Ca, Sr, and Ba Hydrides. Why Are Some Alkaline Earth MX_2 Compounds Bent? *J Chem Phys* (1991) 94:1360–6. doi:10.1063/1.459993
51. Igel-Mann G. Ph.D. thesis. Stuttgart: University of Stuttgart (1987). Untersuchungen an Hauptgruppenelementen und Nebengruppenelementen mit abgeschlossener d-Schale
52. University of Cologne. Energy-consistent Pseudopotentials of Stuttgart/Cologne Group (2014). Available at: http://www.tc.uni-koeln.de/cgi-bin/pp.pl?language=en,format=molpro,element=Zn,job=getecp,ecp=ECP28SDF (Accessed Sept 15, 2021).
53. Fdez. Galván I, Vacher M, Alavi A, Angeli C, Aquilante F, Autschbach J, et al. OpenMolcas: From Source Code to Insight. *J Chem Theor Comput.* (2019) 15:5925–64. doi:10.1021/acs.jctc.9b00532
54. Jmol. *Jmol: An Open-source Java Viewer for Chemical Structures in 3D* (2001). Available from: http://www.jmol.org/.
55.. For an accurate quantitative description of the multiplet structure spanned by the other two irreps b_1 and e, one would need to extend the active space and include the 3d and 4d manifolds of the four neighbouring Ni (Cu) atoms as well as the O 2p orbitals of the same symmetry, resulting in a gigantic 68 electrons in 74 orbitals active space.
56. Lu T, Chen F. Multiwfn: A Multifunctional Wavefunction Analyzer. *J Comput Chem* (2012) 33:580–92. doi:10.1002/jcc.22885
57. Boguslawski K, Tecmer P, Legeza Ö, Reiher M. Entanglement Measures for Single- and Multireference Correlation Effects. *J Phys Chem Lett* (2012) 3:3129–35. doi:10.1021/jz301319v
58. Boguslawski K, Tecmer P, Barcza G, Legeza Ö, Reiher M. Orbital Entanglement in Bond-Formation Processes. *J Chem Theor Comput.* (2013) 9:2959–73. doi:10.1021/ct400247p
59. Boguslawski K, Tecmer P. Orbital Entanglement in Quantum Chemistry. *Int J Quan Chem.* (2015) 115:1289–95. doi:10.1002/qua.24832
60. Legeza Ö, Sólyom J. Optimizing the Density-Matrix Renormalization Group Method Using Quantum Information Entropy. *Phys Rev B* (2003) 68:195116. doi:10.1103/physrevb.68.195116
61. Rissler J, Noack RM, White SR. Measuring Orbital Interaction Using Quantum Information Theory. *Chem Phys* (2006) 323:519–31. doi:10.1016/j.chemphys.2005.10.018
62. Keller S, Dolfi M, Troyer M, Reiher M. An Efficient Matrix Product Operator Representation of the Quantum Chemical Hamiltonian. *J Chem Phys* (2015) 143:244118. doi:10.1063/1.4939000
63. Gunnarsson O, Andersen OK, Jepsen O, Zaanen J. Density-functional Calculation of the Parameters in the Anderson Model: Application to Mn in CdTe. *Phys Rev B* (1989) 39:1708–22. doi:10.1103/physrevb.39.1708
64. Bogdanov NA, Li Manni G, Sharma S, Gunnarsson O, Alavi A. Enhancement of Superexchange Due to Synergetic Breathing and Hopping in Corner-Sharing Cuprates. *Nat Phys* (2021) 18:190–5. doi:10.1038/s41567-021-01439-1
65. Kitatani M, Si L, Janson O, Arita R, Zhong Z, Held K. Nickelate Superconductors – a Renaissance of the One-Band Hubbard Model. *npj Quan Mater* (2020) 5:59. doi:10.1038/s41535-020-00260-y
66. Eskes H, Sawatzky GA. Single-, Triple-, or Multiple-Band Hubbard Models. *Phys Rev B* (1991) 44:9656–66. doi:10.1103/physrevb.44.9656
67. Nomura Y, Arita R. Superconductivty in Infinite-Layer Nickelates. *Rep. Prog. Phys.* (2021) 85:052501. doi:10.1088/1361-6633/ac5a60

Conflict of Interest: The authors declare that the research was conducted in the absence of any commercial or financial relationships that could be construed as a potential conflict of interest.

Publisher's Note: All claims expressed in this article are solely those of the authors and do not necessarily represent those of their affiliated organizations, or those of the publisher, the editors, and the reviewers. Any product that may be evaluated in this article, or claim that may be made by its manufacturer, is not guaranteed or endorsed by the publisher.

Advantages of publishing in Frontiers

OPEN ACCESS
Articles are free to read for greatest visibility and readership

FAST PUBLICATION
Around 90 days from submission to decision

HIGH QUALITY PEER-REVIEW
Rigorous, collaborative, and constructive peer-review

TRANSPARENT PEER-REVIEW
Editors and reviewers acknowledged by name on published articles

Frontiers
Avenue du Tribunal-Fédéral 34
1005 Lausanne | Switzerland

Visit us: www.frontiersin.org
Contact us: frontiersin.org/about/contact

REPRODUCIBILITY OF RESEARCH
Support open data and methods to enhance research reproducibility

DIGITAL PUBLISHING
Articles designed for optimal readership across devices

FOLLOW US
@frontiersin

IMPACT METRICS
Advanced article metrics track visibility across digital media

EXTENSIVE PROMOTION
Marketing and promotion of impactful research

LOOP RESEARCH NETWORK
Our network increases your article's readership